Hierarchical Ammonia Structures in Galactic Molecular Clouds

by

Jared Keown
B.Sc., University of Louisville, 2014

A Dissertation Submitted in Partial Fulfillment of the
Requirements for the Degree of

DOCTOR OF PHILOSOPHY

in the Department of Physics and Astronomy

Hierarchical Ammonia Structures in Galactic Molecular Clouds

by

Jared Keown
B.Sc., University of Louisville, 2014

Supervisory Committee

Dr. James Di Francesco, Co-Supervisor
(Department of Physics and Astronomy)

Dr. Kim Venn, Co-Supervisor
(Department of Physics and Astronomy)

Dr. Charles Curry, Outside Member
(School of Earth and Ocean Sciences)

Supervisory Committee

Dr. James Di Francesco, Co-Supervisor
(Department of Physics and Astronomy)

Dr. Kim Venn, Co-Supervisor
(Department of Physics and Astronomy)

Dr. Charles Curry, Outside Member
(School of Earth and Ocean Sciences)

ABSTRACT

Recent large-scale mapping of dust continuum emission from star-forming clouds has revealed their hierarchical nature, which includes web-like filamentary structures that often harbor clumpy over-densities where new stars form. Understanding the *motions* of these structures and how they interact to form stars, however, can only be learned through observations of emission from their molecular gas. Observations of tracers such as ammonia (NH_3), in particular, reveal the stability of dense gas structures against forces such as the inward pull of gravity and the outward push of their internal pressure, thus providing insights into whether or not those structures are likely to form stars in the future. Due to recent large-scale ammonia surveys that have mapped both nearby and distant clouds in the Galaxy, it is finally possible to investigate and compare the stability of star-forming structures in different environments. In this dissertation, we utilize ammonia survey data to provide one of the largest investigations to date into the stability of structures in star-forming regions. Dense gas structures have been identified in a self-consistent manner across a variety of star-forming regions and the environmental factors (e.g., the presence or lack of local filaments and heating by local massive stars) most influential to their stability were investigated. The analysis has revealed that dense gas structures identified by ammonia observations in nearby star-forming clouds tend to be gravitationally

bound. In high-mass star-forming clouds, however, bound and unbound ammonia structures are equally likely. This result suggests that either gravity is more important to structure stability at the small scales probed in nearby clouds or ammonia is more widespread in high-mass star-forming regions. In addition, a new method to detect and measure emission with multiple velocity components along the line of sight has been developed. Based on convolutional neural networks and named Convnet Line-fitting Of Emission-line Regions (CLOVER), the method is markedly faster than traditional analysis techniques, requires no input assumptions about the emission, and has demonstrated high classification accuracy. Since high-mass star-forming regions are often plagued by multiple velocity components along the line of sight, CLOVER will improve the accuracy of stability measurements for many clouds of interest to the star formation community.

Contents

Supervisory Committee ii

Abstract iii

Table of Contents v

List of Tables ix

List of Figures xi

Acknowledgements xv

Dedication xvi

Co-Authorship xvii

1 Introduction 1

1.1 Dust and Gas as Star Formation Tracers 2
1.2 Observational Perspective 7
1.3 Virial Stability of Dense Gas Structures 11
1.4 Dense Gas Temperatures and Kinematics from Ammonia 13
1.5 Structure Identification Methods 16
1.5.1 Core and Protostar Identification 16
1.5.2 Filament Identification 21
1.6 Machine Learning 23
1.6.1 Supervised Learning 24
1.6.2 Unsupervised Learning 25
1.6.3 Artificial Neural Networks 25
1.6.4 Convolutional Neural Networks 27
1.7 Dissertation Goals - Are cores/clumps truly *bound* structures? 29

2 The Green Bank Ammonia Survey: Observations of Hierarchical Dense Gas Structures in Cepheus-L1251 **31**
2.1 Introduction . . . 32
2.2 Observations . . . 34
2.2.1 GBT NH_3 Data . . . 34
2.2.2 *Herschel* Dust Continuum Data . . . 34
2.3 Analysis and Results . . . 36
2.3.1 NH_3 Line Fitting . . . 36
2.3.2 Dendrogram Structure-Finding . . . 39
2.3.3 Source Masses . . . 43
2.3.4 Virial Analysis . . . 44
2.3.5 Elongated Structure Virial Parameter . . . 50
2.3.6 Source Temperatures and Column Densities . . . 51
2.4 Discussion . . . 54
2.4.1 Comparison with Serpens South Virial Analysis . . . 54
2.4.2 Role of External Pressure . . . 56
2.4.3 Presence of CCS and HC_5N . . . 61
2.5 Summary . . . 70
2.6 Acknowledgments . . . 72
2.7 Appendix . . . 72
2.7.1 Effective Radius . . . 72
2.7.2 Mass . . . 73

3 KFPA Examinations of Young STellar Object Natal Environments: Hierarchical Ammonia Structures in Galactic Giant Molecular Clouds **80**
3.1 Introduction . . . 81
3.2 Observations and Data Reduction . . . 84
3.2.1 Targets . . . 84
3.2.2 GBT NH_3 Data . . . 91
3.2.3 *Herschel* Dust Continuum Data . . . 94
3.2.4 JCMT $C^{18}O$ Data . . . 98
3.3 Analysis and Results . . . 99
3.3.1 NH_3 Line Fitting . . . 99
3.3.2 NH_3 (1,1) Integrated Intensity Maps . . . 113
3.3.3 Identifying NH_3 Structures with Dendrograms . . . 114

3.3.4 Determining Leaf Radii and Masses . . . 129
3.3.5 Virial Analysis . . . 131
3.3.6 Identifying filaments and candidate YSOs . . . 133
3.3.7 Cloud Population Statistics . . . 150
3.4 Discussion . . . 155
3.4.1 Leaf/Filament Relationship . . . 155
3.4.2 Leaf/Protostar Relationship . . . 157
3.4.3 Virial Stability in Low- and High-Mass Star-Forming Regions 159
3.4.4 Cloud Weight Pressure . . . 162
3.4.5 Turbulent Pressure . . . 165
3.5 Summary . . . 170
3.6 Future Work . . . 172
3.7 Appendix . . . 174
3.7.1 Distance Dependence of Virial Parameters . . . 174

4 CLOVER: Convnet Line-fitting Of Velocities in Emission-line Regions 179
4.1 Introduction . . . 180
4.2 Data . . . 183
4.2.1 Training Set: Generating Synthetic Spectra . . . 183
4.2.2 Test Set: Real ^{13}CO, C^{18}O, & HC$_5$N Spectral Cubes . . . 185
4.3 Methods: CNN Architecture . . . 190
4.4 Results . . . 192
4.4.1 Testing on Synthetic Data . . . 192
4.4.2 Performance Versus Two-Component Gaussian Line Fitting . 196
4.4.3 Testing On Real Observations . . . 198
4.4.4 Testing on Three-Component Spectra . . . 203
4.5 Deriving Kinematics From Two-Component Spectra . . . 204
4.5.1 Testing CLOVER's regression CNN on real data . . . 210
4.6 Classifying Spectra with Hyperfine Structure . . . 213
4.6.1 Generating Synthetic NH_3 (1,1) Spectra . . . 214
4.6.2 Testing on Synthetic NH_3 (1,1) Spectra . . . 215
4.6.3 Testing on Real NH_3 (1,1) Observations . . . 217
4.7 Predicting NH_3 (1,1) Kinematics . . . 219
4.8 Improving Virial Analyses with CLOVER . . . 222

4.9 Summary 225
4.10 Appendix 226
4.10.1 Installing and Using CLOVER 226

5 Conclusions **230**
5.1 Virial Stability in Low- and High-mass Clouds 231
5.2 Virial Stability Analysis Improvements: CLOVER 233
5.3 Future Work: Virial Stability Analyses with the VLA 233

A Continuation of Table 3.4 **235**

B Continuation of Table 3.5 **251**

Bibliography **266**

List of Tables

Table 2.1 NH_3 (1,1) Leaves Catalog 76

Table 3.1 KEYSTONE Target GMCs 85
Table 3.2 KEYSTONE Observed Transitions 95
Table 3.3 Beam Gains 95
Table 3.4 W3-west NH_3 (1,1) Leaves Catalog 1 134
Table 3.5 W3-west NH_3 (1,1) Leaves Catalog 2 135
Table 3.6 Cloud Statistics 159
Table 3.7 Leaf Population Statistics 160

Table 4.1 Test Set Spectral Cubes 189

Table A.1 W3 NH_3 (1,1) Leaves Catalog 1 235
Table A.2 MonR2 NH_3 (1,1) Leaves Catalog 1 236
Table A.3 MonR1 NH_3 (1,1) Leaves Catalog 1 237
Table A.4 Rosette NH_3 (1,1) Leaves Catalog 1 238
Table A.5 NGC2264 NH_3 (1,1) Leaves Catalog 1 239
Table A.6 M16 NH_3 (1,1) Leaves Catalog 1 240
Table A.7 M17 NH_3 (1,1) Leaves Catalog 1 241
Table A.8 W48 NH_3 (1,1) Leaves Catalog 1 241
Table A.9 Cygnus X South NH_3 (1,1) Leaves Catalog 1 243
Table A.10 Cygnus X North NH_3 (1,1) Leaves Catalog 1 245
Table A.11 NGC7538 NH_3 (1,1) Leaves Catalog 1 249

Table B.1 W3 NH_3 (1,1) Leaves Catalog 2 251
Table B.2 MonR2 NH_3 (1,1) Leaves Catalog 2 252
Table B.3 MonR1 NH_3 (1,1) Leaves Catalog 2 253
Table B.4 Rosette NH_3 (1,1) Leaves Catalog 2 254
Table B.5 NGC2264 NH_3 (1,1) Leaves Catalog 2 255
Table B.6 M16 NH_3 (1,1) Leaves Catalog 2 255

Table B.7 M17 NH_3 (1,1) Leaves Catalog 2 256
Table B.8 W48 NH_3 (1,1) Leaves Catalog 2 257
Table B.9 Cygnus X South NH_3 (1,1) Leaves Catalog 2 258
Table B.10 Cygnus X North NH_3 (1,1) Leaves Catalog 2 260
Table B.11 NGC7538 NH_3 (1,1) Leaves Catalog 2 264

List of Figures

Figure 1.1 *Herschel* dust continuum emission map of Cygnus X 3
Figure 1.2 Cepheus and Aquila core mass functions 9
Figure 1.3 Rosette H_2 column density filaments 10
Figure 1.4 NH_3 (1,1), (2,2), and (3,3) spectra from Serpens South 14
Figure 1.5 *getsources* single-scale decompositions 18
Figure 1.6 *getsources* cleaned single-scale images 19
Figure 1.7 Example *getsources* protostellar core extraction 20
Figure 1.8 Dendrogram cartoon diagram 21
Figure 1.9 *getfilaments* extraction images 23
Figure 1.10 ANN cartoon diagram 26
Figure 1.11 CNN kernel demonstration 28

Figure 2.1 Cepheus-L1251 H_2 column density map with NH_3 (1,1) contours 35
Figure 2.2 Cepheus-L1251 velocity dispersion and centroid velocity maps 37
Figure 2.3 Cepheus-L1251 kinetic temperature and para-NH_3 abundance maps 38
Figure 2.4 Dendrogram-identified ammonia leaves identified in Cepheus-L1251 42
Figure 2.5 Tree diagram and aspect ratios for Cepheus-L1251 leaves . . 43
Figure 2.6 Effective radius versus mass for Cepheus-L1251 leaves 44
Figure 2.7 Virial parameters for Cepheus-L1251 leaves 48
Figure 2.8 Dust versus kinetic temperature for Cepheus-L1251 52
Figure 2.9 Histograms of para-NH_3 abundance for Cepheus-L1251 . . . 53
Figure 2.10 Virial plane for Cepheus-L1251 leaves 60
Figure 2.11 CCS $(2_0 - 1_0)$ and HC_5N $(9 - 8)$ maps for Cepheus-L1251 . . 63
Figure 2.12 CCS $(2_0 - 1_0)$ and HC_5N $(9 - 8)$ integrated intensity ratios relative to NH_3 (1,1) in Cepheus-L1251 64

Figure 2.13 Velocity dispersion histograms for NH_3 (1,1), CCS ($2_0 - 1_0$), and HC_5N ($9 - 8$) in Cepheus-L1251 leaves 67
Figure 2.14 Comparison of centroid velocities for NH_3 (1,1), CCS ($2_0 - 1_0$), and HC_5N ($9 - 8$) in Cepheus-L1251 leaves 68
Figure 2.15 Effective radii, masses, and virial parameters for Cepheus-L1251 leaves when using alternative radius formulation . . . 77
Figure 2.16 Virial plane using alternative methods to calculate leaf radii and masses 78
Figure 2.17 Virial parameters for alternative mass calculations for Cepheus-L1251 leaves 79

Figure 3.1 KFPA beam gains for NH_3 (1,1) spectral windows 92
Figure 3.2 RMS noise histograms for NH_3 (1,1) and (2,2) 96
Figure 3.3 Stacked histogram of dust emissivities used for SED fitting . 97
Figure 3.4 W3 T_K and σ maps 101
Figure 3.5 W3-west T_K and σ maps 102
Figure 3.6 MonR2 T_K and σ maps 103
Figure 3.7 MonR1 T_K and σ maps 104
Figure 3.8 Rosette T_K and σ maps 105
Figure 3.9 NGC2264 T_K and σ maps 106
Figure 3.10 M16 T_K and σ maps 107
Figure 3.11 M17 T_K and σ maps 108
Figure 3.12 W48 T_K and σ maps 109
Figure 3.13 Cygnus X South T_K and σ maps 110
Figure 3.14 Cygnus X North T_K and σ maps 111
Figure 3.15 NGC7538 T_K and σ maps 112
Figure 3.16 Histograms of T_K and σ 113
Figure 3.17 W3 NH_3 (1,1) integrated intensity maps with leaves 117
Figure 3.18 W3-west NH_3 (1,1) integrated intensity maps with leaves . . 118
Figure 3.19 MonR2 NH_3 (1,1) integrated intensity maps with leaves . . . 119
Figure 3.20 MonR1 NH_3 (1,1) integrated intensity maps with leaves . . . 120
Figure 3.21 Rosette NH_3 (1,1) integrated intensity maps with leaves . . . 121
Figure 3.22 NGC2264 NH_3 (1,1) integrated intensity maps with leaves . . 122
Figure 3.23 M16 NH_3 (1,1) integrated intensity maps with leaves 123
Figure 3.24 M17 NH_3 (1,1) integrated intensity maps with leaves 124

Figure 3.25 W48 NH_3 (1,1) integrated intensity maps with leaves 125
Figure 3.26 Cygnus X South NH_3 (1,1) integrated intensity maps with leaves 126
Figure 3.27 Cygnus X North NH_3 (1,1) integrated intensity maps with leaves 127
Figure 3.28 NGC7538 NH_3 (1,1) integrated intensity maps with leaves . . 128
Figure 3.29 Dendrogram tree diagram for MonR2 129
Figure 3.30 Leaf effective radius versus mass 131
Figure 3.31 Leaf virial parameter versus mass 136
Figure 3.32 W3 on-filament and protostellar virial parameters 138
Figure 3.33 W3-west on-filament and protostellar virial parameters . . . 139
Figure 3.34 MonR2 on-filament and protostellar virial parameters 140
Figure 3.35 MonR1 on-filament and protostellar virial parameters 141
Figure 3.36 Rosette on-filament and protostellar virial parameters 142
Figure 3.37 NGC2264 on-filament and protostellar virial parameters . . . 143
Figure 3.38 M16 on-filament and protostellar virial parameters 144
Figure 3.39 M17 on-filament and protostellar virial parameters 145
Figure 3.40 W48 on-filament and protostellar virial parameters 146
Figure 3.41 Cygnus X South on-filament and protostellar virial parameters 147
Figure 3.42 Cygnus X North on-filament and protostellar virial parameters 148
Figure 3.43 NGC7538 on-filament and protostellar virial parameters . . . 149
Figure 3.44 Correlation coefficient heatmap 153
Figure 3.45 Statistically significant correlations 154
Figure 3.46 Leaf mass, radius, temperature, and velocity dispersion histograms 158
Figure 3.47 NGC7538 spatially filtered H_2 column density map 163
Figure 3.48 Virial plane for KEYSTONE leaves 164
Figure 3.49 $C^{18}O$ (3−2) velocity dispersion maps for DR21, G79.34, W3(OH), and W3-Main 168
Figure 3.50 $C^{18}O$ (3 − 2) velocity dispersion maps for M16, M17, and NGC7538 169
Figure 3.51 Distance-adjusted virial parameters for NGC2264 176
Figure 3.52 Distance-adjusted virial parameters for MonR1 177
Figure 3.53 Distance-adjusted virial parameters for MonR2 178

Figure 4.1 Two-component cartoon 181
Figure 4.2 Training set examples 186

Figure 4.3 Training and test set SNR histograms . . . 187
Figure 4.4 CNN architecture . . . 191
Figure 4.5 Classification confusion matrices . . . 194
Figure 4.6 Misclassified validation set examples . . . 195
Figure 4.7 Classification accuracy versus SNR and centroid velocity separation . . . 198
Figure 4.8 L1689 segmentation . . . 200
Figure 4.9 DR21 segmentation . . . 202
Figure 4.10 B18 segmentation . . . 203
Figure 4.11 Synthetic test set parameter prediction accuracy . . . 206
Figure 4.12 CNN parameter prediction models . . . 207
Figure 4.13 MAE versus SNR and centroid velocity separation . . . 209
Figure 4.14 CNN parameter predictions on real spectra . . . 211
Figure 4.15 CLOVER classification and regression on L1689 . . . 212
Figure 4.16 NH_3 (1,1) classification confusion matrices . . . 216
Figure 4.17 M17 segmentation . . . 218
Figure 4.18 MonR2 segmentation . . . 219
Figure 4.19 NH_3 (1,1) parameter predictions . . . 220
Figure 4.20 Example parameter predictions for NH_3 (1,1) test set . . . 221
Figure 4.21 CLOVER two-component velocity dispersions for M17SW . . . 223
Figure 4.22 Virial parameter versus mass for the three M17SW clumps . . . 224

Acknowledgements

I am eternally grateful to the many people that helped me during and en-route to graduate school:

James Di Francesco, for being an excellent mentor that encouraged me to explore my interests both in and out of astronomy. Your support has made this experience much more enjoyable. The many lessons you have taught me about research, astronomy, writing, public speaking, and leadership are irreplaceable.

My supervisory committee, for pushing me to be a better astronomer.

The New Technologies for Canadian Observatories (NTCO) program, for partially funding my education and providing many unique learning opportunities along the way. The resources your program provided me have springboarded my post-graduation career.

Ned Ladd and Scott Schnee, for giving me the chance to begin research in star formation and helping me get into graduate school.

Gerard Williger and James Lauroesch, for helping me realize as an undergraduate student that a PhD in astronomy was a goal I could achieve.

Mike Chen and Helen Kirk, for always being up for my persistent astronomy questions. You have been great collaborators and friends.

Ben Gerard, for being there from start to finish. Your friendship helped me get through this PhD, but will last far longer.

Connor, Collin, Clare, Nick, Maan, Epson, Mara, Austin, and the many other graduate students that have made my time at UVic enjoyable.

Dave and Gayla Anderson, for making me feel welcome and at home in Victoria. Your kindness will never be forgotten.

Zane Biever, for never losing faith in me and inspiring me to be a better role model.

My family - Mom, Dad, Daniel, Granny, Grandad, and Sofia - for your many sacrifices that have led to countless privileges in my life and your never-ending encouragement that made this achievement possible.

Dedication

In loving memory of Ray and Betty Keown.
Know that I am still “Givin’ ‘em Hell” in everything I do.

Co-Authorship

The research undertaken for this dissertation involved the collaborative effort of a consortium of astronomers. Although I took the lead on all projects described in this dissertation, the projects would not have been possible without the assistance of other astronomers in the following capacities: overseeing parts of the observations and data collection, providing software for data reduction, imparting guidance on the scientific direction of the projects, and providing feedback on the manuscript. In each chapter of this dissertation, all individuals that contributed to the project in any capacity are listed as co-authors.

Chapter 1

Introduction

The gas and dust clouds that serve as the birthplace of stars are characterized by a hierarchy of size, mass, and density. At the top of the hierarchy are molecular clouds, the largest and most massive structures involved in star formation, with sizes of $\sim 10 - 100$ pc and masses of $\sim 10^{3-5}$ $M_\odot$. As these clouds evolve, they form higher density substructures such as *filaments* (a few parsecs in length) and *clumps* ($\sim$1 pc), which can fragment further to form *cores* ($\sim$0.1 pc), the highest density regions of the cloud where stars are born. When cores become dense enough to overcome the outward push of their internal pressures, they can undergo gravitational collapse to form *protostars* or *young stellar objects*. Understanding the processes by which molecular clouds evolve to form these substructures, and ultimately protostars (as well as planets), is a primary goal of modern star formation research.

Although the definitions for the substructures in molecular clouds are loosely defined in the literature, they each have distinct characteristics. Filaments, for instance, are over-densities in the cloud that are highly elongated with large aspect ratios typically > 5 (André et al., 2014). They are also often uni-directional along their long axes without sharp changes in direction or significant curvature (André et al., 2014). The terms "clumps" and "cores" are sometimes used interchangeably because they are both identified as compact density peaks with low to moderate aspect ratios typically < 3. The distinction between the two structures is often made based on their size and mass, wherein clumps are larger and have more mass (diameters $\gtrsim 0.3$ pc and masses $\gtrsim 50$ $M_\odot$) than cores (diameters ~ 0.1 pc and masses $\lesssim 10 - 50$ $M_\odot$). Cores can also be substructures within both filaments and clumps, which is often the case when filaments and clumps are viewed with high angular resolution (e.g., André et al., 2010; Fontani et al., 2018). As such, the cloud substructures probed by a given observation are directly related to the observation's angular resolution.

1.1 Dust and Gas as Star Formation Tracers

Probing the physical characteristics of structures in the star formation hierarchy relies on observations of the two main constituents of molecular clouds: dust and gas. Dust grains in molecular clouds are micron-sized and composed mainly of carbon and silicon (Weingartner & Draine, 2001). While dust contributes only about 1% of the mass of molecular clouds (e.g., Bohlin et al., 1978; Liseau et al., 2015), it is still an important tracer of cloud structure and temperature due to its bright thermal continuum emission at infrared and sub-millimeter wavelengths. The thermal continuum emission of the dust is caused by the heating of the grains as they absorb shorter wavelength (ultraviolet) emission, which originates from either new stars forming within the cloud or from the interstellar radiation field outside the cloud.

The intensity of thermal emission from dust grains at each wavelength λ is governed by the Planck function:

$$B_\lambda(T_D) = \frac{2hc^2}{\lambda^5} \frac{1}{e^{\frac{hc}{\lambda k T_D}} - 1} \tag{1.1}$$

where h is the Planck constant, c is the speed of light, k is the Boltzmann constant, and T_D is the temperature of the dust. The Planck function shows that as the temperature of the dust increases, the peak of its intensity distribution moves to shorter wavelengths. For this reason, the colder regions in clouds produce most of their thermal emission in the sub-millimeter ($250 - 850$ μm) regime. As dust gets heated by forming protostars in its vicinity, its thermal emission intensity peak shifts to shorter, far-infrared wavelengths ($20 - 250$ μm). Figure 1.1 shows a three-color composite image of dust emission at 70 μm, 160 μm, and 250 μm from the Cygnus X molecular cloud, a complex within the Galaxy forming massive stars (> 8 $M_\odot$), as observed by the *Herschel Space Observatory* (see Section 1.2 for a discussion of *Herschel*). There, the locations of forming massive stars are evident by the "bubbles" of 70 μm emission they generate by heating the dust in their surroundings.

When a beam of light travels through a molecular cloud, there is a chance that the light rays in the beam will be either absorbed completely or scattered by the particles in the cloud. The ratio of the light beam's intensity after passing through the cloud (I) to its initial intensity (I_0) is given by:

$$\frac{I}{I_0} = e^{-\kappa \rho s} \tag{1.2}$$

where κ is the *opacity* of the material that is related to how efficient the particles are at absorbing and scattering light, ρ is the volume density of the material, s is the distance traveled by the light through the cloud, and the product ρs is referred to as the *column density* denoted by Σ. As such, when a beam of light must travel far distances through a high density medium with large opacity, its initial intensity is significantly reduced. Oftentimes, the $\kappa\rho s$ term in Equation 1.2 is referred to as the *optical depth* of the material and is represented by the symbol τ. Thus, for each increase in optical depth of 1, the intensity of light after passing through the material decreases by a factor of $1/e$.

Light traveling through environments with high optical depth ($\tau >> 1$) will likely be absorbed or scattered by gas or dust particles along the line of sight. When observing such environments, the majority of the emission we observe originates from an artificial "surface" within the cloud created by the high rate of absorption and scattering of background emission. Such emission is generally called *optically thick*. Conversely, low optical depth environments ($\tau << 1$) allow observers to trace all the emission along the line of sight since there is no significant absorption or scattering. In this case, the emission is generally called *optically thin*.

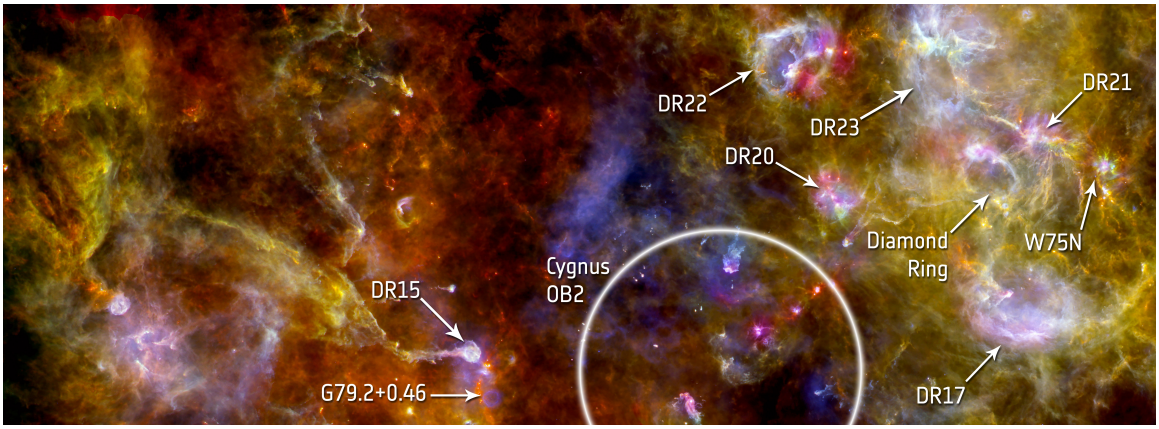

Fig. 1.1 – Figure created by the *Herschel* OB Young Stars Survey showing *Herschel* Space Observatory observations of dust continuum emission from the Cygnus X giant molecular cloud. The three-color image (blue - 70 μm, green - 160 μm, red - 250 μm) shows the effects of heating by forming clusters of massive stars as bright white bubbles silhouetted against the colder dust filaments and clumps shown by red. The image is around six degrees across and Cygnus X is at a distance of 1700 pc. DR15 and DR21 are included in our observations of dense gas emission as part of the KEYSTONE survey (see, e.g., Chapter 3).

In addition to travel distance and density, the optical depth also varies depending

on the wavelength of the observations since the opacity of material is wavelength-dependent. For instance, dust grains in molecular clouds efficiently absorb light with wavelengths much smaller than their sizes, such as optical and ultraviolet light. This absorption causes clouds to be opaque at those shorter wavelengths as most of the light behind the dust is blocked from our point of view. Indeed, since dust acts as an absorptive shield against external ultraviolet radiation, the material in the inner cloud regions where protostars form is generally cold ($15 - 20$ K). In starless dense cores, i.e., cores without an embedded protostar, temperatures are even colder (< 10 K) due to increased shielding by the higher densities of dust grains.

Dust less efficiently absorbs light at wavelengths larger than itself. Hence, it has low opacities at sub-millimeter wavelengths and continuum emission at those wavelengths is generally optically thin. As a result, such emission, radiated by the cold dust in molecular clouds, can be used to trace the internal structures of molecular clouds. Indeed, the intensity of dust emission observed along a line of sight in clouds is related to the column density of dust along that line of sight and the temperature of the emitting dust. The surface brightness (I_λ) as a function of wavelength (λ) and temperature (T_D) of dust emission along a line-of-sight towards a cloud can be approximated in the low optical depth regime as a modified Planck function of the form

$$I_\lambda = B_{\lambda,T_D} \kappa_\lambda \Sigma \tag{1.3}$$

where B_{λ,T_D} is the Planck function at a given wavelength and dust temperature, κ_λ is the dust opacity at a given wavelength, and Σ is the line-of-sight column density. The dust opacity is related to both the relative amount of dust grains compared to gas (i.e., the gas-to-dust ratio) and the efficiency of those grains to absorb light at a given wavelength. In practice, the dust opacity is often assumed to be $\kappa_\lambda = 0.1(\lambda/300\mu\text{m})^{-\beta}$ cm^2/g, following assumptions put forth by Hildebrand (1983) of spherical grains with an average radius of 0.1 μm and gas-to-dust ratio of 100 based on measurements from a single reflection nebula. It is noteworthy, however, that the gas-to-dust ratio has been measured to vary across the Galaxy by ~ 0.09 dex kpc^{-1} due to local metallicity variations (Giannetti et al., 2017). Similarly, β has been shown to vary between 1 and 2.5 depending on the grain size and composition (e.g., Planck Collaboration et al., 2014; Chen et al., 2016).

After assuming a particular dust opacity along a line of sight for an observation at a given wavelength, the only free parameters remaining in Equation 1.3 are the dust

temperature and column density. Fitting this model to a cloud's observed surface brightness across multiple wavelengths (i.e., its spectral energy distribution, or SED) provides a measure of its temperature and mass.

While dust emission serves as an excellent tracer of cloud mass and temperature, it cannot provide insight into the *motions* of the material in clouds. To trace cloud kinematics, one must observe line emission from molecular gas. When the gas molecules in the cloud are excited to higher rotational states (J) through collisions with other molecules, they emit photons of fixed wavelength as they transition to lower energy states. The relative velocity of the emitting gas towards or away from our point of view can then be deduced by measuring the wavelength of its emission and comparing it to the known fixed wavelength of that transition at rest. After placing the relative velocity in a standard reference frame such as the Local Standard of Rest[1], it is known as the *centroid velocity*, if the emission is optically thin. Because we detect the aggregate flux from many molecules emitting a given transition, the width of the detected emission line provides a measure of the distribution of the molecules' line-of-sight velocities about the centroid velocity, again if the emission itself is optically thin. This quantity is termed the *velocity dispersion* or *line width* and is comprised mainly of a thermal component related to the temperature of the emitting gas, as well as a non-thermal component related to the amount of turbulence in the emitting gas. Optically thick emission is generally not a useful probe of centroid velocities and velocity dispersions because its line profiles become non-Gaussian with broadened wings and self-absorption dips that can appear as two distinct intensity peaks (e.g., Stahler & Palla, 2005).

Despite molecular hydrogen (H_2) being the most common molecule in molecular clouds, it is difficult to detect from cold gas since large energies are required to excite the molecule to higher energy levels. This property of H_2 stems from the molecule's low mass and size, which consequently give it a low moment of inertia. When neglecting any stretching or bending of the molecule during its rotation (a.k.a. the "rigid rotor" approximation), the quantized rotational energy levels (E_J) of a linear "dumbbell-shaped" molecule like H_2 are given by:

$$E_J = \frac{\hbar^2}{2I} J(J+1) \tag{1.4}$$

[1]The Local Standard of Rest (LSR) reference frame represents the mean velocity of material within the solar neighborhood as it orbits the Galactic center.

where I is the molecule's moment of inertia, $\hbar$ is the Planck constant divided by 2π, and J is the total rotational angular momentum quantum number that can be integers ≥ 0. It is clear from Equation 1.4 that smaller moments of inertia lead to larger rotational energy level separations. Since H_2 has the smallest moment of inertia of any diatomic molecule, it consequently has the largest rotational energy level separations.

Moreover, the symmetric dumbbell geometry of H_2 also leave it without a gradient in charge between each of its bonded atoms (i.e., zero electric dipole moment). As a result, the rotational transitions for which J decreases by one (e.g., a transition from $J = 1$ to $J = 0$) are inaccessible to H_2 because those transitions require an electric dipole (Stahler & Palla, 2005). Instead, H_2 must radiate through transitions enabled by its quadrupole moment, which require a decrease in J of two (e.g., a transition from $J = 2$ to $J = 0$). Thus, the lowest allowed rotational transition for H_2 is the $J = 2$ to $J = 0$ transition that requires energies of ~ 500 K to excite. Since the energies in molecular clouds are typically far below that threshold, H_2 is essentially undetectable in most molecular clouds.

Instead of relying on H_2, emission lines from other molecules that have lower abundance but also lower excitation requirements are used as proxies for H_2. Carbon monoxide (CO), which is the second-most abundant molecule in molecular clouds, is often the tracer-of-choice for molecular cloud studies because its first excited rotational state is only ~ 5 K above its ground state. The low rotational energy level separations of CO are a result of the molecule's larger moment of inertia relative to H_2 ($I_{CO} \sim 30 I_{H_2}$; Herzberg & Huber, 1979). In addition, the charge difference between the carbon and oxygen atom in CO give it a permanent dipole moment, which makes accessible the $\Delta J = 1$ rotational transitions. These low excitation requirements and still considerable abundances allow CO, as well as its isotopologues (e.g., ^{13}CO, C^{18}O), to emit brightly in molecular clouds across a variety of transitions.

Unfortunately, the high abundance of CO in molecular clouds often makes its emission optically thick towards dense cores, meaning its emission lines become self-absorbed and are no longer clean-cut probes of gas kinematics. In addition, CO begins to freeze onto the surface of dust grains (a.k.a. "freeze-out") at temperatures around 10 K and densities above 10^4 cm^{-3} (Caselli et al., 1999). Thus, emission from CO also does not trace the coldest and densest regions of the cloud where stars form because CO has a very low abundance in those regions. Instead, molecules that can survive in the gas phase at low temperatures and high densities while still having optically thin

emission, such as nitrogen-bearing molecules (e.g., NH_3 and N_2H^+), are a common choice to probe dense gas in molecular clouds (Di Francesco et al., 2007).

The resiliency of nitrogen-bearing molecules against freeze-out is still an open question (see, e.g., Sipilä et al., 2019), but is thought to be related to the longer timescales required to create nitrogen-bearing molecules relative to CO. By the time in a cloud's evolution when it reaches the low temperatures and high densities required for freeze-out, much of the cloud's nitrogen is still in atomic form since N_2 is created through relatively slow gas-phase reactions (Hily-Blant et al., 2010). Conversely, the faster reactions that create CO mean that most of the cloud's gas-phase carbon and oxygen are already locked in CO at the time freeze-out begins (Di Francesco et al., 2007). With an ample supply of gas-phase atomic nitrogen available when freeze-out begins, nitrogen-bearing molecules can continue to be formed to counteract their abundance losses from freeze-out. On the other hand, the abundance of CO drops because there is not enough carbon and oxygen remaining in the gas phase to replenish the molecule's freeze-out losses.

1.2 Observational Perspective

The *Herschel Space Observatory* has been a key instrument for revealing substructures in Galactic molecular clouds due to its: 1) high sensitivities for quick mapping speeds, 2) high spatial resolutions ($8'' - 36''$) for resolving individual filaments and cores, and 3) convenient wavelength coverage centered on the spectral energy distribution peak of cold dust emission from molecular clouds ($70 - 500$ μm). *Herschel* was launched into orbit around the Sun at the second Earth-Sun Lagrangian point (a.k.a. L2) in 2009. The telescope's 3.5-m mirror imaged molecular clouds without the hindrance of Earth's atmosphere, which can be opaque to far-infrared/sub-millimeter wavelengths due to its abundance of water vapor. In addition, *Herschel's* imaging cameras, PACS (Photodetector Array Camera and Spectrometer; bands at 70 μm, 100 μm, and 160 μm; Poglitsch et al., 2010) and SPIRE (Spectral and Photometric Imaging REceiver; bands at 250 μm, 350 μm, and 500 μm; Griffin et al., 2010), provided unprecedented sensitivities to sub-millimeter emission by utilizing "bolometer" detectors that measure small temperature changes in a thin layer of an absorptive metal embedded in a thermally-controlled (~ 0.3 K) reservoir (Griffin et al., 2006). For a given line of sight, the change of the metal's temperature above the thermally-controlled temperature measures the amount of sub-millimeter radiation hitting its

surface. The requirement of a thermally-controlled environment ultimately led to the end of the *Herschel* mission in 2013 after its liquid helium coolant supply ran out, rendering the bolometers useless.

A Key Program of *Herschel* was the Herschel Gould Belt Survey (HGBS), which mapped dust continuum emission throughout 13 nearby molecular clouds out to distances of 500 pc. The HGBS observations demonstrated that filaments are indeed ubiquitous in clouds with little star formation (Miville-Deschênes et al., 2010; Ward-Thompson et al., 2010) and those actively forming stars (André et al., 2010; Men'shchikov et al., 2010). These results, in combination with molecular cloud simulations investigating the physics during the evolution of clouds, suggested that filaments are a by-product of the interplay between turbulence (e.g., Vázquez-Semadeni et al., 2006), magnetic fields (e.g., Hennebelle, 2013; Seifried & Walch, 2015), and gravitational collapse (e.g., Federrath, 2016).

Not only are filaments prevalent throughout molecular clouds, but they are also thought to be closely related to the core and star formation process. For instance, the HGBS also demonstrated that dense cores tend to be coincident with the positions of filaments (Könyves et al., 2015; Marsh et al., 2016; Bresnahan et al., 2018). These filaments often have masses per unit length higher than $M_{line,crit} = 2c_s/G \sim 16$ $M_\odot$ pc^{-1}, which is the theoretical critical threshold for the gravitational fragmentation of an isothermal filament at $T = 10$ K (e.g., André et al., 2014). Thus, the route to making new dense cores and protostars likely relies on the formation of high-density filaments that subsequently undergo gravitational fragmentation.

Recent analysis of the Cepheus molecular clouds as part of the HGBS supports this picture. Di Francesco et al. (2019, in prep) found that 83% of the 835 cores identified in Cepheus reside on $\sim$ 0.1 pc-wide filaments. Additionally, the mass distribution of cores (a.k.a. the core mass function, or CMF) in Cepheus is similar in shape to the general mass distribution of stars (a.k.a. the stellar initial mass function or "IMF"). Figure 1.2 shows that the gravitationally bound starless cores (a.k.a., *prestellar* cores) in both the Cepheus and Aquila molecular clouds have strikingly similar lognormal mass distributions, with peaks occurring at $\sim 0.7 - 0.8$ $M_\odot$. The Cepheus and Aquila core mass functions also have high-mass slopes with power law indices of -1.38 ± 0.24 and -1.33 ± 0.06, respectively, which are both consistent with the -1.35 power law index of, e.g., the Salpeter (1955), Kroupa (2001), and Chabrier (2003) IMFs. The similarities between the core mass function, which may be fixed on molecular cloud scales, and the IMF may imply that stellar masses are determined at

the dense core stage. Thus, understanding the processes that create the CMF may lead to an understanding of the origin of the IMF.

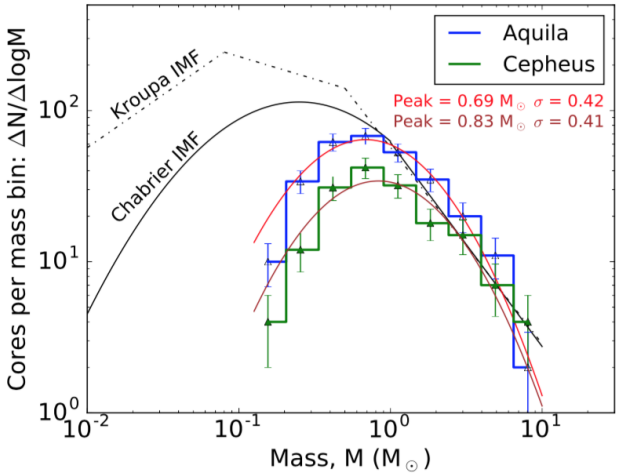

Fig. 1.2 – Left: Core mass functions for 141 prestellar cores identified in the Cepheus molecular cloud (green histogram) and 292 prestellar cores identified in the Aquila molecular cloud (blue histogram) as part of the Herschel Gould Belt Survey (Figure from Di Francesco et al., 2019, in prep). Lognormal fits to the distributions are shown in brown for Cepheus and red for Aquila. These lognormal fits peak at 0.83 $M_\odot$ and 0.69 $M_\odot$, respectively, with standard deviations of 0.41 and 0.42 in $\log_{10}$M. Power-law fits to the high-mass ends of the distributions produce slopes of -1.38 ± 0.24 and -1.33 ± 0.06, respectively. The Kroupa (2001) and Chabrier (2003) stellar Initial Mass Functions are superimposed for comparison.

While the nearby clouds included in the HGBS provide an up-close view of the star formation process, they are not representative of the giant molecular clouds (GMCs) where most of the star formation in our Galaxy takes place. GMCs tend to have larger masses (up to $\sim 10^7$ $M_\odot$), larger sizes (up to $\sim$ 200 pc), and host more high-mass stars (O- and B-types, >8 $M_\odot$) and stellar clusters than nearby clouds (Murray, 2011). As such, GMCs must also be observed to gain a complete understanding of how the star formation process occurs in more typical environments.

One major drawback that arises when observing GMCs is that they are located at much farther distances (>500 pc) than nearby low-mass clouds. Despite the lower linear resolutions encountered when observing more-distant GMCs, the Herschel OB Young Stars Survey (HOBYS, Motte et al., 2010) used *Herschel* to map the dust continuum emission from 13 of the nearest GMCs out to 3 kpc. The HOBYS observations showed that filamentary structures are equally as widespread in GMCs as

they are in low-mass clouds. Moreover, the higher-mass dense cores, high-mass stars, and young stellar clusters forming in the GMCs tend to be located at positions where multiple filaments appear to intersect (Myers, 2009; Schneider et al., 2012; Hennemann et al., 2012; Motte et al., 2018a). An example of these spatial correlations are shown in Figure 1.3, which displays the H_2 column density map for the Rosette GMC with positions of filaments, high-mass dense cores, O-stars, and young stellar clusters overlaid. These results suggest that filaments may be funneling gas onto the central hubs of star and cluster formation, providing the high-density conditions required to form those objects.

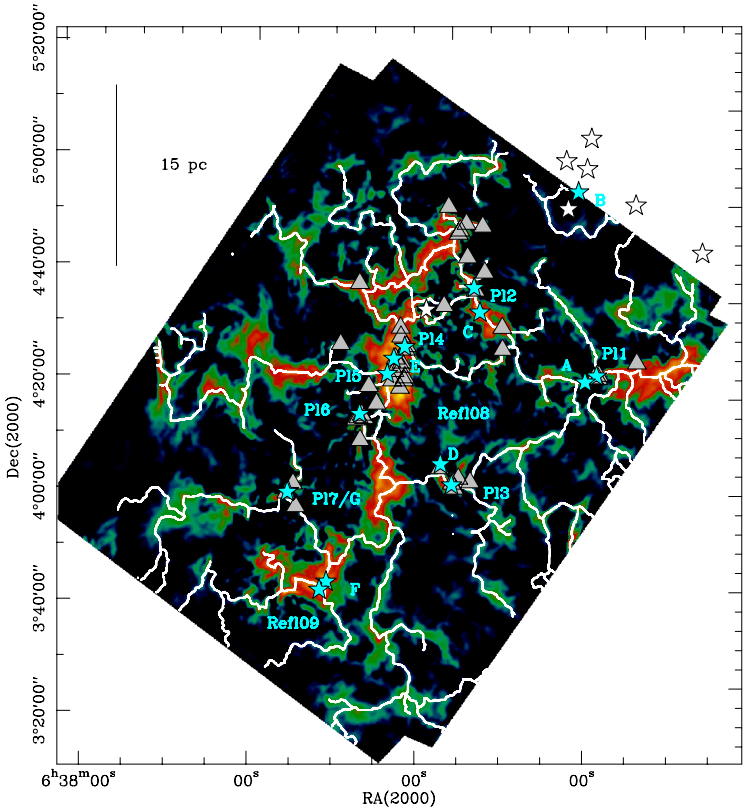

Fig. 1.3 – Figure from Schneider et al. (2012) displaying an H_2 column density map derived from *Herschel* dust continuum observations of the Rosette star-forming region. The map has been spatially filtered to highlight filamentary structures. Filament skeletons identified by the DisPerSE algorithm (Sousbie, 2011) are overlaid in white. Blue stars indicate the positions of known infrared clusters, gray triangles show the positions of massive dense cores, and white stars designate the positions of O-stars (the white stars in the upper right belong to the nearby star-forming region NGC 2264). A strong spatial correlation can be seen between the positions of these objects and the intersections of multiple filaments.

Although *Herschel* data provide exquisite details on the structure and mass of star-forming clouds, they fail to provide any sense of the *motions* of the gas associated with filaments, clumps, or cores. Instead, follow-up kinematics observations of the HGBS and HOBYS clouds with dense molecular gas tracers like ammonia (NH_3) and diazenylium (N_2H^+) were required to measure the motion of gas in star-forming clouds. Early such observations showed several instances of high-mass stars and stellar clusters forming at locations where gas appears to be flowing along filaments onto central junctions with mass flow rates capable of forming massive stars (Kirk et al., 2013a; Friesen et al., 2013; Henshaw et al., 2013; Fukui et al., 2015). Although it is still unclear whether or not the filament intersections are in place *prior* to the formation of stars, the preliminary results lend further credence to the idea that mass flow along filaments creates the environment necessary to form massive stars.

The ideas that the CMF is related to the IMF and that filament intersections form high-mass stars are predicated on the same assumption: that the cores and clumps we include in the CMF and see at filament intersections will indeed form new stars in the future. The validity of this assumption relies on whether or not the observed cores and clumps are gravitationally bound and likely to undergo the gravitational collapse required to form new stars. Measuring the gravitational stability of a given structure involves accounting for the many forces acting upon it. Such analysis also fundamentally requires information about the internal motions of gas associated with the structure. The details of such an analysis, which is known as *virial analysis*, is outlined in the following section.

1.3 Virial Stability of Dense Gas Structures

Whether or not dense cores will undergo the gravitational collapse required to form new stars depends on the interplay of a variety of forces acting on the cores. How this interplay of forces for a cloud or core of fixed shape affects its future is encapsulated by the virial theorem:

$$\frac{1}{2}\ddot{I} = 2(T - T_S) + M + W - \frac{1}{2}\frac{d}{dt}\int_S (\rho v r^2) dS \quad , \tag{1.5}$$

where T is the total kinetic energy due to both turbulent and thermal motions, T_S is the external confining pressure at the structure's surface (indicated by S), M is the net magnetic energy on the structure after considering sources of magnetic pressure both inward (e.g., the cloud magnetic field that compresses a core) and outward

(e.g., a core's internal magnetic field that resists collapse) in direction, W is the structure's gravitational potential energy, and the last integral term is related to the change of the structure's momentum over time (McKee & Zweibel, 1992). Finally, $\ddot{I}$ is the structure's acceleration, which describes its rate of change of expansion (when $\ddot{I}$ is positive) or collapse (when $\ddot{I}$ is negative). Alternatively, if the structure is in equilibrium, $\ddot{I}$ is zero.

In practice, it is often assumed that the structure's momentum is not changing over time, which forces the last term on the right-hand side of Equation 1.5 to zero. The magnetic term (M) is also often neglected due to a lack of reliable magnetic field measurements across clouds and cores. Finally, if external confining pressure on the structure (T_S) is negligible, the virial theorem reduces to:

$$\frac{1}{2}\ddot{I} = 2T + W \quad . \tag{1.6}$$

The expression for a structure in virial equilibrium (when $\frac{1}{2}\ddot{I} = 0$) then becomes $2T = -W$. This expression is the basis for the virial parameter, $\alpha_{vir} = 2T/|W|$, which is often used to express whether or not a structure is gravitationally bound and thus susceptible to gravitational collapse. The kinetic energy term is given by:

$$T = \frac{3}{2}M\sigma^2 \quad , \tag{1.7}$$

where M is the structure's mass and σ is the total one-dimensional (observed along the line-of-sight) velocity dispersion including both turbulent and thermal components. Equation 1.7 assumes that the three-dimensional velocity dispersion is a factor of three times larger than the one-dimensional velocity dispersion. The gravitational potential is given by:

$$W = \frac{-aGM^2}{R} \quad , \tag{1.8}$$

where a is a constant that depends on the shape and density profile of the structure ($a = 3/5$ for the frequent assumption of a uniform sphere; Bertoldi & McKee, 1992), G is the gravitational constant, and R is the structure's radius. Using Equations 1.7 and 1.8 in Equation 1.6 under the condition for virial equilibrium yields the expression for the virial parameter most commonly seen in the literature:

$$\alpha_{vir} = \frac{3\sigma^2 R}{aGM} \quad . \tag{1.9}$$

The appeal of Equation 1.9 is that all its parameters can be easily estimated with a combination of dust continuum and dense gas observations. For instance, a structure can first be identified in either the dust or gas observations to yield its radius (R). Next, the structure mass (M) and density profile (a) can be obtained from its dust continuum emission by summing the H_2 column density within the structure's boundaries and modeling its radial column density profile, respectively. Finally, σ can be determined by measuring the width of emission tracing the structure's dense gas kinematics (e.g., low-level transitions of nitrogen-bearing molecules like NH_3 and N_2H^+).

1.4 Dense Gas Temperatures and Kinematics from Ammonia

Virial stability analyses of core populations across entire clouds have recently become possible after the completion of two spectroscopic follow-up surveys of the clouds included in the HGBS and HOBYS: 1) The Green Bank Ammonia Survey (GAS, Friesen et al., 2017), which used the 100-m Green Bank Telescope (GBT) to map ammonia (NH_3) emission across the nearby HGBS clouds visible from Green Bank, and 2) KFPA Examinations of Young STellar Object Natal Environments (KEYSTONE, PI: J. Di Francesco), which also used the GBT to map ammonia emission across the HOBYS clouds visible from Green Bank.

Ammonia is the tracer-of-choice for GAS and KEYSTONE due to several unique properties that few other molecules detected in the ISM share. For instance, the NH_3 molecule has a trigonal pyramidal structure with the lone nitrogen atom bonded to a lower plane of three hydrogen atoms. This pyramidal structure allows the molecule to de-excite through a combination of rotation and inversion (i.e., when the nitrogen atom quantum mechanically tunnels through the plane of the hydrogen atoms; Ho & Townes, 1983). These collisionally excited rotation-inversion lines are populated across a range of excitation conditions, allowing ammonia to trace a diverse array of star-forming environments (Shirley, 2015). The lower excitation energies required to populate specifically the (1,1) and (2,2) excited states of ammonia cause these transitions to be ideal tracers of the cold, dense gas found in clumps and filaments.

The ammonia rotation-inversion lines are also split by hyperfine interactions between the electric and magnetic fields of the individual nuclei of the molecule. For example, the (1,1) line has 18 components arranged in five groups, as can be seen in Figure 1.4 from Friesen et al. (2016). While the five main groups can be eas-

ily observed in many clouds within the Galaxy, the magnetic hyperfine structures can be resolved only in quiescent, narrow-line regions of molecular clouds since their separations are only ~ 40 kHz (see right panel of Figure 1.4).

The optical depth of ammonia emission can also be measured directly using its hyperfine structures since their relative heights are well known under optically thin conditions. As the optical depth of the emission increases, the ratio between the peaks of the main group and the pairs of satellite lines becomes smaller as all the hyperfine components become saturated. This method for measuring optical depths circumvents the usual requirement of comparing multiple observations of several isotopes, which is commonly adopted for CO surveys (see, e.g., Myers et al., 1983). Unlike CO, NH_3 emission is typically optically thin throughout molecular clouds and does not suffer from the self-absorption that hinders kinematics measurements from CO observations.

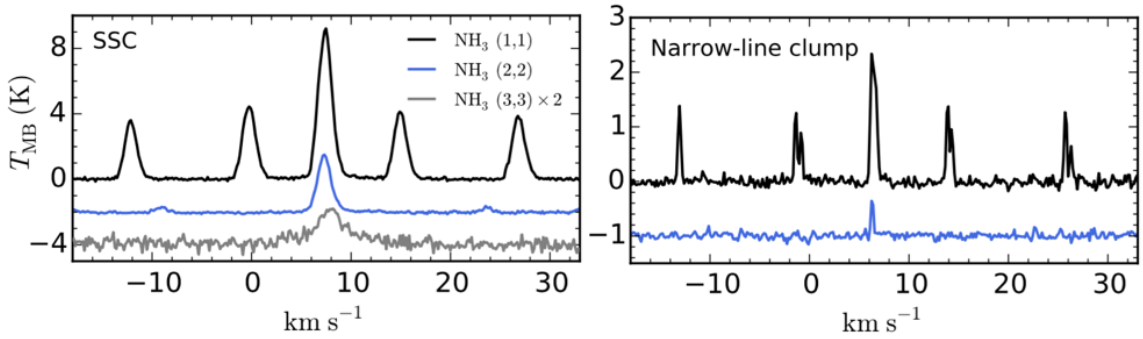

Fig. 1.4 – Figure adapted from Friesen et al. (2016) showing NH_3 (1,1), (2,2), and (3,3) emission observed towards the central protocluster (left panel) and a narrow-line clump (right panel) located in the Serpens South molecular cloud. The (3,3) line was detected in the warmer central protocluster, while the magnetic hyperfine components of the (1,1) transition are clearly resolved in the more quiescent narrow-line clump.

With optical depths for the NH_3 (1,1) transition in hand, calculating the temperature of the emitting gas requires measuring the relative intensities of the central hyperfine groups in the NH_3 (1,1) and (2,2) transitions. This line strength relationship provides the *rotational temperature*, (T_R) which describes the relative distribution of ammonia molecules within each excited state (Ho et al., 1979). Moreover, transitions between the (2,2) and (1,1) excited states are "forbidden," meaning the occurrence of such a transition is very rare (a rate of $\sim 10^{-9}$ transitions per second; Stahler & Palla, 2005). Known as *metastable* states, transitions between any of the ammonia states where the total angular momentum (J) is equal to the angular momentum compo-

nent on the NH_3 symmetry axis (K) are forbidden (e.g., for the (1,1), (2,2), (3,3), (4,4), etc., (J, K) transitions). As a result, excitation and de-excitation between the metastable states occurs mainly through *collisions* of the ammonia molecules with other particles in the cloud. Furthermore, transitions between ΔJ states for given values of K also occur very quickly ($\sim 10^{-1}$ per second), which means most of the ammonia molecules in molecular clouds spend the majority of their time in one of the $J = K$ states. These characteristics mean that rotational temperatures measured from the ammonia $J = K$ states are directly related to the *kinetic gas temperature* (T_K), which describes the velocity distribution of particles in the observed cloud and is more useful in many analyses since it relates to the cloud's total kinetic energy. In the limit where T_K is much less than the energy difference between the two excited states used to calculate the rotational temperature (T_0, which is 41.5 K for the NH_3 (1,1) and (2,2) transitions), T_R is related to T_K with the following expression (Swift et al., 2005):

$$T_R = T_K \left\{ 1 + \frac{T_K}{T_0} \ln \left[1 + \frac{3}{5} \exp \left(\frac{-15.7 \text{ K}}{T_K} \right) \right] \right\} \quad . \tag{1.10}$$

As the temperature of the cloud being observed increases, comparisons between higher excited states must be used to constrain the kinetic temperature. For example, the ratio between the (1,1) and (2,2) excited states begins to break down at $T_K > 40$ K, at which point the (3,3) line must be incorporated into the T_K model. At those temperatures, a new caveat is introduced by the fact that ammonia has two distinct species, ortho-NH_3 and para-NH_3, due to the two potential orientations for the spin of the hydrogen atoms. The (1,1), (2,2), (4,4), and (5,5) transitions are para-NH_3 transitions, while the (3,3) and (6,6) transitions are ortho-NH_3 transitions. When comparing the line intensities between the two different NH_3 species, an ortho- to para-NH_3 ratio must be either assumed or measured. Assuming a fixed ortho- to para-NH_3 ratio undoubtedly introduces uncertainties since the ratio varies depending on the region where the NH_3 was formed (Wilson et al., 1982). In the work described in this dissertation, we use only the (1,1) and (2,2) transitions to avoid assuming an ortho-to-para ratio. Since most regions in molecular clouds have $T_K < 40$ K and lack detectable ammonia emission above the (2,2) transition, this approach provides adequate constraints on T_K.

In addition to optical depth and kinetic temperature, other useful cloud attributes probed by ammonia emission lines are the dense gas velocity dispersion (σ_v) and

centroid velocity in the Local Standard of Rest frame (V_{LSR}). Typically, optically thin emission lines can be modeled as Gaussian distributions with a mean and standard deviation given by V_{LSR} and σ_v, respectively. Thus, measuring V_{LSR} and σ_v involves fitting Gaussian profiles to the observed emission while accounting for the blending of the ammonia hyperfine lines.

1.5 Structure Identification Methods

Identifying structures in the star formation hierarchy is essential to understanding their characteristics and how each level in the hierarchy relates to the others. In particular, the automated identification of protostars, dense cores, clumps, and filaments have become an increasingly important task in the current era of high-resolution, large-scale surveys covering a bevy of molecular clouds. This section provides an overview of the identification methods used in this dissertation.

1.5.1 Core and Protostar Identification

Although there is no strict definition for dense cores, in practice they are typically identified as either intensity peaks in far-infrared/submillimeter, millimeter, and radio emission, or absorption dips in optical or infrared emission (Di Francesco et al., 2007). In this dissertation, the focus is on the former; identifying intensity peaks in dust and ammonia emission.

Since 70 μm point sources are indicative of the internal luminosity of a protostar (Dunham et al., 2008), the working definition of protostars and young stellar objects (YSOs) adopted throughout this dissertation is the presence of a detectable intensity peak at 70 μm. Similarly, cores that are coincident with the position of a 70 μm point source are deemed *protostellar cores*, while those without a detectable 70 μm point source are termed *starless cores*.

getsources

Observations of molecular clouds with the *Herschel Space Observatory* provide dust continuum emission maps at $70 - 500$ μm with angular resolutions of $8'' - 36''$. This factor of $\sim$ 5 variation in resolution poses a major challenge for traditional core or clump extraction algorithms such as *gaussclumps* (Stutzki & Guesten, 1990) and *clumpfind* (Williams et al., 1994) which utilize iterations of Gaussian fits and intensity contours, respectively, to identify cores or clumps in images or position-velocity

data cubes. For example, identifying such objects in *Herschel* observations with *gaussclumps* or *clumpfind* would require five separate extractions, i.e., one for each wavelength band. The five output catalogs produced by each extraction would then need to be cross-matched to produce a final, single catalog of sources identified across all wavelengths. The act of cross-matching extraction catalogs in images with large variations in angular resolution is non-trivial, however, since multiple structures at shorter wavelengths may be identified within a single structure identified at larger wavelengths due to the differences in resolution of each map.

To combat the issue of identifying sources in images with varying angular resolutions, *getsources* was created to identify sources in multiple wavelength images simultaneously (Men'shchikov et al., 2012). *getsources* employs six main steps for extraction that are summarized below:

1 The images at each wavelength are aligned and resampled onto the same pixel grid. This step ensures that each image has the same number of pixels and pixel size to allow for the multi-wavelength extraction.

2 The images are then convolved with circular Gaussians of increasing sizes, which are successively subtracted from the original images to create "single-scale" images at multiple spatial scales for each waveband. This step highlights Gaussian-like structures, from compact protostars to more extended cores, at multiple spatial scales. Figure 1.5 displays example single-scale images for simulated observations included in Men'shchikov et al. (2012).

3 The convolved images are then cleaned of background emission features that do not have Gaussian shapes by masking pixels that are below a predefined noise threshold. The threshold is based on the intensity standard deviation of each map and is iteratively adjusted until convergence is reached, i.e., until the standard deviation changes by less than 1% on successive iterations. Thus, signal is isolated from the noise and background in this step. Figure 1.6 shows the cleaned single-scale images for simulated observations included in Men'shchikov et al. (2012).

4 The single-scale images created from each original waveband image are then summed to produce "combined single-scale" images. This step creates wavelength-independent single-scale images that are cleaned of noise/background and include significant intensity peaks that can be attributed to potential sources.

5 The combined single-scale images are segmented into sources by connecting non-zero pixels that are *4-connected*, which means the square pixels in an individual source are connected to neighboring pixels by a path that runs through the pixel sides (not their corners).

6 All 4-connected sources are assigned a running identification number and their intensity measurements at each wavelength are measured after subtracting the contributions from noise and background. The final catalog of sources includes each source's size and intensity measurements at each wavelength.

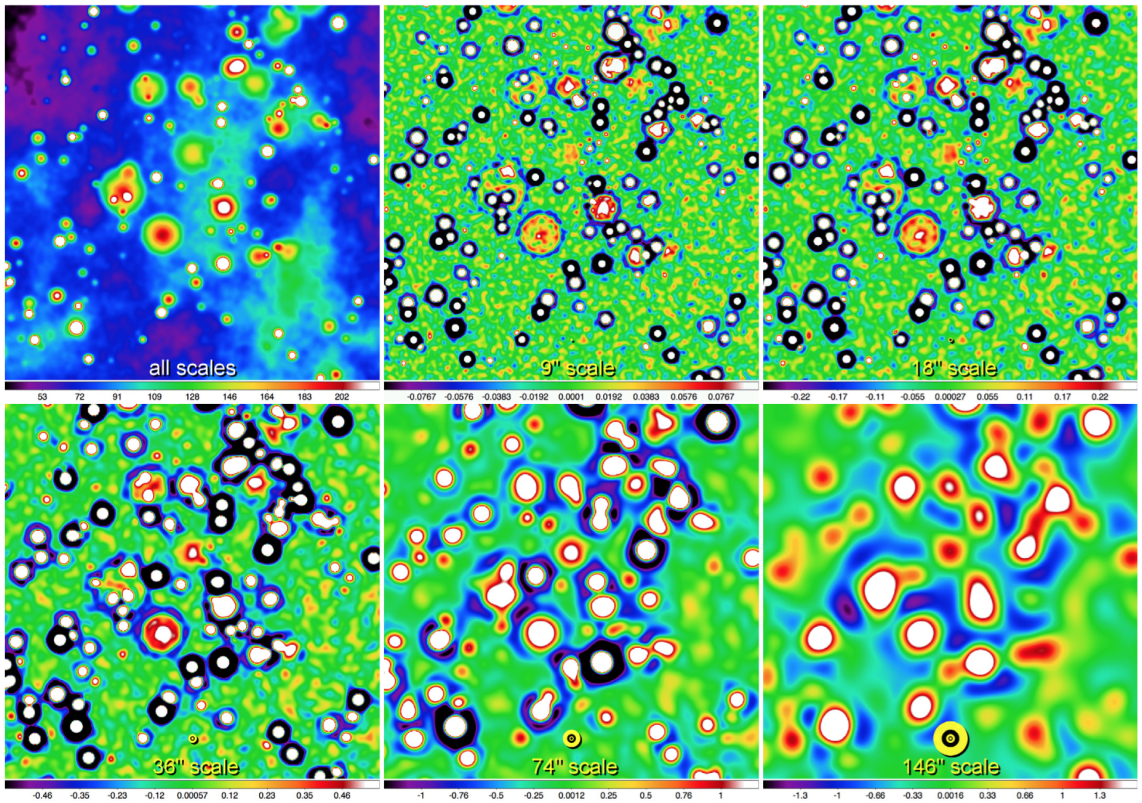

Fig. 1.5 – The upper left panel shows a simulated *Herschel* molecular cloud observation at 350 μm. All other panels show the *getsources* convolved single-scale images at spatial scales from $9'' - 146''$. The color scale in all panels shows intensity in MJy/str. Figure taken from Men'shchikov et al. (2012).

An example protostellar core identified in the *getsources* extraction of the *Herschel* observations of the Cepheus-L1251 molecular cloud is shown in Figure 1.7. The multi-wavelength approach of *getsources* allows the source to have varying sizes across the

five wavebands and in the H_2 column density map. The bright point-source emission at 70 μm also clearly classifies this core as protostellar rather than starless.

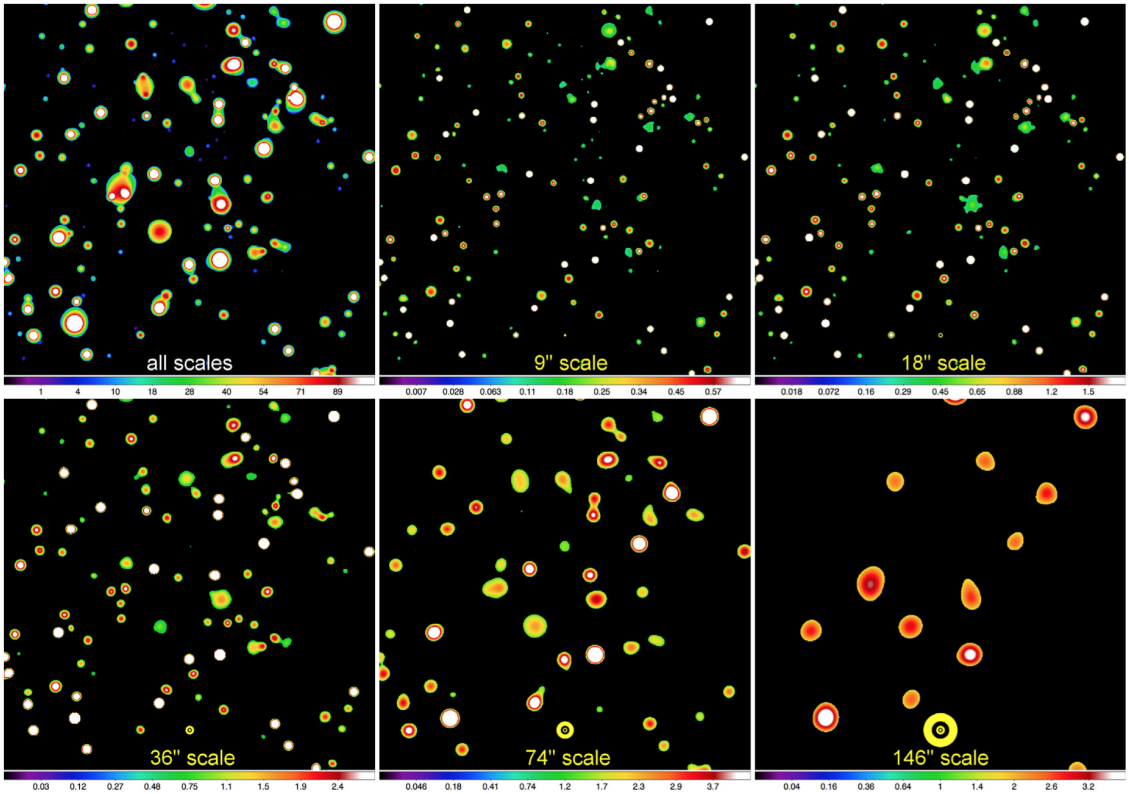

Fig. 1.6 – Cleaned single-scale images from *getsources* for the decompositions shown in Figure 1.5. Noise and background pixels have been masked out, leaving only the signal pixels that will be used for source detection. The color scale in all panels shows intensity in MJy/str. Figure taken from Men'shchikov et al. (2012).

dendrograms

One limitation of *getsources* is that it provides only compact source catalogs while failing to show how sources are related to structures farther up the molecular cloud hierarchy (e.g., filaments and clumps). Dendrograms provide an alternative source extraction method that solves this issue by using a tree-diagram approach that traces the spatial relationships between the sources identified. Although dendrograms will be explained in detail in Chapters 2 and 3 of this dissertation, a cartoon diagram of a dendrogram extraction is shown in Figure 1.8 to provide a visual aid of the algorithm's approach. The top-level *leaf* structures in the tree are analogous to

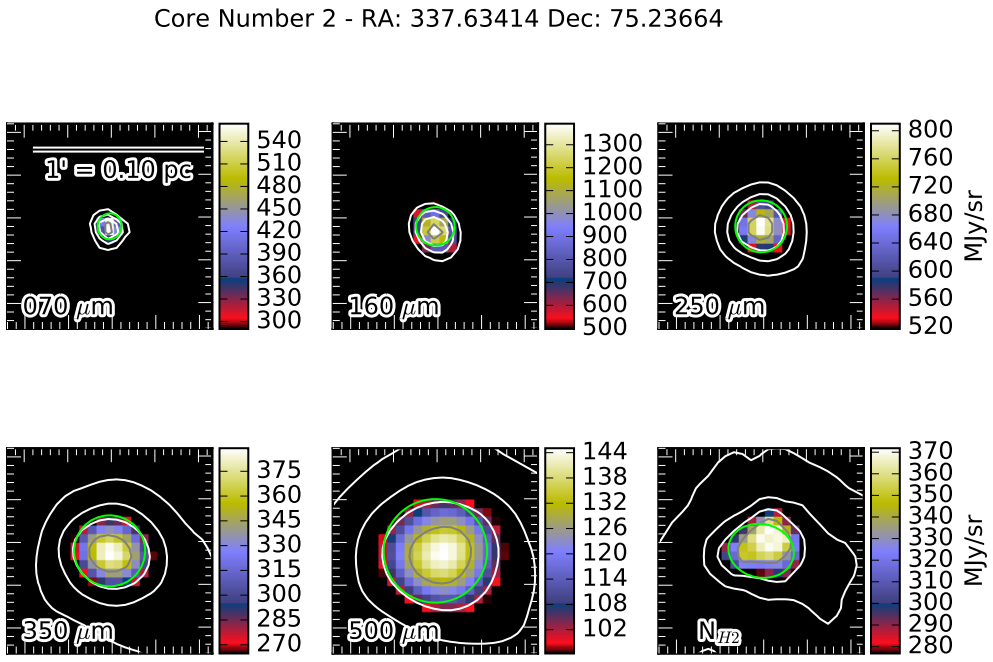

Fig. 1.7 – Example protostellar core identified in a *getsources* extraction of the *Herschel* observations of the Cepheus-L1251 cloud (Di Francesco et al., 2019, in prep) at 70 μm (upper left), 160 μm (upper middle), 250 μm (upper right), 350 μm (bottom left), 500 μm (bottom middle), and in H_2 column density (bottom right). The full-width at half maximum ellipse for the source is shown by a green contour. The remaining contours show 90%, 70%, 50%, and 30% of the peak intensity in each panel. The background color scale in all panels shows intensity in MJy/str.

the compact sources extracted by *getsources*. Instead of stopping at the top-level structures, however, the dendrogram continues connecting pixels to the leaves until they merge into lower-level structures called *branches*. These branches represent the clumps within which the cores are embedded. Further down the dendrogram's tree-diagram are the lowest level structures termed *trunks*. These structures can be thought of as the section of the cloud in which a collection of cores and clumps are embedded. Thus, dendrograms provide a metric to determine how clustered or isolated the star-forming structures in a cloud may be.

Although the dendrogram example shown in Figure 1.8 is for a 2D example (e.g., a map of emission at a single wavelength), dendrograms can easily be scaled to 3D (Rosolowsky et al., 2008). In the 3D case, voxels (the single elements in a data

cube) are connected to one another to form the structure hierarchy rather than pixels. Conversely, *getsources* extractions are limited to 2D images. This disadvantage makes dendrograms a natural choice for identifying structures in the position-position-velocity data cubes commonly obtained in ammonia mapping surveys (e.g., Friesen et al., 2017).

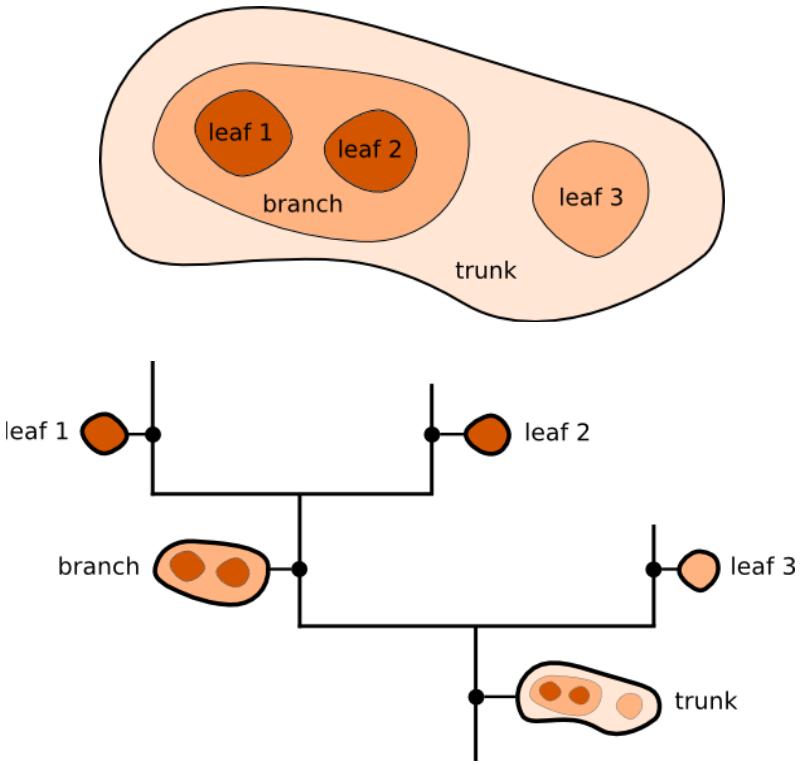

Fig. 1.8 – Cartoon diagram of a dendrogram segmentation on a 2D data set (adapted from figures shown on http://www.dendrograms.org/). The three brightest segments in the map are identified as top-level leaves and all lie within the same trunk, while two of the leaves lie within a mid-level branch.

1.5.2 Filament Identification

Although some authors have deemed filaments as "any elongated ISM structure with an aspect ratio larger than $5 - 10$ that is significantly overdense with respect to its surroundings," (e.g., André et al., 2014; Koch & Rosolowsky, 2015), a formal definition does not exist for filaments. Filaments are also often touted as having

a characteristic width of $\sim$ 0.1 pc, which has been measured in both observations (Arzoumanian et al., 2011) and simulations (Federrath, 2016), and are thought to be created by the turbulence and magnetic fields of clouds. Here, we will loosely define filaments as over-densities in dust or ammonia emission with aspect ratios larger than two.

getfilaments

Although the trunks and branches identified by dendrograms can sometimes have large aspect ratios and may mimic the appearance of filaments, dendrograms are not optimized for identifying filaments in molecular cloud observations. Instead, dedicated filament identification algorithms must be used to extract filaments with high degrees of completeness. Here, we describe the *getfilaments* algorithm (Men'shchikov, 2013), which is run in conjunction with *getsources* to identify the filaments within which cores reside. Like *getsources*, *getfilaments* was designed to identify filaments across the multiple spatial scales and wavelengths covered by *Herschel*.

The issues affecting the extraction of filaments are similar to those encountered in core extractions: Namely, it is difficult to separate background and noise from the intensity distribution of sources, which in this case are filaments. As such, much of the processing required for the *getsources* and *getfilaments* algorithms is identical. In fact, *getfilaments* begins after the second step in *getsources*, which involves creating the convolved single-scale images. When filaments are present in an image, they can be identified using the pixels below the image standard deviation at each spatial scale. An example is illustrated in Figure 1.9, which shows how the image of a simulated filament containing several dense cores on a noisy background is segmented into filament masks at each spatial scale. The upper left and upper right panels in Figure 1.9 show the original simulation image and the convolved single-scale images, respectively. The bottom left panel shows the filament masks obtained after zeroing all pixels below the image standard deviation at each spatial scale. The filament edges are clearly isolated with this simple cutoff, but they are also contaminated by noise. To clean the masked images of noise, *getfilaments* uses the same 4-connected algorithm as *getsources* (listed as step 5 for *getsources*) to segment the masked images into clusters of 4-connected sources. Sources that contain fewer pixels than a threshold set by the spatial scale of each single-scale image are then removed from the filament masks. The result of this final step is displayed in the lower right panel of Figure 1.9,

which shows the final filament masks after the small noise sources have been removed.

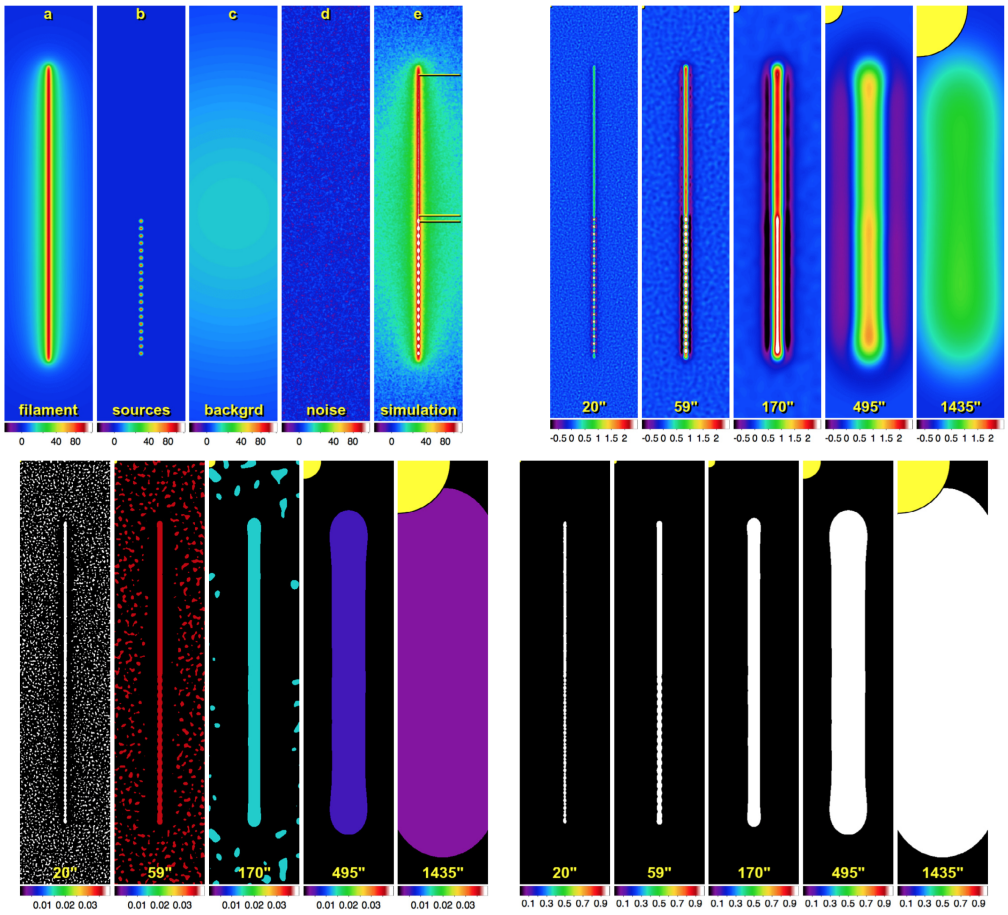

Fig. 1.9 – Example filament extraction for a simulated observation using the *getfilaments* algorithm. The upper left panel shows the individual components (filament, cores, background, and noise) injected into the simulated field. The upper right panel shows the convolved single-scale images at each spatial scale. The lower left panel shows the masks created by isolating all pixels below the standard deviation of each convolved single-scale image. The lower right panel shows the final filament masks after removing 4-connected sources that have fewer pixels than the threshold specified for each spatial scale. The yellow quarter circle shown in each panel represents the spatial scale of the displayed image. Figure adapted from Men'shchikov (2013).

1.6 Machine Learning

Another useful tool for analyzing observations of star-forming molecular clouds is machine learning - the sub-field of computer science focused on using algorithms to identify patterns in data sets and build predictive models for certain tasks. Ma-

chine learning is often split into two regimes: *supervised* learning versus *unsupervised* learning.

1.6.1 Supervised Learning

Supervised learning involves using a *training set* for which each entry has an associated output parameter. For instance, the training set could be a series of 1,000 star and galaxy spectra. In that case, the *input* into the algorithm would be an array of 1D channel intensities for the 1,000 spectra. The *output* would be another array of 1,000 class labels (e.g., "star" versus "galaxy") corresponding to each input spectrum and encoded to a numerical value. For example, the number 0 may represent a star and 1 may represent a galaxy. Oftentimes, the individual input/output pairs in a training set are referred to as a *sample* or *example*.

With the input and output arrays of the training set specified, supervised learning proceeds by tuning (a.k.a. *optimizing*) the parameters of the chosen machine learning algorithm. The goal of this process is often to minimize the amount of misclassifications made by the algorithm on the training set. The chosen machine learning algorithm dictates how the parameter optimization proceeds since each algorithm has its own amount and type of parameters. Typically, *gradient descent* methods are used for parameter optimization. This process involves using the chosen algorithm to predict the class of all or part of the training set input, then comparing those predictions to the true class labels for each sample. The algorithm's parameters are then adjusted to move in the direction that will minimize its misclassifications on the training set. This gradual adjustment of the parameters proceeds iteratively until improvements in the classification accuracy are less than a pre-defined threshold.

After training the algorithm using the training set, its predictive performance is typically evaluated using a separate *test set* that was not used for training. This helps ensure that the algorithm's parameters aren't tuned too specifically for the training set and its predictions can be generalized to new data sets.

Supervised learning can be split further into two categories: *classification* and *regression*. For classification, the outputs are distinct classes that are typically encoded as integers. For regression, the outputs are continuous values. The training process for regression tasks is similar to that of classification, but the algorithm is trained to output a continuous number in the former and an integer in the latter.

1.6.2 Unsupervised Learning

In contrast to supervised learning, the training sets used for unsupervised learning do not have predefined output labels. As such, the goal of unsupervised learning is not to minimize misclassifications, but rather to identify groups of samples in the training set with similar attributes. The output of unsupervised learning is often *clusters* of samples that have been deemed similar by the algorithm. The hierarchical clustering of pixels in a map using dendrograms (as was discussed in Section 1.5) is one example of unsupervised learning. In that case, pixels in a map or voxels in a data cube are grouped together based on their location and intensities.

Unsupervised learning is useful for extracting information from a data set when predefined output labels are not available. For instance, unsupervised learning would be necessary if the spectra in the star versus galaxy classification problem discussed in the previous section had not already been labeled. In that case, clustering algorithms could be used to separate the spectra into clusters based on their appearance.

In general, clustering is often difficult to apply for certain tasks since it can be dependent on the chosen algorithm's input parameters. Such parameters could include the number of clusters to identify, thresholds for separating groups of samples into two separate clusters, etc. Furthermore, without prior knowledge of the samples included in the training set, the clusters identified by an unsupervised learning algorithm can be difficult to interpret. For example, a user would need to have some knowledge of star and galaxy spectral features to understand the physical differences between the clusters identified in the aforementioned star and galaxy spectra data set. This requirement highlights the necessity to complement machine learning tools with domain expertise to extract the most useful insights from a data set.

1.6.3 Artificial Neural Networks

One of the most commonly used supervised learning algorithms in astronomy is the artificial neural network (ANN; see, e.g., the review by Ball & Brunner, 2010). Designed to mimic the functionality of the neurons in the human brain, ANNs rely on interconnected layers of artificial neurons. A cartoon example of an ANN is shown in Figure 1.10. The *input layer* represents the input data for each sample used to train the network. For example, the input layer for the star versus galaxy spectra training set presented in the previous sections would simply be each channel's intensity in the given sample's spectrum.

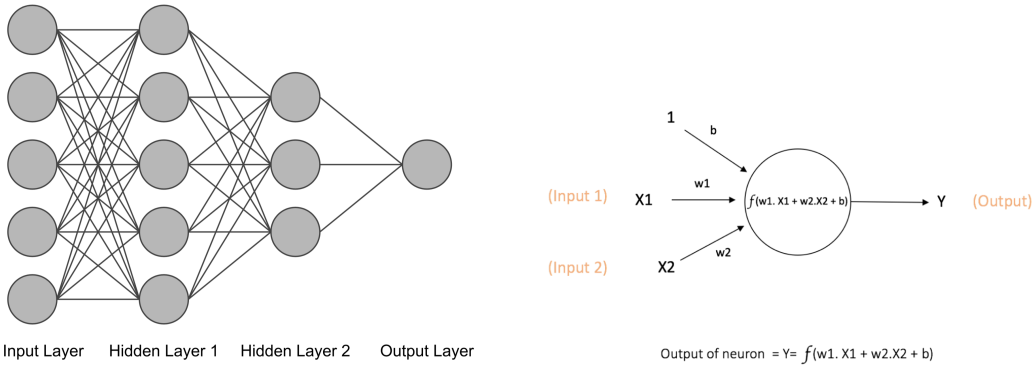

Fig. 1.10 – Left: Example diagram from Shallue & Vanderburg (2018) of a fully connected artificial neural network. The input features that comprise the input layer are fed into each neuron in the first hidden layer, which feed their output into the second hidden layer. Finally, the output of the second hidden layer is used in the output layer to predict either the discrete class of the object (classification) or estimate the value of a continuous variable (regression). Right: Zoom-in view of a single neuron. $X1$ and $X2$ are input features (i.e., numbers) into the neuron, which can come directly from the input layer or the output of a neuron in a previous hidden layer. The output (Y) of the neuron is determined by a pre-defined function (f, e.g., hyperbolic tangent), which applies weights ($w1$ and $w2$) to each input feature and adds a bias variable (b) onto the inputs.

The values in the input layer of the network are passed into each of the artificial neurons in the second layer of the network, as shown in the left panel of Figure 1.10 by the lines connecting each value in the input layer to every artificial neuron in the second layer. Each neuron in the second layer has a non-linear function, known as an *activation function*, associated with it. Commonly used activation functions are the hyperbolic tangent and "rectified linear" ($f(x) = max(0, x)$). These non-linear activation functions allow the network to identify mappings between the input data and output labels in the training set that linear functions cannot distinguish.

A visual representation of the activation function being applied inside an artificial neuron is shown in the right panel of Figure 1.10. $X1$ and $X2$ are input features (i.e., numbers) passed into the neuron from a previous layer in the network. The sum of the products of each input into the neuron and their associated weights ($w1$ and $w2$) are passed into the activation function (f). Oftentimes, a bias variable (b) is also added to the sum fed into the activation function. The bias variable is analogous to the y-intercept in the equation of a line, allowing the activation function to be centered on values that are not zero. Finally, the number produced after passing the

weighted inputs and bias through the activation function becomes the output (Y) of the neuron. This output is then passed onto the neurons in the next layer of the network.

The final layer of the network is known as the *output layer*. It accepts as input the output of the final *hidden layer* in the network, where hidden layers are those in-between the input and output layers. As will be discussed in Chapter 5, the type of activation function used for the output layer dictates whether the network is performing classification or regression.

During training, the weights and bias variables on each artificial neuron in the network are iteratively optimized to return the desired output of the final output layer. As such, the complexity of ANNs is directly related to the size and number of their hidden layers. The advantage of introducing additional neurons and hidden layers is that more complex mappings between the inputs and outputs of the training set can be distinguished. This gain comes at the risk of *overfitting*, which is the term used when a network predicts well on the training set but generalizes poorly to new data sets because it has been tuned too specifically for the training data. Although there are many methods to combat overfitting, one commonly used technique involves averaging the predictions from several independently trained networks. This technique, which is known as *ensemble averaging*, will be described further in Chapter 5.

1.6.4 Convolutional Neural Networks

One of the main drawbacks of using the ANN described in the previous section is that it treats each input independently, disregarding any spatial associations between the inputs. For instance, humans often classify star and galaxy spectra by looking for certain emission and absorption features. Those features are difficult to distinguish by looking at each channel independently. By looking at collections of channels across certain wavelengths, however, the class of the object can be determined more easily. Thus, our ability to classify spectra relies on the spatial awareness we gain by viewing collections of channels together.

Convolutional neural networks (CNNs) were developed to give neural networks the ability to preserve spatial awareness across inputs. CNNs rely on a series of *kernels* that are convolved with the input to produce new "feature maps" that preserve spatial information in the inputs. An example of the kernel convolution process in a CNN trained to detect arrhythmia in electrocardiography (ECG) scans of the human heart

(Yildirim et al., 2018) is shown in Figure 1.11. The raw 1D ECG scans serve as the input into the network. Four 1D kernels of the same length, but with different weights, are slid across the ECG scan starting from the left-most channel. At each position along the ECG scan, the dot product between each of the four kernels' weights and the overlapping ECG scan channels (shown for the first scan segment by red in Figure 1.11) produces a channel in each of the feature maps displayed in the second row of Figure 1.11.

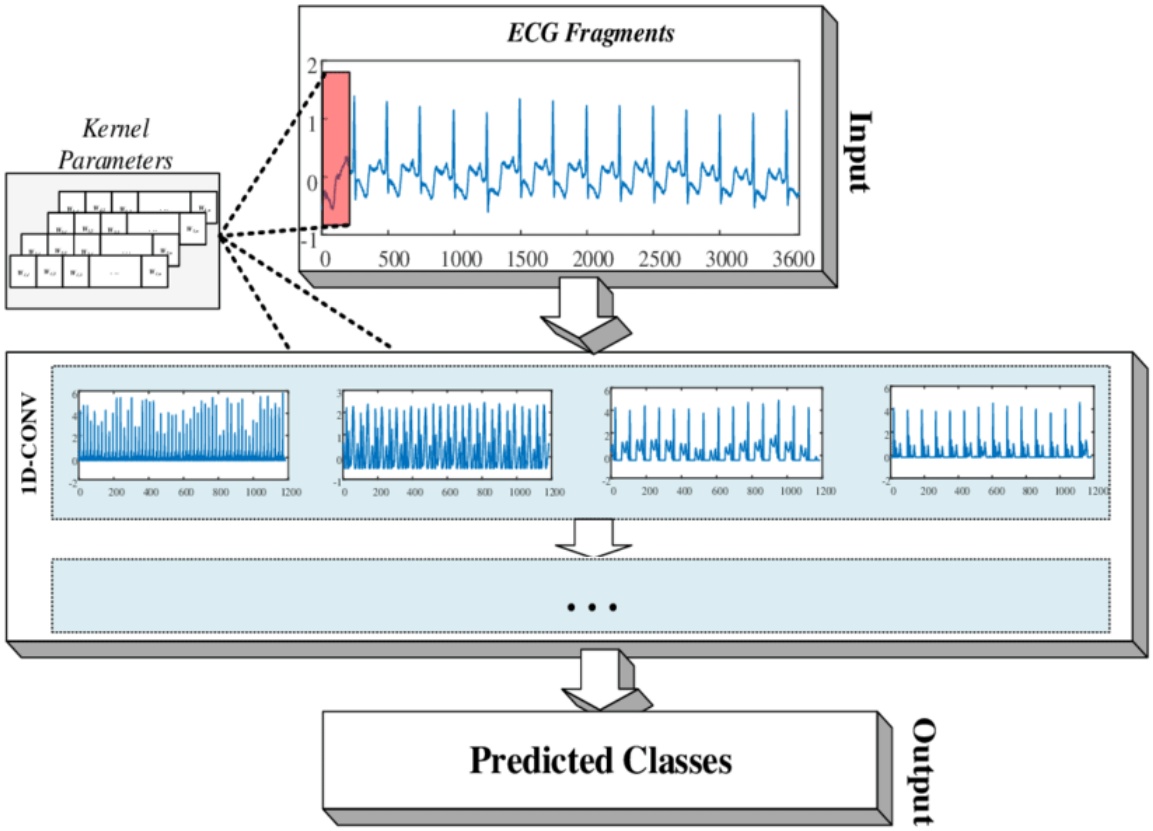

Fig. 1.11 – Example convolutional kernels applied to a 1D electrocardiography signal (top) from Yildirim et al. (2018). Four kernels with different weight combinations are slid across the input and the dot product of every third input channel used to create four convolved feature maps (middle). These feature maps are used as input into subsequent layers of the network to ultimately classify the input signal.

In the example displayed in Figure 1.11, the dot product between each kernel and the ECG channels is calculated for every third channel. This *stride* results in convolved feature maps that have one-third of the length of the input ECG while preserving in each channel the information from neighboring channels in the input.

These convolved feature maps are then either used as input into a traditional ANN or a subsequent convolutional layer using a different set of kernels.

The convolved feature maps in the middle row of Figure 1.11 show the different types of features that can be highlighted by kernels with certain weight combinations. For instance, the kernel that created the left-most feature map appears to accentuate the differences between peaks in the ECG scan. Conversely, the second kernel from the left appears to make the sub-peaks more prominent relative to the main peaks in the ECG scan. Since the weights on the individual kernels are learned during the training process, the network is able to discover the combinations that allow it to optimize its predictions.

Indeed, CNNs have proven to be reliable predictors for a variety of tasks in astronomy involving spectra, time series, and images (e.g., Fabbro et al., 2018; Shallue & Vanderburg, 2018; Zhang et al., 2018). As such, they are excellent choices for a variety of prediction tasks involving the spectroscopic observations of star-forming molecular clouds provided by GAS and KEYSTONE.

1.7 Dissertation Goals - Are cores/clumps truly *bound* structures?

The combination of the *Herschel* dust continuum and GBT ammonia line data provides all the ingredients required to analyze the virial stability of hundreds of cores, clumps, and filaments across a variety of star-forming environments. Such an analysis allows us to investigate the following topics:

1. The CMF/IMF relationship: namely, are most of the cores we include in the CMF gravitationally bound and likely to form stars? Or, will many of them simply dissipate back into the molecular cloud surroundings without forming stars?

2. The effect filaments have on the stability of dense cores: Are the cores/clumps that have been observed to be associated with filaments more likely to be bound structures and form stars? Do filament intersections lead to structures that are more gravitationally bound?

3. Improvements to future virial analyses: Can we improve the methods by which we measure the kinematics of structures to derive more accurate stability estimates? Are machine learning techniques helpful in the analysis of molecular cloud observations?

This dissertation addresses these questions through a series of projects that will be outlined in the following three chapters: In Chapter 2, we investigate whether or not the dense cores in a nearby molecular cloud identified in dust continuum emission are actually associated with dense gas structures as traced by emission line observations of ammonia. A framework will be developed for using the ammonia observations to derive virial stability estimates for the structures, which will provide insight into whether or not they are bound by gravity. In Chapter 3, we use the framework outlined in Chapter 2 to analyze the stability of structures identified by ammonia emission observed in high-mass star-forming GMCs. This chapter will provide one of the largest stability analyses of GMC clumps to date. In addition, we investigate the impact that filaments have upon the stability of the observed structures. Finally, in Chapter 4, we present a new method for detecting emission with multiple velocity components along the line of sight, which can impact the kinematics measurements obtained from traditional emission line fitting techniques. This method improves the accuracy of both core and filament kinematics measurements, which in turn provides better estimates of the stability of those structures.

Chapter 2

The Green Bank Ammonia Survey: Observations of Hierarchical Dense Gas Structures in Cepheus-L1251

Originally published in The Astrophysical Journal, Volume 850, Issue 1, article id. 3, 24 pp. (2017).

Authors: Jared Keown, James Di Francesco, Helen Kirk, Rachel K. Friesen, Jaime E. Pineda, Erik Rosolowsky, Adam Ginsburg, Stella S. R. Offner, Paola Caselli, Felipe Alves, Ana Chacón-Tanarro, Anna Punanova, Elena Redaelli, Young Min Seo, Christopher D. Matzner, Michael Chun-Yuan Chen, Alyssa A. Goodman, How-Huan Chen, Yancy Shirley, Ayushi Singh, Hector G. Arce, Peter Martin, and Philip C. Myers

ABSTRACT

We use Green Bank Ammonia Survey observations of NH_3 (1,1) and (2,2) emission with $32''$ FWHM resolution from a ~ 10 pc^2 portion of the Cepheus-L1251 molecular cloud to identify hierarchical dense gas structures. Our dendrogram analysis of the NH_3 data results in 22 top-level structures, which reside within 13 lower-level, parent structures. The structures are compact (0.01 pc $\lesssim R_{eff} \lesssim$ 0.1 pc) and are spatially correlated with the highest H_2 column density portions of the cloud. We also compare the ammonia data to a catalog of dense cores identified by higher-resolution ($18.2''$ FWHM) *Herschel Space Observatory* observations of dust continuum emission from Cepheus-L1251. Maps of kinetic gas temperature, velocity dispersion, and NH_3 column density, derived from detailed modeling of the NH_3 data, are used to investigate the stability and chemistry of the ammonia-identified and *Herschel*-identified

structures. We show that the dust and dense gas in the structures have similar temperatures, with median T_{dust} and T_K measurements of 11.7 ± 1.1 K and 10.3 ± 2.0 K, respectively. Based on a virial analysis, we find that the ammonia-identified structures are gravitationally dominated, yet may be in or near a state of virial equilibrium. Meanwhile, the majority of the *Herschel*-identified dense cores appear to be not bound by their own gravity and instead confined by external pressure. CCS $(2_0 - 1_0)$ and HC_5N $(9 - 8)$ emission from the region reveal broader line widths and centroid velocity offsets when compared to the NH_3 (1,1) emission in some cases, likely due to these carbon-based molecules tracing the turbulent outer layers of the dense cores.

2.1 Introduction

Recent large-scale surveys of dust continuum emission from nearby star-forming regions have provided unprecedented insights into the structure of molecular clouds. The Gould Belt Legacy surveys on the *Herschel Space Observatory* (HGBS; André et al., 2010) and James Clerk Maxwell Telescope (JGBS; Ward-Thompson et al., 2007) have fueled these advancements, providing photometric censuses of nearby (< 500 pc) Galactic molecular clouds. In particular, they have revealed that filaments pervade both active (André et al., 2010; Men'shchikov et al., 2010) and quiescent (Miville-Deschênes et al., 2010; Ward-Thompson et al., 2010) molecular clouds. Dense cores, the high density regions of molecular clouds where stars are born, also appear to be spatially correlated with filaments (Könyves et al., 2010, 2015). These results suggest mass flow onto or through filaments may be a requirement to gain the locally high density conditions necessary for core formation and subsequent gravitational collapse to form stars.

The HGBS has shown that the mass distribution of prestellar dense cores, i.e., gravitationally-bound structures on the verge of forming new stars, bears a resemblance to the stellar initial mass function (IMF) across several star-forming environments (Aquila, Könyves et al. 2015; Taurus, Marsh et al. 2016; Cepheus, Di Francesco et al. 2019, in prep). Assuming the observed prestellar cores will indeed form stars in the future, the relationship between the IMF and core mass function lends credence to the theory that stellar masses are set at the dense core stage. Without adequate spectral line measurements for the prestellar cores, however, it is difficult to determine whether these structures are truly gravitationally bound objects or rather they

are simply pressure-confined by the molecular cloud within which they reside.

To provide a large-scale spectral counterpart to the photometry-based HGBS and JGBS, the Green Bank Ammonia Survey (GAS; Friesen et al., 2017) has mapped NH_3 emission across the highest H_2 column density portions of the northern Gould Belt molecular clouds. NH_3 is an ideal tracer for such a survey because it is excited in the cold, dense gas ($n > 2 \times 10^3$ cm^{-3} at 10 K) found in cores and filaments (Shirley, 2015). Observing both NH_3 (1,1) and (2,2) emission also provides a convenient way of measuring kinetic gas temperatures (Ho & Townes, 1983), which, along with velocity dispersion measurements, can be used to determine the stability of filaments and dense cores.

In this paper, we analyze the stability of dense gas structures identified in the Cepheus-L1251 molecular cloud by combining HGBS photometry with GAS NH_3 spectral data for the region. Cepheus-L1251 is a prime candidate for such an analysis due to its large population of both starless and protostellar dense cores (Lee et al., 2007; Kun et al., 2009; Kim et al., 2015), as well as its prominent network of parsec-length filaments (Sato et al., 1994). The cloud consists of three main submillimeter-bright regions - L1251A in the west, L1251C in the center, and L1251E/B in the east - all of which contain protostar-driven outflows (L1251A: Lee et al. 2010; L1251C: Kim et al. 2015, L1251E/B: Lee et al. 2007). These outflows are indicative of the active nature of the region and may produce noticeable chemo-dynamical effects upon the surrounding gas.

Furthermore, the dense core population in Cepheus-L1251 has been catalogued by both the HGBS (Di Francesco et al., 2019, in prep), which identified 187 dense cores in a ~ 3 square degree field in the region, and the JGBS (Pattle et al., 2017), which found 51 sources in a ~ 1.6 square degree field. Newly obtained NH_3 observations of Cepheus-L1251 by GAS provide the link necessary to determine the dynamical states of dust continuum-identified structures. Here, we analyze the stability of cores in the Di Francesco et al. (2019, in prep) catalog since the Pattle et al. (2017) observations do not include the southwestern portion of Cepheus-L1251 observed by the HGBS and GAS. We also use the NH_3 (1,1) data to identify hierarchical dense gas structures in Cepheus-L1251, which are cataloged here and compared to the continuum-identified structures. We assume a distance of 300 pc to Cepheus-L1251 throughout this paper, which appears to be a consistent distance measurement found from a variety of methods (Kun & Prusti, 1993; Kun, 1998; Balázs et al., 2004).

In § 2.2, we describe the observations and data sets used for our analysis. In § 2.3,

we outline the methods used to identify structures in the NH_3 data and derive stability parameters for those structures. In § 2.4, we compare our results to a similar analysis performed by Friesen et al. (2016) in Serpens South, discuss the role of external pressure within the observed structures, and investigate potential chemical effects within L1251 by analyzing CCS $(2_0 - 1_0)$ and HC_5N $(9-8)$ emission from the region. We conclude, in § 2.5, with a summary of the paper.

2.2 Observations

2.2.1 GBT NH_3 Data

Our ammonia data were obtained as part of the Green Bank Ammonia Survey (GAS; Friesen et al., 2017), a large project on the Green Bank Telescope which mapped NH_3 $(J,K) = (1,1)$, $(2,2)$, and $(3,3)$, HC_7N $J = (21-20)$ and $(22-21)$, HC_5N $J = (9-8)$, and CCS $J = (2_0 - 1_0)$ emission across much of the northern Gould Belt star-forming regions where $A_V > 7$ mag. The Cepheus-L1251 region was observed for a total of $\sim$ 21 hours between October 2015 and February 2016. Observations covered the highest H_2 column density portions of L1251 and totaled $\sim$ 0.36 square degrees ($\sim$ 10 pc^2 at a distance of 300 pc). Figure 2.1 shows the outline of the region observed by GAS overlaid onto the *Herschel*-derived H_2 column density map for L1251 (Di Francesco et al., 2019, in prep). The angular resolution for all observed lines is $32''$ (FWHM), which is equivalent to $\sim$ 0.05 pc at a distance of 300 pc. The spectral resolution is 5.7 kHz, or $\sim$ 0.07 km s^{-1} at 23.7 GHz. The median rms noise in the off-line channels of both NH_3 (1,1) and (2,2) is 0.12 K. If the noisy map edges are excluded, the median rms noise in the maps is 0.09 K. Emission was detected from all observed transitions except NH_3 (3,3), HC_7N $(21-20)$, and HC_7N $(22-21)$. All GAS-observed data and parameter maps used in this paper are publicly available at https://dataverse.harvard.edu/dataverse/Cepheus-L1251.

2.2.2 *Herschel* Dust Continuum Data

As part of the *Herschel* Gould Belt Survey (HGBS; André et al., 2010), five separate fields in the Cepheus star-forming region, including L1251, were mapped by the PACS and SPIRE instruments at $70-500$ μm. After subtracting background sub-millimeter emission observed toward the region by *Planck*, Di Francesco et al. (2019, in prep) fit modified blackbody functions (of the form shown in Equation 1.3

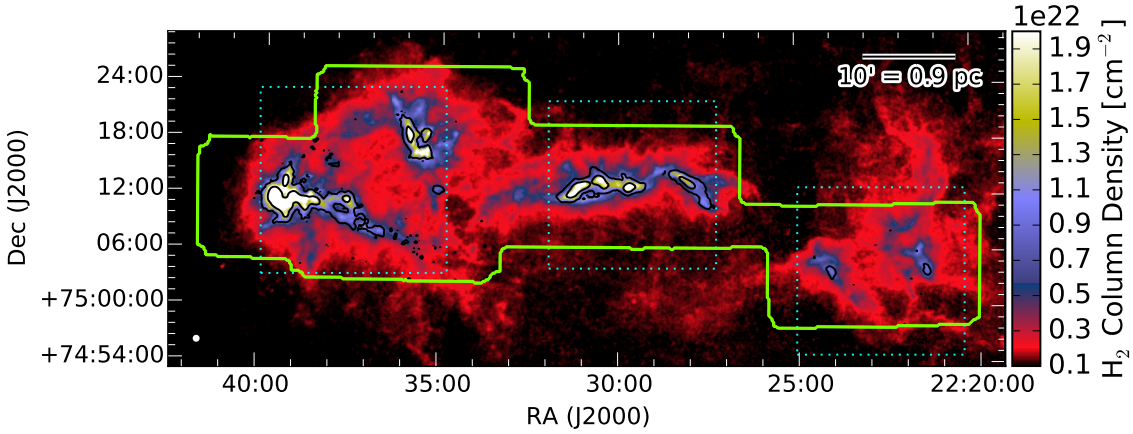

Fig. 2.1 – Background colorscale shows the H_2 column density map of Cepheus-L1251 derived by Di Francesco et al. (2019, in prep). The green contour outlines the region observed in NH_3 (1,1) and (2,2) by GAS (Friesen et al., 2017) using the Green Bank Telescope. The black contours show the NH_3 (1,1) integrated intensity at 0.5 and 3.5 K km s^{-1}. The cyan dotted lines denote the extents of the three zoomed panels shown in Figure 2.2. The 32″ FWHM beam-size is shown by the white circle in the lower left corner.

and assuming $\beta = 2$) to the *Herschel* photometric measurements to derive H_2 column densities and dust temperatures across the observed fields. In this paper, we adopt the "high-resolution" (18.2″) H_2 column density map produced by Di Francesco et al., which was created using a multi-scale decomposition method outlined in Palmeirim et al. (2013). In addition, Di Francesco et al. (2019, in prep) used the multi-scale, multi-wavelength source extraction algorithm *getsources* (Men'shchikov et al., 2012) to identify dense cores and protostars throughout Cepheus. They classified cores depending on the likelihood they were gravitationally bound based on the ratio of their critical Bonnor-Ebert mass (Ebert, 1955; Bonnor, 1956) to their observed mass ($\alpha_{BE} = M_{BE,crit}/M_{obs}$), which provides an estimate for the virial state of a core in the absence of spectroscopically obtained velocity dispersion and gas temperature measurements. Cores with $\alpha_{BE} > 5$ are deemed gravitationally unbound and termed "starless," cores with $\alpha_{BE} \leq 5$ are classified as "prestellar candidate" cores that are likely to be gravitationally bound, while cores with $\alpha_{BE} \leq 2$ are coined "robust prestellar" cores that are most likely to be gravitationally bound. Such a core classification scheme depends heavily on whether or not the dust-derived temperatures are representative of the *gas* temperatures of structures and excludes any non-thermal motions that could support the structures against gravity. In this paper, we use

NH_3 data to determine whether or not these prestellar-classified cores are truly gravitationally bound structures. Such an analysis allows up to make a more informed interpretation of the relationship between the IMF and core mass function.

2.3 Analysis and Results

2.3.1 NH_3 Line Fitting

Although we detect NH_3 (1,1) and (2,2) emission throughout Cepheus-L1251, both of which are caused by the para-NH_3 species, we do not detect emission from the ortho-NH_3 species (e.g., the NH_3 (3,3) transition). Thus, we are unable to determine an ortho-to-para NH_3 ratio and must focus our analysis on the (1,1) and (2,2) para-NH_3 transitions. The GAS analysis pipeline[1] was used for data calibration, imaging, and NH_3 (1,1) and (2,2) line fitting. This pipeline, and the methods used in the GAS line-fitting procedure, are discussed in detail by Friesen et al. (2017). The GAS line-fitting pipeline simultaneously fits the NH_3 (1,1) and (2,2) lines pixel-by-pixel, assuming LTE and a single velocity component along the line-of-sight, to produce a set of best-fit parameter maps which includes kinetic gas temperature (T_K), excitation temperature (T_{ex}), para-NH_3 column density ($N_{para-NH_3}$), velocity dispersion (σ), and centroid velocity (V_{LSR}).

In this paper, we use the GAS analysis pipeline to fit all pixels in Cepheus-L1251 with signal-to-noise ratio (SNR) > 3 in the NH_3 (1,1) spectrum, where the SNR has been estimated from the peak emission channel and rms. The resulting best-fit parameter maps were used to calculate the kinematic and chemical properties of the structures presented in our analysis. All pixels with peak SNR ≤ 3 in the NH_3 (1,1) spectrum are not included in our analysis. We also exclude any pixels from our analysis that do not meet the following requirements: 5 K $< T_K <$ 30 K (outside this range, the NH_3 (1,1) and (2,2) lines cannot constrain T_K), 0.05 km s^{-1} $< \sigma <$ 2.0 km s^{-1}, -7 km s^{-1} $< V_{LSR} < -1$ km s^{-1}, $T_{K,err} < 5$ K, $\sigma_{err} < 2.0$ km s^{-1}, and $V_{LSR,err} <$ 1 km s^{-1}. For the para-NH_3 abundance analysis presented in § 3.6, we additionally require $T_{ex} < 30$ K and $T_{ex,err} < 5$ K since reliable abundance estimates are dependent upon accurate T_{ex} measurements. The final parameter maps used for the analyses are shown in Figures 2.2 (σ and V_{LSR}) and 2.3 (T_K and para-NH_3 abundance). Detailed analyses and discussions of these maps are presented in the following sections.

[1] available at http://gas.readthedocs.io/

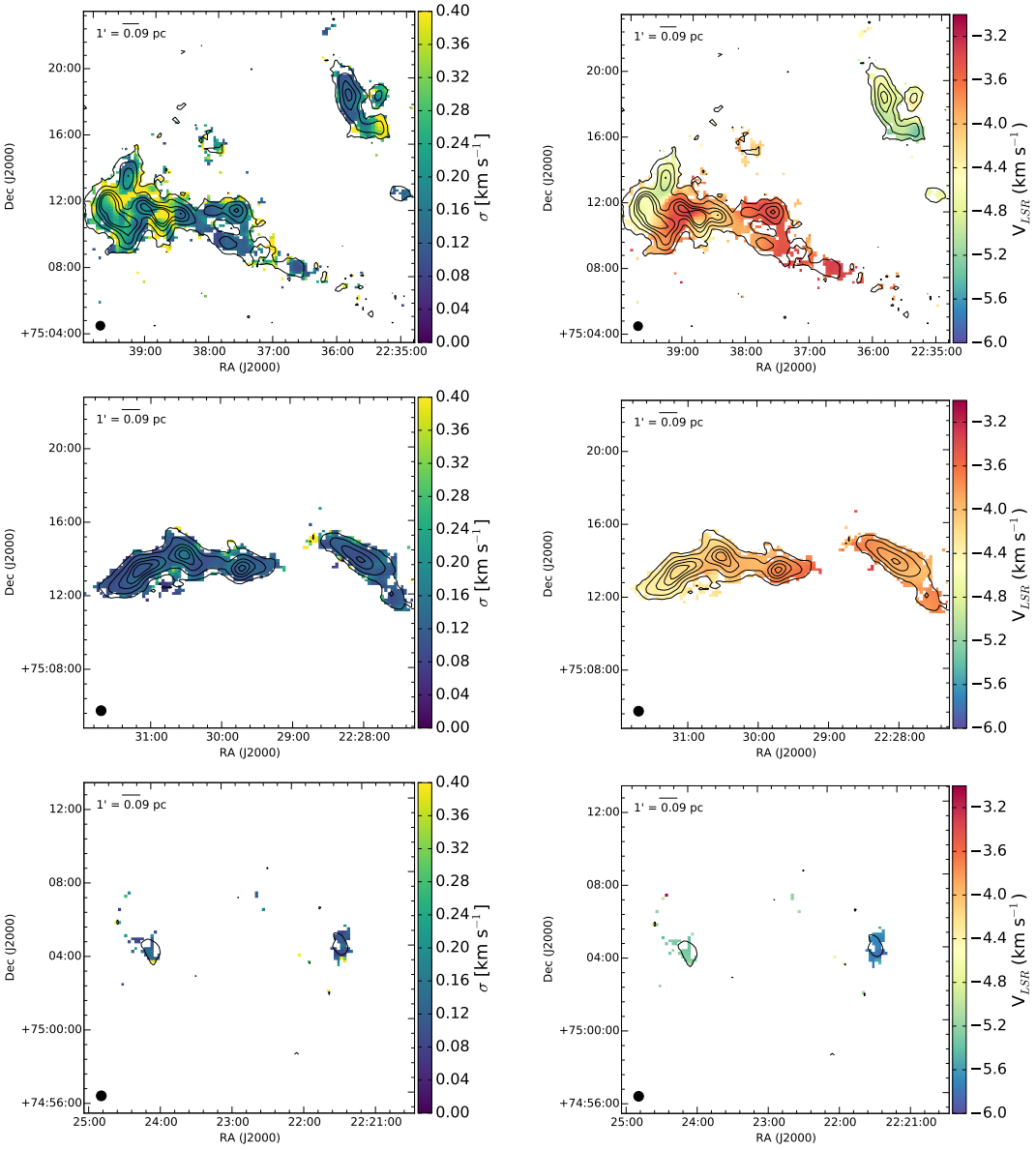

Fig. 2.2 – Velocity dispersion (left column) and centroid velocity (right column) of the NH_3 (1,1) emission from Cepheus-L1251. Black contours represent the NH_3 (1,1) integrated intensity at 0.5, 1.5, 3.5, 5.5, and 7.5 K km s^{-1}. The panels display the eastern (L1251E/B, top panel), central (L1251A, middle panel), and western (L1251C, bottom panel) portions of L1251. The 32″ FWHM beam-size is shown as a black circle in the lower left corner of each panel.

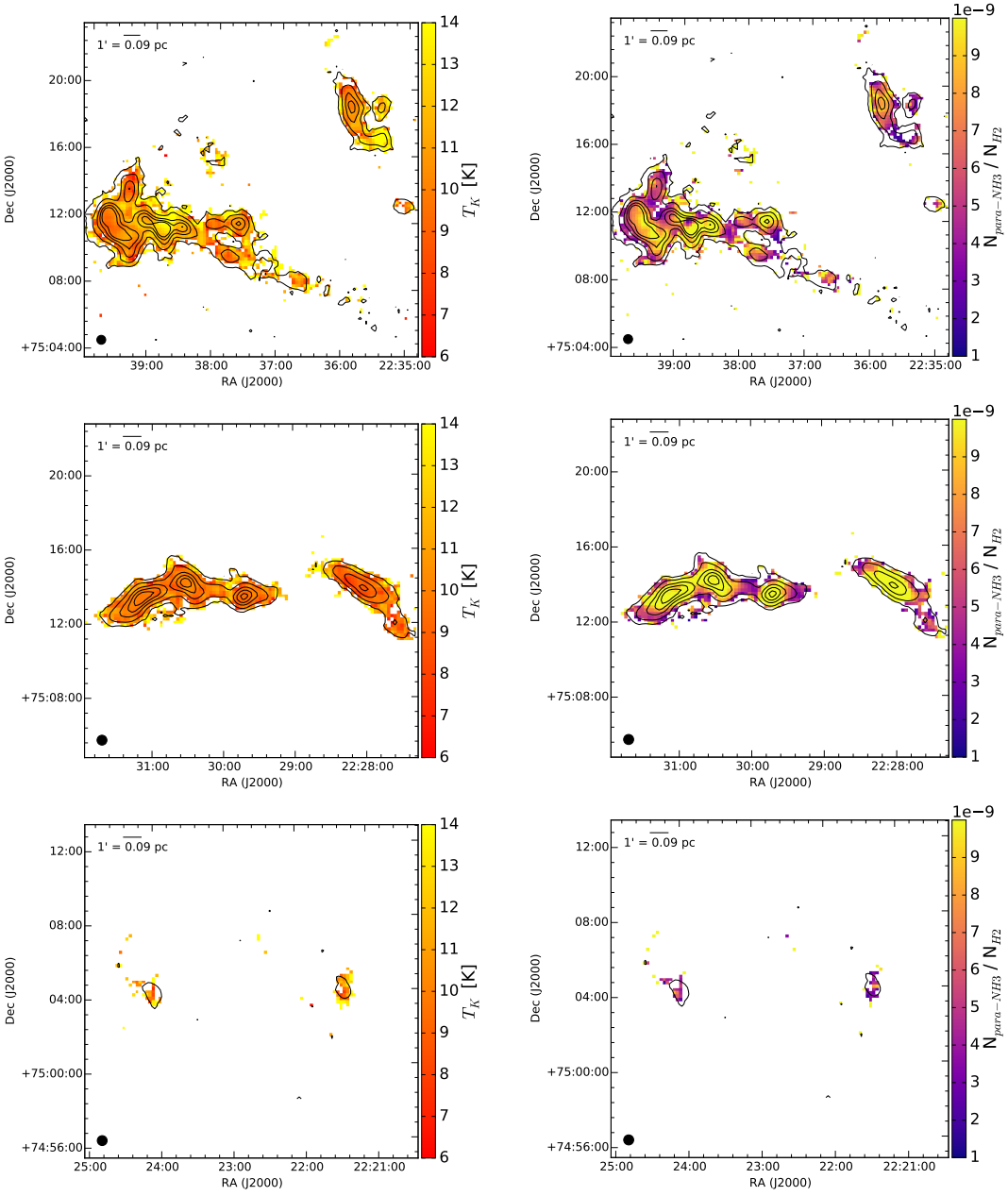

Fig. 2.3 – Same as Figure 2.2 but for kinetic temperature (left column) and para-NH_3 abundance (right column).

2.3.2 Dendrogram Structure-Finding

Although there exists a variety of methods for extracting structures from both 2D and 3D emission maps of molecular clouds, dendrograms capture the hierarchical nature of clouds better than most other extraction products. This is due to the dendrogram's basis on tree diagrams, which display the relationship between the various structures found within a map. The analysis begins by locating the emission peaks in a map, then proceeds by grouping the fainter surrounding pixels until two or more local maxima, i.e., *leaves*, contain adjoining pixels, at which point they merge at a *branch*. Fainter pixels are continually added to this merged structure until it is either merged with another local maximum, or reaches a user-defined noise threshold, at which point it becomes a *trunk*. A detailed description of dendrograms as a source extraction method is discussed in Rosolowsky et al. (2008). Throughout this paper, we use the term "parent" for structures that are either a branch or a trunk.

Due to the 18 hyperfine components of the NH_3 (1,1) line, running a dendrogram extraction algorithm on our NH_3 (1,1) data cube produces spurious identifications, as well as inaccurate source sizes and velocity dispersions. To circumvent this complication, we constructed a simulated Gaussian emission data cube based on the parameters obtained from the line-fitting procedure described in Section 2.3.1. Namely, a Gaussian spectrum was created for each pixel with SNR > 3 in the observed NH_3 (1,1) map. The Gaussian profile was scaled to each pixel's peak brightness temperature, centroid velocity, and velocity dispersion as measured in the NH_3 (1,1) map. Friesen et al. (2016) note that some error is introduced when using this method on spectra that contain multiple velocity components, for which our single component fit would produce skewed estimates for V_{LSR} and σ. Cepheus-L1251 is a relatively quiescent environment compared to the Serpens South region observed by Friesen et al. (2016), however, and our data show no signs of the multiple velocity components that they observed. Furthermore, Friesen et al. (2016) add the residual of their single velocity component fit of the NH_3 (1,1) emission back into their simulated Gaussian profile, which can lead to spurious sources being identified by the dendrogram when multiple velocity components are present. To circumvent this complication, in our analysis, random noise was added back into each simulated Gaussian spectrum with an rms equivalent to the rms measured for that pixel in the observed NH_3 (1,1) cube. We also mask out the edges of the map where rms noise levels were high in the original NH_3 (1,1) cube.

In this paper, we use the *astrodendro* package to identify hierarchical structures in our simulated Gaussian data cube. The input parameters for the dendrogram algorithm are: (1) `min_value`, the minimum threshold value to consider in the data cube (i.e., the lowest intensity a pixel can have to be joined to a structure). We chose to set `min_value` at 0.45 K, which is equivalent to 5 times the median rms noise. (2) `min_delta`, the minimum difference in brightness between two structures before they are merged into a single structure. We set `min_delta` to 0.18 K, or 2 times the median rms noise. (3) `min_npix`, the minimum number of pixels a structure must contain to remain independent. We set `min_npix` to 10, which reduces the number of noise spikes identified by the extraction. Our choices for the *astrodendro* input parameters follow the NH_3 structure-finding prescription outlined by Friesen et al. (2016), which based their parameter selections on standard recommendations for dendrogram-based source extraction (e.g., Rosolowsky et al., 2008).

The major and minor axes of sources identified in our dendrogram analysis are calculated by *astrodendro* based on the intensity weighted second moment in the direction of greatest elongation in the position-position (PP) plane. After completing source identification with *astrodendro*, we also require that the major and minor axes of all sources be larger than $6''$ in projection on the sky to be included in our final catalog. We note that the major and minor axes for many of the *astrodendro*-identified sources in this paper are much smaller than the full extent of their associated pixels on the PP plane. All of the structures with minor and major axes larger than $6''$, however, have total pixel areas larger than the area of the $32''$ GBT beam. Thus, our $6''$ major and minor axes cut successfully removes noise spikes while preserving real structures that are larger than the $32''$ beam-size of our GBT observations.

Imposing these parameters and selection criteria results in a dendrogram with 22 top-level "leaf" structures, nine mid-level "branches," and four low-level "trunks." Figure 2.4 displays the outlines of the leaves (green) and trunks (cyan) that were identified in the dendrogram overlaid onto the NH_3 (1,1) integrated intensity map. The integrated intensity map was created using the channels surrounding all five hyperfine groups of the NH_3 (1,1) emission. The dendrogram leaves highlight both the peaks in the integrated intensity map, as well as the highest H_2 column density portions of the cloud. Eight of the branches fall within the eastern L1251E/B trunk shown in the upper left panel of Figure 2.4, indicating the region is highly sub-structured and contains many pockets of dense gas potentially forming within a larger filamentary structure. The ninth branch is located in the larger trunk in the eastern

half of L1251A shown in the middle left panel of Figure 2.4. The full tree diagram for the identified sources is shown in the left panel of Figure 2.5. The highly substructured portion of L1251E/B begins at structure 30 in the diagram. Visual checks for all leaves were also completed, but no spurious sources were identified that also pass our selection criteria. Table 2.1 contains the full catalog of leaves identified in the dendrogram which also pass our selection criteria.

For each 3D structure, we obtain the mean R.A., Dec., major axis (σ_{major}), minor axis (σ_{minor}), and position angle (θ_{PA}) projected in the PP plane. Additionally, we define the projected effective radius of each structure as the geometric mean of the major and minor axes: R_{eff}=(σ_{major} σ_{minor})$^{1/2}$. We note that this effective radius is an upper limit because we have not applied any deconvolution to the measured sizes, which can be unstable when applied to dendrogram-identified objects (see Rosolowsky et al. 2008 for a discussion of this issue). As mentioned above, however, all structures have total areas much larger than the area of the 32″ GBT beam. Specifically, the median ± standard deviation for the ratio of the GBT beam area to the areas of the leaves is 0.22 ± 0.19. The low relative size of the beam compared to the size of the identified structures suggests that deconvolution would have a small effect on the structure sizes. Nevertheless, in Section 2.3.4 we show that lowering the effective radius for the dendrogram-identified structures does not alter their virial state. Moreover, in Appendix 2.7.1, we also demonstrate that using an alternative formulation for the effective radius, based on a structure's total surface area, increases their virial parameters by factors of a few but does not change the main conclusions of the virial analysis presented in this paper.

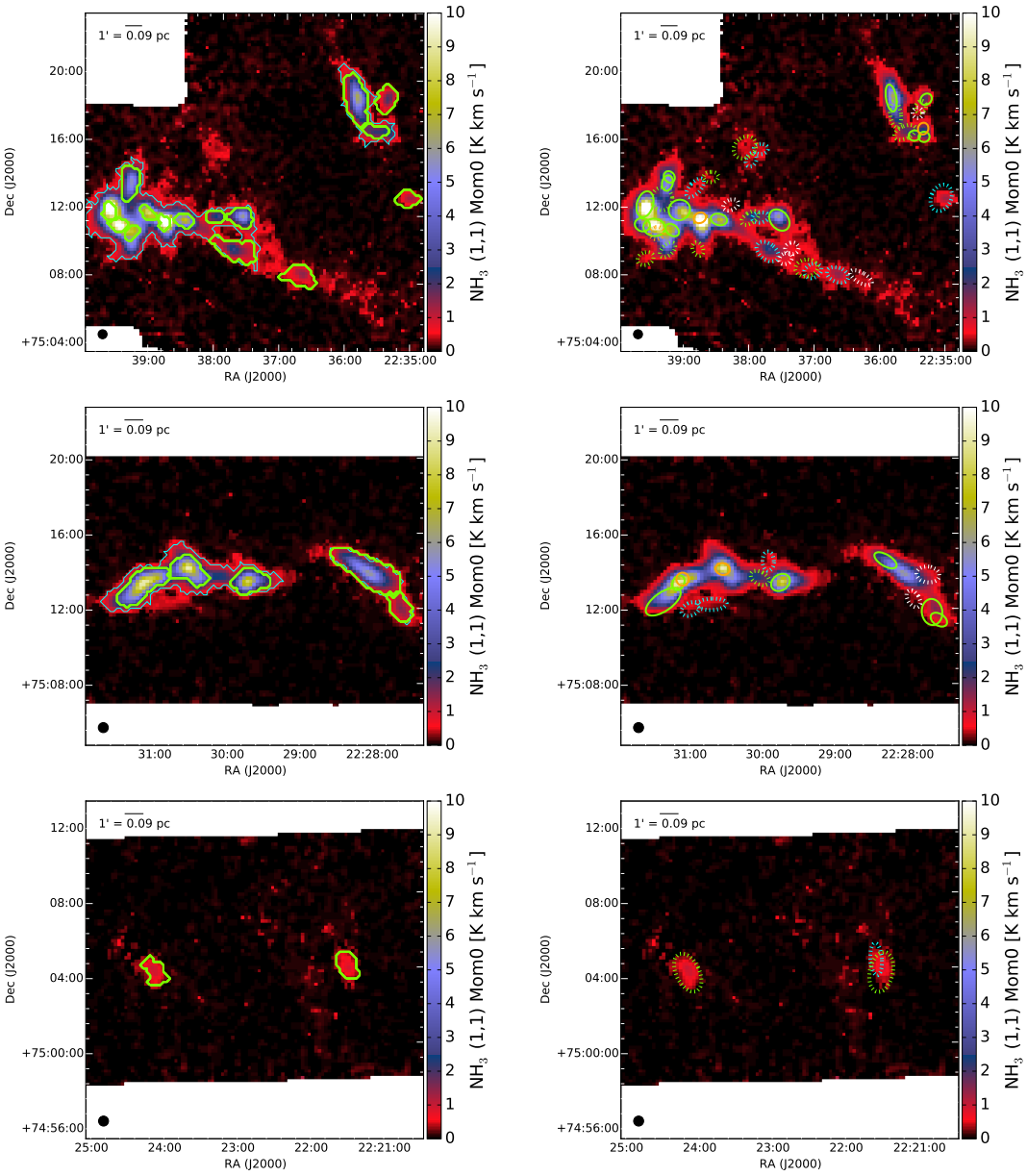

Fig. 2.4 – Left column: Top-level, "leaf" structures (outlined in green) identified from our dendrogram analysis of the NH_3 (1,1) emission from Cepheus-L1251. The background image is the NH_3 (1,1) integrated intensity map and the panels outline the same fields shown in Figure 2.2. The four lowest-level, "trunks" identified by the dendrogram are outlined in cyan. Right column: Positions of *Herschel*-identified dense cores that have reliable kinematic measurements (see text). Each ellipse represents twice the FWHM for the source. Robust prestellar cores are shown in green, prestellar candidate cores in cyan, starless cores in white, and protostellar cores in orange. Structures with $\alpha_{vir} < 2$ are shown in solid lines, while those with $\alpha_{vir} \geq 2$ are shown by dotted lines.

Figure 2.5 plots effective radius versus aspect ratio ($\sigma_{major}/\sigma_{minor}$) for the leaves and parent structures identified in the dendrogram. The parent structures tend to have larger aspect ratios (median $\sigma_{major}/\sigma_{minor} = 2.7 \pm 0.6$) than the leaves (median $\sigma_{major}/\sigma_{minor} = 1.7 \pm 0.5$), likely a result of the tendency of dense gas to lie along filamentary structures within the cloud (Friesen et al., 2016).

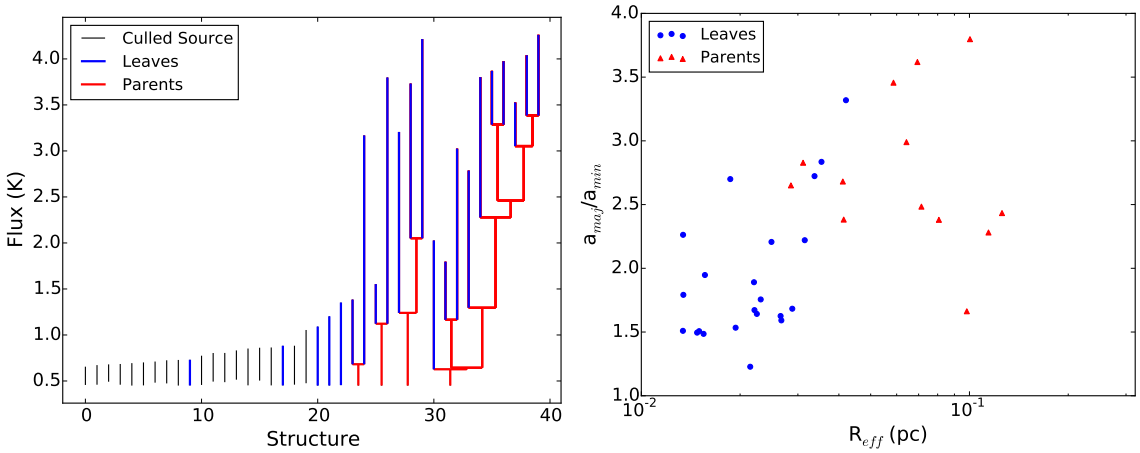

Fig. 2.5 – Left panel: Dendrogram tree identified for our ammonia observations of Cepheus-L1251. Black denotes sources that have major and minor axes smaller than 6″ in projection on the sky and were not included in our analysis. Blue and red show the "leaf" and "parent" structures, respectively, that are larger than 6″ and were included in our analysis. Right panel: Effective radius versus aspect ratio for the leaves (blue dots) and parents (red triangles) shown in the left panel. The parent structures include both the "branches" and "trunks" in the dendrogram.

2.3.3 Source Masses

We estimate the masses of the ammonia-identified structures based on their corresponding H_2 column density as measured by *Herschel* dust continuum observations of Cepheus (Di Francesco et al., 2019, in prep). Each source's 2D mask, based on its projection onto the PP plane, is used to define the region over which pixels in the H_2 column density map (convolved from a resolution of 18.2″ to 32″ to match the beam-size of the NH_3 observations) are integrated and converted to mass. We assume a distance of 300 pc to Cepheus-L1251 and a mean molecular weight per hydrogen molecule (μ_H) of 2.8 (see, e.g., Appendix A in Kauffmann et al., 2008). Figure 2.6 shows source effective radius versus mass for the leaves and parents identified in our dendrogram analysis. The structures have a range in mass from 0.9 $M_\odot$ for the small-

est top-level structure to 80 $M_\odot$ for the largest parent structure. A power-law fit to the data produces a best-fit slope of 1.94 ± 0.18, where the uncertainty on the slope has been estimated from the square-root of the diagonal term of the covariance matrix from the total least squares curve-fitting method. This slope is consistent with the Larson (1981) $M \propto R^2$ relation. In Appendix 2.7.2, we show that determining the masses of the ammonia-identified leaves based on continuum maps that have been spatially filtered to remove emission from large-scale structures has little impact on their calculated virial parameters.

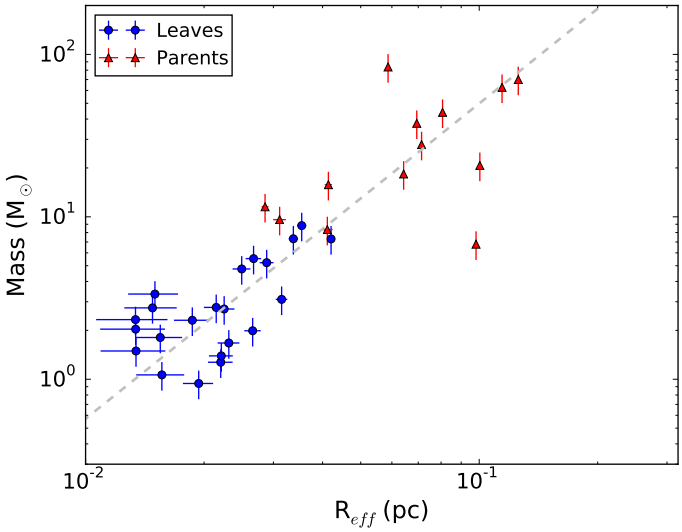

Fig. 2.6 – Effective radius versus observed mass for the same structures as in Figure 2.5. The dashed line is a power-law fit to the combined leaf and parent data points. The best-fit slope is found to be 1.94 ± 0.18. Errorbars in the y-axis direction indicate 20% uncertainty on the H_2 column densities used to calculate mass. Errorbars in the x-axis direction represent $\sqrt{A_{pix}/\pi N_{pix}}$, where A_{pix} is the area of a pixel in the NH_3 (1,1) emission map and N_{pix} is the number of pixels falling within the structure.

2.3.4 Virial Analysis

Ammonia-identified Structures

The stability of our ammonia-identified structures can be estimated from a virial analysis. Neglecting external pressure and magnetic fields, the virial parameter (α_{vir}) can be used to determine whether a cloud structure is gravitationally bound or unbound. We follow the virial analysis method outlined in Friesen et al. (2016) and define the virial mass as:

$$M_{vir} = \frac{5\sigma^2 R}{aG} \tag{2.1}$$

where σ is the velocity dispersion of the core, R is the core radius (which we set to be R_{eff}), G is the gravitational constant, and

$$a = \frac{1 - k/3}{1 - 2k/5} \tag{2.2}$$

is a term which accounts for the radial power-law density profile of a core, where $\rho(r) \propto r^{-k}$ (Bertoldi & McKee, 1992). We note that recent virial analyses by Pattle et al. (2017) and Kirk et al. (2017) assume a spherically symmetric Gaussian density distribution (derived in Pattle (2016), for reference). For such a distribution, Equation 2.2 instead becomes $a = 5/6\sqrt{\pi} \sim 0.47$. In the virial analysis we present here, we adopt Equation 2.2 with $k = 1.5$ (thus, $a = 1.25$) as the assumed density profile of the observed structures to be consistent with Friesen et al. (2016). In the analysis presented in Section 2.4.2, in which we add pressure to the virial equation as was done by Pattle et al. (2017) and Kirk et al. (2017), we assume a Gaussian density distribution. For both virial analyses presented in this paper, however, we also show the effect that using the alternative density profile would have on the calculated virial parameters.

Both the thermal and non-thermal components of the velocity dispersion for a particle of mean mass are included in σ. Using the parameter maps obtained from the NH_3 line fitting mentioned in Section 2.3.1, we calculate σ as

$$\sigma^2 = \sigma_v^2 - \frac{k_B T}{m_{NH_3}} + \frac{k_B T}{\mu_p m_H} \tag{2.3}$$

where k_B is Boltzmann's constant, m_{NH_3} is the molecular mass of NH_3, m_H is the atomic mass of hydrogen, and μ_p is the mean molecular mass of interstellar gas (2.33; see, e.g., Appendix A in Kauffmann et al., 2008). σ_v is found by first creating a 2D mask from each 3D structure's projection onto the PP plane. This mask is then overlaid onto the velocity dispersion map created from the line fitting procedure of Section 2.3.1. All pixels in the velocity dispersion map falling within the mask are used to calculate an average velocity dispersion for the structure, weighted by the NH_3 (1,1) integrated intensity maps, which is used as σ_v in Equation 2.3. The same procedure is followed to obtain an average T_K value for each structure, which is used for T in Equation 2.3.

The virial parameter, α_{vir}, is defined as $\alpha_{vir} = M_{vir}/M$, where M_{vir} is given in Equation 2.1 and M is the observed mass for the structure found using the method described in Section 2.3.3. For $\alpha_{vir} \geq 2$, gas motions alone are presumed to be strong enough to prevent gravitational collapse. For $\alpha_{vir} < 2$, without the presence of magnetic pressure, structures are unable to provide support against gravitational collapse. Since the virial parameter assumes spherical symmetry, we only calculate α_{vir} for structures with aspect ratios less than 2. The top panel of Figure 2.7 displays the observed mass versus measured virial parameter for all the leaves identified in our ammonia dendrogram analysis that pass this aspect ratio criterion. We find that all the ammonia structures sit below $\alpha_{vir} = 2$, suggesting they are gravitationally bound structures when magnetic pressure is not considered and a power-law density profile is assumed for the structures.

The dotted horizontal line in Figure 2.7 shows where $\alpha_{vir} = 1$ would be located if we assume a Gaussian density profile for the structures rather than a power-law density profile. Using this alternative density profile assumption and $\alpha_{vir} = 1$ as the virial stability threshold, only two of the leaves are bound by gravity. While this change in the virial state of the ammonia-identified structures between the two sets of assumptions highlights the large uncertainties in virial parameter estimations, it may also indicate that the leaves are currently at or near a state of virial equilibrium (see Sections 2.4.1 and 2.4.2 for further evidence of this scenario).

Herschel-identified Dense Cores

In addition to our virial analysis of the ammonia structures identified in this paper, we also derive virial parameters for the *Herschel*-identified dense cores in the Cepheus-L1251 region that were originally identified by Di Francesco et al. (2019, in prep). We treat these *Herschel*-identified dense cores as a separate set of structures because they were identified using higher-resolution observations (18.2″ FWHM at 250 μm) and a different source extraction algorithm than the ammonia-identified structures. The Di Francesco et al. catalog features 187 dense cores identified by the *getsources* (Men'shchikov et al., 2012) extraction algorithm within the Cepheus-L1251 region as part of the *Herschel* Gould Belt Survey. Each core in the Di Francesco et al. catalog is classified as either "protostellar," "starless," "prestellar candidate," or "robust prestellar" (see Section 2.2.2 for a discussion of this classification scheme). The "prestellar candidate" and "robust prestellar" cores are thought to be gravitationally

bound and likely to form stars in the future due to their higher critical Bonnor-Ebert mass ratio ($\alpha_{BE} = M_{BE,crit}/M_{obs}$), which is an appropriate substitute for the virial mass ratio in the absence of spectroscopic information. The critical Bonnor-Ebert mass (Bonnor, 1956) is given by

$$M_{BE,crit} = \frac{2.4 c_s^2 R}{G} \tag{2.4}$$

where c_s is the isothermal sound speed, R is the radius, and G is the gravitational constant. Thus, dense cores with $\alpha_{BE} < 2$ should likely have $\alpha_{vir} \lesssim 2$ in the absence of magnetic pressure.

To test whether or not the *Herschel*-identified cores are truly "prestellar," we use the R.A., Dec., major FWHM, minor FWHM, and position angle provided for each source in the Di Francesco et al. catalog to construct elliptical, 2D masks. We follow the method adopted by Kirk et al. (2017) and set the outline of the mask to be twice the size of the core's FWHM ellipse (i.e., the full extent of the structure), as measured in the *Herschel* H_2 column density map. If the core's ellipse falls within the area mapped in NH_3 (1,1) and (2,2) by GAS, and at least one-fourth of the pixels in the 2D mask contain reliable fits to the NH_3 (1,1) and (2,2) spectra, we use its 2D mask to obtain mean values for σ_v and T_K, weighted by the NH_3 (1,1) integrated intensity map. This criterion eliminates 87 of 94 "starless" cores, 28 of 40 "prestellar candidate" cores, 9 of 42 "robust prestellar" cores, and 6 of 11 "protostellar" cores from the analysis. The "starless" dense cores are preferentially eliminated due to their lower H_2 column densities, where NH_3 (2,2) emission was rarely detected, and thus did not produce reliable fits during our line-fitting procedure. The right column of Figure 2.4 shows the outlines of the 2D elliptical masks used for the *Herschel*-identified cores that match our selection criteria overlaid onto the NH_3 (1,1) integrated intensity map. In many cases, the NH_3-identified structures are consistent with the positions of *Herschel*-identified cores. The higher spatial resolution of the *Herschel* observations, as well as the different source extraction algorithm used for the *Herschel*-identified sources, leads to two or more *Herschel*-identified cores being identified within several of the NH_3 leaves.

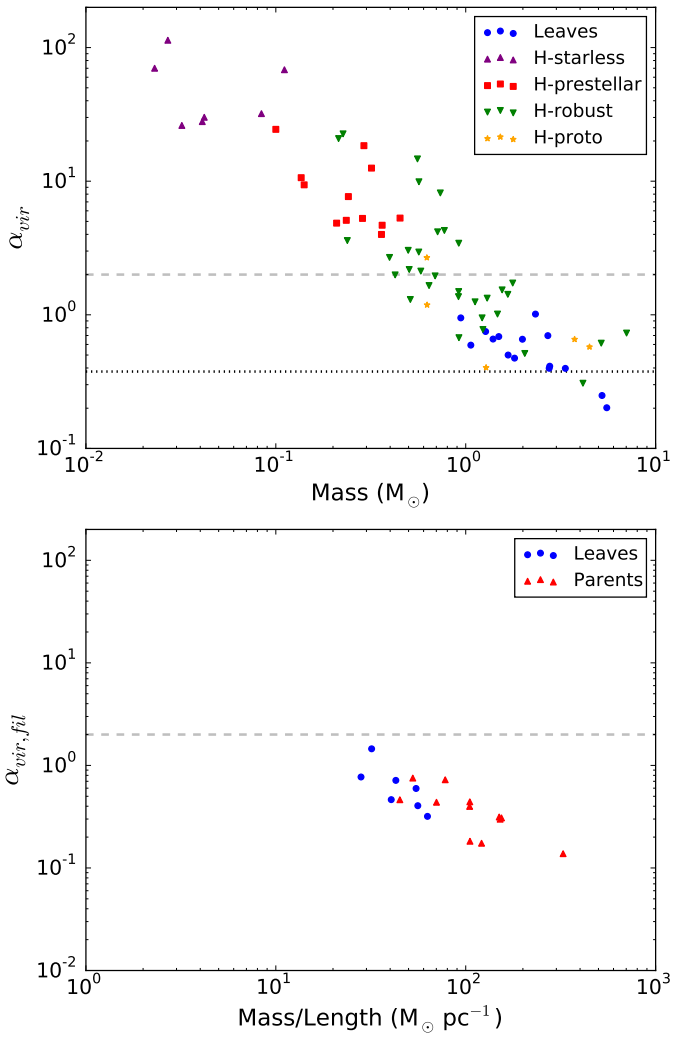

Fig. 2.7 – Top: Virial parameter, α_{vir}, versus observed mass for the NH_3 (1,1) top-level structures identified in our dendrogram analysis (blue), as well as the *Herschel*-identified "starless" (purple), "prestellar candidate" (red), "robust prestellar" (green), and "protostellar" (orange) dense cores from Di Francesco et al. (2019, in prep). The dashed line denotes $\alpha_{vir} = 2$, above which structures are gravitationally unbound in the absence of magnetic pressure and assuming a power-law density profile for the structures. The dotted line represents where $\alpha_{vir} = 1$ would occur if a Gaussian density profile is assumed for the structures (for reference, this line is consistent with the vertical dotted line shown in the left panel of Figure 2.10). Bottom: Filamentary virial parameter, $\alpha_{vir,fil}$, versus mass per unit length for the structures identified in our dendrogram analysis with $a_{maj}/a_{min} \geq 2$. Blue denotes top-level, leaf structures. Red signifies lower-level, parent structures within which the leaves reside.

The intensity-weighted mean values of σ_v and T_K, along with the SED-derived mass and deconvolved R_{eff} quoted in the Di Francesco et al. catalog for each core, are used to derive the virial parameter for each source using the same method described above for the ammonia-identified structures. We note that the mass and effective radius used for the *Herschel*-identified cores in the virial analysis presented in this paper are the same values used by Di Francesco et al. to determine the critical Bonnor-Ebert classification of the cores. The R_{eff} of the *Herschel*-identified cores have a mean and standard deviation of 0.029 ± 0.014 pc, which is consistent with the R_{eff} of the ammonia-identified leaves ($R_{eff,mean} = 0.023 \pm 0.008$ pc). In Appendix 2.7.1, we show that using the surface area of the *Herschel*-identified cores to determine their effective radius increases their virial parameters by factors of a few. Similarly, in Appendix 2.7.2, we show that the virial parameters for the *Herschel*-identified dense cores are significantly lower when their observed mass is calculated by summing all the pixels in the *Herschel*-derived H_2 column density map that fall within their elliptical mask. These lower virial parameters are driven by the larger core masses measured directly from the H_2 column density map, which includes large-scale structure that was filtered out by the *getsources* extraction algorithm prior to the original mass estimate for the *Herschel*-identified cores.

The top panel of Figure 2.7 displays the observed mass versus virial parameter for the *Herschel*-identified cores overlaid atop the results for the ammonia-identified structures. All of the "starless" and "prestellar candidate" cores have $\alpha_{vir} \gtrsim 4$, while the "robust prestellar" cores are split almost evenly above and below $\alpha_{vir} = 2$. When assuming a Gaussian density profile for the structures and setting $\alpha_{vir} = 1$ as the virial stability threshold, only one *Herschel*-identified core is gravitationally bound. This result suggests that many of the *Herschel*-identified cores that have been deemed "prestellar" based on a critical Bonnor-Ebert sphere analysis, may actually be gravitationally unbound structures. Additionally, the cores with $\alpha_{vir} < 2$ tend to be located over the brightest NH_3 (1,1) emission. The right column of Figure 2.4 shows the *Herschel*-identified cores that have $\alpha_{vir} < 2$ as solid ellipses and those with $\alpha_{vir} \geq 2$ as dotted ellipses. None of the cores with $\alpha_{vir} < 2$ correspond to regions that contain the lowest detectable levels of NH_3 (1,1) emission.

2.3.5 Elongated Structure Virial Parameter

The aforementioned virial analysis assumes spherical symmetry for structures. This assumption means elongated and filamentary structures must be analyzed independently to reduce the risk of misrepresenting their virial parameters. Thus, we use instead the mass per unit length of the ammonia-identified leaves and parents with aspect ratios ≥ 2 to calculate a filament virial parameter, $\alpha_{vir,fil}$. We define the filament virial mass per unit length as (Fiege & Pudritz, 2000)

$$m_{vir,fil} = \frac{2\sigma^2}{G} \ , \tag{2.5}$$

where the velocity dispersion, σ, is calculated from Equation 2.3 using the same method described in Section 2.3.4. We obtain the observed mass, M, for the structures in the same way described in Section 2.3.3. The length of the structures, L, is set to twice the FWHM of its major axis:

$$L = 2\sqrt{2\ln 2}\ \sigma_{major} \ . \tag{2.6}$$

The filament virial parameter then becomes $\alpha_{vir,fil} = m_{vir,fil}/(M/L)$. In the bottom panel of Figure 2.7, we plot M/L versus $\alpha_{vir,fil}$ for all leaves and parent structures with aspect ratios ≥ 2. All such structures fall below $\alpha_{vir,fil} = 2$. The high spatial correlation of dense cores with the positions of filamentary structures in dust continuum observations (e.g., Könyves et al., 2015), combined with the larger prevalence of elongated structures being gravitationally bound, provides further evidence in support of star formation being driven by the gravitational collapse and fragmentation of filaments within molecular clouds.

It should be noted that while dendrograms are viable options for uncovering hierarchies of related structures, they are not optimized for detecting elongated, filamentary structures. While the structures we include in our elongated structure analysis do indeed have large aspect ratios, they are not necessarily the parsec-length filamentary networks found in dust continuum observations of star-forming regions by dedicated filament-finding algorithms (Könyves et al., 2015). As a result, we are likely excluding a large number of filaments in our analysis, particularly those at low surface brightness that the dendrogram has excluded from the hierarchy tree.

2.3.6 Source Temperatures and Column Densities

Along with the kinematics of the ammonia-identified structures and *Herschel*-identified dense cores, we also compare their temperatures and column densities. Our NH_3 (1,1) and (2,2) line fitting procedure produces T_K and NH_3 column density ($N_{para-NH_3}$) maps over the portion of Cepheus-L1251 mapped by our GBT observations. We also utilize the T_{dust} and H_2 column density maps derived by Di Francesco et al. (2019, in prep) for the entire Cepheus-L1251 cloud. These maps were convolved and re-gridded to match the resolution and pixel scale of the NH_3 observations, allowing a pixel-by-pixel comparison between the NH_3 and dust continuum measurements.

Figure 2.8 shows a scatter plot of T_{dust} versus T_K for all pixels that fall within either an ammonia-identified leaf or *Herschel*-identified core. A Gaussian kernel density estimate of the data is also shown as a background colorscale in Figure 2.8. Despite many of the pixels falling within a small range of temperatures and a large amount of scatter, a slight positive correlation does exist between the two temperature measurements. The distributions of T_{dust} and T_K have median $\pm$ standard deviation values of 11.7 $\pm$ 1.1 K and 10.3 $\pm$ 2.0 K, respectively. The side histograms in Figure 2.8 show temperature distributions for all pixels falling within the individual structure categories (i.e., the ammonia-identified leaves and the *Herschel*-identified dense core sub-categories). The overall median values appear to be representative of each individual structure type, considering all the sub-categories show similar distributions of T_{dust} and T_K. These results suggest the dust and gas in the structures is likely coupled, which is predicted to occur at H_2 volume densities $n(H_2) > 10^{4.5}$ (Goldsmith, 2001). The slightly higher (but not significant) median T_{dust} value may be caused by heated material on the outskirts of the cloud which falls along the line of sight to the observed structures. The kinetic temperatures, derived from the dense gas emission originating in the center of the cloud, are less affected by the warmer outer layers of the cloud, which may explain the lower median T_K value.

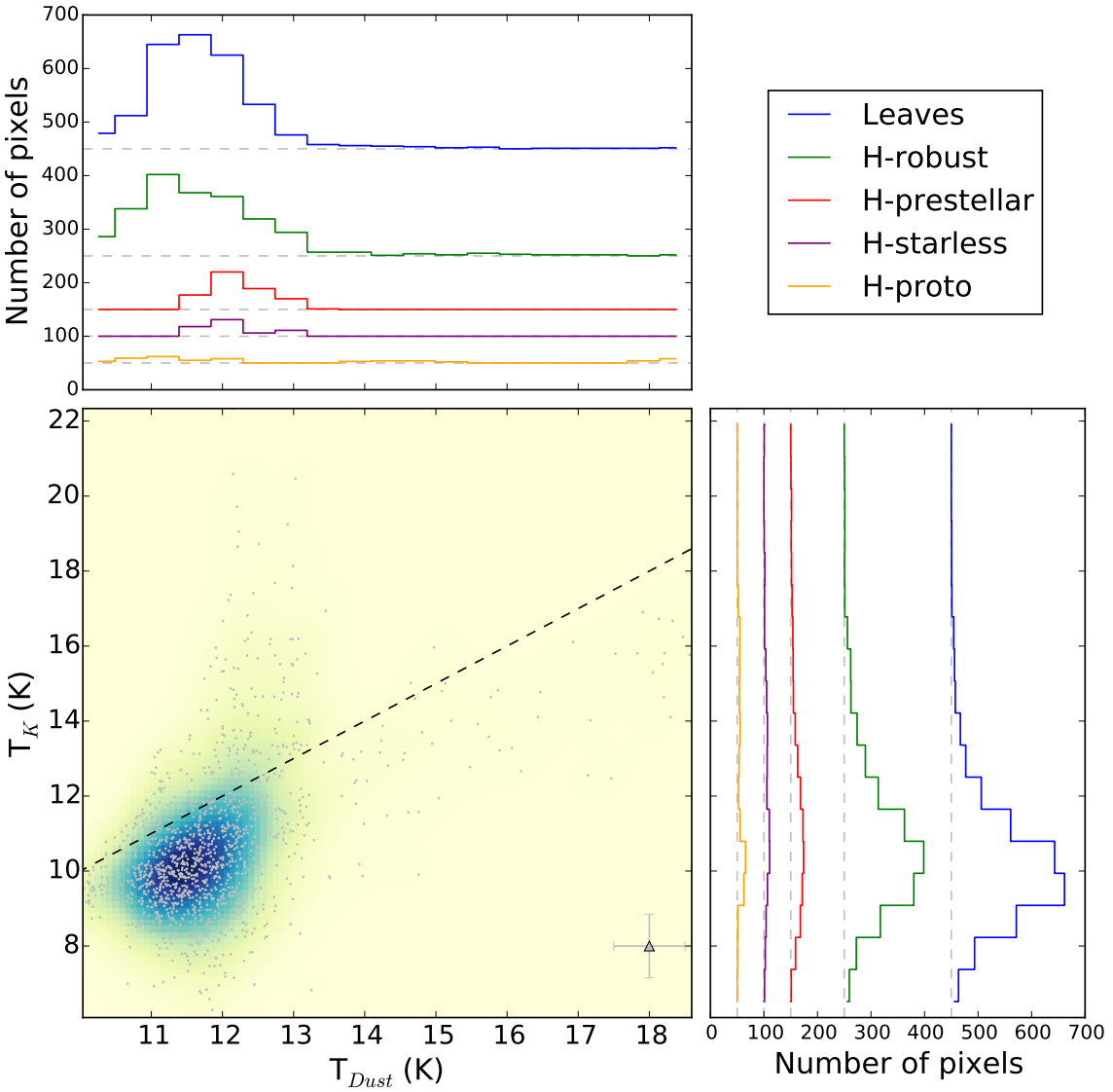

Fig. 2.8 – Dust versus kinetic temperature for all pixels that fall within the 2D mask of either a *Herschel*-identified dense core or ammonia-identified leaf. The background colorscale represents a Gaussian kernel density estimate of the actual measurements, which are shown as grey dots. Typical errorbars for the data are shown in the bottom right corner and the black dashed line shows the 1:1 line between the two parameters. The histograms show the distributions of T_K (right) and T_{dust} (top) for the pixels that fall within each structure type (ammonia-identified leaves in blue, *Herschel* robust prestellar cores in green, prestellar candidates in red, starless cores in purple, and protostellar cores in orange). The orange, purple, red, green, and blue histograms are offset from the zero position on the y-axis by 50, 100, 150, 250, and 450, respectively. The dashed grey lines beneath each histogram represent the y=0 position for the distribution.

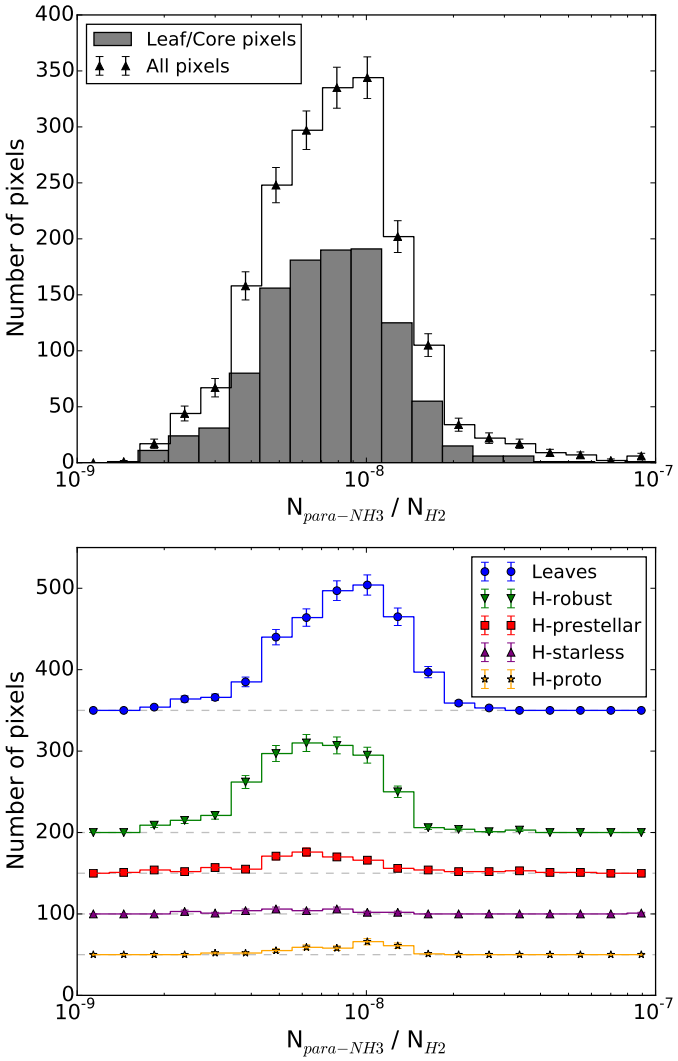

Fig. 2.9 – Top: Histogram of para-NH_3 abundance ($N_{para-NH3}$ / N_{H2}) for all pixels with reliable kinematic measurements (black line) and all pixels that fall within either an ammonia-identified leaf or *Herschel*-identified dense core (grey bars). Bottom: Histograms of para-NH_3 abundance for all pixels falling within each structure type (colors represent the same structures as those shown in Figure 2.8). The orange, purple, red, green, and blue histograms are offset from the zero position on the y-axis by 50, 100, 150, 200, and 350, respectively. The dashed grey lines represent the y=0 position for each histogram.

The abundance of para-NH_3 is defined as $\chi_{NH_3} = (N_{para-NH_3}/N_{H_2})$. We divide the $N_{para-NH_3}$ map presented in this paper by the Di Francesco et al. (2019, in prep) *Herschel*-derived H_2 column density map to obtain a map of χ_{NH_3} (shown in the right column of Figure 2.3). Figure 2.9 shows a histogram of χ_{NH_3} for all pixels in the $N_{para-NH_3}$ map (shown as a black line) along with a similar histogram for only the pixels which fall within either an ammonia-identified leaf or *Herschel*-identified dense core (grey bars). Both distributions peak at $\chi_{NH_3} \sim 10^{-8}$ and have a range between $\chi_{NH_3} \sim 10^{-9} - 10^{-7}$. Assuming a typical ortho-to-para ratio of 1:1 for NH_3, this abundance range is consistent with measurements of the *total* NH_3 abundance observed in other nearby star-forming environments, which is generally found to be between $\sim 10^{-9}$ and $\sim 10^{-8}$ (Hotzel et al., 2001; Tafalla et al., 2006; Crapsi et al., 2007; Friesen et al., 2009; Battersby et al., 2014) but has been found to be as low as 7×10^{-10} in B68 (Di Francesco et al., 2002) and as high as a few times 10^{-7} in Serpens South (Levshakov et al., 2013) and infrared dark clouds (Ragan et al., 2011). The bottom panel of Figure 2.9 plots χ_{NH_3} histograms for each sub-category of structures included in our analysis. No significant shifts in abundance are observed for any of the structure categories.

2.4 Discussion

2.4.1 Comparison with Serpens South Virial Analysis

For comparative purposes, we modeled our virial analysis on the methodology adopted by Friesen et al. (2016), who analyzed dendrogram-identified NH_3 structures in the Serpens South region. Cepheus-L1251 and Serpens South provide an interesting comparison because they have similar total masses ($\sim 700 - 800$ $M_\odot$), yet the latter is a much more clustered star-forming environment with higher H_2 column densities than the former. Nevertheless, similar to our results in Cepheus-L1251, Friesen et al. (2016) found that nearly all of the ammonia-identified structures (both leaves and parents) in Serpens South had $\alpha_{vir} < 2$. Friesen et al. (2016) also found that the elongated, filamentary structures in their sample had the lowest virial parameters and the region's magnetic field is unable to provide sufficient support to prevent their gravitational collapse. This result lends credence to the radial infall motions observed both along and onto the main filament in Serpens South (Friesen et al., 2013; Kirk et al., 2013a). Despite the lack of large-scale magnetic field measurements in Cepheus, our virial analysis of L1251, which also showed that nearly all the ammonia-identified

structures in the region are gravitationally bound when magnetic pressure is neglected and a power-law density profile is assumed for the structures, matches the results of Friesen et al. (2016).

The similarity in virial parameters for structures in Serpens South and Cepheus-L1251 is an intriguing result, especially when considering the two clouds constitute drastically different star-forming environments. For instance, Serpens South resides in the Aquila Rift cloud complex, which Könyves et al. (2015) showed had an H_2 column density PDF peak (i.e., the most common column density in the region) of $4-5\times10^{21}$ cm^{-2}. In contrast, Di Francesco et al. (2019, in prep) found that Cepheus has a comparatively much lower amount of material at high column density, with an H_2 column density PDF peak of only $\sim 1\times10^{21}$ cm^{-2}. Furthermore, Serpens South has a higher average gas mass surface density compared to Cepheus-L1251. We use the *Herschel* H_2 column density maps derived by Könyves et al. (2015) for Serpens South and by Di Francesco et al. (2019, in prep) for Cepheus-L1251 to derive total masses for the two clouds. In a 0.1 square degree area centered on Serpens South, we find its mass to be ~ 800 M$_\odot$ assuming a distance of 260 pc (Straižys et al., 2003). Alternatively, if we adopt the more recently measured distance of 430 pc to Serpens South (Dzib et al., 2011; Ortiz-León et al., 2017), its total mass becomes ~ 2200 M$_\odot$. Assuming a distance of 300 pc for Cepheus-L1251 and using the 0.36 square degree area observed for our NH_3 observations, we find its total mass to be ~ 680 M$_\odot$. We convert these values to mass surface densities and find $\Sigma \sim 370$ M$_\odot$ pc^{-2} for Serpens South and ~ 70 M$_\odot$ pc^{-2} for Cepheus-L1251. Even if we calculate the mass within a 0.1 square degree box centered on L1251E/B, the most active and clustered portion of L1251, we find $\Sigma \sim 100$ M$_\odot$ pc^{-2}. Thus, independent of the cloud-scale environment, it appears that dense ammonia structures are gravitationally bound when magnetic pressure is not considered and a power-law density distribution is assumed for the structures.

An additional, noteworthy difference between Serpens South and Cepheus-L1251 is the *number* of gravitationally bound NH_3 structures in each cloud. Friesen et al. (2016) found 85 NH_3 leaves in Serpens South compared to the 22 leaves we identify in Cepheus-L1251 over a larger area. Similarly, Serpens South has a higher amount of YSOs compared to Cepheus-L1251. We use the Dunham et al. (2015) YSO catalog, which includes Class 0−III sources identified by the *Spitzer* "cores-to-disks" and "Gould Belt" Legacy surveys, to determine the number of protostars within each region. We find that 133 Class 0−III sources fall within the 0.1 square degree area

in Serpens South used above to calculate the cloud's mass, while Cepheus-L1251 contains only 36 Class 0−III sources within the 0.36 square degree area observed for our NH_3 observations. These discrepancies show that Serpens South is producing both gravitationally bound structures and protostars at a higher rate than Cepheus-L1251. This production difference may be linked to the clustered star-forming environment that is found in Serpens South, which is likely more efficient at funneling gas onto forming dense cores than the more isolated environs of Cepheus-L1251. While stars and dense cores are still being formed in Cepheus-L1251, its lower overall column densities might be preventing a higher rate of dense core and protostar production.

Yet another dissimilarity between Serpens South and Cepheus-L1251 is the alignment between their NH_3 leaves and *Herschel* cores. For instance, 75 of the 85 NH_3 leaves ($\sim 88\%$) in Serpens South were found to have a *Herschel* core counterpart with a center within one R_{eff} of the leaf center. In Cepheus-L1251, the same matching criterion reveals that only 4 of its 22 NH_3 leaves ($\sim 18\%$) have a *Herschel* core counterpart. Even when using $32''$ (the FWHM beam-size of the NH_3 observations) as the maximum angular offset for the cross-match, which is larger than the R_{eff} of all sources, only 13 of 22 NH_3 leaves ($\sim 60\%$) in Cepheus-L1251 have a matched *Herschel* core. In either case, the higher ratio of ammonia leaves that contain continuum counterparts observed in Serpens South may be due to its highly clustered environment. Alternatively, chemical effects related to higher density could be causing the continuum in Serpens South to be a better probe of NH_3 gas when compared with Cepheus-L1251.

Despite their different levels of correspondence between dense gas and continuum structures, the NH_3 in both Serpens South and Cepheus-L1251 is tracing a higher fraction of prestellar and protostellar cores than the continuum. Namely, the *Herschel* core counterpart for 66 of the 75 matched NH_3 leaves (88%) in Serpens South were classified as either prestellar or protostellar. Likewise, all 13 of the matched NH_3 leaves in Cepheus-L1251 had either a prestellar or protostellar counterpart. This result provides further evidence that ammonia is predominately tracing dense, gravitationally bound structures regardless of cloud-scale environment.

2.4.2 Role of External Pressure

Although the virial analysis presented in this paper has shown the gravitational boundedness of structures in L1251, we have not yet considered the role of external

pressure by the ambient cloud. Seo et al. (2015) combined CO and NH_3 observations to show that the majority of NH_3 dendrogram-identified leaves in Taurus B211/213 that were unbound gravitationally are confined by the external pressure exerted by the filaments and clouds within which the leaves reside. Similarly, Pattle et al. (2017) combined ^{13}CO observations with a JCMT GBS-identified dense core catalog for several Cepheus Flare regions (including L1251) and determined that the majority of Cepheus dense cores are pressure-confined rather than gravitationally bound. Our virial analysis for L1251, which was able to incorporate the internal line widths of structures that the Pattle et al. (2017) analysis lacked, supports their result since we have shown that the *Herschel*-identified structures in the region are mostly gravitationally unbound when magnetic pressure is neglected. Furthermore, Kirk et al. (2017) use GAS observations of Orion A to determine the virial states of dense cores identified by the JCMT Gould Belt Survey and found that while few cores in the region are bound by self-gravity, nearly all are pressure-confined when taking into consideration the weight of the encompassing molecular cloud. Therefore, many of the structures we find within L1251 that are gravitationally unbound could also be predominantly pressure-confined. We calculate below the effect of external pressure from the L1251 molecular cloud upon the virial stability of its structures.

We follow the methodology outlined in Pattle et al. (2015) and Kirk et al. (2017) to express the virial contributions of external pressure, self-gravity, and thermal plus non-thermal motions using the following energy density equations:

$$\Omega_P = -4\pi P R^3 \tag{2.7}$$

$$\Omega_G = \frac{-1}{2\sqrt{\pi}} \frac{GM^2}{R} \tag{2.8}$$

$$\Omega_K = \frac{3}{2} M \sigma^2 \tag{2.9}$$

where M is the observed structure mass, R is the effective radius, G is the gravitational constant, σ^2 is the same as Equation 2.3, and P is pressure. As noted in Section 2.3.4, Equation 2.8 assumes that the structures have a Gaussian density profile. This contrasts with the power-law density distribution assumed by Friesen et al. (2016) that we adopted in Section 2.3.4. Due to this discrepancy, we calculate Ω_G using each density profile and compare the resulting virial parameters in the forthcoming

discussion.

We estimate the pressure on the structures consists of two main components: 1) the turbulent pressure (P_T) exerted by turbulent motions within the parental cloud and 2) the pressure supplied by the weight of the parental cloud (P_W).[2] Thus, $P = P_T + P_W$, where the turbulent component is given by:

$$P_T = \mu_H m_H \times \rho_{^{13}CO} \times \sigma^2_{^{13}CO} \ , \tag{2.10}$$

$\sigma^2_{^{13}CO}$ is the line width of emission from ^{13}CO (1−0), a transition that traces the outer envelopes of dense cores, and $\rho_{^{13}CO}$ is the volume density at which the ^{13}CO $(1-0)$ emission originates. Here, we use a previously measured value of $\sigma_{^{13}CO} = 0.8$ km s^{-1} obtained by Yonekura et al. (1997) for a single pointing at 2.4 arcminute resolution in the eastern portion of Cepheus-L1251. In the absence of other data, we assume this single line width for all structures in our analysis, which is consistent with the virial analysis presented in Pattle et al. (2017). We also set $\rho_{^{13}CO} = 5.5 \times 10^3$ cm^{-3}, which is the average of the typical density range traced by ^{13}CO $(1-0)$ ($n \sim 10^3 - 10^4$ cm^{-3}; Di Francesco et al., 2007). The cloud weight pressure term is given by:

$$P_W = \pi G \bar{N} N (\mu_H m_H)^2 \tag{2.11}$$

where $\bar{N}$ is the mean cloud column density and N is the column density at the structure (e.g., McKee, 1989; Kirk et al., 2006, 2017). We note that Equation 2.11 applies only to spherical clouds with a density profile given by $\rho \propto r^{-k}$, with $k = 1$ (see Appendix C in Kirk et al., 2017). When $1 < k < 3$, an additional positive term is added to the expression for P_W, making the estimate presented here a lower limit.

To isolate the large-scale features of Cepheus-L1251 that are contributing to the cloud weight pressure, we calculate $\bar{N}$ and N using a spatially filtered version of the Di Francesco et al. (2019, in prep) H_2 column density map. Following a method outlined in Kirk et al. (2017), we use the *a Trous* wavelet transform to determine the column density contribution at each spatial scale[3]. The wavelet transform smooths the image on pixel scales with increasing powers of 2^N and subtracts the contribution

[2]We do not consider the pressure exerted by filaments, as was included by Kirk et al. (2017) in their Orion A virial analysis, due to the following reasons: 1) There is less obvious filamentary structure in Cepheus-L1251 compared to Orion A. 2) Kirk et al. estimated the filament pressure did not contribute significantly to the total external pressure on cores in Orion A.

[3]We use the *atrous.pro* IDL script developed by Erik Rosolowsky that is available at https://github.com/low-sky/idl-low-sky/blob/master/wavelet/atrous.pro

of that scale from the image until the pixel scale exceeds the image size. Since the clumps within which dense cores reside have sizes larger than a few tenths of a parsec, we add the column density contribution of the scales ≥ 128 pixels, which corresponds to ~ 0.6 pc. We calculate $\bar{N}$ using the portion of the spatially filtered map that was observed for our NH_3 observations, which produces a mean of 2.1×10^{21} cm^{-2}.

Under this formalism, a structure is in virial equilibrium when $2\Omega_K = -1(\Omega_G + \Omega_P)$. We define all structures with an observed mass larger than their virial mass to be "sub-virial." Conversely, any structure with a mass smaller than its corresponding virial mass is designated "super-virial." The left panel of Figure 2.10, which we refer to as the "virial plane," displays the balance between the three aforementioned energy densities for the same structures included in the virial analysis presented in Section 2.3.4. Structures to the right of the vertical line in Figure 2.10 are sub-virial, while structures on the left are super-virial. Structures that lie below the horizontal dotted line in Figure 2.10 are dominated by pressure over gravity, while structures above the line are dominated by gravity over pressure. When adding pressure to the virial equation and assuming a Gaussian density profile for the structures (shown in the left panel of Figure 2.10), many of the *Herschel*-identified cores are revealed to be dominated by pressure rather than gravity. Specifically, fourteen of the 57 *Herschel*-identified cores are dominated by gravity over pressure, with only two of those being sub-virial. For the other 43 pressure-dominated *Herschel*-identified cores, 16 are super-virial and 27 are sub-virial. On the other hand, all the ammonia-identified leaves are dominated by their gravitational potential energy.

In the right panel of Figure 2.10, we show how the virial plane would shift if the density profile for the structures is assumed to be a power-law consistent with the virial analysis presented in Section 2.3.4. Since the density profile is incorporated into the Ω_G term, the virial parameters of the gravitationally-dominated structures are more sensitive to these assumptions. When a Gaussian density profile is assumed, nearly all of the gravitationally-dominated structures are super-virial. Conversely, when a power-law density profile is assumed, nearly all the gravitationally-dominated structures become sub-virial. While this result demonstrates the uncertainty surrounding virial parameter measurements, it may also indicate that these gravitationally-dominated structures, many of which are ammonia-identified leaves, are currently in or near a state of virial equilibrium. Such a scenario would explain why the NH_3 emission is less well matched to the dense cores in L1251, as was discussed in Section 2.4.1, since structures in virial equilibrium are unable to undergo

the gravitational collapse required to form cores and protostars.

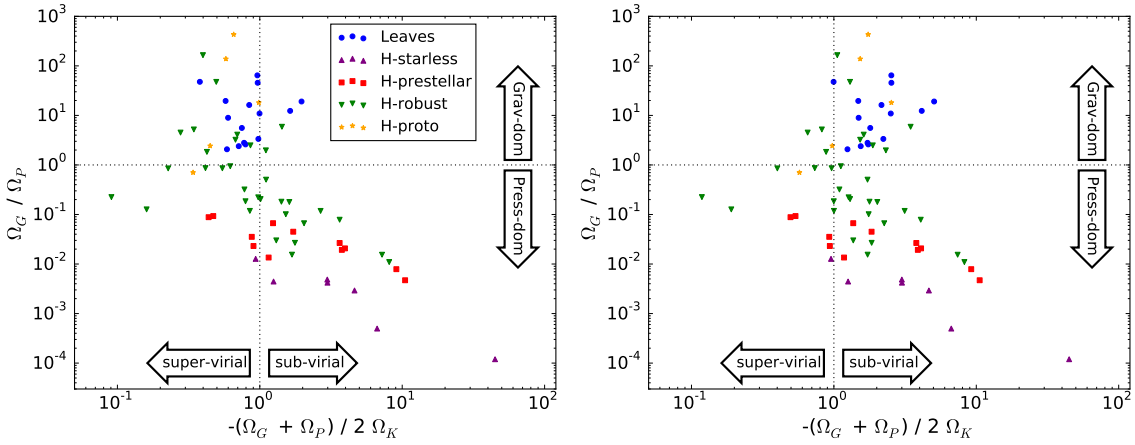

Fig. 2.10 – Left: Virial plane, including the contributions of gravity, pressure, and kinetic energy, for the same structures shown in the top panel of Figure 2.7. Structures to the right of the vertical line are sub-virial, while structures on the left are super-virial. Structures below the horizontal line are dominated by pressure over gravity, while structures above the line are dominated by gravity over pressure. The density profile used in Ω_G is assumed to be Gaussian, consistent with Kirk et al. (2017). Right: Virial plane for the same structures as in the left panel when a power-law density profile is assumed for Ω_G, consistent with Friesen et al. (2017).

Our results after adding pressure to the virial equation contrast with the aforementioned work of Pattle et al. (2017). Pattle et al. (2017) found that all 34 of the sources they identified in L1251 from the region's 850 μm emission were sub-virial and all but four of those 34 were pressure-dominated. The discrepancy between our results likely arises because the virial parameters presented in Pattle et al. (2017) were upper limits due to the lack of non-thermal line width measurements for their cores. Our spectroscopic information shows that the structures in Cepheus-L1251 are dominated by non-thermal motions, which results in higher Ω_K terms (i.e., structures become more super-virial) than those reported by Pattle et al. (2017).

Similarly, our results differ from those of Kirk et al. (2017), which did incorporate GAS NH_3 spectroscopic information into their virial parameter calculations. They find that most of the cores in Orion A are pressure-dominated and sub-virial, with a much lower fraction of gravitationally-dominated structures than we observe in Cepheus-L1251. The giant molecular cloud environment of Orion A is likely the culprit causing the higher rate of pressure-dominated and sub-virial cores in the Kirk et al. (2017) analysis. For instance, Kirk et al. (2017) measure the average column

density of the large-scale structures in Orion A to be over an order of magnitude larger ($\bar{N} = 3.9{\times}10^{22}$ cm^{-2}) than our estimate for Cepheus-L1251 ($\bar{N} = 2.1{\times}10^{21}$ cm^{-2}). Assuming the column density measured at each core (i.e., N in Equation 2.11) in Orion A is also roughly an order of magnitude larger than those measured for the structures in Cepheus-L1251, that would cause the P_W estimates in Orion A to be over two orders of magnitude larger than those of Cepheus-L1251. Such an increase in pressure would move many of the structures in our analysis into the sub-virial and pressure-dominated regime of the virial plane.

The low column densities and high non-thermal motions in Cepheus-L1251 cause the turbulent pressure to be the dominant term in Ω_P for our analysis, with P_T being a factor of $2-9$ larger than P_W for all structures. This result displays the need for similar resolution ^{13}CO measurements across Cepheus-L1251, which are required to understand whether or not the 0.8 km s^{-1} estimate of $\sigma_{^{13}CO}$ adequately represents the motions of the parental cloud nearest to each structure identified in our analysis. We also note that the internal magnetic fields of the structures, which may provide additional support against gravitational collapse, could cause the virial terms presented on the x-axis of Figure 2.10 to move toward being super-virial. Additional sources of external pressure may also be acting on the observed structures, however, which would move the data points in Figure 2.10 towards the sub-virial regime on the right side of the virial plane. Such sources of pressure include radiation from the interstellar field (Seo & Youdin, 2016) and the weight of the filaments in which the observed structures are embedded (Kirk et al., 2017).

2.4.3 Presence of CCS and HC_5N

Although our analysis has focused on the identification of dense gas structures in Cepheus-L1251, the GAS observations also reveal significant amounts of CCS (2_0-1_0) and HC_5N ($9-8$) emission towards the highest H_2 column density portions of the region. The presence of carbon-chain molecules, including CCS and HC_5N, is thought to indicate the early stages of chemical evolution in dense cloud cores (Benson & Myers, 1983; Suzuki et al., 1992; Friesen et al., 2013). As cores evolve, large carbon-chain molecules deplete onto the surface of dust grains and their production rate decreases as higher fractions of the available carbon atoms react to form CO (Caselli et al., 1999). When densities are large enough for CO to be heavily frozen onto dust grains, nitrogen-bearing molecules, such as NH_3 and N_2H^+, increase their abundance.

Thus, the presence or absence of CCS and HC_5N can provide insight into the chemical evolution of the structures identified within Cepheus-L1251.

Here, we perform Gaussian line-fitting on the CCS $(2_0 - 1_0)$ and HC_5N $(9 - 8)$ maps observed toward Cepheus-L1251 to understand which parts of the region contain significant emission from these carbon-chain molecules. The CCS $(2_0 - 1_0)$ and HC_5N $(9 - 8)$ maps observed by GAS toward Cepheus-L1251 contain median rms noise in the off-line channels of 0.23 K and 0.11 K, respectively. CCS $(2_0 - 1_0)$ was only observed in the central beam of the seven beam GBT K-band Focal Plane Array, hence its higher rms values. Due to the faint nature of the CCS and HC_5N emission, we first convolve each map to an angular resolution of $64''$ (FWHM). A Gaussian profile is then fit to all pixels with SNR > 3, where the SNR is defined as the ratio of the peak brightness temperature of the emission line to the standard deviation of the off-line channels. The Levenberg-Marquardt implementation of non-linear least squares is adopted for the fitting. Synthetic Gaussian cubes, along with individual parameter maps for peak brightness temperature, V_{LSR}, and σ, are obtained from the best-fit results. 1-σ statistical uncertainties on the best-fit parameters in each pixel are estimated from the diagonal terms in the covariance matrix.

Figure 2.11 displays integrated intensity maps constructed from the synthetic Gaussian cubes created from our line-fitting of the CCS $(2_0 - 1_0)$ and HC_5N $(9 - 8)$ emission. For comparative purposes, the plots shown in Figure 2.11 match the NH_3 (1,1) integrated intensity fields displayed in Figure 2.4. Although the CCS $(2_0 - 1_0)$ and HC_5N $(9 - 8)$ emission tend to correlate with the positions where NH_3 (1,1) and (2,2) are detected, spatial differences are seen between the three molecular species. The positions of the dendrogram-identified NH_3 leaves found in this paper are also overlaid onto Figure 2.11. While some of the NH_3 structures coincide with CCS $(2_0 - 1_0)$ and HC_5N $(9 - 8)$ emission, others contain no detectable emission in either carbon-chain molecule or contain emission from only one of the carbon-chain molecules. Specifically, 17 of 22 ammonia-identified leaves contain detectable CCS $(2_0 - 1_0)$ emission in at least one-third of the pixels falling within their 2D mask. Using the same criteria, 16 of 22 ammonia-identified leaves contain detectable HC_5N $(9 - 8)$ emission.

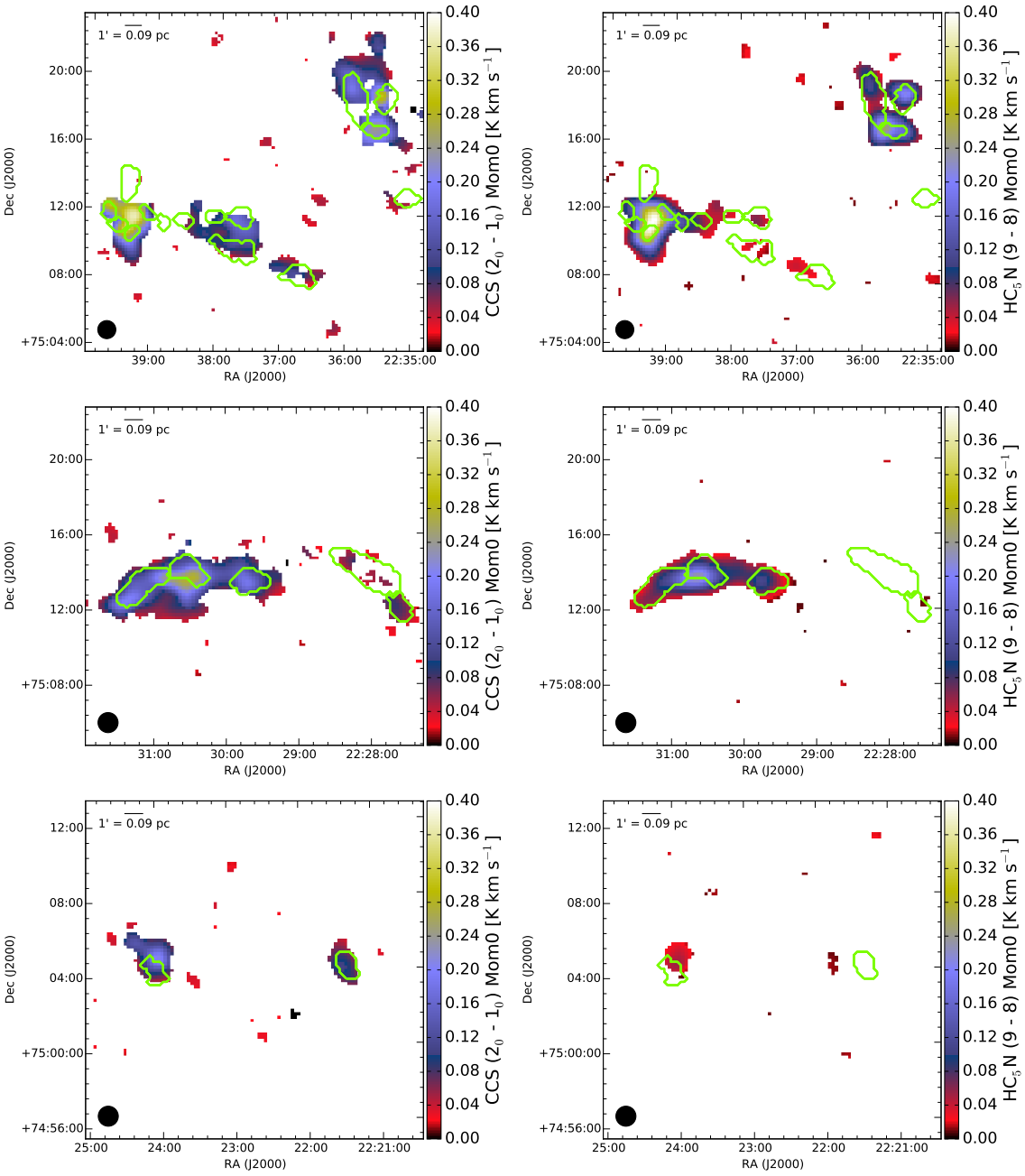

Fig. 2.11 – Comparison of CCS ($2_0 - 1_0$) (left column) versus HC_5N ($9 - 8$) (right column) emission observed towards Cepheus-L1251. The colorscale shows the integrated intensity map created from Gaussian fits to the real molecular emission that was first convolved to a spatial resolution of 64″ (see text for details; new beam-size shown in lower left corner of all plots). The ammonia-identified leaves detected in this paper are outlined in green. Each row shows the same fields displayed in Figure 2.4.

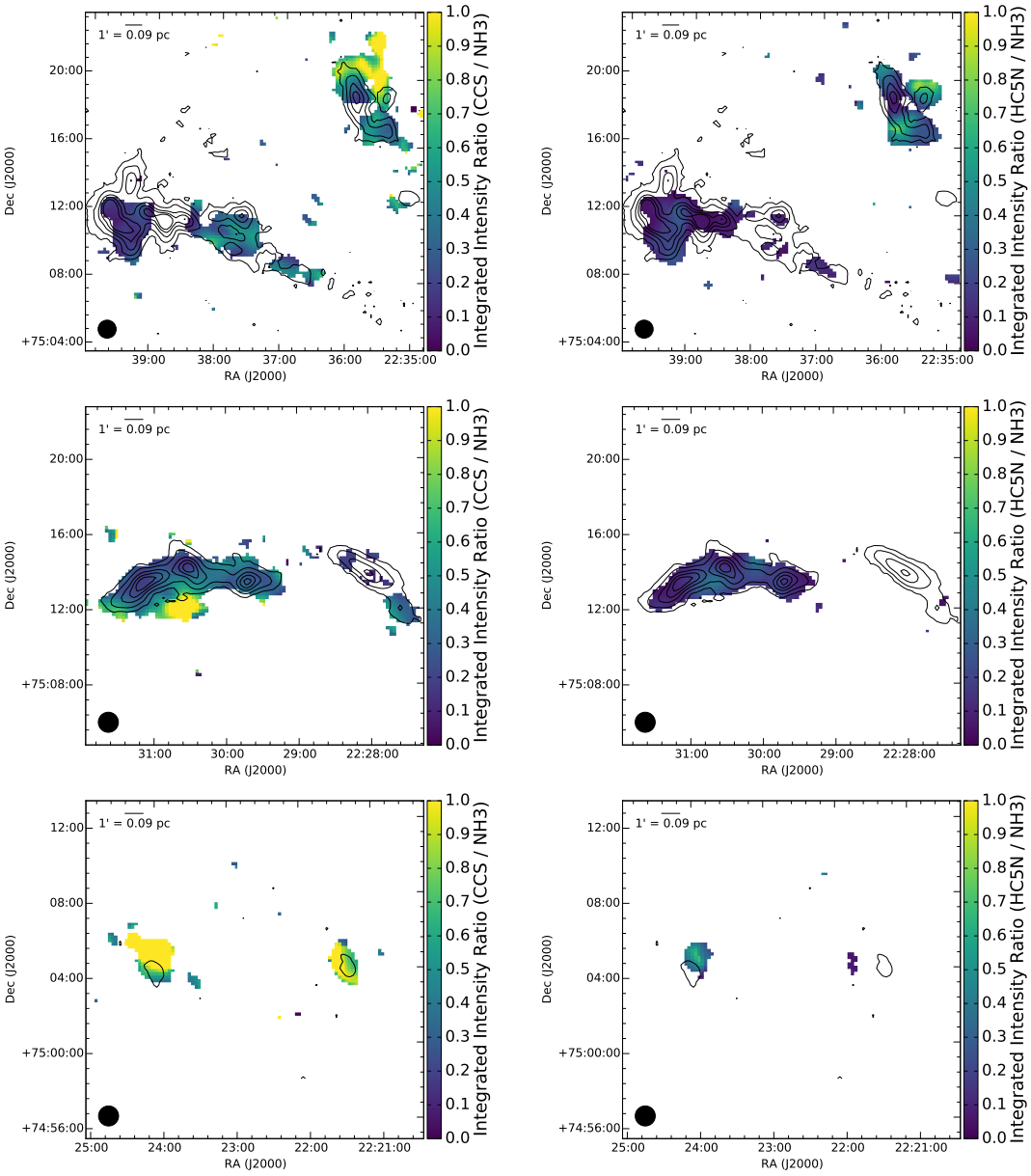

Fig. 2.12 – Ratios of CCS ($2_0 - 1_0$) integrated intensity (left column) and HC_5N ($9 - 8$) integrated intensity (right column) to NH_3 (1,1) integrated intensity for the same fields shown in Figure 2.11. Black contours represent the NH_3 (1,1) integrated intensity at 0.5, 1.5, 3.5, 5.5, and 7.5 K km s^{-1}.

Maps of the ratio of the integrated intensity of CCS ($2_0 - 1_0$) and HC_5N ($9 - 8$) to NH_3 (1,1) are shown in Figure 2.12. In the optically thin limit, these intensity ratios serve as proxies for the abundance ratios of CCS and HC_5N relative to NH_3. L1251E/B, located in the eastern-most portion of Cepheus-L1251, contains the lowest relative ratios of both CCS ($2_0 - 1_0$) and HC_5N ($9 - 8$) emission relative to NH_3 (1,1) compared with L1251C and L1251A in the central and western portions of the cloud, respectively. L1251E/B also corresponds with the most star and core formation throughout Cepheus-L1251. The lower relative levels of carbon-chain emission from L1251E/B may be indicating it is the most chemically evolved sub-region within Cepheus-L1251. Similarly, the sub-region's higher levels of star-formation activity suggest it is dynamically more evolved as well.

In Figure 2.13, we compare the measured line widths of the CCS ($2_0 - 1_0$) and HC_5N ($9 - 8$) emission to those measured in the NH_3 (1,1) map, which was also convolved to a resolution of $64''$ and re-run through the GAS line-fitting pipeline. Comparisons are made for all pixels meeting the following criteria: 1) the pixel falls within the 2D mask of an ammonia-identified leaf and 2) the pixel contains reliable fits for all three transitions. The top panel of Figure 2.13 shows that the line width distributions for each transition peak at different values, with the NH_3 peak occurring at $\sigma \sim 0.15$ km s^{-1} and the HC_5N peak occurring at $\sigma \sim 0.2$ km s^{-1}. The CCS line width distribution is much broader than those of the other two molecules, but its median value of $\sigma \sim 0.18$ km s^{-1} lies between the medians of the other molecules. The small peaks near 0.3 km s^{-1} in the NH_3 and HC_5N distributions are driven by several leaves in L1251E/B, the most active region throughout L1251.

In the bottom panel of Figure 2.13, we plot a histogram of the difference between the NH_3 line width and the HC_5N or CCS line width ($\Delta\sigma$) for each individual pixel. The $\Delta\sigma$ distribution for $HC_5N - NH_3$ peaks at 0.05 km s^{-1} and shows that the majority of the pixels in the map have $\Delta\sigma \gtrsim 0.05$ km s^{-1}. This difference is equivalent to about a single resolution element in the spectrum (i.e., ~ 0.07 km s^{-1}). The $\Delta\sigma$ distribution for CCS $- NH_3$ is also skewed to values greater than zero, but the distribution is much broader than that of $HC_5N - NH_3$. We estimate uncertainties on $\Delta\sigma$ by adding in quadrature the 1-σ uncertainties on the best-fit values for σ at each pixel. The median uncertainty on $\Delta\sigma$ is ~ 0.02 km s^{-1} for both $HC_5N - NH_3$ and CCS $- NH_3$, which suggests the observed values of $\Delta\sigma$ are significantly different from zero for most pixels.

This result is interesting when considering CCS and HC_5N are ~ 3 and ~ 4 times more massive than NH_3, respectively. If all three molecules are tracing the same

volume of gas imbued with common turbulent motions, one would naively expect NH_3 to have the largest line widths of the three tracers due to its lower molecular mass. Namely, the lighter NH_3 molecules would, on average, have greater thermal velocities than the heavier molecules. The larger line widths for the carbon-based species, however, suggest they are not tracing the same gas as NH_3. Instead, the carbon-based molecules may be tracing the outer layers of the cloud, which are likely more turbulent than its central regions. This claim supports previous observations by Pineda et al. (2010) that suggest the dissipation of turbulence within dense cores provides the conditions necessary for their gravitational collapse to form protostars. The de-coupling of the carbon-based molecular species observed in this paper from NH_3 could be caused by the depletion of the carbon-based species in the central, colder regions of the cloud. This scenario would also explain the offsets observed between the NH_3 (1,1) emission peaks and those of the carbon-based tracers.

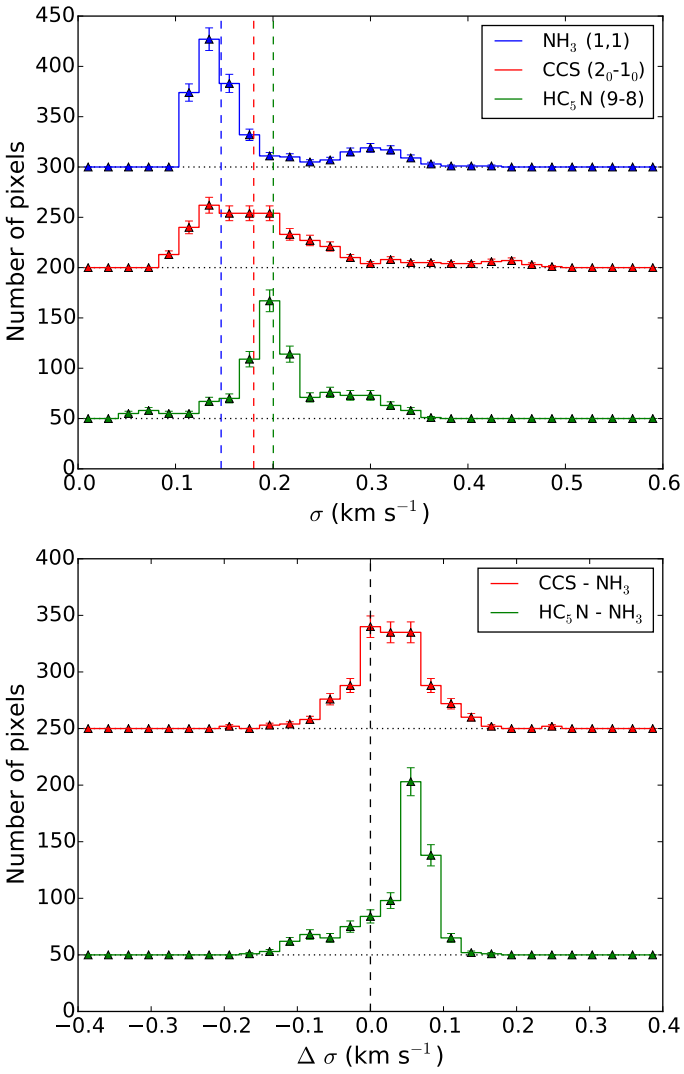

Fig. 2.13 – Top: histograms of velocity dispersion for all pixels falling within an ammonia-identified leaf in the NH_3 (1,1) (blue), CCS $(2_0 - 1_0)$ (red) and HC_5N $(9-8)$ (green) emission maps. All maps were convolved to a spatial resolution of $64''$ before line-fitting and only pixels with reliable fits in all three transitions are included in the histograms. The vertical dashed lines represent the median value of σ for each distribution. The HC_5N $(9-8)$, CCS $(2_0 - 1_0)$, and NH_3 (1,1) histograms have been offset from the zero position of the y-axis by 50, 200, and 300, respectively (denoted by the horizontal dotted lines). Bin widths are set to 0.021 km s^{-1}. Bottom: $\Delta\sigma$ offset between HC_5N $(9-8)$ and NH_3 (1,1) (green) and between CCS $(2_0 - 1_0)$ and NH_3 (1,1) (red) for all pixels in the top panel. Bin widths are set to 0.028 km s^{-1}. The green and red histograms have been offset from the zero position of the y-axis by 50 and 250, respectively. The vertical dotted black line denotes $\Delta\sigma = 0$.

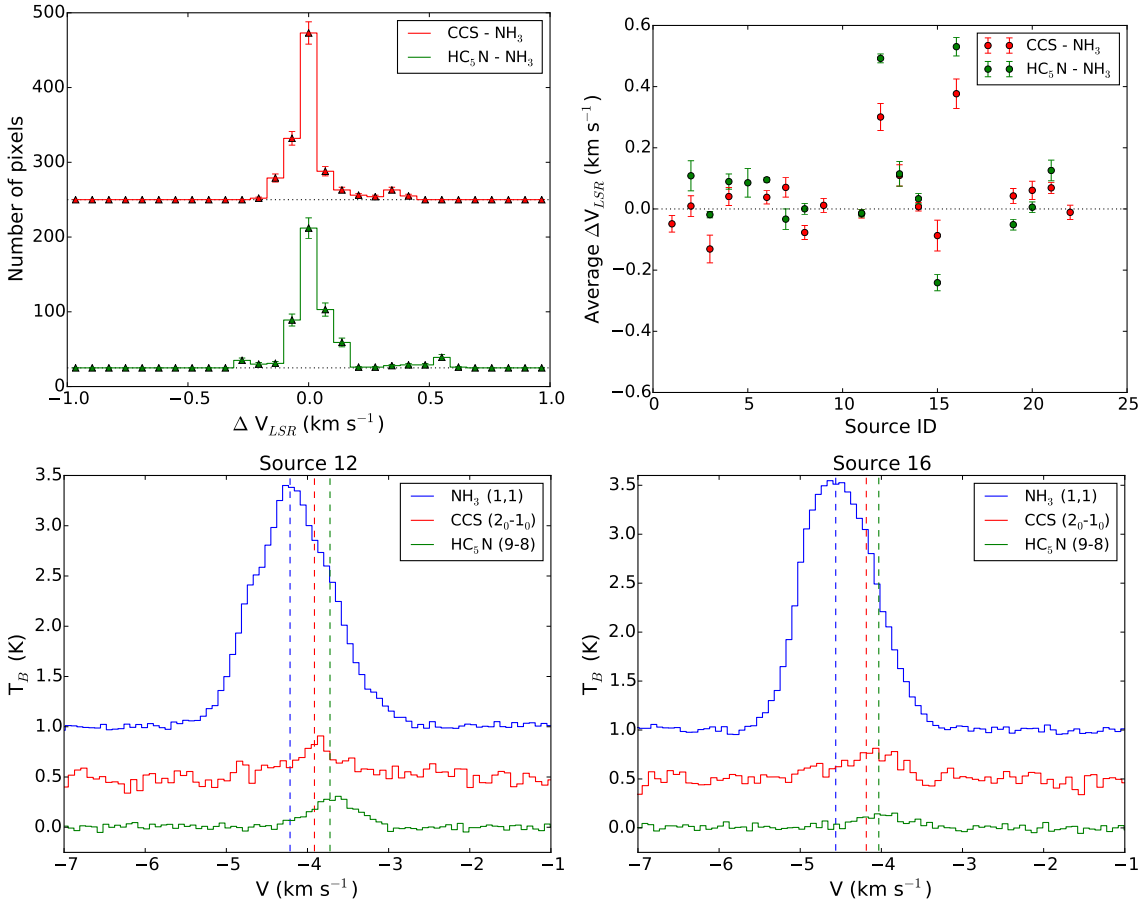

Fig. 2.14 – Top left: histograms of the difference between the centroid velocity of HC_5N $(9-8)$ (green) or CCS (2_0-1_0) (red) and the centroid velocity of NH_3 (1,1) for all pixels falling within an ammonia-identified leaf. The green and red histograms have been offset from the zero position of the y-axis by 25 and 250, respectively (denoted by the horizontal dotted black lines). Top right: Average ΔV_{LSR} for all pixels falling within each individual ammonia-identified source, weighted by the integrated intensity maps of each respective molecular transition. The horizontal dotted line marks ΔV_{LSR} = 0. Bottom row: Average observed spectra for all pixels falling within source 12 (left) and source 16 (right) listed in Table 2.1, weighted by the integrated intensity maps of each respective molecular transition. Vertical lines represent the average V_{LSR} for the source in each transition. The CCS (2_0-1_0) and NH_3 (1,1) spectra have been offset from the zero position on the y-axis by 0.5 and 1.0 K, respectively. Only the central hyperfine group of the NH_3 (1,1) spectrum is shown.

In addition, we also observe significant centroid velocity offsets (up to ~ 0.5 km s^{-1}) between the emission from NH_3 and the carbon-based molecules for several sources. These offsets can clearly be seen in Figure 2.14, which plots the ΔV_{LSR} distribution for all pixels falling within an ammonia-identified leaf. While most of the V_{LSR} measurements between the three transitions are in agreement, there is a considerable number of pixels with $\Delta V_{LSR} > 0.5$ km s^{-1} for HC_5N and $\Delta V_{LSR} \sim 0.3$ km s^{-1} for CCS. Such large offsets are significant considering the median uncertainty on ΔV_{LSR}, estimated using the same method discussed above for the uncertainty on $\Delta\sigma$, is ~ 0.02 km s^{-1} for both $HC_5N - NH_3$ and $CCS - NH_3$. Furthermore, the pixels with high ΔV_{LSR} values are not dispersed evenly throughout the map, but rather isolated within specific leaves. This isolation can clearly be seen in the top right panel of Figure 2.14, which plots the weighted average ΔV_{LSR} for all pixels falling within the 2D mask of each individual ammonia-identified leaf, weighted by the peak brightness temperature of each respective emission line. While most of the leaves hover around $\Delta V_{LSR} = 0$ km s^{-1}, sources 12 and 16 show $\Delta V_{LSR} > 0.5$ km s^{-1} for HC_5N and $\Delta V_{LSR} > 0.3$ km s^{-1} for CCS. The weighted average spectra for each source, plotted in the bottom panels of Figure 2.14 and weighted by the peak brightness temperature of each respective emission line, show that the calculated offsets do indeed correspond to real features in the spectra.

For sources 12 and 16, the largest centroid velocity offsets are observed between NH_3 and HC_5N, which is the heavier of the two observed carbon-based species. Ohashi et al. (2016b) observed a similar offset between NH_3 (1,1), ^{13}CO $(1-0)$, and CS $(2-1)$ emission toward a starless dense core in the Orion A molecular cloud named TUKH122. There, they found the NH_3 (1,1) emission had a centroid velocity 0.7 km s^{-1} lower than the ^{13}CO $(1-0)$ and CS $(2-1)$ emission. Similarly, Swift et al. (2005) observed a 0.16 km s^{-1} offset between the centroid velocities of NH_3 (1,1) and C_2S (3_2-2_1) emission towards a pre-protostellar core in L1551. They interpret their result as arising from either an infalling or outflowing, lower-density envelope surrounding the high-density gas forming the protostar. The former is a more likely explanation for sources 12 and 16 in our analysis, since both are likely prestellar cores because they lack a *Herschel*-identified or *Spitzer*-identified protostellar counterpart.

Alternatively, the relative motions we observe between the low and high density gas could be related to the positions of these particular sources within the molecular cloud. Sources 12 and 16 are the two eastern-most leaves in our sample (shown in the far-left side of the top left panel of Figure 2.4). As can be seen in Figure 2.1,

the positions of these sources correspond to a sharp change in H_2 column density. Thus, sources 12 and 16, which lie on the outskirts of the high-density central regions of Cepheus-L1251, may be more exposed to the turbulent outer layers of the parental molecular cloud. Furthermore, these sources lie at the edge of a "comet-like" feature in the east of Cepheus-L1251 (also shown in Figure 2.1), which may indicate some external forces (e.g., winds or radiation) moving in the east to west direction are producing a larger influence upon the outer gas layers in that portion of the cloud. Chemical differentiation of carbon-based species has been observed toward sharp edges of H_2 column density (Spezzano et al., 2016), which may also explain why the centroid velocity offsets we observe are more extreme for the emission from HC_5N than that of CCS. In total, these results suggest such centroid velocity offsets between certain molecular transitions may be a common occurrence at sharp transitions between high and low density gas.

2.5 Summary

We have performed a dendrogram analysis on Green Bank Ammonia Survey observations of the Cepheus-L1251 molecular cloud to identify hierarchical dense gas structures that may form stars in the future. Our final catalog consists of 22 top-level structures, which reside within 13 lower-level parent structures. We also use the ammonia data to characterize the gas properties of a dense core population identified by Di Francesco et al. (2019, in prep) using *Herschel* photometric observations of thermal dust continuum emission across the region. The results of our analysis for the ammonia-identified and *Herschel*-identified structures are summarized below:

1. The observed masses for the top-level ammonia-identified sources, estimated from a dust continuum-derived H_2 column density map for the region, range from 0.9 $M_\odot$ for the smallest top-level structure to 80 $M_\odot$ for the largest parent structure. The top-level structures are predominantly compact, with $R_{eff} < 0.05$ pc, and show a strong spatial correspondence with the highest H_2 column density portions of the observed field.

2. The virial parameters for the top-level ammonia-identified structures suggest they are gravitationally dominated, yet may be in or near a state of virial equilibrium. Conversely, the majority of the *Herschel*-identified dense cores are pressure-confined, sub-virial objects rather than gravitationally bound structures. These results appear to hold for multiple sets of assumptions on the density profile, radius, and mass of the

structures. Our NH_3 results are also consistent with a similar virial analysis conducted by Friesen et al. (2016) for the more active star-forming Serpens South region, despite Cepheus-L1251 and Serpens South being drastically different environments (as indicated by their significantly different cloud mass surface densities, column densities, numbers of YSOs, and numbers of dense cores). As such, it appears that, independent of the cloud-scale environment, dense ammonia structures are gravitationally dominated, while most *Herschel*-identified cores are pressure-confined.

3. All of the elongated, filamentary, ammonia-identified structures with aspect ratios greater than 2 appear to be gravitationally bound. This finding lends credence to the idea that filamentary collapse and fragmentation gives rise to dense core and protostar formation.

4. The median value of T_{dust} amongst the ammonia- and *Herschel*-identified structures is 11.7 ± 1.1 K, while the median value of T_K is 10.3 ± 2.0 K. These results suggest the dust and dense gas within the structures are coupled. The slightly higher median T_{dust} value is potentially caused by heated material on the outskirts of the cloud, which is not traced by NH_3, that falls along the line of sight to the observed structures.

5. The abundance of para-NH_3, $\chi_{NH_3} = (N_{para-NH_3}/N_{H_2})$, is measured for all structures and found to peak just below $\chi_{NH_3} = 10^{-8}$, which is consistent with χ_{NH_3} measurements from many other star-forming regions. The ammonia-identified leaves and *Herschel*-identified cores show similar χ_{NH_3} distributions, with no significant variations between the different structure types.

6. 17 of 22 ammonia-identified leaves contain detectable CCS ($2_0 - 1_0$) emission in at least one-third of the pixels falling within their 2D mask. Similarly, 16 of 22 ammonia-identified leaves contain detectable HC_5N ($9 - 8$) emission. The line widths measured for the carbon-based molecular tracers, particularly HC_5N ($9 - 8$), are generally higher than the line width measured from NH_3 (1,1). This difference suggests the carbon-based molecules are tracing the more turbulent outer layers of the molecular cloud where they have not yet suffered depletion at higher densities and colder temperatures.

7. Two of the ammonia-identified leaves (sources 12 and 16 in Table 2.1) show centroid velocity offsets of $\Delta V_{LSR} > 0.5$ km s^{-1} between NH_3 (1,1) and HC_5N ($9-8$) and $\Delta V_{LSR} > 0.3$ km s^{-1} between NH_3 (1,1) and CCS (2_0-1_0). The position of these structures on the outskirts of the high-density regions of the cloud suggest they may be located at a sharp transition between the turbulent parental cloud and quiescent

star-forming region.

2.6 Acknowledgments

We thank the entire *Herschel* Gould Belt Survey team for their efforts obtaining and preparing the data used for the dense core catalogs utilized in this paper. We particularly appreciate the efforts of Bilal Ladjelate, Vera Könyves, and Alexander Men'shchikov for their contributions to the *getsources* extractions used for our analysis. JK, JDF, ER, MCC, and CDM acknowledge the financial support of a Discovery Grant from NSERC of Canada. RKF is a Dunlap Fellow at the Dunlap Institute for Astronomy & Astrophysics. The Dunlap Institute is funded through an endowment established by the David Dunlap family and the University of Toronto. PC, JP, AP, and ACT acknowledge the financial support of the European Research Council (ERC; project PALs 320620). The National Radio Astronomy Observatory is a facility of the National Science Foundation operated under cooperative agreement by Associated Universities, Inc. This research made use of *astrodendro*, a Python package to compute dendrograms of Astronomical data (http://www.dendrograms.org/). This research also made use of Astropy (http://www.astropy.org), a community-developed core Python package for Astronomy (Astropy Collaboration et al., 2013).

2.7 Appendix

2.7.1 Effective Radius

As discussed in Section 2.3.4, the virial parameter presented in this paper depends upon the radius (R) of the structure being analyzed. In this paper, we chose to use $R = R_{eff} = (\sigma_{major}\sigma_{minor})^{1/2}$ (i.e., the geometric mean of the major and minor axes) for the ammonia-identified leaves to be consistent with the virial analysis presented in Friesen et al. (2016). Similarly, the effective radius used for the *Herschel*-identified dense cores is the deconvolved geometric mean of their FWHM axes, which was chosen to be consistent with the effective radius used for the Bonnor-Ebert core classification presented in Di Francesco et al. (2019, in prep). Previous studies that have involved virial analyses, however, have determined the radii of sources in other ways. For instance, Kauffmann et al. (2013) adopt $R = (A/\pi)^{1/2}$ as the effective radii used in their virial analysis of low- and high-mass star-forming regions (where A represents the structure's area on the PP plane).

To investigate the dependence of our virial parameter calculations upon our chosen formulation for the effective radius, we re-calculate the virial parameters of both the ammonia-identified structures and *Herschel*-identified dense cores using $R = (A/\pi)^{1/2}$ as input into Equation 2.1. The altered virial parameters are used to create Figure 2.15, which plots updated versions of Figures 2.5, 2.6, and 2.7, showing the impact the changes in effective radius make upon our conclusions. The new radii formulation increases the R_{eff} of all the leaves, while it increases some of the parent structures and decreases others. The amorphous shapes that some of the parent structures exhibit are likely not well-characterized by the assigned major and minor axes, causing a more extreme change in their R_{eff} estimates between the two formulations. The mean effective radii of the ammonia-identified leaves and Herschel-identified cores increase to 0.052 $\pm$ 0.019 pc and 0.040 $\pm$ 0.011 pc, respectively, when using the altered formulation.

The virial parameters of the ammonia-identified leaves increase as a result of their larger effective radii. The bottom panel of Figure 2.15, however, shows that while their virial parameters increase, nearly all the ammonia-identified leaves remain below $\alpha_{vir} = 2$. Similarly, the top panel of Figure 2.16 shows that most of the ammonia-identified leaves move into the sub-virial, pressure-dominated portion of the virial plane when using the altered R_{eff}.

The change in effective radii, and hence virial parameter, for the *Herschel*-identified cores is similar to the effect observed for the ammonia-identified leaves. The radii of the *Herschel*-identified cores increase by factors of a few, likely because deconvolution is not being applied to the core sizes in this altered analysis, which increases their virial parameters by factors of a few. Regardless, the majority of the *Herschel*-identified cores remain in the sub-virial and pressure-dominated portion of the virial plane.

2.7.2 Mass

The method used for obtaining the observed mass of structures also has a bearing on the calculated virial parameters. For instance, our analysis of the *Herschel*-identified dense cores in Cepheus-L1251 uses the masses presented in Di Francesco et al. (2019, in prep). The masses presented in that paper were obtained from SED fits to the integrated dust continuum fluxes for each source after emission from large-scale background structures (i.e., the filaments within which the cores reside) was subtracted.

Such filtering reduces the total amount of flux associated with each core, causing derived masses to be significantly lower than if all the emission along the line of sight to the core were used in the mass derivation.

To understand the impact large-scale filtering has upon the virial parameters derived in this paper, we re-derive masses for the *Herschel*-identified dense cores by summing all the H_2 column density within the pixels that fall inside their respective elliptical 2D masks. This method is consistent with the method described in Section 2.3.3, which we used to estimate the observed masses for the top-level ammonia-identified structures. Figure 2.17 re-plots Figure 2.7 using the re-derived masses for the *Herschel*-identified dense cores. The higher observed masses for the *Herschel*-identified cores result in lower virial parameters and a higher fraction of the structures falling below $\alpha_{vir} = 2$. Relatedly, the middle panel of Figure 2.16 shows that many of the cores move into the super-virial zone of the virial plane after altering the method by which their mass is calculated. When combining both the altered mass calculation for the *Herschel*-identified cores with the altered R_{eff} calculation discussed in Appendix 2.7.1, however, the structures remain split between the sub-virial and super-virial portions of the virial plane (as can be seen in the bottom panel of Figure 2.16).

An additional caveat arises when comparing the virial parameters derived for the *Herschel*-identified dense cores and ammonia-identified structures when considering the former were identified in 2D while the latter were identified in 3D. To circumvent any issues related to these projection effects and provide a direct comparison between the two types of structures, we first perform a cross-match to find the *Herschel*-identified counterpart to each ammonia-identified leaf. If the center of a *Herschel*-identified dense core is within $32''$ of an ammonia-identified leaf (i.e., the GBT beam size for our NH_3 (1,1) observations), the two structures are considered matched. Nine of the 15 ammonia-identified leaves with aspect ratios less than two were found to have a *Herschel*-identified counterpart using this criterion. For matched pairs, we re-calculate the virial parameter of the ammonia-identified structure using the SED-derived mass determined for its *Herschel*-identified counterpart.

The bottom panel of Figure 2.17 shows the originally calculated virial parameters for the ammonia-identified leaves (blue points) that contained a *Herschel*-identified counterpart, and the re-calculated virial parameters using the *Herschel* mass, which are shown in the color corresponding to the core type of the *Herschel*-identified counterpart. Although the virial parameters calculated using the (lower) *Herschel* masses

tend to be higher, nearly all remain below $\alpha_{vir} = 2$. This result shows that, at least for the ammonia-identified structures, filtering out large-scale structure prior to estimating masses does not significantly alter the conclusions of our virial analysis.

Table 2.1. NH_3 (1,1) Leaves Catalog

ID	x_{center}[a] (deg)	y_{center}[a] (deg)	σ_{major}[b] ($''$)	σ_{minor}[b] ($''$)	PA[c] (deg)	R_{eff}[d] (10^{-2} pc)	M_{obs}[e] ($M_\odot$)	σ_{obs}[f] (km s^{-1})	T_K[g] (K)	T_{dust}[h] (K)	$N_{para-NH_3}$[i] (10^{13} cm^{-2})	N_{H_2}[j] (10^{21} cm^{-2})	α_{vir}[k]	$\alpha_{vir,fil}$[l]
1	339.173424	75.139485	23.3	14.3	162	2.7 ± 0.1	2.0 ± 0.4	0.14 ± 0.06	11.0 ± 1.7	12.7 ± 0.2	6.1 ± 1.9	7.9 ± 1.3	0.7	···
2	339.403121	75.195569	16.4	13.3	157	2.1 ± 0.1	2.8 ± 0.6	0.16 ± 0.01	10.5 ± 0.6	11.5 ± 0.2	15.1 ± 3.8	15.2 ± 3.0	0.4	···
3	339.762110	75.196272	13.9	6.1	139	1.3 ± 0.3	2.0 ± 0.4	0.18 ± 0.02	11.3 ± 0.5	11.5 ± 0.7	24.3 ± 2.2	31.7 ± 5.0	0.4	0.7
4	339.422677	75.162841	32.3	14.5	163	3.1 ± 0.1	3.1 ± 0.6	0.12 ± 0.01	10.3 ± 1.6	12.0 ± 0.2	5.8 ± 1.5	8.7 ± 1.1	0.4	0.8
5	339.697981	75.187238	11.3	7.5	99	1.3 ± 0.3	2.3 ± 0.5	0.39 ± 0.05	13.1 ± 0.7	14.3 ± 0.6	36.9 ± 6.8	43.6 ± 27.9	1.0	···
6	339.822184	75.176348	12.4	6.9	-136	1.3 ± 0.3	1.5 ± 0.3	0.22 ± 0.05	10.7 ± 0.5	11.0 ± 0.1	22.1 ± 2.8	23.3 ± 2.5	0.7	···
7	339.503914	75.194370	15.0	7.7	-177	1.6 ± 0.2	1.1 ± 0.2	0.12 ± 0.01	9.4 ± 0.7	12.0 ± 0.1	8.2 ± 1.6	12.4 ± 1.1	0.6	···
8	337.418972	75.225552	23.2	14.6	-171	2.7 ± 0.1	5.5 ± 1.1	0.13 ± 0.01	9.5 ± 0.6	11.1 ± 0.3	24.7 ± 9.6	19.9 ± 6.3	0.2	···
9	336.896899	75.201494	21.1	12.0	115	2.3 ± 0.1	1.7 ± 0.3	0.11 ± 0.01	8.9 ± 1.3	11.8 ± 0.1	4.7 ± 1.2	8.9 ± 1.1	0.5	···
10	337.004425	75.233212	52.7	15.9	150	4.2 ± 0.1	7.3 ± 1.5	0.11 ± 0.01	9.1 ± 0.9	11.5 ± 0.3	14.4 ± 5.8	10.2 ± 3.1	0.2	0.5
11	337.630159	75.235730	25.7	15.3	151	2.9 ± 0.1	5.2 ± 1.0	0.14 ± 0.02	9.8 ± 0.5	11.5 ± 0.3	22.0 ± 7.0	17.4 ± 5.7	0.2	···
12	339.875346	75.183526	12.4	8.3	172	1.5 ± 0.2	2.8 ± 0.6	0.22 ± 0.03	10.0 ± 0.6	10.3 ± 0.2	30.7 ± 2.8	34.3 ± 5.0	0.4	···
13	339.622874	75.190326	13.0	8.7	165	1.5 ± 0.2	1.8 ± 0.4	0.16 ± 0.05	11.6 ± 0.4	12.4 ± 0.4	21.9 ± 2.4	19.9 ± 2.9	0.5	···
14	337.789904	75.222149	41.0	14.5	-145	3.5 ± 0.1	8.8 ± 1.8	0.11 ± 0.01	9.9 ± 0.4	11.1 ± 0.2	23.4 ± 7.8	19.7 ± 6.5	0.2	0.3
15	338.852562	75.314655	19.8	12.1	70	2.2 ± 0.1	2.7 ± 0.5	0.23 ± 0.06	12.5 ± 1.6	12.4 ± 0.3	6.2 ± 1.7	13.0 ± 3.2	0.7	···
16	339.910415	75.196766	12.7	8.4	90	1.5 ± 0.2	3.3 ± 0.7	0.26 ± 0.04	9.5 ± 0.3	10.2 ± 0.1	31.9 ± 4.9	39.1 ± 6.9	0.4	···
17	338.764785	75.217186	16.5	10.8	173	1.9 ± 0.2	0.9 ± 0.2	0.14 ± 0.01	10.3 ± 1.7	12.2 ± 0.2	5.1 ± 1.8	6.8 ± 1.1	0.9	···
18	339.834372	75.224749	25.5	11.5	81	2.5 ± 0.1	4.8 ± 1.0	0.20 ± 0.04	9.4 ± 1.3	11.0 ± 0.3	11.7 ± 2.9	19.9 ± 4.9	0.3	0.6
19	338.970673	75.312996	38.3	14.0	102	3.4 ± 0.1	7.3 ± 1.5	0.13 ± 0.02	10.5 ± 0.8	12.0 ± 0.5	12.9 ± 4.5	15.9 ± 3.9	0.2	0.4
20	338.889854	75.282631	21.1	7.8	172	1.9 ± 0.2	2.3 ± 0.5	0.25 ± 0.09	12.9 ± 2.7	15.3 ± 1.7	5.0 ± 1.2	20.6 ± 2.6	0.8	1.5
21	336.016977	75.072091	20.8	11.0	126	2.2 ± 0.2	1.3 ± 0.3	0.13 ± 0.02	10.0 ± 1.9	12.1 ± 0.2	4.2 ± 1.0	7.9 ± 1.1	0.7	···
22	335.354540	75.072309	19.7	11.8	115	2.2 ± 0.2	1.4 ± 0.3	0.11 ± 0.02	10.5 ± 1.7	12.4 ± 0.2	3.6 ± 1.6	8.1 ± 0.9	0.7	···

Note. — Top-level, "leaves" identified in our dendrogram analysis of the NH_3 (1,1) data.

[a]Mean position of the structure in R.A. and Dec. (J2000) coordinates.

[b]Major and minor axis of the structure, projected onto the position-position plane.

[c]Position angle of the major axis, measured in degrees counter-clockwise from the west direction on the sky.

[d]Geometric mean of σ_{major} and σ_{minor}. Uncertainty represents $\sqrt{A_{pix}/\pi N_{pix}}$, where A_{pix} is the area of a pixel in the NH_3 (1,1) emission map and N_{pix} is the number of pixels falling within the structure.

[e]Observed mass estimated from the *Herschel*-derived H_2 column density map presented in Di Francesco et al. (2019, in prep). Uncertainties estimated assuming a 20% error on the H_2 column densities used to calculate mass.

[f]Average and standard deviation of the velocity dispersion measured from the NH_3 (1,1) emission for all pixels falling within the structure, weighted by the NH_3 (1,1) integrated intensity.

[g]Average and standard deviation of the kinetic gas temperature for all pixels falling within the structure, weighted by the NH_3 (1,1) integrated intensity.

[h]Average and standard deviation of the dust temperature for all pixels falling within the structure in the *Herschel*-derived T_{dust} map presented in Di Francesco et al. (2019, in prep).

[i]Average and standard deviation of the para-NH_3 column density for all pixels falling within the structure, weighted by the NH_3 (1,1) integrated intensity.

[j]Average and standard deviation of the H_2 column density for all pixels falling within the structure in the *Herschel*-derived N_{H_2} map presented in Di Francesco et al. (2019, in prep).

[k]Virial parameter ($\alpha_{vir} = M_{vir}/M_{obs}$) for the structure.

[l]Filamentary virial parameter for the leaves with $a_{maj}/a_{min} \geq 2$.

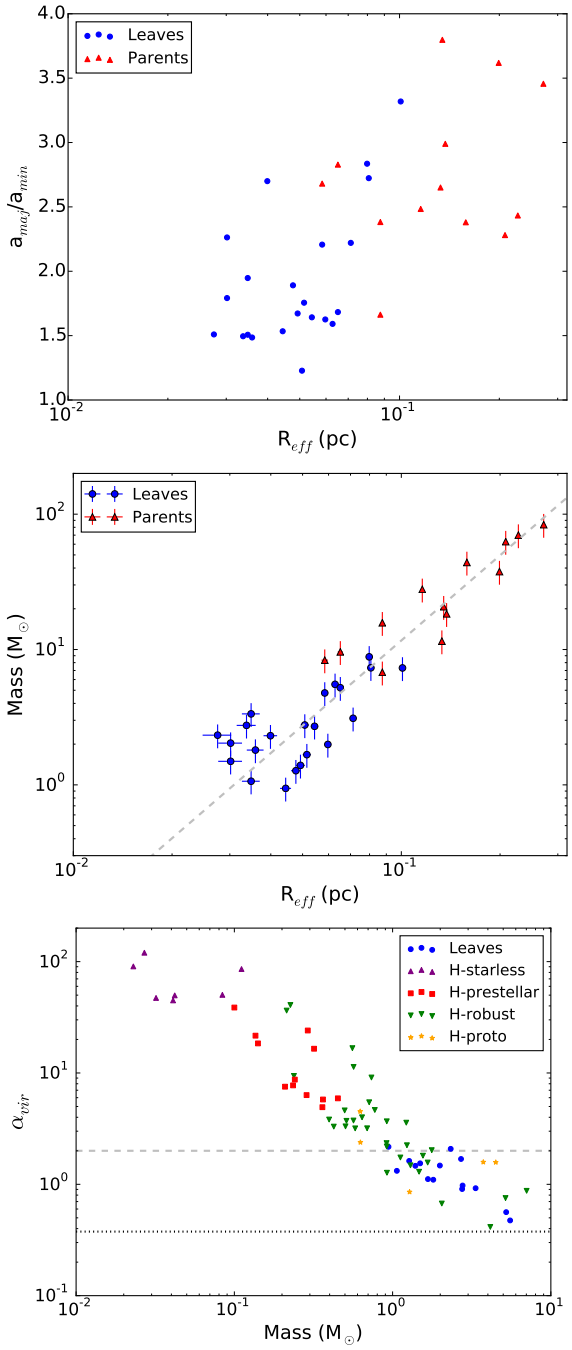

Fig. 2.15 – Same as Figure 2.5 (top), Figure 2.6 (middle), and Figure 2.7 (bottom), but using $R = (A/\pi)^{1/2}$ as the effective radius for all structures. The best-fit power law slope in the middle panel is 2.09 ± 0.15.

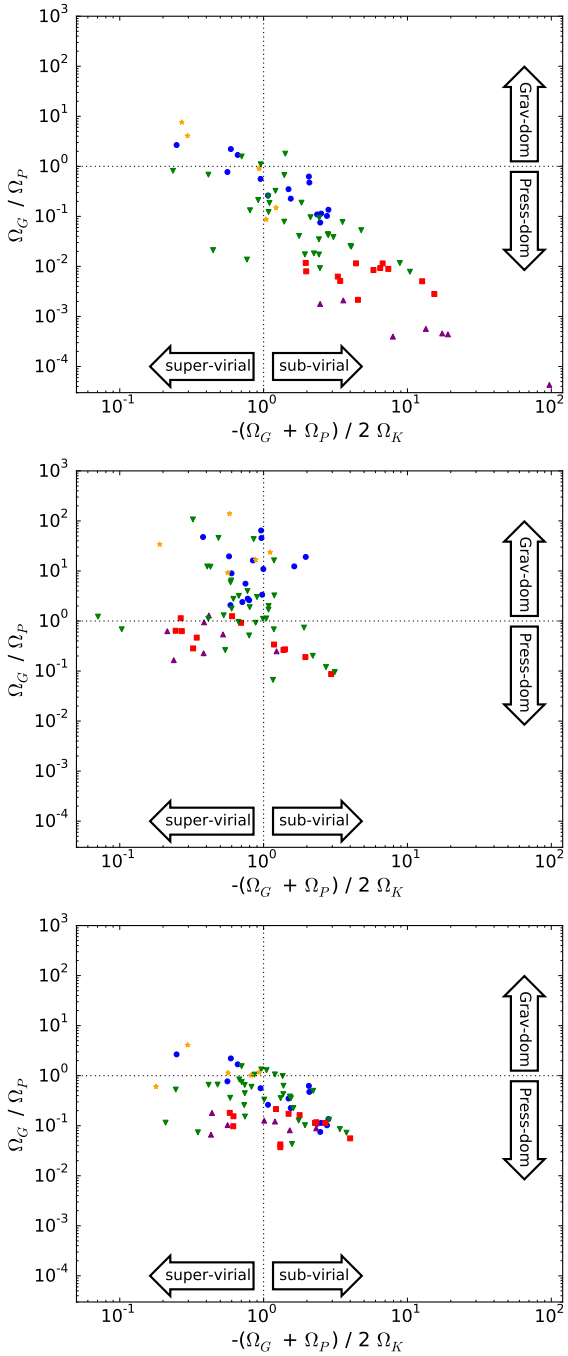

Fig. 2.16 – Top: Virial plane for the same structures as in Figure 2.10 when using $R_{eff} = (A/\pi)^{1/2}$ as the effective radius (see Appendix 2.7.1 for details). Middle: Virial plane when using the H_2 column density map to determine the masses of the *Herschel*-identified dense cores (see Appendix 2.7.2 for details). Bottom: Virial plane when using both $R_{eff} = (A/\pi)^{1/2}$ and the H_2 column density map to determine structure masses. In all panels, a Gaussian density profile is assumed for the structures, which is consistent with the virial analysis presented in Kirk et al. (2017).

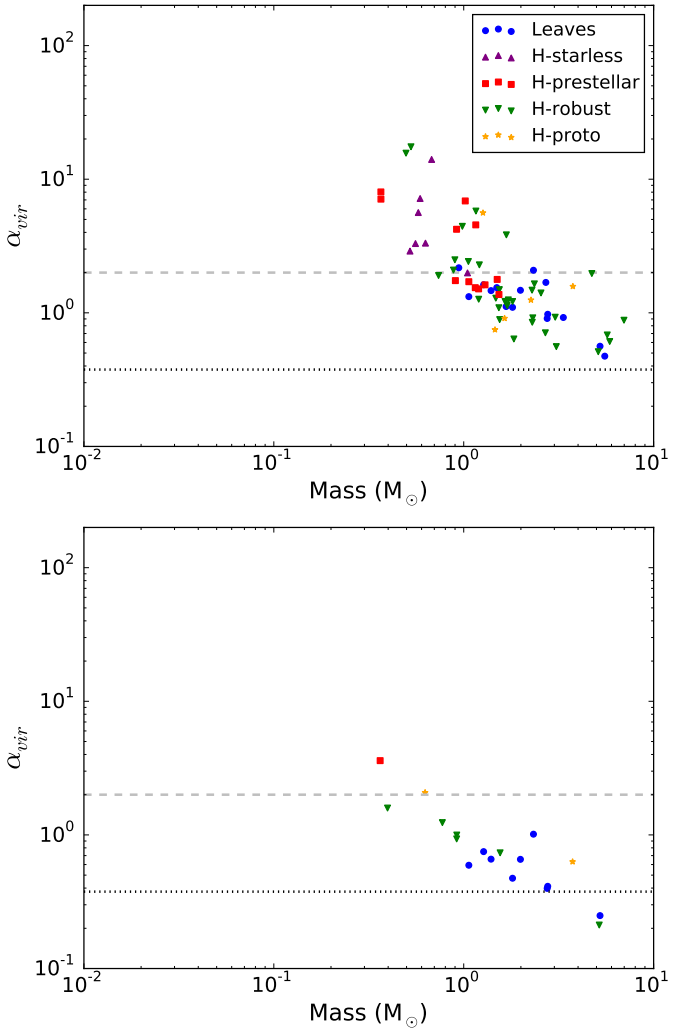

Fig. 2.17 – Top panel: Same as Figure 2.7, but using an alternative method for obtaining the observed mass for the *Herschel*-identified cores. Namely, the observed mass for each *Herschel*-identified core was obtained by summing all pixels in the *Herschel*-derived H_2 column density map that fall within its elliptical mask. Bottom panel: Where ammonia-identified leaves have a *Herschel*-identified counterpart, the mass of the *Herschel*-identified core is used to calculate the virial parameter of the ammonia-identified structure. The blue points represent the original virial parameter calculations (see Section 2.3.4) for the leaves which have *Herschel*-identified core counterparts. The non-blue points represent the virial parameters for the leaves when using their *Herschel*-identified core counterpart's SED-derived mass. The color and shape of the non-blue points represent the core type for the cross-matched *Herschel*-identified source.

Chapter 3

KFPA Examinations of Young STellar Object Natal Environments: Hierarchical Ammonia Structures in Galactic Giant Molecular Clouds

Originally published in The Astrophysical Journal, Volume 884, Issue 1, article id. 4, 45 pp. (2019).

Authors: Jared Keown, James Di Francesco, Erik Rosolowsky, Ayushi Singh, Charlie Figura, Helen Kirk, L. D. Anderson, Michael Chun-Yuan Chen, Davide Elia, Rachel Friesen, Adam Ginsburg, A. Marston, Stefano Pezzuto, Eugenio Schisano, Sylvain Bontemps, Paola Caselli, Hong-Li Liu, Steven Longmore, Frédérique Motte, Philip C. Myers, Stella S. R. Offner, Patricio Sanhueza, Nicola Schneider, Ian Stephens, James Urquhart, and the KEYSTONE collaboration

ABSTRACT

We present initial results from the K-band focal plane array Examinations of Young STellar Object Natal Environments (KEYSTONE) survey, a large project on the 100-m Green Bank Telescope mapping ammonia emission across eleven giant molecular clouds at distances of $0.9 - 3.0$ kpc (Cygnus X North, Cygnus X South, M16, M17, MonR1, MonR2, NGC2264, NGC7538, Rosette, W3, and W48). This data release includes the NH_3 (1,1) and (2,2) maps for each cloud, which are modeled to produce maps of kinetic temperature, centroid velocity, velocity dispersion, and ammonia column density. Median cloud kinetic temperatures range from 11.4 ± 2.2 K in the coldest cloud (MonR1) to 23.0 ± 6.5 K in the warmest cloud (M17). Using dendrograms on the NH_3 (1,1) integrated intensity maps, we identify 856 dense gas clumps across the eleven clouds. Depending on the cloud observed, $40 - 100\%$ of

the clumps are aligned spatially with filaments identified in H_2 column density maps derived from SED-fitting of dust continuum emission. A virial analysis reveals that 523 of the 835 clumps ($\sim 63\%$) with mass estimates are bound by gravity alone. We find no significant difference between the virial parameter distributions for clumps aligned with the dust-continuum filaments and those unaligned with filaments. In some clouds, however, hubs or ridges of dense gas with unusually high mass and low virial parameters are located within a single filament or at the intersection of multiple filaments. These hubs and ridges tend to host water maser emission, multiple 70μm-detected protostars, and have masses and radii above an empirical threshold for forming massive stars.

3.1 Introduction

The ubiquity of filaments in star-forming environments was first revealed by continuum observations of nearby (<300 pc), low-mass star-forming molecular clouds, which showed that filaments are present in both quiescent (Miville-Deschênes et al., 2010; Ward-Thompson et al., 2010) and active (André et al., 2010; Men'shchikov et al., 2010) star-forming regions. These results suggest filaments are created during the molecular cloud formation process prior to the onset of star formation, likely as a result of turbulence (Vázquez-Semadeni et al., 2006; Smith et al., 2014a,b; Federrath, 2016) and magnetic fields (Hennebelle, 2013; Palmeirim et al., 2013; Seifried & Walch, 2015). Furthermore, prestellar cores, the arguably gravitationally bound structures that likely collapse to form stars, are predominantly found along filaments (Könyves et al., 2010, 2015; Marsh et al., 2016). These results provide evidence that the formation and gravitational collapse of filaments is related to the core and star formation processes in low-mass star-forming environments.

Although the study of nearby molecular clouds undoubtedly provides us with a close-up view of the star formation process, such clouds are not representative of the most productive star-forming engines in our Galaxy due to their low abundance of O- and B-type stars and clusters. To observe large samples of high-mass stars (>8 $M_\odot$) and stellar clusters, we must probe giant molecular clouds (GMCs) at distances typically >300 pc from our Solar system. While these distant environments require higher spatial resolution and sensitivity, they are more indicative of the majority of clouds in the Galaxy. Similar to nearby clouds, filamentary networks of dense gas are also prevalent throughout GMCs and have been found to be spatially correlated with

signposts of high-mass star formation (e.g., Nguyen Luong et al., 2011; Hill et al., 2012b; Motte et al., 2018b). In particular, massive young stellar objects (MYSOs) and embedded stellar clusters appear to be preferentially located at the intersections of multiple filaments seen in dust continuum observations (Myers, 2009; Schneider et al., 2010a, 2012; Hennemann et al., 2012; Li et al., 2016; Motte et al., 2018a). The combination of the pervasiveness of filaments throughout molecular clouds with the finding that clusters form at the intersections of multiple filaments motivates the idea that mass flow along filaments provides the localized high-density conditions necessary to form stellar clusters and the MYSOs that form within them (Kirk et al., 2013a; Friesen et al., 2013; Henshaw et al., 2013; Schneider et al., 2010a; Fukui et al., 2015; Motte et al., 2018a).

While dust continuum emission provides a detailed look at the distribution of dense cores and filaments within molecular clouds, it does not provide the gas velocity dispersion measurements required to understand whether or not those structures are gravitationally bound. Rather, observations of dense gas emission from molecules such as NH_3 (ammonia) and N_2H^+ (diazenylium) are necessary to probe core and filament kinematics. These tracers provide an advantage over commonly observed carbon-based molecules (e.g., CO) for tracing dense gas because they suffer less from freeze-out onto dust grains at the high densities within dense cores (see, e.g., Di Francesco et al., 2007) and they are also typically optically thin with Gaussian-like profiles that allow an easier interpretation of kinematics. In addition, the hyperfine splitting of ammonia emission provides a convenient method for obtaining optical depths. Since the relative heights of the NH_3 hyperfine structures are well known in the optically thin limit, optical depths and excitation temperatures can easily be determined by measuring the intensities of the hyperfine components (Ho & Townes, 1983). Furthermore, observations of multiple NH_3 transitions allow a kinetic gas temperature to be calculated from the relative intensities of the central hyperfine groups in each transition. This line strength relationship serves as a proxy for the distribution of populations within each excited state (Ho et al., 1979), i.e., the kinetic energy over the observed portion of the cloud.

The combination of dense gas kinematics and temperatures with continuum observations provides a way to measure the virial stability of dense cores and filaments (e.g., Friesen et al., 2016; Kirk et al., 2017; Keown et al., 2017), the dissipation of turbulence from clouds and filaments to cores ("transition to coherence," Pineda et al., 2010; Chen et al., 2019a), and the flow of gas along or onto filaments (e.g., Schneider

et al., 2010a; Kirk et al., 2013a; Friesen et al., 2013; Henshaw et al., 2013). Such measurements can also be used to determine if dense structures associated with filament intersections are susceptible to gravitational collapse. If so, the structures may be the precursors of future stellar clusters, further linking filament intersections to the star formation process in GMCs.

Recent large surveys have set out to investigate the connection between dense gas kinematics and star formation by observing ammonia emission throughout different regions of the Galaxy. The Green Bank Ammonia Survey (GAS) mapped NH_3 emission throughout the nearby Gould Belt molecular clouds ($d < 500$ pc) where $A_v > 7$ (e.g., Friesen et al., 2017; Kirk et al., 2017; Keown et al., 2017; Redaelli et al., 2017; Kerr et al., 2019; Chen et al., 2019a). The Galactic plane, which typically excludes nearby (< 3 kpc) GMCs, has been mapped in ammonia by the Radio Ammonia Mid-Plane Survey (RAMPS; covering $10° < l < 40°$, $-0.5° < b < +0.5°$; Hogge et al., 2018) and the H_2O Southern Galactic Plane Survey (HOPS; covering $-70° > l > 30°$, $-0.5° < b < +0.5°$; Purcell et al., 2012). Similarly, Urquhart et al. (2011, 2015) observed ammonia and water maser emission from ~ 600 massive young stellar objects and ultra-compact H II regions as part of the Red MSX Source Survey. While these surveys trace the kinematics of the most quiescent and extreme environments in the Galaxy, they do not cover the nearest GMCs producing massive stars.

Here, we present KFPA Examinations of Young STellar Object Natal Environments (KEYSTONE, PI: J. Di Francesco), a large project on the Green Bank Telescope (GBT) that has mapped NH_3 emission in eleven GMCs at intermediate distances (0.9 kpc $< d <$ 3.0 kpc) using the K-band Focal Plane Array (KFPA) receiver and VEGAS spectrometer on the GBT. KEYSTONE targeted GMCs observable from Green Bank that are part of the Herschel OB Young Stars Survey (HOBYS, Motte et al., 2010), which mapped dust continuum emission in all GMCs out to 3 kpc using the *Herschel Space Observatory*. This sample of molecular cloud complexes presented in Motte et al. (2018a) (see also Schneider et al. (2011)) gives a complete view of high-mass star formation at distances less than 3 kpc. This sample notably contains the Cygnus X molecular complex (Hennemann et al., 2012; Schneider et al., 2016), the M16/M17 complex (Hill et al., 2012b; Tremblin et al., 2013, 2014), the Monoceres complex (Didelon et al., 2015; Rayner et al., 2017), Rosette (Motte et al., 2010; Di Francesco et al., 2010; Schneider et al., 2010b, 2012), W48 (Nguyen Luong et al., 2011; Rygl et al., 2014), the W3/KR140 complex (Rivera-Ingraham et al., 2013, 2015), NGC7538 (Fallscheer et al., 2013) plus southern regions not presented

here (Hill et al., 2012a; Minier et al., 2013; Tigé et al., 2017). Thus, KEYSTONE provides the kinematic counterpart to the HOBYS survey that is required to understand the relationship between dense gas dynamics and massive stars.

This paper, which is the first KEYSTONE publication, provides an initial look at the NH_3 (1,1) and (2,2) emission maps observed in each region, catalogs each region's dense gas clumps, estimates the virial stability of those clumps, and compares the spatial distribution of the clumps to the positions of filaments and protostars identified in *Herschel* observations. Dendrograms, tree-diagrams that identify intensity peaks in a map and determine their hierarchical structure, are used to select dense gas clumps in each cloud. The top-level structures in the dendrogram hierarchy are often called "leaves," a term that we use synonymously with "clumps" throughout this paper. In § 3.2, we describe our GBT observations and data reduction techniques, along with the archival data that were retrieved for our analysis. In § 3.3, we outline the methods used to model the NH_3 data, identify NH_3 structures, derive their stability parameters, and compare their spatial distributions to those of dust continuum filaments. In § 3.4, we estimate the cloud weight pressure and turbulent pressure exerted on the NH_3 structures. We conclude with a summary of the paper in § 3.5 and a discussion of future analyses using the KEYSTONE data in § 3.6.

3.2 Observations and Data Reduction

3.2.1 Targets

Table 3.1 lists the eleven clouds observed by KEYSTONE and their distances. Here, we provide a brief overview of each cloud. For more detailed comparisons between the clouds, see the review by Motte et al. (2018a).

W3

W3 is part of a larger complex located in the Perseus spiral arm that also includes the W4 and W5 molecular clouds (Megeath et al., 2008). The W3 Main, W3(OH), and AFGL 333 regions on the eastern edge of W3 all show signatures of high-mass star formation that may have been triggered by superbubbles from previous generations of star formation (Oey et al., 2005). W3 Main is a particularly popular source for high-mass star formation studies due to its array of H II regions (Colley, 1980; Tieftrunk et al., 1997) powered by a cluster of OB stars (Megeath et al., 1996; Ojha et al.,

Table 3.1. KEYSTONE Target GMCs

Region	R.A. (J2000)	Dec. (J2000)	Distance (kpc)	Total Mass ($M_\odot$)	Total Area (pc^2)	Footprints[a] Observed	Completeness $A_V > 10$
W3	02:23:22.140	+61:36:17.432	2.0 ± 0.1[b]	1.0E5	2.7E3	26+	98%
Mon R2	06:08:25.657	−06:14:32.812	0.9 ± 0.1[c,d]	4.9E3	1.4E2	5+	100%
Mon R1	06:32:32.294	+10:27:13.335	0.9 ± 0.1[c,e]	8.8E3	1.4E2	5	98%
Rosette	06:33:38.530	+04:29:10.771	1.4 ± 0.1[c]	3.2E4	7.2E2	15	85%
NGC2264	06:40:41.339	+09:25:42.177	0.9 ± 0.1[e]	1.0E4	2.2E2	8+	99%
M16	18:18:38.140	−13:39:30.050	1.8 ± 0.5[f]	8.6E4	5.6E2	5	52%
M17	18:19:35.479	−16:19:09.088	2.0 ± 0.1[g]	5.0E5	1.9E3	9	31%
W48	19:00:52.657	+01:41:55.338	3.0[h]	1.4E6	8.8E3	13+	60%
Cygnus X South	20:33:42.800	+39:35:41.356	1.4 ± 0.1[i]	2.2E5	2.3E3	43	84%
Cygnus X North	20:37:14.998	+41:56:04.742	1.4 ± 0.1 [i]	2.7E5	3.3E3	36+	82%
NGC7538	23:14:50.333	+61:29:04.744	2.7 ± 0.1[j]	9.3E4	1.4E3	17	100%

Note. — The right ascensions and declinations listed are the mid-point of the entire mapped area. The total mass and total area are calculated as the sum of all H_2 column density and area, respectively, mapped in each cloud by *Herschel*. The completeness represents the percentage of pixels with $A_V > 10$ in the *Herschel* H_2 column density maps that were observed by KEYSTONE. We assumed an extinction conversion factor of $N_{H2} \,/\, A_V = 0.94 \times 10^{21}$ (Bohlin et al., 1978). The completion percentages for M16, M17, and W48 account for the RAMPS intended coverage of those regions.

[a]Each footprint is $10' \times 10'$. A '+' denotes that a partially completed tile was also observed in that region.

[b]Hachisuka et al. (2006)

[c]Schlafly et al. (2014)

[d]Lombardi et al. (2011)

[e]Baxter et al. (2009)

[f]Bonatto et al. (2006)

[g]Xu et al. (2011)

[h]Rygl et al. (2010)

[i]Rygl et al. (2012)

[j]Moscadelli et al. (2009)

2004). For instance, Tieftrunk et al. (1998) used NH_3 (1,1) and (2,2) observations of W3 Main and W3(OH) to show that the stellar clusters are littered with cold dense gas clumps. More recently, Nakano et al. (2017) mapped the AFGL 333 ridge in NH_3 and found evidence for triggered star formation at the edges of the ridge but quiescent (non-triggered) formation in the ridge center. Similarly, Rivera-Ingraham et al. (2011) argued that both triggered and quiescent star formation are required to explain the YSO population detected in the cloud. More recent large-scale *Herschel* mapping of W3 by Rivera-Ingraham et al. (2013, 2015) suggested that the triggered star formation was a result of "convergent constructive feedback," which involves massive stars serving as triggers for subsequent star formation by funneling gas onto a central massive structure.

In this paper, we present the observations of the southwestern half of W3, which includes the small H II region KR 140 (Kallas & Reich, 1980), as a separate region that we named W3-west.

Mon R2

Monoceros R2 (Mon R2) is the most distant member of the larger Orion-Monoceros molecular cloud complex, which also includes the Orion A and Orion B clouds. Wilson et al. (2005) contend that Mon R2 and the Orion clouds share a common origin, as evidenced by the alignment of spurs in their CO emission with the Vela supershell. Mon R2 hosts a central reflection nebula with a high stellar volume density ($\sim$ 9000 stars pc^{-3}), including several B-type stars (Carpenter et al., 1997). Didelon et al. (2015) estimated that the size of the four main H II regions in Mon R2 range from 0.1 pc for the central ultra-compact H II region, which they suggest is undergoing pressure-driven large-scale collapse, to 0.8 pc for the most extended classical H II region. Previous NH_3 mapping by Willson & Folch-Pi (1981) and Montalban et al. (1990) have shown that the H II regions are surrounded by dense gas clumps with masses of $1-65$ $M_\odot$ and kinetic temperatures of $15-30$ K. Moreover, recent *Herschel* dust continuum and $C^{18}O$ observations by Rayner et al. (2017) showed that the gas and dust in Mon R2 has a distinct hub-spoke geometry, with a central hub of protostars and dense cores that may be fed by several connected filaments. The column density probability distribution function from the *Herschel* observations also shows two power-law tails, suggesting both turbulent- and gravity-dominated regimes in Mon R2 (Schneider et al., 2015; Pokhrel et al., 2016).

A *Herschel*-derived sample of 177 dense cores in MonR2 was published by Rayner et al. (2017). Their masses span 0.084 $M_\odot$ to 24 $M_\odot$ and their radii span 0.023 pc to 0.3 pc. Of the 177 dense cores identified by Rayner et al. (2017), 29 ($\sim$ 16%) were found to be protostellar and eleven had masses > 10 $M_\odot$.

Mon R1 and NGC 2264

The Monoceros OB1 (Mon OB1) GMC includes NGC 2264, one of the most massive star clusters ($\sim$ 1400 members) within 1 kpc of our position in the Galaxy (Dahm, 2008; Teixeira et al., 2012; Rapson et al., 2014). Initial CO and CS mapping of the region revealed several outflows associated with the cluster (e.g., Margulis & Lada, 1986; Wolf-Chase et al., 1995). Six Herbig-Haro objects have also been detected within this region (Adams et al., 1979; Walsh et al., 1992; Wang et al., 2003). Ammonia mapping by Lang & Willson (1980) and Pagani & Nguyen-Q-Rieu (1987) revealed that the dense gas in NGC 2264 is comprised of two components, each $\sim$ 0.9 pc in diameter and separated by 0.9 pc, with kinetic temperatures of $\sim$ 20 K. In addition, Peretto et al. (2006) used more recent observations of dust continuum and molecular line emission to show that several massive clumps in NGC 2264 indicate infall motions and may comprise an intermediate mode of massive star formation.

Just north of NGC 2264 is a more quiescent region of dense gas where a collection of Class 0/I and II objects are forming (Rapson et al., 2014). We henceforth refer to this northern region as "Mon R1," which it has been referred to in previous literature (Kutner et al., 1979; Ogura, 1984). Large-scale CO mapping covering NGC 2264 and Mon R1 by Oliver et al. (1996) revealed that the kinematics of the region are dominated by the Perseus and Local spiral arms.

Rosette

The Rosette complex is located in the Monoceros constellation south in declination from Mon OB1, NGC 2264, and Mon R2 (Román-Zúñiga & Lada, 2008). The cloud's emission is dominated by NGC 2244, its central OB association of 70 high-mass stars that has created a large H II region (Wang et al., 2008). Rosette has been mapped extensively in CO (Blitz & Thaddeus, 1980; Blitz & Stark, 1986; Schneider et al., 1998; Heyer et al., 2006), which revealed outflows from the massive proto-binary AFGL 961 (Castelaz et al., 1985). Large-scale *Herschel* dust continuum mapping by Di Francesco et al. (2010) revealed 473 dense clumps throughout Rosette, 371 being

starless and 102 being protostellar, which includes 6 protostellar massive dense cores and 3 prestellar massive dense cores with masses between 20 $M_\odot$ and 40 $M_\odot$ (Motte et al., 2010). Schneider et al. (2010b) also used the *Herschel* observations to show a negative temperature gradient, positive density gradient, and age sequence (more evolved to younger) as distance from the NGC 2244 cluster increases, highlighting the influence of the OB association upon the star formation in the cloud. In addition, Schneider et al. (2012) note that the massive stars and infrared clusters discovered in Rosette tend to align with the intersections of dust-identified filaments, providing compelling evidence that massive star formation occurs at the sites of filament mergers.

M16

M16, which is also known as the Eagle Nebula, is an H II region located in the Sagittarius spiral arm (Oliveira, 2008). The cloud's structure and temperature are influenced by the open cluster NGC 6611 at its center, which contains 52 OB stars (Evans et al., 2005). For example, Hill et al. (2012b) used *Herschel Space Observatory* dust continuum mapping to show there is a clear dust temperature gradient moving away from the NGC 6611 cluster. Tremblin et al. (2014) also show that the dust-derived column density probability distribution function in M16 has a second peak at high densities, which they attribute to a compressed zone of gas caused by an expanding shell of ionized gas from NGC 6611. In the south of M16 are the famous "Pillars of Creation" or "elephant trunks" imaged with the *Hubble Space Telescope* (Hester et al., 1996) and with *Herschel* (Hill et al., 2012b; Tremblin et al., 2013). The morphology of the Pillars is caused by the ionizing radiation from the central OB stars in M16 (White et al., 1999; Williams et al., 2001; Gritschneder et al., 2010). In addition, recent CO mapping of M16 by Nishimura et al. (2017) revealed a 10 pc diameter cavity of molecular gas near NGC 6611, providing further evidence of the cluster's impact on the star formation in the GMC.

M17

M17 (the Omega Nebula) is located south in declination from M16 by an angular separation of 2.5° (Oliveira, 2008). Elmegreen et al. (1979) used CO mapping, however, to show that M17 and M16 form a continuous molecular cloud structure despite their large angular separation, which is a conclusion supported by recent near-infrared

imaging (Comerón et al., 2019). Similar to M16, M17 has a central H II region created by an open cluster (NGC 6618) of 53 OB stars (Hoffmeister et al., 2008). While much of the literature is focused on mapping the molecular gas (e.g., Thronson & Lada, 1983; Stutzki et al., 1988; Stutzki & Guesten, 1990; Pérez-Beaupuits et al., 2015) and dust continuum (e.g., Gatley et al., 1979; Povich et al., 2009) of the M17SW region near NGC 6618, the whole of M17 has recently been mapped in ^{12}CO, ^{13}CO, and C^{18}O by Nishimura et al. (2018) and in ^{12}CO, ^{13}CO, HCO$^+$ and HCN by Nguyen Luong et al. (2019, submitted). M17SW has also been mapped in NH_3 by Lada (1976) and Guesten & Fiebig (1988), which revealed several distinct velocity components in the dense gas and kinetic temperatures of $30 - 100$ K.

W48

At 3 kpc (Rygl et al., 2010), W48 is the most distant HOBYS and thus KEYSTONE target. *Herschel* observations of the cloud by Nguyen Luong et al. (2011) revealed numerous H II regions with extended warm dust emission. The IRDC G035.39−00.33 region in the north of W48 was also found to host 13 high-mass ($M > 20$ M$_\odot$), compact (diameters of $0.1 - 0.2$ pc), and dense ($2 - 20{\times}10^5$ cm^{-3}) massive dense cores that could be the precursors of massive stars (Nguyen Luong et al., 2011). Liu et al. (2018) used dust polarization and NH_3 measurements to show that these clumps are likely supported against gravitational collapse by magnetic fields and turbulence. Similarly, Pillai et al. (2011) used interferometric observations of G35.20−1.74 in the east of W48 to show that the cores there were also massive ($\sim 9 - 250$ M$_\odot$), dense ($> 10^5$ cm^{-3}), cold (< 20 K), and highly deuterated ([NH_2D/NH_3] $> 10\%$), which suggest they are on the verge of forming protoclusters. With several methanol maser emission line detections (Slysh et al., 1995; Minier et al., 2000; Sugiyama et al., 2008; Surcis et al., 2012), which are a signpost of massive stars, it is clear that W48 is an interesting testbed for high-mass star formation studies.

Cygnus X

The Cygnus X molecular cloud complex is one of the most active star-forming regions in the nearby Galaxy (Schneider et al., 2016). It hosts over 1800 protostars (Kryukova et al., 2014) and is a favored target for studies of high-mass star formation due to its high concentration of OB associations (e.g., Hanson, 2003; Comerón & Pasquali, 2012; Wright et al., 2014). The OB associations range in age and size from the young

proto-globular cluster Cyg OB2 (Knödlseder, 2000; Wright et al., 2014), harboring nearly one hundred O-stars, to the slightly older and smaller Cyg OB1, OB3, and OB9 (Uyanıker et al., 2001). It has been mapped extensively in a variety of molecular gas tracers (Schneider et al., 2006, 2010b; Wilson & Mauersberger, 1990; Csengeri et al., 2011a,b; Duarte-Cabral et al., 2013, 2014; Dobashi et al., 2014; Schneider et al., 2016; Pillai et al., 2012), dust continuum (Motte et al., 2007; Bontemps et al., 2010; Hennemann et al., 2012), and dust polarization (e.g., Ching et al., 2017).

Although previous papers have treated Cygnus X as a single complex (Schneider et al., 2006; Rygl et al., 2012), our observations split the Cygnus X cloud into a North and South region. The choice to treat Cygnus X North and South as separate regions in our analysis is motivated by the observations of Kryukova et al. (2014), which showed that each have distinct luminosity functions and morphological differences indicative of dissimilar star-forming environments. Cygnus X North contains DR21, the massive ridge where a slew of massive stars are forming, including the high-mass core DR21(OH) (e.g., Mangum et al., 1991; Csengeri et al., 2011b). Previous observations of the DR21 H II region by Guilloteau et al. (1983) mapped the region in NH_3 (1,1), (2,2), (3,3), and (4,4), which revealed absorption in the (1,1) and (2,2) emission that indicates high excitation temperatures ≥ 100 K. The southern section of Cygnus X is home to DR15, a cluster of ~ 200 protostars that sits atop a filamentary pillar extended over 10 pc to the south (Rivera-Gálvez et al., 2015).

NGC 7538

NGC 7538 is a GMC associated with the Perseus spiral arm (Kun et al., 2008). It harbors several bright H II regions, most notably around the IRS $1-11$ sources in its center (Werner et al., 1979; Mallick et al., 2014). Strong outflows have been observed throughout the cloud (Campbell, 1984; Scoville et al., 1986; Sandell et al., 2005; Qiu et al., 2011), one of which has signatures of a massive (~ 40 $M_\odot$) accreting Class 0 protostar (Sandell et al., 2003). Dust continuum observations covering the IRS $1-11$ sources by Reid & Wilson (2005) showed that the bright IR sources are surrounded by massive cold clumps. *Herschel* observations by Fallscheer et al. (2013) that covered a wider field-of-view revealed an evacuated ring structure in the east of NGC 7538, with a string of cold clumps detected along the ring's edge. Fallscheer et al. also detected 13 massive ($M > 40$ $M_\odot$) and cold ($T < 15$ K) clumps that may be starless or contain embedded Class 0 sources, further highlighting the high-mass star-forming

potential of the cloud.

Previous ammonia observations in NGC 7538 have been focused primarily on IRS 1, which has shown a slew of rare emission features such as: maser emission in H_2O, the nonmetastable $^{14}NH_3$ (10,6), (10,8), (9,8), and (9,6) transitions, and $^{15}NH_3$ (3,3) (Johnston et al., 1989; Hoffman & Seojin Kim, 2011; Hoffman, 2012) as well as vibrationally excited ammonia (Schilke et al., 1990).

3.2.2 GBT NH_3 Data

Data were obtained as part of the KEYSTONE (KFPA Examinations of Young STellar Object Natal Environments) survey, a large project on the GBT that mapped NH_3, HC_5N, HC_7N, HNCO, H_2O, CH_3OH, and CCS emission across eleven GMCs at distances between 0.9 kpc and 3 kpc. Observations were conducted between 2016 October and 2019 March for a total of 356.25 observing hours, including overheads. Table 3.2 summarizes all observed transitions along with their rest frequencies. The eleven GMCs observed by KEYSTONE were selected from the HOBYS survey. The observing strategy for KEYSTONE targeted all filamentary structures where $A_V >$ 10 mag in the HOBYS column density maps (see Ladjelate et al., in preparation), which is slightly higher than that used in the GAS survey ($A_V > 7$; Friesen et al., 2017). Due to the large amount of foreground and/or background contamination along the line of sight to some of the clouds, this extinction threshold does not have much physical meaning but rather is meant to highlight the densest regions in each cloud. The KEYSTONE observations also exclude parts of M16, M17, and W48 that will be mapped with the GBT by the Radio Ammonia Mid-Plane Survey (RAMPS, Hogge et al., 2018).

Observations were made with the GBT's K-band Focal Plane Array, which has seven beams arranged in the shape of a hexagon with beam centers separated by $\sim 95''$ on the sky. Following the observational setup used in GAS, each cloud was segmented into $10' \times 10'$ tiles that were observed using on-the-fly mapping and frequency-switching for 11 seconds of on+off integration time (5.5 seconds on-source and 5.5 seconds at reference frequency) per beam (i.e., a total of 77 seconds when summing over all seven beams) for each resolution element. The $10' \times 10'$ tiles were scanned using on-the-fly mapping, covering the observed region in the Right Ascension and Declination directions. The row separation ($\sim 13''$) and spectrometer dump cadence ensured that each resolution element in the map was sampled by > 3 samples in both

directions, ensuring Nyquist sampling. Each tile took ~ 1.3 hours to complete, with 1 to 3 tiles observed per session. Table 3.1 lists the number of tiles completed for each cloud. The survey's completeness, defined as the percentage of the HOBYS maps with $A_V > 10$ mag observed by KEYSTONE, ranged from 31% for M17 to 100% for MonR2 and NGC7538 (see Table 3.1).

The telescope's pointing and focus were aligned before mapping each tile to account for changes in the optical performance due to, e.g., temperature- and weather-dependent structural deformations. The KFPA receiver's noise diodes were used to measure the off-source system temperatures for each observing session, which are also temperature- and weather-dependent. Since each of the KFPA's beams has an independent response (i.e., gain), the Moon was observed at least once per session for flux density calibration, if available. The Moon's large angular size compared to the size of the KFPA beam allowed for beam gains to be calculated from single on-source and off-source observations during each observing session. Figure 3.1 shows the beam gains for the NH_3 (1,1) spectral windows (IFs 6, 7, and 8) averaged over all observations of the Moon for each polarization. Table 3.3 displays the final beam gains used for flux density calibration, along with the standard deviation for each average.

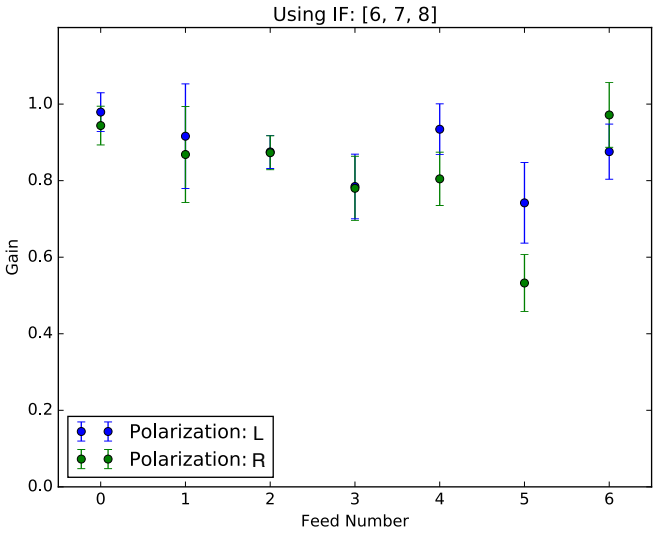

Fig. 3.1 – Beam gains for the NH_3 (1,1) spectral windows (IFs 6, 7, and 8) averaged over all Moon observations for each feed and polarization.

The GBT's VEGAS backend was configured with eight spectral windows, each 23.44 MHz wide. All five NH_3 transitions (1,1) up to (5,5), along with HC_7N $(9-8)$ and CH_3OH $(10_1 - 9_2)$ A^-, were observed in seven of the windows across all seven of

the KFPA beams. The eighth VEGAS window covered H_2O ($6_{16}-5_{23}$), HC_5N (8−7), HC_7N (19 − 18), HNCO ($1_{0,1} - 0_{0,0}$), CH_3OH ($12_2 - 11_1$) A^-, and CCS ($2_0 - 1_0$) in only the central KFPA beam. The GBT beam has a FWHM of 32″ at the NH_3 (1,1) rest frequency. This VEGAS configuration is the same as that used by the RAMPS survey (Hogge et al., 2018).

In this paper, we present the NH_3 (1,1) and (2,2) emission. Other lines will be presented in future KEYSTONE papers. We also identify H_2O ($6_{16} - 5_{23}$) maser emission by eye in the spectral cubes to include in figures presented in Section 3.4, but leave the full presentation of those data and a more thorough maser identification technique to White et al. (in prep.). The NH_3 data were reduced using `gbtpipe`[1], a Python-packaged version of the standard GBT reduction pipeline. The data were calibrated and output as 3D FITS spectral cubes, with R.A., Dec., and spectral frequency comprising each axis. The on-the-fly observations were mapped to a grid of square pixels with width of 8.8″, which corresponds to $\sim$ 3.5 pixels per FWHM beam of the NH_3 (1,1) line. The spectrum corresponding to each spatial pixel was determined using a weighted average of on-the-fly integrations from all seven beams of the K-band Focal Plane array, including those samples with separations less than one FWHM beam size away from a given map pixel. The weighting scheme is a Gaussian-tapered Bessel function, as described in Friesen et al. (2017) following Mangum et al. (2007). This procedure results in data cubes with a resolution of 32″ and the dense sampling from the mapping strategy and multiple receiver feeds produces high-quality maps without discernible scanning patterns in the image or Fourier domain.

The pipeline also subtracts a first-order polynomial fit to the channels on the edges of each scan prior to gridding to remove any shape in the spectral baselines introduced by, e.g., instrumental effects. The pixel size of the final data cubes is 8.8″, with a spectral resolution of 5.7 kHz, or 0.07 km s^{-1}.

To remove any remaining shape in the spectral baselines, we perform an additional round of per-pixel baseline fitting similar to the method described in Hogge et al. (2018). Namely, a sliding window with a width of 31 channels is used to calculate a "local" standard deviation for every channel in a spectrum. For the 15 channels at each end of the spectrum, the first and last 31 channels are used as the "local" windows, while all other channels are at the center of their "local" window. From the standard deviation distribution of all "local" windows, the central channels belonging to the lowest two quintiles are used for the baseline fit. Thus, channels that belong

[1] https://github.com/GBTSpectroscopy/gbtpipe

to an emission line or noise spike are excluded from the baseline fit due to their high "local" standard deviation relative to the non-emission-line channels in the spectrum. Next, polynomials up to a third order are fit to the selected channels. A reduced chi-squared value is then calculated for each of the best-fit polynomials against the full spectrum. Finally, the polynomial with the lowest reduced chi-squared value is subtracted from the original spectrum. This baseline subtraction technique is publicly available[2], along with the full KEYSTONE data reduction code base. The final baseline-subtracted NH_3 (1,1) and (2,2) data cubes are publicly available[3].

The system temperatures for the observations were typically $40 - 50$ K, with a median of ~ 43 K. Figure 3.2 shows histograms of the RMS noise for the NH_3 (1,1) and (2,2) maps of each cloud. We calculate the RMS using the channels in the best-fit model from our line-fitting procedure (see Section 3.3.1) with brightness lower than 0.0125 K. While the medians of the RMS distributions for each cloud range from 0.13 K to 0.2 K, most of the distributions have a peak below 0.15 K. M17 and M16 have slightly higher noise (medians of 0.2 K and 0.18 K, respectively) than the other regions since they are the lowest declination sources observed ($\sim -16°$ and $-13°$, respectively).

3.2.3 *Herschel* Dust Continuum Data

Herschel Space Observatory Level 2.5 data products at 70 μm, 160 μm, 250 μm, 350 μm, and 500 μm for each KEYSTONE region were downloaded from the European Space Agency Herschel Science Archive[4]. These maps were originally observed by the Herschel OB Young Stars Survey (Motte et al., 2010) and have spatial resolutions of 8.4″, 13.5″, 18.2″, 24.9″, and 36.3″, respectively. Although the HOBYS team has released dense core and protostar catalogs for MonR2 (Rayner et al., 2017), W3 (Rivera-Ingraham et al., submitted), Cygnus X North (Bontemps et al., in preparation), NGC 6334 (Tigé et al., 2017), and NGC 6537 (Russeil et al. 2019, in press), no catalogs have been yet released for many of the clouds targeted by KEYSTONE. In this paper, we use the *Herschel* $160 - 500$ μm maps to estimate the H_2 column densities and masses of structures identified in the KEYSTONE observations (see Section 3.3.4). Additionally, we use the 70 μm maps to identify embedded protostars in each cloud (see Section 3.3.6).

[2] https://github.com/GBTAmmoniaSurvey/keystone
[3] https://doi.org/10.11570/19.0074
[4] http://archives.esac.esa.int/hsa/whsa/

Table 3.2. KEYSTONE Observed Transitions

Molecule	Transition	Rest Frequency[a] (MHz)	Number of Beams
HC_5N	$(8-7)$	21301.26	1
HC_7N	$(19-18)$	21431.93	1
CH_3OH	(12_2-11_1) A^-	21550.34	1
HNCO	$(1_{0,1}-0_{0,0})$	21981.4706(1)	1
H_2O	$(6_{16}-5_{23})$	22235.08	1
CCS	(2_0-1_0)	22344.030	1
CH_3OH	(10_1-9_2) A^-	23444.78	7
NH_3	(1,1)	23694.4955	7
NH_3	(2,2)	23722.6336	7
NH_3	(3,3)	23870.1296	7
HC_5N	$(9-8)$	23963.9010	7
NH_3	(4,4)	24139.35	7
NH_3	(5,5)	24532.92	7

[a]Accessed from Lovas (2004)

Table 3.3. Beam Gains

Beam	Polarization L	Polarization R
0	0.979 (0.050)	0.944 (0.051)
1	0.916 (0.137)	0.868 (0.126)
2	0.875 (0.043)	0.873 (0.044)
3	0.785 (0.084)	0.780 (0.084)
4	0.934 (0.066)	0.805 (0.070)
5	0.742 (0.105)	0.533 (0.074)
6	0.876 (0.072)	0.972 (0.085)

Note. — Average beam gains with one-σ variations shown in parentheses.

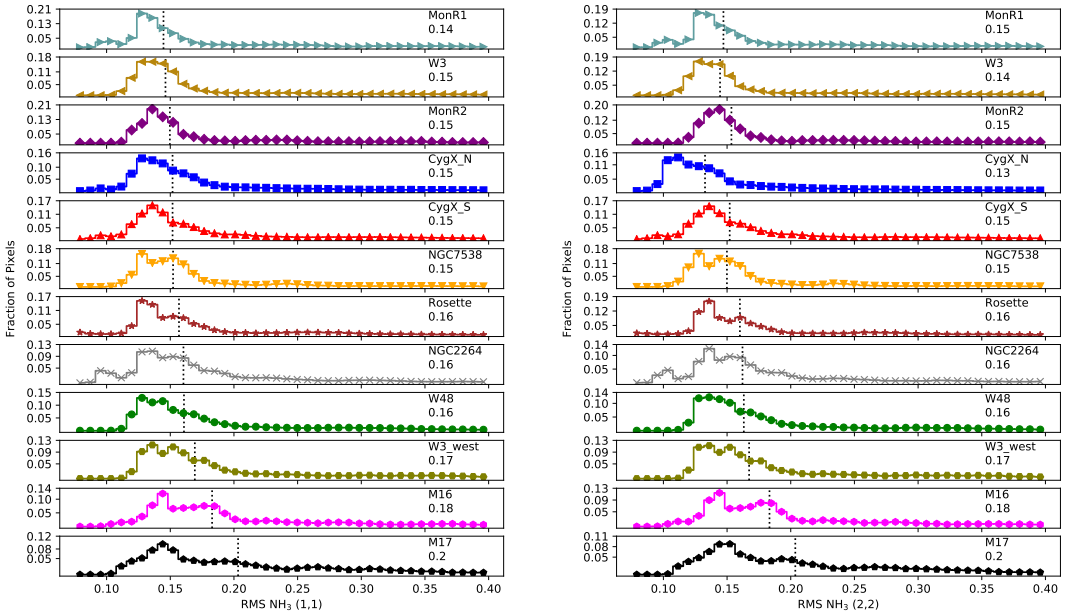

Fig. 3.2 – Histograms of the RMS noise for the NH_3 (1,1) (left) and NH_3 (2,2) (right) maps of each cloud. The median of the distribution is displayed as a vertical dotted line, with the corresponding value shown in the upper right corner of each panel. The clouds are ordered from top to bottom by increasing median NH_3 (1,1) RMS noise.

To estimate H_2 column densities for each region, spectral energy distributions (SEDs) were created by combining the $160-500$ μm maps for each observed pixel. Full details of the SED-fitting method are described in Singh et al. (2019, in preparation), but are similar to the method applied in all HOBYS papers (see, e.g., Ladjelate et al. in preparation). Here, we provide a brief summary of the process: first, a zero-level offset was added to the 160 μm map based on *Planck* observations to account for background continuum emission not included in the *Herschel* data. The *Herschel* Level 2.5 products for $250 - 500$ μm already have this offset applied, so no additional offsets were added to those maps. Next, all maps were convolved to a resolution of $36.3''$ and aligned to the same pixel grid as the 500 μm map. SEDs were then assembled on a pixel-by-pixel basis and a modified blackbody model of the form $I_\lambda = B_\lambda(T_D)\kappa_\lambda\Sigma$ was fit to the data, where I_λ is the surface brightness of the emission, $B_\lambda(T_D)$ is the Planck blackbody function at dust temperature T_D, and κ_λ is the dust opacity defined as $\kappa_\lambda = 0.1(\lambda/300\mu\text{m})^{-\beta}$ cm^2/g following Hildebrand (1983) and assuming a gas-to-dust ratio of 100. The dust emissivity index, β, is fixed for each pixel and is based on *Planck*-derived dust models (Planck Collaboration et al., 2014) that were resampled to the same pixel grid as the *Herschel* maps. A stacked

histogram showing the β distribution across all pixels used for SED fitting in each region is displayed in Figure 3.3. The values of β vary between 1.2 and 2.0. The β distributions also vary from cloud to cloud, with the highest values observed in clouds close to the Galactic plane such as W48, M17, and M16. We used *Planck*-derived values of β because the *Herschel* data include only the portion of the dust SED close to the intensity peak. The position of the intensity peak is a function of both T_D and β (e.g., $\lambda_{peak} = 1.493/T_D(3+\beta)$ for a modified blackbody, Elia & Pezzuto, 2016) and it is not possible to remove the degeneracy between these two parameters unless data at longer wavelengths, where $I_\nu \propto \lambda^{-\beta}$, are used. Since the *Planck* data include observations down to 850 μm, they are more capable of constraining β than the *Herschel* data.

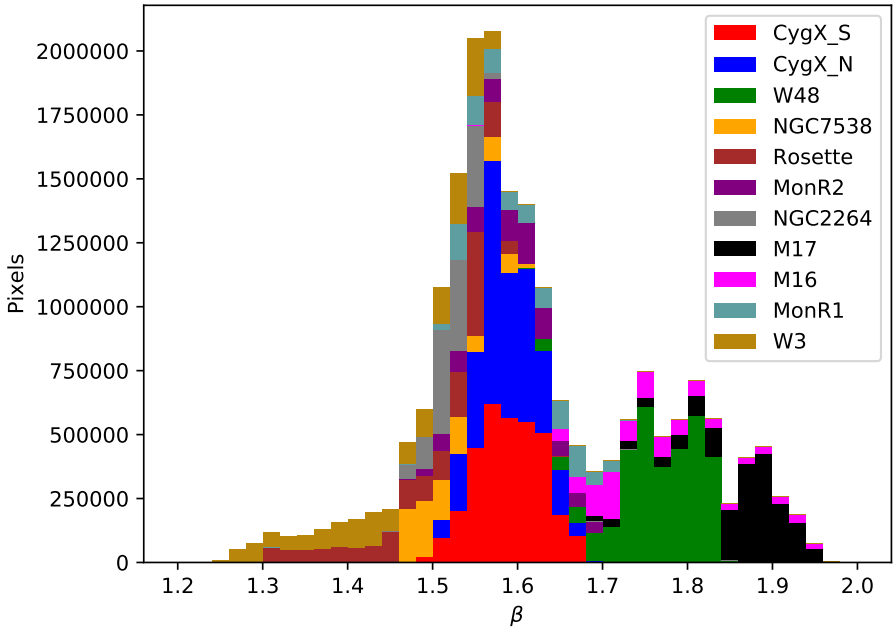

Fig. 3.3 – Stacked histogram of the dust emissivity, β, used for SED fitting of each pixel in the *Herschel* dust continuum maps for all clouds observed by KEYSTONE. The β values are from *Planck*-derived dust models (Planck Collaboration et al., 2014) that have been resampled to the same pixel grid as the *Herschel* data.

The gas surface mass density, Σ, and dust temperature were left as free parameters during the fitting procedure. The resulting best-fit model's Σ was converted to H_2 column density, $N(H_2)$, using $\Sigma = \mu_H m_H N(H_2)$, where μ_H=2.8 is the mean molecular weight per hydrogen molecule, which assumes the relative mass ratios of hydrogen, helium, and metals are 0.71, 0.27, and 0.02, respectively (see, e.g., Appendix A in

Kauffmann et al., 2008), and m_H is the mass of a hydrogen atom. The SED fitting procedure failed to converge for a small fraction of pixels where the dust continuum emission was saturated. The percentage of affected pixels for the KEYSTONE clouds affected are: M17 (0.09%), W48 (0.008% of pixels), Cygnus X North (0.006% of pixels), NGC7538 (0.01% of pixels), W3 (0.01% of pixels), and MonR2 (0.001% of pixels). For the affected pixels, we replace their values with the median column density of the ten closest pixels with reliable SED fits. As such, this is likely a lower limit to the true column density for those pixels. Any dendrogram-identified leaf (see Section 3.3.3) that overlaps with one of these affected pixels is also flagged in all catalogs and analyses. The number of leaves in each cloud that include affected pixels are: M17 (1 of 38 leaves), W48 (1 of 100 leaves), Cygnus X North (2 of 200 leaves), NGC7538 (1 of 73 leaves), and W3 (2 of 84 leaves).

The main difference between the column densities derived in this paper and those of the HOBYS collaboration (Ladjelate et al. in preparation) involve the assumptions on β. Specifically, the HOBYS column density maps assume $\beta = 2$ for all pixels while we use $1.2 \leq \beta \leq 2.0$ based on *Planck* dust models that constrain β on large spatial scales (Planck Collaboration et al., 2014). Our lower values of β result in comparatively lower column densities in our maps. For instance, the HOBYS team has released the H_2 column density maps and core/protostar catalog for MonR2 (Rayner et al., 2017). We find that the Rayner et al. (2017) column densities are on average a factor of ~ 2.5 higher than those derived in this paper. Although the higher column densities in the HOBYS maps would lead to larger structure masses in our analysis, we discuss in Section 3.3.4 that the method used to convert the column densities into structure masses is likely a larger source of uncertainty than the β assumption. Moreover, we also recovered 22 of the 28 ($\sim 79\%$) protostars identified by Rayner et al. (2017), with the six discrepant sources located in the central MonR2 hub that is bright at 70 μm. This suggests that our protostar extraction is likely confusion limited in bright hubs, but can efficiently recover sources that are more isolated.

3.2.4 JCMT $C^{18}O$ Data

$C^{18}O$ $(3-2)$ data cubes observed by the HARP-ACSIS spectrometer on the James Clerk Maxwell Telescope (JCMT) were obtained from the JCMT Science Archive[5],

[5] http://www.cadc-ccda.hia-iha.nrc-cnrc.gc.ca/en/

which is hosted by the Canadian Astronomy Data Centre. Of the eleven clouds observed by KEYSTONE, six were found to have publicly available $C^{18}O$ $(3-2)$ data cubes in the JCMT Science Archive: Cygnus X North, Cygnus X South, M16, M17, NGC7538, and W3. The native spectral resolution of the $C^{18}O$ $(3-2)$ cubes is ~ 0.056 km s^{-1} and the spatial resolution is $15.3''$. To match better the spatial and spectral resolution of our NH_3 observations and improve sensitivity, we smoothed the $C^{18}O$ $(3-2)$ maps to a spatial resolution of $32''$ and spectral resolution of 0.11 km s^{-1}. In Section 3.4.3, we describe how Gaussian line fitting of these data cubes is used to estimate the external, turbulent pressure on the ammonia structures observed by KEYSTONE.

3.3 Analysis and Results

3.3.1 NH_3 Line Fitting

The NH_3 (1,1) and (2,2) lines were used to estimate the excitation temperature (T_{ex}), kinetic gas temperature (T_K), centroid velocity (V_{LSR}), velocity dispersion (σ), and para-NH_3 column density ($N_{para-NH_3}$) for each pixel. We adopted the line fitting method of the Green Bank Ammonia Survey (GAS) described in Friesen et al. (2017), which uses the `coldammonia` model in the `pyspeckit` Python package (Ginsburg & Mirocha, 2011) to generate model ammonia spectra under the assumptions of LTE and a single velocity component along the line of sight. While most of the KEYSTONE spectra are well characterized by a single velocity component, we do see signs of multiple velocity components that are closely separated along the spectral axis in regions of W48 and M17. For those spectra, our single velocity component fitting will produce a best-fit model that has a broadened line width to account for the larger width of the emission line features in the spectrum. In a future KEYSTONE paper, we plan to implement a multiple velocity component fitting method that will robustly identify spectra with more than one velocity component and estimate better the line widths for those spectra (see Chapter 4 of this dissertation).

The GAS line-fitting pipeline[6] was applied to all pixels with NH_3 (1,1) signal-to-noise ratio (SNR) > 3, where SNR is measured from the ratio of peak emission-line intensity to the rms of the off-line channels in the spectrum. In addition to the minimum SNR threshold, pixels were excluded from our final parameter maps if

[6]available at http://gas.readthedocs.io/

they did not meet the following constraints on the best-fit model parameters and uncertainties:

1. 5 K $< T_K <$ 40 K (outside this range, the NH_3 (1,1) and (2,2) lines cannot constrain T_K);
2. 0.05 km s^{-1} $< \sigma <$ 2.0 km s^{-1} (below 0.05 km s^{-1} is unrealistic since our channel width is only $\sim$ 0.07 km s^{-1}; above 2.0 km s^{-1} is uncharacteristic of NH_3 (1,1) emission in the observed star-forming environments (e.g., Pillai et al., 2011; Olmi et al., 2010) and likely indicates the presence of strong outflows or multiple velocity components along the line of sight);
3. $N_{para-NH_3} < 10^{16}$ cm^{-2} (above 10^{16} cm^{-2} is uncharacteristic of NH_3 emission in the observed star-forming environments (e.g., Olmi et al., 2010));
4. $T_{K,err} < 5$ K;
5. $\sigma_{err} < 2.0$ km s^{-1};
6. $V_{LSR,err} < 1$ km s^{-1};
7. $(\log N_{para-NH_3})_{err} < 2$;

where $4 - 7$ are included to cull fits that were unable to converge.

The final parameter maps for each region are shown in Figures 3.4-3.15. To compare each region's ammonia emission to its dust continuum emission, we also plot *Herschel* H_2 column density contours overtop the ammonia parameter maps presented in Figures 3.4-3.15. The ammonia emission tends to occur where total extinction in the V band (A_V) is larger than $\sim 6 - 8$ mag.

A comparison of the T_K and σ histograms for each region is presented in Figure 3.16. Although the T_K distributions are consistent for most of the regions, there are significant temperature differences between the regions with the lowest temperatures (MonR1 and W3-west) compared to the highest temperature regions (M17 and MonR2). Similarly, the σ distributions are fairly consistent across regions, with peak values of $0.3 - 0.7$ km s^{-1}. There are several regions (NGC7538, W48, M17), however, that have a tail of pixels with large line widths > 1 km s^{-1}. These large line width tails are likely due to a higher fraction of pixels with strong outflows or multiple velocity components along the line of sight.

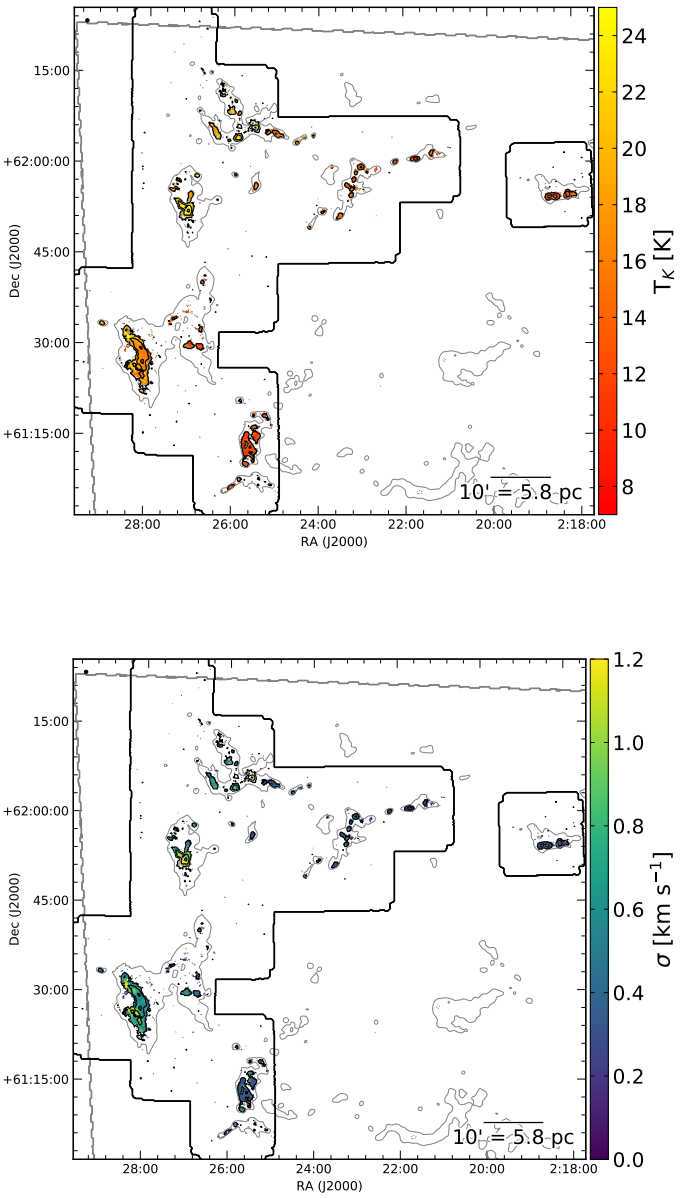

Fig. 3.4 – Kinetic temperature (top) and NH_3 (1,1) velocity dispersion (bottom) derived from NH_3 (1,1) and (2,2) line fitting of the W3 observations. The black contours show the NH_3 (1,1) integrated intensity at 1.0, 3.5, and 10 K km s^{-1}. The solid and dotted grey contours outline H_2 column densities of 2.8×10^{21} cm^{-2} and 9.4×10^{21} cm^{-2}, respectively, which are equivalent to a total extinction in the V band of $A_V = 3$ mag and 10 mag. The 32″ beam size is shown as a black dot in the upper left corner of each plot. The thick black and gray lines outline the KEYSTONE and *Herschel* mapping boundaries, respectively.

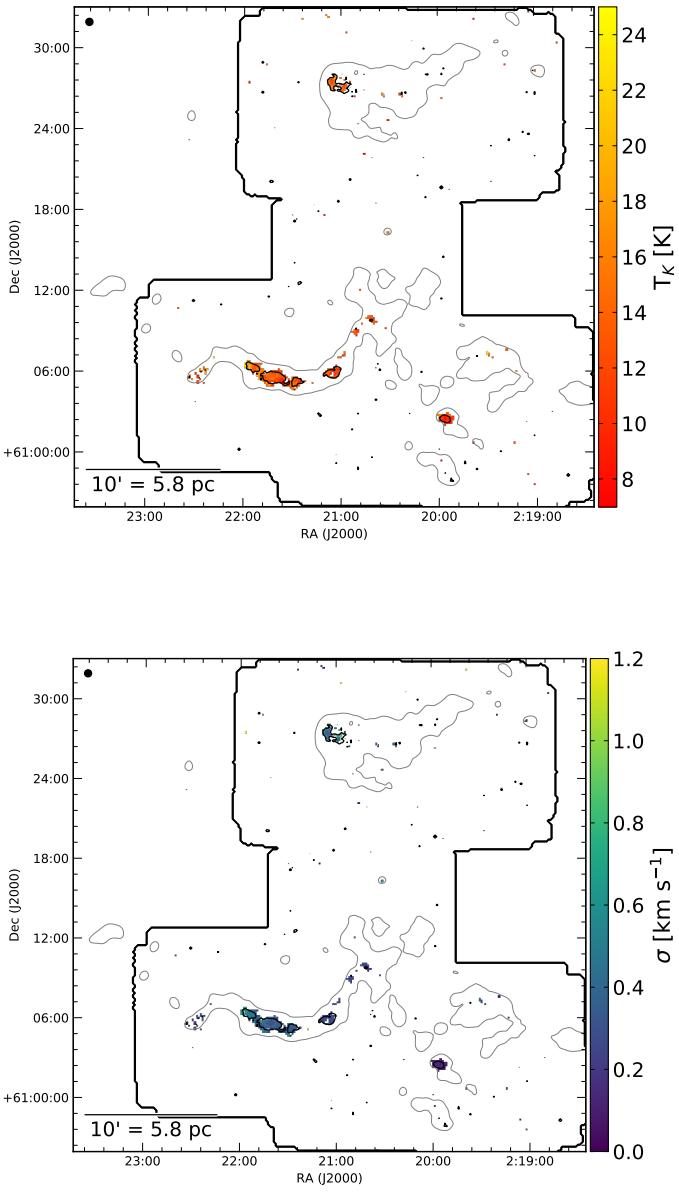

Fig. 3.5 – Same as Figure 3.4 for W3-west.

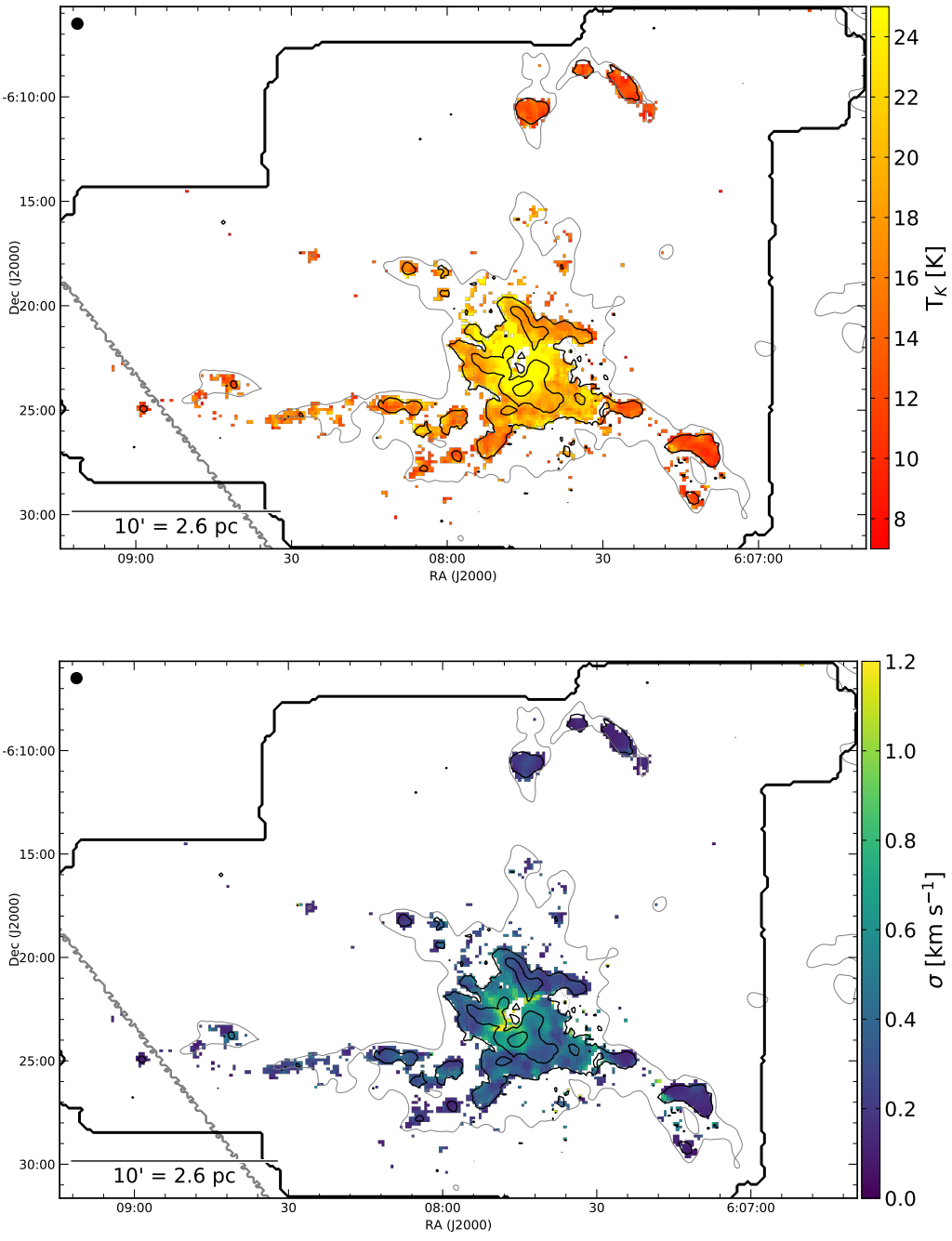

Fig. 3.6 – Same as Figure 3.4 for MonR2.

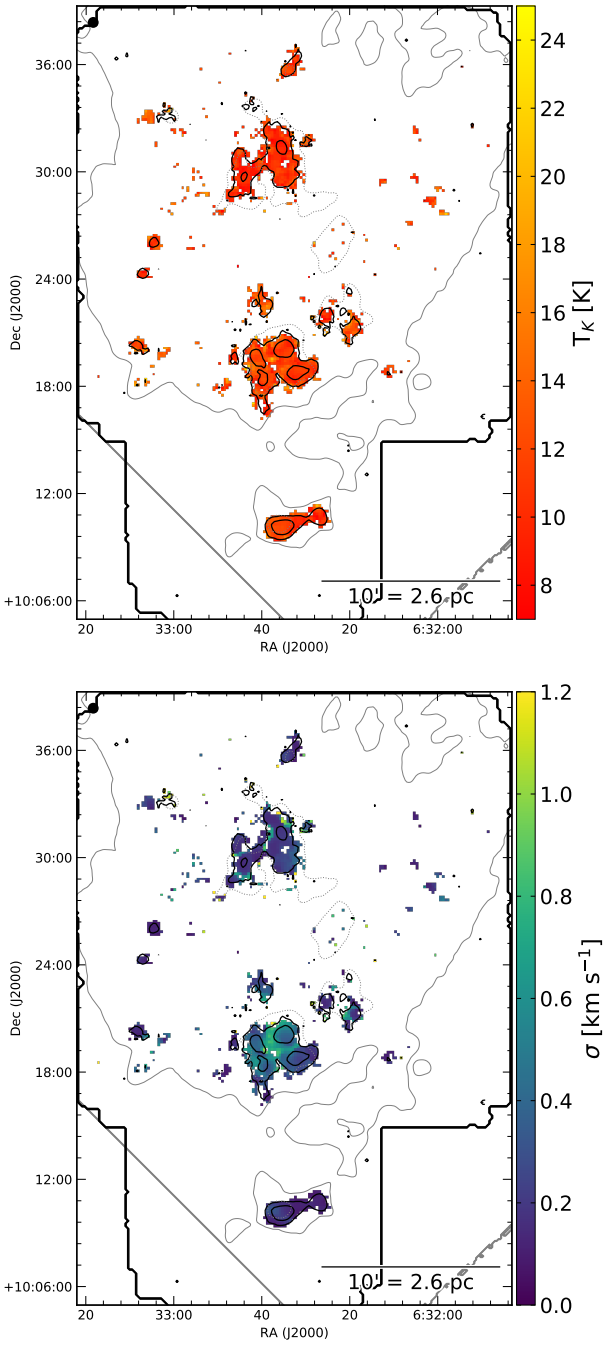

Fig. 3.7 – Same as Figure 3.4 for MonR1.

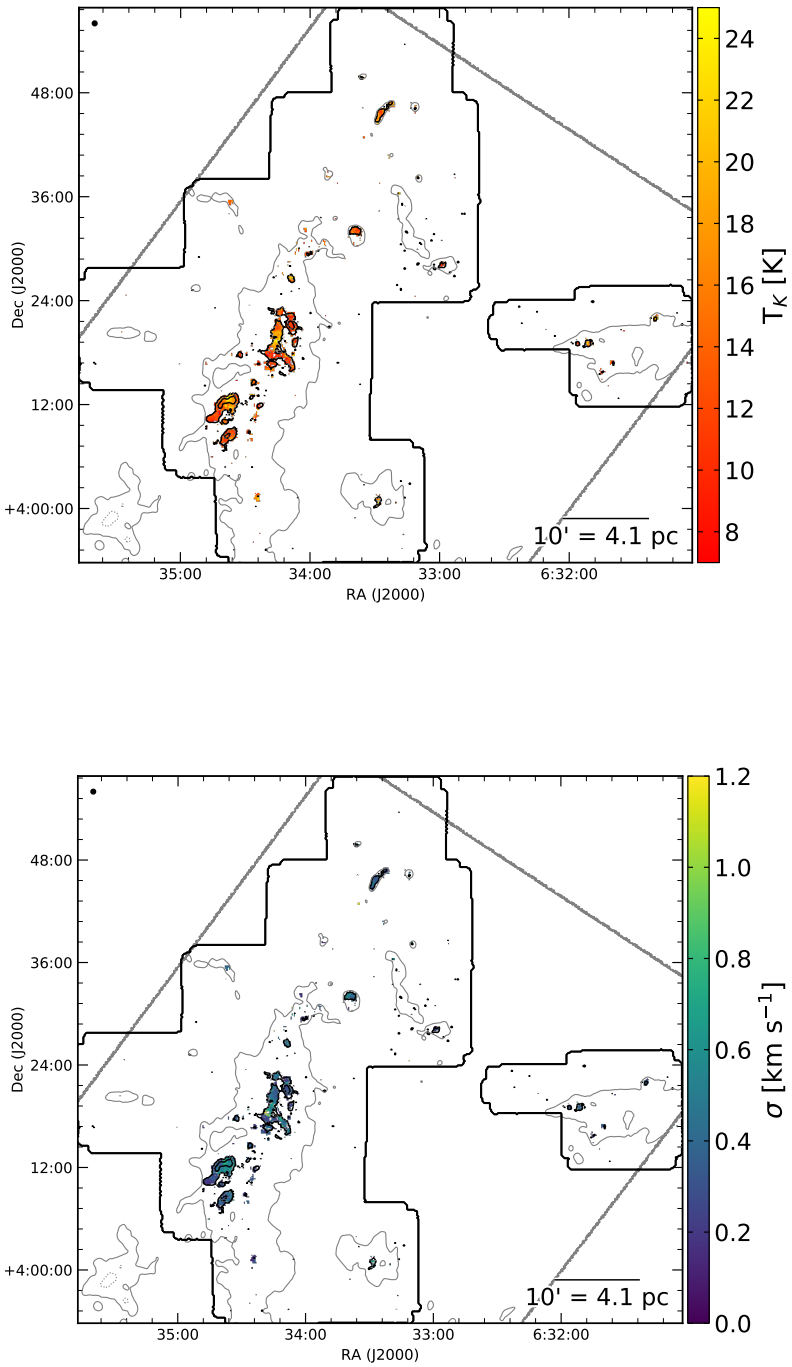

Fig. 3.8 – Same as Figure 3.4 for Rosette.

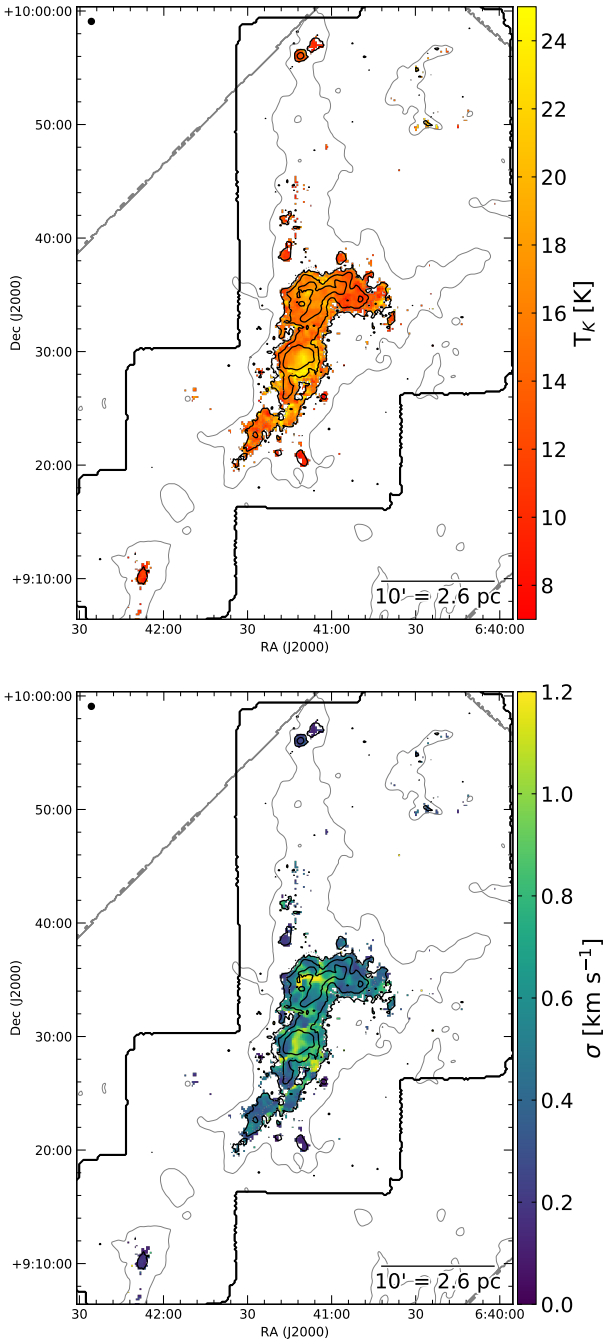

Fig. 3.9 – Same as Figure 3.4 for NGC2264.

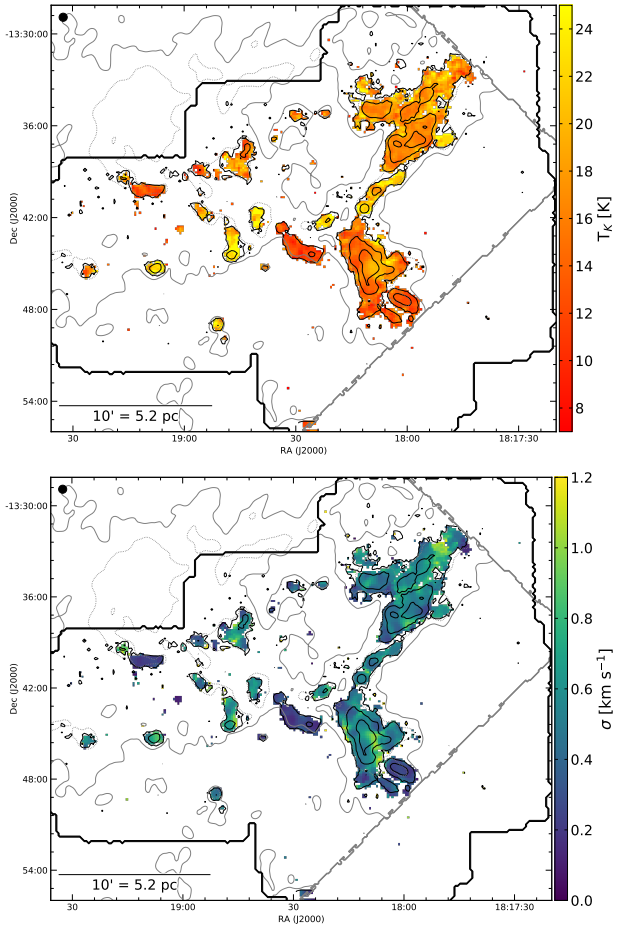

Fig. 3.10 – Same as Figure 3.4 for M16. The solid and dotted grey contours outline H_2 column densities of 5.6×10^{21} cm^{-2} and 9.4×10^{21} cm^{-2}, respectively, which are equivalent to a total extinction in the V band of $A_V = 6$ mag and 10 mag.

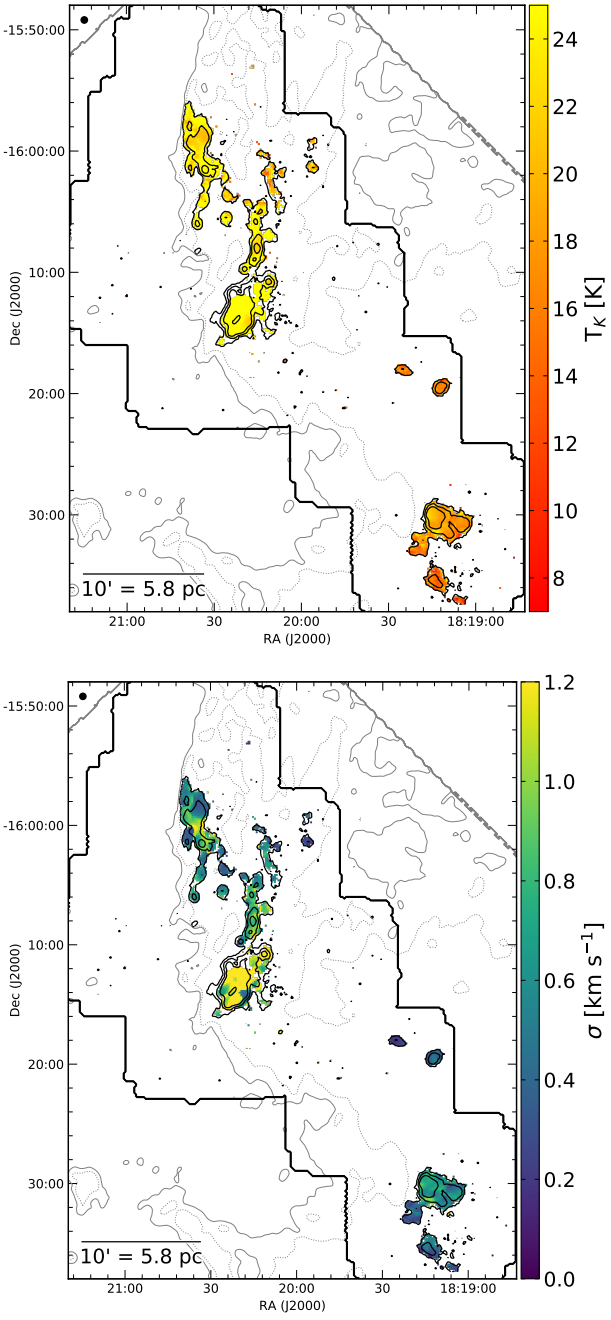

Fig. 3.11 – Same as Figure 3.4 for M17. The solid and dotted grey contours outline H_2 column densities of 7.5×10^{21} cm^{-2} and 9.4×10^{21} cm^{-2}, respectively, which are equivalent to a total extinction in the V band of $A_V = 8$ mag and 10 mag.

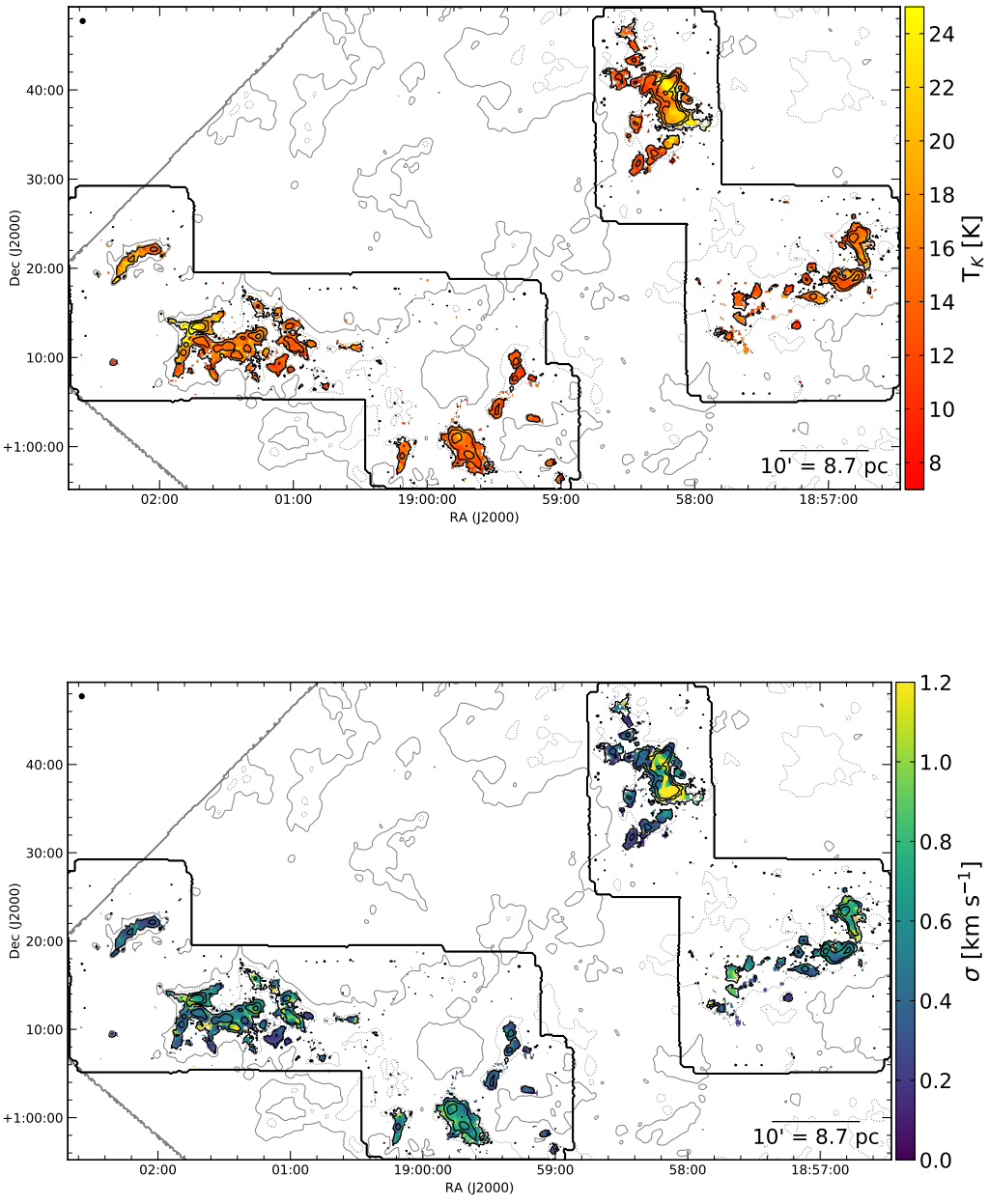

Fig. 3.12 – Same as Figure 3.10 for W48.

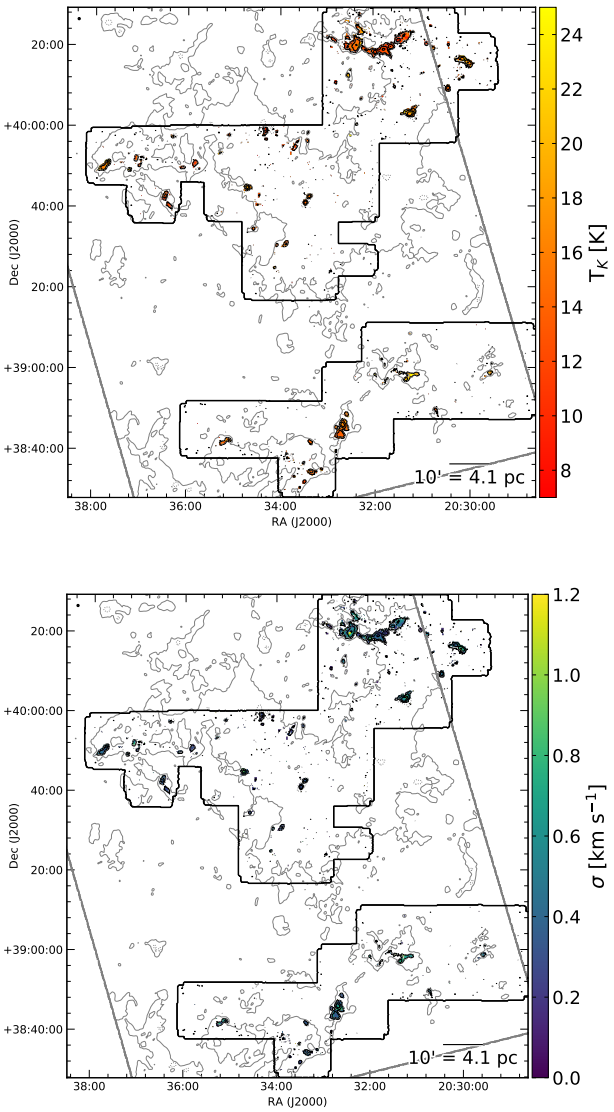

Fig. 3.13 – Same as Figure 3.4 for Cygnus X South. The solid and dotted grey contours outline H_2 column densities of 4.7×10^{21} cm^{-2} and 9.4×10^{21} cm^{-2}, respectively, which are equivalent to a total extinction in the V band of $A_V = 5$ mag and 10 mag.

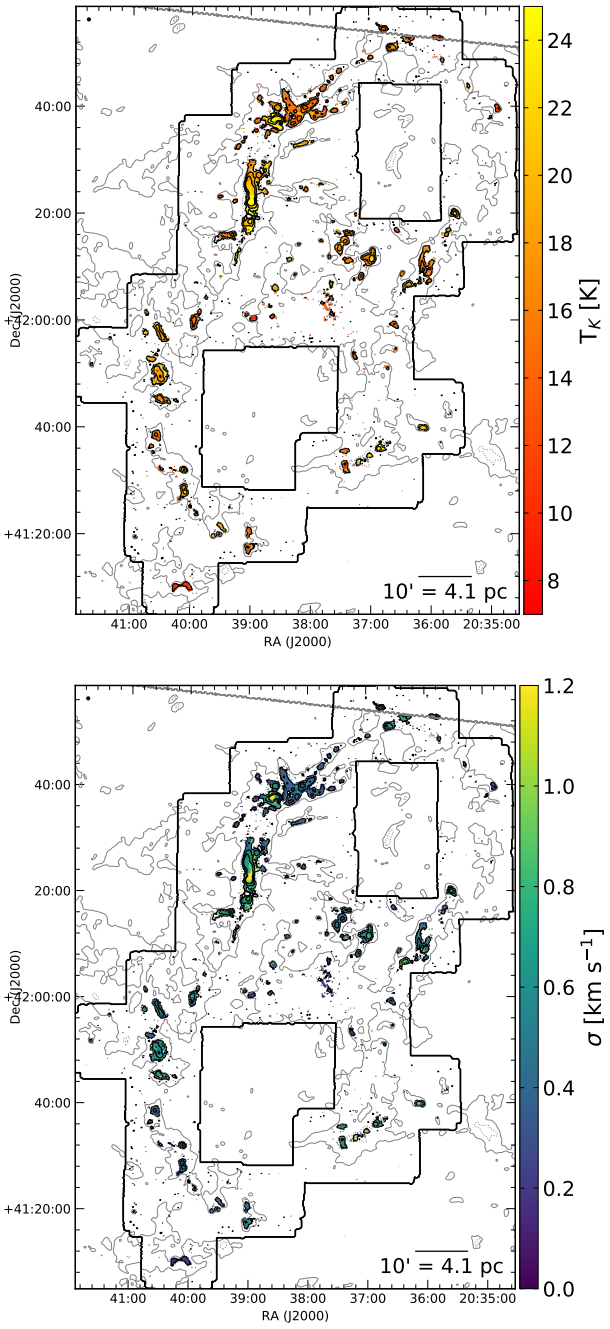

Fig. 3.14 – Same as Figure 3.13 for Cygnus X North.

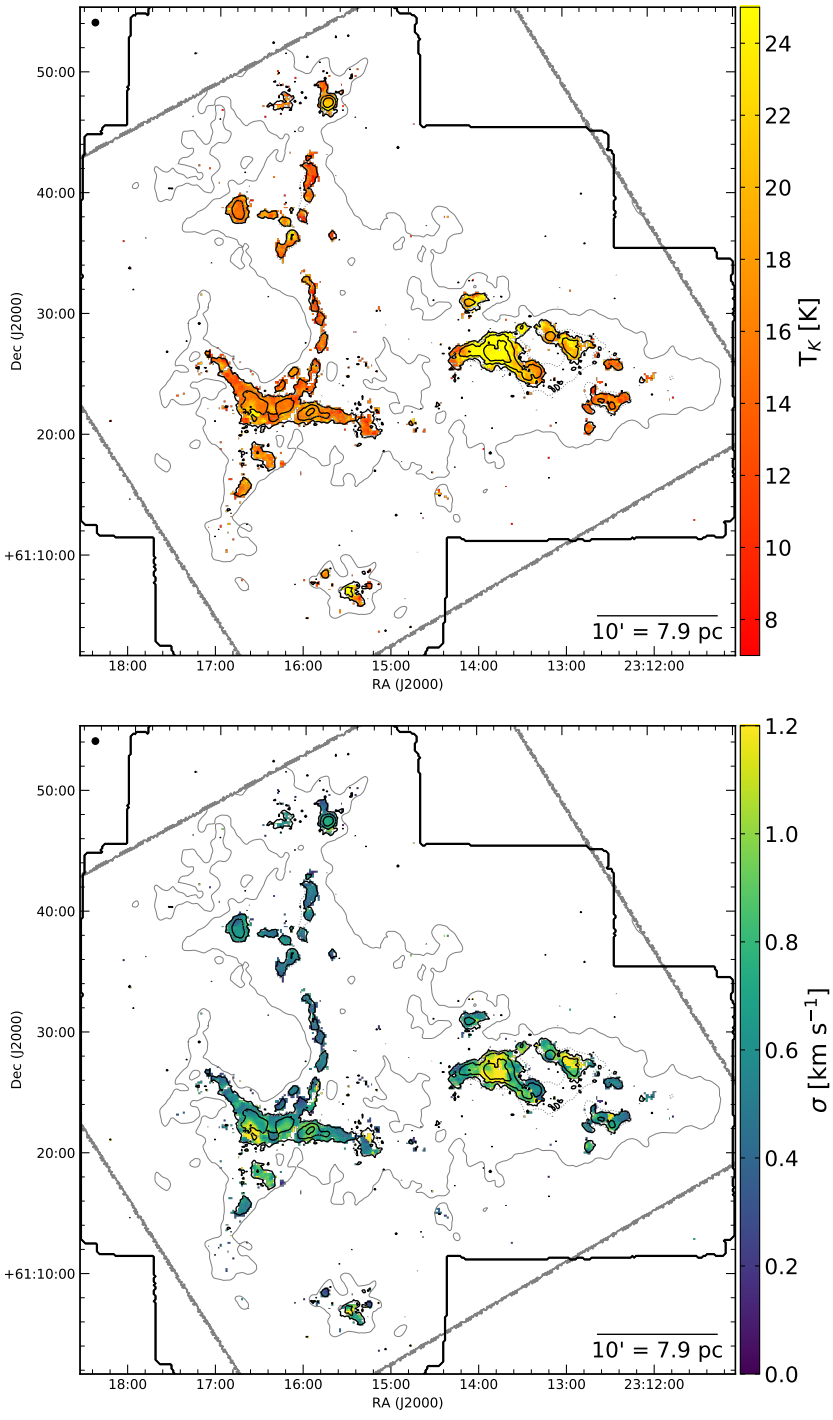

Fig. 3.15 – Same as Figure 3.4 for NGC7538.

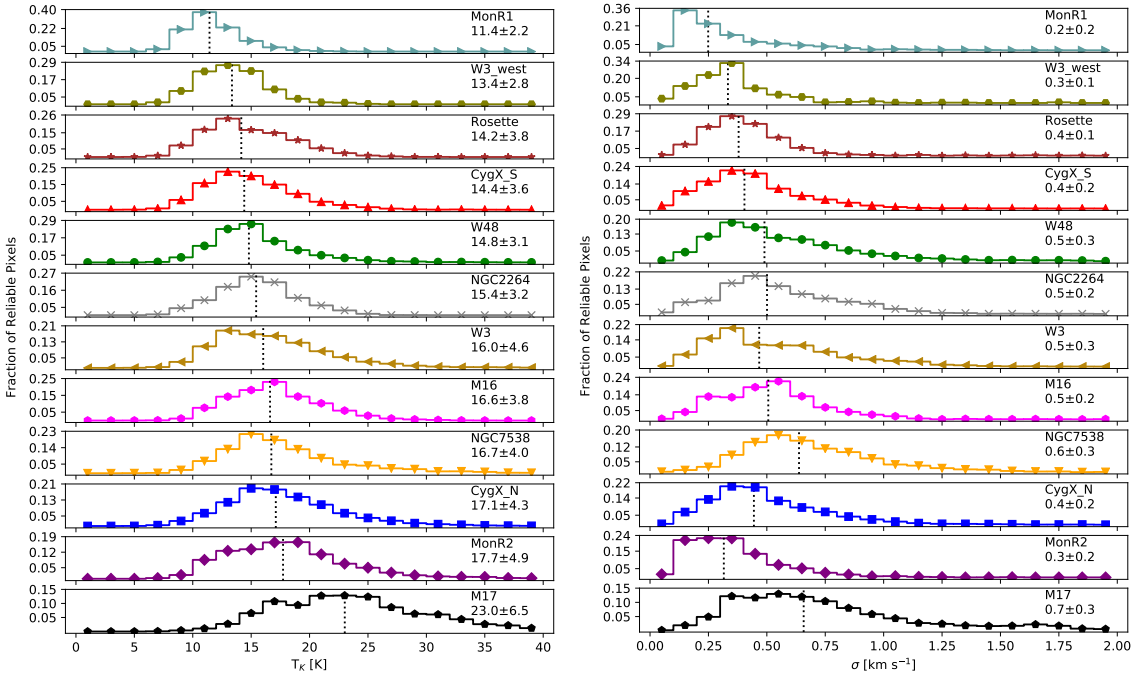

Fig. 3.16 – Histograms of kinetic temperature (left) and NH_3 (1,1) velocity dispersion (right) for the reliably fit pixels in each region. The median and median absolute deviation of each distribution is printed in the top right corner of each panel. The clouds are ordered from top to bottom by increasing median kinetic temperature.

3.3.2 NH_3 (1,1) Integrated Intensity Maps

The best-fit models from the NH_3 (1,1) line fitting described in Section 3.3.1 were used to identify the channels to integrate for producing NH_3 (1,1) integrated intensity maps. Namely, the spectral channels in the best-fit models that were brighter than 0.0125 K were included in the integration. This threshold was selected to include only the channels that are part of an emission line in the best-fit models. Since the off-line channels in a `pyspeckit` model are slightly above zero due to machine precision, the threshold of 0.0125 K provides a conservative distinction between emission-line and off-line channels in the models. For pixels that did not have any channels above that brightness criterion, we use the set of spectral channels centered on the mean cloud centroid velocity with a range defined by the mean cloud line width. In addition, we blank all pixels within three pixels from the map edges since they have lower coverage by the KFPA and typically have higher noise. Figures 3.17-3.28 show the final NH_3 (1,1) integrated intensity maps for each region.

3.3.3 Identifying NH_3 Structures with Dendrograms

The hierarchical nature of molecular clouds (e.g., Falgarone & Puget, 1986; Lada, 1992; Bonnell et al., 2003) warrants a structure-identification method that handles features with different sizes, shapes, and spatial scales. Dendrograms are a proven identification method that excel at identifying such hierarchical features in both continuum (e.g., Kirk et al., 2013b; Könyves et al., 2015) and molecular line emission observations (e.g., Rosolowsky et al., 2008; Goodman et al., 2009; Lee et al., 2014; Seo et al., 2015; Friesen et al., 2017; Keown et al., 2017) and simulations (Boyden et al., 2016; Koch et al., 2017; Boyden et al., 2018). This ability arises from the tree-diagram architecture of dendrogram algorithms, which first identifies the pixels in a map that represent local maxima. Next, structures are assembled around the local maxima by joining nearby fainter pixels. These top-level *leaves* are grown until they either merge with another nearby leaf, at which point they are connected by a *branch*, or reach a pre-defined noise threshold below which no more pixels are added to the structure. The lowest-level structures above this noise threshold that are connected to branches are known as *trunks*.

Due to the hyperfine structure of NH_3 (1,1) emission, each hyperfine group would be detected as a distinct structure in a 3D dendrogram extraction of the KEYSTONE spectral cubes. To "remove" the hyperfine structures of NH_3 (1,1), some authors have created a single-Gaussian cube from the line width, peak brightness temperature, and centroid velocity measured from the NH_3 (1,1) emission (e.g., Friesen et al., 2017; Keown et al., 2017). Such a single-Gaussian cube attempts to represent how the ammonia emission would appear without hyperfine splitting. Unless the ammonia emission is fit using a model with multiple velocity components along the line of sight, however, the output single-Gaussian cube does not account for emission with multiple velocity components. Instead, a robust multiple velocity component line-fitting method would first need to be applied to the data to take full advantage of a 3D dendrogram extraction of NH_3 (1,1) cubes. The multiple velocity component models would then allow for the creation of a "multi-Gaussian" cube that removes the hyperfine structures of NH_3 (1,1) while preserving the presence of multiple velocity components along the line of sight. Although a multiple velocity component NH_3 (1,1) line-fitting method has been developed in another KEYSTONE paper (Keown et al., 2019a), the analysis presented here neglects multiple velocity components along the line of sight.

Here, we instead perform a dendrogram analysis of the NH_3 (1,1) integrated intensity maps described in Section 3.3.2. When the observed emission has only a single velocity component along the line of sight, a 2D dendrogram extraction of the integrated intensity maps will produce similar results as a 3D extraction of the full emission cube. Since the majority of the KEYSTONE observations appear to lack multiple velocity components, a 2D analysis is warranted. We defer a 3D dendrogram analysis of the ammonia data to a future KEYSTONE paper.

The `astrodendro` Python package was applied to the integrated intensity map for each region. For consistency with the ammonia dendrogram analyses by Friesen et al. (2016) and Keown et al. (2017), we chose the following values for the dendrogram algorithm input parameters:

- `min_value` = 5 × RMS, where RMS is the rms noise measured in a region of the integrated intensity map where no emission was detected. For clouds with highly variable noise in the integrated intensity map, the RMS was calculated using an emission-free region representative of the highest noise portion of the map. While this conservative approach may leave some low brightness sources undetected, it reduces the amount of spurious noise sources detected by the dendrogram. `min_value` is the lowest intensity a pixel can have to be joined to a neighboring structure.

- `min_delta` = 2 × RMS, where RMS is the same as described for `min_value`. `min_delta` is the minimum difference in brightness between two structures before they are merged into a single structure.

- `min_npix` = 10 pixels. `min_npix` is the minimum number of pixels a structure must contain to remain independent. This parameter prevents noise spikes from being identified as sources.

After running the dendrogram algorithm on the maps, we cull *leaf* sources from our final catalog that do not meet the following criteria:

- The total area of the leaf, in terms of all the pixels associated with it, must be larger than the total area of the GBT beam. This criterion ensures further that small noise spikes are excluded from our final catalog and analyses.

- The leaf contains at least one pixel that was reliably fit by the NH_3 line fitting method described in Section 3.3.1. Here, a reliably fit pixel is one that passes the seven constraints listed in Section 3.3.1.

Figure 3.29 shows an example tree diagram for the dendrogram extraction of the MonR2 region. Leaves that do not pass our selection criteria are shown as black vertical lines, while robust leaves are shown in blue and parent structures are shown in red. The tree diagram shows that our selection criteria preferentially cull isolated leaves that are not associated with larger-scale parent structures and are likely noise spikes in the map. Table 3.4 provides a sample catalog of the leaves that pass our selection criteria in W3-west. Similar catalogs for all eleven KEYSTONE regions are available in Appendix A. Of the 970 total leaves identified by the dendrograms in each region, the final catalog includes a total of 856 leaves ($\sim 88\%$) that passed all of the culling criteria. Figures 3.17-3.28 show the final catalog leaf masks overlaid atop the NH_3 (1,1) integrated intensity map for each region. These masks show the full extent of all pixels associated with each leaf. For the remainder of the paper, we refer to leaves and clumps synonymously since the ammonia-identified leaves represent the dense gas structures from which new stars may form.

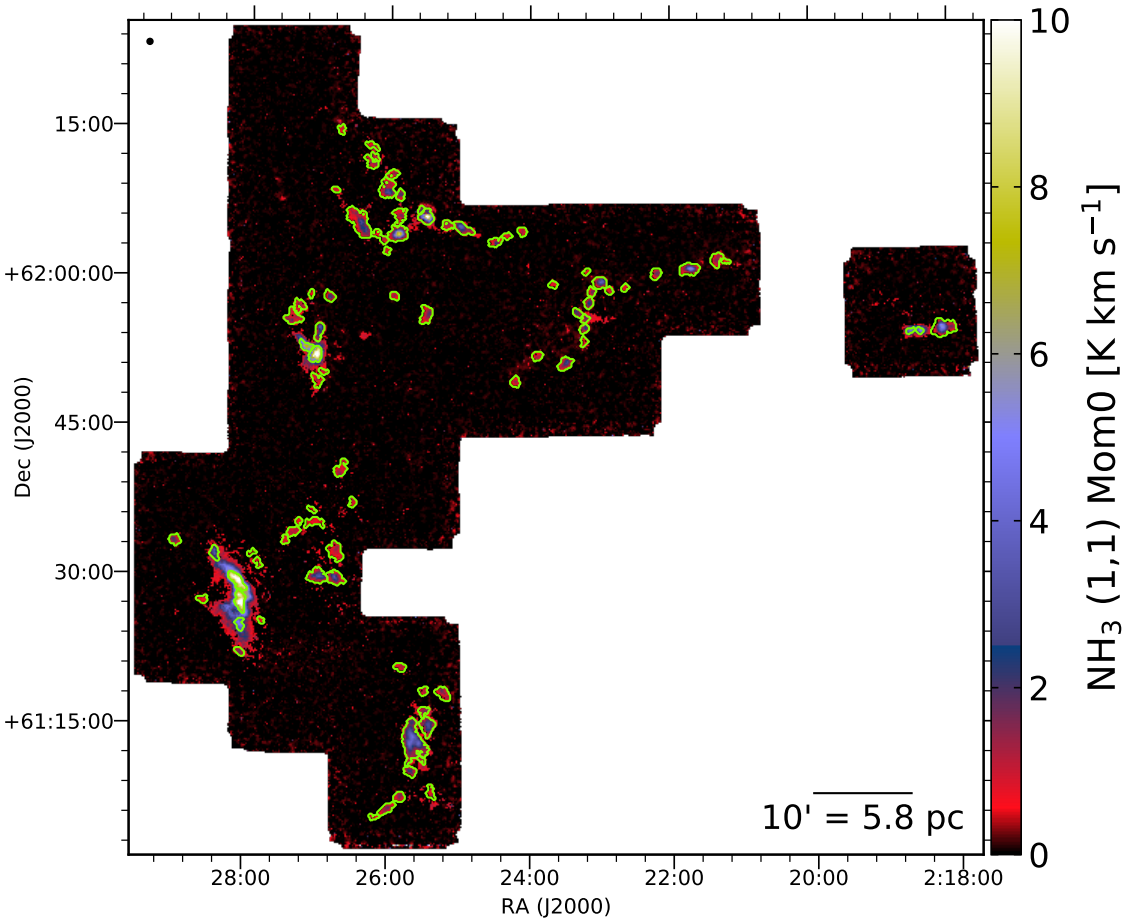

Fig. 3.17 – NH_3 (1,1) integrated intensity map for W3. Green contours outline leaves identified by a dendrogram analysis of the map that passed the culling criteria listed in Section 3.3.3.

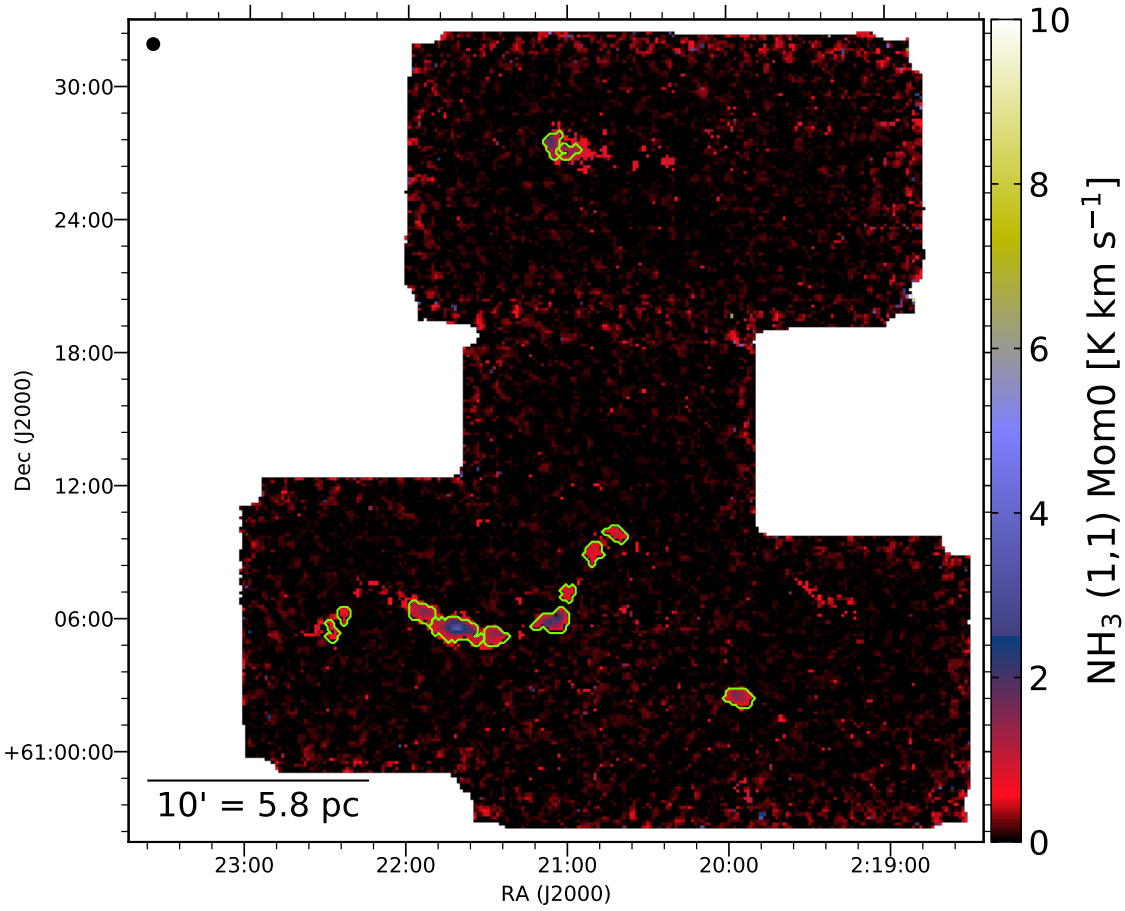

Fig. 3.18 – Same as Figure 3.17 for W3-west.

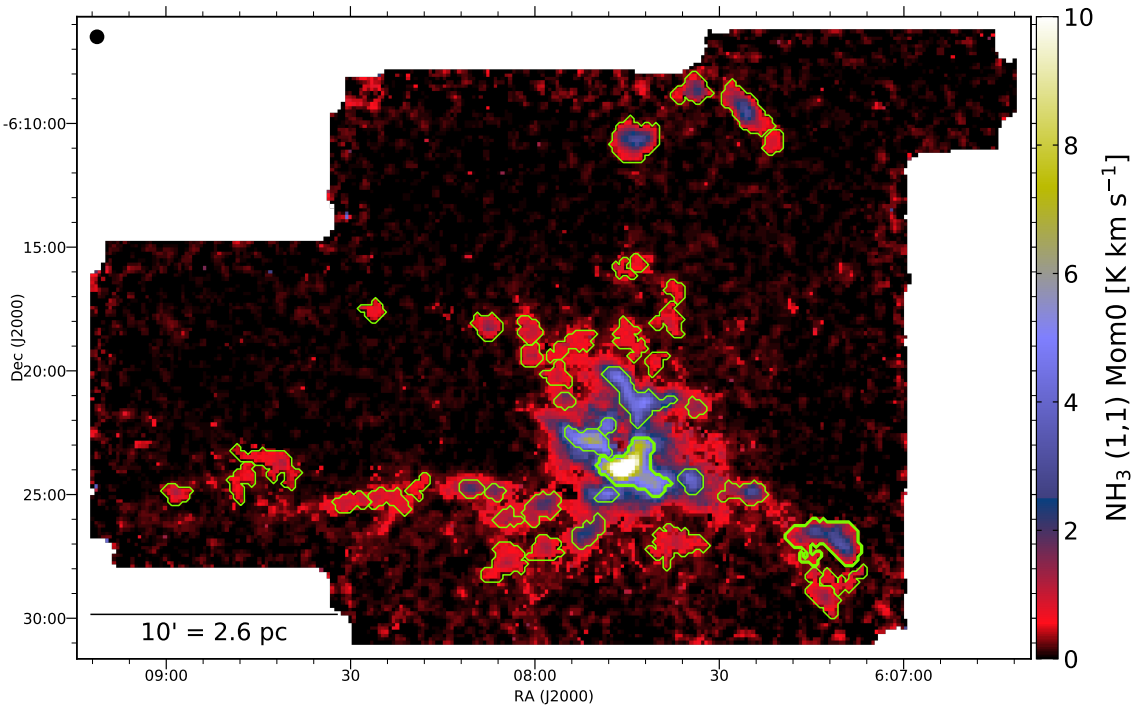

Fig. 3.19 – Same as Figure 3.17 for MonR2.

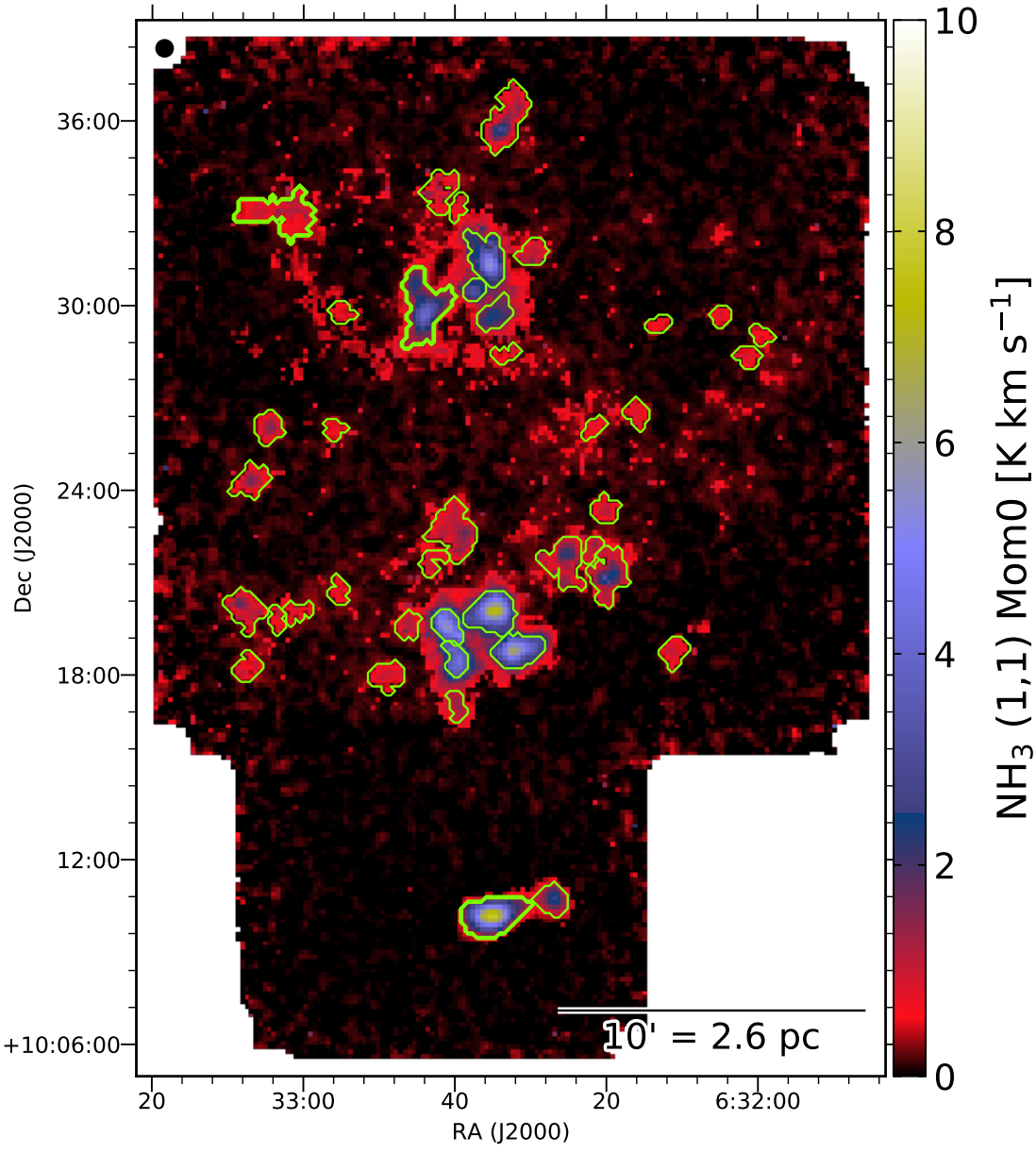

Fig. 3.20 – Same as Figure 3.17 for MonR1.

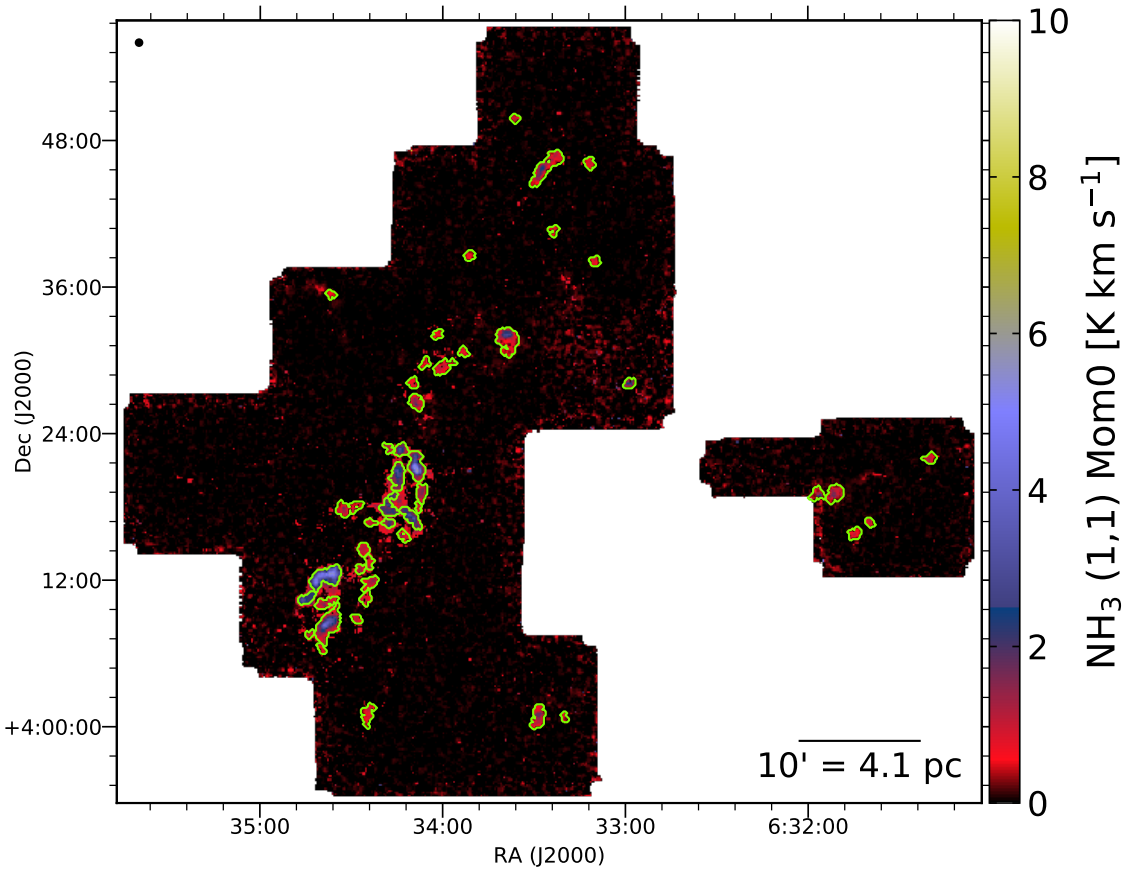

Fig. 3.21 – Same as Figure 3.17 for Rosette.

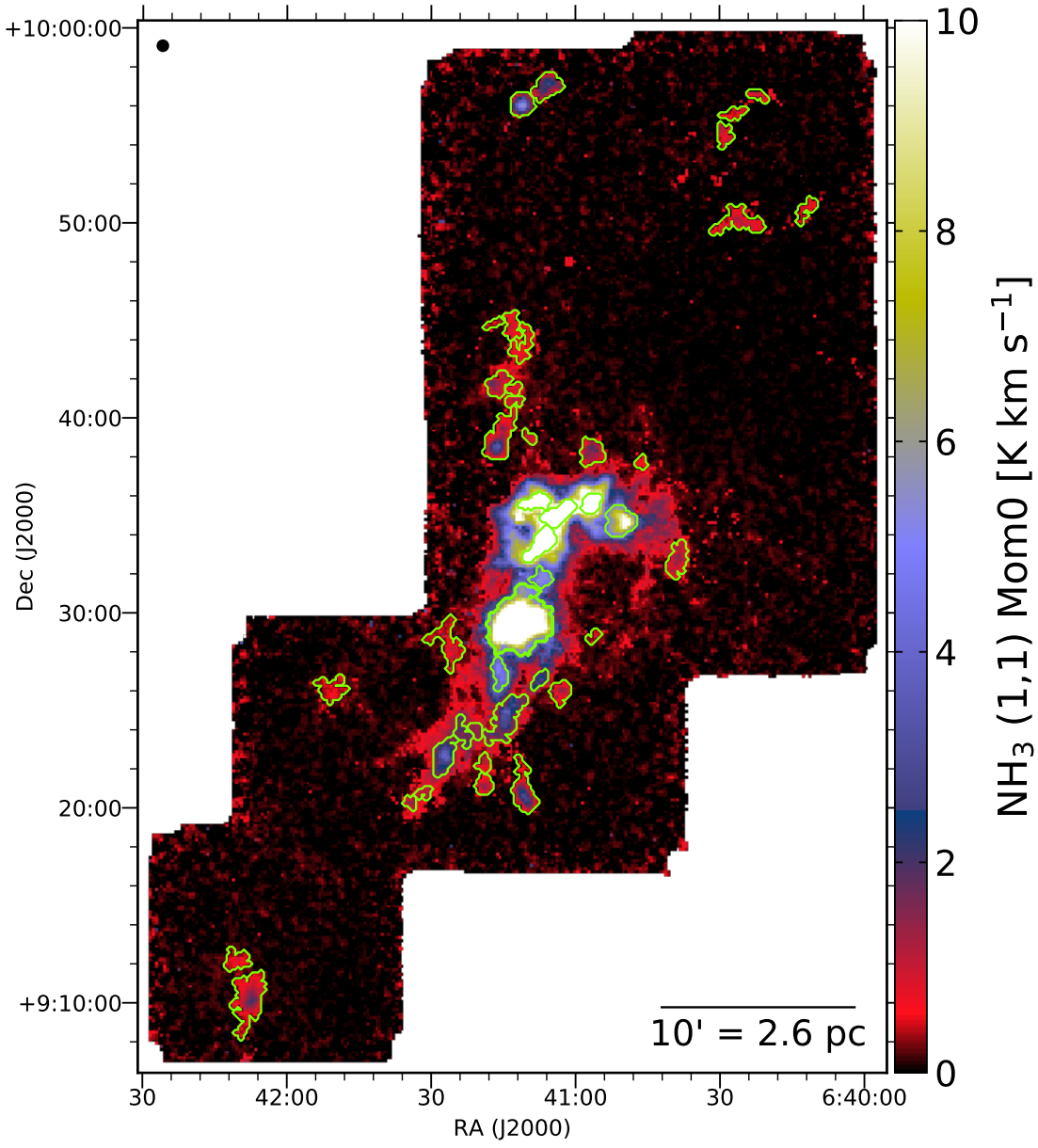

Fig. 3.22 – Same as Figure 3.17 for NGC2264.

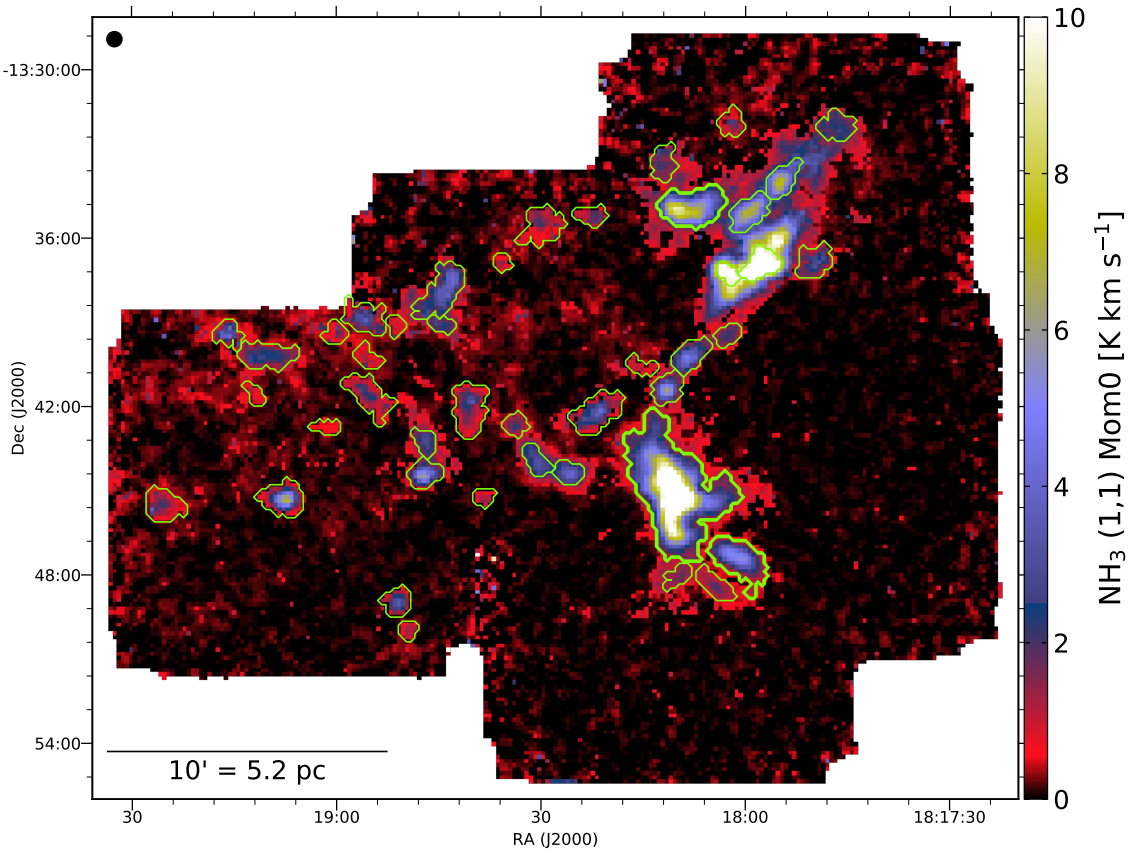

Fig. 3.23 – Same as Figure 3.17 for M16.

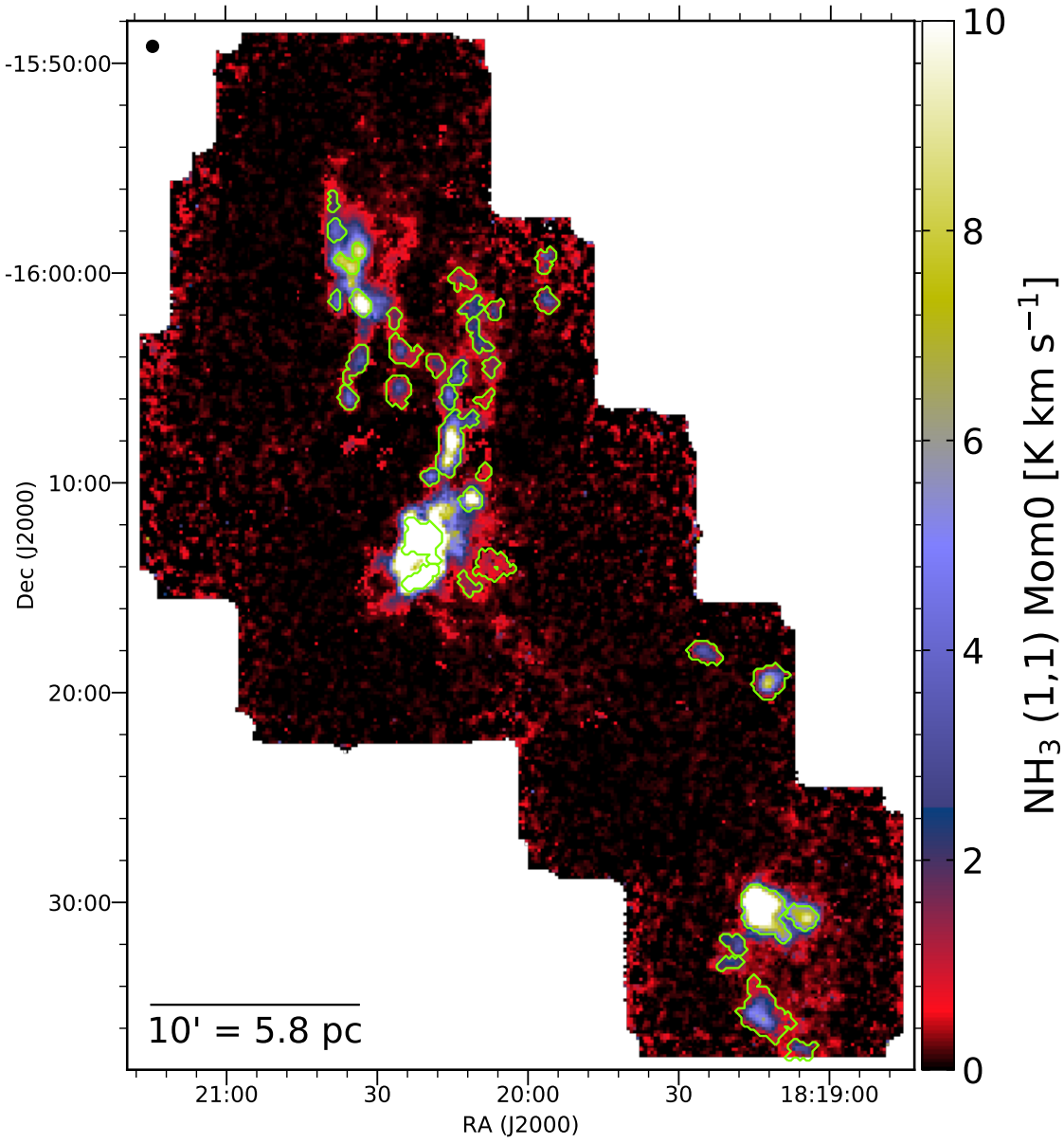

Fig. 3.24 – Same as Figure 3.17 for M17.

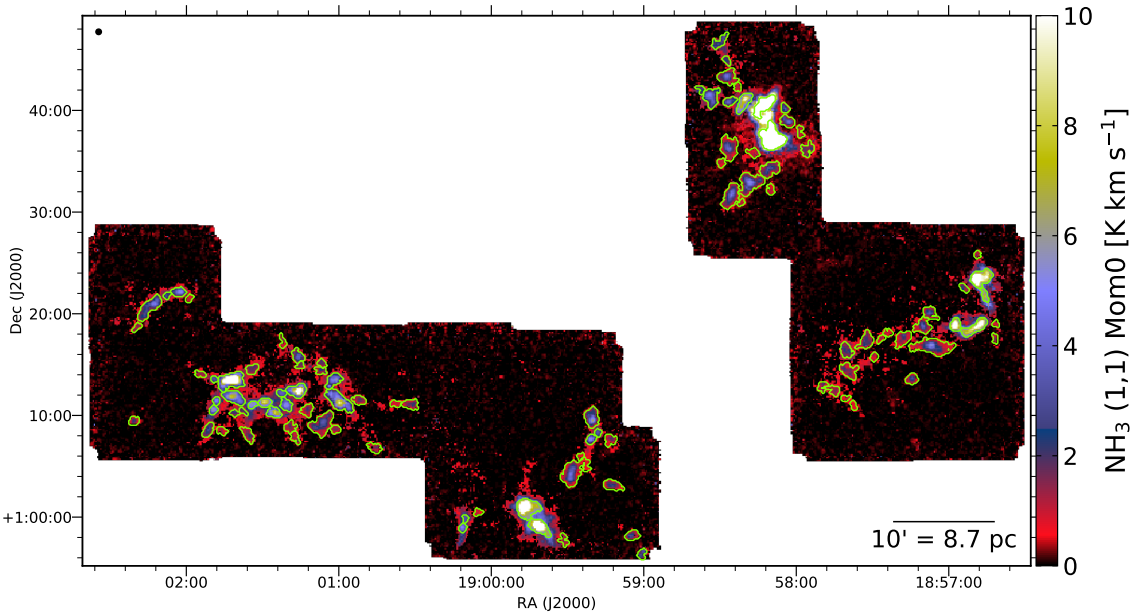

Fig. 3.25 – Same as Figure 3.17 for W48.

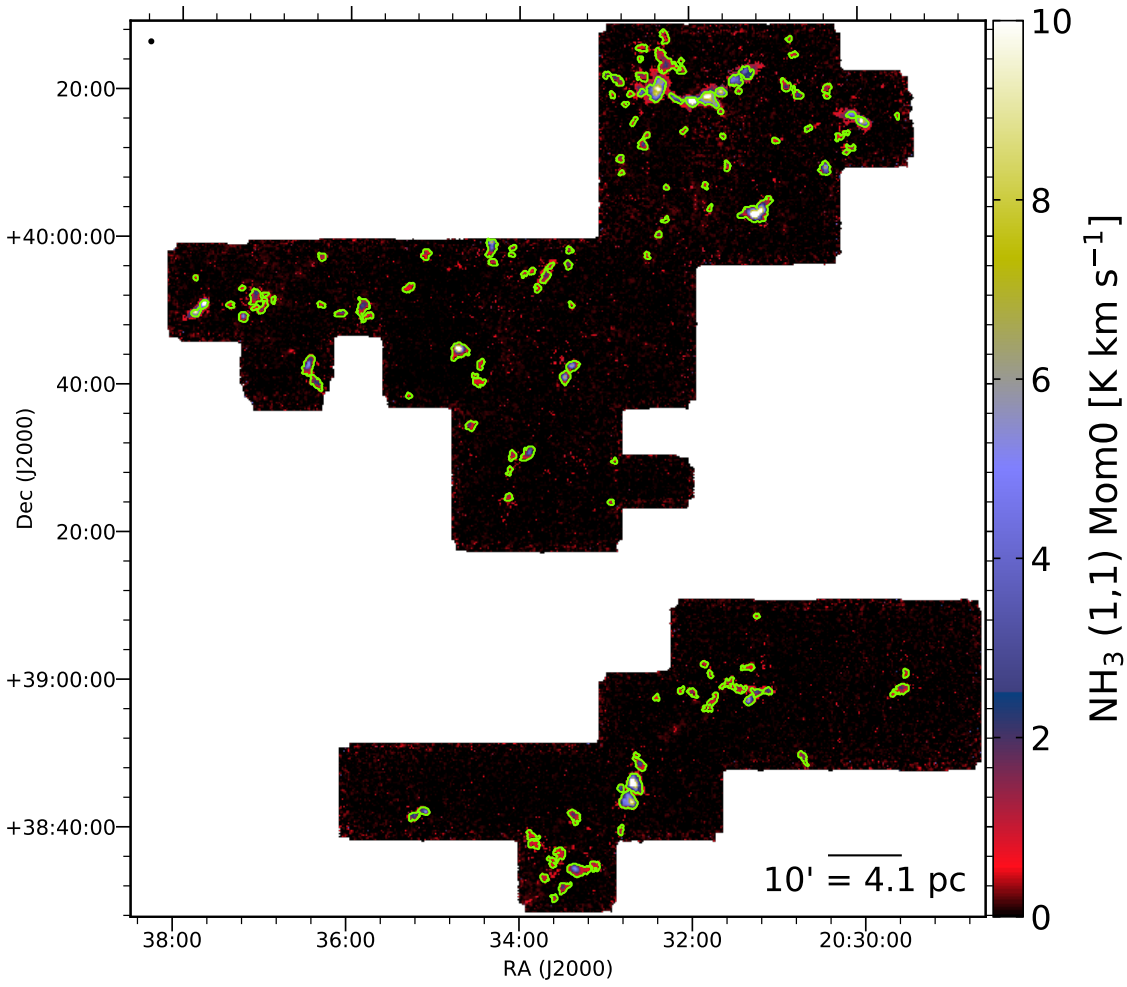

Fig. 3.26 – Same as Figure 3.17 for Cygnus X South.

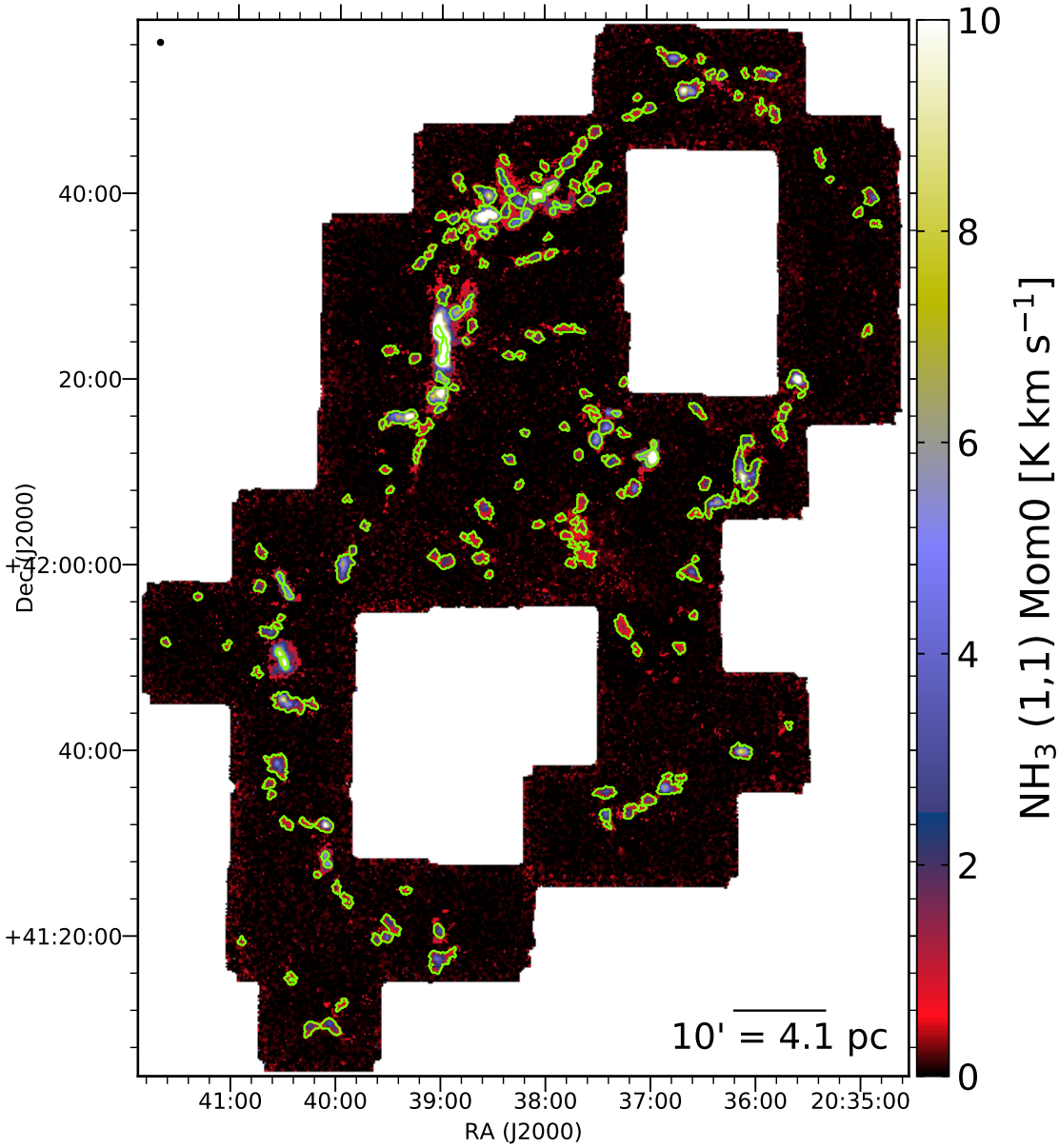

Fig. 3.27 – Same as Figure 3.17 for Cygnus X North.

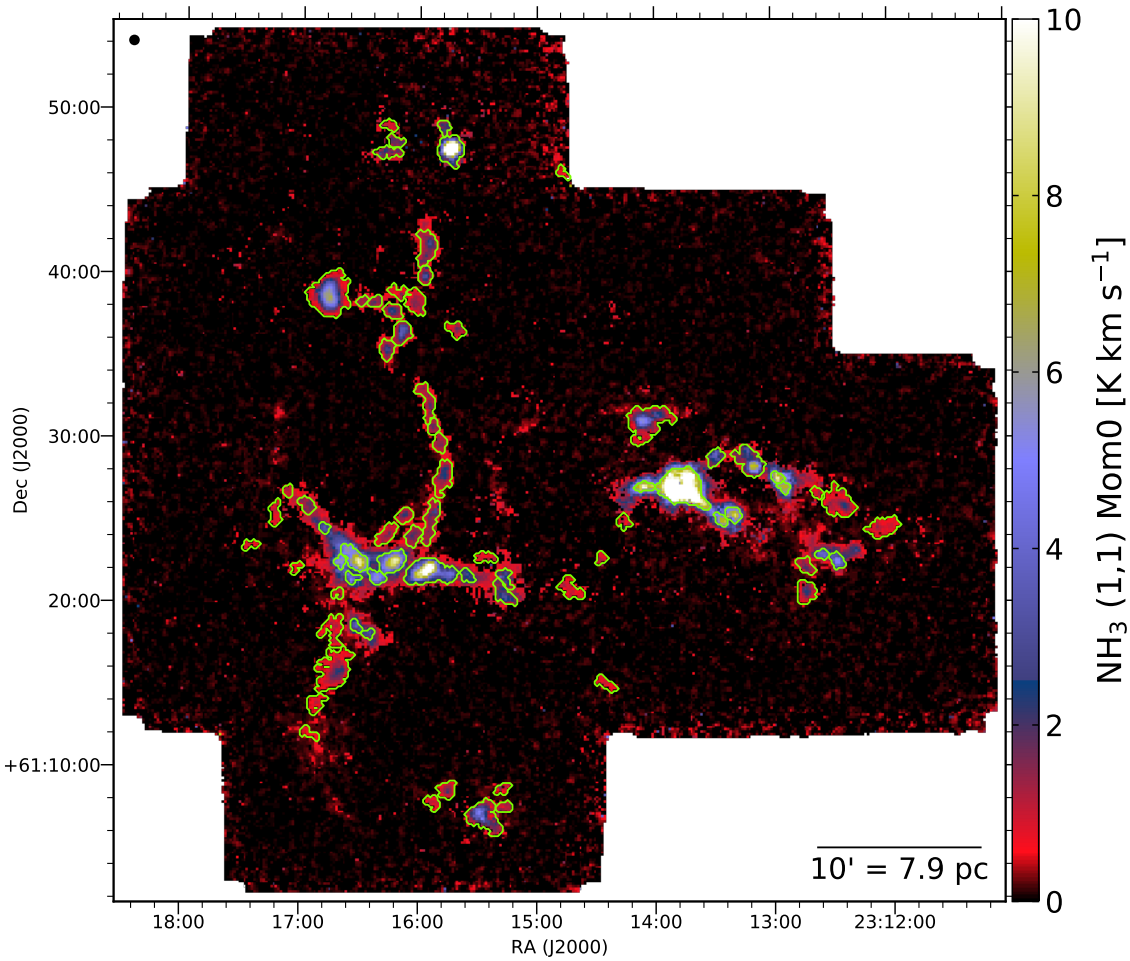

Fig. 3.28 – Same as Figure 3.17 for NGC7538.

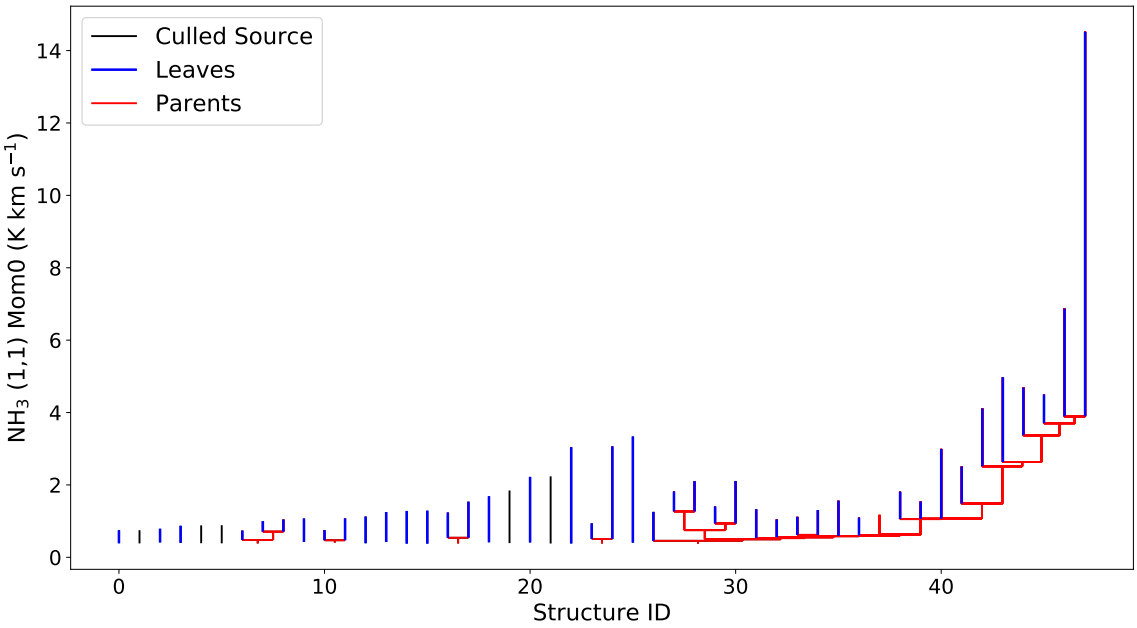

Fig. 3.29 – Dendrogram tree diagram for MonR2 showing the peak intensity for each structure identified. Leaves are shown in blue and branches are shown in red. Leaves that were culled based on the selection criteria described in Section 3.3.3 are shown in black. Leaves that are red denote culled leaves that are part of a branch with an accepted leaf.

3.3.4 Determining Leaf Radii and Masses

The effective radii of the ammonia-identified leaves were estimated using the area of the leaf masks identified by the dendrogram analysis. Following Kauffmann et al. (2013), we adopt $R_{eff} = (A/\pi)^{1/2}$ as the effective radius, where A is the area of all pixels in the leaf's mask on the position-position plane. Rosolowsky & Leroy (2006) showed that this area-based radius formulation becomes inaccurate for structures with low SNR and sizes much larger or smaller than the beam size. Although we do enforce that leaves are comprised of pixels with at least 5σ detections (see Section 3.3.3) and limit structures to being larger than the beam size, R_{eff} may still be susceptible to such biases. To estimate the uncertainties on our measured radii, we use the method described by Chen et al. (2019a), which uses the radii of the largest circle that fits inside the leaf boundary as the leaf's radii lower limit and the radii of the smallest circle that encompasses the leaf as its radii upper limit. The corresponding uncertainties on R_{eff} based on these upper and lower limits are listed in Table 3.4.

The uncertainties range from 0.1% to 153% of R_{eff}, with a median of 35%.

Masses for the ammonia-identified leaves were estimated by summing all the H_2 column density for the pixels inside each leaf's mask. The integrated column densities are then converted to mass assuming the distances to each region listed in Table 3.1 and a mean molecular weight per hydrogen molecule $\mu_H = 2.8$. In Cygnus X and MonR2, a small number of leaves (six in Cygnus X North, 14 in Cygnus X South, and one in MonR2) fall outside the boundaries of our H_2 column density maps. Those sources are, therefore, excluded from our analyses that require a mass determination.

Summing all the column density within the leaf boundaries is likely an upper limit on the mass of the structure. Conversely, a lower limit on the structure's mass can be obtained by using the "clipping" technique described in Rosolowsky et al. (2008) and Chen et al. (2019a). Namely, before summing the column density pixels within the leaf boundary, the lowest column density pixel's value is subtracted from all other pixels. This method aims to remove contributions to the structure's observed column density from background sources, but is likely over-estimating the true background contribution in most cases. As such, we adopt the regular integrated column density masses throughout this paper, but show the range the mass could be assuming the "clipped" mass is a lower limit. The clipped masses are also displayed in Table 3.4 alongside the integrated column density masses. The clipped masses are typically a factor of ~ 5 (median) lower than the integrated column density masses.

The left panel of Figure 3.30 shows the effective radii versus mass for all leaves in our final catalog. A power-law fit to the radius versus mass distribution reveals a best-fit slope of 2.43 ± 0.45, which is consistent with the value of 2 expected for clumps of constant surface density and the value of 3 expected for clumps of constant volume number density. The data were fit using a Markov Chain Monte Carlo (MCMC) sampler[7]. The MCMC sampling used an orthogonal least-squares likelihood function and uniform priors on the power-law slope and intercept. The best-fit model parameters were taken to be the medians of the accepted parameters in the MCMC chain, while the uncertainty on the best-fit parameters was taken to be the standard deviations of the accepted parameter distributions.

[7]the `emcee` package: https://emcee.readthedocs.io

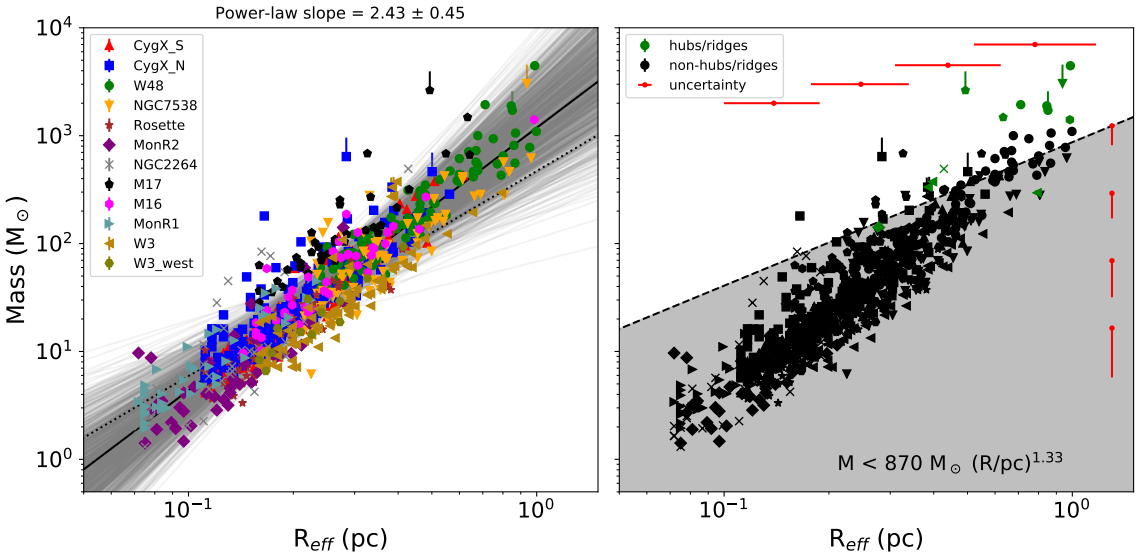

Fig. 3.30 – Left: effective radius versus mass for the leaves identified in each region. The solid black line shows the best power-law fit to the data using an MCMC sampler. The grey lines show 1000 random selections from the full MCMC chain. The dotted line shows a power-law slope of 1.9 (Larson, 1981) for comparison. Right: effective radius versus mass for hubs (green) and non-hubs (black) identified in each region (see Section 3.4.1 for discussion of hubs). The dashed black line denotes the empirically-derived threshold for massive star formation determined by Kauffmann & Pillai (2010). The red dots with errorbars show the median mass and radius uncertainties in different bins along each axis. All other errorbars show leaves that have mass lower limits due to saturated pixels in the H_2 column density map (see Section 3.2.3).

3.3.5 Virial Analysis

To estimate the virial stability of the ammonia-identified leaves, we adopt the virial analysis method described in Keown et al. (2017), which uses the ammonia-derived line widths to derive a virial mass (M_{vir}) for each structure given by:

$$M_{vir} = \frac{5\sigma^2 R}{aG} \tag{3.1}$$

where σ is the velocity dispersion of the core (including both the thermal and non-thermal components), R is the core radius, G is the gravitational constant, and

$$a = \frac{1 - k/3}{1 - 2k/5} \tag{3.2}$$

is a term which accounts for the radial power-law density profile of a core, where $\rho(r) \propto r^{-k}$ (Bertoldi & McKee, 1992). M_{vir} represents the mass that a structure with a given radius and internal kinetic energy would have if it were in virial equilibrium when considering only its gravitational potential and kinetic energies. We also assume that the structure is in a steady state, spherical, isothermal, and has a radial power-law density profile of the form: $\rho(r) \propto r^{-1.5}$. Our density profile assumption is motivated by recent observations that found $\rho(r) \propto r^{-1.5\pm0.3}$ for the inner regions of dense cores (e.g., Kurono et al., 2013; Pirogov, 2009) and is likely a more accurate choice than the Gaussian density profile chosen in previous virial analyses (e.g., Pattle et al., 2017; Kirk et al., 2017; Keown et al., 2017). See Keown et al. (2017) for a discussion of the implications of assuming a power-law density profile for sources in a virial analysis. We also set R in Equation 3.1 to be R_{eff} and calculate the thermal plus nonthermal velocity dispersion as:

$$\sigma^2 = \sigma_v^2 - \frac{k_B T}{m_{NH_3}} + \frac{k_B T}{\mu_p m_H} \tag{3.3}$$

where k_B is Boltzmann's constant, m_{NH_3} is the molecular mass of NH_3, m_H is the atomic mass of hydrogen, and μ_p is the mean molecular mass of interstellar gas. We use μ_p rather than μ_H for this analysis since μ_p considers the additional contributions of helium, assuming a hydrogen-to-helium abundance ratio of 10 and a negligible admixture of metals, that are required to calculate the thermal gas pressure accurately (2.33; see, e.g., Appendix A in Kauffmann et al., 2008). σ_v and T are the average velocity dispersion and kinetic temperature, respectively, within the core boundaries measured from the NH_3 line-fitting parameter maps. Both the σ_v and T averages are weighted by the NH_3 (1,1) integrated intensity map such that $\sigma_{v,avg} = w_1\sigma_1 + w_2\sigma_2 \cdots w_n\sigma_n$, where w_n and σ_n are the fraction of the source's integrated intensity and value of the velocity dispersion, respectively, for pixel n.

The ratio of M_{vir} to the actual observed mass of the structure (M_{obs}) is known as the virial parameter ($\alpha_{vir} = M_{vir}/M_{obs}$). This virial parameter can also be written as $\alpha_{vir} = a2\Omega_K/|\Omega_G|$, where Ω_K, Ω_G, and a represent the structure's total kinetic energy, gravitational potential energy, and density profile (Equation 3.2), respectively (Bertoldi & McKee, 1992). Thus, the virial parameter neglects the surface term for the kinetic energy that considers the ambient gas pressure exerted on the structure by the cloud. When $\alpha_{vir} \geq 2$, the structure's internal kinetic energy is large enough to prevent it from being gravitationally bound. Conversely, when $\alpha_{vir} < 2$, the

structure is deemed gravitationally bound since its gravitational potential energy is large enough relative to its internal kinetic energy (neglecting the effects of magnetic fields and external pressure). Figure 3.31 shows observed mass versus virial parameter for all leaves in our final catalog. Of the 835 leaves, 523 ($\sim$ 63%) fall below the $\alpha_{vir} = 2$ threshold to be considered gravitationally bound. When looking at each cloud individually, the bound leaf fraction varies from $\sim$0.3 in MonR2 to $\sim$0.9 in M17 and W48. Table 3.5 lists the virial parameters for the leaves identified in W3-west (similar tables for the other regions are provided in Appendix B). Table 3.6 shows the bound leaf fractions for each individual cloud, while Table 3.7 lists the bound fraction and other population statistics for the full leaf sample.

We note that the variations in distance to each KEYSTONE target provide a variety of linear scales resolved by our observations. These linear resolution effects are not accounted for with the analysis presented here. In Appendix 3.7, however, we show the impact on the virial parameters of NGC 2264, MonR1, and MonR2 ($d = 0.9$ kpc) if those maps were convolved and downsampled to the linear resolution of the W48 ($d = 3.0$ kpc) observations. We show that there is indeed a tendency for the identified structures in the distance-adjusted analysis to be bound, which might be affecting the higher fraction of bound structures observed in W48 and M17 ($d = 2.0$ kpc).

3.3.6 Identifying filaments and candidate YSOs

Although dendrograms are able to identify the hierarchical parent structures in which leaves are embedded, they are not optimized for isolating the elongated, filamentary structures that are commonly observed in molecular clouds. To understand how the ammonia-identified leaves in this paper relate to surrounding filamentary structures, we employ a dedicated filament extraction algorithm called `getfilaments` (Men'shchikov, 2013) to identify filaments in each region's H_2 column density map. The `getfilaments` algorithm is a multi-scale extraction approach designed to identify filamentary background structures in *Herschel* maps (e.g., Könyves et al., 2015; Rivera-Ingraham et al., 2016; Marsh et al., 2016; Bresnahan et al., 2018). As such, it performs far better than dendrograms at identifying filaments. `getfilaments` was run on all the *Herschel* H_2 column density maps using the standard extraction parameters for the algorithm (see Men'shchikov (2013) for the extensive list of `getfilaments` parameters). The top left panels in Figures 3.32-3.43 display the final filament masks,

Table 3.4 W3-west NH_3 (1,1) Leaves Catalog 1

ID	RA (deg)	decl. (deg)	PA (deg)	σ_{major} ($''$)	σ_{minor} ($''$)	R_{eff} (pc)	M_{obs} ($M_\odot$)	M_{clip} ($M_\odot$)	T_K (K)	σ_{NH_3} (km s^{-1})	V_{LSR,NH_3} (km s^{-1})	$\log(N_{para-NH_3})$ (cm^{-2})	$\log(N_{H_2})$ (cm^{-2})
0	34.9844	61.0428	166	16.6	9.9	$0.27^{+0.07}_{-0.06}$	18.7	3.8	10.9 ± 2.4	0.13 ± 0.02	-15.2	13.7	21.4
1	35.4211	61.0938	167	30.7	12.8	$0.41^{+0.27}_{-0.15}$	93.7	37.2	13.1 ± 1.7	0.36 ± 0.04	-49.9	13.9	21.5
2	35.3625	61.0890	180	14.6	10.8	$0.24^{+0.08}_{-0.13}$	23.0	4.2	13.0 ± 2.4	0.36 ± 0.05	-49.7	14.1	21.5
3	35.6144	61.0918	101	14.5	7.0	$0.17^{+0.09}_{-0.12}$	6.6	1.5	10.2 ± 3.6	0.21 ± 0.04	-49.4	13.6	21.3
4	35.2711	61.1001	196	22.1	12.1	$0.33^{+0.22}_{-0.19}$	47.5	14.3	12.2 ± 2.5	0.27 ± 0.04	-49.7	14.0	21.5
5	35.5964	61.1042	90	10.8	6.2	$0.16^{+0.05}_{-0.01}$	8.4	1.3	16.5 ± 3.0	0.34 ± 0.06	-50.1	13.4	21.3
6	35.4752	61.1064	152	17.8	10.6	$0.27^{+0.07}_{-0.07}$	29.2	7.2	15.4 ± 2.6	0.52 ± 0.07	-50.0	13.8	21.5
7	35.2490	61.1213	63	10.2	8.1	$0.17^{+0.02}_{-0.03}$	9.7	1.6	13.0 ± 3.9	0.23 ± 0.06	-49.6	13.9	21.5
8	35.2099	61.1515	68	13.8	9.7	$0.23^{+0.08}_{-0.03}$	14.4	2.3	12.3 ± 3.2	0.25 ± 0.05	-48.8	13.1	21.5
9	35.1733	61.1655	155	14.4	8.2	$0.21^{+0.1}_{-0.03}$	15.2	4.8	12.8 ± 2.8	0.25 ± 0.05	-48.7	13.8	21.5
10	35.2731	61.4578	86	16.1	9.5	$0.22^{+0.13}_{-0.04}$	30.8	7.6	14.8 ± 2.5	0.46 ± 0.06	-51.0	13.8	21.5
11	35.2470	61.4522	191	13.4	9.0	$0.18^{+0.08}_{-0.08}$	16.4	1.2	12.6 ± 3.5	0.67 ± 0.11	-51.4	14.0	21.5

Columns show the following values for each leaf: (1) Leaf ID, $(2-3)$ Mean Right Ascension and Declination in J2000 coordinates, (4) Position angle of the major axis, measured in degrees counterclockwise from the west on sky, $(5-6)$ Major and minor axis measured by *astrodendro* based on the intensity weighted second moment in the direction of greatest elongation, (7) Effective radius defined as $R_{eff} = (A/\pi)^{1/2}$, where A is the area of all pixels in the leaf's mask on the position-position plane, (8) Observed mass of leaf from the sum of its H_2 column density, (9) lower limit mass of leaf calculated using the "clipping" technique (see text), $(10-13)$ Average kinetic gas temperature, velocity dispersion, NH_3 (1,1) centroid velocity, and para-NH_3 column density for leaf, all weighted by the NH_3 (1,1) integrated intensity map, along with their 1-sigma uncertainties, (14) Median H_2 column density for leaf measured from the spatially-filtered column density map and used as N in Equation 3.7. Both column densities are shown in logarithmic scale. Similar tables for all other KEYSTONE regions are available in Appendix A. Although the intensity-weighted major and minor axes of some sources are less than the $32''$ beam size of the observations, our culling criteria ensure that their total areas when considering all their associated pixels are larger than $32''$.

Table 3.5 W3-west NH_3 (1,1) Leaves Catalog 2

ID	α_{vir}	M_{vir} ($M_\odot$)	σ_{nt} (km s^{-1})	$\log\lvert\Omega_G\rvert$ (erg)	$\log\Omega_K$ (erg)	$\log\lvert\Omega_{Pw}\rvert$ (erg)	$\log\lvert\Omega_{Pt}\rvert$ (erg)	on-filament	hub	N_{proto}	Bad $N(H_2)$ Pixels
0	0.67	12.6	0.10	43.8	43.4	44.2	NaN	True	False	0	0
1	0.71	66.3	0.36	45.0	44.7	44.8	NaN	True	False	4	0
2	1.68	38.6	0.36	44.1	44.1	44.1	NaN	True	False	1	0
3	1.82	12.0	0.20	43.1	43.2	43.5	NaN	True	False	0	0
4	0.70	33.3	0.26	44.5	44.2	44.5	NaN	True	False	2	0
5	2.92	24.5	0.33	43.4	43.6	43.5	NaN	True	False	1	0
6	2.72	79.6	0.51	44.2	44.4	44.3	NaN	True	False	0	0
7	1.53	14.9	0.21	43.4	43.4	43.7	NaN	True	False	1	0
8	1.47	21.2	0.24	43.7	43.6	44.0	NaN	True	False	0	0
9	1.32	20.0	0.24	43.8	43.7	43.9	NaN	True	False	1	0
10	1.72	52.9	0.45	44.3	44.4	44.0	NaN	True	False	1	0
11	5.01	82.0	0.67	43.9	44.4	43.8	NaN	True	False	0	0

Columns show the following values for each leaf: (1) Leaf ID, (2) virial parameter defined as M_{vir}/M_{obs}, (3) virial mass calculated using Equation 3.1, (4) non-thermal component of the velocity dispersion, (5) gravitational energy density calculated using Equation 3.5, (6) kinetic energy density calculated using Equation 3.6, (7) cloud weight pressure energy density calculated using Equation 3.4, (8) turbulent pressure energy density calculated using Equation 3.4, with NaN representing a lack of $C^{18}O$ data for that leaf, $(9-10)$ whether or not the leaf is on-filament or a hub, (11) number of 70 μm point sources within the leaf's boundary, (12) fraction of pixels in the leaf that were saturated in the H_2 column density map. Similar tables for all other KEYSTONE regions are available in Appendix B.

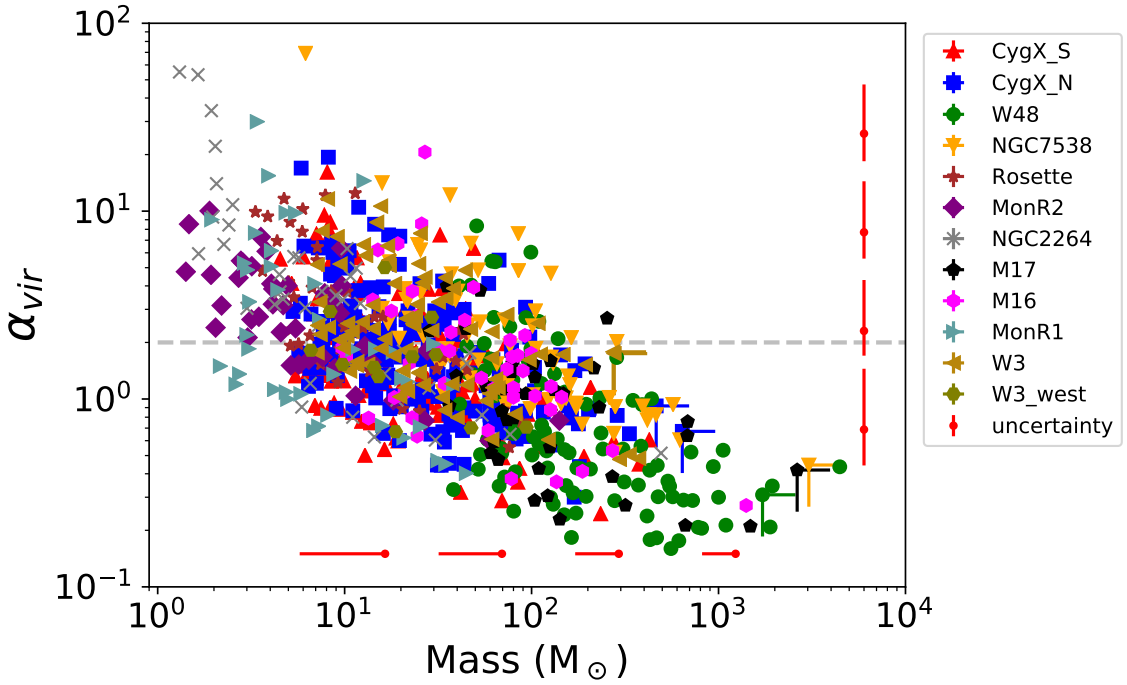

Fig. 3.31 – Virial parameter (α_{vir}) versus mass for the leaves identified in each region. The dashed line denotes $\alpha_{vir} = 2$ when assuming a power-law density profile for the structures. Above this line, structures are deemed to be gravitationally unbound in the absence of magnetic fields or external pressure. The red dots with errorbars show the median mass and radius uncertainties in different bins along each axis. All other errorbars show leaves that have mass lower limits due to saturated pixels in the H_2 column density map (see Section 3.2.3).

reconstructed up to spatial scales of 145″.

A leaf that has at least one of its pixels corresponding to at least one pixel in a filament mask is designated "on-filament" and all other leaves are termed "off-filament." The "on-filament fraction," i.e., the fraction of leaves in a cloud that are on-filament, is listed in Table 3.6 and ranges from 0.35 in Cygnus X South to 1.0 in W3-west. For the full sample of 835 leaves with *Herschel* observations, 454 are on-filament (on-filament fraction of ~ 54 %).

To compare the number of star-forming leaves in each KEYSTONE region, we identify young, embedded protostars using the *Herschel* 70 μm maps observed for each cloud. `getsources` (Men'shchikov et al., 2012), a multi-scale source extraction algorithm designed to identify dense cores and protostars in *Herschel* observations, was employed to extract point sources at 70 μm only. We adopt the *Herschel* Gould Belt Survey selection criteria for candidate young stellar objects (YSOs) described in

Section 3.4.5 of Könyves et al. (2015). The final candidate YSOs are shown as red circles in Figures 3.32-3.43. We note that at the distances of the KEYSTONE clouds (0.9 kpc $< d <$ 3.0 kpc), there may be significant incompleteness plus insufficient resolution to separate close sources in the *Herschel* 70 μm maps. For some regions, there may also be contamination by photodissociation regions that can appear as 70 μm point sources. Since we are only using these 70 μm point sources to indicate which leaves are currently star-forming, rather than using them as a complete catalog of YSOs, the extraction is sufficient for our goals.

We perform a cross-match between the candidate YSO catalogs and leaf catalogs to determine which leaves are protostellar. Leaves with at least one candidate YSO falling within their dendrogram-identified boundary are designated "protostellar." Conversely, leaves without a candidate YSO are termed "starless." The protostellar leaf fraction is listed in Table 3.6 and ranges from 0.17 in MonR1 to 0.58 in W3-west. For the 835 leaves with *Herschel* observations, 288 are protostellar ($\sim$ 34 %).

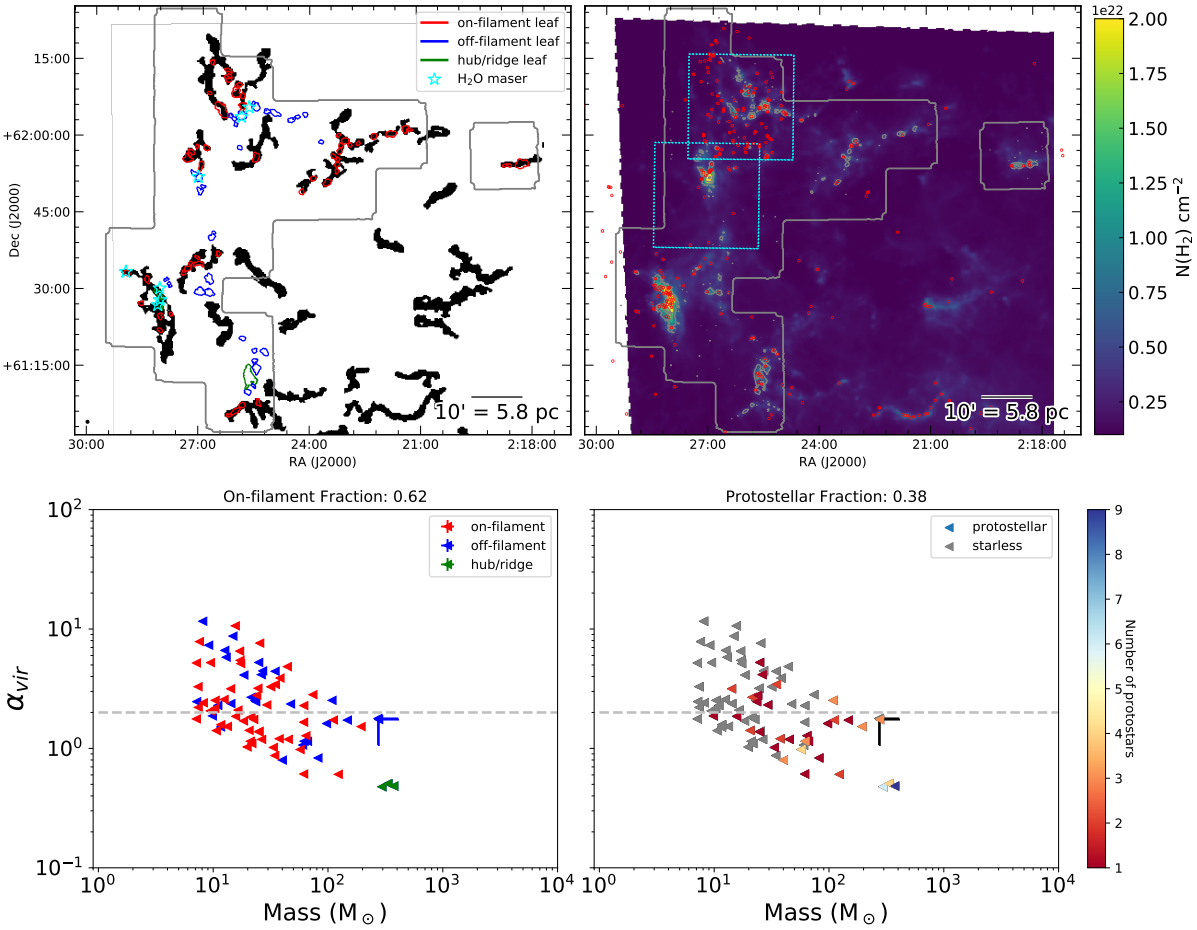

Fig. 3.32 – Top Right: *Herschel* H_2 column density map of W3 with positions of candidate YSOs identified by `getsources` at 70 μm overlaid as red dots. The outer grey outline denotes the area mapped by KEYSTONE. The grey contours show NH_3 (1,1) integrated intensity at 1.0 K km s^{-1}, 3.5 K km s^{-1}, and 10 K km s^{-1}. The cyan dotted line outlines the area observed in $C^{18}O$ $(3-2)$ by the JCMT, which we fit to derive external pressure terms for the subset of leaves falling within those observations (see Section 3.4.5). Top Left: masks of filaments identified in the *Herschel* H_2 column density map by *getfilaments*, reconstructed up to scales of 145″. The positions of our ammonia-identified leaves are overlaid, with red denoting an "on-filament" leaf, blue representing an "off-filament" leaf, and green showing "hubs/ridges" that have uncharacteristically larger masses than the majority of leaves in their respective cloud and tend to be located at filament intersections (see Section 3.4.1). Cyan stars show the positions of H_2O maser emission. Bottom row: virial parameters versus mass for the protostellar and starless leaves (right) as well as the on-filament, off-filament, and hub sources shown in the top left panel (left). The data point shape in these plots is the same as in Figure 3.2. Errorbars show leaves that have mass lower limits due to saturated pixels in the H_2 column density map (see Section 3.2.3).

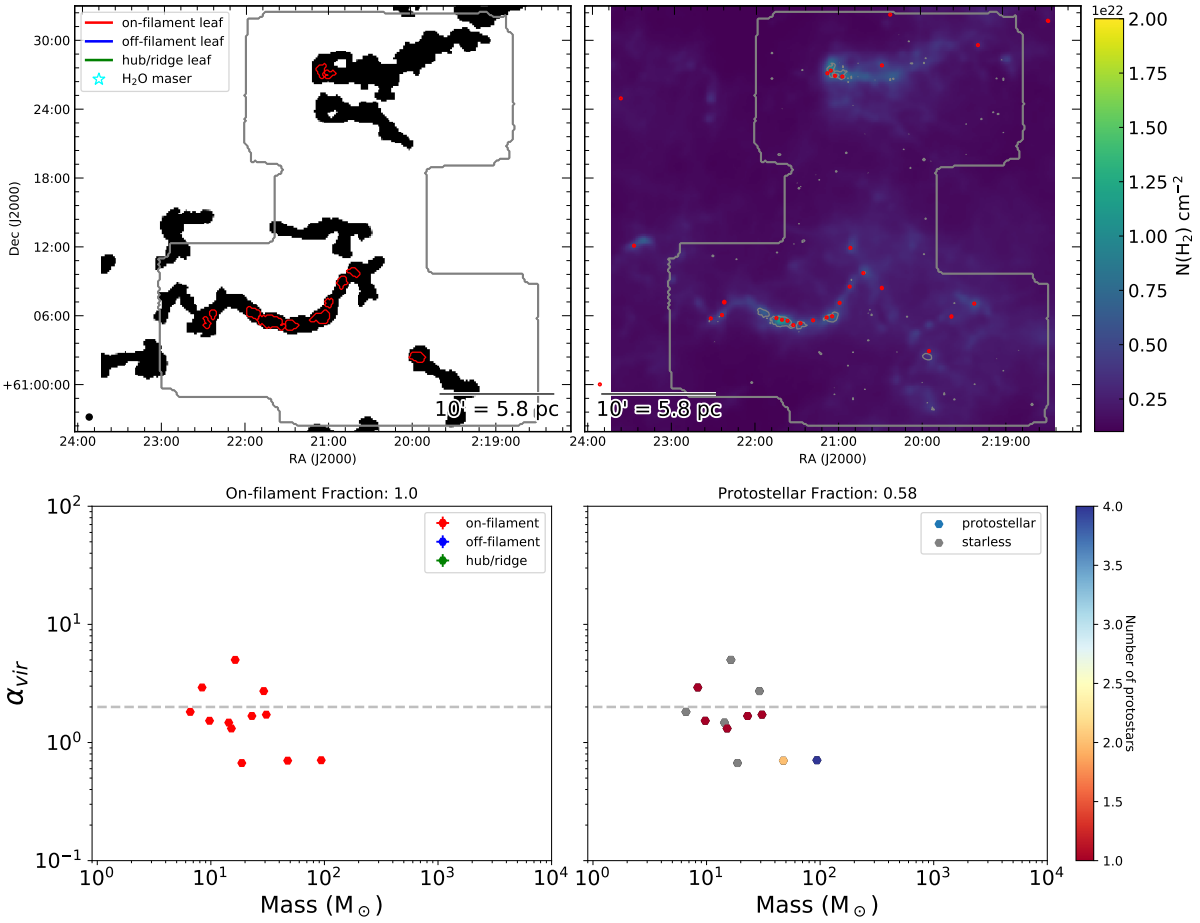

Fig. 3.33 – Same as Figure 3.32 for W3-west.

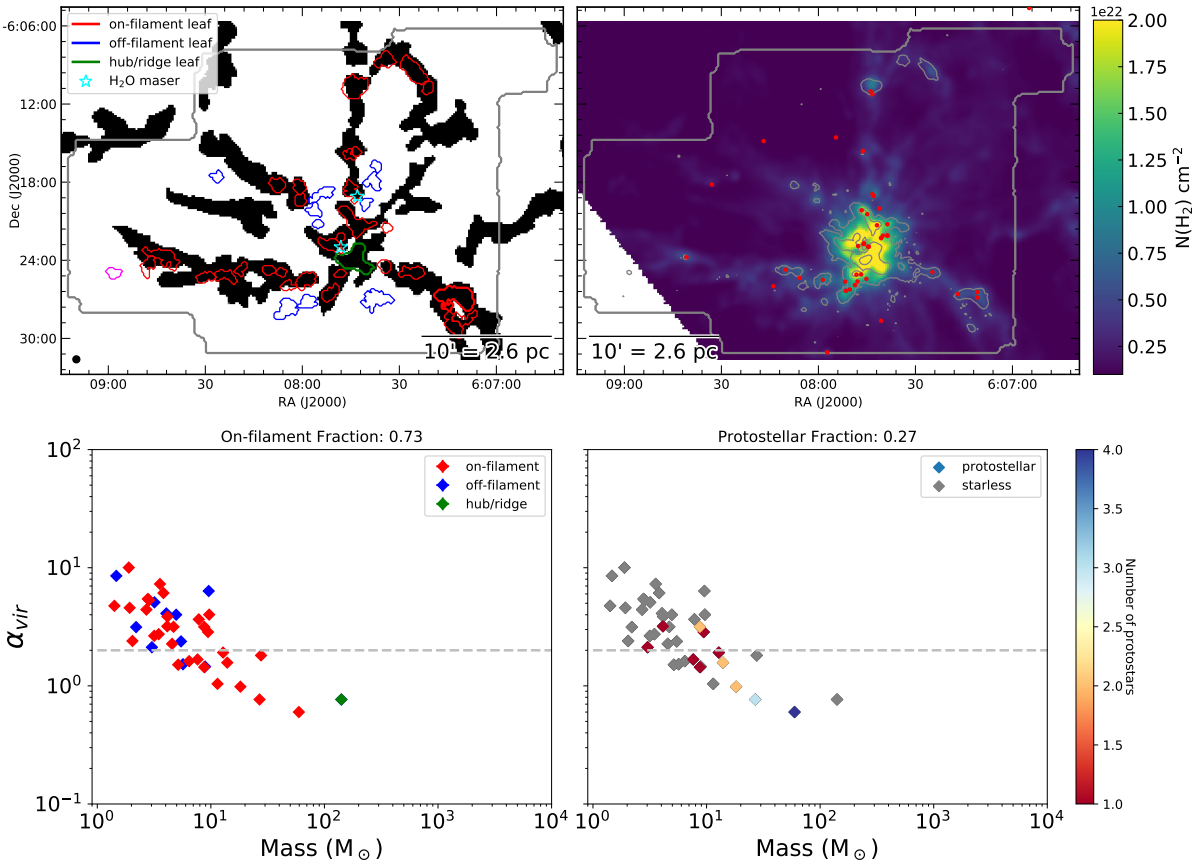

Fig. 3.34 – Same as Figure 3.32 for MonR2. Magenta contours on the left side of the upper left panel denote leaves that were not included in our virial analysis since their masses could not be estimated due to their locations being outside our H_2 column density map boundaries.

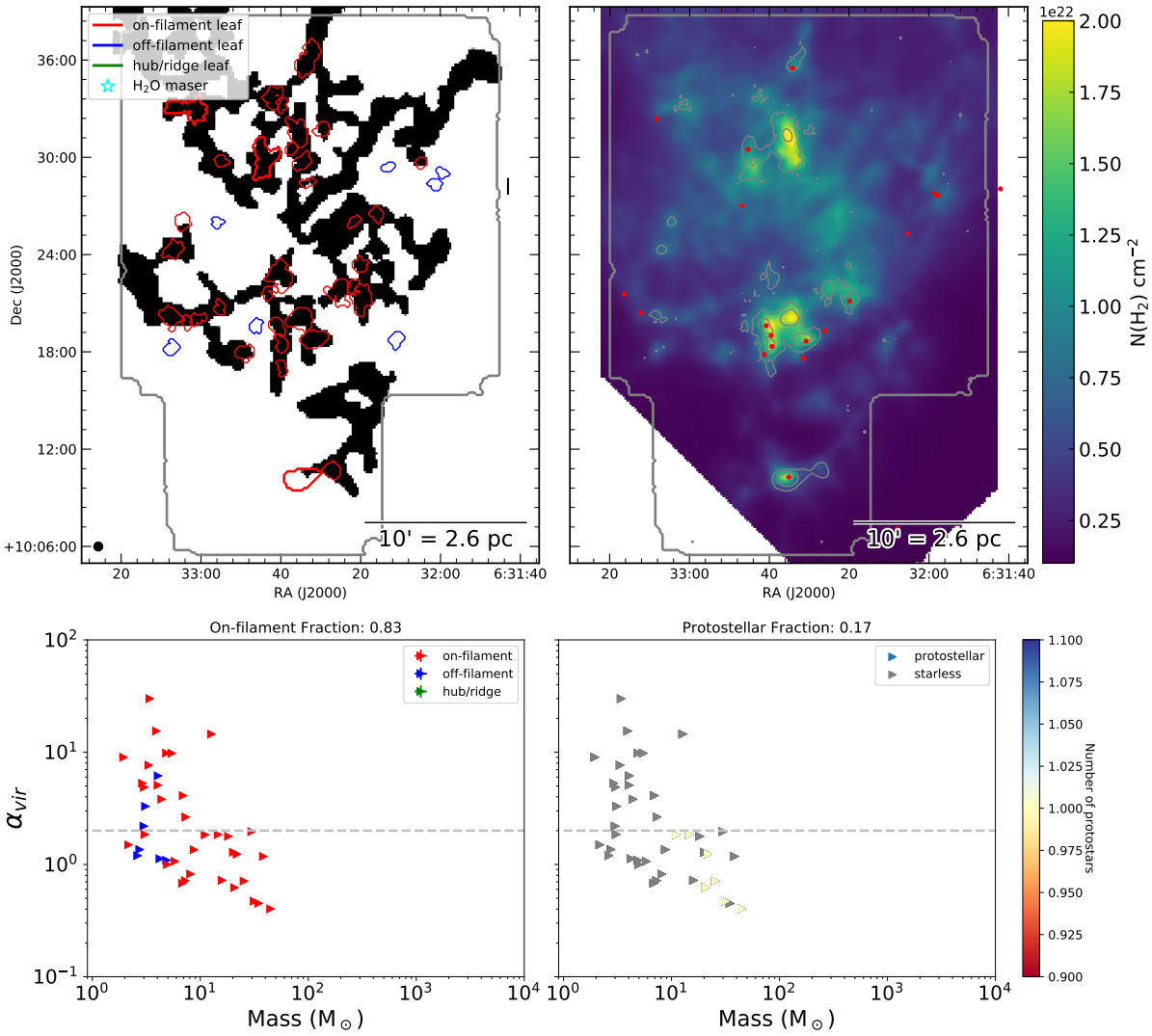

Fig. 3.35 – Same as Figure 3.32 for MonR1.

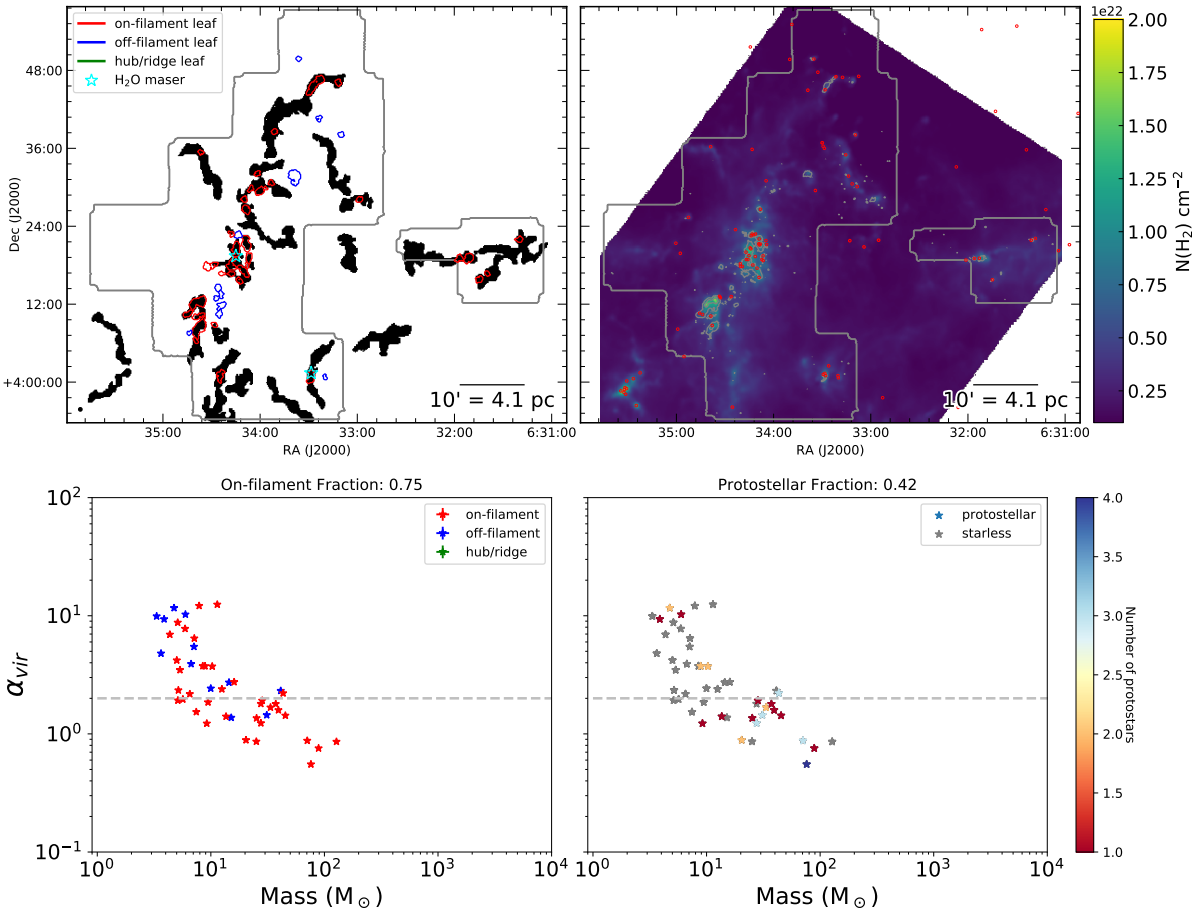

Fig. 3.36 – Same as Figure 3.32 for Rosette.

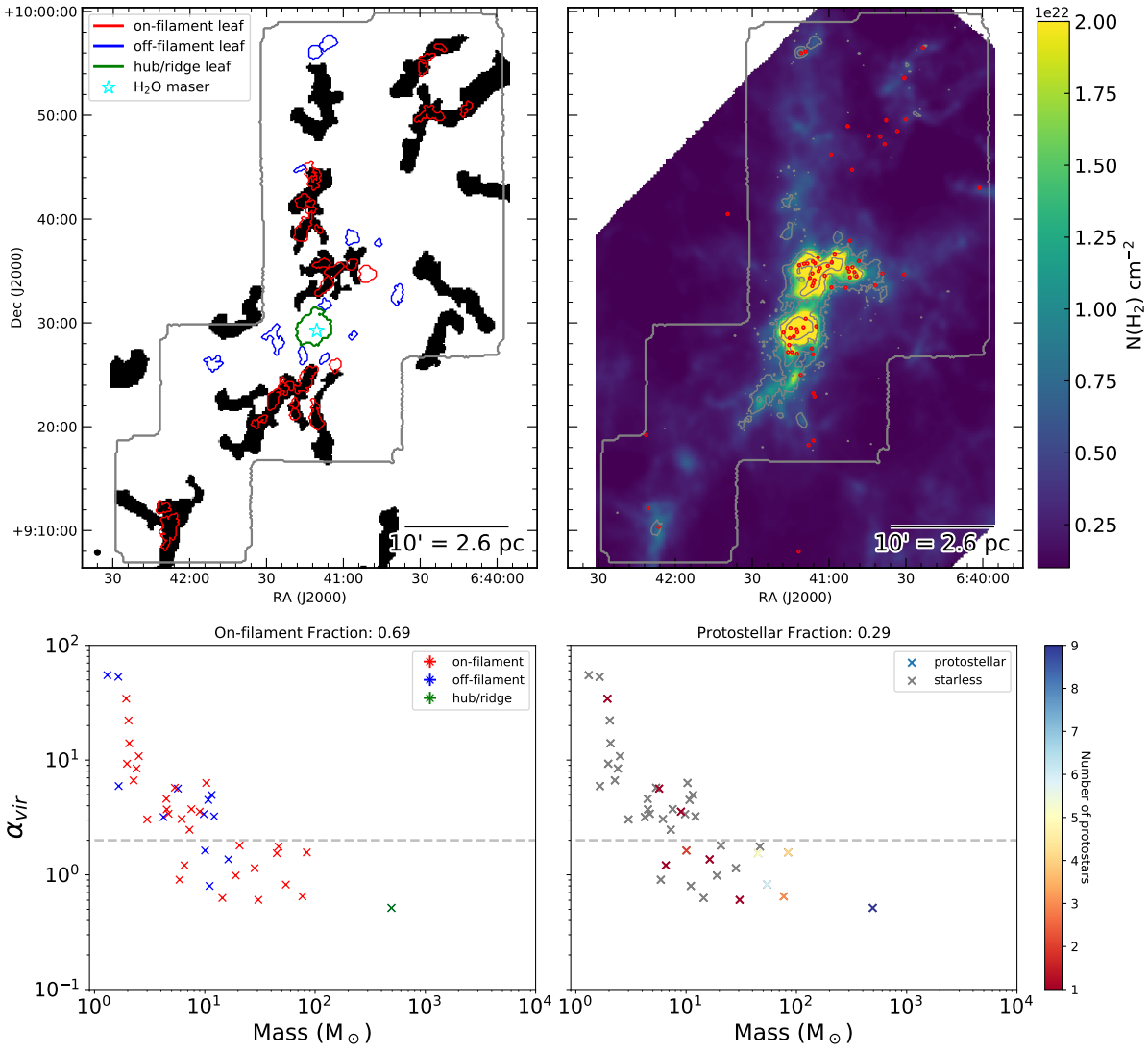

Fig. 3.37 – Same as Figure 3.32 for NGC2264.

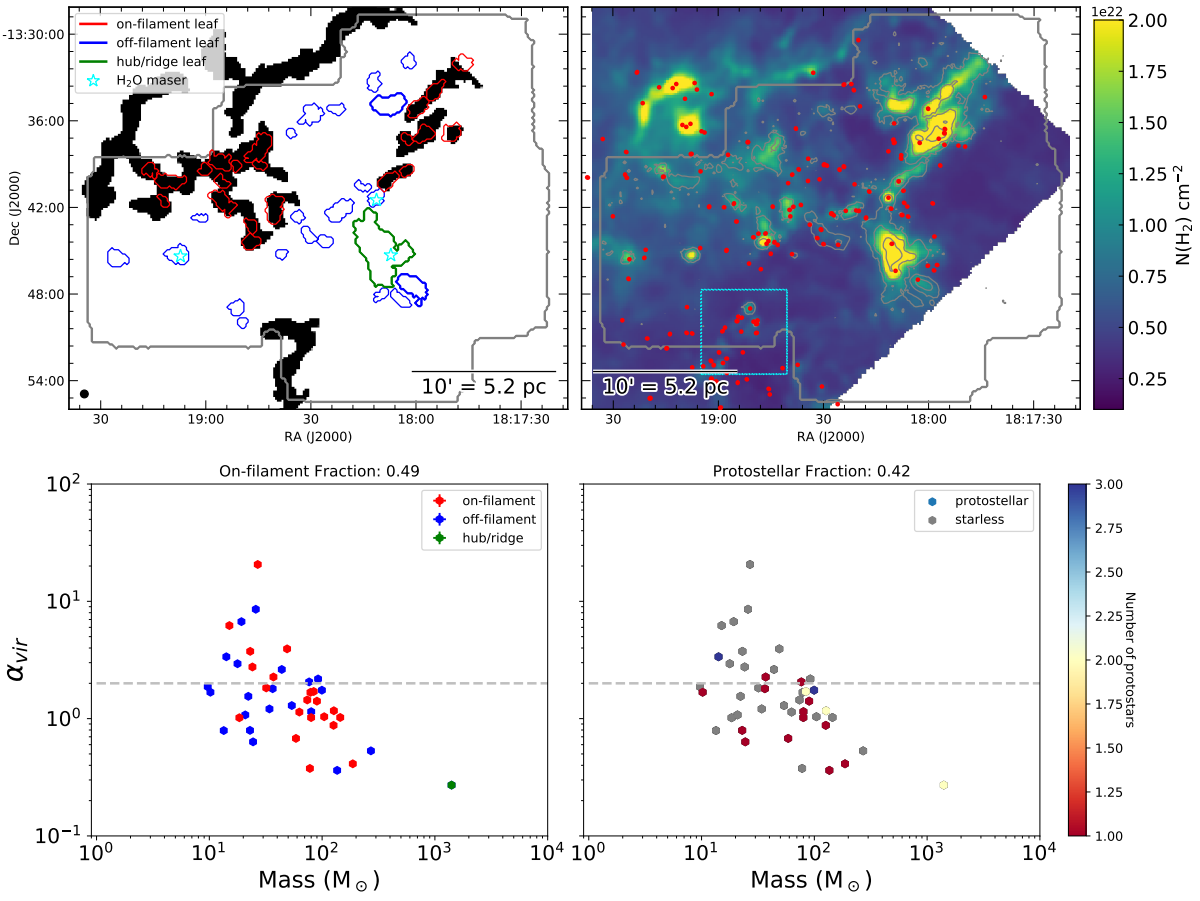

Fig. 3.38 – Same as Figure 3.32 for M16.

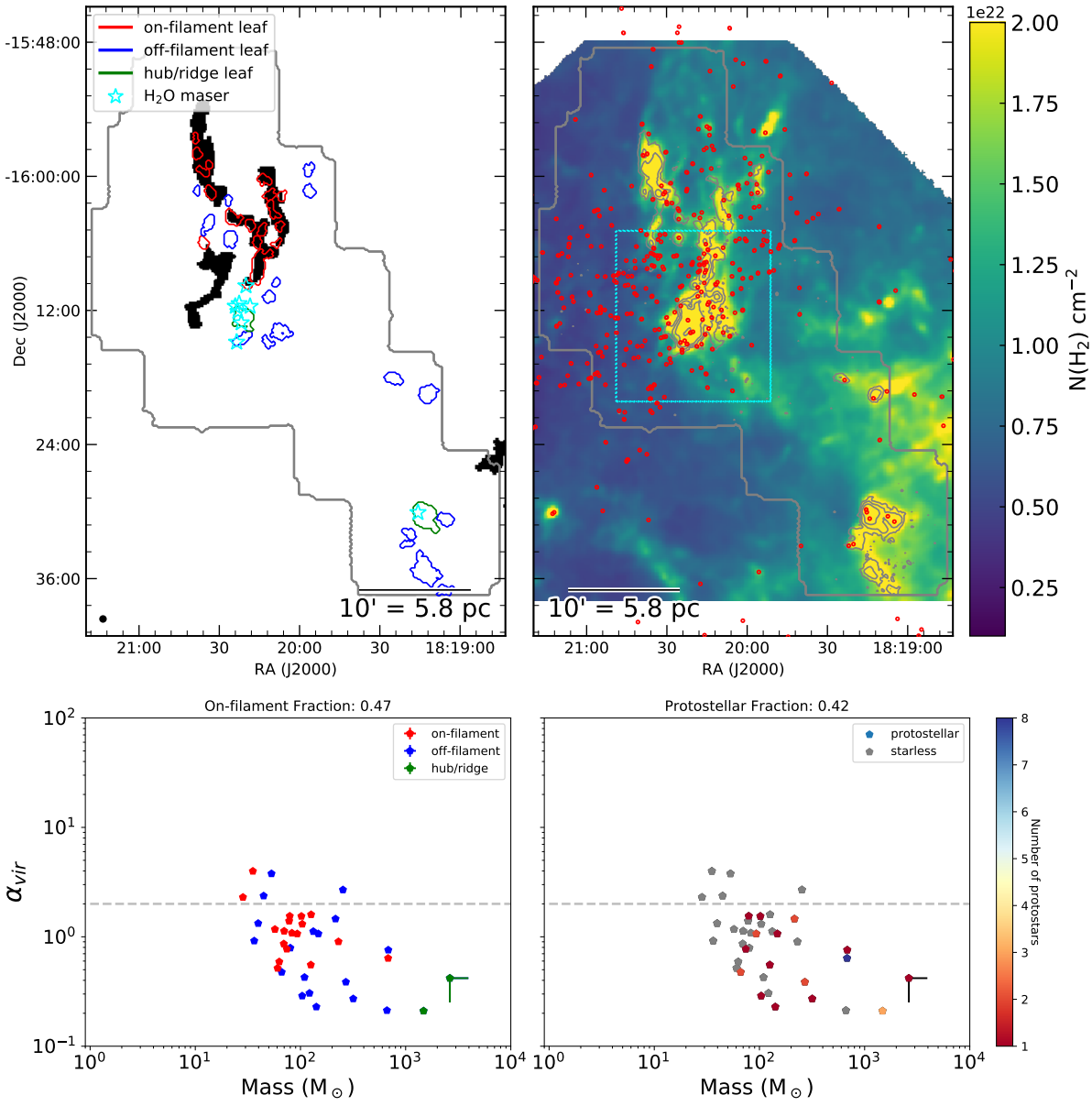

Fig. 3.39 – Same as Figure 3.32 for M17.

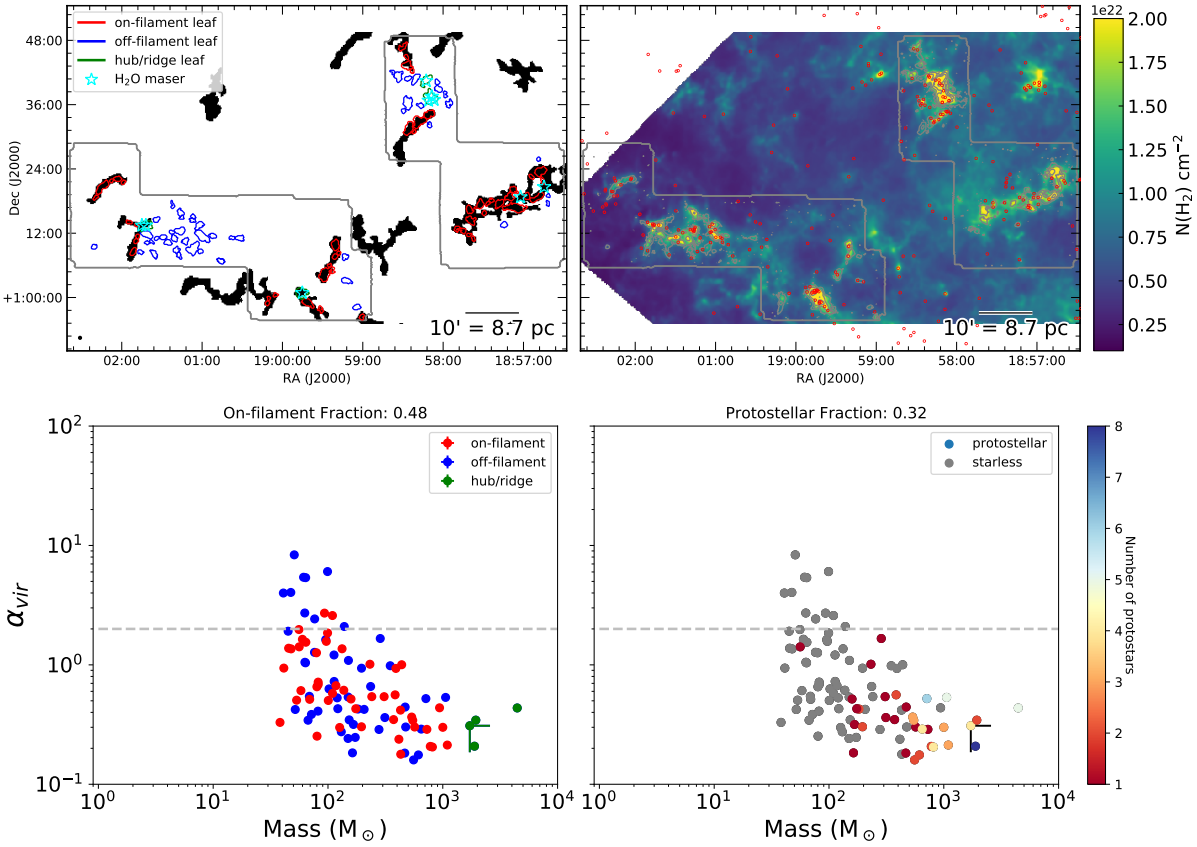

Fig. 3.40 – Same as Figure 3.32 for W48.

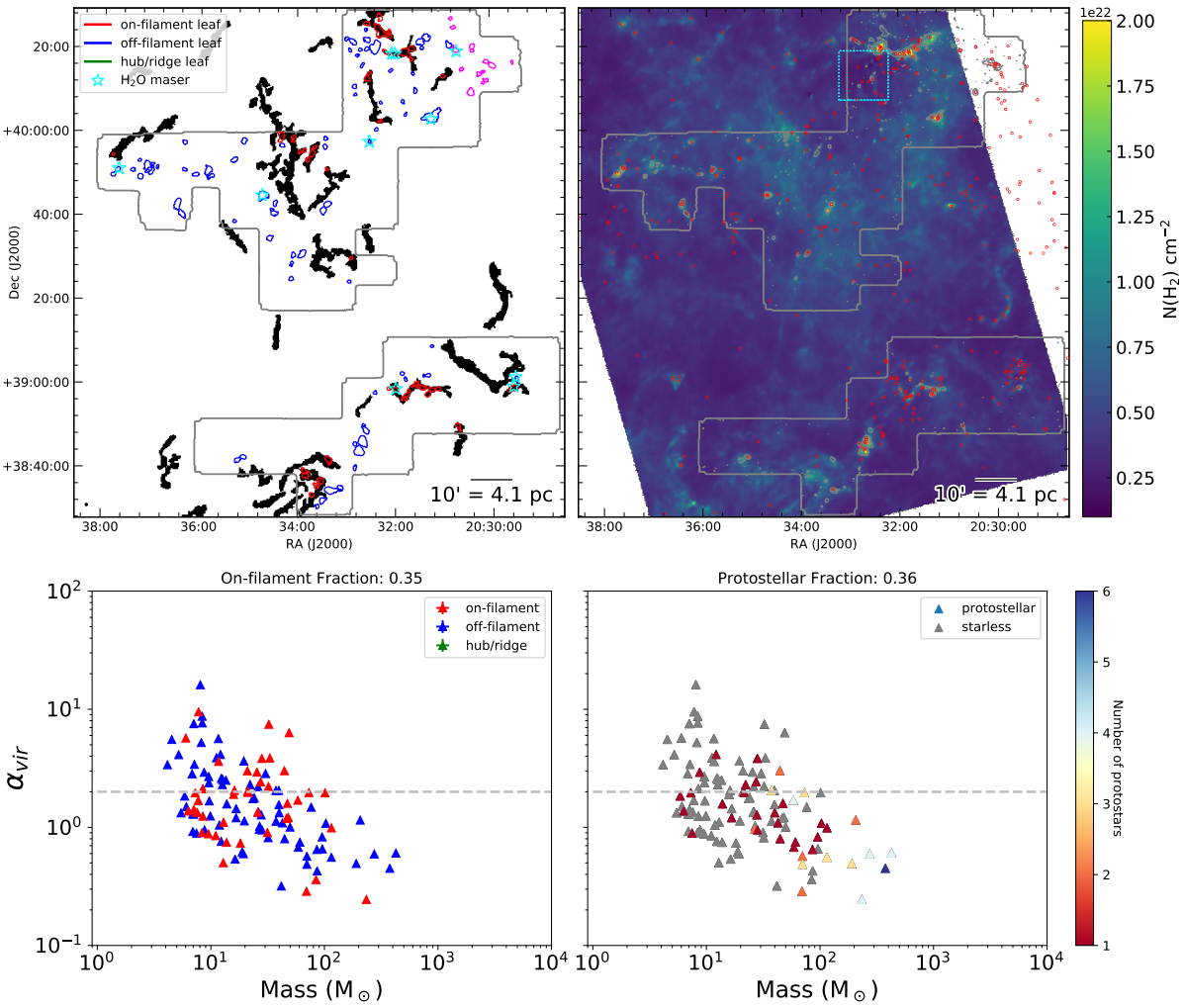

Fig. 3.41 – Same as Figure 3.34 for Cygnus X South.

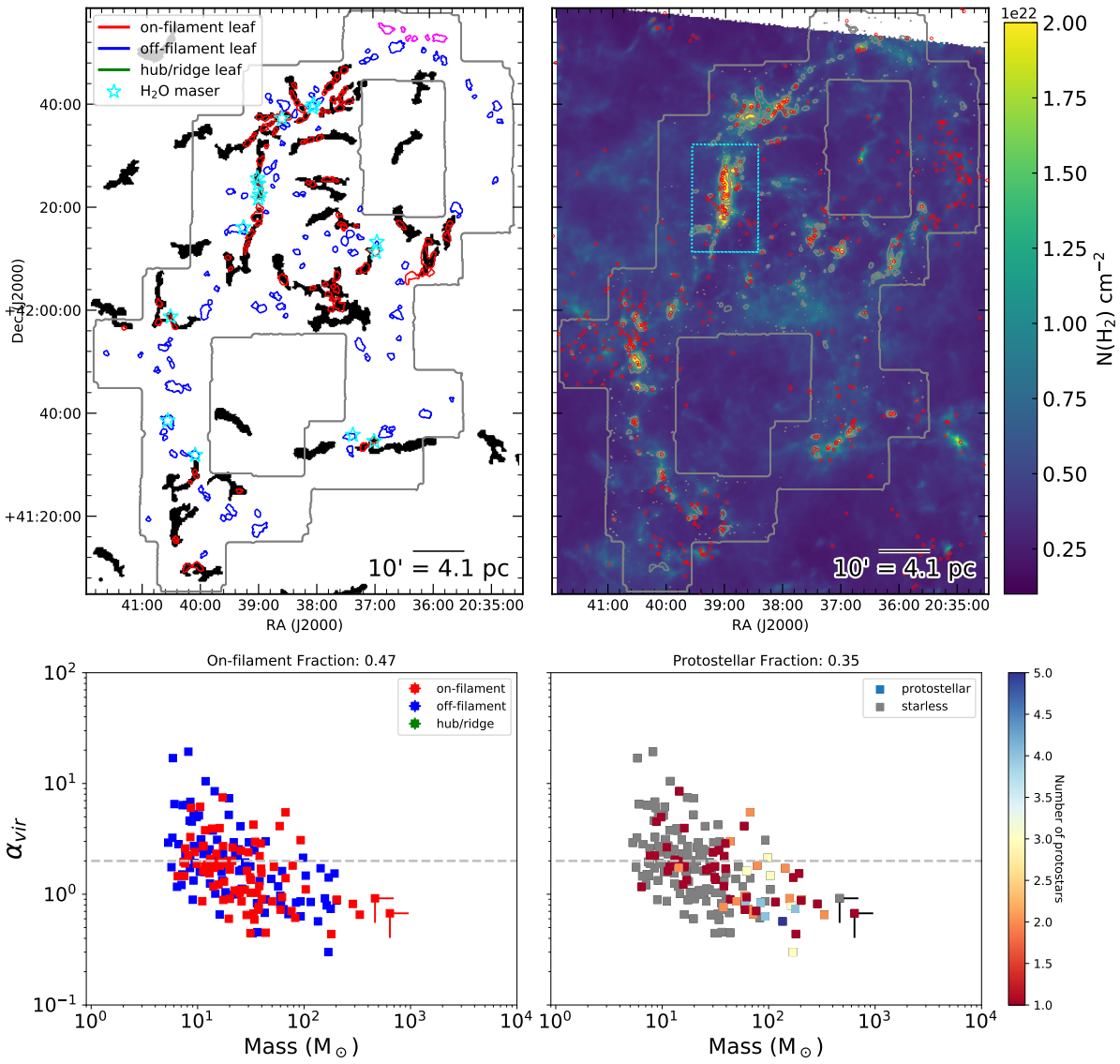

Fig. 3.42 – Same as Figure 3.34 for Cygnus X North.

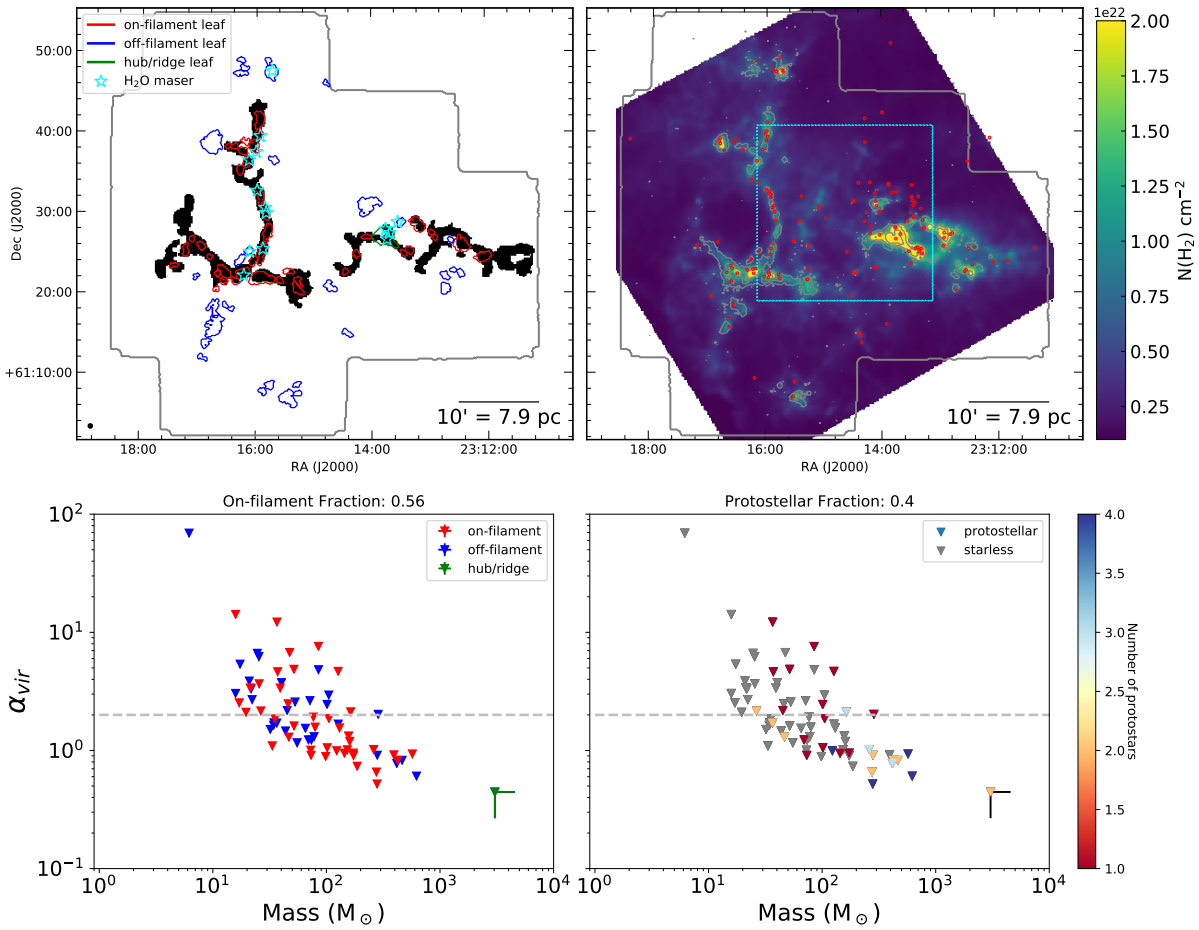

Fig. 3.43 – Same as Figure 3.32 for NGC7538.

3.3.7 Cloud Population Statistics

To understand the impact environment has upon the star formation in the KEYSTONE clouds, we search for relationships between ten variables of interest: leaf on-filament fraction, "bound" leaf fraction (i.e., the fraction of leaves with $\alpha_{vir} < 2$), protostellar leaf fraction, total dense gas mass, total protostar count, total leaf count, dense gas surface mass density, surface protostar density, median cloud kinetic temperature, and cloud distance. The dense gas mass, total protostar count, dense gas surface mass density, and surface protostar density are calculated over the KEYSTONE-mapped boundaries of the cloud where the NH_3 (1,1) integrated intensity is greater than 1.0 K km s^{-1}. The dense gas mass is defined as the integrated H_2 column density within the NH_3 (1,1) 1.0 K km s^{-1} integrated intensity contour, while the total protostar count is defined as the number of candidate YSOs identified by `getsources` within that same contour. The threshold of NH_3 (1,1) integrated intensity above 1.0 K km s^{-1} was chosen since it typically highlights the extent of pixels that were robustly fit during our line-fitting procedure (see, e.g., the lowest NH_3 (1,1) integrated intensity contours in Figures 3.4-3.15). Median values of H_2 column density within the NH_3 (1,1) 1.0 K km s^{-1} integrated intensity contours are typically around 1×10^{22} cm^{-2}, with a minimum of 4.2×10^{21} cm^{-2} measured in W3-west and a maximum of 2.3×10^{22} cm^{-2} measured in M17.

Figure 3.44 shows the Pearson correlation coefficients for the matrix of ten variables. The Pearson correlation coefficient can range from -1 to 1, where -1 and 1 signify the data fall on a straight line with a negative or positive correlation, respectively. A Pearson correlation coefficient of zero indicates there is no correlation between the variables. For 12 data points and using the Student's t-distribution to test for statistical significance, the null hypothesis that the data have no relationship is rejected at the 99.5% confidence level when the absolute value of the Pearson correlation coefficient is greater than ~ 0.71. As such, correlations that meet this threshold are outlined by black in Figure 3.44 and the corresponding scatter plots are shown in Figure 3.45.

Eight statistically significant correlations were found in the data: 1) decreasing leaf on-filament fraction with increasing dense gas mass, 2) decreasing leaf on-filament fraction with increasing number of protostars, 3) decreasing leaf on-filament fraction with increasing number of leaves, 4) decreasing bound leaf fraction with increasing protostellar surface density, 5) increasing dense gas mass with increasing number

of protostars, 6) increasing number of protostars with increasing number of leaves, 7) increasing surface mass density with increasing temperature, and 8) decreasing protostellar surface density with increasing cloud distance.

Since the Pearson correlation coefficient does not take into consideration the uncertainties on each data point, we visualize the scatter of each parameter in Figure 3.45 by adding errorbars as follows: The lower and upper leaf on-filament fraction errorbars represent the on-filament fractions obtained when using the `getfilaments` filament masks reconstructed up to spatial scales of 72″ and 290″, respectively, rather than the 145″ scale map. Errorbars for the bound leaf fraction reflect the fractions obtained when assuming the virial parameters for each leaf are at the extremes of their individual uncertainty range. Errorbars for the total protostars, protostellar surface density, and NH_3-leaves represent the $\sqrt{N}$ counting uncertainty. Errorbars for the median kinetic temperature represent the median absolute deviation of each cloud's T_K distribution.

Many of these correlations can be explained with our current understanding of the star formation process. For instance, the positive correlation between dense gas mass and protostars (Panel 5 in Figure 3.45) is related to the relationship between star formation rate (SFR) and dense gas mass that is well-established (e.g., Gao & Solomon, 2004; Wu et al., 2005, 2010; Lada et al., 2012; Stephens et al., 2016; Burkhart, 2018). Similarly, the correlation we observe between protostars and total ammonia-identified leaves (Panel 6 in Figure 3.45) is also related to the SFR-Mass relation since the leaves are tracing the dense gas mass in each cloud. Moreover, the negative relationship observed between leaf on-filament fraction and dense gas mass (Panel 1 in Figure 3.45) may also be loosely related to the SFR-Mass relation. Since the lower mass clouds in our sample tend to have higher leaf on-filament fractions, this trend may suggest that the star formation in those environments is more heavily dependent on filaments creating the high densities required to form ammonia leaves. Clouds with higher dense gas mass, however, can form clumps and stars even when filaments are not present due to their more widespread dense gas. The same argument can be applied to the anti-correlations observed between leaf on-filament fraction versus protostars and ammonia-identified leaves (Panels 2 and 3 in Figure 3.45). The SFR-Mass relation could also explain the positive relationship between temperature and surface mass density displayed in Panel 7 of Figure 3.45 since a higher SFR could lead to higher gas temperatures. Panel 7 has the lowest Pearson coefficient absolute value (0.71) of all the relationships shown in Figure 3.45 and is dominated by two

data points, however, which suggests it is not as robust as the other relationships presented.

In addition, the negative trend observed between bound leaf fraction and protostellar surface density (Panel 4 in Figure 3.45) may be related to the heating and turbulence injected into the cloud by protostars (e.g., Krumholz & McKee, 2008; Hansen et al., 2012; Offner & Chaban, 2017; Offner & Liu, 2018; Cunningham et al., 2018). As the protostellar density increases, the virial parameters of the leaves may increase due to the higher velocity dispersions and temperatures caused by nearby protostellar (or cluster) feedback (e.g., radiation and outflows). Such a scenario is also suggested by the magneto-hydrodynamic simulations of Offner & Chaban (2017), which showed that cores become unbound soon after (< 0.1 Myr) the onset of protostar formation due to outflow-induced turbulence. Lastly, the negative correlation between protostar surface density and cloud distance shown in Panel 8 is likely related to the larger areas observed for the more distant clouds, which would lower their protostar surface densities. Since protostellar surface density is the only parameter significantly correlated with distance, the distance dependency of the other parameters shown in Figure 3.44 is likely minimal.

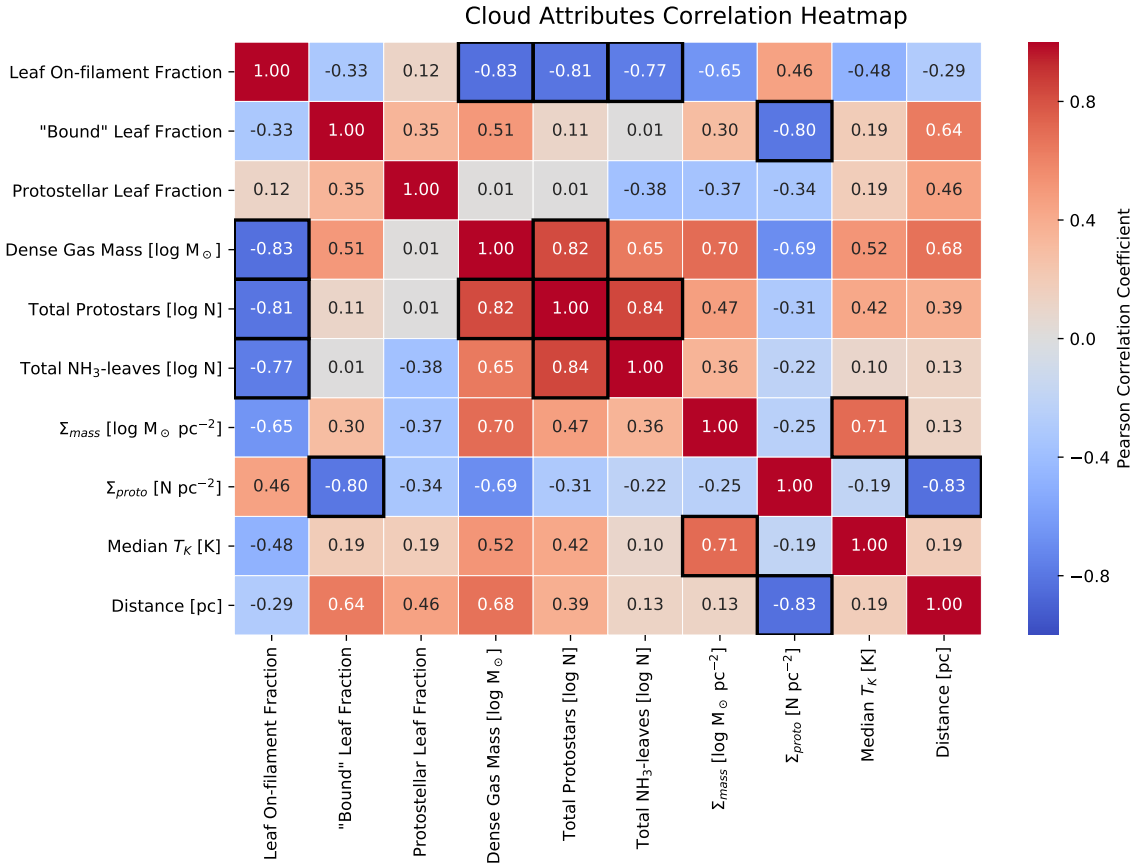

Fig. 3.44 – Heatmap of Pearson correlation coefficients for the ten variables of interest examined: leaf on-filament fraction, "bound" leaf fraction (i.e., the fraction of leaves with $\alpha_{vir} < 2$), protostellar leaf fraction, total dense gas mass, total protostar count, total leaf count, dense gas surface mass density, surface protostar density, median cloud kinetic temperature, and cloud distance. The colorbar ranges from -1 (perfect anti-correlation) to 1 (perfect positive correlation). Panels with a black outline denote statistically significant correlations that are displayed in Figure 3.45.

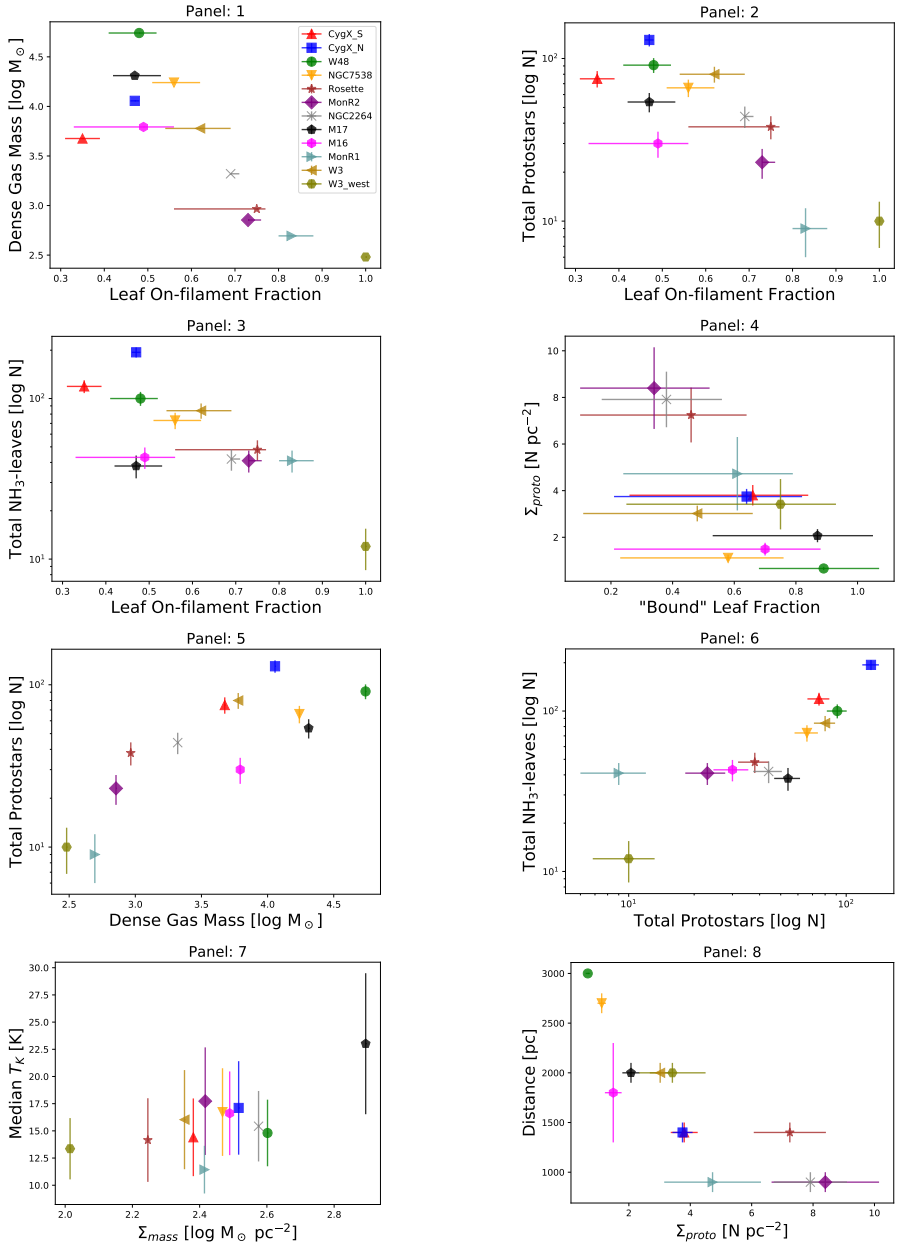

Fig. 3.45 – Statistically significant correlations found from Figure 3.44 when neglecting data errorbars. The dense gas mass, number of protostars, and surface protostar density are calculated within the boundaries of the KEYSTONE-mapped regions in each cloud where NH_3 (1,1) integrated intensity was greater than 1.0 K km s^{-1}. The errorbars on each data point are calculated as described in Section 3.3.7.

3.4 Discussion

3.4.1 Leaf/Filament Relationship

A relationship between dense cores and filamentary structures in dust continuum observations has been noted in several nearby star-forming environments. Polychroni et al. (2013) show that 67% of the dense cores they identified with CuTEx, a Gaussian fitting and background subtraction source extraction algorithm developed by Molinari et al. (2011), were coincident with filamentary structures in L1641 of Orion A. Using the same filament identification algorithm adopted in this paper, Könyves et al. (2015), Marsh et al. (2016), and Di Francesco et al. (2019, in prep) also found that 75%, 40%, and $40-80$% of starless dense cores in Aquila, Taurus-L1495, and five regions of the Cepheus Flare, respectively, are coincident with filamentary structures. In addition, hydrodynamical simulations of molecular clouds (e.g., Offner et al., 2013) also show a strong correspondence between cores and filamentary structures (Mairs et al., 2014). Although the KEYSTONE clouds analyzed in this paper are located at much farther distances ($0.9-3.0$ kpc) than L1641 (400 pc), Aquila ($250-450$ pc), Taurus-L1641 (140 pc), and Cepheus ($\sim$ 300 pc), we find consistent values for the on-filament fraction ($\sim 0.4-1.0$ for KEYSTONE clouds).

Despite the apparent relationship observed between leaves and filaments, we find no significant variations between the virial parameters of the on- and off-filament leaf populations in any of the clouds. For the 454 on-filament leaves, 294 ($\sim$ 65 %) have $\alpha_{vir} < 2$, which is consistent with the bound fraction for the entire leaf population ($\sim$ 63 %). Furthermore, Figure 3.46 shows that the mass, effective radius, average kinetic temperature, and average velocity dispersion for the on-filament and off-filament leaves are essentially identical. Although the more distant clouds (e.g., W48 and NGC7538) tend to have larger masses and radii than the nearest clouds in our sample (e.g., MonR1, MonR2, and NGC2264; see Appendix 3.7 for a discussion of the distance dependency of our results), the similarities between the on-filament and off-filament leaf parameter distributions appear to hold for the individual clouds as well. These similarities indicate that star formation away from filaments might be equally as likely as star formation on filaments in high-mass GMCs since dense gas may be more widespread in those environments. Such a scenario is also suggested by the anti-correlation found between leaf on-filament fraction and dense gas mass discussed in Section 3.3.7. As dense gas becomes more widespread in high-mass GMCs, the fraction of star formation taking place on filaments may decrease since dense

gas is equally as likely to be found away from filaments as it is to be found within filaments.

We also note the existence of a group of ammonia-identified leaves with uncharacteristically larger masses ($10^2 - 10^3$ $M_\odot$) than the majority of leaves in their respective clouds. Deemed "hubs" or "ridges" based on the nomenclature suggested in Myers (2009), these high-mass leaves are shown by the color green in Figures 3.32-3.43. The hubs are located at the intersection of multiple filaments (e.g., MonR2, NGC2264, eastern and northern regions in W48) and the ridges are massive filaments (e.g., NGC7538, M16, southern region of W48). Due to their high masses, these structures all have low virial parameters ($\alpha_{vir} = 0.2 - 0.5$) and are likely gravitationally bound or collapsing. As such, the hubs and ridges may be a result of mass build-up at the locations where filaments are transporting mass from other parts of the cloud.

In addition to the hubs and ridges being coincident with filaments, their mass and size indicate they are likely the precursors of massive young stellar objects and stellar clusters. For example, the right panel of Figure 3.30 shows the Mass-Radius plot for the hub/ridge and non-hub/ridge leaves in relation to the Kauffmann & Pillai (2010) empirically-derived threshold for massive star formation: m(r) > 870 $M_\odot$ $(r/pc)^{1.33}$. The hubs and ridges tend to be above this threshold, indicating that they will likely form high-mass stars. As shown in Figure 3.46, the hubs and ridges tend to have higher masses (median $\log(M_{obs}) = 3.2 \pm 0.5$), larger radii (median R_{eff} $= 0.7 \pm 0.3$), warmer temperatures (median $T_{K,avg} = 19.5 \pm 5.1$), and larger velocity dispersions (median $\sigma = 0.7 \pm 0.1$) than the starless leaf population. Instead, the hub and ridge masses, radii, and virial parameters are more similar to the massive star-forming clumps identified by Urquhart et al. (2015), highlighting further their propensity to form massive stars. Furthermore, the hubs and ridges tend to align with the positions of H_2O maser emission (identified by eye and shown as cyan stars in Figures 3.32-3.43) also detected by KEYSTONE (White et al., in prep.), which is frequently associated with massive young stellar objects. If dense gas hubs and ridges are indeed the current, or future, sites of massive young stellar object and stellar cluster formation, it would explain the high correspondence observed between those objects and filament intersections (e.g., Myers, 2009; Schneider et al., 2012; Hennemann et al., 2012; Li et al., 2016; Motte et al., 2018a).

3.4.2 Leaf/Protostar Relationship

Figures 3.32-3.43 also show the virial parameters of the leaves identified as protostellar and starless in each of the clouds observed by KEYSTONE. In many regions (e.g., MonR1, Rosette, Cygnus X North, MonR2, W48), the protostellar core population clearly has larger masses and lower virial parameters than the starless core population. For the 288 protostellar leaves identified, 229 ($\sim$ 80 %) have $\alpha_{vir} < 2$. In comparison, 294 of the 547 starless leaves identified ($\sim$ 54 %) have $\alpha_{vir} < 2$. As shown in Figure 3.46, the protostellar population's mass distribution peaks at higher values (Median log(Mass) = 1.8 $\pm$ 0.6 $M_{\odot}$) than that of the starless population (Median log(Mass) = 1.3 $\pm$ 0.5 $M_{\odot}$), which could explain the lower protostellar virial parameters. In addition, the hubs and ridges identified in the previous section tend to host multiple protostars (see, e.g., NGC7538, NGC2264, W48, W3, M16). In several regions, the hubs and ridges host over six protostars. Since the 70 μm maps are typically confusion-limited in the hubs and ridges, their protostar counts are likely under-estimated. This attribute highlights the exceptional environment hubs and ridges provide for cluster formation.

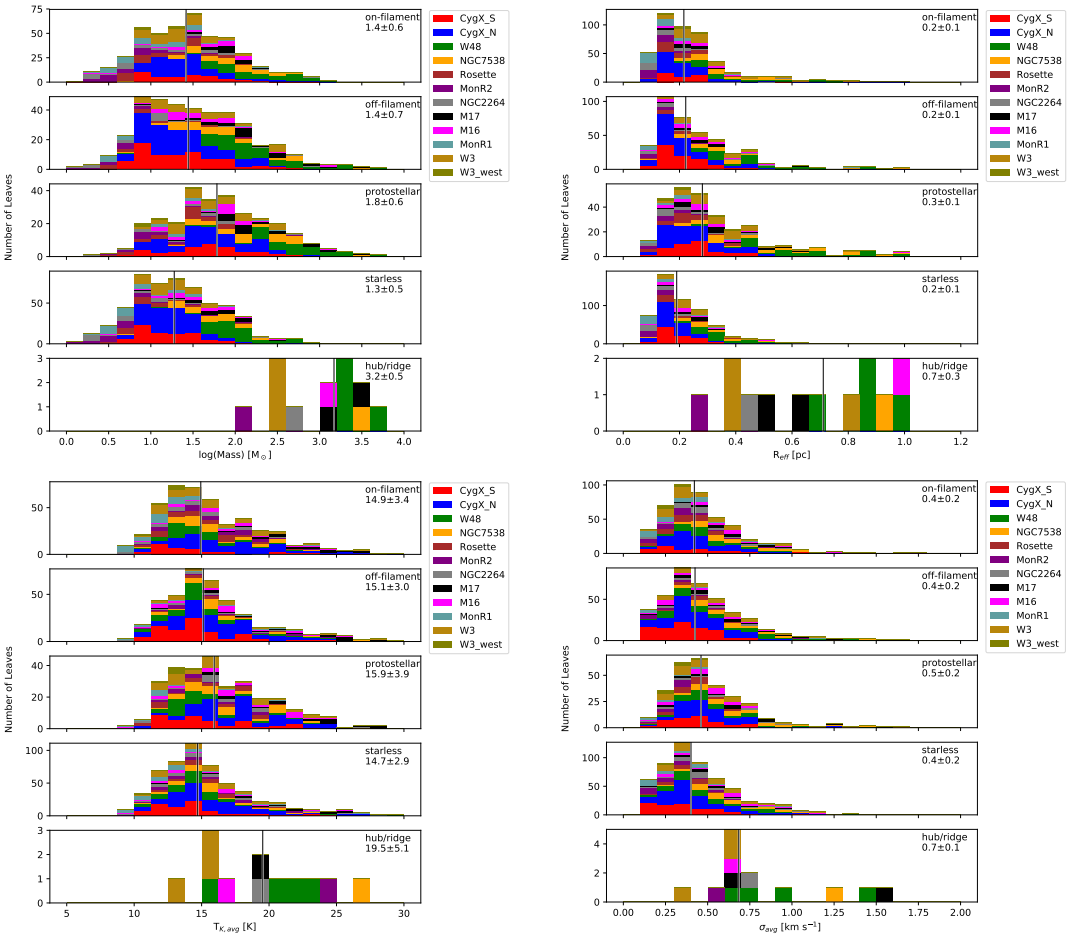

Fig. 3.46 – Stacked histograms of mass (upper left), effective radius (upper right), average kinetic temperature (lower left), and average velocity dispersion (lower right) for the leaves identified as on-filament, off-filament, protostellar, starless, and hub/ridge. The median and median absolute deviation of the distributions are shown in the upper right corner of each panel. The black vertical lines show the distribution median.

Table 3.6. Cloud Statistics

Cloud	T_{med} K	σ_{med} km s^{-1}	Protos	Area pc^2	Mass $M_\odot$	Tot Leaves	Fil Leaves fraction	Proto Leaves fraction	Bound Leaves fraction
W3	16.0 ± 4.6	0.5 ± 0.3	80	26.5	5999	84	0.62	0.38	0.48
W3-west	13.4 ± 2.8	0.3 ± 0.1	10	2.9	303	12	1.00	0.58	0.75
MonR2	17.7 ± 4.9	0.3 ± 0.2	23	2.7	715	41	0.73	0.27	0.34
MonR1	11.4 ± 2.2	0.2 ± 0.2	9	1.9	494	41	0.83	0.17	0.61
Rosette	14.2 ± 3.8	0.4 ± 0.1	38	5.2	924	48	0.75	0.42	0.46
NGC2264	15.4 ± 3.2	0.5 ± 0.2	44	5.6	2091	42	0.69	0.29	0.38
M16	16.6 ± 3.8	0.5 ± 0.2	30	20.1	6207	43	0.49	0.42	0.70
M17	23.0 ± 6.5	0.7 ± 0.3	54	26.1	20439	38	0.47	0.42	0.87
W48	14.8 ± 3.1	0.5 ± 0.3	91	137.6	55013	100	0.48	0.32	0.89
Cygnus X South	14.4 ± 3.6	0.4 ± 0.2	75	19.7	4744	119	0.35	0.36	0.66
Cygnus X North	17.1 ± 4.3	0.4 ± 0.2	130	34.7	11383	194	0.47	0.35	0.64
NGC7538	16.7 ± 4.0	0.6 ± 0.3	66	59.2	17393	73	0.56	0.40	0.58

Note. — Columns show the following: (1) cloud name, (2-3) median kinetic gas temperature and velocity dispersion for all reliably fit ammonia pixels, (4) number of protostars identified where NH_3 (1,1) integrated intensity is greater than 1 K km s^{-1}, (5) area of map where NH_3 (1,1) integrated intensity is greater than 1 K km s^{-1}, (6) total mass where NH_3 (1,1) integrated intensity is greater than 1 K km s^{-1}, (7) total number of ammonia leaves identified in cloud, (8) fraction of total leaves that are on-filament, (9) fraction of total leaves that are protostellar, (10) fraction of total leaves that are bound ($\alpha_{vir} < 2$).

3.4.3 Virial Stability in Low- and High-Mass Star-Forming Regions

Our final sample of 835 ammonia-identified leaves, for which virial parameters have been measured in a consistent manner, forms one of the largest current samples of dense gas structure virial parameters in high-mass star-forming regions. While many studies have derived virial parameters for single molecular clouds or sub-samples of clumps/cores (e.g., Dunham et al., 2010; Schneider et al., 2010a; Urquhart et al., 2011; Tan et al., 2013; Li et al., 2013; Urquhart et al., 2015; Friesen et al., 2016; Kirk et al., 2017; Billington et al., 2019), few have viewed virial stability across many clouds. Wienen et al. (2012) observed ammonia emission from a sample of 862 clumps in the inner Galactic disk, but only $\sim$ 300 of those had known distance measurements required to estimate masses and virial parameters. Similarly, Kauffmann et al. (2013) compiled a catalog of 1325 virial parameter estimates from previously published catalogs of sources in both high- and low-mass star-forming regions. The Kauffmann et al. (2013) catalog, however, featured virial parameters that had been measured using a variety of molecular tracers (^{13}CO, NH_3, N_2D^+), mass estimation methods (dust continuum and NIR extinction), and probed varying scales (clouds, clumps, and cores). Nevertheless, we can usefully compare the Kauffmann et al. (2013) catalog to our data since it deals primarily with high-mass star-forming regions, uses the same formulation for source effective radius, and uses dust continuum emission to derive the masses for most sources.

Overall, our virial parameters are consistent with those found for the high-mass

Table 3.7. Leaf Population Statistics

Leaf Statistic	Fraction
Bound	523 of 835 ($\sim 63\%$)
Starless	547 of 835 ($\sim 66\%$)
Protostellar	288 of 835 ($\sim 34\%$)
On-filament	454 of 835 ($\sim 54\%$)
Bound Starless	294 of 547 ($\sim 54\%$)
Bound Protostellar	229 of 288 ($\sim 80\%$)
Bound On-filament	294 of 454 ($\sim 65\%$)
Sub-virial (cloud weight pressure)	573 of 835 ($\sim 69\%$)

Note. — Leaf population statistics quoted throughout the paper. All fractions are in relation to the sample of leaves with mass estimates.

cores, clumps, and clouds included in the Kauffmann et al. (2013) compilation, which included the clumps observed by Wienen et al. (2012). α_{vir} ranges from $\sim 10^{-1}$ to 10^2 and roughly half of the sources fall below the α_{vir}=2 threshold for both the Kauffmann et al. (2013) sources and those presented in this paper. This result is in contrast to the virial analyses of Friesen et al. (2016) in Serpens South and Keown et al. (2017) in Cepheus-L1251, which found that nearly all their ammonia-identified leaves had $\alpha_{vir} < 2$. Serpens South and Cepheus-L1251 are closer ($d \sim 250 - 450$ pc and 300 pc, respectively) than the clouds observed by KEYSTONE and are thus probing smaller scale structures, which may explain the higher rate of gravitationally bound leaves in those papers. These results are supported by those of Ohashi et al. (2016a) and Chen et al. (2019b), which used ALMA observations of infrared dark clouds to show that α_{vir} decreases with decreasing spatial scales from filaments to clumps to cores, and may be showing that gravity is more important in the stability of structures at small scales. Alternatively, the KEYSTONE observations may indicate that ammonia is more widespread throughout GMCs than it is in low-mass clouds, producing detectable ammonia emission in both bound and unbound sources. Such a scenario is supported by the observations of Henshaw et al. (2013), which found N_2H^+ $(1-0)$ to be more extended in the infrared dark cloud G035.39-00.33 than in low-mass star-forming environments.

Observations of more distant cloud clumps ($\sim 2-11$ kpc) by the Bolocam Galactic Plane Survey (BGPS; Rosolowsky et al., 2010; Ginsburg et al., 2013), which mapped 1.1 mm dust continuum emission across the Galactic plane, have also indicated low virial parameters ($\alpha_{vir} < 2$) for clumps. For instance, Svoboda et al. (2016) combined NH_3 observations with BGPS clump detections to calculate virial parameters for 1640 clumps and found that 76% of starless candidates and 86% of protostellar candidates had $\alpha_{vir} < 2$. Similarly, Dunham et al. (2011) found that a separate sample of 456 BGPS clumps had a median $\alpha_{vir} = 0.74$. We note, however, that the NH_3 observations used for those analyses were targeted follow-ups to previously identified clumps in the BGPS data. Thus, they may not be tracing the faint NH_3 emission probed by KEYSTONE and included in our leaf catalog. These low brightness NH_3 sources comprise the lower mass leaves in our sample that have $\alpha_{vir} > 2$ and may be the reason we detect unbound sources that are lacking in the BGPS data.

A similar selection bias for high brightness sources is likely also impacting clump virial analyses using *Herschel* Hi-GAL (Molinari et al., 2010) and *APEX Telescope* ATLASGAL (Schuller et al., 2009) observations. For example, Merello et al. (2019)

combined Hi-GAL clump detections with NH_3 catalogs to derive virial parameters for 1068 clumps at distances typically between ~ 2 kpc and ~ 15 kpc. 72% of the 1068 clumps had $0.1 < \alpha_{vir} < 1$, with a median α_{vir} of 0.3. A similar virial analysis of 213 Hi-GAL clumps by Traficante et al. (2018) found that 76% have $\alpha_{vir} < 1$. Using a sample of 1244 ATLASGAL clump detections with masses much larger (typically $> 10^3 M_\odot$) than the leaves presented in this paper, Contreras et al. (2017) found a median α_{vir} of 1.1. Since these analyses rely on clump catalogs identified by dust continuum observations, however, they likely exclude the faint NH_3 sources detected by KEYSTONE.

3.4.4 Cloud Weight Pressure

Although the virial analysis presented in Section 3.3.5 compares the gravitational energy of the ammonia-identified leaves with their kinetic energy, it excludes the possible influence of external pressure applied by the leaves' surroundings (Field et al., 2011). For instance, the weight of the molecular cloud in which the leaves are embedded can contribute to their confinement (e.g., Pattle et al., 2015, 2017; Kirk et al., 2017). Here, we add the cloud weight pressure energy density (Ω_{Pw}) to the virial equation using the technique described in Keown et al. (2017) and Kirk et al. (2017). The three energy densities in the virial equation considered in our analysis are given by the following expressions:

$$\Omega_{Pw} = -4\pi P_w R^3 \tag{3.4}$$

$$\Omega_G = \frac{-1}{2\sqrt{\pi}} \frac{GM^2}{R} \tag{3.5}$$

$$\Omega_K = \frac{3}{2} M\sigma^2 \tag{3.6}$$

where M is the observed structure mass, R is the effective radius, G is the gravitational constant, σ^2 is the same as Equation 3.3, and P_w is cloud weight pressure:

$$P_w = \pi G \bar{N} N (\mu_H m_H)^2 \tag{3.7}$$

where $\bar{N}$ is the mean cloud column density and N is the column density at the structure (e.g., McKee, 1989; Kirk et al., 2006, 2017). Both $\bar{N}$ and N are measured from a spatially filtered column density map to determine the cloud's mass contribution from

large-scale structures. Following other recent virial analyses incorporating turbulent pressure (Kirk et al., 2017; Keown et al., 2017; Kerr et al., 2019), the *a trous* transform[8] is used to filter spatially each column density map to spatial scales larger than 2^n pixels, where we have chosen n=4 or 16 pixels for all regions. Figure 3.47 shows an example spatially filtered column density map for NGC 7538, where 16 pixels is equivalent to $\sim 96''$ or ~ 1.3 pc. $\bar{N}$ is calculated as the mean of the spatially filtered column density map, while N represents the mean spatially filtered column density within each leaf's dendrogram-identified boundary.

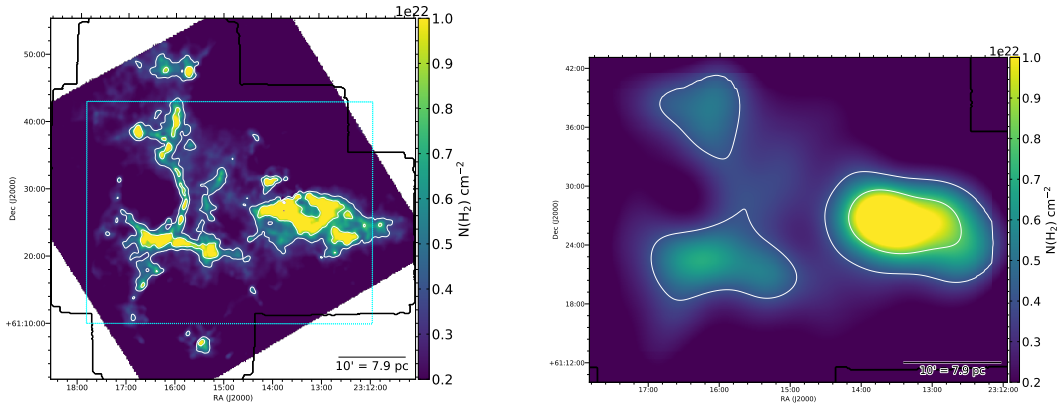

Fig. 3.47 – Left: H_2 column density map of NGC7538 with white contours at 4×10^{21} cm^{-2} and 8×10^{21} cm^{-2}. Black outlines the extent of the KEYSTONE mapping of the region. Right: Spatially filtered H_2 column density map over the cyan dotted area overlaid in the left panel. The map includes spatial scales larger than 16 pixels, which is equivalent to $\sim 96''$ or ~ 1.3 pc at the distance of NGC7538.

Although we have chosen a single scale for the spatial filtering, a recent virial analysis by Kerr et al. (2019) investigated the impact that varying this scale has upon the cloud weight pressure term. In their analysis of L1688, B18, and NGC1333, Kerr et al. find that increasing or decreasing the spatial filtering scale by a factor of two results in less than a factor of two difference in the average P_w values for those clouds. As shown below, such a factor is not enough to change our overall conclusions about the virial stability of the observed structures.

The left panel of Figure 3.48 shows the balance between cloud weight pressure (Ω_{Pw}), kinetic energy (Ω_K), and gravitational potential energy (Ω_G) for the 835 leaves with mass estimates. Leaves to the right of the vertical dotted line are deemed "sub-

[8]The *atrous.pro* IDL script developed by Erik Rosolowsky, which is available at https://github.com/low-sky/idl-low-sky/blob/master/wavelet/atrous.pro, was used for this analysis.

virial" since their gravitational potential and external pressure are enough to overcome their internal kinetic energy in the absence of magnetic fields. Leaves to the left of the vertical line are "super-virial" since they are not bound by their gravitational and external pressure energy densities. Below the horizontal dotted line are "pressure-dominated" sources that have a higher external pressure energy density than their gravitational energy density. Conversely, "gravity-dominated" sources lie above the horizontal line.

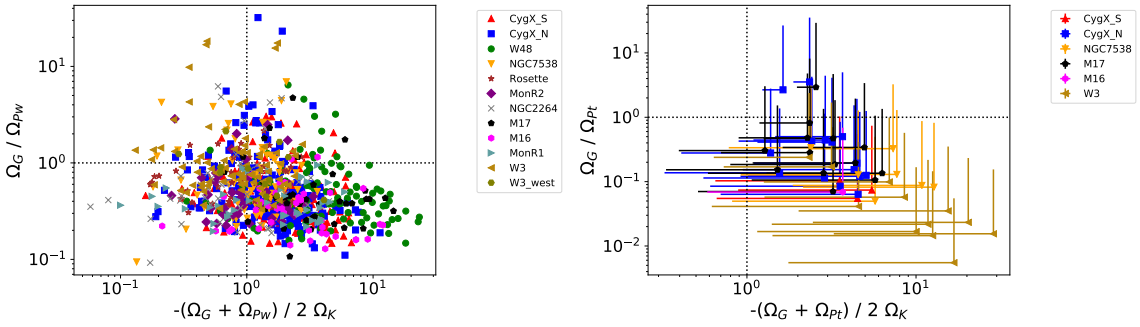

Fig. 3.48 – Left: Virial plane for all ammonia-identified leaves displayed in Figure 3.31 showing the balance between three energy densities in the virial equation: Gravitational (Ω_G), Cloud Weight Pressure (Ω_{Pw}), and Kinetic (Ω_K). Sources to the right of the vertical line are sub-virial, while sources to the left are super-virial. Sources above the horizontal line are gravitationally-dominated, while sources below the line are pressure-dominated. Right: Virial plane using instead the Turbulent Pressure energy density (Ω_{Pt}) for all ammonia-identified leaves with reliable $C^{18}O$ (3−2) velocity dispersion measurements. The data points are calculated using the critical density (3×10^4 cm^{-3}) of $C^{18}O$ (3 − 2) as the volume density traced by its emission. The errorbars show where the source would fall on the plot if the density traced by the $C^{18}O$ were a factor of ten lower (3×10^3 cm^{-3}).

As previous virial analyses in nearby low-mass star-forming regions have shown (Pattle et al., 2015, 2017; Kirk et al., 2017; Keown et al., 2017; Chen et al., 2019a; Kerr et al., 2019), most of the leaves are sub-virial and pressure-dominated. In particular, Kerr et al. (2019) showed that 79 of 134 ($\sim$ 59%) of the cores in their combined sample from the NGC1333, L1688, and B18 clouds were sub-virial when considering both cloud weight pressure and turbulent pressure. Similarly, we find that $\sim$ 69% of the leaves presented in this paper are deemed sub-virial when considering only the cloud weight pressure in the pressure energy density. This implies that the larger H_2 column densities and total cloud masses observed for GMCs are sufficient to create virially bound structures without the necessity of large levels of turbulent pressure

that appear to be required in low-mass star-forming environments (see Section 3.4.5 below for a discussion of turbulent pressure).

Although many of the structures are pressure-dominated, the large surrounding reservoirs of dense gas in GMCs may facilitate their evolution into the gravitationally-dominated regime. For instance, some recent simulations have shown that even though dense cores may appear as pressure-confined and stable structures at various stages in their evolution, they are still likely to be gaining mass by accreting material from their surroundings and will eventually undergo gravitational collapse (e.g., "global hierarchical collapse," Naranjo-Romero et al., 2015; Vázquez-Semadeni et al., 2017; Ballesteros-Paredes et al., 2018; Vázquez-Semadeni et al., 2019). As such, the observed pressure-dominated state of our ammonia-identified leaves may be a common stage in their evolution from dense gas structures to protostars and clusters. Furthermore, the dearth of structures in the sub-virial and gravitationally-dominated regime may indicate that clumps spend the majority of their time being pressure-dominated, with a quick transition to being gravitationally-dominated and subsequently collapsing to form protostars.

3.4.5 Turbulent Pressure

In addition to cloud weight, pressure due to cloud-scale turbulence may have a significant impact on the virial stability of dense cores (e.g., Kerr et al., 2019; Pattle et al., 2015, 2017; Kirk et al., 2017; Keown et al., 2017; Chen et al., 2019a). Here, we calculate the turbulent pressure energy density (Ω_{Pt}) for a subset of our ammonia-identified leaves following the method described by Keown et al. (2017) (see also Pattle et al. (2017) and Kirk et al. (2017) for detailed discussions of turbulent pressure). Ω_{Pt} is calculated from Equation 3.4, with P_w being replaced with P_t given by:

$$P_T = \mu_H m_H \times \rho_{C^{18}O} \times \sigma^2_{C^{18}O} \ , \tag{3.8}$$

where $\sigma_{C^{18}O}$ is the velocity dispersion measured from $C^{18}O$ $(3-2)$, a moderate density tracer, and $\rho_{C^{18}O}$ is the volume density at which the $C^{18}O$ $(3-2)$ emission originates. Here, we assume the $C^{18}O$ $(3-2)$ emission is tracing a volume density of 3×10^4 cm^{-3}, which is the critical density ($n_{cr}(u-l) = A_{ul}/\gamma_{ul}$, where A_{ul} is the Einstein A coefficient and γ_{ul} is the collisional rate coefficient for collisions with H_2) of $C^{18}O$ $(3-2)$ at 20 K (calculated using collisional rate coefficients accessed from the Leiden Atomic and Molecular Database, Schöier et al., 2005).

Six of the eleven KEYSTONE regions were found to have partial JCMT observations of $C^{18}O$ $(3-2)$ (see Section 3.2.4 for a discussion of these data and our reduction techniques). A Gaussian model with three free parameters (peak brightness temperature, centroid velocity, and velocity dispersion) was fit to all pixels in the $C^{18}O$ $(3-2)$ data cubes with SNR > 6 using the non-linear least squares curve-fitting method in the `scipy.optimize.curvefit` Python package. SNR is measured from the ratio of the peak brightness temperature in each spectra to the standard deviation of the off-line spectral channels. The conservative cutoff of SNR > 6 was chosen to remove low SNR spectra from consideration since they often have higher uncertainties in the fitted parameters. The initial parameter guesses of each fit are based on the brightness and velocity of the peak brightness channel, with a set guess of 1.5 km s^{-1} for the velocity dispersion. After the line fitting, pixels must meet the following criteria to be included in our final parameter maps:

1. $\sigma > 0.05$ km s^{-1} (below 0.05 km s^{-1} is unrealistic since our channel width is only ~ 0.11 km s^{-1};
2. $T_{peak,err} < 1$ K;
3. $\sigma_{err} < 0.5$ km s^{-1};
4. $V_{LSR,err} < 0.75$ km s^{-1}.

The final parameter maps for the velocity dispersion, σ_{C18O}, are shown in Figures 3.49-3.50. The 52 leaves with at least one reliably fit $C^{18}O$ $(3-2)$ pixel are shown by red contours in Figures 3.49-3.50. The median value of σ_{C18O} is calculated within the boundaries of each leaf and converted into a turbulent pressure using Equations 3.4 and 3.8. Although most of the $C^{18}O$ $(3-2)$ spectra are well-characterized by a single Gaussian, some do show wings that may be due to outflows or multiple velocity components along the line of sight. These areas can be seen in the velocity dispersion maps as sharp increases in σ_{C18O}. Since most of the leaves do not overlap with these sharp transitions, our single Gaussian fit is likely sufficient for our velocity dispersion estimates.

The right panel of Figure 3.48 shows the virial plane for structures with $C^{18}O$ $(3-2)$ measurements when using Ω_{Pt} as the pressure term in the virial equation. All of these structures fall within the pressure-dominated, sub-virial quadrant. The ratio of Ω_{Pt}/Ω_{Pw} for these structures ranges from ~ 1 to ~ 200, with a median of ~ 7.

This would suggest that cloud-scale turbulence or global collapse, rather than cloud weight, is the dominant contributor to the pressure term in the virial equation for these ammonia-identified leaves.

Since the turbulent pressure calculation is sensitive to the assumed value of $\rho_{C^{18}O}$, we also calculate P_T using a factor of ten lower value (3×10^3 cm^{-3}) for $\rho_{C^{18}O}$ and show the difference as errorbars in Figure 3.48. This lower density is more characteristic of the effective excitation density of C^{18}O $(3-2)$, which is often $1-2$ orders of magnitude lower than critical densities (Shirley, 2015). Under this assumption, the ratio of Ω_{Pt}/Ω_{Pw} correspondingly drops by a factor of ten, with a range from ~ 0.1 to ~ 20 and a median of ~ 0.7. In contrast to the scenario using the higher $\rho_{C^{18}O}$ assumption, this new estimation would suggest that cloud weight is dominant over turbulent pressure.

Several recent virial analyses of nearby star-forming regions such as Ophiuchus, B18, and NGC1333 have shown that turbulent pressure tends to be larger than cloud weight pressure (e.g., Kerr et al., 2019; Pattle et al., 2015). Conversely, cloud weight pressure appears to be larger than turbulent pressure in Orion A (Kirk et al., 2017). We note, however, that these analyses included turbulent pressure measurements across entire clouds. This approach is in contrast to the analysis we present here, which has turbulent pressure measurements for only a small subset of leaves that are generally concentrated on the most active star formation sites in each cloud observed (e.g., DR21 in Cygnus X, W3(OH) and W3 Main in W3, and M17SW in M17) and tend to qualify as hubs or ridges. As such, this biased sample cannot be used to draw generalizations for the full ammonia-identified leaf catalog presented in this paper. Instead, widespread C^{18}O mapping across the KEYSTONE clouds is required to investigate further the role of turbulent pressure on cloud structure and core dynamics.

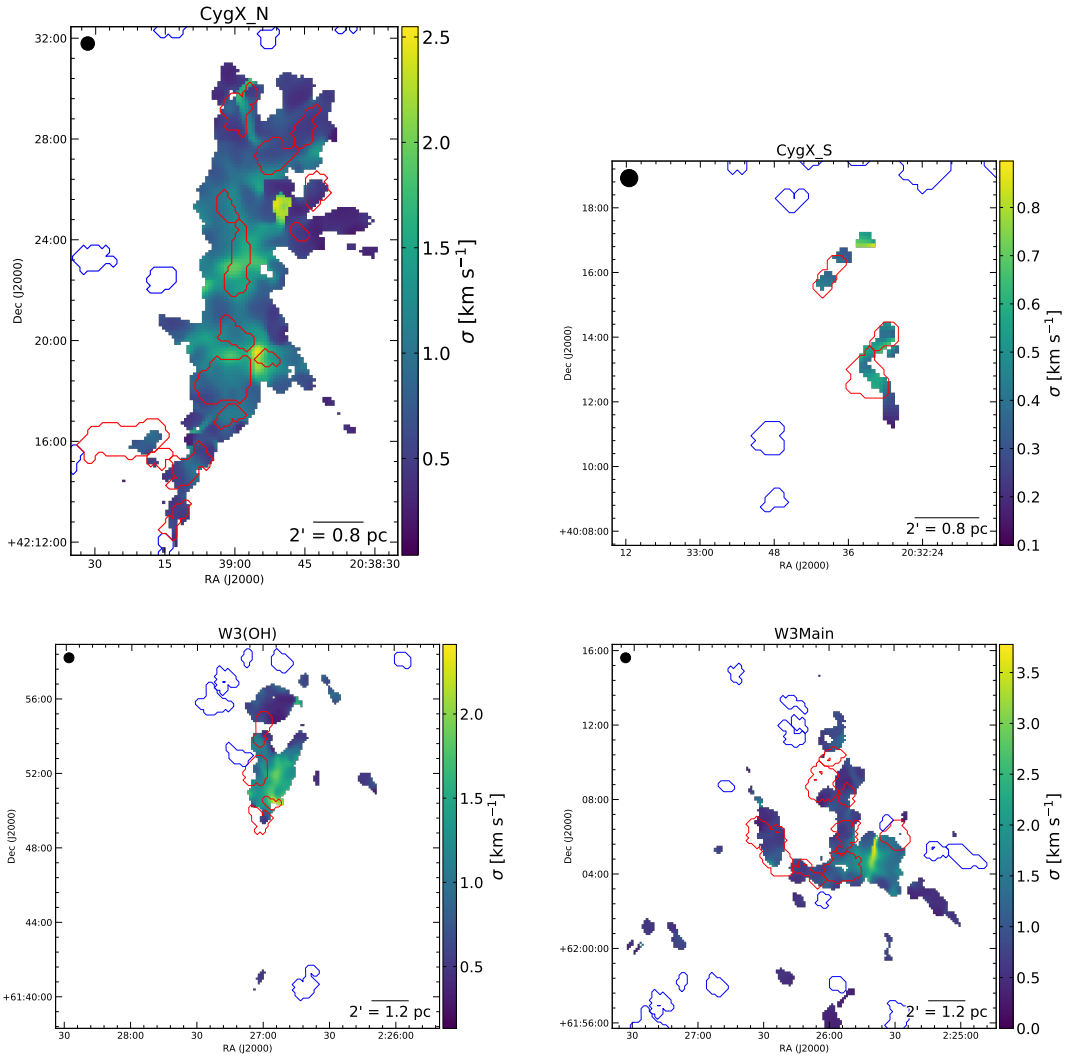

Fig. 3.49 – $C^{18}O$ $(3-2)$ velocity dispersion measured from Gaussian fits to JCMT observations of DR21 in Cygnus X North (top left), G79.34 in Cygnus X South (top right), W3(OH) (bottom left), and W3-Main (bottom right). Red contours denote ammonia-identified leaves that have at least one reliably fit $C^{18}O$ $(3-2)$ pixel and were included in our turbulent pressure virial analysis. Blue contours show all other ammonia-identified leaves in the field of view.

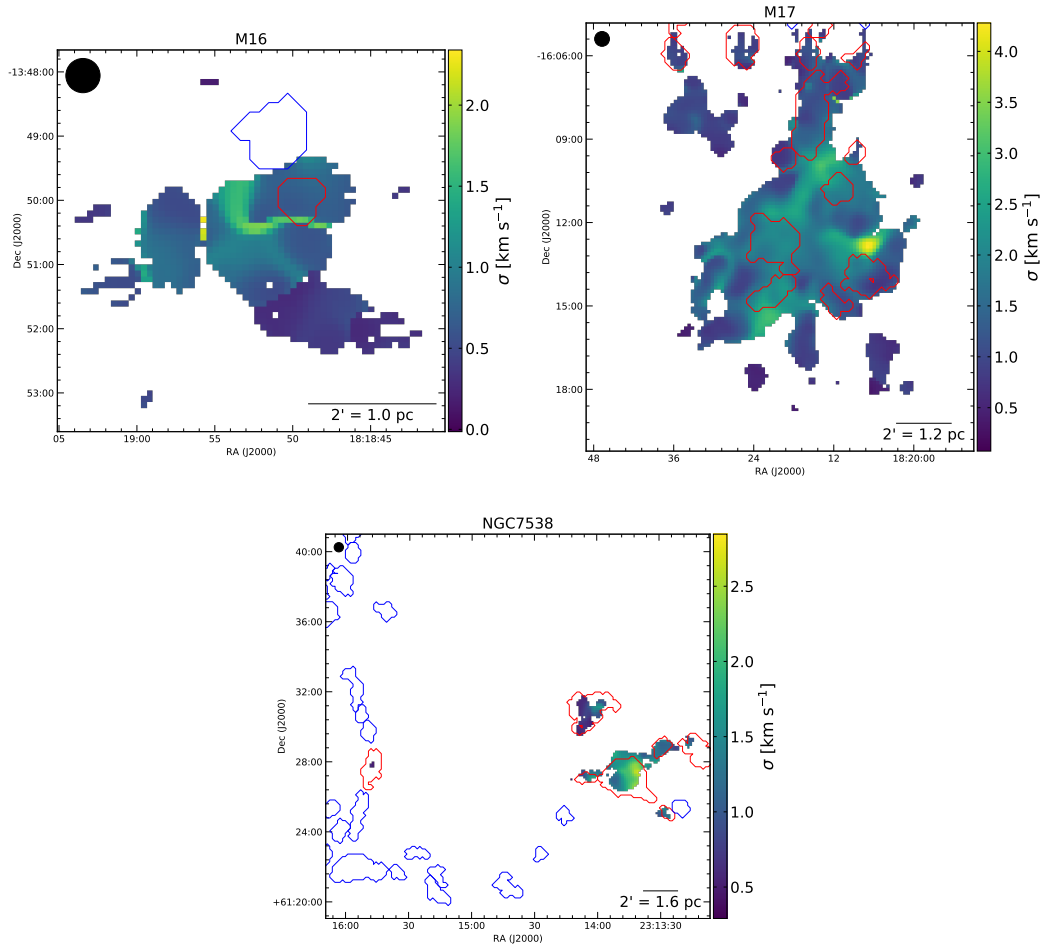

Fig. 3.50 – Same as Figure 3.49 for M16 (top left), M17 (top right), and NGC7538 (bottom).

In addition to external pressure, the magnetic field may also play an important role in the virial stability of the ammonia-identified leaves. For instance, both observations (e.g., Tan et al., 2013; Pillai et al., 2015) and simulations (e.g. Peters et al., 2011) suggest that magnetic fields are equally as important as turbulence and gravity for high-mass star formation. Although we currently lack large-scale magnetic field measurements for the KEYSTONE clouds, Auddy et al. (2019) have recently developed a "core field structure" model that predicts the magnetic field strength and fluctuation profile using dense gas kinematics. We reserve a detailed analysis of the clump magnetic fields, however, to a future KEYSTONE paper.

3.5 Summary

We have presented initial observations and results from KFPA Examinations of Young STellar Object Natal Environments (KEYSTONE), a survey of filamentary dense gas structure in eleven GMCs (Cygnus X North, Cygnus X South, M16, M17, MonR1, MonR2, NGC2264, NGC7538, Rosette, W3, and W48) at distances of $0.9 - 3.0$ kpc. We identified 856 dense gas clumps, traced by NH_3 (1,1) emission, across all the observed clouds using a dendrogram analysis. Simultaneous line fitting of the NH_3 (1,1) and (2,2) emission provided estimates of kinetic gas temperature, centroid velocity, velocity dispersion, and para-NH_3 column density for the dense gas. These parameter maps and the NH_3 (1,1) and (2,2) data cubes are publicly available.[9]

The ammonia parameter maps were used to derive virial stability parameters for each dense gas structure identified, providing insight into whether or not the gravitational potential energy of the structures is enough to overcome their internal kinetic energies in the absence of magnetic fields or external pressure. HOBYS *Herschel Space Observatory* observations of dust continuum emission were utilized to create H_2 column density maps, identify young protostellar candidates, and identify filamentary structures in each region. James Clerk Maxwell Telescope observations of $C^{18}O$ $(3 - 2)$ emission were accessed to determine the turbulent pressure applied by the ambient molecular cloud upon a subset of the dendrogram-identified dense gas structures. Our main results are listed below:

1. Significant variations in kinetic gas temperature are observed between clouds, with median $T_K = 11.4 \pm 2.2$ K in the coldest region (MonR1) and $T_K = 23.0 \pm 6.5$ K in the warmest (M17). The velocity dispersion distributions are more similar between clouds, with characteristic median values of $0.3 - 0.7$ km s^{-1}.

2. Of the 835 ammonia-identified clumps with mass estimates, 523 ($\sim$ 63 %) have virial parameters less than two, suggesting the mass of those structures is gravitationally bound and more susceptible to gravitational collapse when neglecting the effects of magnetic fields or external pressure. Similar analyses in nearby, low-mass star-forming clouds have found much higher rates of gravitationally bound ammonia-identified cores, which may suggest ammonia is more

[9] https://doi.org/10.11570/19.0074

widespread in GMCs than in nearby clouds or that gravity is more important to structure stability at small scales.

3. The fraction of ammonia-identified clumps that are spatially coincident with filaments identified in the H_2 column density maps ranges from 0.35 in Cygnus X South to 1.0 in W3-west. These values are consistent with core on-filament fractions found from dust continuum observations of nearby star-forming regions, which tend to be from $\sim 0.4 - 0.8$ depending on the cloud and core class considered.

4. On- and off-filament clumps show no substantial differences in their virial parameter, mass, radius, temperature, and velocity dispersion distributions. We do find, however, a tendency for clouds with low dense gas mass to have a higher fraction of on-filament clumps. These findings may indicate that filaments play a lesser role in the star formation process of high-mass GMCs. In those environments, dense gas may be more widespread allowing for clump formation to be equally as likely on and off filaments. In lower mass environments where dense gas is less widespread, however, clump formation may be limited to the filaments that harbor the main supply of dense gas.

5. In several regions there are "hubs" or "ridges" of dense gas that have much higher masses and lower virial parameters than the other clumps in their respective cloud. These hubs and ridges tend to be located at the intersections of multiple filaments or located near/within a single filament, are often associated with H_2O maser emission, and typically host multiple protostars. Based on these characteristics, hubs may be the sites of future cluster formation.

6. When considering the external pressure exerted on the clumps, most are considered sub-virial and pressure-dominated structures. This characteristic state may indicate that high-mass clumps spend the majority of their lifetime confined by external pressure. Over time, as the clumps accrete mass from their surroundings, they may gain enough mass to be gravitationally dominated and undergo gravitational collapse or fragmentation.

3.6 Future Work

Although it was not the focus of this paper, a key use-case of the KEYSTONE data is the analysis of filament kinematics in GMCs. For instance, in regards to the observed spatial relationship between massive young stellar objects and stellar clusters with filament intersections, the KEYSTONE data could be used to determine: 1) whether or not the observed clumps and filaments are truly velocity coherent structures (Pineda et al., 2010; Chen et al., 2019a), and 2) if the mass flow rates along them are large enough to produce MYSOs. Several independent studies have already measured gas motions in individual filaments such as Serpens South (Kirk et al., 2013a; Friesen et al., 2013), G035.39-00.33 (Henshaw et al., 2013), DR21 (Schneider et al., 2010a), W43-MM1 (Nguyen-Lu'o'ng et al., 2013), M17SW (Chen et al., 2019b), and eight other high-mass filaments (Lu et al., 2018), noting that the observed mass flow rates could supply the mass required to assemble the stellar clusters at their centres. Similarly, observations of the Large Magellanic Cloud by Fukui et al. (2015) showed two separate instances of MYSOs forming at the centers of adjoining filaments that have gas flowing into the central junction. Svoboda et al. (2016) and Motte et al. (2018a) also contend that such mass flow onto sites of cluster formation is prominent throughout Galactic high-mass star-forming regions, providing the mass build-up and compression necessary to form stellar clusters. These studies, however, have focused primarily on regions that have already formed clusters/MYSOs and do not address the conditions of the parental clumps, i.e., the dense gas out of which stellar clusters form, prior to the onset of star formation. As such, the gas velocity patterns of those regions are susceptible to distortions due to stellar feedback, which raises questions about the applicability of their kinematic measurements. Furthermore, observations after the onset of star formation cannot be used to decipher whether clumps form before or after filaments collide to form intersections. Using the clump catalog presented in this paper, in conjunction with an analysis of the adjacent filament kinematics, it is now possible to investigate these questions across multiple high-mass star-forming environments.

In addition to dense gas kinematics, the KEYSTONE data can provide insight into temperature and chemistry variations as a function of environment within GMCs. For example, the KEYSTONE observations of the NH_3 (1,1), (2,2), (3,3), (4,4), and (5,5) transitions probe a range of gas temperatures up to ~ 200 K. Since dust temperatures derived from *Herschel* data become increasingly uncertain above 20 K as the spectral

energy distribution peak moves toward wavelengths shorter than 160 μm (Chen et al., 2016), ammonia-derived gas temperatures will be important for understanding how the OB associations are impacting the star formation in the KEYSTONE target clouds. Furthermore, the KEYSTONE observations will constrain the abundances of NH_3 in GMCs. These abundances, in combination with the gas temperatures, will provide a way to understand how temperature impacts the formation/destruction of ammonia in GMCs.

Acknowledgments

JK, JDF, ER, and MCC acknowledge the financial support of a Discovery Grant from NSERC of Canada. SB and NS acknowledge support by the French ANR and the German DFG through the project "GENESIS" (ANR-16-CE92-0035-01/DFG1591/2-1). The Green Bank Observatory is a facility of the National Science Foundation operated under cooperative agreement by Associated Universities, Inc. *Herschel* is an ESA space observatory with science instruments provided by European-led Principal Investigator consortia and with important participation from NASA. The James Clerk Maxwell Telescope is operated by the East Asian Observatory on behalf of The National Astronomical Observatory of Japan; Academia Sinica Institute of Astronomy and Astrophysics; the Korea Astronomy and Space Science Institute; Center for Astronomical Mega-Science (as well as the National Key R&D Program of China with No. 2017YFA0402700). Additional funding support is provided by the Science and Technology Facilities Council of the United Kingdom and participating universities in the United Kingdom and Canada. This research made use of astrodendro, a Python package to compute dendrograms of Astronomical data (http://www.dendrograms.org/), Astropy (http://www.astropy.org), a community-developed core Python package for Astronomy (Astropy Collaboration et al., 2013), and pyspeckit (https://pyspeckit.readthedocs.io/en/latest/), a Python spectroscopic analysis and reduction toolkit (Ginsburg & Mirocha, 2011).

Facility: GBT, Herschel, JCMT

3.7 Appendix

3.7.1 Distance Dependence of Virial Parameters

The virial analysis presented in this paper used the native KEYSTONE resolution for all clouds analyzed, despite the cloud distances ranging from 0.9 kpc to 3 kpc. Such distance variations provide a factor of ~ 3 range of linear spatial resolutions, which may lead to different types of structures (in terms of size and mass) being identified in each cloud. To test whether or not the distance dependence has any influence on the main results of this paper, we convolved the NH_3 (1,1) and (2,2) cubes for NGC 2264, MonR1, and MonR2 ($d = 0.9$ kpc, $\theta \sim 0.13$ pc), the closest clouds in KEYSTONE, to the linear resolution of W48 ($d = 3.0$ kpc, $\theta \sim 0.45$ pc), the most distant cloud observed. This process degrades the resolution of the observations by a factor of $3.0/0.9 \sim 3.3$ to a final resolution of $\sim 103''$. Following a similar distance bias analysis by Baldeschi et al. (2017) on *Herschel* maps, we also downsampled the cubes by the same factor along each spatial axis. Finally, Gaussian noise with a mean of zero and standard deviation of $s_N\sqrt{1 - d_0/d_1}$ is added to the cubes, where s_N is the median of the original cube's RMS map, d_0 is 0.9 pc and d_1 is 3.0 kpc. This noise addition attempts to return the native RMS level to the convolved and resampled cubes, which have lower noise levels due to the spatial averaging.

These processes allow us to simulate what might be observed if NGC 2264, MonR1, and MonR2 were at a distance of 3 kpc. The convolved, downsampled, noise-injected cubes were then run through the line-fitting pipeline to produce a new set of ammonia parameter maps and integrated intensity maps. Finally, we repeat the virial analysis presented in Section 3.3.5 using the new set of maps and assuming their distance is 3.0 kpc.

In Figures 3.51-3.53, we compare the results of the original virial analyses in NGC 2264, MonR1, and MonR2 to their distance-adjusted virial analysis. Leaves from the original analysis that fall within a leaf identified in the distance-adjusted analysis are tagged with a specific color in each plot of Figures 3.51-3.53. As expected, much fewer structures are identified by the dendrogram in the distance-adjusted analysis. Many of the small structures in the original analysis are lumped together into a single large structure in the distance-adjusted analysis due to the lower resolution. In terms of virial parameters, the structures in the distance-adjusted analysis are all gravitationally bound. This distance bias is likely why more bound structures are observed in W48 than these closer clouds. At 900 pc, NGC2264, MonR1, and MonR2

represent the extreme examples of the distance bias in our sample. The impact will undoubtedly be less for the moderate distance clouds in our sample (e.g., Cygnus X, W3, NGC7538, etc.), for which the distance difference is lower. This statement is echoed by the fact that many of the cloud attributes analyzed in this paper (e.g., dense gas mass, leaf on-filament fraction, number of leaves, etc.) do not depend strongly on cloud distance (see Section 3.3.7 and Figure 3.44). Nevertheless, we are indeed tracing different scales in the star formation hierarchy by including a range of cloud distances in our analysis. Future high-resolution observations of the more distant KEYSTONE targets with the Karl G. Jansky Very Large Array (VLA) or Next Generation VLA (ngVLA) could provide the means to compare cloud structures between clouds on more similar spatial scales.

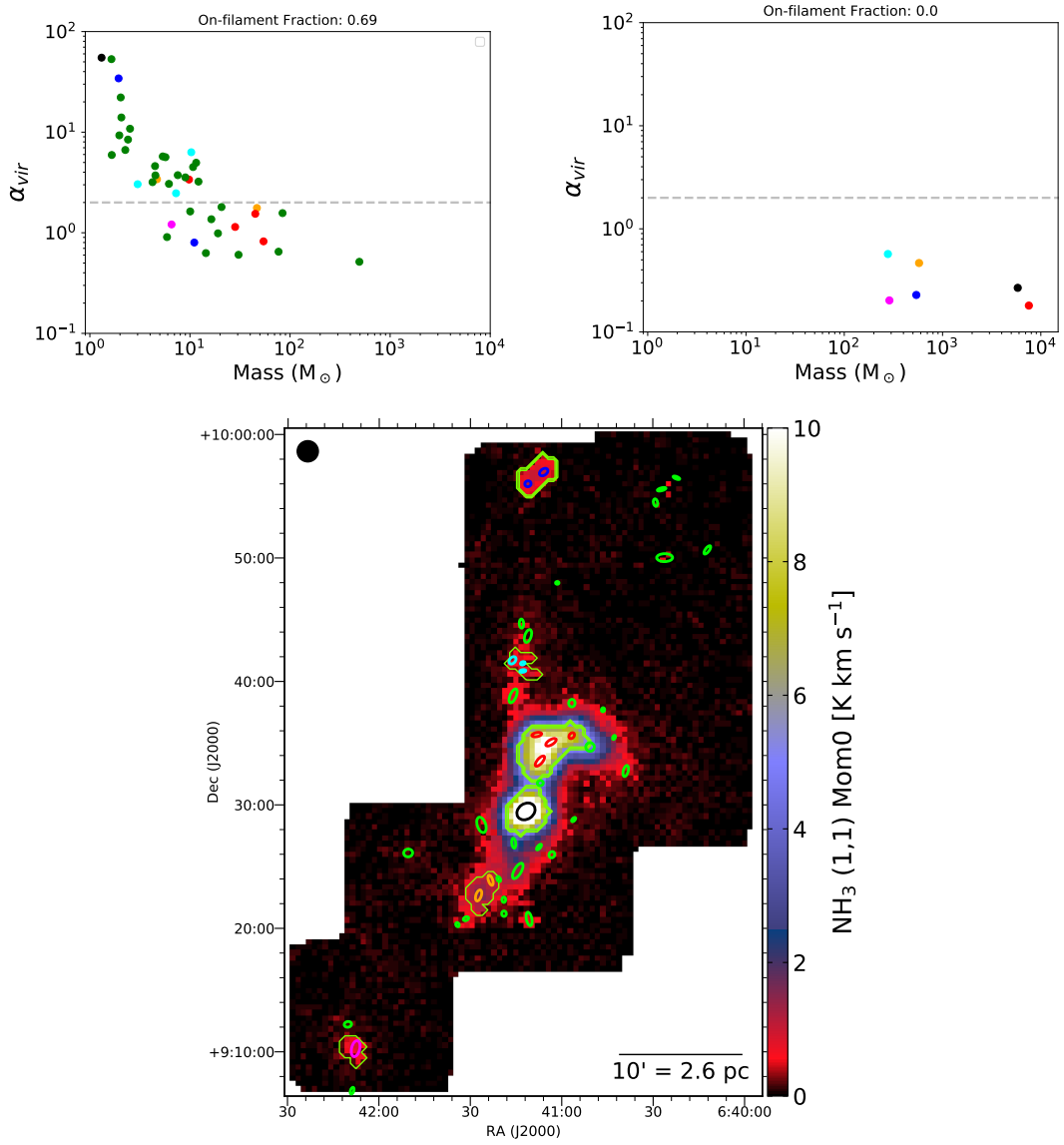

Fig. 3.51 – Top row: Leaf virial parameters in NGC2264 using native KEYSTONE resolution (left) and after convolving the NH_3 (1,1) and (2,2) cubes to the linear resolution of W48 ($\theta \sim 0.45$ pc), downsampling the number of pixels, adding white noise, and re-running the full analysis (right). Bottom: Integrated intensity map obtained using the convolved NH_3 (1,1) cube. Ellipses represent the peaks of leaves identified when using the native resolution data. The green dendrogram masks show the extent of the leaves identified using the convolved data. Ellipses falling within a dendrogram mask were tagged as a colored pair in the top row plots.

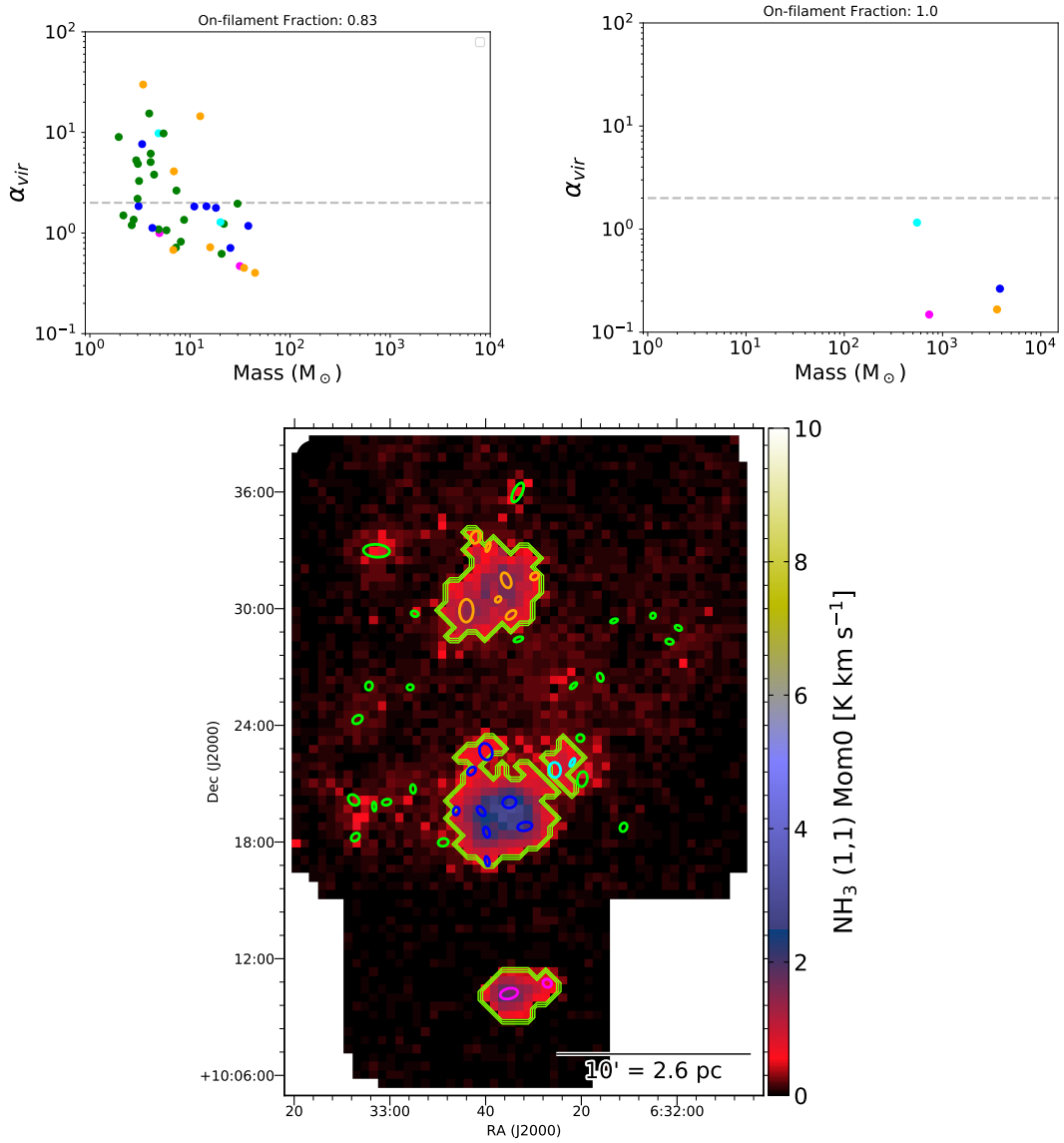

Fig. 3.52 – Same as Figure 3.51 for MonR1.

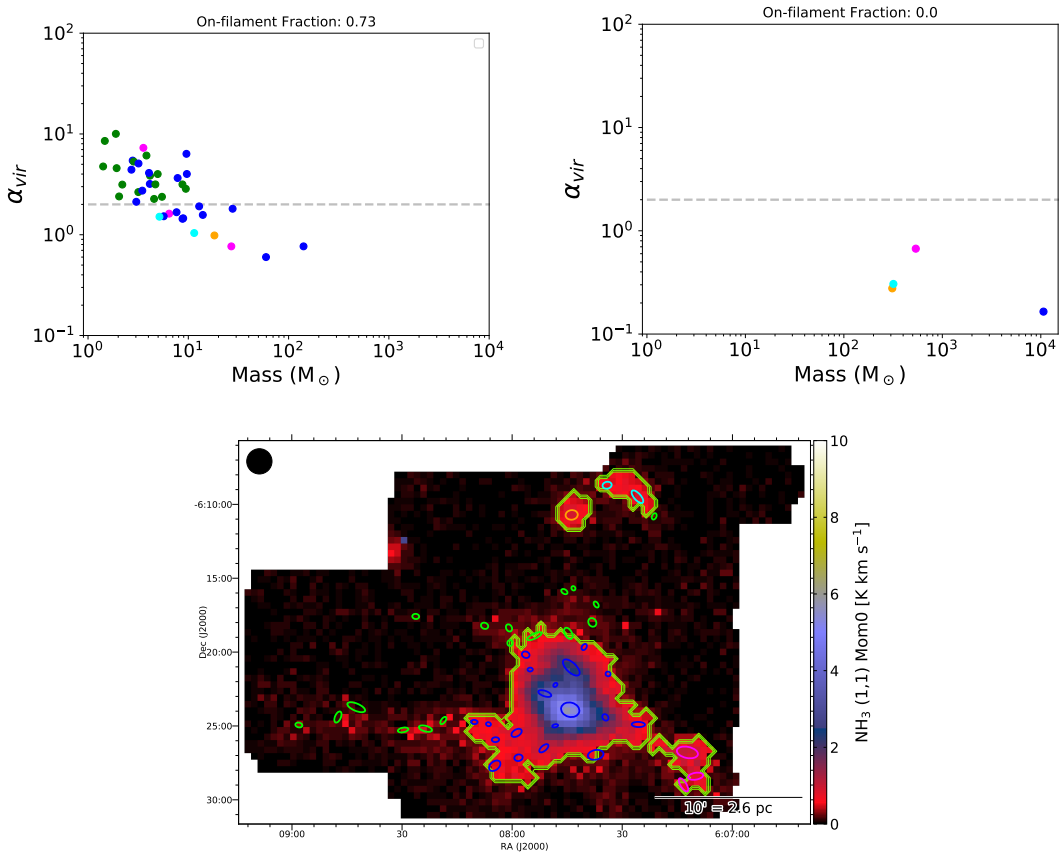

Fig. 3.53 – Same as Figure 3.51 for MonR2.

Chapter 4

CLOVER: Convnet Line-fitting Of Velocities in Emission-line Regions

Accepted for publication in The Astrophysical Journal

Authors: Jared Keown, James Di Francesco, Hossen Teimoorinia, Erik Rosolowsky, and Michael Chun-Yuan Chen

ABSTRACT

When multiple star-forming gas structures overlap along the line of sight and emit optically thin emission at significantly different radial velocities, the emission can become non-Gaussian and often exhibits two distinct peaks. Traditional line-fitting techniques can fail to account adequately for these double-peaked profiles, providing inaccurate measurements of cloud kinematics. We present a new method, called Convnet Line-fitting Of Velocities in Emission-line Regions (CLOVER), for distinguishing between one-component, two-component, and noise-only emission lines using 1D convolutional neural networks trained with synthetic spectral cubes. CLOVER utilizes spatial information in spectral cubes by predicting on 3×3 pixel sub-cubes, using both the central pixel's spectrum and the average spectrum over the 3×3 grid as input. On an unseen set of 10,000 synthetic spectral cubes in each predicted class, CLOVER has classification accuracies of $\sim 99\%$ for the one-component class and $\sim 97\%$ for the two-component class. For the noise-only class, which is analogous to a signal-to-noise cutoff of four for traditional line-fitting methods, CLOVER has classification accuracy of 100%. CLOVER also has exceptional performance on real observations, correctly distinguishing between the three classes across a variety of star-forming regions. In addition, CLOVER quickly and accurately extracts kinematics directly from spectra

identified as two-component class members. Moreover, we show that CLOVER is easily scalable to emission lines with hyperfine splitting, making it an attractive tool in the new era of large-scale NH_3 and N_2H^+ mapping surveys.

4.1 Introduction

Kinematics observations of star-forming molecular clouds reveal the turbulent motions of the clouds' gas and provide an understanding of how gas is funneled onto sites of star formation (e.g., Pineda et al., 2010; Kirk et al., 2013a; Friesen et al., 2013). Such kinematics measurements are obtained by modeling the emission lines from molecular transitions in the gas. Typically, emission lines without self-absorption (i.e., optically thin lines) are modeled as Gaussian distributions with a single centroid velocity and velocity dispersion. A major limitation of this "single-Gaussian" line fitting approach is its inability to account for spectra that display multiple velocity components along the line of sight. For instance, if two slabs of emitting gas with slightly offset centroid velocities lie along our line of sight to a particular cloud, a broadened second peak or "shoulder" is produced in the observed spectrum. Figure 4.1 shows a schematic of this situation. Traditional single-Gaussian line fitting methods, which assume the observed emission contains a single velocity component, would fit this broadened spectrum with a line width that is much larger than those of the individual line components that produced the observed spectrum. In addition, the centroid measurement would be skewed to a value in-between those of the individual line components. These inaccuracies have significant impacts on many analyses of star-forming regions. For example, virial stability analyses (e.g., Kauffmann et al., 2013; Pattle et al., 2015, 2017; Seo et al., 2015; Kirk et al., 2017) and velocity gradient calculations (e.g., Schneider et al., 2010b; Henshaw et al., 2013; Kirk et al., 2013a; Peretto et al., 2014) are highly dependent on velocity dispersion and centroid, respectively.

High spatial and spectral resolutions can provide observers with a lower chance of viewing multiple velocity component spectra, as there can be less chance of "smearing" together slabs of gas that are close to one another in the spatial and spectral dimensions. When observing clouds at farther distances, however, there can be a higher chance of observing multiple velocity component spectra due to the worsened spatial resolving power. Thus, modern spectroscopic surveys of molecular clouds at large distances must incorporate a line-fitting strategy that considers multiple velocity

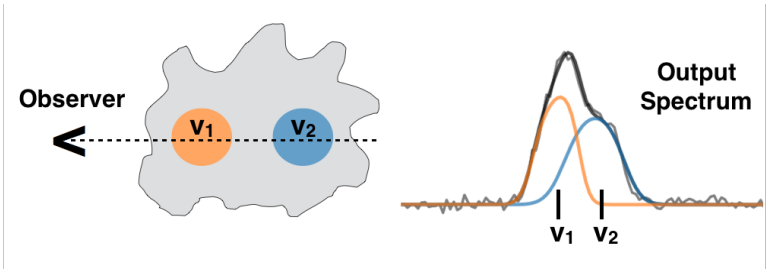

Fig. 4.1 – Schematic diagram of a molecular cloud observation that would result in a spectrum with two velocity components. The observer views two cores along the line of sight (dashed line) at slightly offset centroid velocities (v_1 and v_2). The combination of the two Gaussian emission line profiles for each core (orange and blue spectra) results in a broadened observed spectrum (black spectrum) with a "shoulder" at one side.

components along the line-of-sight to obtain the most accurate kinematics measurements from their data.

Although several multi-component line fitting methods have been developed for molecular emission line observations, they either require user input and direction during the line fitting procedure (e.g., SCOUSE: Semi-automated multi-COmponent Universal Spectral-line fitting Engine, Henshaw et al., 2016), or they require several iterations of fitting both single and multiple-component models to test which model produces the "best" fit (Lindner et al., 2015; Sokolov et al., 2017; Clarke et al., 2018; Riener et al., 2019; Chen et al., in prep). These semi-automated and brute-force methods are plagued by several issues: 1) They are highly dependent on the model's initial parameter guesses and degrees of freedom used for their χ^2-minimization fits. For example, for χ^2-minimization to converge onto the optimal solution, it must be fed initial conditions for the model parameters (e.g., velocity dispersion and centroid) that are near the "true" values of the emission. This requirement often leads to large amounts of pre-processing the data to obtain estimates for the centroid and dispersion of each velocity component that can be used as initial guesses for the line fitting procedure. Alternatively, one can blindly repeat the line fitting procedure using a large grid of initial parameter guesses to search for the optimal fit. 2) Due to this pre-processing or grid search requirement, traditional methods tend to be computationally expensive, often requiring hours to fit typical spectral cubes. 3) Furthermore, traditional methods tend to neglect spectra in neighboring pixels that could confirm the presence or absence of multiple velocity components.

This paper provides a solution for efficiently identifying multiple velocity compo-

nent spectra using artificial neural networks (ANNs). ANNs are a type of machine learning model that attempts to map input features to output classes or values using hierarchical feature representations that are learned during the training process. These hierarchical features are learned by stacked layers of artificial neurons that use a weighted function to map the inputs they receive into outputs that are fed into subsequent layers. The complexity of features learned by each layer increases with depth into the network. For example, a neural network trained for facial recognition might first detect facial edges and contours, which can then be used to detect facial features such as noses, ears, and eyes, until the final layer is able to build facial templates that can be used to predict which face is being viewed in a given image.

In terms of astronomy, ANNs are becoming increasingly prevalent due to the advantages they can provide by learning non-linear patterns that traditional methods struggle to reproduce and making quick predictions once trained. For example, ANNs have been successfully applied to a variety of problems across many different fields of research, such as: detecting planets in the Kepler archive that were missed by the standard Kepler identification pipeline (Shallue & Vanderburg, 2018), discriminating galaxies with an active galactic nucleus from star-forming galaxies in Sloan Digital Sky Survey (SDSS) observations (Teimoorinia & Keown, 2018), deriving stellar temperature, metallicity, and gravity from SDSS APOGEE stellar spectra (Fabbro et al., 2018), detecting 72 previously missed fast radio burst (FRB) pulses from the first-discovered repeating FRB (Zhang et al., 2018), and identifying wind-driven shells in magneto-hydrodynamic molecular cloud simulations (Van Oort et al., 2019). ANNs have also been used for multiple-component emission line identification of optical spectra. For instance, Hampton et al. (2017) have trained an ANN to classify optical spectra of galaxies using parameters output by a traditional Gaussian line-fitting approach called LZIFU (Ho et al., 2016).

Many of the ANNs used for astronomy applications rely on a particular type of ANN called a convolutional neural network (CNN or convnet), which preserves the spatial structure of its input features using convolutional kernels that are learned during training. The convolution involves taking the dot product between the network's input (which can be an image, spectrum, light curve, etc.) and a sliding kernel that is moved across the input in predefined steps. The output is a convolved feature map that is used in subsequent layers of the network to make a prediction on the input's class (in the case of classification). The convolved feature map not only preserves the spatial structure in the input image, but also reduces the number of input features

into the next layer of the network, which leads to faster training times.

This paper will utilize the advantages of training a 1D CNN to classify input spectra as either single or multiple velocity components and predict the kinematics of each velocity component. The method requires no initial parameter guesses, incorporates spectra from nearby pixels to make predictions, and analyzes typical spectral cubes in seconds. Such improvements are welcome with the advent of large multi-receiver arrays where thousands of spectra can be collected in a reasonable time. Named Convnet Line-fitting of Velocities in Emission-line Regions (CLOVER), the method is also publicly available as a Python package called `astroclover`[1].

The paper is organized as follows: Section 4.2 describes the data used for training CLOVER and testing its performance; Section 4.3 outlines the CNN architecture of CLOVER; Section 4.4 compares CLOVER's classification performance to that of a traditional single-Gaussian line fitting method on both synthetic and real data; Section 4.5 discusses predicting kinematics from two-component spectra with CLOVER; Section 4.6 describes further applications of CLOVER classifications to emission lines with hyperfine splitting; Section 4.7 presents CLOVER kinematics predictions for NH_3 (1,1) synthetic data; Section 4.8 shows how CLOVER can be used to improve the accuracy of virial stability analyses of structures with multiple velocity components; and Section 4.9 summarizes the paper. In addition, Appendix 4.10 provides an overview of the installation and usage instructions for the `astroclover` Python package.

4.2 Data

4.2.1 Training Set: Generating Synthetic Spectra

All machine learning classification projects require a training set composed of input feature vectors (a.k.a., "samples" or "examples") that belong to one of the possible output classes the model will be trained to predict. In this paper, we train a network that has three distinct output classes: "one-component" spectra with only one velocity component along the line of sight, "two-component" spectra with two velocity components along the line of sight, and "noise-only" spectra with negligible emission.

To generate the training set, synthetic spectral cubes on a 3×3 pixel grid with 500 spectral channels were created. For the "one-component" class, a single Gaussian spectrum was injected into the grid's central pixel with peak intensity (T_{peak}) set to 1

[1] https://github.com/jakeown/astroclover/

K and values of velocity dispersion (σ) and centroid velocity (V_{LSR}) chosen at random from a uniform distribution with the following limits:

- σ: $2 - 11$ channels, which produces both narrow and broad Gaussians similar to real emission lines.
- V_{LSR}: channel 112 to channel 388 of the 500 channel spectrum. This range is equivalent to -0.55 km s^{-1} to 0.55 km s^{-1} when the spectral axis has been normalized to -1.0 km s^{-1} for the lowest velocity channel and 1.0 km s^{-1} for the highest velocity channel. This range provides a variety of centroid velocities while ensuring the emission line edges do not spill off the edges of the spectrum.

The Gaussians for the surrounding pixels in the 3×3 grid are determined by applying a perturbation to the central pixel's Gaussian parameters. This step was done by drawing values from three normal distributions (one for each parameter) with a mean of zero and variance of 0.05. The randomly drawn values were then added to the central pixel's parameter values to generate new Gaussians with slight offsets in σ, V_{LSR}, and T_{peak}. Finally, noise with an RMS drawn from a uniform distribution between 0.05 K and 0.25 K was injected into each spectral cube, creating training examples with low, moderate, and high signal-to-noise ratios (SNRs).

For the "two-component" class, two Gaussians were injected into the central pixel of the 3×3 grid. The values of σ for the two Gaussians were both drawn at random as described above for the one-component class. The value of T_{peak} for the second Gaussian was drawn randomly from a uniform distribution between 2×RMS and 1 K, where RMS is the noise level selected for the cube. Similarly, the V_{LSR} for the second Gaussian was randomly drawn from a uniform distribution between $V_{LSR,1} \pm 1.5 \times \sigma_{max}$ and $V_{LSR,1} \pm 5 \times \sigma_{max}$, where σ_{max} is the value of σ for the wider of the two Gaussians, $V_{LSR,1}$ is the centroid of the first component, and the sign of the offset ($\pm$) is chosen at random. Thus, the second component can be on either the left or right of the first component along the spectral axis.

This two-component sample generation approach created variations in the relative heights, velocity dispersions, and centroids of each velocity component. Moreover, the velocity centroid separation threshold for each velocity component minimized the number of two-component samples that are indistinguishable from one-component samples. This characteristic of the training set was necessary to prevent the CNN from overfitting (a tendency to predict the two-component class when it was clear

the one-component class was more appropriate). Such separation thresholds are also often implemented in traditional line-fitting methods (see, e.g., Lindner et al., 2015; Henshaw et al., 2016; Riener et al., 2019) when deciding whether or not a multiple-component fit is appropriate. The outer pixels in the 3×3 grid were filled by adding perturbations to both of the Gaussian components, as described above for the one-component class.

For each training example cube, only two spectra are used as input into the CNN: 1) the spectrum of the central pixel in the 3×3 grid and 2) the averaged spectrum over all nine spectra in the 3×3 grid. The first spectrum provides a "local" view of the pixel for which the class prediction is being made, while the second spectrum provides a "global" view of neighboring pixels that can provide insight into whether the central pixel is a one-component, two-component, or noise-only spectrum. Both spectra are normalized by dividing by the value of the brightest channel. This "local+global" setup also provides for a simple way to make predictions on real observations. In that case, a sliding window of size 3×3 pixels is moved across the position-position plane of a spectral cube and a class prediction is made on the central pixel after feeding its "local" and "global" spectra into the trained network.

Following the aforementioned method, 300,000 synthetic samples (100,000 for each training set class, i.e., a "balanced" training set) were generated. Figure 4.2 shows example local and global spectra for training set samples in the one-component, two-component, and noise-only classes. A validation set of 90,000 additional synthetic spectra (30,000 in each class) was also generated for monitoring performance during training (see Section 4.3). After training, the network's performance is tested on ten additional collections of 30,000 synthetic spectra (10,000 in each class).

4.2.2 Test Set: Real ^{13}CO, C^{18}O, & HC$_5$N Spectral Cubes

The test sets used to gauge the trained CNN's performance included three real spectral cubes observed from three different surveys of three distinct star-forming regions. The first cube was a ^{13}CO $(1-0)$ observation of L1689 in the Ophiuchus molecular cloud from the COMPLETE survey[2] (Ridge et al., 2006) on the Five College Radio Astronomy Observatory (FCRAO). This cube has a spectral resolution of ~ 0.07 km s^{-1}, the pixel size is $23''$, and the FCRAO has an angular resolution of $\sim 46''$ at the rest frequency of ^{13}CO $(1-0)$.

[2]available at https://www.cfa.harvard.edu/COMPLETE/

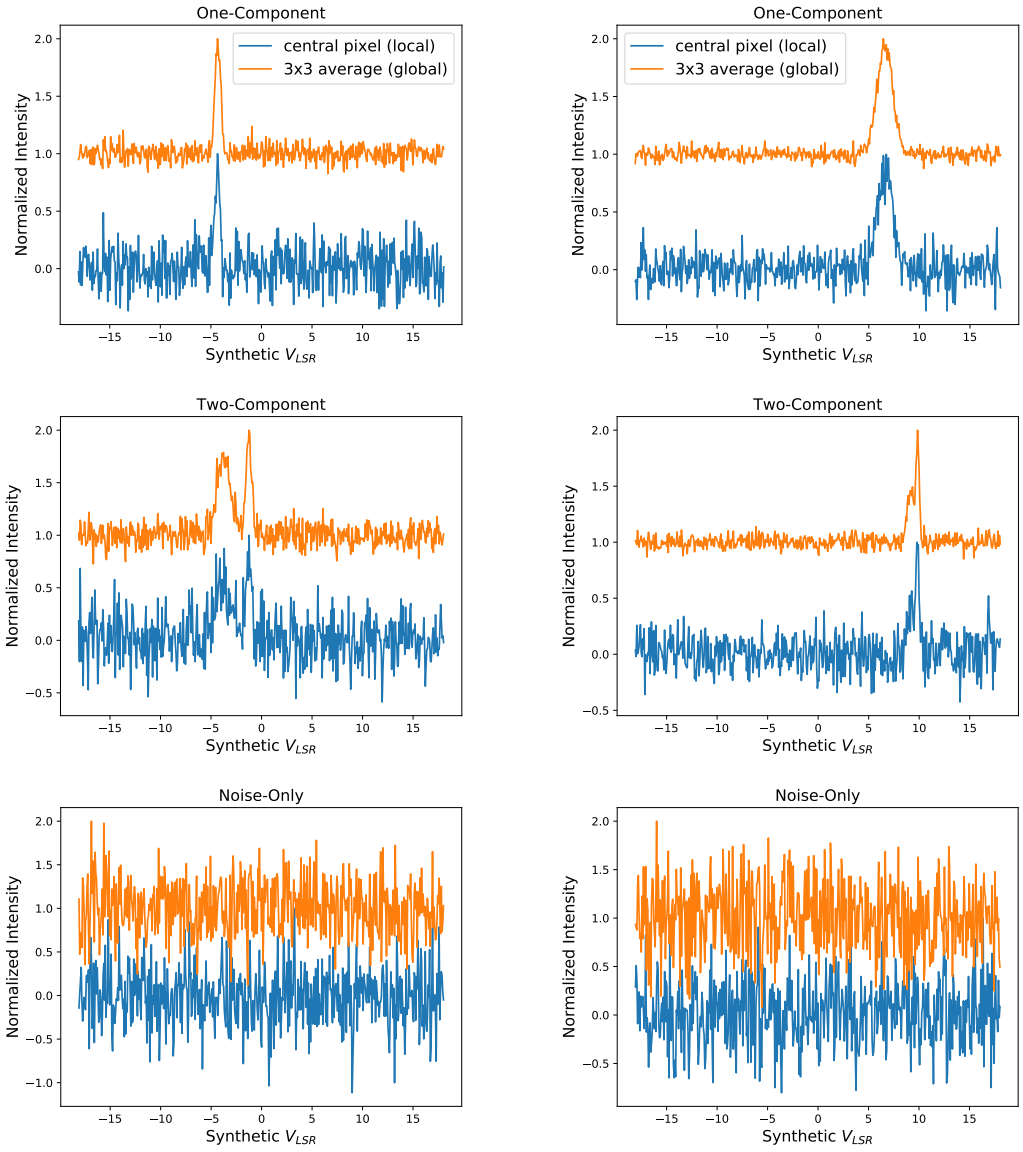

Fig. 4.2 – Example synthetic spectra included in the one-component (top row), two-component (middle row), and noise-only (bottom row) training set classes. Blue spectra show the central pixel in the spectral cube window (i.e., the "local" spectrum) and the orange spectra represent the 3×3 pixel average around the central pixel (i.e., the "global" spectrum).

The second cube was a $C^{18}O$ $(3-2)$ observation of DR21[3] in the Cygnus X giant molecular cloud complex observed by the James Clerk Maxwell Telescope (JCMT). The observations were accessed from the JCMT archive and have not been previously published, but were originally observed as part of a ^{12}CO $(3-2)$ survey by Gottschalk et al. (2012). The native spectral resolution of the cube was ~ 0.056 km s^{-1}, but to improve the spectral SNR, we smooth spectrally with a Gaussian kernel to half the original spectral resolution: 0.11 km s^{-1}. The native angular resolution of the JCMT at the rest wavelength of $C^{18}O$ $(3-2)$ is $\sim 15''$, which we convolve to $32''$ to improve SNRs further. The pixel scale of the cube is $7.2''$.

The third cube was a HC_5N $(9-8)$ observation of B18[4] in the Taurus molecular cloud observed by the Green Bank Ammonia Survey (Friesen et al., 2017) on the 100m Green Bank Telescope. This cube has a spectral resolution of ~ 0.07 km s^{-1}, a pixel scale of $\sim 11''$, and an angular resolution of $\sim 31''$.

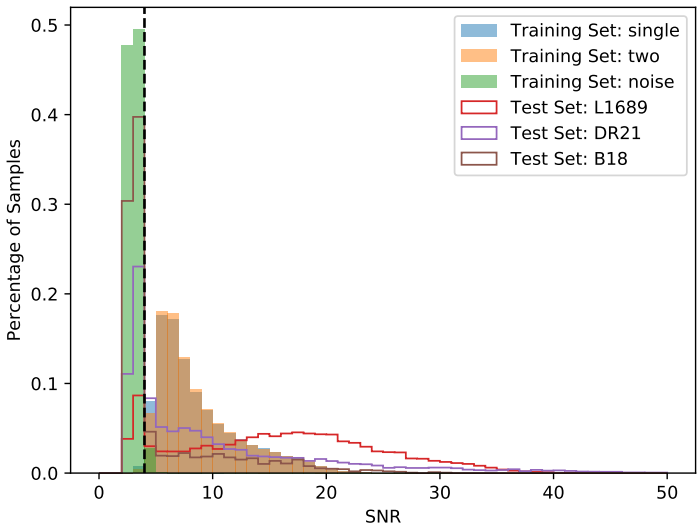

Fig. 4.3 – Histograms of signal-to-noise ratio for the "local" spectra in the training and test sets. Blue, orange, and green represent the one-component, two-component, and noise-only classes of the synthetic training set, respectively. Red, purple, and brown show the distributions for the real observations of L1689, DR21, and B18, respectively. The black dashed line shows SNR=4.

Table 4.1 outlines the characteristics of each spectral cube and star-forming region

[3]available at http://www.cadc-ccda.hia-iha.nrc-cnrc.gc.ca/en/ with proposal ID: M10BD01

[4]available at https://dataverse.harvard.edu/dataverse.xhtml?alias=GAS_Project

in the test set. These three regions were chosen due to their differing levels of star formation activity. B18 is a fairly quiescent, nearby ($d \sim 135$ pc), star-forming region, while L1689 is a more active nearby cloud ($d \sim 119$ pc) and DR21 is a distant ($d \sim 1700$ pc) high-mass star-forming region producing O- and B-type stars. Thus, these spectral cubes provide a thorough test of the CNN performance across a variety of star-forming environments, instruments, and emission line transitions.

To be consistent with the synthetic spectra used to train the CNN, the spectral axis on all cubes was clipped to 500 channels centered on the line-of-sight velocity to each cloud. The "local" and "global" view spectra were extracted from each cube by sliding a 3×3 pixel window across the position-position plane of the cube. The CNN then makes a prediction on the class of the central pixel in the window using the "local" and "global" view spectra as input.

Figure 4.3 shows the distributions of SNR, defined as the ratio of the peak emission line channel to the standard deviation of the off-line channels, for the "local" spectra in the test set cubes. Figure 4.3 also displays the SNR distributions for the one-component, two-component, and noise-only training set classes. The one- and two-component training set classes have similar SNR distributions, which ensures that the network must use morphological differences rather than SNR differences to distinguish those classes. In addition, the one- and two-component training set distributions have a similar range in SNR as the majority of the real data. This similarity suggests the training set is representative of real data, which is necessary for the trained network to generalize its predictions for handling real observations with a wide range of SNR. Although the high SNR end of the training set is less populated than the real data, this difference is acceptable since the high SNR examples are typically much easier to classify than low SNR examples. We also note that the one- and two-component classes in the training set have a significant drop-off below SNR=4, which is effectively the SNR threshold where the "noise" class begins. An SNR of 4 is similar to typical minimum thresholds set for traditional line-fitting methods, however, making it a reasonable signal versus noise threshold for the network's predictions.

In Section 4.6, we also use NH_3 (1,1) cubes observed by the KFPA Examinations of Young STellar Object Natal Environments (KEYSTONE) survey (PI: James Di Francesco; Keown et al., 2019b) using the 100m Green Bank Telescope. Our analysis is focused on the KEYSTONE observations of MonR2 and M17 at distances of 900 pc and 2000 pc, respectively. These cubes have a spectral resolution of 0.07 km s^{-1}, beam size of $32''$, and pixel width of $8.8''$.

Table 4.1. Test Set Spectral Cubes

Region	Cloud	Distance (pc)	Transition	Telescope	Rest Freq.[e] (MHz)	Spectral Res. (km s^{-1})	Spatial Res. ($''$)	Pixel Scale ($''$)
L1689	Ophiuchus	119±6[a]	^{13}CO $(1-0)$	FCRAO	110201.354	0.07	46	23
DR21	Cygnus X	1700[b]	$C^{18}O$ $(3-2)$	JCMT	329330.552	0.11	32	7.2
B18	Taurus	135±20[c]	HC_5N $(9-8)$	GBT	23963.9010	0.07	31	11
M17SW	M17	2000[d]	NH_3 (1,1)	GBT	23694.4955	0.07	32	8.8
MonR2	Orion-Monoceros	900[c]	NH_3 (1,1)	GBT	23694.4955	0.07	32	8.8

[a]Lombardi et al. (2008)

[b]Schneider et al. (2006)

[c]Schlafly et al. (2014)

[d]Xu et al. (2011)

[e]Accessed from Lovas (2004).

4.3 Methods: CNN Architecture

The architecture of the 1D CNN adopted in this paper is shown in Figure 4.4. The network's hyper-parameters were set based on the success of previously published 1D CNNs featured in Fabbro et al. (2018) and Shallue & Vanderburg (2018), which used spectra and light curves, respectively, as input. Following those papers, we also use a 1D CNN because each sample in our training set consists of two 1D spectra with 500 channels. The "local" and "global" view spectra are fed into individual convolutional columns before being reconnected into a joint fully-connected layer. The convolutional columns consist of two convolutional layers, each with 16 kernels with a width of 3 spectral channels. The "convolution" in the convolutional layers involves taking the dot product between the input spectra and the kernels, which are moved across each channel of the input spectra. The output are convolved feature maps (one for each kernel) that are used as input into the next layer of the network.

The weights on the convolutional kernels are learned during training and attempt to create convolved feature maps that highlight spectral features that can be used to make a decision about the class of the sample. The resulting convolved features from the two convolutional columns are then combined as inputs into a joint column of two fully-connected layers with 3000 artificial neurons each. All of the neurons in these layers have a rectified-linear ('relu') activation function, which transforms the inputs it receives into an output that is sent to the next layer in the network. The rectified-linear activation function is commonly used in deep neural networks because it solves the "vanishing gradients problem," wherein large networks fail to train properly because the error of neurons deep in the network go to zero and can't be properly updated by gradient descent methods (Hochreiter et al., 2001).

The final output layer has three artificial neurons with a 'softmax' activation function. Each of these neurons has its own weight vector (w) that is the length of the output vector (x) from the previous network layer. The neurons first apply a weighted sum of x by performing the dot product of x and w. The output of the three dot products performed by each individual neuron form a new vector (y) of length three that is then passed to the softmax function, which is given by $e^{y_i}/\Sigma_j e^{y_j}$ where y_i is every element of y and $\Sigma_j e^{y_j}$ is the sum of the exponential of each element in y. Thus, the softmax activation function output is a length three vector that always sums to one and is interpreted as the probability of the input sample being in each of the three input classes.

The weights on the artificial neurons and convolutional kernels are optimized by minimizing the categorical cross-entropy loss function, using the 'Adam' gradient descent optimization method (Kingma & Ba, 2014). Since the categorical cross-entropy loss function increases as the predicted probabilities of the training set samples diverge from their ground-truth values, the model prediction accuracy is maximized if the cross-entropy function is minimized. For instance, an input training set sample that is a one-component class member has a label of [1, 0, 0]. If the softmax output of the network is [0.1, 0.5, 0.4] for that sample, the loss function output is high and thus the weights of the network need to be adjusted to minimize the loss. The gradient of the loss function is then calculated to determine in which directions the model weights should be updated to get closer to the minimum loss.

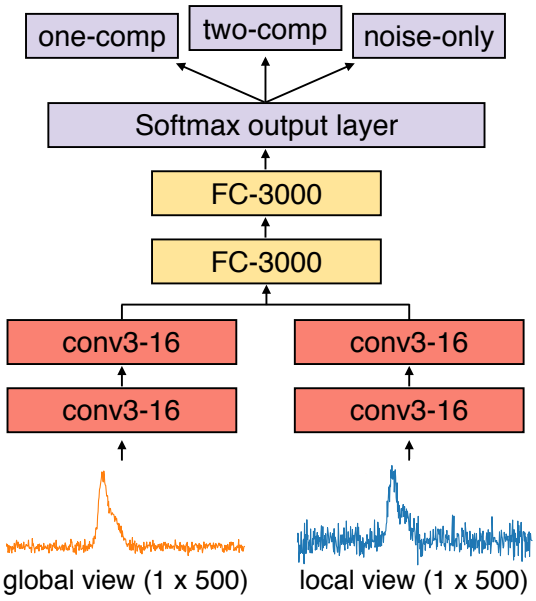

Fig. 4.4 – Architecture of the CNN chosen for this paper. The "local" and "global" view spectra for each sample are fed into individual columns of convolutional layers with 16, three-channel width kernels. The convolved features maps from each column are then joined into a single column of fully-connected layers with 3000 artificial neurons. The final layer predicts the class of the object using the softmax activation function. All other layers use a rectified-linear (relu) activation function.

The weights of the CNN are updated by iteratively moving through the training set in batches of 100 samples (a.k.a. 'mini-batch gradient descent'). To prevent over-

fitting, 'early-stopping' is implemented by monitoring the model's performance on a validation set of 90,000 additional synthetic spectra (30,000 in each class) during training. After each epoch in the training process, where an epoch represents using all samples in the training set to update the weights of the CNN, the validation set loss is measured. If the validation set loss does not improve for five epochs in a row, training is stopped and the model from the epoch with the best validation set loss is saved.

As an additional comparison to the architecture using the local and global spectra as inputs, we also train two additional networks using only the local and only the global spectra as input. The results for these architectures are presented in Section 4.4. Tests of more complex architectures with additional layers, neurons, and larger kernel sizes produced models that overfit the training data. As such, the simpler architecture presented in Figure 4.4 was chosen for CLOVER.

4.4 Results

4.4.1 Testing on Synthetic Data

After training the three CNN architectures (local-only, global-only, and local+global), we test their performance using ten independent validation sets of 30,000 synthetic spectra (10,000 in each class) described in Section 4.2.1. Predictions are made on each of the ten validation sets by the trained CNNs. The mean and standard deviation of the ten confusion matrices for each architecture are shown in Figure 4.5. Each square in the confusion matrix shows the amount of correct or incorrect classifications the CNN has made for each class. For a perfect classification of all samples in the validation set, the upper left, central, and lower right squares in the matrices would each be 10,000. The off-diagonal squares represent the number of misclassifications in each class.

The mean classification accuracies and standard deviations for the CNN using only the local spectrum as input across the ten independent validation sets are $96.39 \pm 0.19\%$, $99.95 \pm 0.02\%$, and $90.56 \pm 0.36\%$ for the one-component, noise, and two-component classes, respectively. For the CNN using only the global spectrum as input, the classification accuracies improve to $99.31 \pm 0.03\%$, 100%, and $96.82 \pm 0.13\%$ for the three classes. This improvement can be attributed to the higher SNR of the global spectra, which makes it easier to classify the samples. When using both the local and global spectra as input to the CNN, the classification accuracies become

$99.35 \pm 0.07\%$, 100%, and $96.08 \pm 0.24\%$, which are similar to those of the global-only CNN.

Although the global-only and local+global CNNs show similar performance, we opt to use the local+global CNN for the remainder of our analysis since the local spectra can be useful for preventing overfitting on real data. For instance, there are scenarios in real observations where the global spectrum may appear to have two velocity components, but the local spectrum shows only a single component. For those cases, using the local spectrum as input prevents misclassification.

The accuracy of the local+global CNN is improved further by averaging the outputs of six independently trained CNNs. Since each CNN is trained with different random initializations for their parameter weights, there is a variance in their output predictions on a given test set. Averaging their predictions, however, reduces this variance and often leads to improved overall performance since each CNN may perform better or worse on particular samples. Known as 'ensembling' or model 'averaging,' this technique involves summing the three output class probabilities predicted by each CNN before selecting the class with the highest probability as the predicted class for a given sample. The confusion matrix for this ensemble CNN is shown in the middle right panel of Figure 4.5. The accuracies for the one-component, noise, and two-component classes improves to $99.92 \pm 0.02\%$, 100%, and $96.72 \pm 0.18\%$. We refer to this ensemble of CNNs as the "ensemble CNN" for the remainder of the paper.

Visual inspection of the ensemble CNN misclassifications in the validation set also reveals that many of those samples indeed exhibit characteristics of the misclassified class. Several examples of these misclassified samples are shown in Figure 4.6. For instance, the true one-component samples that the ensemble CNN incorrectly identified as two-components often have a visible, but subtle, second peak due to the randomness of the noise injection. Similarly, the true two-component samples identified as one-components by the ensemble CNN are often indistinguishable from a true one-component sample. As such, these misclassifications are actually a positive sign that the ensemble CNN has "learned" the subtle differences between the one- and two-component classes rather than simply memorizing the samples in the training set.

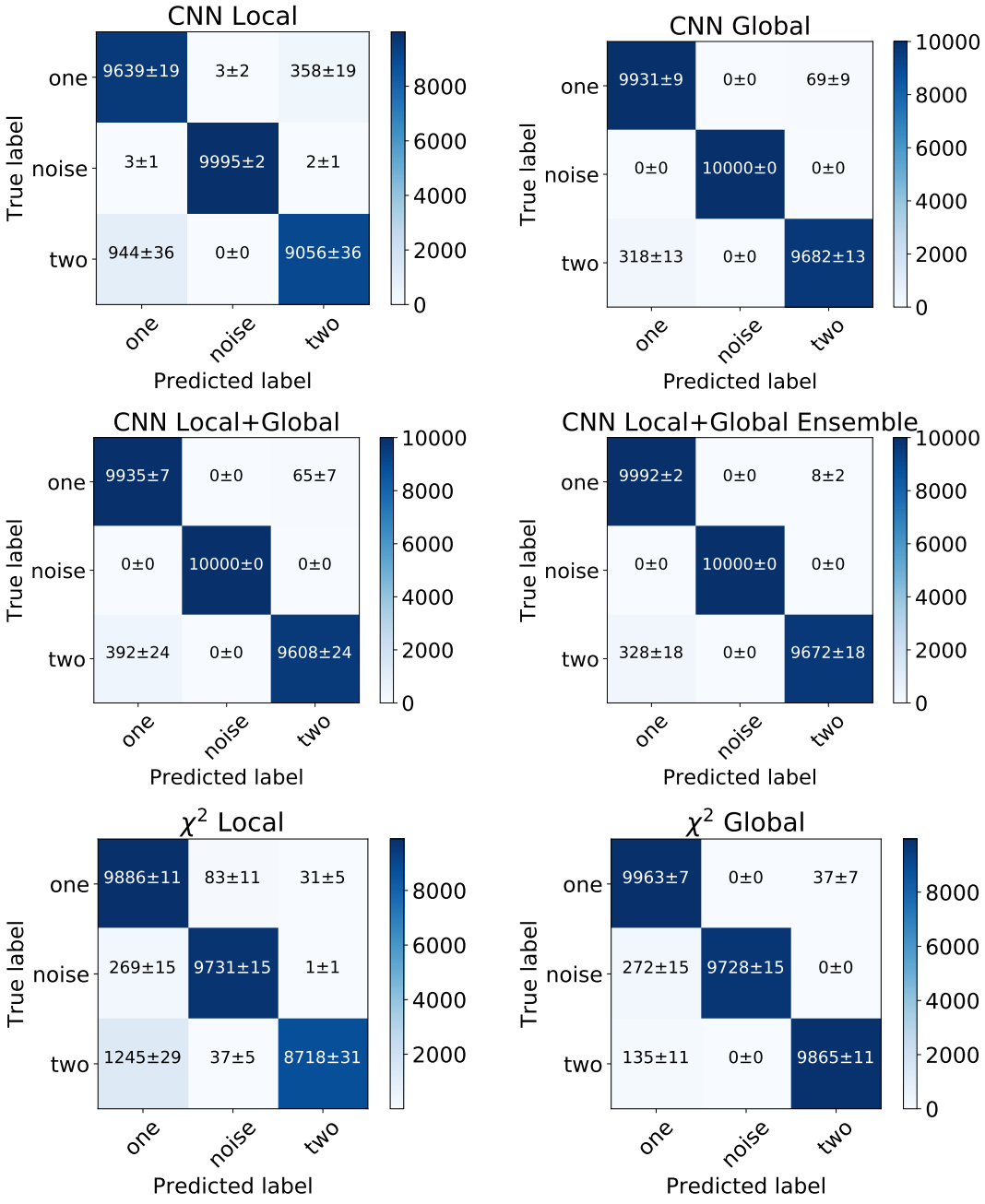

Fig. 4.5 – Confusion matrices for ten validation sets of 30,000 synthetic spectra (10,000 in each class) classified by the CNN using only the "local" spectrum (top left), CNN using only the "global" spectrum (top right), CNN using both the local and global spectra (middle left), averaged ensemble of six CNNs (middle right), traditional χ^2-minimization on the local spectrum (bottom left), and the traditional χ^2-minimization on the global view spectrum (bottom right). The "noise" class for the χ^2-minimization panels was selected based on a SNR threshold of 4. Each panel in the confusion matrices shows the mean and standard deviation for the ten validation sets.

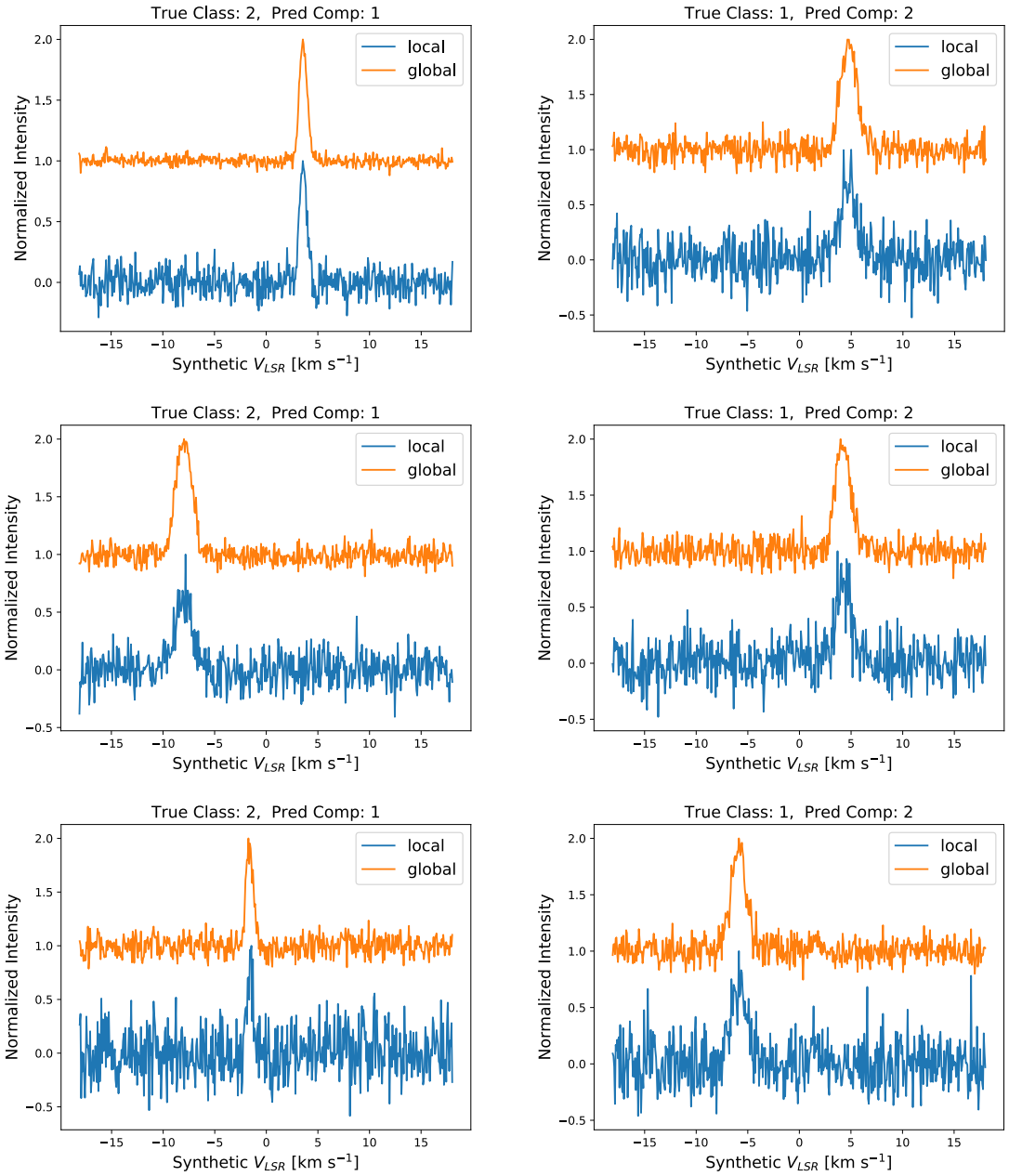

Fig. 4.6 – Samples in the synthetic validation set misclassified by the ensemble CNN. The left column shows true two-component samples (True Class: 2) classified as one-component (Pred Comp: 1) by the ensemble CNN. The right column shows true one-component samples (True Class: 1) classified as two-component (Pred Comp: 2) by the ensemble CNN.

4.4.2 Performance Versus Two-Component Gaussian Line Fitting

To gauge the ensemble CNN's performance against traditional line fitting methods, we also use a χ^2-minimization model selection technique to make class predictions on the validation set. Both a single- and two-component Gaussian model are fit to the "local" spectrum for each validation set sample using the Levenberg-Marquardt χ^2-minimization method in the `scipy.optimize.curve_fit` Python package. For the one-component fit, we use the peak channel in the spectrum as the initial guess for centroid velocity, a set value of 1.0 for the peak intensity guess (spectra are scaled to a max value of 1.0), and a set value of 10 channels for the velocity dispersion guess. To find the optimal solution for the two-component fit, which is more susceptible to falling into local minima solutions rather than global minima, we perform the line-fitting using a grid of initial parameter guesses. The model with the lowest χ^2 value was selected as the best-fitting two-component model. The initial guess for the first velocity component in the two-component model was set in the same way as the one-component model, while the second velocity component guesses were set as follows:

- T_{peak}: 0.1 less than the solution found for the one-component fit.
- V_{LSR}: [± 10, ± 30, ± 50, ± 70, ± 90, ± 110, ± 130, ± 150, ± 170, ± 190] channels from the solution found for the one-component fit. Thus, we search for centroids to the left and right of the one-component fit.
- σ: 0.1 channel larger than the solution found for the one-component fit.

The χ^2 values for the best-fitting single- and two-component models are then compared to select the "better" model for the spectrum. To penalize the larger number of model parameters in the two-component model and consider the number of data points being fit, we apply the Bayesian Information Criterion (BIC; Schwarz, 1978) to each model's χ^2 value. This approach is similar to the Akaike Information Criterion used in other traditional two-component line fitting methods (e.g., Henshaw et al., 2016), but has a built-in penalty for the number of data points in the models being compared. Namely, the model with the lowest BIC value is selected as the preferred model, where the BIC is given by the following expression:

$$BIC = N \ln(\chi^2) + p \ln(N) \quad , \tag{4.1}$$

where p is the number of model parameters and N is the number of fitted data points. The BIC attempts to balance goodness-of-fit (e.g, χ^2 value) against model complexity (i.e., the number of model parameters in relation to data set size) when comparing models. This approach tries to avoid overfitting (selecting a model that is too complex simply because it fits the data better), but at the same time limit underfitting (selecting a simpler model when a more complex model is more appropriate for the data).

The results of the BIC comparisons for the "local" spectra in the validation set are also shown in the bottom left panel of Figure 4.5. The "noise" class in this case is defined by any spectrum below SNR=4.0. For this traditional model selection approach, the classification accuracies for the one-component, noise-only, and two-component classes are $98.86 \pm 0.11\%$, $97.31 \pm 0.15\%$, and $87.18 \pm 0.31\%$, respectively. These accuracies are similar to those from the CNN local-only classifications, with slightly lower accuracies for the noise-only and two-component classes, but a slight increase in accuracy for the one-component class.

We also repeat the traditional line fitting and model selection method using the "global" spectrum for each training sample. The lower right panel in Figure 4.5 shows the accuracy for those classifications. The classification accuracies in this case are $99.63 \pm 0.07\%$, $97.28 \pm 0.15\%$, and $98.65 \pm 0.11\%$ for the one-component, noise-only, and two-component classes, respectively. The higher SNR of the "global" spectra are likely contributing to this accuracy improvement.

As an additional comparison between the ensemble CNN and χ^2-minimization predictions, we also show in Figure 4.7 each method's classification accuracy for the two-component samples in the synthetic test set versus SNR and centroid velocity separation (ΔV_{LSR}). Figure 4.7 shows that the classification accuracy for the χ^2-global and ensemble CNN methods is stable between an SNR range of $4 - 20$, with variations less than a few percent. In contrast, the χ^2-local method has a severe drop-off in accuracy for the lowest SNR bin. Since the χ^2-global and ensemble CNN methods incorporate the higher SNR global spectra into their classifications, they are less affected by the lower SNRs of the local spectra.

In terms of centroid velocity separation, all three methods show a significant drop-off in classification accuracy below $\Delta V_{LSR} \sim 1$ km s^{-1}. This effect is due to many of the low velocity separation two-component samples being indistinguishable in appearance to one-component class members. At $\Delta V_{LSR} > 1$ km s^{-1}, the components are distinct and easy to identify, causing accuracies to be near 100% for all three

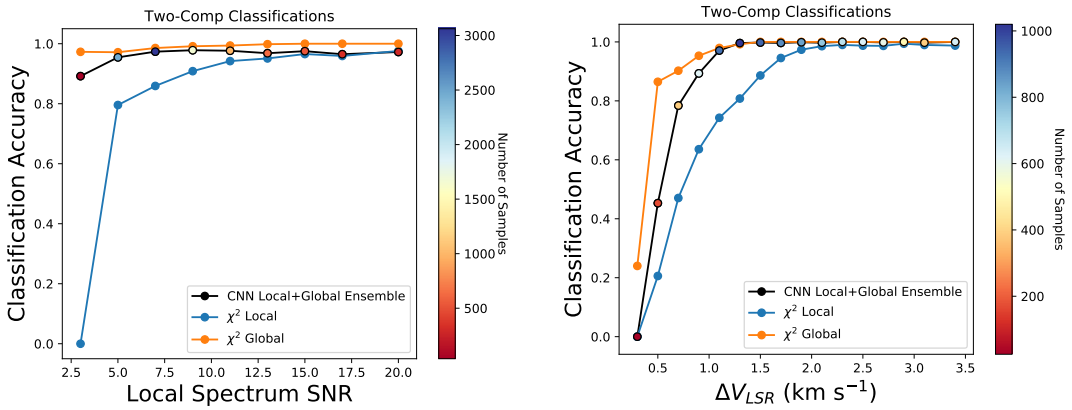

Fig. 4.7 – Model classification accuracy versus SNR (left) and centroid velocity separation (right) for two-component samples in the synthetic test set. Each data point represents the classification accuracy for samples within a bin centered on the data point's x-axis position. The classifications for the traditional χ^2-minimization methods on the "local" and "global" spectra are shown in blue and orange, respectively. The color of the CNN Local+Global Ensemble data points (outlined in black) show the amount of test set samples within each bin. The centroid velocity separation calculation assumes each spectral channel is separated by ~ 0.07 km s^{-1}.

methods. We also see that the χ^2-local method's accuracy begins to decrease at higher velocity separations $\Delta V_{LSR} \sim 2$ km s^{-1} than the other two methods. This behavior is once again likely related to the lower SNR of the local spectrum, which makes classifying close velocity components more difficult.

We also note that using solely an averaged spectrum (e.g., the global spectrum) to make classifications is not common for other traditional line-fitting methods (Henshaw et al., 2016; Sokolov et al., 2017; Clarke et al., 2018). Typically, a fit to an averaged spectrum is used to set the initial parameter guesses for a second fit to an individual spectrum. For this reason, all further comparisons will be between the χ^2-local and the ensemble CNN methods.

4.4.3 Testing On Real Observations

L1689 - ^{13}CO $(1-0)$

Although the ensemble CNN has demonstrated high classification accuracy on synthetic data, it is only useful if it can accurately classify real emission-line spectra. To test the model's performance on real observations, we have collected a ^{13}CO $(1-0)$ spectral cube from L1689 in the Ophiuchus molecular cloud observed by the COM-

PLETE survey (Ridge et al., 2006). This cube provides an excellent test for the ensemble CNN since it displays spectra that belong in all three of the classes in our training set. For this test, we implicitly assume that the line emission observed is optically thin everywhere. The use of CLOVER or traditional two-component line-fitting techniques on data with self-absorbed single-component lines will likely result in erroneous conclusions about the nature of the emission. Nevertheless, even if the observed emission is optically thick and self-absorbed, it still provides an adequate test set since self-absorption features mimic the appearance of optically thin emission with two velocity components along the line of sight.

Figure 4.8 shows the output predictions after a sliding window of size 3×3 pixels has been moved across the position-position plane of the cube, the "local" and "global" spectra are extracted, and fed into the ensemble CNN. Gray pixels in Figure 4.8 denote those that were predicted to be in the noise class, while black represents pixels predicted to be in the one-component class and white shows those predicted to be two-component class members. The red-lettered panels in Figure 4.8 show the "global" spectra at different locations on the data cube. Since we have no *a priori* knowledge of the physical processes that created any apparent two-component features in these real spectra, we must rely only on the appearance of the spectra when determining the success of the CNN's predictions. Nevertheless, comparing the spectra highlighted in Figure 4.8 to the ensemble CNN prediction map reveals that the CNN can distinguish the spectral differences between each class. Even two-component spectra with closely separated velocity components are correctly identified by the model (see, e.g., spectrum C in Figure 4.8).

Figure 4.8 also displays the class predictions of each pixel obtained from the traditional BIC model selection method using the "local" spectrum. For this method, any pixel with SNR < 4 is deemed noise. The red-lettered panels in Figure 4.8 show locations where the traditional model selection method agrees with the ensemble CNN predictions. As can be seen, these tend to be high SNR spectra where the class of the object is obvious. The green-numbered panels in Figure 4.8 show spectra from locations where the two methods disagree in their class predictions. These disagreeing cases reveal clear examples of the χ^2-minimization method underfitting (labeled panels 1 and 2 in Figure 4.8) and overfitting (labeled panels 3 and 4 in Figure 4.8) the spectra. Visual inspection of the individual best-fit models for the χ^2-minimization approach at those locations reveals that they are not cases in which the method fails to provide good fits to each spectrum, but rather they are failures

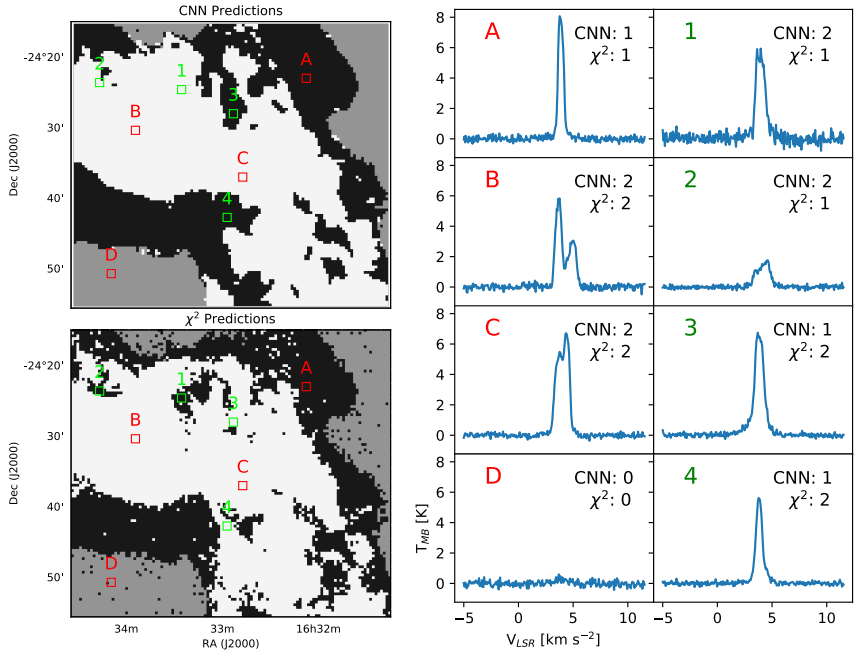

Fig. 4.8 – Left panels: example segmentations of a ^{13}CO $(1-0)$ spectral cube observation of L1689 into three classes: single velocity component spectrum (black), multiple velocity component spectrum (white), and noise (grey) using CLOVER's ensemble CNN (top) and traditional χ^2-minimization model fitting (bottom). Right panels: The "global" view spectra extracted from the observed spectral cube at the positions of the 3×3 pixel windows overlaid onto the left panels. Red letters denote positions where CLOVER and the χ^2 technique agree in their class predictions, while the green numbers show positions where they disagree. The text in the upper right corner of each panel shows the class predicted by CLOVER and the χ^2 technique for that spectrum, where 2=two-component, 1=one-component, and 0=noise.

of the BIC model selection technique. Conversely, the ensemble CNN is able to identify weak two-component features that are deemed to be one-component by the χ^2-minimization approach (labeled panels 1 and 2 in Figure 4.8), but is also resilient against predicting the two-component class when it is not warranted (labeled panels 3 and 4 in Figure 4.8). These examples serve as evidence for the advantage that the ensemble CNN can provide for identifying multiple velocity component spectra.

Moreover, the ensemble CNN predictions on the entire spectral cube, which has dimensions of 118×106 pixels (i.e., $\sim$ 12,500 individual predictions), take only 137 seconds ($\sim$ 23 seconds for each of the six CNN predictions in the ensemble) on a single core of a 2.8 GHz Intel Core i7 CPU. Although CLOVER's prediction speed could improve by utilizing multiple cores on a single CPU or GPU, the low computing

power required for CLOVER to obtain fast performance is a marked advantage over traditional methods (see Section 4.5.1 for a comparison involving both classification and parameter predictions). The number of pixels in typical spectral cubes is also growing with the advent of focal plane arrays that quickly map large areas of the sky (e.g., Morgan et al., 2008; Devaraj et al., 2014) and interferometers (e.g., ALMA, ngVLA, etc.) that map at high spatial resolutions. As such, the quick prediction speeds provided by CLOVER make it an attractive tool for the next generation of large-scale spectroscopic surveys of star-forming regions.

DR21 - $C^{18}O$ ($3-2$)

Although ^{13}CO $(1-0)$ emission is a common tracer of molecular gas in star-forming regions, it can become optically thick in some environments. The high opacity emission sometimes leads to self-absorption dips, which can mimic the double-peaked structure of optically-thin two-component spectra (e.g., Lee et al., 1999; Sohn et al., 2007; Schnee et al., 2013; Keown et al., 2016). To ensure that self-absorption is not affecting the CNN predictions, we also test the CNN on a $C^{18}O$ $(3-2)$ spectral cube of DR21 in the Cygnus X star-forming region. Since $C^{18}O$ is a much rarer isotopomer than ^{13}CO, its emission is almost always optically thin and rarely suffers from self-absorption dips.

We advise users of CLOVER to determine whether or not the emission they are inputting into the algorithm is optically thin or thick. Since CLOVER makes its predictions under the assumption that the emission is optically thin, any significantly self-absorbed optically thick spectrum it receives as input will most likely be classified in the two-component class.

Figure 4.9 shows the results of both the ensemble CNN and χ^2-minimization model selection technique on the $C^{18}O$ $(3-2)$ spectral cube. Once again, we see that the ensemble CNN and χ^2-minimization methods show overall agreement between their predictions. As seen in the green numbered panels of Figure 4.9, the ensemble CNN method is less susceptible to overfitting than the χ^2-minimization method. For instance, the χ^2-minimization method frequently classifies spectra that appear to have a single velocity component (or very subtle wings) as two-components.

In addition to showing the differences between one- and two-component class predictions for the ensemble CNN and χ^2-minimization approach, Figure 4.9 also highlights the advantages of the CNN's noise class predictions over simple SNR thresh-

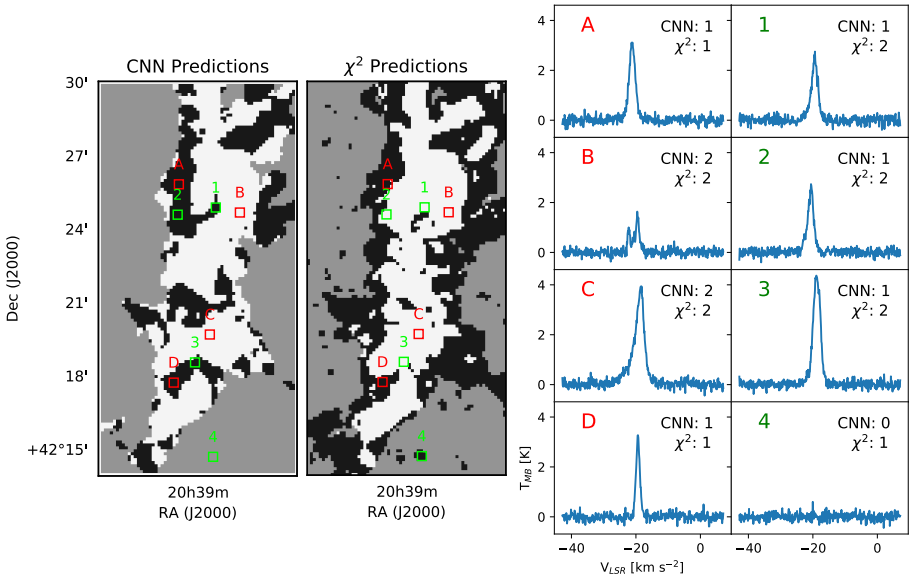

Fig. 4.9 – Same as Figure 4.8, but for the $C^{18}O$ $(3-2)$ observations of DR21.

olds. For example, the χ^2-minimization approach's SNR cutoff leads to many islands of one-component members that should instead be classified as noise (see, e.g., green spectrum 4 in Figure 4.9). Conversely, the ensemble CNN segmentation is much smoother, showing a clear distinction between the core of signal at the center of the cube and noise at the edges. A similar distinction between the noise and signal can be seen in the L1689 CNN segmentation shown in Figure 4.8. This behavior provides further evidence of the advantages gained by incorporating CNNs into the line-fitting procedure.

B18 - HC_5N $(9-8)$

As an additional comparison between the ensemble CNN and χ^2-minimization approaches, we also test their performance on a HC_5N $(9-8)$ spectral cube from B18 in the Taurus star-forming region observed by the Green Bank Ammonia Survey (Friesen et al., 2017). B18 is a much more quiescent region than L1689 and DR21, which means its emission tends to have only a single velocity component. HC_5N $(9-8)$ is also an optically thin transition, ensuring that self-absorption is not affecting the spectra. Thus, this cube provides a test to see how robust the ensemble CNN

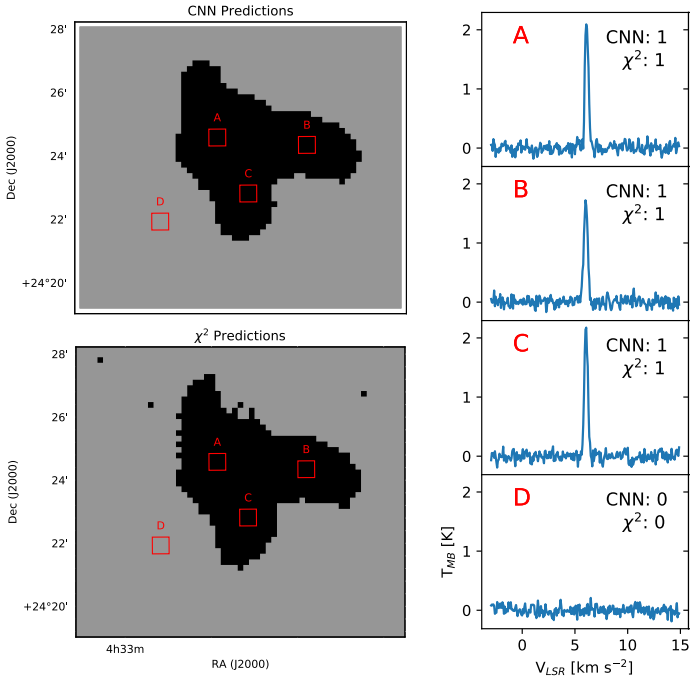

Fig. 4.10 – Same as Figure 4.8, but for the HC_5N $(9-8)$ observations of B18.

is for cubes that lack two-component class members.

Figure 4.10 displays the segmentation results for the ensemble CNN and χ^2-minimization approach applied to the B18 cube. Overall, the two methods are in good agreement. Both correctly identify that only one-component and noise-only spectra are within the cube. As in the other test regions, we once again see that the ensemble CNN noise segmentation for B18 is superior to the SNR threshold of the χ^2-minimization approach since there is a clear distinction between the noise and signal in the former.

4.4.4 Testing on Three-Component Spectra

One important assumption of CLOVER's ensemble CNN classifications are that they assume the input spectra belong to one of the three classes they were trained to predict (one-component, two-component, or noise-only). In real observations, however, three or more velocity components may be present in a single spectrum (e.g., Sokolov et al., 2017; Clarke et al., 2018; Chen et al., 2019b). As a simple test to see how CLOVER would classify spectra with three velocity components, we generate an additional synthetic test set of 30,000 three-component spectra. The first and second

velocity components for each sample in the test set were generated using the same steps described in Section 4.2.1 for generating the two-component samples. A third velocity component was introduced by injecting a third Gaussian spectrum into each sample. The velocity dispersion and centroid for this third Gaussian were randomly drawn from a uniform distribution with the following limits: 2 channels $\leq \sigma \leq$ 11 channels, and -0.55 km s^{-1} $\leq V_{LSR} \leq$ 0.55 km s^{-1} (where the spectral axes have been normalized between -1 km s^{-1} and 1 km s^{-1}). The value of T_{peak} for the third Gaussian was drawn randomly from a uniform distribution between 2×RMS and 1 K, where RMS is the noise level selected for the cube. The RMS level for each sample was set as described in Section 4.2.1.

When predicting the class of the 30,000 three-component spectra, CLOVER assigns the two-component class to 29,827 ($\sim$ 99%) and the one-component class to only 173. Thus, CLOVER's two-component classifications can be thought of as a "multi-component" class. If presented with a sample containing more than two velocity components, the current implementation of CLOVER will likely place that sample in its two-component class.

4.5 Deriving Kinematics From Two-Component Spectra

The quick and accurate classifications provided by CLOVER can be used to improve kinematics measurements in one of two ways: 1) As a preprocessing technique that will predict the class of each pixel, then a traditional line fitting method can be used to find the best-fitting parameters for that model. 2) As a preprocessing technique into a second neural network that will predict the centroid velocity and line width directly from the spectra of the pixels identified as two-component class members. In this section, we demonstrate the latter case - deriving kinematics directly from spectra.

Fabbro et al. (2018) showed that CNNs have similar performance as traditional least-squares template fitting for deriving stellar parameters from APOGEE spectra. More importantly, the Fabbro et al. (2018) CNN made stellar parameter predictions significantly faster than least-squares template fitting, highlighting the advantages gained by utilizing neural network architectures. With those results in mind, it is likely that neural networks can perform similarly to the traditional least-squares model fitting commonly used to derive kinematics from emission-line spectral data of star-forming regions.

Using a similar neural network architecture described in Section 4.3 for CLOVER's spectral classification, we trained an additional network to use the local and global spectra for a two-component class member (i.e., a pixel predicted to be a two-component by the ensemble CNN) to predict the velocity centroid, dispersion, and peak intensity of each component. There are two main changes to the architecture of this network from the spectral classification network: 1) Instead of the training set labels being classes, they are now the velocity centroid, dispersion, and peak intensity of each component (i.e., in the most general case, both the inputs and outputs of a machine learning problem can be multidimensional. Here, we have a multidimensional-output regression.). The training set labels are a six-number array, with the first being the centroid of the lower-velocity component, the second being the centroid of the higher-velocity component, the third being the dispersion of the lower-velocity component, the fourth being the dispersion of the higher-velocity component, the fifth being the peak intensity of the lower-velocity component, and the sixth being the peak intensity of the higher-velocity component. This setup ensures that the network always predicts the labels in the same order so that no label switching occurs. 2) The output layer consists of six output neurons (one for each label) with linear activation functions that predict continuous values rather than the probability of each class. The centroid velocity labels are normalized between -1 and 1, with -1 being the left (lowest-velocity) edge of the spectrum and 1 being the right (highest-velocity) edge of the spectrum. The velocity dispersion labels are represented in units of spectral channels.

The training set for this regression network included 300,000 two-component spectra generated using the same method discussed in Section 4.2.1. A validation set of an additional 90,000 spectra was also used to monitor the network's performance during training in order to apply early-stopping. After training, a test set of 30,000 additional two-component samples were generated and used to gauge the network's performance. The top row of Figure 4.11 displays the regression accuracy of the CNN predictions for the test set. The model's predictions are accurate to mean absolute errors (MAE $= \frac{1}{n}\sum_{t=1}^{n}|e_t|$, where e_t is the error in the prediction of sample t) of ~ 0.01 for centroid velocity, ~ 0.35 for velocity dispersion, and ~ 0.06 for peak intensity.

Figure 4.12 shows the trained network's predictions for two samples in the test set. The model can accurately predict the kinematics of components that have large velocity separations (e.g., left panel of Figure 4.12), but also those that are blended together (e.g., right panel of Figure 4.12).

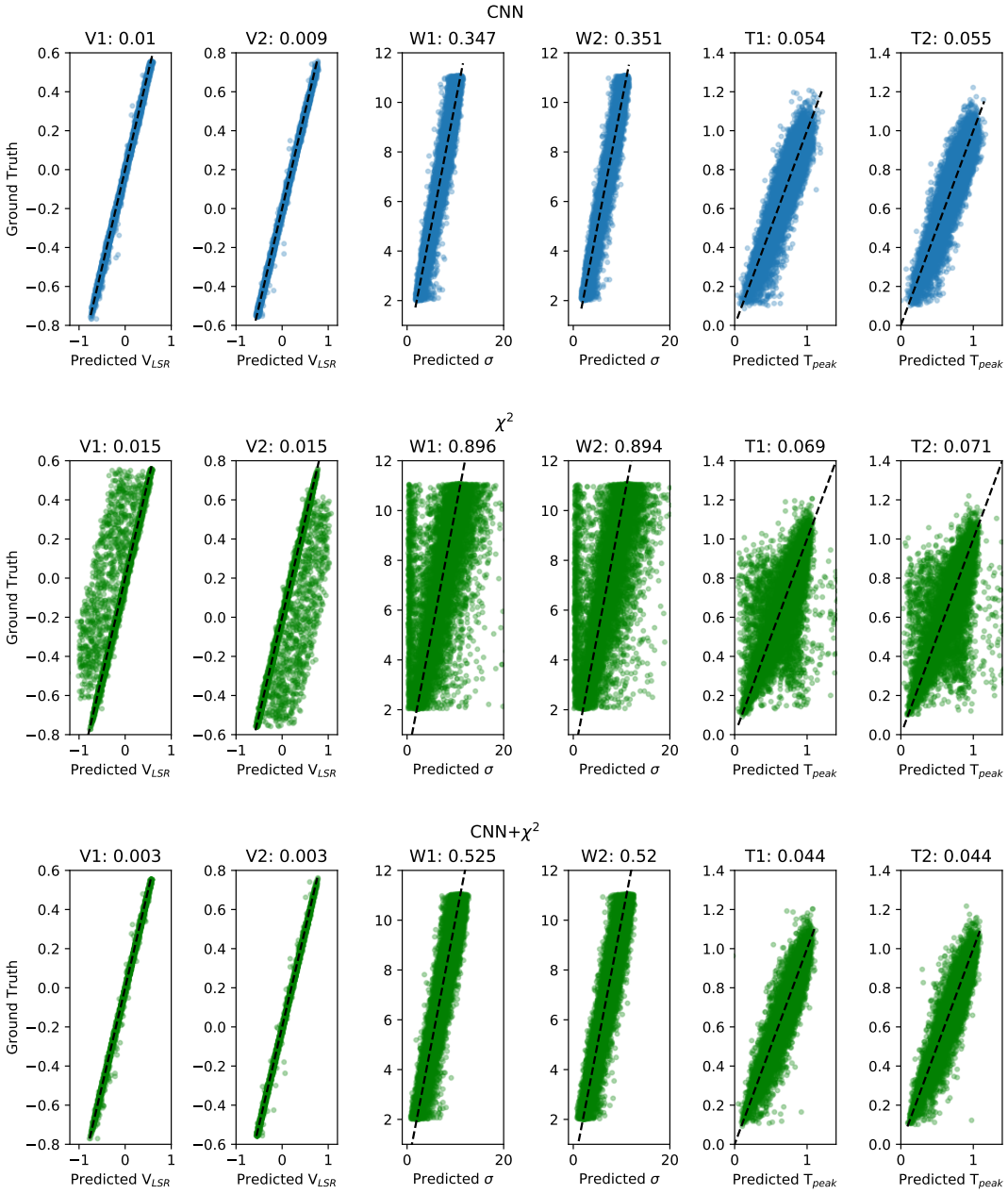

Fig. 4.11 – Velocity centroid (two left columns), dispersion (middle two columns), and peak intensity (two right columns) predictions by CLOVER's trained regression CNN (top row), χ^2-minimization grid search method (middle row), and χ^2-minimization method with CNN initial guesses (bottom row) versus the "ground-truth" for the low-velocity component (V1, W1, T1) and high-velocity component (V2, W2, T1) for the 30,000 two-component spectra in the synthetic test set. The dashed lines show a one-to-one correspondence. In all panels, the centroid velocities are normalized between -1 and 1. The velocity dispersion units are the number of channels in the spectrum. The subtitle above each panel shows the mean absolute error for that parameter.

The middle row in Figure 4.11 shows the performance of the χ^2-minimization method's best-fit two-component model for every sample's local spectrum in the test set. Using this method, the mean absolute errors increase to ~ 0.015 for centroid velocity, ~ 0.9 for velocity dispersion, and ~ 0.07 for peak intensity, with a significant number of poor fits as shown by the abundance of outliers in each panel. Disregarding the outliers, the spread of the χ^2-minimization predictions about the one-to-one line is similar to the CNN predictions. The lack of outliers in the CNN predictions, however, suggests that it is more resilient against fitting noise and/or falling into local minimum solutions compared to the χ^2-minimization method.

Figure 4.13 shows the mean absolute error for each predicted parameter in bins of SNR and centroid velocity offset for the χ^2-minimization method and CNN predictions. It is clear from Figure 4.13 that the χ^2-minimization method's outliers are caused by samples with low SNR and low centroid velocity offsets, which show higher values of MAE compared to samples with higher SNR and larger centroid velocity offsets. Although the MAE values for the CNN predictions are more stable than those of the χ^2-minimization method, the CNN still suffers from a moderate increase in MAE for samples with low SNR and low centroid velocity offsets.

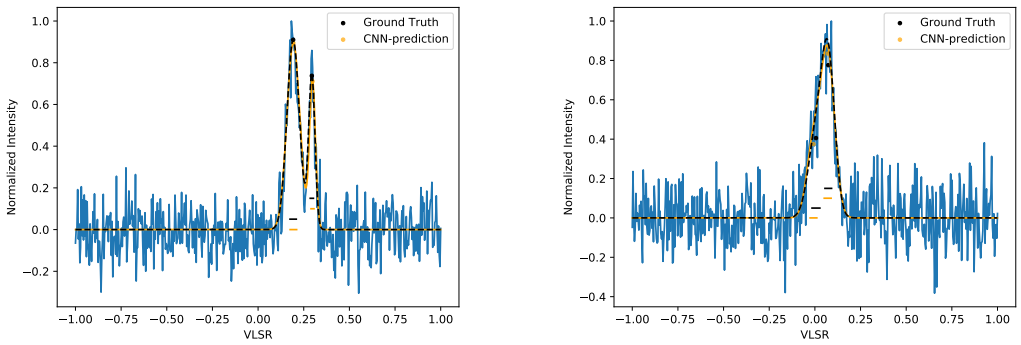

Fig. 4.12 – Example predictions by CLOVER on previously unseen "local-view" spectra from the synthetic test set. The black dots/bars show the positions of the "ground-truth" velocity centroids, peak intensities, and velocity dispersions used to generate the synthetic sample. For comparison, the orange dots/bars show CLOVER's parameter predictions. The dashed black line shows the ground-truth model used to generate the synthetic sample, while the orange solid line shows the corresponding two-component model generated using CLOVER's parameter predictions.

Since the χ^2-minimization method is susceptible to falling into local minimum solutions for samples with low SNR and low centroid velocity offsets, its performance

can be improved by making better initial guesses and providing constraints on the parameter space explored. One way to set these initial guesses is by using the CNN predictions, which are more resilient to low SNR and low centroid velocity offsets. To demonstrate this use-case, we perform a second round of fitting on the test set using the χ^2-minimization method. Instead of using the initial guess grid-search method described in Section 4.4.2, the CNN predictions are used as the initial parameter guesses. We also constrain the parameter space explored by the χ^2-minimization method to be within the scatter of the CNN predictions, which also helps prevent fitting noise or falling into local minimum solutions. In the bottom panel of Figure 4.11, we show the results using this combined CNN and χ^2-minimization method. Using the CNN parameter constraints, the χ^2-minimization method no longer falls into local minimum solutions. The mean absolute errors improve to ~ 0.003 for centroid velocity, ~ 0.5 for velocity dispersion, and ~ 0.04 for peak intensity. Moreover, Figure 4.13 also shows that using the CNN, rather than the grid-search technique, to set initial guesses for the χ^2-minimization method reduces the MAE for samples with low SNR and low centroid velocity offsets. As such, CLOVER provides a convenient way to improve existing line fitting methods that require initial guesses for centroid velocity, dispersion, and peak intensity.

In addition, Figures 4.11 and 4.13 show that the CNN+χ^2-minimization approach has better performance than the CNN alone for both centroid velocity and peak intensity predictions. Conversely, the accuracies of the velocity dispersion predictions for both χ^2 methods are lower than those of the CNN. The middle left panel of Figure 4.13, however, shows that the velocity dispersion prediction accuracy of all three methods converges at high SNR. The poorer performance of the χ^2 methods are limited to the low SNR spectra, which make up the majority of the test set samples. The better performance of the CNN is likely a result of its usage of the higher SNR "global" spectrum, which can provide better constraints on a given sample's velocity dispersions than the "local" spectrum alone.

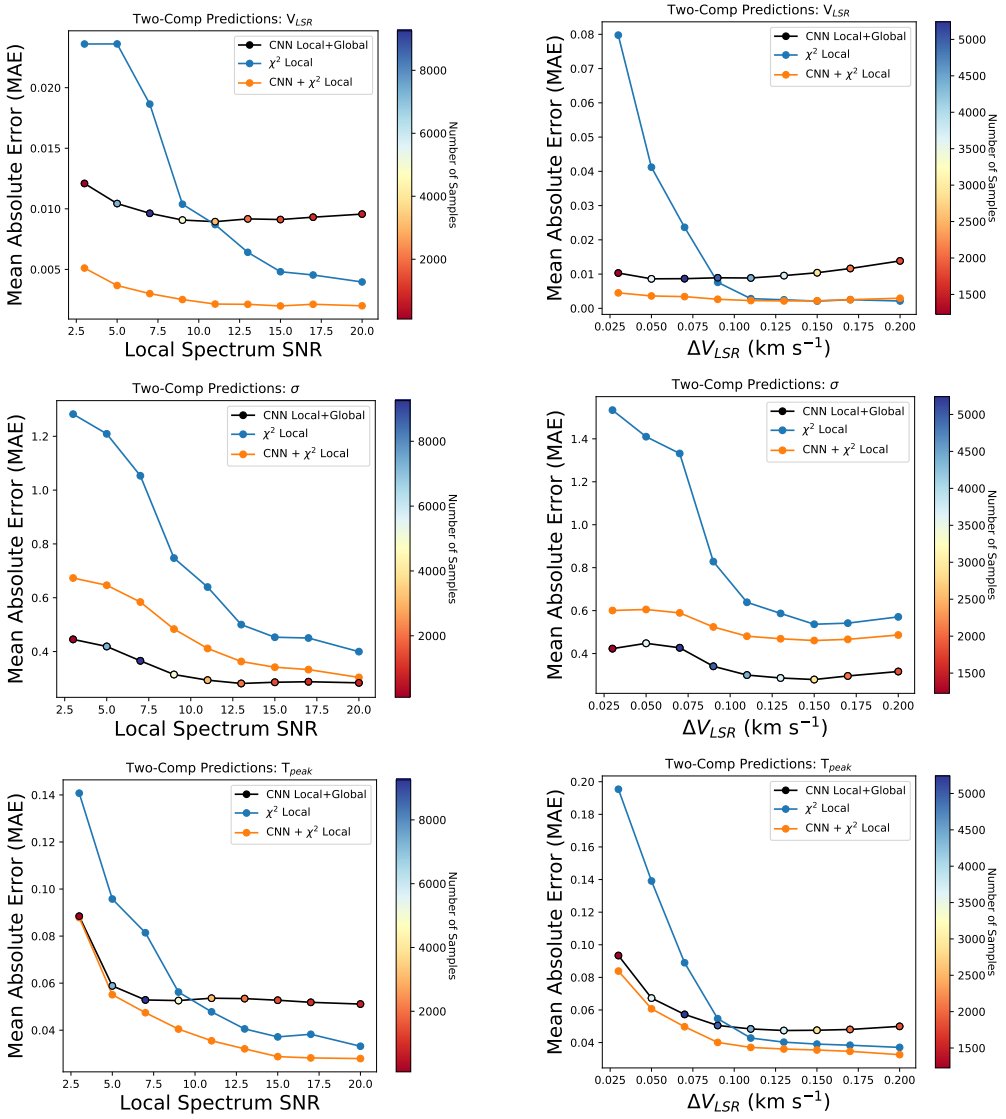

Fig. 4.13 – Mean absolute error (MAE) versus SNR (left column) and centroid velocity separation (right column) for centroid velocity (top row), velocity dispersion (middle row), and peak intensity (bottom row) predictions. Each data point represents the MAE for test set samples within a bin centered on the data point's x-axis position, averaged over both velocity components for each parameter (e.g., the average MAE for both V1 and V2 from Figure 4.11). The results for the traditional χ^2-minimization method are shown for both the grid-search initial guess technique (blue, see Section 4.4.2) and when using CLOVER's regression CNN predictions to set initial guesses (orange, see Section 4.5). The color of the regression CNN Local+Global data points (outlined in black) show the amount of test set samples within each bin. The centroid velocity separation calculation uses the spectral axis after normalization between -1 km s^{-1} and 1 km s^{-1}.

4.5.1 Testing CLOVER's regression CNN on real data

To test the performance of CLOVER's regression CNN on real observations, we use the L1689 ^{13}CO $(3-2)$ spectra that were predicted to belong to the two-component class by CLOVER's classification CNN presented in Section 4.4. Figure 4.14 shows example predictions by the regression CNN on six of the L1689 spectra. CLOVER is able to predict accurately the kinematics of blended two-component spectra with both broad and narrow components. Figure 4.14 also shows the kinematics and best-fit model determined by fitting a two-component Gaussian model to the data using the traditional χ^2-minimization approach described in Section 4.4.2. Overall, the predictions of the two methods are in good agreement across all of these test examples. In most cases, however, the χ^2-minimization approach provides a better fit visually to the data. These better fits are likely related to the fact that the χ^2-minimization approach uses only the local spectrum for fitting while CLOVER uses both the local and global spectra. Since CLOVER also uses the global spectrum for its predictions, there is some bias in its predictions when viewed on the local spectrum. Nevertheless, using the global spectrum allows CLOVER's predictions to have lower variance and suffer less from falling into the local minima solutions that plague the χ^2-minimization approach (see, e.g., the discussion in Section 4.5).

Moreover, the design of the χ^2-minimization approach provides an advantage over the CNN for producing visually optimal fits. The χ^2-minimization approach is based on minimizing the residual between the spectrum and model. When provided adequate initial model parameter guesses, the χ^2-minimization approach will oftentimes produce a visually optimal fit. Conversely, the CNN is attempting to "guess" the Gaussian model parameters based on similar examples it has seen during training. The CNN knows nothing about the residual of the model it generates for the six parameters it predicts. Rather, the CNN knows only that the new spectrum it receives has activated similar artificial neurons as examples it saw during training. This approach is very different to residual minimization and does not always lead to the best possible visual fit. The CNN approach can, however, get very close to the best possible visual fit (as shown in Figure 4.14). To obtain the most robust parameter predictions possible, we therefore recommend users use CLOVER's regression predictions as initial guesses for a χ^2-minimization approach.

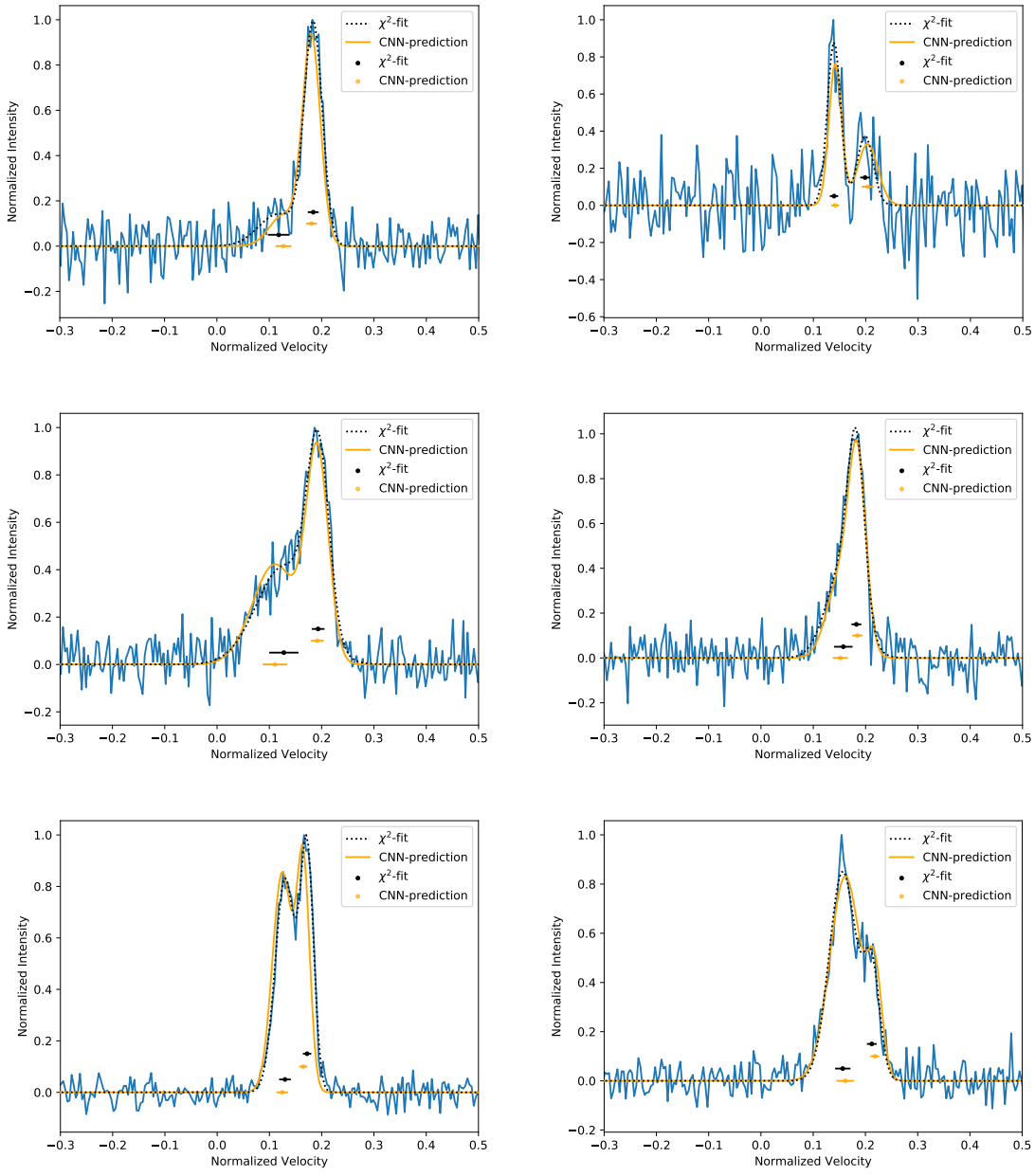

Fig. 4.14 – Velocity centroid (orange dots) and dispersion (orange bars) predictions by CLOVER versus the centroids and dispersions obtained from a two-component Gaussian fit using χ^2-minimization (black dots and bars) for six spectra observed in L1689. In all panels, the "local" view spectrum is shown in blue, while the best-fit two-component model from the χ^2-minimization is displayed as a dotted black line. The orange solid line shows the corresponding two-component model generated using CLOVER's parameter predictions.

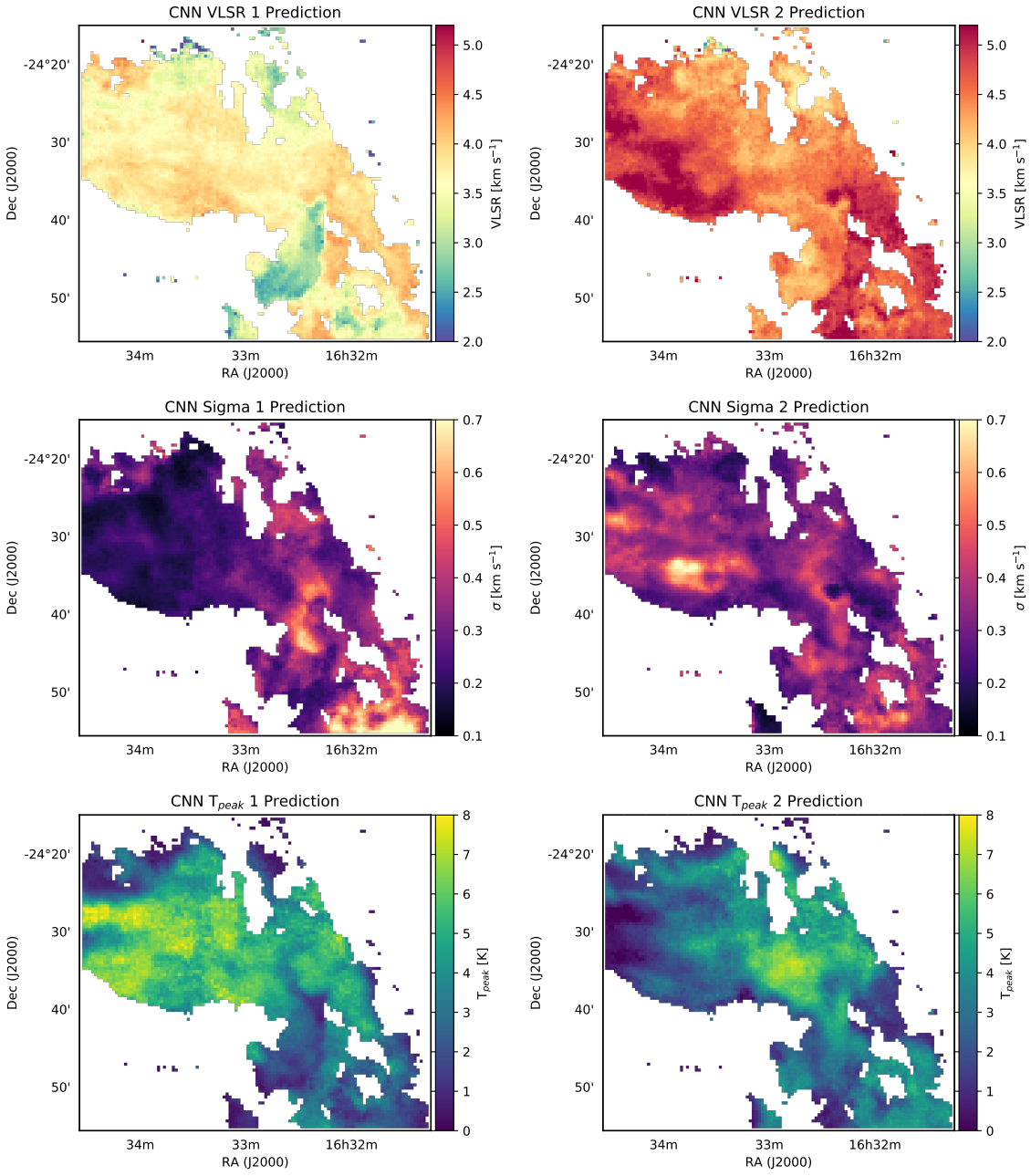

Fig. 4.15 – Velocity centroid (top row), velocity dispersion (middle row), and peak brightness temperature (bottom row) predicted by CLOVER's regression CNN for all pixels predicted to be "two-component" class members by CLOVER's classification CNN for L1689.

Figure 4.15 shows the result of running both CLOVER's classification and regression CNNs (i.e., the complete CLOVER method) on the full L1689 data cube. In each panel, colored pixels represent those that were designated "two-component" class members by CLOVER's classification CNN. The top row displays the predicted centroids for each pixel, the middle row shows the predicted dispersion, and the bottom row shows the predicted peak intensity. The maps suggest a stronger gradient in centroid velocity for the lower-velocity component than the higher-velocity component, which is typically at $V_{LSR} > 4.0$ km s^{-1}. The lower-velocity component also tends to have smaller velocity dispersion, especially on the eastern side of the cloud.

In addition, the full CLOVER classifications and parameter predictions take only ~ 154 seconds on a single core of a 2.8 GHz Intel Core i7 CPU. This is over an order of magnitude faster than the 3,209 seconds required for the χ^2-minimization approach, which simultaneously provides classifications and parameter predictions, when run on the same CPU.

4.6 Classifying Spectra with Hyperfine Structure

Hyperfine splitting is an additional mechanism that can cause an emission line to appear non-Gaussian. The emission from the NH_3 (1,1) transition, for instance, is split across 18 different velocity components (see, e.g., Ho & Townes, 1983). For NH_3 (1,1), this splitting results in a central group of blended Gaussians with four satellite groups of blended Gaussians (two on each side). Such spectra would be problematic when making classifications with CLOVER as described in Section 4.4, since it would undoubtedly select the two-component class for every spectrum due to the multiple hyperfine groups.

With ammonia being a popular tracer of modern large-scale molecular cloud mapping surveys (e.g., Friesen et al., 2017; Hogge et al., 2018), CLOVER would be much more useful to the star formation community if it were adaptable to transitions with hyperfine splitting. Since the relative frequency separations of the NH_3 (1,1) hyperfine lines are well-known, however, we can train a new CNN to distinguish between the transition's intrinsic frequency separations and an actual second velocity-component source along the line of sight. Here, we train such a CNN using synthetic NH_3 (1,1) spectra.

4.6.1 Generating Synthetic NH_3 (1,1) Spectra

3×3 pixel cubes for 300,000 training samples (100,000 in each of the three training classes) were generated using the `cold_ammonia` model generator within the `pyspeckit` Python package (Ginsburg & Mirocha, 2011). The generator creates NH_3 (1,1) emission models using the following input parameters that were randomly selected from the listed distributions:

- T_K (kinetic gas temperature): uniformly distributed from $8 - 25$ K
- V_{off} (centroid velocity offset from spectrum center): -2.5 to 2.5 km s^{-1}, which is equivalent to channels $465 - 534$ of the 1000 channel spectrum. Here, the spectral axis has been normalized so that each channel is separated by ~ 0.07 km s^{-1}.
- log$N$ (logarithm of the NH_3 column density): uniformly distributed in $\log_{10}$ space from $13 - 14.5$ log(cm^{-2})
- σ_{nt} (non-thermal velocity dispersion): log-normally distributed in natural logarithm space with a 1-sigma range of $0.02 - 0.45$ km s^{-1}
- σ_{tot} (total velocity dispersion) $= \sqrt{\sigma_{nt} + 0.08^2}$ km s^{-1}

These distributions aim to mimic those seen in real NH_3 (1,1) observations by the Green Bank Ammonia Survey (Friesen et al., 2017) and KEYSTONE (Keown et al., 2019b). For the two-component class, two randomly chosen models were added together. The velocity centroid of the second velocity component was drawn with respect to the first component (i.e., the range of possible centroids for individual components in the two-component samples is -5 km s^{-1} to 5 km s^{-1}). We also ensure that the centroids of the two components are separated by at least $1.0 \times \sigma_{max}$.

As described in Section 4.2.1, each model generated represented the central pixel in the 3×3 pixel grid. The outer pixels were filled by adding a perturbation to the central pixel model by drawing values from four normal distributions (one for each parameter) with mean of zero and variance of 0.2 K, 0.1 km s^{-1}, 0.1 km s^{-1}, and 0.01 cm^{-2} for T_K, V_{off}, σ_{nt}, and log$N$, respectively. Random noise with an RMS of 0.1 K was also added to the cubes, a noise level that is typical for recent ammonia mapping surveys of nearby star-forming regions (Friesen et al., 2017; Keown et al., 2017). For the noise class, only noise was added to an otherwise emission-free cube.

The final features for each sample are again the local (central pixel's spectrum) and global (averaged spectrum of all nine pixels) spectra, but in this case these have 1000 channels each to account for the hyperfine structure of the NH_3 (1,1) line that typically spreads over 500 channels. We note also that the narrow range of possible centroid velocities for the NH_3 (1,1) synthetic spectra create a challenging training set since the majority of the samples have blended velocity components. This choice was observationally motivated, however, since typical ammonia observations show few spectra with large centroid separations between each velocity component along the line of sight.

4.6.2 Testing on Synthetic NH_3 (1,1) Spectra

We adopt the same neural network architecture described in Section 4.3 to train the network. An additional synthetic validation set of 90,000 samples (30,000 in each class) was also used to monitor model performance during training to implement early-stopping. The trained CNN's performance on a separate synthetic test set of 30,000 additional samples (10,000 in each class) is shown in the top left panel of Figure 4.16. The CNN prediction accuracy is $\sim$ 98%, 100%, and $\sim$ 92%, for the one-component, noise-only, and two-component classes, respectively. As shown in the right panel of Figure 4.16, the prediction accuracy of ensemble averaging six independently trained CNNs improves to $\sim$ 99%, 100%, and $\sim$ 93%, for the one-component, noise-only, and two-component classes, respectively. For this reason, all further comparisons and analysis of the NH_3 data will use the ensemble CNN.

To compare the ensemble CNN performance to traditional line fitting methods, we use the χ^2-minimization model selection approach to classify each spectrum in the training set using the same technique described in Section 4.4.2. The `cold_ammonia` model generator within `pyspeckit` was used to generate one- a two-component models that were fit to the data using the χ^2-minimization method. The initial guesses for T_K, σ_{nt}, and log$N$ were set at 14 K, 0.3 km s^{-1}, and 13.5 cm^{-2}. A grid of V_{LSR} initial guesses were used, which included one guess centered on the peak intensity channel and increments of $\pm$0.4, $\pm$1.3, $\pm$2.2, $\pm$3.1, $\pm$4.0, and $\pm$4.9 km s^{-1} offset from the peak intensity channel.

The bottom panels in Figure 4.16 show that the CNN performance is better than the χ^2-minimization model selection approach on the local (95%, 94%, and 85% for the one-component, noise-only, and two-component classes, respectively) and global

(90%, 94%, and 92% for the one-component, noise-only, and two-component classes, respectively) spectra. These results indicate that the χ^2-global approach is actually susceptible to overfitting the hyperfine spectra, tending to classify incorrectly the one-component samples as two-component at a slightly higher rate than the χ^2-local method. In contrast, the ensemble CNN is more resilient to this overfitting while still incorporating the global spectrum as input.

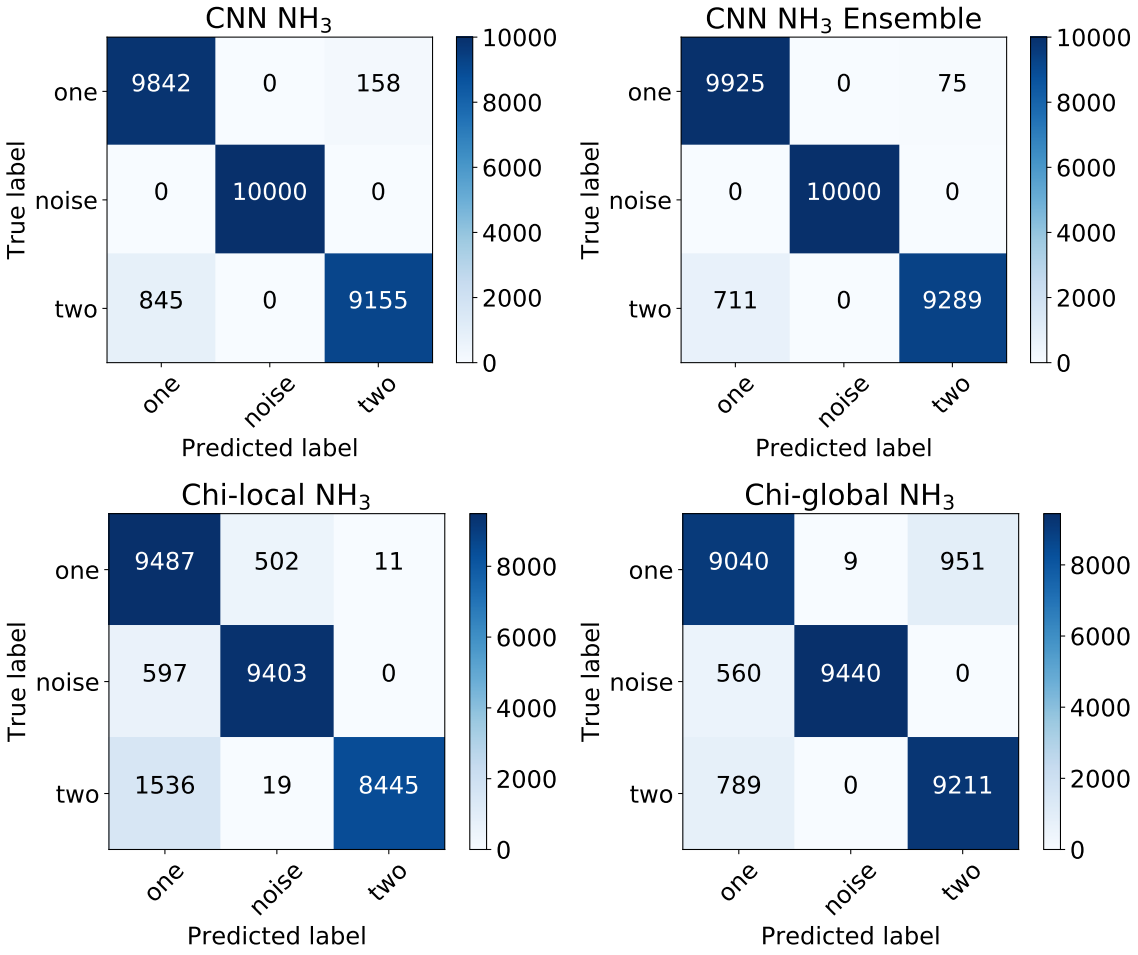

Fig. 4.16 – Confusion matrices for a validation set of 30,000 synthetic NH_3 (1,1) spectra (10,000 in each class) classified by a single CNN (top left), an averaged ensemble of six CNNs (top right), traditional χ^2-minimization on the "local" view spectrum (bottom left), and traditional χ^2-minimization on the "global" view spectrum (bottom right). The "noise" class for the χ^2-minimization panels was selected based on a SNR threshold of 4.

4.6.3 Testing on Real NH_3 (1,1) Observations

To demonstrate that CLOVER can accurately predict the class of real ammonia spectra, we utilize two NH_3 (1,1) cubes observed by the KFPA Examinations of Young STellar Object Natal Environments (KEYSTONE) survey (PI: James Di Francesco; Keown et al., 2019b). KEYSTONE used the 100m Green Bank Telescope to map ammonia emission across eleven of the nearest giant molecular clouds (0.9 kpc $< d <$ 3 kpc). Here, we use the KEYSTONE observations of two clouds: 1) M17, which has a core of emission (M17SW) with obvious multiple velocity components, and 2) MonR2, which is composed mainly of single velocity component spectra. To match the size of the spectra used to train CLOVER's CNNs, the ammonia cubes are clipped to 1000 channels along the spectral axis.

Following the method described in Section 4.4.3, predictions are made for each pixel using both CLOVER's ensemble CNN and the χ^2-minimization technique. Figures 4.17 and 4.18 show the resulting segmentation maps for M17 and MonR2, respectively. Similar to the results of CLOVER's non-hyperfine classifications, we see clear cases where CLOVER's hyperfine classifications are more robust than the χ^2-minimization technique across all three classes. In particular, CLOVER appears to provide better noise classifications and be more resilient to overfitting the spectra than the χ^2-minimization technique.

There is also evidence that CLOVER is able to identify spectra with more than two-components (e.g., three or more velocity components). For instance, labeled spectrum C in Figure 4.17 shows a location in M17 that clearly has three velocity components. Even without including three-component spectra in the training set, CLOVER is able to correctly identify that the spectrum has more than one velocity component.

To test robustly how CLOVER will classify three-component spectra that it receives as input, we perform a three-component classification test similar to the test described in Section 4.4.4. An additional test set of 3,000 synthetic three-component NH_3 (1,1) samples were created by injecting three synthetic spectra into the test cubes by creating models at random from the distributions listed in Section 4.6.1. For these 3000 synthetic three-component samples, CLOVER classifies 2945 ($\sim 98\%$) as "two-component" and 55 ($\sim 2\%$) as "one-component." This result suggests that CLOVER's two-component class can be thought of as "multi-component" (i.e., emission with more than one velocity component), which is similar to the result found for

CLOVER's non-hyperfine classification discussed in Section 4.4.4.

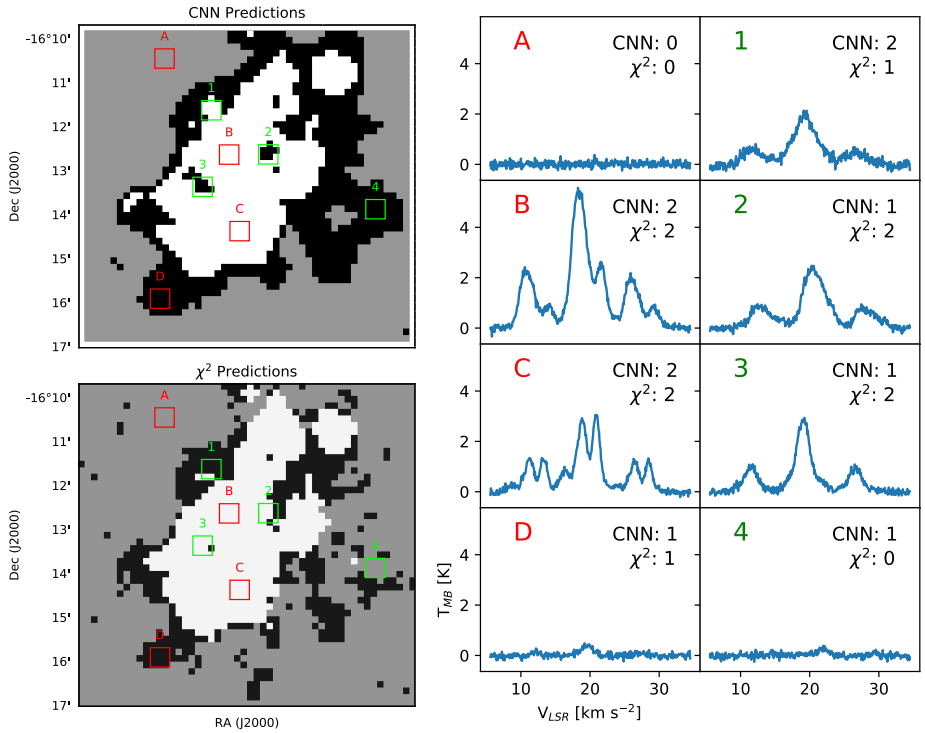

Fig. 4.17 – Left panels: segmentation of a NH_3 (1,1) spectral cube observation of M17 into three classes: single velocity component spectrum (black), multiple velocity component spectrum (white), and noise (grey) using CLOVER's CNN ensemble (top) and traditional χ^2-minimization model fitting (bottom). Right panels: The "global" view spectra extracted from the observed spectral cube at the positions of the 3×3 pixel windows overlaid onto the left panels. Red letters denote positions where CLOVER and the χ^2 technique agree in their class predictions, while the green numbers show positions where they disagree. The spectra in all panels have been clipped around the central three hyperfine groups. The text in the upper right corner of each panel shows the class predicted by CLOVER and the χ^2 technique for that spectrum, where 2=two-component, 1=one-component, and 0=noise.

Furthermore, CLOVER is again remarkably faster at making classifications than the χ^2-minimization technique. CLOVER's predictions for M17 and MonR2 take 82 seconds and 170 seconds, respectively, on a single CPU core. In comparison, the full χ^2-minimization technique requires 3918 seconds for M17 and 8435 seconds for MonR2 with the computations run in parallel on eight CPU cores. This implies CLOVER's classifications provide several orders of magnitude in speed improvements over traditional methods.

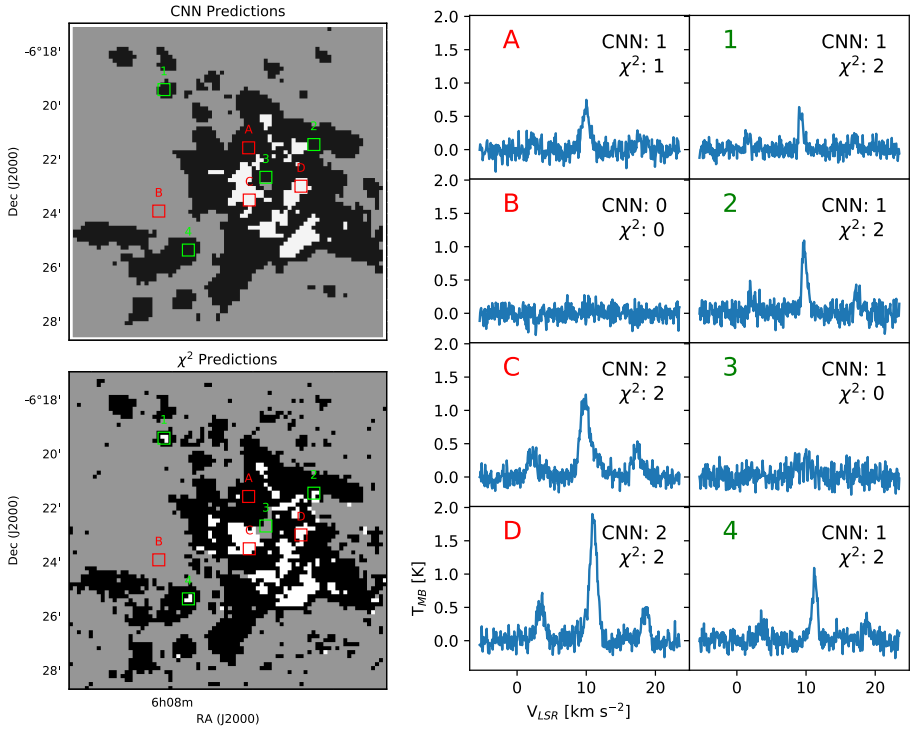

Fig. 4.18 – Same as Figure 4.17 for MonR2.

4.7 Predicting NH_3 (1,1) Kinematics

Hyperfine splitting also poses a challenge for predicting the kinematics of spectra when using CLOVER. The predictions from CLOVER's regression CNN discussed in Section 4.5, for example, become unreliable for transitions with hyperfine splitting since the emission is implicitly split across multiple lines with distinct centroid velocities. To overcome this issue, we train an additional regression CNN to predict the velocity centroids, velocity dispersions, and peak intensities for NH_3 (1,1) spectra with two velocity components. A training set of 300,000 synthetic two-component NH_3 (1,1) spectra was generated as described in Section 4.6.1. The labels for the training set were a six-number array including the values of V_{off}, σ_{tot}, and the peak intensity (T_{peak}) for both of the velocity components.

The performance of the trained network on a validation set of 30,000 additional synthetic spectra is shown in Figure 4.19. The mean absolute errors for the validation set are ~ 0.002 for centroid velocity, ~ 0.6 for velocity dispersion, and ~ 0.06 for peak intensity. Since these MAEs have been calculated after normalizing the velocity centroids, dispersions, and peak intensities in the same way as those for the non-hyperfine

regression CNN, the MAEs between the two models can be directly compared. Although the MAEs for velocity dispersion are smaller for the non-hyperfine regression CNN ($\sim$ 0.4), its centroid velocity and peak intensity MAEs are larger ($\sim$ 0.01 and $\sim$ 0.064). These differences are to be expected since the hyperfine training set was generated using slightly different parameter distributions than the non-hyperfine training set.

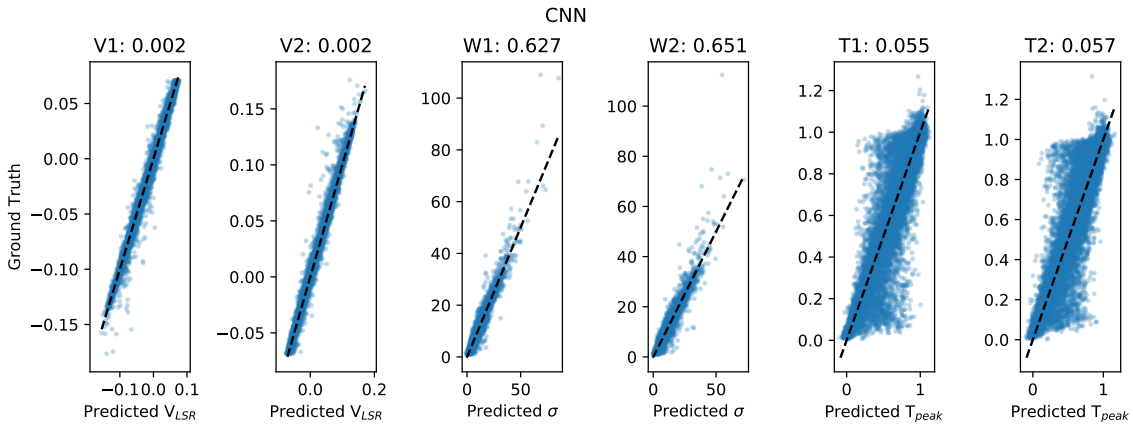

Fig. 4.19 – Velocity centroid (two left panels), dispersion (two middle panels), and peak intensity (two right panels) predictions by CLOVER's trained NH_3 (1,1) regression CNN versus the "ground-truth" for the low-velocity component (V1, W1, T1) and high-velocity component (V2, W2, T2) for the 30,000 two-component spectra in the synthetic test set. The dashed lines show a one-to-one correspondence. In all panels, the centroid velocities are normalized between -1 km s^{-1} and 1 km s^{-1}. The velocity dispersion units are the number of channels in the spectrum. The subtitle above each panel shows the mean absolute error for that parameter.

The horizontal flaring at large and small T_{peak} values seen in Figure 4.19 also indicates that the hyperfine peak intensity predictions have a slight degeneracy at large and small values. This effect is also likely related to the way in which the hyperfine training set was generated. For example, the non-hyperfine training set generator ensured that the velocity components for two-component samples were separated by at least $1.5 \times \sigma_{max}$ (see Section 4.2.1). For the hyperfine training set, we instead chose the minimum centroid separation to be $1.0 \times \sigma_{max}$ to probe closer velocity component separations. This alteration leads to a slightly higher fraction of the hyperfine samples being indistinguishable from single velocity component spectra. A degeneracy in the peak intensity predictions for those samples is created because it becomes unclear which of the blended components is brighter.

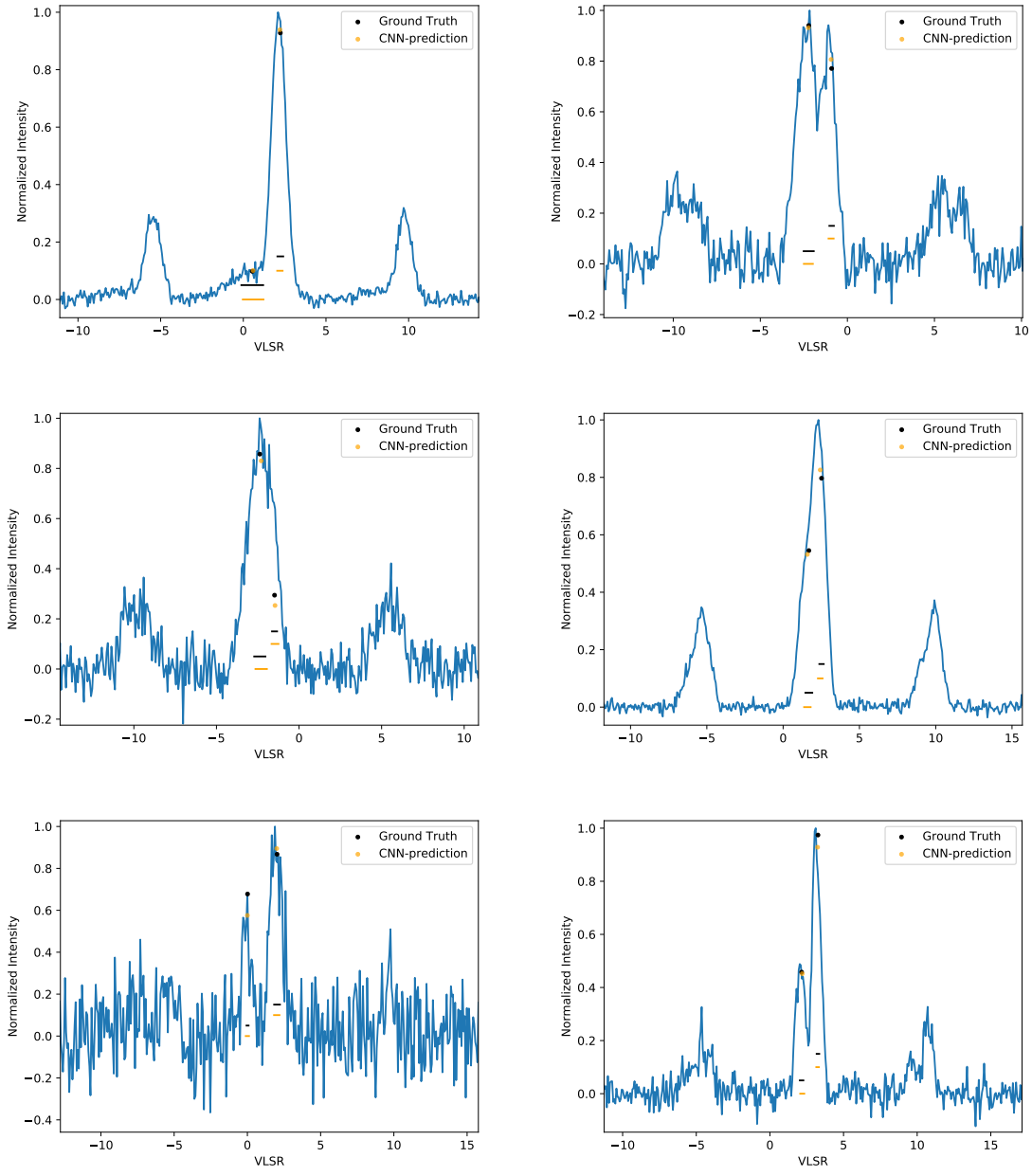

Fig. 4.20 – Example predictions by CLOVER on previously unseen spectra from the hyperfine synthetic test set. The horizontal bars show the positions of each velocity component's centroid and dispersion for the "ground-truth" (black) and CLOVER predictions (orange) overlaid onto the "local" spectrum. The black and orange dots show the peak intensity for each velocity component for the ground-truth and CLOVER predictions, respectively. In all panels, the central three hyperfine groups are shown.

Figure 4.20 displays CLOVER's centroid, dispersion, and peak intensity predictions overlaid onto the local spectra for six unseen samples included in the synthetic test set. In most cases, CLOVER's predictions are well-matched to the ground-truth values used to create the samples. Even for blended components (middle panels in Figure 4.20) and those with shallow wings (top left panel in Figure 4.20), CLOVER can accurately recover the underlying kinematics.

These tests prove that CNNs can be trained to not only classify spectra with hyperfine structure and multiple velocity components, but also predict with high accuracy the kinematics of the emitting gas. Moreover, this method can easily be adjusted to incorporate other molecular tracers of interest that exhibit hyperfine splitting (e.g., HCN, N_2H^+, etc.). Although the current implementation of CLOVER considers only the one- versus two-component classes of emission, the method could also be generalized to emission with three- or more velocity components.

4.8 Improving Virial Analyses with CLOVER

CLOVER's two-component spectral classifications and kinematics predictions can be used to improve existing analyses that neglect the presence of multiple velocity components. For instance, many virial stability analyses of star-forming structures rely on velocity dispersions measured from models that assume a single velocity component along the line of sight (e.g., Keown et al., 2017; Kirk et al., 2017; Chen et al., 2019a; Kerr et al., 2019). When multiple velocity components are present along the line of sight, however, models assuming a single velocity component typically fit the observed spectrum with a much wider velocity dispersion than would be obtained by using a model with multiple velocity components. Since the virial parameter is proportional to σ^2, the wider velocity dispersions measured from one-component fits have a significant impact on the stability measurement of a given structure.

To demonstrate CLOVER's ability to improve virial analyses, we use two-component velocity dispersions measured by CLOVER to update the virial analysis of M17SW by Keown et al. (2019b). The Keown et al. analysis used the KEYSTONE NH_3 (1,1) integrated intensity maps of M17 to identify dense gas clumps, which are shown as black contours in Figure 4.21. Virial parameters were calculated by Keown et al. for each structure using a velocity dispersion map (top right panel of Figure 4.21) measured from an ammonia model assuming a single velocity component along the line of sight. The velocity dispersion maps predicted by CLOVER for pixels identified as

two-component in M17SW are shown in the bottom row of Figure 4.21. Figure 4.21 clearly shows that the one-component fit produces larger velocity dispersions than the two velocity components identified by CLOVER.

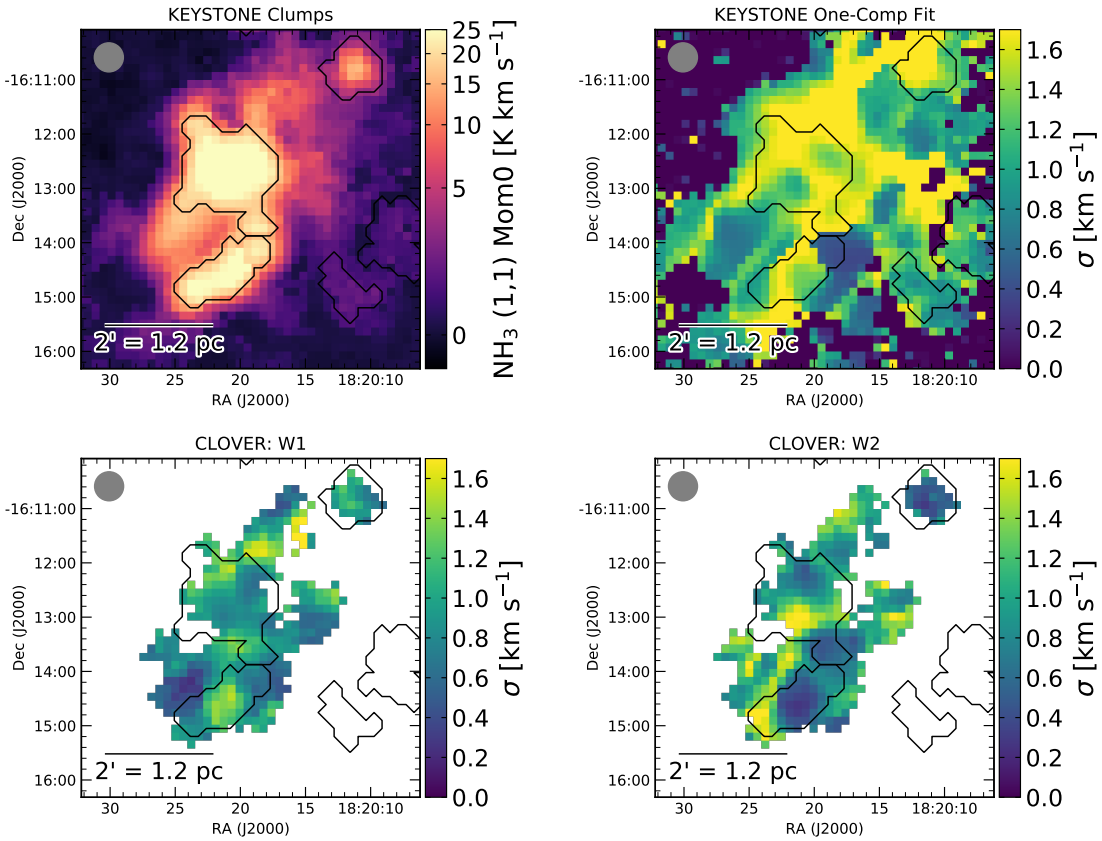

Fig. 4.21 – Top left: NH_3 (1,1) integrated intensity map of the M17SW region observed by KEYSTONE with dendrogram-identified clumps overlaid as black contours (Keown et al., 2019b). Top right: KEYSTONE velocity dispersion measurements from modeling the NH_3 (1,1) emission with one velocity component. Bottom row: Velocity dispersion measured by CLOVER for pixels classified as "two-component."

Three of the clumps identified by Keown et al. fall on pixels identified as two-component by CLOVER. Here, we re-calculate the virial parameters for these three structures using the same mass, average temperature, and radius measured by Keown et al., but replace the average velocity dispersion with values measured from the CLOVER velocity dispersion maps. Although this approach neglects mass and/or size differences in the multiple structures along the line of sight, it serves as a test to see how much the two-component kinematics might affect their calculated virial parameters.

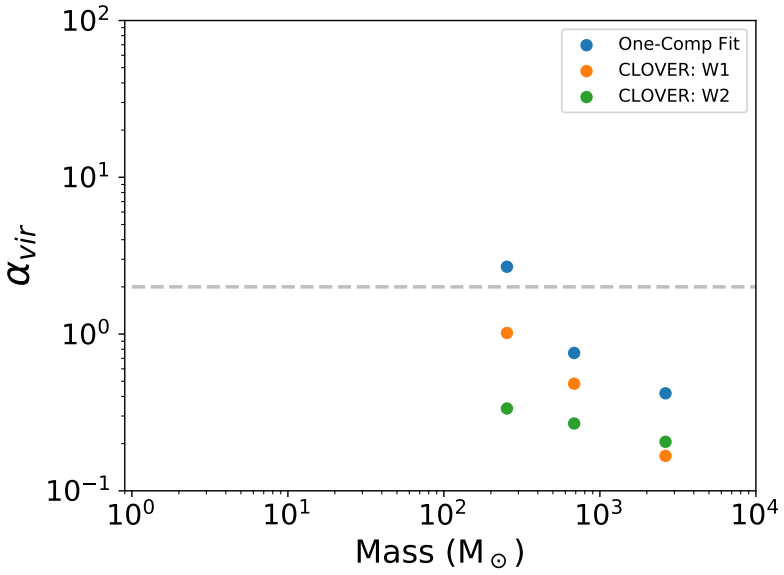

Fig. 4.22 – Virial parameter versus mass for the three dendrogram-identified clumps in Figure 4.21 falling on pixels classified as "two-component" by CLOVER. Blue shows the virial parameters derived by Keown et al. (2019b) using the KEYSTONE velocity dispersions from a one-component fit to the NH_3 (1,1). Orange and green show the virial parameters derived when using the CLOVER velocity dispersion predictions for each identified velocity component (W1 and W2). Sources falling below the grey dashed line are gravitationally bound when neglecting magnetic fields and external pressure.

Following the method described in Keown et al., each structure's average velocity dispersion is calculated as the average of all pixels falling within its 2D mask shown in Figure 4.21. The average is weighted by the integrated intensity map such that $\sigma_{v,avg} = w_1\sigma_1 + w_2\sigma_2 \cdots w_n\sigma_n$, where w_n and σ_n are the fraction of the source's integrated intensity and value of the velocity dispersion, respectively, for pixel n. Since CLOVER predicts two velocity dispersions for every pixel (one for each velocity component), we calculate two virial parameters for each structure based on the weighted average velocity dispersion measured in each map. Figure 4.22 compares these new virial parameters with the original values presented in Keown et al. (2019b).

As expected, the virial parameters using the CLOVER velocity dispersions are lower than the Keown et al. measurements. Specifically, the CLOVER-measured virial parameters are a factor of $1.5 - 8$ times lower depending on the structure and which velocity component map is used. The lowest mass structure also moves from the upper "gravitationally unbound" half of the plot to the lower "gravitationally

bound" half when using the CLOVER measurements. Although only three structures are analyzed here, this example shows the usefulness of CLOVER for virial analyses that include structures with multiple velocity components along the line of sight.

4.9 Summary

We present a new method for identifying emission line spectra with two velocity components by training an ensemble of convolutional neural networks (CNNs) using synthetic spectral cubes. The networks predict the class of 3×3 pixel windows, utilizing the spatial information of pixels adjacent to the central pixel to make a prediction. The trained network ensemble has classification accuracies of $99.92 \pm 0.02\%$, 100%, and $96.72 \pm 0.18\%$ for one-component, noise-only, and two-component synthetic spectral windows. This performance is a significant improvement over traditional line fitting approaches that do not consider the spatial information in adjacent pixels. The ensemble CNN's high classification performance was also demonstrated on real spectral cubes, which revealed that the ensemble CNN is able to segment accurately real observations into each of the three training set classes. Moreover, the speed with which the ensemble CNN makes its classifications was measured to be over an order of magnitude faster than a traditional line fitting approach.

A regression CNN is also trained to extract kinematics directly from the spectra identified as two-component class members by the ensemble CNN classifications. We show that the regression CNN has high prediction accuracy for two-component spectra that exhibit large centroid velocity separations and those that are blended. The combination of the ensemble and regression CNNs provides a quick way to measure accurately kinematics from two-component spectra. Named Convnet Line-fitting Of Velocities in Emission-line Regions (CLOVER), this combination unlocks a new method to analyze large spectral cubes of emission lines from star-forming molecular clouds.

After testing CLOVER on observations of four different molecular emission lines from five distinct star-forming regions observed by three separate observatories, it is clear that its predictions can be generalized to many data sets. In particular, we show that the method can be applied to transitions with hyperfine splitting. The versatility and speed of CLOVER's predictions make it an attractive option for signal versus noise segmentation and line fitting for large-scale spectral mapping surveys. The higher accuracy kinematics measurements provided by CLOVER also make it a

useful tool for improving virial stability analyses of star-forming structures. CLOVER is publicly available as a Python package called `astroclover` at https://github.com/jakeown/astroclover/.

Acknowledgments

We would like to thank Stella Offner for helpful recommendations regarding CLOVER's network architecture and training set. We also thank the anonymous referee for their thoughtful comments that have undoubtedly improved our manuscript. JK, JDF, ER, and MCC acknowledge the financial support of a Discovery Grant from NSERC of Canada. The Green Bank Observatory is a facility of the National Science Foundation operated under cooperative agreement by Associated Universities, Inc. The James Clerk Maxwell Telescope is operated by the East Asian Observatory on behalf of The National Astronomical Observatory of Japan; Academia Sinica Institute of Astronomy and Astrophysics; the Korea Astronomy and Space Science Institute; Center for Astronomical Mega-Science (as well as the National Key R&D Program of China with No. 2017YFA0402700). Additional funding support is provided by the Science and Technology Facilities Council of the United Kingdom and participating universities in the United Kingdom and Canada. This research made use of Astropy (http://www.astropy.org), a community-developed core Python package for Astronomy (Astropy Collaboration et al., 2013), pyspeckit (https://pyspeckit.readthedocs.io/en/latest/), a Python spectroscopic analysis and reduction toolkit (Ginsburg & Mirocha, 2011), and Keras, a Python API for neural networks (Chollet et al., 2015).

4.10 Appendix

4.10.1 Installing and Using CLOVER

CLOVER is publicly available for use as a Python package called `astroclover`. Here, we provide a brief description of the installation and usage instructions for the package.

Users must first ensure that they have Python 3 and all required packages installed. This can easily be done by installing the `Anaconda` Python package manager at https://www.anaconda.com/distribution/, which has many of `astroclover's` package dependencies pre-installed. `Anaconda` version 4.6.11 or later is recommended

for `astroclover`, but other `Anaconda` versions have not been tested.

Once `Anaconda` is installed, users can run the following commands in a Linux or Mac terminal to setup a new environment and install the remaining packages required for `astroclover`:

- conda create −n clover_env python=3.6 anaconda
- conda activate clover_env
- pip install tensorflow==1.8.0 keras==2.2.0 spectral_cube

The first two commands will setup an `Anaconda` virtual environment named `clover_env`, which must be entered when running `astroclover` by running the `conda activate clover_env` command. The last command installs `tensorflow` version 1.8.0, `keras` version 2.2.0, and `spectral_cube`, which are the CLOVER package dependencies not included by default in `Anaconda`. Although Python version 3.6 is recommended, `astroclover` has also been tested on Python 2.7 for users that wish to use Python version 2.

After successfully setting up the `Anaconda` environment, users can clone or download `astroclover` at https://github.com/jakeown/astroclover. This will create a new directory called *astroclover* at the download location. Users must enter this directory and run the following command from their `Anaconda` environment:

- python download_models.py

which will download the trained convolutional neural networks that CLOVER uses from a remote directory into the user's local *astroclover* directory. The 14 files are $\sim$ 12 GB in total.

Once the neural network files have been downloaded, users must ensure the spectral cube they input into CLOVER is formatted properly. CLOVER's predictions require FITS data cubes with position-position-spectral axes. A spectral axis of 500 channels is required for Gaussian emission lines and 1000 channels for NH_3 (1,1). If the cube a user inputs into CLOVER is smaller than those sizes, CLOVER will add random noise channels to each end of the spectral axis up to the required size. If the input cube's spectral axis is larger than the required input size, CLOVER will clip channels from each end of the spectral axis until the required size is obtained.

It is also recommended that the centroids of the emission lines in an input cube be located within the central $\sim$ 275 channels for Gaussian emission lines and the

central $\sim$ 140 channels for NH_3 (1,1). These bounds are set by the range of possible centroids used to train CLOVER. If a cube has large centroid velocity gradients that cause some of the emission lines to fall outside these bounds, it is recommended that users split their cube into sub-cubes so that all emission is within the aforementioned channel bounds.

To run CLOVER on a prepared data cube, simply use the `predict(f=cube.fits)` function in the `clover.py` script. If the cube is NH_3 (1,1), add `nh3=True` in the call to `predict()`. For example, if the user is predicting on a NH_3 (1,1) cube using an iPython session within the *astroclover* directory, they would use the following commands:

- import clover
- clover.predict(f=your_nh3_cube.fits, nh3=True)

The classification step uses an ensemble of six independently trained CNNs to make the final class prediction. These six predictions can be done in parallel by specifying the number of desired parallel processes. For example, to run all six predictions at once, use `predict(f=your_nh3_cube.fits, nproc=6)`.

CLOVER will output its classification map and parameter predictions as individual FITS files. In total, up to eight files are generated:

1. input_name +'_clover.fits' - cube after the spectral axis has been corrected (not generated if input cube already has proper spectral length)
2. input_name +'_class.fits' - predicted class of each pixel (2=two-component, 1=noise, 0=one-component)
3. input_name +'_vlsr1.fits' - predicted centroid velocity of component with lowest centroid
4. input_name +'_vlsr2.fits' - predicted centroid velocity of component with highest centroid
5. input_name +'_sig1.fits' - predicted velocity dispersion of component with lowest centroid
6. input_name +'_sig2.fits' - predicted velocity dispersion of component with highest centroid

7. input_name +'_tpeak1.fits' - predicted peak intensity of component with lowest centroid

8. input_name +'_tpeak2.fits' - predicted peak intensity of component with highest centroid

where input_name is the name of the FITS file input into CLOVER.

Please refer to https://github.com/jakeown/astroclover for the most up-to-date install and usage instructions since new features may be developed in the future.

Chapter 5

Conclusions

A new era of detailed virial stability analyses of star-forming structures has been unlocked thanks to recent large-scale spectroscopic surveys like GAS and KEYSTONE. These surveys have mapped the ammonia emission from many nearby molecular clouds, which provides measurements of both the temperature and kinematics of each cloud's dense gas. With these data in hand, it has finally become possible to determine if the cores and clumps observed by *Herschel* in dust continuum observations are truly gravitationally bound and are en-route to forming new stars. This dissertation has utilized the GAS, KEYSTONE, and *Herschel* data sets to analyze the virial stability of nearly 900 dense gas structures across 13 molecular clouds. With that unprecedented sample size, new comparisons of structure stability between clouds became possible. These comparisons, combined with analyses of the environmental factors affecting each cloud, have revealed important insights into the nature of how stars form in both low-mass and high-mass clouds.

In addition, the newly acquired high-resolution spectroscopic information has revealed that emission with multiple velocity components is widespread in some star-forming regions. Since multi-component emission leads to inaccurate kinematics measurements when using traditional line-fitting techniques, virial stability analyses of those regions must account properly for multiple velocity components along the line of sight. To meet this need, a multiple velocity component line-fitting method named CLOVER was also developed as part of this dissertation.

The following sections outline the contributions this dissertation has made to the field of star formation.

5.1 Virial Stability in Low- and High-mass Clouds

As was discussed in Chapter 2, this dissertation has shown that cores identified in dust continuum observations of nearby clouds like Cepheus-L1251 may not all be gravitationally bound structures. Rather, many cores are held together by the external pressure applied upon them by the surrounding molecular cloud. This pressure support may be enough to prevent the cores from dissipating back into the ambient molecular cloud. In addition, this pressure-confinement might allow the cores time to accrete mass from their surroundings and eventually become gravitationally bound, ultimately undergoing the gravitational collapse required to form new stars. Conversely, dense gas structures identified directly from ammonia observations in nearby clouds appear to be gravitationally dominated.

These results directly address the questions related to the CMF/IMF relationship posed in Section 1.7. For instance, the cores typically included in core mass functions from dust continuum observations may not all be gravitationally bound structures. Instead, core mass functions should be assembled using cores identified from dense gas tracers like ammonia, which is predominately tracing gravitationally bound structures. Building CMFs in such a manner will likely improve their reliability, which may clarify whether or not there is indeed a relationship between the CMF and IMF.

Furthermore, the virial analyses performed in this dissertation highlighted the uncertainties in virial parameter calculations introduced by different density profile assumptions, structure identification algorithms, mass estimation methods, and radius estimation methods. Self-consistent virial stability analyses across different star-forming regions are, therefore, necessary to understand how virial parameters vary between different clouds and how the local environment of the observed structures might impact their stability.

With those consistency considerations in mind, Chapter 3 utilized a self-consistent stability analysis of dense gas clumps in twelve of the closest GMCs. That analysis revealed that GMCs tend to have both bound and unbound clumps as traced by ammonia. Specifically, $\sim 40\%$ of the clumps identified are unbound by gravity alone. This result is in contrast to our results from Cepheus-L1251, which showed that nearly all ammonia-identified cores are bound by gravity alone. Such a descrepancy suggests two possibilities: 1) The clumps observed at farther distances and with lower spatial resolution contain unresolved cores that are indeed bound. Testing this scenario would require higher resolution follow-up observations of the KEYSTONE clouds

with, e.g., the Jansky Very Large Array (see Section 5.3 for further discussion of future KEYSTONE follow-up observations). 2) Alternatively, the discrepancy could indicate that ammonia is more widespread in GMCs than the lower-mass clouds in the solar neighbourhood. Comparisons of the extent of ammonia emission between the GAS and KEYSTONE observations of low- and high-mass star-forming regions, respectively, could determine if such a scenario is true.

The analyses presented in Chapter 3 also addressed the second main goal of this dissertation: understanding the effect filaments have on the stability of dense gas structures. Although the stability of dense gas clumps coincident with filaments appears to be no different than clumps unassociated with filaments, cloud mass may dictate where clumps are likely to form. For instance, comparisons between the KEYSTONE clouds showed that their total dense gas mass is anti-correlated with the fraction of their clumps that were found to be coincident with filaments. This result likely ties into the idea that ammonia is more widespread in higher mass clouds, which allows clumps to form both along and away from filaments. The dense gas clumps in lower mass clouds, however, appear to form only at the locations of filaments because ammonia is not found outside filaments. This restriction in the extent of dense gas would boost the on-filament fraction in low-mass clouds. Conversely, the on-filament fraction in high-mass clouds would be suppressed since they are equally as likely to form clumps away from filaments due to the presence of ammonia (i.e., dense gas) elsewhere in the cloud. Thus, filaments may have a lesser role in the star formation process of high-mass clouds than they do in low-mass clouds.

Although filaments may play a lesser role in the star formation process of high-mass clouds as a whole, filaments appear to play a major role in the formation of stellar clusters and massive stars in GMCs. In particular, many of the KEYSTONE GMCs have gravitationally bound hubs of dense gas where multiple filaments appear to intersect. Not only do these dense gas hubs tend to host multiple protostars, but their masses and sizes are also consistent with clumps that tend to form high-mass stars and clusters. Moreover, the hubs also often host water maser emission, which is sometimes associated with the outflows produced during the formation of massive stars. Since hubs have the characteristics of forming proto-clusters, they support the theory that filament collisions or mass flow along multiple filaments provide the high densities required to form massive stars and clusters.

5.2 Virial Stability Analysis Improvements: CLOVER

The final endeavor of this dissertation was to improve the methods used by the star formation community for virial stability analyses. The CLOVER line-fitting method presented in Chapter 4 achieves that goal. Much like the GAS and KEYSTONE observations have allowed for more detailed virial analyses of star-forming structures, CLOVER provides a deeper level of accuracy in stability measurements. Specifically, CLOVER allows researchers to account correctly for structures with multiple velocity components along the line of sight. As was shown in Chapter 4, multi-component emission can lead to over-estimating the virial parameter by factors of 1.5 to 8 if the emission is assumed to be from one velocity component. In some cases, those over-estimates of virial parameters can make a structure appear gravitationally unbound when it is in fact gravitationally bound after accounting correctly for its multiple velocity components.

In addition, CLOVER is easy to use and its predictions are much more efficient than traditional two-component line-fitting methods. CLOVER's predictions were demonstrated to require less time than traditional methods by over an order of magnitude. This efficiency improvement is necessary for future spectroscopic surveys of molecular clouds with higher resolution and covering larger areas of the sky, which will pose computational difficulties for traditional line-fitting methods.

More importantly, CLOVER provides a foundation from which additional line-fitting innovations can be made in the field of star formation. The benefits provided by neural networks are only just beginning to be explored in astronomy, but they have already proven to be beneficial for a variety of problems. CLOVER, in particular, has already demonstrated it is adaptable to a variety of emission lines and instruments. As such, the prospects are promising for expanding CLOVER to incorporate additional hyperfine emission lines of interest to the star formation community like those from HCN, HNC, and N_2H^+.

5.3 Future Work: Virial Stability Analyses with the VLA

Comparisons between the GMCs included in KEYSTONE and the nearby clouds targeted by GAS require higher resolution follow-up observations of the KEYSTONE clouds. Such observations can be obtained using the Jansky Very Large Array (JVLA), which would provide an angular resolution of $\sim 4''$ at 23 GHz (the rest frequency of NH_3 (1,1)) when in the array's compact D configuration. This resolu-

tion would be sufficient to resolve 0.1 pc width filaments and cores at a distance of 2 kpc (i.e., $4'' \sim 0.04$ pc at 2 kpc). In fact, a 40 hour pilot follow-up observation of the AFGL333 ridge in the W3 GMC was recently completed on the JVLA (PI: J. Keown). Since AFGL333 includes two of the dense gas hubs identified in Chapter 3, it provides a prime initial testbed of the advantages gained by observing the KEYSTONE clouds at higher angular resolutions.

CLOVER can also be utilized alongside the JVLA observations of AFGL333 to showcase further the advantages of using multiple velocity component information in analyses incorporating cloud kinematics. These analyses include not only the virial stability analysis of the dense gas hubs in AFGL333, but also determining whether or not gas is flowing onto those hubs through the surrounding filaments. Such high spatial resolution will also allow us to resolve substructures in the filaments. For instance, Hacar et al. (2013) used $C^{18}O$ emission to find multiple velocity-coherent "bundles" of filaments within the nearby Taurus B213 filament that were observed as a single structure in continuum emission. Additionally, Palmeirim et al. (2013) observed "striations" oriented perpendicular to the Taurus B211/213 filament in dust continuum emission, which they propose may be feeding mass onto the main filament. The AFGL333 GBT+JVLA observations combined with CLOVER finally provide the information necessary to determine if similar mechanisms are prevalent in high-mass star-forming environments.

If the analysis of the AGFL333 JVLA observations is worthwhile, it could serve as motivation to follow-up all the KEYSTONE GMCs at higher angular resolution. Such a large survey could be completed on either the current JVLA or the Next Generation Very Large Array (ngVLA), a proposed replacement of the JVLA that would add 218 $\times$ 18-m dishes. With the ngVLA, however, the number of hours required to complete a KEYSTONE follow-up would decrease by an order of magnitude ($\sim$ 1000 hours if targeting the KEYSTONE ammonia detections; see, e.g., the time estimates provided in Di Francesco et al., 2018). An efficiency improvement of that magnitude would make it much more feasible to embark on a full KEYSTONE follow-up survey.

Appendix A

Continuation of Table 3.4

This appendix provides a continuation of the NH_3 (1,1) Leaves Catalog 1 shown in Table 3.4, which only presented the W3-west catalog. The catalogs for the remaining KEYSTONE clouds are listed below.

Table A.1: W3 NH_3 (1,1) Leaves Catalog 1

ID	RA (deg)	decl. (deg)	PA (deg)	σ_{maj} ($''$)	σ_{min} ($''$)	R_{eff} (pc)	M_{obs} ($M_\odot$)	M_{clip} ($M_\odot$)	T_K (K)	σ_{NH_3} (km s^{-1})	V_{NH_3} (km s^{-1})	$\log(N_{p-NH_3})$ (cm^{-2})	$\log(N_{H_2})$ (cm^{-2})
0	36.5415	61.0964	185	16.1	7.6	$0.18^{+0.14}_{-0.14}$	7.1	1.1	12.3 ± 4.1	0.19 ± 0.05	-49.2	13.6	21.2
1	36.4968	61.1103	213	26.0	9.4	$0.33^{+0.21}_{-0.13}$	26.5	7.0	12.0 ± 2.8	0.25 ± 0.04	-49.7	13.7	21.3
2	36.4520	61.1305	200	14.4	12.4	$0.28^{+0.05}_{-0.01}$	25.2	6.7	11.0 ± 3.1	0.31 ± 0.05	-50.2	13.7	21.3
3	36.3429	61.1377	104	22.2	9.6	$0.25^{+0.17}_{-0.13}$	17.4	5.0	14.2 ± 4.1	0.58 ± 0.12	-47.5	13.9	21.4
4	36.4152	61.1731	150	16.8	12.0	$0.3^{+0.05}_{-0.05}$	26.2	8.1	12.5 ± 2.4	0.59 ± 0.07	-48.0	13.8	21.4
5	36.4070	61.2240	101	55.6	29.5	$0.79^{+0.67}_{-0.31}$	295.6	149.7	12.5 ± 1.5	0.39 ± 0.03	-47.8	14.0	21.4
6	36.3754	61.1927	137	15.3	6.2	$0.17^{+0.11}_{-0.08}$	8.1	1.2	15.0 ± 3.2	0.75 ± 0.12	-48.7	13.9	21.4
7	36.3567	61.2493	97	25.0	18.2	$0.44^{+0.24}_{-0.14}$	81.9	31.3	12.1 ± 1.8	0.36 ± 0.04	-48.7	13.9	21.4
8	36.3695	61.2742	214	15.7	11.8	$0.24^{+0.12}_{-0.1}$	24.9	4.7	14.9 ± 2.8	0.73 ± 0.1	-48.3	14.0	21.4
9	36.3028	61.3043	137	24.1	13.6	$0.36^{+0.14}_{-0.09}$	40.1	9.2	12.4 ± 2.9	0.24 ± 0.04	-47.2	13.8	21.4
10	36.3714	61.3075	56	12.6	11.2	$0.23^{+0.06}_{-0.09}$	14.3	3.7	13.3 ± 3.4	0.35 ± 0.07	-47.4	13.9	21.4
11	36.4519	61.3472	162	16.3	10.2	$0.26^{+0.08}_{-0.07}$	21.4	6.5	19.0 ± 3.1	0.42 ± 0.07	-50.6	13.9	21.3
12	37.0143	61.3707	140	14.8	7.9	$0.22^{+0.06}_{-0.05}$	25.4	4.5	14.8 ± 3.1	0.95 ± 0.12	-48.5	14.0	21.6
13	37.0152	61.4164	101	18.5	10.7	$0.26^{+0.08}_{-0.12}$	74.0	7.7	15.7 ± 1.0	0.9 ± 0.04	-47.7	14.3	21.7
14	36.9407	61.4235	129	10.5	7.0	$0.16^{+0.02}_{-0.03}$	9.5	1.8	16.0 ± 3.7	0.53 ± 0.1	-48.2	14.3	21.7
15	37.0146	61.4554	96	31.2	12.7	$0.39^{+0.3}_{-0.15}$	333.6	83.4	16.0 ± 0.4	0.65 ± 0.01	-48.6	14.4	21.8
16	37.1458	61.4572	177	15.2	9.7	$0.23^{+0.09}_{-0.06}$	15.7	5.3	23.2 ± 3.6	0.25 ± 0.05	-46.6	13.1	21.6
17	37.0260	61.4890	131	35.7	12.0	$0.4^{+0.29}_{-0.2}$	374.8	80.6	16.1 ± 0.4	0.66 ± 0.01	-48.4	14.4	21.8
18	36.6832	61.4956	151	22.7	15.6	$0.41^{+0.2}_{-0.08}$	66.4	29.1	12.2 ± 1.9	0.4 ± 0.04	-47.5	13.9	21.5
19	36.7455	61.4983	178	25.2	17.5	$0.45^{+0.17}_{-0.11}$	97.3	37.0	13.3 ± 2.1	0.58 ± 0.06	-47.5	13.9	21.5
20	36.9543	61.5194	117	17.2	8.7	$0.2^{+0.08}_{-0.16}$	12.6	1.7	17.4 ± 4.1	0.63 ± 0.13	-50.1	14.2	21.7
21	36.6824	61.5405	111	28.9	18.2	$0.44^{+0.15}_{-0.15}$	60.2	19.0	13.3 ± 3.0	0.34 ± 0.06	-47.6	13.6	21.5
22	37.1072	61.5351	101	20.9	10.7	$0.29^{+0.16}_{-0.09}$	61.6	12.3	18.8 ± 1.4	0.68 ± 0.04	-49.9	13.9	21.6
23	36.9769	61.5363	207	15.4	7.2	$0.17^{+0.08}_{-0.07}$	9.9	0.4	17.2 ± 3.6	0.26 ± 0.06	-50.3	13.9	21.7
24	37.2483	61.5560	152	15.2	11.7	$0.29^{+0.06}_{-0.05}$	24.0	10.5	19.9 ± 2.4	0.43 ± 0.05	-51.3	13.9	21.2
25	36.8599	61.5586	91	14.1	9.9	$0.2^{+0.04}_{-0.11}$	14.2	2.2	15.6 ± 3.1	0.44 ± 0.07	-49.6	13.9	21.6
26	36.8319	61.5727	199	19.5	10.9	$0.29^{+0.09}_{-0.1}$	29.4	5.6	15.9 ± 3.0	0.45 ± 0.07	-49.6	13.6	21.5
27	36.7580	61.5883	184	31.0	13.2	$0.33^{+0.27}_{-0.2}$	33.4	6.9	13.3 ± 3.5	0.27 ± 0.05	-47.0	13.7	21.5
28	36.8128	61.5898	63	10.8	8.1	$0.18^{+0.01}_{-0.07}$	10.7	1.2	16.1 ± 3.8	0.2 ± 0.05	-49.4	13.6	21.5
29	36.7663	61.6091	145	16.6	5.2	$0.17^{+0.12}_{-0.07}$	10.4	1.4	14.3 ± 4.0	0.36 ± 0.08	-49.6	14.0	21.5
30	36.6247	61.6225	90	14.5	8.8	$0.22^{+0.05}_{-0.09}$	12.5	1.6	11.7 ± 3.2	0.35 ± 0.06	-46.0	13.9	21.4
31	36.6671	61.6776	64	28.5	13.4	$0.36^{+0.23}_{-0.21}$	47.3	15.0	15.8 ± 3.3	0.54 ± 0.09	-46.9	13.4	21.4
32	36.7546	61.8260	119	20.8	13.3	$0.3^{+0.15}_{-0.16}$	34.7	7.7	17.5 ± 3.0	0.7 ± 0.09	-47.7	14.1	21.5
33	36.0531	61.8251	93	13.9	11.2	$0.26^{+0.06}_{-0.05}$	13.3	5.0	11.9 ± 2.5	0.22 ± 0.03	-43.8	13.9	21.2
34	36.7332	61.8404	162	14.1	7.2	$0.18^{+0.06}_{-0.05}$	14.9	3.5	17.0 ± 2.9	0.85 ± 0.12	-47.9	14.0	21.5

Continued on next page

Table A.1 – *Continued from previous page*

ID	RA (deg)	decl. (deg)	PA (deg)	σ_{maj} ($''$)	σ_{min} ($''$)	R_{eff} (pc)	M_{obs} ($M_\odot$)	M_{clip} ($M_\odot$)	T_K (K)	σ_{NH_3} (km s^{-1})	V_{NH_3} (km s^{-1})	$\log(N_{p-NH_3})$ (cm^{-2})	$\log(N_{H_2})$ (cm^{-2})
35	35.8751	61.8562	221	20.8	12.6	$0.36^{+0.12}_{-0.09}$	37.6	16.6	15.4 ± 1.9	0.3 ± 0.04	-43.0	13.8	21.3
36	36.7611	61.8690	67	22.1	15.5	$0.38^{+0.06}_{-0.04}$	273.1	105.3	28.5 ± 0.8	1.13 ± 0.03	-46.7	14.3	21.6
37	35.9743	61.8680	210	15.1	10.5	$0.25^{+0.04}_{-0.07}$	18.4	4.4	13.2 ± 2.9	0.3 ± 0.05	-41.9	13.8	21.3
38	36.7951	61.8824	149	21.1	10.6	$0.28^{+0.19}_{-0.09}$	108.6	32.7	24.0 ± 0.9	1.0 ± 0.03	-48.6	14.3	21.6
39	35.8095	61.8925	83	15.3	8.9	$0.2^{+0.08}_{-0.16}$	8.2	1.9	14.7 ± 4.2	0.25 ± 0.06	-42.9	13.8	21.3
40	36.7496	61.9087	78	27.2	9.9	$0.33^{+0.24}_{-0.12}$	64.4	21.0	19.3 ± 1.6	0.46 ± 0.04	-45.1	13.9	21.6
41	34.5379	61.9100	189	29.4	20.8	$0.55^{+0.27}_{-0.18}$	123.0	71.4	12.8 ± 1.2	0.33 ± 0.02	-41.9	14.3	21.3
42	35.8087	61.9139	225	13.3	9.8	$0.24^{+0.03}_{-0.02}$	16.5	2.6	14.0 ± 1.9	0.34 ± 0.04	-43.5	14.1	21.4
43	34.6511	61.9054	203	13.2	5.7	$0.17^{+0.07}_{-0.04}$	19.8	3.9	12.1 ± 0.6	0.31 ± 0.01	-43.2	14.4	21.3
44	34.6179	61.9053	153	10.5	7.3	$0.17^{+0.01}_{-0.03}$	21.1	4.4	12.5 ± 0.6	0.33 ± 0.01	-43.0	14.3	21.3
45	36.8435	61.9302	169	25.0	20.2	$0.39^{+0.18}_{-0.26}$	61.4	17.1	20.5 ± 3.1	0.47 ± 0.07	-48.5	13.6	21.5
46	36.3685	61.9374	73	25.1	13.7	$0.39^{+0.19}_{-0.13}$	57.3	28.4	18.3 ± 2.0	0.32 ± 0.04	-43.1	13.8	21.3
47	35.8053	61.9307	62	12.0	9.6	$0.2^{+0.04}_{-0.07}$	17.0	2.5	14.4 ± 2.6	0.75 ± 0.09	-42.9	14.3	21.4
48	35.8327	61.9406	141	15.6	8.7	$0.24^{+0.05}_{-0.03}$	24.9	4.3	13.5 ± 1.9	0.34 ± 0.04	-42.1	14.2	21.4
49	36.8202	61.9505	100	18.7	16.8	$0.3^{+0.11}_{-0.24}$	38.2	9.2	19.9 ± 3.2	0.68 ± 0.1	-48.1	14.0	21.5
50	35.7930	61.9571	77	14.6	10.5	$0.27^{+0.07}_{-0.04}$	22.6	4.1	12.0 ± 1.8	0.35 ± 0.04	-43.6	14.3	21.4
51	36.7123	61.9662	142	14.5	11.1	$0.28^{+0.1}_{-0.03}$	34.9	16.9	23.2 ± 2.8	0.62 ± 0.07	-44.2	13.7	21.5
52	36.4833	61.9684	143	12.2	9.0	$0.22^{+0.05}_{-0.02}$	13.0	3.8	20.3 ± 2.8	0.55 ± 0.07	-37.5	13.9	21.3
53	36.7786	61.9715	81	12.6	5.8	$0.17^{+0.11}_{-0.05}$	9.4	1.0	16.7 ± 3.5	0.27 ± 0.05	-46.9	13.7	21.4
54	35.7822	61.9754	88	12.2	9.7	$0.23^{+0.06}_{-0.02}$	20.6	3.2	14.9 ± 2.2	0.31 ± 0.04	-43.3	13.9	21.4
55	35.7194	61.9775	139	10.4	9.0	$0.2^{+0.0}_{-0.01}$	11.7	2.1	15.6 ± 2.7	0.23 ± 0.04	-43.4	13.7	21.3
56	35.6635	61.9823	48	11.9	7.6	$0.19^{+0.02}_{-0.05}$	10.3	1.0	12.7 ± 3.2	0.3 ± 0.06	-42.3	14.1	21.3
57	35.9207	61.9880	175	11.7	8.6	$0.2^{+0.04}_{-0.04}$	11.6	1.1	15.5 ± 3.1	0.21 ± 0.04	-40.5	14.0	21.3
58	35.7525	61.9911	184	16.9	13.9	$0.35^{+0.06}_{-0.04}$	45.2	14.3	12.4 ± 1.6	0.36 ± 0.03	-43.6	14.2	21.3
59	35.5528	62.0052	59	15.1	11.8	$0.29^{+0.02}_{-0.05}$	21.8	5.5	12.9 ± 2.1	0.22 ± 0.03	-42.9	14.1	21.3
60	35.8011	62.0093	45	11.1	6.0	$0.17^{+0.03}_{-0.07}$	7.4	1.1	18.1 ± 3.7	0.22 ± 0.04	-43.1	14.2	21.3
61	35.4334	62.0133	183	22.8	13.7	$0.43^{+0.15}_{-0.11}$	61.5	31.3	13.2 ± 1.1	0.23 ± 0.02	-43.7	14.2	21.2
62	35.3379	62.0289	68	21.3	13.8	$0.33^{+0.11}_{-0.14}$	34.4	9.5	14.9 ± 2.2	0.23 ± 0.03	-43.3	13.8	21.2
63	35.3035	62.0257	172	14.1	5.3	$0.16^{+0.06}_{-0.07}$	7.4	0.6	11.7 ± 3.5	0.36 ± 0.07	-43.9	13.7	21.2
64	36.5114	62.0431	82	10.4	8.6	$0.18^{+0.02}_{-0.05}$	9.1	2.2	19.8 ± 3.9	0.58 ± 0.1	-38.3	14.0	21.5
65	36.1253	62.0582	199	17.4	10.8	$0.29^{+0.16}_{-0.08}$	23.5	10.7	16.2 ± 2.5	0.41 ± 0.05	-39.7	14.2	21.3
66	36.5332	62.0660	141	28.8	10.3	$0.29^{+0.25}_{-0.22}$	27.0	6.0	17.6 ± 3.1	0.62 ± 0.09	-39.0	14.0	21.5
67	36.4711	62.0714	196	21.4	16.8	$0.48^{+0.13}_{-0.1}$	147.7	94.3	22.0 ± 1.1	0.71 ± 0.03	-38.7	14.2	21.5
68	36.0825	62.0695	188	13.0	7.6	$0.2^{+0.07}_{-0.05}$	7.2	2.4	15.7 ± 2.8	0.22 ± 0.04	-40.4	14.0	21.3
69	36.6070	62.0885	121	50.3	18.6	$0.65^{+0.44}_{-0.33}$	194.5	110.3	19.8 ± 2.2	0.65 ± 0.06	-39.3	13.7	21.5
70	36.0297	62.0763	119	12.2	10.7	$0.24^{+0.03}_{-0.03}$	11.0	4.6	15.1 ± 2.6	0.26 ± 0.04	-41.0	13.8	21.2
71	36.2424	62.0819	152	28.3	12.3	$0.39^{+0.32}_{-0.14}$	62.1	27.3	15.3 ± 1.5	0.39 ± 0.03	-39.6	14.0	21.4
72	36.2950	62.0867	179	16.7	12.8	$0.26^{+0.07}_{-0.13}$	23.1	4.9	17.4 ± 2.5	0.43 ± 0.06	-40.0	13.5	21.5
73	36.4663	62.1018	79	23.5	16.4	$0.36^{+0.19}_{-0.13}$	44.3	20.9	27.4 ± 4.5	0.75 ± 0.11	-38.6	13.9	21.5
74	36.3712	62.0998	155	18.2	16.5	$0.39^{+0.08}_{-0.12}$	276.9	237.4	36.0 ± 1.2	1.11 ± 0.03	-42.5	14.2	21.5
75	36.3907	62.1127	56	11.5	5.8	$0.16^{+0.06}_{-0.04}$	18.5	9.5	34.6 ± 3.3	0.64 ± 0.06	-45.9	13.6	21.5
76	36.4645	62.1372	75	14.1	9.7	$0.25^{+0.06}_{-0.06}$	21.3	7.7	16.6 ± 2.3	0.34 ± 0.04	-38.1	14.2	21.5
77	36.5105	62.1454	90	25.7	21.1	$0.48^{+0.23}_{-0.2}$	111.7	48.2	20.5 ± 2.4	0.61 ± 0.06	-39.7	13.9	21.5
78	36.6952	62.1448	170	10.9	6.5	$0.17^{+0.02}_{-0.01}$	7.6	0.7	16.4 ± 2.8	0.57 ± 0.08	-38.4	13.9	21.3
79	36.4921	62.1713	200	18.9	11.0	$0.26^{+0.1}_{-0.17}$	24.6	5.2	16.8 ± 3.1	0.52 ± 0.08	-41.7	14.2	21.5
80	36.5694	62.1907	134	24.7	11.8	$0.29^{+0.19}_{-0.22}$	31.8	9.3	19.1 ± 2.9	0.57 ± 0.08	-40.7	13.6	21.4
81	36.5571	62.2009	138	14.8	8.2	$0.19^{+0.1}_{-0.07}$	15.6	1.6	18.1 ± 4.8	0.93 ± 0.2	-41.3	13.9	21.4
82	36.5664	62.2188	157	21.8	7.9	$0.23^{+0.19}_{-0.15}$	17.2	2.9	15.3 ± 3.5	0.62 ± 0.1	-42.0	14.2	21.3
83	36.6769	62.2462	89	13.6	9.5	$0.2^{+0.1}_{-0.06}$	7.2	0.6	17.6 ± 3.6	0.38 ± 0.07	-43.0	14.1	21.2

Table A.2: MonR2 NH_3 (1,1) Leaves Catalog 1

ID	RA (deg)	decl. (deg)	PA (deg)	σ_{maj} ($''$)	σ_{min} ($''$)	R_{eff} (pc)	M_{obs} ($M_\odot$)	M_{clip} ($M_\odot$)	T_K (K)	σ_{NH_3} (km s^{-1})	V_{NH_3} (km s^{-1})	$\log(N_{p-NH_3})$ (cm^{-2})	$\log(N_{H_2})$ (cm^{-2})
0	91.8054	-6.4832	122	30.7	12.0	$0.16^{+0.11}_{-0.07}$	6.4	1.9	12.3 ± 2.7	0.18 ± 0.03	10.0	13.8	21.4
1	91.7917	-6.4735	190	31.1	13.9	$0.13^{+0.12}_{-0.1}$	3.6	0.6	14.5 ± 4.2	0.42 ± 0.1	11.2	14.1	21.5
2	92.0198	-6.4617	219	26.4	17.1	$0.18^{+0.1}_{-0.06}$	8.9	3.2	13.7 ± 3.0	0.19 ± 0.03	10.5	13.3	21.5
3	91.9051	-6.4493	191	32.1	19.4	$0.2^{+0.14}_{-0.1}$	9.6	2.6	16.9 ± 3.9	0.53 ± 0.1	9.6	14.0	21.6
4	91.8010	-6.4466	168	43.4	22.7	$0.29^{+0.17}_{-0.2}$	26.8	9.3	12.1 ± 1.6	0.2 ± 0.02	11.9	13.9	21.5

Continued on next page

Table A.2 – *Continued from previous page*

ID	RA (deg)	decl. (deg)	PA (deg)	σ_{maj} ($''$)	σ_{min} ($''$)	R_{eff} (pc)	M_{obs} ($M_\odot$)	M_{clip} ($M_\odot$)	T_K (K)	σ_{NH_3} (km s^{-1})	V_{NH_3} (km s^{-1})	$\log(N_{p-NH_3})$ (cm^{-2})	$\log(N_{H_2})$ (cm^{-2})
5	91.9928	-6.4526	192	17.0	13.2	$0.13^{+0.06}_{-0.01}$	5.7	1.3	14.2 ± 2.5	0.16 ± 0.03	10.9	13.6	21.6
6	91.9640	-6.4419	221	22.6	10.7	$0.14^{+0.07}_{-0.06}$	14.0	3.1	15.5 ± 1.6	0.36 ± 0.03	10.8	13.7	21.9
7	92.0189	-6.4322	183	14.9	9.8	$0.1^{+0.05}_{-0.03}$	2.8	0.6	19.4 ± 2.7	0.33 ± 0.05	10.4	13.5	21.6
8	91.9949	-6.4246	211	23.0	13.6	$0.16^{+0.05}_{-0.06}$	12.8	5.4	16.7 ± 2.0	0.34 ± 0.04	11.0	13.5	21.7
9	92.0984	-6.4198	165	27.5	11.4	$0.13^{+0.09}_{-0.1}$	4.2	1.2	17.0 ± 3.0	0.28 ± 0.05	9.7	13.3	21.4
10	92.1238	-6.4213	191	21.7	9.2	$0.12^{+0.05}_{-0.05}$	2.9	1.0	15.7 ± 2.8	0.3 ± 0.05	9.4	13.2	21.3
11	92.2422	-6.4156	168	14.3	9.6	$0.11^{+0.04}_{-0.03}$	NaN	NaN	11.4 ± 2.1	0.12 ± 0.02	9.6	13.9	NaN
12	92.1978	-6.4067	67	24.1	11.9	$0.13^{+0.1}_{-0.09}$	3.2	1.7	13.8 ± 3.8	0.17 ± 0.04	9.3	13.3	21.3
13	91.8567	-6.4151	178	26.9	10.5	$0.15^{+0.13}_{-0.05}$	7.6	1.7	13.9 ± 1.5	0.23 ± 0.03	9.6	14.0	21.6
14	92.0781	-6.4106	54	17.5	8.5	$0.09^{+0.04}_{-0.04}$	1.9	0.4	14.8 ± 3.9	0.24 ± 0.06	10.0	13.7	21.4
15	92.0269	-6.4147	166	10.1	7.8	$0.08^{+0.01}_{-0.01}$	2.7	0.4	15.5 ± 1.9	0.34 ± 0.04	10.6	13.6	21.6
16	91.9512	-6.4166	193	12.1	6.2	$0.08^{+0.03}_{-0.01}$	8.7	1.0	19.0 ± 0.8	0.34 ± 0.02	11.1	14.1	22.2
17	92.0430	-6.4123	177	13.2	8.5	$0.1^{+0.01}_{-0.01}$	4.1	0.8	15.0 ± 1.7	0.32 ± 0.03	10.4	13.7	21.5
18	91.9340	-6.3985	166	37.6	29.1	$0.28^{+0.15}_{-0.1}$	140.9	71.3	24.3 ± 0.7	0.59 ± 0.02	10.6	14.2	22.3
19	91.8941	-6.4071	128	14.2	11.3	$0.11^{+0.0}_{-0.02}$	7.8	1.5	20.4 ± 1.2	0.45 ± 0.03	10.5	13.9	21.9
20	92.1770	-6.3956	157	38.7	14.8	$0.19^{+0.25}_{-0.12}$	9.4	4.8	14.4 ± 3.4	0.34 ± 0.06	8.6	13.7	21.4
21	91.9629	-6.3802	161	27.5	11.1	$0.15^{+0.11}_{-0.05}$	27.7	9.3	23.0 ± 0.9	0.53 ± 0.02	10.7	14.0	22.2
22	91.9509	-6.3704	45	9.5	7.0	$0.07^{+0.0}_{-0.0}$	9.7	1.4	33.5 ± 1.5	0.69 ± 0.03	9.5	13.9	22.2
23	91.9328	-6.3508	137	43.1	19.7	$0.22^{+0.2}_{-0.16}$	59.6	29.2	19.2 ± 0.9	0.35 ± 0.02	9.5	14.0	22.1
24	91.8911	-6.3581	152	10.2	9.3	$0.08^{+0.01}_{-0.01}$	3.5	0.2	18.1 ± 2.3	0.26 ± 0.04	9.8	13.3	21.8
25	91.9795	-6.3531	182	10.7	7.8	$0.08^{+0.0}_{-0.0}$	3.2	0.9	22.2 ± 2.3	0.38 ± 0.04	10.4	13.5	21.8
26	91.9846	-6.3364	159	15.9	12.7	$0.11^{+0.04}_{-0.02}$	4.1	0.9	21.8 ± 3.5	0.3 ± 0.05	10.0	13.6	21.7
27	91.9182	-6.3277	57	13.8	9.2	$0.09^{+0.04}_{-0.02}$	3.0	0.4	13.4 ± 3.3	0.18 ± 0.04	9.4	14.0	21.8
28	92.0024	-6.3232	82	12.1	10.8	$0.1^{+0.02}_{-0.01}$	4.7	0.8	17.6 ± 2.5	0.32 ± 0.05	9.3	13.4	21.6
29	91.9747	-6.3154	205	32.2	10.0	$0.14^{+0.14}_{-0.09}$	5.0	1.2	21.8 ± 3.7	0.29 ± 0.06	10.3	13.4	21.6
30	91.9362	-6.3123	119	25.2	14.0	$0.14^{+0.08}_{-0.07}$	8.7	2.4	18.6 ± 3.5	0.39 ± 0.07	9.8	13.8	21.7
31	92.0036	-6.3061	118	15.4	11.6	$0.12^{+0.03}_{-0.02}$	3.8	1.1	18.3 ± 3.2	0.39 ± 0.07	9.5	13.6	21.5
32	92.0313	-6.3038	157	15.2	12.3	$0.13^{+0.03}_{-0.02}$	4.6	0.9	16.2 ± 2.2	0.19 ± 0.03	8.9	13.8	21.4
33	91.9090	-6.2999	124	18.6	15.5	$0.14^{+0.05}_{-0.07}$	5.5	1.4	15.1 ± 3.0	0.24 ± 0.05	9.6	13.9	21.5
34	92.1094	-6.2932	174	14.0	10.5	$0.1^{+0.03}_{-0.03}$	1.5	0.4	13.1 ± 3.3	0.32 ± 0.07	8.9	13.8	21.1
35	91.9046	-6.2797	124	13.8	8.2	$0.09^{+0.02}_{-0.02}$	2.2	0.4	13.4 ± 4.3	0.21 ± 0.05	10.1	14.0	21.5
36	91.9407	-6.2652	147	13.9	8.9	$0.08^{+0.06}_{-0.04}$	1.9	0.5	16.5 ± 3.7	0.45 ± 0.08	10.8	14.4	21.4
37	91.9304	-6.2614	120	9.1	7.7	$0.08^{+0.0}_{-0.0}$	1.4	0.2	18.7 ± 3.6	0.2 ± 0.04	10.4	13.7	21.4
38	91.9324	-6.1787	187	24.8	19.5	$0.22^{+0.04}_{-0.06}$	18.2	9.6	13.1 ± 1.6	0.22 ± 0.02	10.4	13.8	21.5
39	91.8388	-6.1803	65	13.6	8.9	$0.1^{+0.01}_{-0.01}$	2.0	0.3	11.7 ± 2.8	0.13 ± 0.02	10.9	13.6	21.3
40	91.8578	-6.1582	132	32.3	13.6	$0.21^{+0.12}_{-0.07}$	11.4	4.3	12.3 ± 1.8	0.15 ± 0.02	11.0	13.8	21.4
41	91.8922	-6.1452	191	18.6	13.9	$0.15^{+0.08}_{-0.04}$	5.2	1.4	12.9 ± 2.9	0.13 ± 0.02	10.7	13.7	21.4

Table A.3: MonR1 NH_3 (1,1) Leaves Catalog 1

ID	RA (deg)	decl. (deg)	PA (deg)	σ_{maj} ($''$)	σ_{min} ($''$)	R_{eff} (pc)	M_{obs} ($M_\odot$)	M_{clip} ($M_\odot$)	T_K (K)	σ_{NH_3} (km s^{-1})	V_{NH_3} (km s^{-1})	$\log(N_{p-NH_3})$ (cm^{-2})	$\log(N_{H_2})$ (cm^{-2})
0	98.1463	10.1702	193	27.5	16.0	$0.22^{+0.13}_{-0.05}$	31.5	16.4	11.6 ± 0.7	0.19 ± 0.01	3.0	14.1	21.7
1	98.1130	10.1790	146	13.6	12.1	$0.12^{+0.02}_{-0.01}$	5.0	1.1	9.6 ± 1.6	0.12 ± 0.01	2.8	13.8	21.5
2	98.1653	10.2836	103	15.0	6.3	$0.08^{+0.03}_{-0.03}$	3.1	0.8	10.0 ± 2.6	0.21 ± 0.03	3.7	13.9	21.7
3	98.2036	10.2998	191	15.9	11.7	$0.12^{+0.01}_{-0.03}$	5.8	1.5	11.9 ± 3.0	0.14 ± 0.03	4.0	13.7	21.7
4	98.2801	10.3043	222	14.6	10.6	$0.1^{+0.01}_{-0.05}$	4.1	1.0	17.2 ± 4.1	0.46 ± 0.1	4.6	13.7	21.5
5	98.1659	10.3084	106	16.2	9.1	$0.1^{+0.05}_{-0.05}$	11.1	2.2	11.8 ± 0.9	0.43 ± 0.02	3.2	14.1	22.0
6	98.0466	10.3127	65	13.9	10.6	$0.11^{+0.03}_{-0.02}$	4.9	1.4	11.3 ± 3.2	0.13 ± 0.02	3.9	13.3	21.6
7	98.1325	10.3134	190	22.5	13.1	$0.16^{+0.05}_{-0.04}$	25.4	7.0	10.9 ± 0.8	0.3 ± 0.01	4.0	14.2	22.0
8	98.1705	10.3265	127	16.6	10.0	$0.11^{+0.04}_{-0.02}$	14.6	5.1	12.0 ± 0.8	0.46 ± 0.02	3.2	14.2	22.1
9	98.1923	10.3266	76	12.4	9.3	$0.09^{+0.01}_{-0.01}$	4.2	1.4	9.9 ± 2.7	0.15 ± 0.02	5.8	13.9	21.8
10	98.2816	10.3361	137	19.2	14.0	$0.15^{+0.06}_{-0.03}$	8.7	3.7	12.7 ± 2.5	0.22 ± 0.03	5.7	13.8	21.6
11	98.2637	10.3304	95	13.7	5.7	$0.08^{+0.03}_{-0.04}$	1.9	0.5	13.9 ± 4.0	0.46 ± 0.11	5.5	14.3	21.6
12	98.1460	10.3341	189	21.0	17.2	$0.18^{+0.05}_{-0.02}$	38.3	6.8	11.0 ± 0.9	0.49 ± 0.02	4.9	14.1	22.1
13	98.2529	10.3342	193	14.0	9.2	$0.08^{+0.04}_{-0.03}$	3.0	0.5	14.4 ± 3.6	0.38 ± 0.08	5.2	14.0	21.7
14	98.0824	10.3539	79	23.4	15.0	$0.17^{+0.08}_{-0.06}$	21.8	8.6	13.2 ± 2.0	0.37 ± 0.04	4.2	14.0	21.9
15	98.2299	10.3456	95	13.6	8.0	$0.08^{+0.03}_{-0.04}$	2.9	0.3	14.0 ± 4.3	0.39 ± 0.1	5.3	14.3	21.7
16	98.1065	10.3618	94	23.3	18.0	$0.16^{+0.1}_{-0.08}$	20.2	6.1	11.7 ± 2.8	0.37 ± 0.05	5.2	13.9	22.0

Continued on next page

Table A.3 – *Continued from previous page*

ID	RA (deg)	decl. (deg)	PA (deg)	σ_{maj} ($''$)	σ_{min} ($''$)	R_{eff} (pc)	M_{obs} ($M_\odot$)	M_{clip} ($M_\odot$)	T_K (K)	σ_{NH_3} (km s^{-1})	V_{NH_3} (km s^{-1})	$\log(N_{p-NH_3})$ (cm^{-2})	$\log(N_{H_2})$ (cm^{-2})
17	98.1789	10.3609	45	14.7	9.9	$0.08^{+0.04}_{-0.06}$	3.3	0.2	14.6 ± 4.0	0.53 ± 0.11	3.8	14.0	21.8
18	98.1664	10.3775	108	26.1	19.2	$0.19^{+0.08}_{-0.06}$	18.2	3.0	13.7 ± 2.7	0.38 ± 0.06	4.6	13.5	21.8
19	98.0911	10.3683	61	13.6	5.5	$0.08^{+0.03}_{-0.02}$	4.9	0.3	12.5 ± 4.4	0.8 ± 0.17	4.8	14.1	22.0
20	98.0842	10.3892	175	11.6	11.1	$0.1^{+0.02}_{-0.01}$	7.3	0.9	11.3 ± 3.9	0.41 ± 0.08	3.9	13.8	22.0
21	98.2783	10.4050	214	16.4	11.6	$0.13^{+0.06}_{-0.02}$	8.1	2.0	9.9 ± 2.7	0.16 ± 0.02	5.7	13.7	21.7
22	98.2684	10.4338	79	13.0	10.9	$0.11^{+0.01}_{-0.01}$	7.3	0.9	11.2 ± 2.0	0.12 ± 0.01	4.7	13.8	21.8
23	98.2325	10.4327	182	9.8	8.6	$0.08^{+0.02}_{-0.02}$	2.6	0.1	10.4 ± 4.0	0.11 ± 0.03	5.4	14.1	21.8
24	98.0901	10.4340	221	13.0	5.7	$0.08^{+0.04}_{-0.01}$	4.4	0.5	11.5 ± 4.1	0.45 ± 0.09	5.5	13.8	22.0
25	98.0668	10.4412	109	13.4	9.0	$0.1^{+0.03}_{-0.03}$	5.4	0.4	13.4 ± 4.4	0.74 ± 0.15	5.6	13.9	21.9
26	98.0064	10.4718	169	11.9	8.3	$0.09^{+0.01}_{-0.02}$	3.0	0.9	11.1 ± 3.1	0.22 ± 0.04	5.7	13.8	21.7
27	98.1381	10.4738	199	14.7	6.8	$0.08^{+0.03}_{-0.05}$	3.9	0.2	13.3 ± 4.0	0.91 ± 0.17	4.6	14.3	22.0
28	98.1835	10.4983	89	35.2	21.2	$0.23^{+0.13}_{-0.1}$	44.7	16.9	9.7 ± 1.2	0.23 ± 0.01	5.0	14.0	22.0
29	97.9987	10.4836	153	11.1	7.1	$0.08^{+0.02}_{-0.02}$	3.1	0.3	14.4 ± 3.9	0.32 ± 0.08	5.6	13.7	21.7
30	98.1446	10.4947	219	18.0	10.7	$0.12^{+0.05}_{-0.04}$	15.9	4.3	10.5 ± 1.2	0.27 ± 0.02	6.5	13.9	22.1
31	98.0548	10.4896	200	11.5	5.8	$0.08^{+0.01}_{-0.02}$	2.7	0.2	11.1 ± 3.3	0.14 ± 0.03	6.3	13.8	21.7
32	98.0209	10.4940	68	8.8	7.7	$0.08^{+-0.0}_{-0.0}$	2.2	0.4	10.0 ± 3.7	0.13 ± 0.02	6.2	13.2	21.7
33	98.2285	10.4957	159	11.4	8.5	$0.08^{+0.03}_{-0.01}$	4.0	0.3	12.5 ± 4.0	0.47 ± 0.1	6.5	13.8	21.8
34	98.1558	10.5080	224	10.0	7.7	$0.08^{+0.0}_{-0.0}$	6.8	1.4	10.3 ± 0.6	0.17 ± 0.01	6.4	14.2	22.1
35	98.1488	10.5244	112	24.5	14.0	$0.17^{+0.11}_{-0.05}$	34.7	12.3	9.6 ± 0.8	0.27 ± 0.01	6.4	14.2	22.1
36	98.1240	10.5279	216	14.0	10.4	$0.1^{+0.02}_{-0.02}$	6.9	0.9	12.5 ± 3.1	0.51 ± 0.08	5.5	13.5	22.0
37	98.2619	10.5496	176	40.3	19.7	$0.22^{+0.16}_{-0.17}$	29.9	10.4	14.1 ± 3.0	0.49 ± 0.08	4.3	13.8	21.8
38	98.1646	10.5529	70	15.0	5.3	$0.07^{+0.04}_{-0.03}$	3.4	0.2	12.9 ± 4.4	1.22 ± 0.24	5.8	14.4	21.9
39	98.1753	10.5613	63	20.1	14.9	$0.14^{+0.06}_{-0.08}$	12.7	2.2	11.9 ± 4.1	1.19 ± 0.23	4.9	14.6	21.9
40	98.1388	10.5997	64	32.3	13.3	$0.19^{+0.12}_{-0.1}$	20.7	6.4	11.4 ± 2.0	0.19 ± 0.02	6.8	13.9	21.8

Table A.4: Rosette NH_3 (1,1) Leaves Catalog 1

ID	RA (deg)	decl. (deg)	PA (deg)	σ_{maj} ($''$)	σ_{min} ($''$)	R_{eff} (pc)	M_{obs} ($M_\odot$)	M_{clip} ($M_\odot$)	T_K (K)	σ_{NH_3} (km s^{-1})	V_{NH_3} (km s^{-1})	$\log(N_{p-NH_3})$ (cm^{-2})	$\log(N_{H_2})$ (cm^{-2})
0	98.6014	4.0181	77	27.5	11.9	$0.24^{+0.21}_{-0.11}$	25.2	5.1	16.5 ± 3.2	0.22 ± 0.04	16.0	13.3	21.6
1	98.3692	4.0146	77	28.4	13.0	$0.27^{+0.12}_{-0.16}$	43.3	18.2	18.6 ± 3.3	0.57 ± 0.09	14.8	13.7	21.5
2	98.3335	4.0146	100	12.5	6.2	$0.12^{+0.04}_{-0.05}$	4.7	0.5	18.6 ± 4.7	0.67 ± 0.15	14.8	13.8	21.5
3	98.6651	4.1077	120	15.2	6.0	$0.13^{+0.04}_{-0.05}$	5.1	0.6	16.5 ± 3.7	0.58 ± 0.11	11.9	14.1	21.6
4	98.6565	4.1400	55	39.4	18.9	$0.41^{+0.36}_{-0.15}$	88.8	33.8	13.1 ± 1.8	0.37 ± 0.04	11.3	13.9	21.7
5	98.6810	4.1273	225	12.2	6.8	$0.12^{+0.02}_{-0.05}$	3.6	0.3	14.5 ± 3.3	0.34 ± 0.07	12.0	13.8	21.6
6	98.6171	4.1479	149	12.6	8.1	$0.14^{+0.04}_{-0.01}$	7.4	1.1	13.2 ± 2.9	0.21 ± 0.04	11.3	13.6	21.7
7	98.6596	4.1695	199	28.8	9.7	$0.22^{+0.21}_{-0.12}$	25.3	6.8	15.1 ± 3.0	0.35 ± 0.06	12.2	13.8	21.8
8	98.6047	4.1757	70	16.2	11.8	$0.17^{+0.08}_{-0.1}$	10.0	1.4	15.1 ± 3.6	0.32 ± 0.07	11.6	13.9	21.6
9	98.6853	4.1758	208	23.4	9.7	$0.2^{+0.11}_{-0.08}$	20.4	5.6	11.6 ± 1.5	0.25 ± 0.02	13.3	13.8	21.7
10	98.6590	4.2055	203	42.2	19.3	$0.38^{+0.21}_{-0.23}$	127.6	59.1	16.9 ± 1.2	0.51 ± 0.03	12.7	14.0	21.7
11	98.5984	4.1971	218	22.5	11.7	$0.21^{+0.13}_{-0.07}$	15.1	2.6	11.9 ± 3.1	0.26 ± 0.04	11.5	13.5	21.6
12	98.6119	4.2156	223	11.9	9.2	$0.14^{+0.03}_{-0.02}$	6.7	0.8	14.6 ± 3.9	0.4 ± 0.08	12.0	13.6	21.7
13	98.6000	4.2256	97	19.8	8.4	$0.15^{+0.08}_{-0.12}$	7.1	0.5	15.9 ± 4.1	0.49 ± 0.11	12.4	14.2	21.7
14	98.6076	4.2427	97	14.7	12.2	$0.18^{+0.02}_{-0.04}$	14.4	2.4	15.4 ± 2.7	0.43 ± 0.07	13.3	13.6	21.7
15	98.5530	4.2608	137	16.6	9.5	$0.16^{+0.06}_{-0.08}$	11.4	1.4	13.5 ± 4.0	0.96 ± 0.18	11.6	14.1	21.7
16	97.9372	4.2634	215	15.4	11.0	$0.18^{+0.03}_{-0.06}$	9.2	1.7	10.8 ± 3.2	0.18 ± 0.03	12.7	13.4	21.5
17	98.5425	4.2862	132	33.0	10.9	$0.26^{+0.21}_{-0.11}$	45.3	9.2	12.4 ± 2.3	0.48 ± 0.05	11.5	13.9	21.8
18	98.5733	4.2781	175	13.6	9.2	$0.15^{+0.06}_{-0.02}$	12.5	1.8	11.7 ± 2.7	0.42 ± 0.05	12.7	13.6	21.8
19	97.9162	4.2793	122	10.8	7.8	$0.13^{+0.03}_{-0.01}$	5.3	0.5	12.0 ± 3.3	0.33 ± 0.06	10.5	14.0	21.5
20	98.5982	4.2789	175	13.7	6.9	$0.13^{+0.09}_{-0.02}$	5.7	0.8	11.1 ± 3.1	0.24 ± 0.04	12.9	13.8	21.7
21	98.6299	4.2977	195	31.9	15.0	$0.27^{+0.27}_{-0.2}$	27.6	6.8	13.1 ± 3.4	0.39 ± 0.07	12.3	13.4	21.6
22	98.5736	4.2979	140	22.7	16.6	$0.23^{+0.12}_{-0.2}$	33.5	4.1	11.2 ± 2.5	0.47 ± 0.06	11.1	13.8	21.8
23	98.5327	4.2998	94	13.5	5.5	$0.11^{+0.05}_{-0.05}$	6.5	0.4	15.4 ± 3.6	0.3 ± 0.06	15.7	13.2	21.8
24	98.5284	4.3195	83	22.8	10.6	$0.21^{+0.13}_{-0.05}$	27.6	6.4	13.9 ± 2.6	0.36 ± 0.06	15.8	13.8	21.8
25	97.9643	4.3181	224	21.4	14.9	$0.27^{+0.06}_{-0.08}$	39.4	17.5	17.1 ± 2.8	0.44 ± 0.07	13.7	13.9	21.5
26	97.9869	4.3179	196	15.9	13.4	$0.2^{+0.12}_{-0.07}$	13.6	4.0	12.3 ± 3.0	0.26 ± 0.05	13.2	14.2	21.5
27	98.5672	4.3157	209	11.8	6.7	$0.11^{+0.03}_{-0.03}$	10.3	0.9	18.8 ± 2.2	0.56 ± 0.06	9.9	13.8	21.8
28	98.5608	4.3425	86	33.2	13.9	$0.29^{+0.16}_{-0.13}$	70.6	22.4	16.4 ± 2.2	0.42 ± 0.05	10.8	13.7	21.8
29	98.5358	4.3558	99	32.4	14.9	$0.33^{+0.14}_{-0.14}$	76.1	25.0	11.5 ± 1.5	0.32 ± 0.03	12.5	14.1	21.8

Continued on next page

Table A.4 – *Continued from previous page*

ID	RA (deg)	decl. (deg)	PA (deg)	σ_{maj} ($''$)	σ_{min} ($''$)	R_{eff} (pc)	M_{obs} ($M_\odot$)	M_{clip} ($M_\odot$)	T_K (K)	σ_{NH_3} (km s^{-1})	V_{NH_3} (km s^{-1})	$\log(N_{p-NH_3})$ (cm^{-2})	$\log(N_{H_2})$ (cm^{-2})
30	97.8343	4.3663	195	15.1	10.8	$0.17^{+0.07}_{-0.03}$	8.9	3.4	19.4 ± 2.9	0.39 ± 0.06	18.5	13.5	21.4
31	98.5562	4.3783	213	14.9	13.2	$0.2^{+0.04}_{-0.03}$	31.0	11.1	13.9 ± 2.3	0.45 ± 0.05	11.4	13.8	21.8
32	98.5737	4.3807	133	15.5	9.0	$0.13^{+0.07}_{-0.08}$	7.9	1.5	21.5 ± 4.0	0.85 ± 0.14	11.5	13.6	21.7
33	98.5358	4.4427	123	18.6	12.8	$0.23^{+0.05}_{-0.06}$	28.4	7.4	18.6 ± 2.6	0.45 ± 0.06	15.0	13.7	21.6
34	98.5404	4.4689	122	12.7	10.3	$0.15^{+0.04}_{-0.1}$	8.5	1.4	16.5 ± 3.4	0.41 ± 0.07	15.8	13.6	21.5
35	98.2447	4.4683	208	15.0	9.4	$0.16^{+0.04}_{-0.08}$	9.4	3.4	13.1 ± 3.2	0.28 ± 0.05	16.5	14.0	21.3
36	98.4988	4.4907	209	26.5	12.9	$0.24^{+0.2}_{-0.18}$	16.0	5.3	14.1 ± 2.9	0.39 ± 0.06	15.9	13.5	21.5
37	98.5237	4.4961	54	17.1	8.4	$0.15^{+0.06}_{-0.05}$	5.9	0.8	14.3 ± 4.0	0.54 ± 0.1	15.9	14.1	21.5
38	98.4709	4.5113	133	12.6	9.0	$0.14^{+0.03}_{-0.04}$	5.0	0.9	14.7 ± 3.2	0.34 ± 0.06	15.9	13.4	21.4
39	98.4115	4.5303	107	30.2	22.3	$0.37^{+0.23}_{-0.13}$	41.2	13.5	13.9 ± 2.2	0.48 ± 0.06	13.6	13.9	21.3
40	98.5069	4.5350	214	13.7	8.8	$0.14^{+0.04}_{-0.04}$	5.1	0.6	13.8 ± 3.6	0.18 ± 0.04	15.5	13.8	21.4
41	98.6522	4.5898	155	11.8	8.1	$0.13^{+0.03}_{-0.04}$	4.4	1.3	15.0 ± 4.0	0.45 ± 0.1	14.7	13.9	21.3
42	98.2916	4.6352	222	10.9	10.9	$0.15^{+0.01}_{-0.03}$	6.0	2.5	21.0 ± 3.7	0.6 ± 0.1	20.3	13.9	21.1
43	98.4631	4.6427	218	11.5	10.6	$0.15^{+0.0}_{-0.01}$	5.2	0.7	15.7 ± 3.6	0.19 ± 0.04	12.5	13.8	21.3
44	98.3478	4.6767	60	13.9	11.1	$0.14^{+0.03}_{-0.11}$	3.3	1.0	20.7 ± 3.9	0.43 ± 0.08	9.9	13.4	21.1
45	98.3595	4.7624	48	53.1	14.2	$0.38^{+0.37}_{-0.24}$	37.2	18.2	16.1 ± 2.2	0.37 ± 0.05	10.5	13.9	21.2
46	98.2988	4.7686	104	13.9	10.9	$0.17^{+0.04}_{-0.04}$	7.2	3.2	17.5 ± 3.4	0.49 ± 0.08	11.3	14.1	21.1
47	98.4009	4.8288	163	10.6	8.5	$0.13^{+-0.0}_{-0.01}$	3.9	1.5	19.4 ± 3.4	0.48 ± 0.08	10.4	13.6	21.0

Table A.5: NGC2264 NH_3 (1,1) Leaves Catalog 1

ID	RA (deg)	decl. (deg)	PA (deg)	σ_{maj} ($''$)	σ_{min} ($''$)	R_{eff} (pc)	M_{obs} ($M_\odot$)	M_{clip} ($M_\odot$)	T_K (K)	σ_{NH_3} (km s^{-1})	V_{NH_3} (km s^{-1})	$\log(N_{p-NH_3})$ (cm^{-2})	$\log(N_{H_2})$ (cm^{-2})
0	100.5318	9.1710	77	39.8	19.8	$0.26^{+0.28}_{-0.11}$	30.6	13.1	11.0 ± 2.3	0.21 ± 0.03	7.8	14.0	21.6
1	100.5425	9.2038	190	17.8	13.8	$0.13^{+0.04}_{-0.06}$	6.5	2.7	9.1 ± 4.1	0.19 ± 0.04	7.4	14.0	21.5
2	100.2946	9.3462	102	33.2	13.2	$0.2^{+0.3}_{-0.08}$	14.4	4.1	9.7 ± 1.8	0.14 ± 0.01	4.4	14.0	21.6
3	100.3926	9.3385	118	10.5	7.9	$0.08^{+0.02}_{-0.01}$	2.0	0.1	13.6 ± 3.0	0.47 ± 0.07	8.0	13.9	21.5
4	100.3810	9.3465	204	13.5	8.6	$0.08^{+0.03}_{-0.06}$	2.4	0.2	13.9 ± 2.9	0.49 ± 0.07	8.2	13.6	21.6
5	100.3290	9.3533	94	13.3	11.2	$0.11^{+0.03}_{-0.01}$	5.9	2.0	10.5 ± 2.7	0.13 ± 0.02	4.8	13.9	21.7
6	100.3637	9.3779	71	27.8	13.1	$0.17^{+0.11}_{-0.05}$	20.7	6.9	13.6 ± 1.2	0.43 ± 0.03	8.1	13.9	21.7
7	100.3292	9.3721	88	13.2	8.9	$0.09^{+0.03}_{-0.03}$	4.7	0.4	13.7 ± 3.0	0.38 ± 0.06	4.9	13.9	21.8
8	100.3474	9.3984	108	25.7	10.3	$0.11^{+0.1}_{-0.08}$	7.6	2.3	14.3 ± 1.7	0.48 ± 0.04	7.7	13.8	21.8
9	100.3101	9.4110	60	42.2	17.0	$0.23^{+0.19}_{-0.12}$	46.7	18.3	18.4 ± 1.8	0.58 ± 0.05	5.6	13.7	21.9
10	100.3362	9.4000	119	13.1	8.0	$0.08^{+0.02}_{-0.06}$	4.5	0.6	17.7 ± 2.1	0.41 ± 0.05	7.6	13.5	21.8
11	100.2635	9.4329	62	15.6	13.7	$0.13^{+0.05}_{-0.02}$	6.2	1.2	11.0 ± 3.3	0.35 ± 0.06	4.9	13.9	21.8
12	100.4601	9.4352	186	21.8	18.9	$0.15^{+0.08}_{-0.09}$	4.2	1.2	14.3 ± 3.8	0.22 ± 0.05	7.5	13.7	21.2
13	100.3157	9.4484	97	24.2	9.5	$0.13^{+0.08}_{-0.04}$	16.4	5.9	15.6 ± 0.7	0.38 ± 0.02	7.7	14.0	22.1
14	100.2811	9.4432	50	16.7	7.0	$0.09^{+0.05}_{-0.02}$	5.7	0.7	16.5 ± 1.6	0.56 ± 0.05	6.2	14.0	22.0
15	100.3598	9.4732	108	38.9	20.5	$0.19^{+0.18}_{-0.13}$	12.2	6.7	12.3 ± 3.3	0.43 ± 0.08	6.7	14.1	21.8
16	100.2989	9.4913	215	47.2	37.4	$0.43^{+0.09}_{-0.08}$	492.7	322.3	18.8 ± 0.4	0.76 ± 0.01	7.3	14.5	22.2
17	100.2337	9.4803	48	12.4	6.7	$0.08^{+0.02}_{-0.03}$	1.3	0.1	10.0 ± 5.0	1.0 ± 0.22	5.6	14.6	21.8
18	100.2793	9.5296	185	14.4	12.5	$0.11^{+0.04}_{-0.02}$	11.5	0.8	15.3 ± 0.9	0.72 ± 0.03	6.5	14.2	22.2
19	100.1623	9.5459	75	27.6	11.9	$0.16^{+0.08}_{-0.05}$	10.7	3.6	14.4 ± 3.3	0.53 ± 0.08	5.4	13.8	21.7
20	100.2798	9.5593	49	31.1	12.7	$0.17^{+0.13}_{-0.07}$	76.8	28.3	15.7 ± 0.3	0.51 ± 0.01	6.1	14.6	22.3
21	100.2112	9.5783	121	21.0	20.7	$0.19^{+0.02}_{-0.03}$	54.3	21.3	12.3 ± 0.6	0.47 ± 0.01	5.1	14.4	22.1
22	100.2646	9.5847	212	28.8	12.3	$0.16^{+0.07}_{-0.08}$	84.1	24.7	16.0 ± 0.4	0.91 ± 0.02	5.3	14.6	22.3
23	100.2363	9.5936	51	15.9	11.5	$0.12^{+0.02}_{-0.01}$	28.3	2.2	14.5 ± 0.3	0.49 ± 0.01	5.6	14.6	22.2
24	100.2841	9.5950	191	24.0	10.0	$0.13^{+0.1}_{-0.05}$	45.0	10.8	16.6 ± 0.4	0.72 ± 0.02	5.1	14.5	22.2
25	100.1934	9.6285	78	9.8	7.8	$0.07^{+0.01}_{-0.01}$	1.7	0.1	15.0 ± 3.8	0.32 ± 0.08	5.5	14.2	21.8
26	100.2361	9.6375	86	18.2	15.6	$0.15^{+0.04}_{-0.02}$	9.8	3.5	13.3 ± 2.8	0.44 ± 0.06	5.5	13.7	21.9
27	100.3165	9.6474	66	36.0	14.8	$0.21^{+0.27}_{-0.1}$	19.1	5.7	11.4 ± 2.0	0.24 ± 0.03	4.7	13.8	21.7
28	100.2896	9.6495	134	11.9	5.8	$0.07^{+0.04}_{-0.01}$	2.0	0.1	15.7 ± 4.4	0.79 ± 0.17	5.5	14.1	21.8
29	100.3032	9.6809	188	14.5	6.4	$0.08^{+0.04}_{-0.04}$	2.5	0.3	14.7 ± 3.8	0.57 ± 0.1	5.2	14.0	21.7
30	100.3173	9.6953	49	20.4	13.9	$0.14^{+0.05}_{-0.04}$	10.3	2.2	12.8 ± 3.0	0.67 ± 0.1	5.8	14.0	21.6
31	100.3032	9.6913	198	11.5	7.5	$0.08^{+0.01}_{-0.02}$	3.0	0.1	9.8 ± 4.3	0.31 ± 0.06	5.1	13.8	21.6
32	100.2961	9.7281	72	32.5	15.4	$0.13^{+0.15}_{-0.09}$	7.3	1.5	12.2 ± 3.9	0.33 ± 0.07	5.0	13.8	21.6
33	100.3050	9.7449	93	22.1	10.5	$0.12^{+0.06}_{-0.07}$	5.3	0.4	11.5 ± 4.4	0.48 ± 0.1	4.8	14.0	21.6
34	100.3208	9.7473	205	19.9	3.8	$0.07^{+0.06}_{-0.03}$	1.6	0.3	12.2 ± 3.2	1.13 ± 0.17	5.6	14.5	21.5
35	100.1089	9.8339	181	38.6	19.3	$0.19^{+0.2}_{-0.1}$	9.0	2.1	19.7 ± 3.7	0.35 ± 0.07	10.4	13.5	21.3

Continued on next page

Table A.5 – *Continued from previous page*

ID	RA (deg)	decl. (deg)	PA (deg)	σ_{maj} ($''$)	σ_{min} ($''$)	R_{eff} (pc)	M_{obs} ($M_\odot$)	M_{clip} ($M_\odot$)	T_K (K)	σ_{NH_3} (km s^{-1})	V_{NH_3} (km s^{-1})	$\log(N_{p-NH_3})$ (cm^{-2})	$\log(N_{H_2})$ (cm^{-2})
36	100.0504	9.8443	53	24.2	9.6	$0.11^{+0.1}_{-0.1}$	2.3	0.5	16.1 ± 4.4	0.31 ± 0.08	10.1	13.7	21.2
37	100.1214	9.9082	100	18.3	10.1	$0.11^{+0.06}_{-0.05}$	4.5	1.2	20.3 ± 3.1	0.36 ± 0.06	10.0	13.9	21.4
38	100.1130	9.9262	195	21.3	7.0	$0.1^{+0.09}_{-0.03}$	2.1	0.3	18.0 ± 5.0	0.51 ± 0.13	10.0	14.0	21.3
39	100.2962	9.9336	211	15.2	14.2	$0.15^{+0.01}_{-0.01}$	10.1	3.7	13.1 ± 1.5	0.28 ± 0.03	4.5	14.1	21.4
40	100.2746	9.9494	216	22.7	15.2	$0.17^{+0.05}_{-0.04}$	11.0	3.0	10.3 ± 2.8	0.16 ± 0.02	4.7	13.9	21.4
41	100.0927	9.9416	158	16.9	6.1	$0.09^{+0.05}_{-0.03}$	1.9	0.2	16.0 ± 4.3	0.88 ± 0.18	9.8	13.9	21.3

Table A.6: M16 NH_3 (1,1) Leaves Catalog 1

ID	RA (deg)	decl. (deg)	PA (deg)	σ_{maj} ($''$)	σ_{min} ($''$)	R_{eff} (pc)	M_{obs} ($M_\odot$)	M_{clip} ($M_\odot$)	T_K (K)	σ_{NH_3} (km s^{-1})	V_{NH_3} (km s^{-1})	$\log(N_{p-NH_3})$ (cm^{-2})	$\log(N_{H_2})$ (cm^{-2})
0	274.7056	-13.8326	70	8.9	8.1	$0.16^{+-0.0}_{-0.03}$	14.1	2.4	16.6 ± 3.5	0.53 ± 0.09	22.8	13.6	NaN
1	274.7125	-13.8160	58	12.7	12.2	$0.25^{+0.04}_{-0.03}$	36.4	15.6	22.0 ± 2.4	0.47 ± 0.05	24.9	14.3	21.5
2	274.5189	-13.8058	141	23.3	8.5	$0.25^{+0.14}_{-0.11}$	34.1	1.7	13.0 ± 2.0	0.37 ± 0.04	20.2	13.8	21.8
3	274.5047	-13.7902	143	31.9	16.9	$0.46^{+0.29}_{-0.15}$	135.9	42.9	12.9 ± 0.9	0.28 ± 0.02	20.8	14.1	21.9
4	274.5413	-13.8005	218	17.1	7.9	$0.19^{+0.12}_{-0.08}$	22.2	1.5	12.2 ± 1.9	0.4 ± 0.04	21.0	14.0	21.9
5	274.5439	-13.7509	113	61.1	35.8	$0.98^{+0.6}_{-0.42}$	1405.7	931.9	16.3 ± 0.6	0.61 ± 0.02	20.8	14.4	22.2
6	274.8560	-13.7584	171	18.7	15.2	$0.3^{+0.13}_{-0.12}$	76.7	21.4	15.7 ± 2.9	0.72 ± 0.1	21.6	13.8	21.9
7	274.7816	-13.7548	177	17.9	13.6	$0.34^{+0.14}_{-0.07}$	92.1	43.3	22.9 ± 1.5	0.75 ± 0.04	24.7	14.3	21.8
8	274.6596	-13.7542	181	9.7	8.1	$0.16^{+0.04}_{-0.02}$	10.2	0.6	17.1 ± 3.1	0.25 ± 0.05	20.2	13.8	21.7
9	274.6960	-13.7402	194	15.3	11.7	$0.26^{+0.05}_{-0.03}$	84.2	40.1	24.3 ± 1.6	0.72 ± 0.04	19.9	14.2	21.9
10	274.6080	-13.7393	166	14.4	10.1	$0.22^{+0.03}_{-0.05}$	22.9	4.1	11.7 ± 0.8	0.23 ± 0.01	21.7	14.1	21.8
11	274.6275	-13.7322	127	18.9	9.0	$0.23^{+0.09}_{-0.08}$	24.4	3.3	11.6 ± 1.0	0.2 ± 0.01	21.8	14.0	21.8
12	274.6955	-13.7213	117	14.7	8.9	$0.2^{+0.09}_{-0.05}$	37.0	8.3	21.9 ± 1.9	0.62 ± 0.05	20.7	14.0	22.0
13	274.6686	-13.7007	88	27.2	14.5	$0.37^{+0.15}_{-0.15}$	127.1	40.2	23.1 ± 2.7	0.6 ± 0.06	28.6	13.8	22.0
14	274.6405	-13.7108	200	11.3	10.2	$0.19^{+0.02}_{-0.02}$	20.8	3.1	13.1 ± 2.0	0.29 ± 0.04	22.3	14.1	21.9
15	274.7550	-13.7123	176	16.3	6.1	$0.16^{+0.13}_{-0.06}$	13.4	1.0	16.8 ± 3.9	0.14 ± 0.03	22.4	13.9	21.8
16	274.5915	-13.7040	213	26.2	13.3	$0.37^{+0.19}_{-0.12}$	99.6	40.9	22.4 ± 2.2	0.66 ± 0.06	26.4	13.9	21.9
17	274.7298	-13.6936	136	29.4	12.9	$0.34^{+0.22}_{-0.12}$	89.9	28.7	18.4 ± 2.4	0.59 ± 0.07	20.2	14.0	21.9
18	274.7992	-13.6927	126	14.7	5.7	$0.16^{+0.08}_{-0.06}$	15.1	0.8	13.3 ± 4.4	0.78 ± 0.17	22.8	14.3	21.9
19	274.5480	-13.6897	48	15.5	11.7	$0.26^{+0.06}_{-0.04}$	80.0	35.5	22.2 ± 1.5	0.55 ± 0.03	19.2	14.2	22.0
20	274.5642	-13.6761	163	17.8	7.5	$0.18^{+0.08}_{-0.08}$	19.3	3.2	25.9 ± 4.7	0.84 ± 0.13	24.7	14.0	21.9
21	274.5344	-13.6704	220	21.1	11.1	$0.29^{+0.12}_{-0.08}$	79.9	25.4	19.4 ± 1.3	0.5 ± 0.03	25.4	14.1	22.0
22	274.7923	-13.6701	177	30.3	11.8	$0.34^{+0.22}_{-0.17}$	77.9	10.4	12.9 ± 1.7	0.23 ± 0.03	22.9	14.0	21.9
23	274.7307	-13.6715	141	15.4	9.5	$0.2^{+0.08}_{-0.08}$	26.9	2.6	16.2 ± 3.7	1.72 ± 0.27	22.7	14.9	21.9
24	274.8157	-13.6569	145	14.3	11.8	$0.22^{+0.11}_{-0.06}$	48.9	14.0	18.4 ± 3.1	0.94 ± 0.13	21.9	14.5	22.0
25	274.5110	-13.6579	213	13.9	8.4	$0.19^{+0.03}_{-0.04}$	32.0	7.7	21.5 ± 2.1	0.51 ± 0.05	24.9	13.5	22.0
26	274.7497	-13.6565	52	11.5	9.1	$0.19^{+0.04}_{-0.04}$	23.0	1.2	11.6 ± 4.5	0.68 ± 0.13	22.6	14.2	21.9
27	274.7133	-13.6527	95	11.8	7.8	$0.16^{+0.02}_{-0.05}$	18.5	2.1	15.4 ± 3.9	0.29 ± 0.07	25.1	13.5	22.0
28	274.7320	-13.6481	153	21.6	13.3	$0.31^{+0.17}_{-0.1}$	62.8	14.0	13.0 ± 3.0	0.46 ± 0.08	23.5	14.1	21.9
29	274.6854	-13.6516	164	14.3	6.4	$0.17^{+0.04}_{-0.07}$	24.1	2.0	16.3 ± 2.2	0.61 ± 0.07	22.9	14.0	22.0
30	274.6849	-13.6319	54	34.4	14.6	$0.39^{+0.29}_{-0.23}$	144.8	46.7	16.3 ± 1.9	0.6 ± 0.06	23.8	13.9	22.0
31	274.5111	-13.6214	135	13.3	7.1	$0.17^{+0.03}_{-0.06}$	58.6	4.4	16.4 ± 0.4	0.45 ± 0.01	19.5	14.5	22.2
32	274.4910	-13.6162	211	20.7	13.3	$0.28^{+0.12}_{-0.09}$	187.1	36.3	16.1 ± 0.4	0.49 ± 0.01	19.8	14.6	22.3
33	274.4583	-13.6144	219	19.7	13.4	$0.29^{+0.08}_{-0.06}$	78.8	18.6	23.2 ± 2.9	0.65 ± 0.08	23.9	13.5	22.1
34	274.6487	-13.6150	154	8.1	7.3	$0.14^{+0.01}_{--0.01}$	9.7	0.7	19.5 ± 3.4	0.28 ± 0.05	20.6	13.4	21.8
35	274.6239	-13.5921	208	22.1	17.9	$0.33^{+0.22}_{-0.15}$	53.9	15.1	16.6 ± 3.3	0.42 ± 0.08	20.5	13.7	21.8
36	274.5341	-13.5826	187	34.0	18.5	$0.48^{+0.18}_{-0.17}$	270.9	102.3	17.0 ± 1.0	0.52 ± 0.03	19.1	14.2	22.1
37	274.4981	-13.5851	222	23.0	12.2	$0.31^{+0.12}_{-0.07}$	126.3	39.4	15.8 ± 0.9	0.58 ± 0.03	18.9	14.2	22.2
38	274.5939	-13.5876	175	16.4	8.3	$0.21^{+0.1}_{-0.05}$	17.8	2.9	15.6 ± 3.2	0.47 ± 0.08	20.0	13.7	21.7
39	274.4785	-13.5665	51	21.2	10.6	$0.27^{+0.2}_{-0.06}$	104.3	14.8	17.5 ± 1.0	0.61 ± 0.03	18.9	14.2	22.1
40	274.5505	-13.5559	87	19.1	11.6	$0.25^{+0.1}_{-0.08}$	43.9	8.5	19.8 ± 3.5	0.66 ± 0.1	17.8	13.7	21.9
41	274.4450	-13.5347	178	18.5	14.1	$0.27^{+0.05}_{-0.08}$	73.9	17.4	17.5 ± 2.3	0.6 ± 0.07	19.9	13.7	21.9
42	274.5085	-13.5329	122	12.4	11.1	$0.22^{+0.07}_{-0.07}$	25.8	6.4	12.2 ± 3.7	1.03 ± 0.18	19.0	13.9	21.8

Table A.7: M17 NH_3 (1,1) Leaves Catalog 1

ID	RA (deg)	decl. (deg)	PA (deg)	σ_{maj} ($''$)	σ_{min} ($''$)	R_{eff} (pc)	M_{obs} ($M_\odot$)	M_{clip} ($M_\odot$)	T_K (K)	σ_{NH_3} (km s^{-1})	V_{NH_3} (km s^{-1})	$\log(N_{p-NH_3})$ (cm^{-2})	$\log(N_{H_2})$ (cm^{-2})
0	274.7744	-16.6161	172	18.1	11.5	$0.28^{+0.14}_{-0.09}$	121.9	18.1	12.4 ± 2.8	0.32 ± 0.05	17.6	14.2	22.2
1	274.8064	-16.5884	125	35.6	24.4	$0.64^{+0.42}_{-0.19}$	664.3	229.8	15.1 ± 1.8	0.44 ± 0.04	18.9	14.1	22.2
2	274.8333	-16.5475	191	18.3	6.7	$0.21^{+0.11}_{-0.09}$	66.3	10.5	15.9 ± 1.8	0.34 ± 0.04	19.1	14.1	22.2
3	274.8293	-16.5325	144	18.4	10.5	$0.26^{+0.12}_{-0.09}$	109.3	41.9	18.1 ± 1.8	0.37 ± 0.04	19.3	14.2	22.3
4	274.8074	-16.5044	123	35.9	23.8	$0.63^{+0.45}_{-0.17}$	1480.8	878.3	19.5 ± 0.5	0.68 ± 0.01	18.4	14.7	22.3
5	274.7729	-16.5110	156	20.3	13.8	$0.33^{+0.09}_{-0.05}$	270.3	53.7	17.2 ± 0.8	0.53 ± 0.02	17.6	14.3	22.3
6	274.8011	-16.3247	225	20.5	15.8	$0.43^{+0.12}_{-0.07}$	317.6	92.4	16.5 ± 1.3	0.41 ± 0.03	21.9	14.2	22.2
7	274.8543	-16.3014	161	20.7	11.6	$0.34^{+0.12}_{-0.08}$	141.6	30.6	16.1 ± 1.7	0.23 ± 0.03	22.3	14.1	22.1
8	275.0490	-16.2479	136	18.8	10.5	$0.22^{+0.13}_{-0.13}$	53.0	8.5	27.6 ± 2.9	0.94 ± 0.09	19.7	13.7	22.5
9	275.0884	-16.2424	212	27.9	10.1	$0.33^{+0.19}_{-0.16}$	683.8	298.6	24.2 ± 0.3	1.28 ± 0.01	18.8	14.9	22.7
10	275.0293	-16.2319	165	25.7	19.2	$0.4^{+0.19}_{-0.32}$	215.5	67.8	27.8 ± 3.7	0.88 ± 0.11	21.7	13.8	22.4
11	275.0869	-16.2116	133	27.4	22.6	$0.49^{+0.26}_{-0.08}$	2634.3	2131.9	30.0 ± 0.3	1.52 ± 0.01	19.4	15.0	22.8
12	275.0469	-16.1802	58	12.7	12.0	$0.27^{+0.02}_{-0.04}$	253.6	95.5	24.8 ± 1.1	1.62 ± 0.05	20.0	14.6	22.6
13	275.0805	-16.1622	203	10.7	9.2	$0.2^{+0.01}_{-0.02}$	74.2	24.4	27.4 ± 2.0	0.47 ± 0.03	18.2	14.4	22.6
14	275.0363	-16.1586	65	11.7	7.0	$0.18^{+0.02}_{-0.04}$	44.6	5.2	25.4 ± 4.7	0.74 ± 0.12	17.2	13.9	22.4
15	275.0635	-16.1364	74	43.2	16.0	$0.55^{+0.51}_{-0.25}$	681.3	332.0	24.0 ± 1.0	0.88 ± 0.03	17.6	14.5	22.4
16	275.1484	-16.0998	110	14.3	9.6	$0.25^{+0.06}_{-0.02}$	79.1	26.4	28.0 ± 2.2	0.66 ± 0.04	19.3	14.3	22.0
17	275.1070	-16.0935	89	18.8	14.1	$0.36^{+0.11}_{-0.03}$	147.9	46.2	26.1 ± 2.2	0.63 ± 0.05	17.1	13.9	22.1
18	275.0655	-16.0987	92	15.0	8.5	$0.23^{+0.05}_{-0.04}$	102.0	18.6	24.5 ± 1.7	0.81 ± 0.05	17.3	13.8	22.2
19	275.0350	-16.1007	224	15.2	7.8	$0.17^{+0.1}_{-0.06}$	35.3	1.7	14.6 ± 4.0	0.91 ± 0.16	18.8	13.9	22.2
20	275.1407	-16.0711	63	25.2	10.8	$0.32^{+0.31}_{-0.1}$	132.5	44.1	26.0 ± 2.2	0.64 ± 0.05	17.4	14.0	22.1
21	275.0581	-16.0814	71	16.9	8.3	$0.23^{+0.13}_{-0.05}$	82.9	10.1	21.8 ± 2.0	0.6 ± 0.04	18.2	14.3	22.2
22	275.0761	-16.0734	115	14.2	9.7	$0.24^{+0.06}_{-0.03}$	70.0	8.1	22.7 ± 3.2	0.53 ± 0.07	17.4	14.1	22.2
23	275.0306	-16.0751	72	13.4	8.6	$0.19^{+0.05}_{-0.07}$	57.2	10.7	23.8 ± 3.8	0.55 ± 0.08	18.6	14.1	22.2
24	275.1040	-16.0628	144	21.4	13.9	$0.35^{+0.16}_{-0.1}$	125.5	28.1	21.0 ± 2.3	0.39 ± 0.04	19.3	14.1	22.2
25	275.0416	-16.0511	115	29.8	9.9	$0.26^{+0.23}_{-0.22}$	104.0	17.4	19.0 ± 3.0	0.7 ± 0.09	19.1	13.8	22.2
26	275.1101	-16.0363	89	13.9	6.8	$0.19^{+0.06}_{-0.05}$	39.6	2.0	25.9 ± 3.1	0.47 ± 0.05	18.9	13.8	22.2
27	275.0458	-16.0286	211	16.5	11.8	$0.24^{+0.1}_{-0.08}$	78.0	26.8	20.1 ± 3.4	0.65 ± 0.1	19.2	13.9	22.1
28	275.0279	-16.0305	77	12.4	9.1	$0.21^{+0.09}_{-0.03}$	60.6	10.8	19.3 ± 2.8	0.32 ± 0.05	21.6	14.0	22.1
29	275.1376	-16.0251	118	16.3	10.2	$0.27^{+0.08}_{-0.04}$	229.8	100.8	26.2 ± 0.8	0.86 ± 0.02	20.7	14.7	22.2
30	274.9847	-16.0227	131	15.2	11.8	$0.28^{+0.03}_{-0.05}$	103.9	28.7	20.0 ± 3.1	0.23 ± 0.04	19.7	14.1	22.1
31	275.1587	-16.0225	89	12.3	5.6	$0.16^{+0.07}_{-0.03}$	36.3	4.7	21.2 ± 1.2	0.4 ± 0.02	19.0	14.1	22.1
32	275.0543	-16.0058	157	18.6	10.2	$0.26^{+0.09}_{-0.15}$	69.4	15.6	18.7 ± 3.9	0.43 ± 0.08	19.6	13.8	22.1
33	275.1489	-15.9936	148	19.2	7.8	$0.23^{+0.1}_{-0.07}$	126.2	10.9	22.2 ± 0.6	0.94 ± 0.02	21.2	14.4	22.2
34	274.9853	-15.9901	65	16.8	10.2	$0.25^{+0.09}_{-0.13}$	80.1	24.5	17.6 ± 4.1	0.46 ± 0.1	20.3	14.0	22.1
35	275.1398	-15.9835	105	9.3	6.7	$0.16^{+0.0}_{--0.01}$	62.9	7.4	20.5 ± 0.4	0.43 ± 0.01	20.4	14.4	22.2
36	275.1584	-15.9672	98	14.3	10.3	$0.24^{+0.03}_{-0.03}$	93.2	17.6	22.6 ± 1.1	0.62 ± 0.03	21.5	14.2	22.1
37	275.1605	-15.9448	93	15.4	5.4	$0.16^{+0.09}_{-0.09}$	28.4	6.0	27.0 ± 2.4	0.6 ± 0.04	20.3	13.9	22.0

Table A.8: W48 NH_3 (1,1) Leaves Catalog 1

ID	RA (deg)	decl. (deg)	PA (deg)	σ_{maj} ($''$)	σ_{min} ($''$)	R_{eff} (pc)	M_{obs} ($M_\odot$)	M_{clip} ($M_\odot$)	T_K (K)	σ_{NH_3} (km s^{-1})	V_{NH_3} (km s^{-1})	$\log(N_{p-NH_3})$ (cm^{-2})	$\log(N_{H_2})$ (cm^{-2})
0	284.7530	0.9409	64	16.5	9.5	$0.35^{+0.07}_{-0.2}$	126.4	23.8	12.6 ± 2.9	0.28 ± 0.05	47.6	14.3	21.9
1	284.8809	0.9637	109	20.4	11.5	$0.34^{+0.21}_{-0.26}$	96.6	14.5	13.5 ± 2.9	0.66 ± 0.1	45.4	13.8	22.0
2	284.7698	0.9709	194	18.5	11.3	$0.46^{+0.19}_{-0.19}$	120.3	22.5	13.8 ± 2.1	0.33 ± 0.04	47.1	14.2	21.9
3	284.9213	0.9851	147	30.3	14.9	$0.68^{+0.51}_{-0.16}$	1000.5	374.7	14.8 ± 0.3	0.66 ± 0.01	45.6	14.7	22.0
4	285.0465	0.9835	71	11.9	9.0	$0.31^{+0.03}_{-0.02}$	80.1	10.2	13.5 ± 0.7	0.37 ± 0.02	43.2	14.4	21.9
5	285.0422	0.9984	91	11.5	6.8	$0.24^{+0.08}_{-0.04}$	59.9	5.0	14.0 ± 1.1	0.63 ± 0.04	42.9	14.2	21.9
6	284.9416	1.0159	186	30.8	24.9	$0.85^{+0.36}_{-0.18}$	1888.7	942.6	16.2 ± 0.4	0.67 ± 0.01	46.0	14.6	22.0
7	285.0214	1.0089	201	12.3	9.1	$0.29^{+0.1}_{-0.06}$	56.1	16.7	16.3 ± 2.7	0.5 ± 0.07	41.1	13.3	21.9
8	284.8016	1.0532	167	25.6	11.4	$0.55^{+0.43}_{-0.18}$	182.7	45.4	13.2 ± 1.9	0.33 ± 0.04	46.1	14.1	21.9
9	284.8671	1.0730	54	40.1	23.0	$0.96^{+0.78}_{-0.45}$	778.4	281.5	13.0 ± 1.4	0.38 ± 0.03	41.8	14.1	21.9
10	284.8538	1.1006	222	10.9	7.5	$0.24^{+0.06}_{-0.07}$	45.4	2.4	12.9 ± 3.7	0.49 ± 0.09	41.8	13.8	21.9
11	285.1903	1.1140	155	18.9	12.4	$0.43^{+0.26}_{-0.18}$	153.0	18.0	12.3 ± 3.0	0.31 ± 0.06	37.0	13.9	21.9
12	284.8044	1.1276	206	16.0	14.5	$0.44^{+0.16}_{-0.24}$	130.6	20.1	10.5 ± 2.7	0.24 ± 0.04	41.8	14.0	21.9
13	285.3979	1.1357	123	24.5	10.9	$0.48^{+0.36}_{-0.17}$	166.6	51.5	14.3 ± 2.1	0.27 ± 0.04	42.1	13.7	21.9
14	285.3207	1.1310	119	20.2	9.5	$0.35^{+0.22}_{-0.18}$	95.5	11.3	14.8 ± 2.9	0.65 ± 0.09	42.5	13.8	21.9

Continued on next page

Table A.8 – *Continued from previous page*

ID	RA (deg)	decl. (deg)	PA (deg)	σ_{maj} ($''$)	σ_{min} ($''$)	R_{eff} (pc)	M_{obs} ($M_\odot$)	M_{clip} ($M_\odot$)	T_K (K)	σ_{NH_3} (km s^{-1})	V_{NH_3} (km s^{-1})	$\log(N_{p-NH_3})$ (cm^{-2})	$\log(N_{H_2})$ (cm^{-2})
15	284.8362	1.1283	223	14.2	10.4	$0.38^{+0.08}_{-0.03}$	174.6	40.6	12.1 ± 0.8	0.42 ± 0.02	41.6	14.3	21.9
16	285.2771	1.1536	224	37.9	21.9	$0.87^{+0.39}_{-0.36}$	556.6	145.9	12.9 ± 1.4	0.27 ± 0.02	37.7	13.9	22.0
17	285.4633	1.1433	61	22.0	10.5	$0.47^{+0.18}_{-0.15}$	158.7	33.0	13.5 ± 1.8	0.38 ± 0.04	43.7	13.9	21.8
18	284.8249	1.1388	88	10.0	8.2	$0.27^{+0.0}_{-0.03}$	69.3	8.2	11.2 ± 1.0	0.33 ± 0.02	41.4	14.3	21.9
19	285.4410	1.1420	159	14.1	9.7	$0.34^{+0.14}_{-0.11}$	62.9	7.9	12.4 ± 3.4	0.41 ± 0.07	43.6	14.0	21.8
20	285.3290	1.1483	205	16.0	15.1	$0.43^{+0.12}_{-0.15}$	150.7	31.0	15.3 ± 2.6	0.6 ± 0.08	41.7	13.3	22.0
21	285.2546	1.1445	187	12.6	10.0	$0.35^{+0.0}_{-0.06}$	71.7	11.6	11.8 ± 1.9	0.22 ± 0.03	38.3	13.8	21.9
22	284.8349	1.1628	94	25.4	16.6	$0.67^{+0.27}_{-0.16}$	568.9	151.2	13.3 ± 1.2	0.48 ± 0.03	41.2	14.3	21.9
23	285.5849	1.1580	205	12.7	10.5	$0.37^{+0.06}_{-0.02}$	51.9	10.1	10.3 ± 1.8	0.18 ± 0.02	38.6	14.2	21.4
24	285.4203	1.1711	173	12.5	8.3	$0.29^{+0.12}_{-0.03}$	63.9	11.7	13.9 ± 2.2	1.11 ± 0.11	42.2	14.4	21.9
25	285.3549	1.1718	162	19.9	12.7	$0.48^{+0.13}_{-0.11}$	285.4	71.9	14.8 ± 0.8	1.01 ± 0.04	41.3	14.5	22.0
26	285.3010	1.1760	62	17.3	13.5	$0.46^{+0.14}_{-0.12}$	206.5	50.7	17.7 ± 2.0	0.39 ± 0.04	38.1	13.7	22.0
27	285.4056	1.1737	143	15.8	5.6	$0.24^{+0.16}_{-0.09}$	50.8	2.6	15.4 ± 2.4	1.36 ± 0.14	41.7	13.6	21.9
28	285.4546	1.1762	60	12.1	9.5	$0.33^{+0.03}_{-0.01}$	109.5	37.4	17.1 ± 0.7	0.39 ± 0.02	42.7	14.3	21.9
29	285.2489	1.1906	141	42.4	17.8	$0.87^{+0.53}_{-0.33}$	1058.2	467.0	13.7 ± 0.9	0.81 ± 0.04	36.1	14.4	22.0
30	285.3356	1.1845	123	18.6	13.0	$0.46^{+0.18}_{-0.09}$	278.2	49.3	14.6 ± 0.8	0.38 ± 0.02	41.4	14.2	22.0
31	285.1315	1.1853	176	22.4	12.3	$0.49^{+0.26}_{-0.12}$	195.9	41.4	16.7 ± 2.7	0.59 ± 0.08	38.2	13.8	21.9
32	284.4067	1.1835	109	14.4	6.4	$0.28^{+0.08}_{-0.09}$	53.3	3.1	16.1 ± 3.2	0.23 ± 0.04	46.7	13.8	21.9
33	285.3905	1.1846	204	13.2	7.7	$0.3^{+0.09}_{-0.05}$	121.8	23.4	14.4 ± 0.5	0.38 ± 0.01	41.9	14.3	22.0
34	285.3705	1.1882	185	17.6	10.8	$0.43^{+0.1}_{-0.06}$	312.9	90.0	14.7 ± 0.5	0.49 ± 0.01	41.6	14.4	22.0
35	285.1567	1.1863	175	16.8	8.1	$0.31^{+0.14}_{-0.19}$	63.7	5.0	15.6 ± 3.1	0.43 ± 0.07	38.6	13.8	21.9
36	285.4499	1.1909	86	10.7	8.4	$0.29^{+0.01}_{-0.02}$	82.2	17.5	20.9 ± 0.9	0.38 ± 0.02	42.7	14.3	21.9
37	285.4214	1.1969	159	31.6	15.2	$0.68^{+0.31}_{-0.22}$	475.1	122.8	15.0 ± 0.7	0.43 ± 0.02	40.0	14.2	21.9
38	285.2161	1.1924	169	18.4	11.0	$0.43^{+0.15}_{-0.08}$	172.8	32.8	15.3 ± 1.7	0.25 ± 0.03	39.1	13.9	21.9
39	284.4195	1.1954	188	13.8	6.5	$0.27^{+0.11}_{-0.11}$	64.1	6.4	16.3 ± 3.3	0.59 ± 0.1	46.8	13.9	22.0
40	285.3170	1.2074	185	24.7	16.1	$0.64^{+0.28}_{-0.23}$	712.4	313.8	16.9 ± 0.7	0.76 ± 0.02	41.5	14.5	22.0
41	285.3434	1.2036	167	13.8	8.2	$0.31^{+0.04}_{-0.09}$	113.1	10.1	14.5 ± 1.0	0.49 ± 0.03	41.2	14.2	22.0
42	284.4387	1.2080	153	19.4	12.4	$0.4^{+0.32}_{-0.2}$	137.3	18.7	14.5 ± 2.1	0.43 ± 0.05	47.6	14.0	22.0
43	284.4575	1.2148	61	16.4	11.7	$0.35^{+0.17}_{-0.21}$	109.4	20.1	13.2 ± 2.7	0.92 ± 0.12	46.9	14.1	22.0
44	285.4257	1.2243	193	32.4	17.4	$0.85^{+0.3}_{-0.35}$	1719.3	1226.3	23.4 ± 0.6	0.77 ± 0.02	42.7	14.7	21.9
45	285.2580	1.2245	223	25.7	14.2	$0.56^{+0.27}_{-0.18}$	470.3	163.5	14.3 ± 1.1	0.59 ± 0.03	40.9	14.1	21.9
46	284.3109	1.2269	199	15.2	12.3	$0.45^{+0.08}_{-0.03}$	163.4	43.1	11.3 ± 1.4	0.19 ± 0.02	11.6	14.0	22.0
47	285.4533	1.2264	156	9.1	7.8	$0.25^{+-0.01}_{-0.01}$	93.2	31.1	30.0 ± 2.3	1.0 ± 0.06	44.0	14.0	21.9
48	284.4150	1.2401	145	27.5	17.4	$0.6^{+0.26}_{-0.24}$	438.5	100.4	14.8 ± 2.4	0.86 ± 0.09	45.2	13.6	22.0
49	285.4763	1.2349	167	17.1	7.5	$0.31^{+0.12}_{-0.15}$	55.8	11.8	18.6 ± 2.8	0.57 ± 0.08	42.7	13.9	21.8
50	285.3914	1.2429	205	17.7	11.7	$0.42^{+0.12}_{-0.1}$	112.9	24.9	20.4 ± 2.2	0.54 ± 0.06	43.0	13.5	21.9
51	285.2790	1.2405	168	16.3	9.6	$0.34^{+0.16}_{-0.08}$	99.1	13.7	16.0 ± 3.1	1.36 ± 0.17	39.6	14.4	21.9
52	285.3126	1.2493	210	12.1	8.7	$0.27^{+0.12}_{-0.03}$	76.5	7.8	14.3 ± 2.3	0.83 ± 0.09	36.5	13.5	21.9
53	285.2771	1.2525	141	12.8	9.1	$0.31^{+0.07}_{-0.06}$	76.3	13.8	16.5 ± 2.1	0.53 ± 0.06	40.6	13.6	21.9
54	285.3161	1.2638	124	18.7	13.7	$0.48^{+0.18}_{-0.1}$	348.6	91.9	14.8 ± 1.6	0.85 ± 0.06	36.7	13.8	21.9
55	284.3729	1.2631	75	12.4	8.9	$0.31^{+0.04}_{-0.02}$	100.6	5.7	15.0 ± 2.7	0.36 ± 0.05	46.2	13.7	22.0
56	284.4186	1.2734	115	22.1	14.7	$0.53^{+0.14}_{-0.12}$	390.4	65.6	13.4 ± 2.2	0.84 ± 0.08	43.5	13.6	22.0
57	284.2771	1.2796	174	50.1	18.3	$1.0^{+0.98}_{-0.51}$	1095.0	454.6	16.2 ± 1.5	0.45 ± 0.04	46.2	14.0	22.0
58	285.3412	1.2877	99	22.3	7.9	$0.31^{+0.37}_{-0.28}$	61.3	12.9	14.3 ± 3.9	1.06 ± 0.21	42.1	14.6	21.9
59	284.3859	1.2889	61	25.9	16.8	$0.59^{+0.46}_{-0.16}$	384.6	58.8	13.1 ± 1.8	0.59 ± 0.05	44.3	14.1	22.0
60	284.3256	1.2931	47	24.6	15.1	$0.6^{+0.37}_{-0.1}$	428.4	69.6	12.5 ± 2.4	0.53 ± 0.06	45.3	13.9	22.0
61	284.3615	1.2926	225	14.8	6.2	$0.28^{+0.16}_{-0.1}$	79.4	6.2	14.9 ± 3.1	0.58 ± 0.1	43.2	13.9	22.0
62	284.1749	1.2925	97	15.1	6.2	$0.27^{+0.17}_{-0.11}$	47.4	4.1	16.4 ± 3.1	0.84 ± 0.12	40.8	14.1	22.0
63	284.3504	1.3022	176	13.0	9.6	$0.31^{+0.03}_{-0.15}$	99.2	14.2	12.3 ± 3.4	0.77 ± 0.11	44.3	14.0	22.0
64	284.2068	1.3114	211	44.6	12.6	$0.67^{+0.55}_{-0.43}$	726.8	266.6	15.4 ± 0.5	0.54 ± 0.01	44.6	14.5	22.0
65	284.2929	1.3132	191	20.0	18.9	$0.6^{+0.27}_{-0.16}$	372.8	78.6	12.6 ± 1.9	0.44 ± 0.04	47.1	14.1	22.0
66	285.5802	1.3111	224	16.8	6.6	$0.3^{+0.14}_{-0.11}$	47.7	8.5	22.0 ± 2.7	0.41 ± 0.05	40.7	14.0	21.5
67	284.2398	1.3149	88	16.8	13.1	$0.46^{+0.07}_{-0.04}$	308.4	63.6	14.5 ± 0.4	0.59 ± 0.01	45.3	14.7	22.0
68	284.1739	1.3171	122	9.6	8.6	$0.25^{+0.05}_{-0.03}$	40.9	3.9	18.8 ± 3.8	0.8 ± 0.14	41.8	13.5	22.0
69	285.5585	1.3447	45	45.9	15.1	$0.77^{+0.63}_{-0.48}$	547.5	237.2	18.4 ± 1.4	0.45 ± 0.03	42.2	14.0	21.6
70	284.2817	1.3348	146	19.5	14.2	$0.51^{+0.37}_{-0.18}$	240.8	34.1	14.1 ± 2.1	0.48 ± 0.06	46.8	14.1	22.0
71	285.4941	1.3584	47	12.4	7.3	$0.28^{+0.07}_{-0.08}$	41.2	9.2	16.2 ± 3.3	0.32 ± 0.06	42.2	13.8	21.6
72	284.1919	1.3637	109	21.5	6.5	$0.33^{+0.26}_{-0.12}$	132.6	11.1	16.2 ± 0.7	0.73 ± 0.03	42.4	14.3	22.0
73	285.5307	1.3632	218	11.1	7.4	$0.26^{+0.08}_{-0.06}$	58.1	6.3	16.2 ± 1.3	0.31 ± 0.03	43.4	14.0	21.6
74	285.5112	1.3690	181	19.0	11.1	$0.46^{+0.15}_{-0.08}$	195.8	48.5	14.2 ± 0.8	0.31 ± 0.02	43.7	14.1	21.6
75	284.2259	1.3757	137	15.6	7.4	$0.32^{+0.1}_{-0.08}$	117.3	13.5	13.3 ± 2.7	0.47 ± 0.07	47.8	13.9	22.0
76	284.1989	1.3917	204	31.7	19.6	$0.75^{+0.28}_{-0.27}$	937.5	295.5	15.1 ± 0.5	0.74 ± 0.02	41.7	14.6	22.0

Continued on next page

Table A.8 – *Continued from previous page*

ID	RA (deg)	decl. (deg)	PA (deg)	σ_{maj} ($''$)	σ_{min} ($''$)	R_{eff} (pc)	M_{obs} ($M_\odot$)	M_{clip} ($M_\odot$)	T_K (K)	σ_{NH_3} (km s^{-1})	V_{NH_3} (km s^{-1})	$\log(N_{p-NH_3})$ (cm^{-2})	$\log(N_{H_2})$ (cm^{-2})
77	284.2040	1.4298	75	9.9	7.9	$0.27^{+-0.0}_{-0.05}$	45.0	3.7	13.8 ± 3.1	0.55 ± 0.09	41.4	14.1	22.0
78	284.6071	1.5266	66	35.0	16.5	$0.79^{+0.35}_{-0.22}$	430.2	104.4	11.7 ± 1.4	0.26 ± 0.02	35.7	14.1	21.9
79	284.5908	1.5147	48	12.5	6.4	$0.24^{+0.08}_{-0.09}$	38.2	2.6	11.9 ± 2.4	0.14 ± 0.02	34.8	13.9	21.9
80	284.5755	1.5473	208	32.4	25.3	$0.86^{+0.36}_{-0.34}$	812.2	279.7	13.0 ± 1.4	0.41 ± 0.03	32.7	14.1	22.0
81	284.5425	1.5360	94	15.7	9.6	$0.34^{+0.12}_{-0.21}$	67.0	5.2	10.6 ± 3.2	0.2 ± 0.04	32.0	13.9	22.0
82	284.5441	1.5694	208	28.9	17.0	$0.68^{+0.22}_{-0.33}$	536.0	138.8	19.9 ± 2.1	0.5 ± 0.05	35.0	13.6	22.1
83	284.6235	1.5801	84	11.5	9.9	$0.31^{+0.05}_{-0.03}$	81.8	9.3	14.5 ± 2.9	0.27 ± 0.05	34.2	13.7	22.0
84	284.6107	1.6049	99	29.6	20.2	$0.8^{+0.31}_{-0.16}$	649.3	243.7	14.0 ± 1.8	0.46 ± 0.04	31.6	14.0	22.1
85	284.5700	1.5962	157	17.3	11.4	$0.4^{+0.24}_{-0.06}$	149.9	21.2	13.0 ± 2.9	0.42 ± 0.07	32.0	13.6	22.1
86	284.4820	1.6022	52	21.5	16.1	$0.46^{+0.26}_{-0.27}$	138.6	10.4	24.6 ± 4.0	0.77 ± 0.11	34.4	13.8	22.1
87	284.5391	1.6197	134	33.6	29.2	$0.99^{+0.49}_{-0.34}$	4451.6	2672.0	20.1 ± 0.3	1.43 ± 0.01	33.2	14.9	22.2
88	284.4939	1.6315	99	20.2	8.6	$0.31^{+0.15}_{-0.23}$	62.8	9.1	11.3 ± 4.2	0.75 ± 0.12	33.4	14.1	22.1
89	284.5149	1.6483	151	20.0	12.5	$0.51^{+0.07}_{-0.16}$	235.2	54.6	15.3 ± 1.7	0.53 ± 0.05	31.9	14.1	22.1
90	284.5529	1.6751	223	35.7	15.1	$0.71^{+0.47}_{-0.25}$	1939.1	1027.7	22.2 ± 0.3	0.97 ± 0.01	33.8	14.9	22.2
91	284.5859	1.6797	59	32.6	12.3	$0.6^{+0.46}_{-0.23}$	613.3	250.1	13.1 ± 0.6	0.39 ± 0.01	35.7	14.4	22.1
92	284.5187	1.6695	119	13.5	9.4	$0.35^{+0.08}_{-0.04}$	102.1	20.1	13.9 ± 1.6	0.4 ± 0.04	33.2	13.9	22.1
93	284.6399	1.6874	95	26.8	19.4	$0.66^{+0.3}_{-0.17}$	466.4	156.9	11.6 ± 1.4	0.32 ± 0.03	36.5	14.2	22.0
94	284.6094	1.6806	199	18.8	9.8	$0.41^{+0.19}_{-0.1}$	149.5	24.6	10.3 ± 1.4	0.25 ± 0.02	35.1	14.2	22.1
95	284.6564	1.6999	131	14.5	9.6	$0.27^{+0.19}_{-0.2}$	68.8	6.2	12.7 ± 2.8	0.33 ± 0.05	36.4	14.0	22.0
96	284.5964	1.7045	85	12.1	8.8	$0.3^{+0.04}_{-0.06}$	82.1	8.1	15.9 ± 3.3	0.41 ± 0.07	36.3	13.7	22.1
97	284.6133	1.7210	180	23.8	18.5	$0.66^{+0.29}_{-0.15}$	414.6	102.1	12.2 ± 1.7	0.35 ± 0.04	37.1	14.1	22.1
98	284.6143	1.7476	126	14.3	7.2	$0.3^{+0.14}_{-0.07}$	80.2	5.3	13.0 ± 1.3	0.18 ± 0.02	38.2	14.1	22.0
99	284.6256	1.7783	223	31.4	11.2	$0.46^{+0.49}_{-0.41}$	231.9	50.2	13.7 ± 2.7	0.71 ± 0.09	37.9	13.8	21.9

Table A.9: Cygnus X South NH_3 (1,1) Leaves Catalog 1

ID	RA (deg)	decl. (deg)	PA (deg)	σ_{maj} ($''$)	σ_{min} ($''$)	R_{eff} (pc)	M_{obs} ($M_\odot$)	M_{clip} ($M_\odot$)	T_K (K)	σ_{NH_3} (km s^{-1})	V_{NH_3} (km s^{-1})	$\log(N_{p-NH_3})$ (cm^{-2})	$\log(N_{H_2})$ (cm^{-2})
0	308.3976	38.5130	92	12.9	9.9	$0.16^{+0.06}_{-0.03}$	9.6	0.6	12.4 ± 2.9	0.34 ± 0.05	-2.6	14.0	21.7
1	308.3713	38.5369	221	21.3	13.9	$0.26^{+0.2}_{-0.08}$	26.9	3.8	11.9 ± 1.8	0.28 ± 0.03	-2.9	13.9	21.7
2	308.4271	38.5588	142	14.7	11.9	$0.19^{+0.03}_{-0.02}$	18.2	5.8	12.8 ± 2.3	0.19 ± 0.03	-1.7	13.7	21.7
3	308.3334	38.5773	173	35.5	18.6	$0.42^{+0.32}_{-0.15}$	95.4	34.9	14.9 ± 1.3	0.4 ± 0.03	-0.9	14.1	21.7
4	308.2804	38.5865	118	19.7	15.9	$0.22^{+0.1}_{-0.09}$	23.5	6.5	14.4 ± 2.8	0.39 ± 0.06	-1.1	13.7	21.7
5	308.4036	38.5938	119	23.0	14.3	$0.21^{+0.14}_{-0.16}$	21.0	4.2	12.4 ± 3.0	0.54 ± 0.08	1.8	13.4	21.8
6	308.3819	38.6140	112	23.0	20.8	$0.28^{+0.13}_{-0.2}$	48.9	8.8	14.1 ± 4.1	1.07 ± 0.19	0.5	14.2	21.8
7	308.4574	38.6348	172	22.4	14.5	$0.24^{+0.09}_{-0.13}$	48.1	6.4	15.6 ± 3.7	0.46 ± 0.09	0.9	13.5	21.8
8	308.4640	38.6538	153	26.4	15.5	$0.23^{+0.21}_{-0.16}$	32.2	7.9	13.2 ± 3.8	0.55 ± 0.1	1.4	13.9	21.7
9	308.2060	38.6649	81	19.5	8.0	$0.17^{+0.13}_{-0.07}$	11.9	1.1	16.1 ± 3.3	0.17 ± 0.04	-0.7	13.7	21.7
10	308.3408	38.6987	125	27.2	15.6	$0.29^{+0.2}_{-0.1}$	46.4	10.9	14.9 ± 2.1	0.4 ± 0.05	-1.7	13.8	21.7
11	308.8029	38.6970	207	22.1	12.8	$0.23^{+0.09}_{-0.04}$	39.6	9.4	14.6 ± 1.9	0.58 ± 0.06	-2.7	14.2	21.7
12	308.7735	38.7086	163	18.9	11.1	$0.22^{+0.09}_{-0.06}$	40.0	10.8	15.0 ± 1.2	0.46 ± 0.03	-3.4	14.2	21.7
13	308.1824	38.7321	138	31.9	27.5	$0.45^{+0.15}_{-0.1}$	190.7	93.9	13.9 ± 0.8	0.43 ± 0.02	-0.0	14.3	21.7
14	308.1681	38.7713	115	30.6	22.2	$0.45^{+0.21}_{-0.08}$	274.8	168.1	16.3 ± 0.6	0.58 ± 0.02	-0.7	14.4	21.7
15	308.2061	38.7609	93	12.7	10.2	$0.17^{+0.02}_{-0.01}$	16.7	5.4	15.6 ± 1.5	0.28 ± 0.03	0.2	14.1	21.7
16	308.1507	38.8163	121	30.8	13.9	$0.31^{+0.32}_{-0.12}$	49.9	15.0	15.6 ± 1.8	0.36 ± 0.04	1.0	14.1	21.7
17	307.6774	38.8283	118	29.4	10.3	$0.23^{+0.26}_{-0.12}$	21.5	4.3	12.6 ± 3.1	0.4 ± 0.06	-4.1	14.0	21.6
18	307.9428	38.9525	55	46.3	14.3	$0.3^{+0.31}_{-0.2}$	58.3	21.3	22.4 ± 3.6	0.54 ± 0.08	0.5	13.6	21.7
19	307.8325	38.9579	224	19.9	13.4	$0.25^{+0.11}_{-0.05}$	73.0	32.3	21.6 ± 1.3	0.74 ± 0.04	-0.5	14.1	21.7
20	308.1021	38.9645	66	11.8	10.5	$0.14^{+0.04}_{-0.02}$	8.2	1.1	14.3 ± 4.5	0.53 ± 0.13	0.8	13.9	21.6
21	307.9971	38.9762	132	19.3	11.2	$0.2^{+0.15}_{-0.08}$	28.1	10.3	30.7 ± 3.2	0.69 ± 0.07	-4.5	13.5	21.7
22	307.8106	38.9757	170	22.0	13.8	$0.22^{+0.12}_{-0.09}$	44.4	9.7	22.6 ± 2.2	0.76 ± 0.07	-0.0	13.6	21.7
23	307.4157	38.9689	208	10.7	7.8	$0.13^{+0.03}_{-0.01}$	7.3	0.6	16.9 ± 3.2	0.26 ± 0.05	-3.2	13.8	21.6
24	308.0311	38.9812	51	15.3	9.4	$0.15^{+0.08}_{-0.09}$	7.8	0.5	12.4 ± 4.6	0.71 ± 0.16	0.1	14.1	21.6
25	307.7785	38.9787	179	16.3	11.6	$0.19^{+0.07}_{-0.04}$	25.4	5.8	20.0 ± 2.0	0.6 ± 0.05	-0.3	13.7	21.7
26	307.3896	38.9809	196	24.3	16.3	$0.3^{+0.18}_{-0.05}$	47.2	14.7	19.1 ± 2.4	0.46 ± 0.05	-3.4	13.9	21.6
27	307.8590	38.9836	176	23.3	14.5	$0.23^{+0.12}_{-0.07}$	32.4	7.4	20.6 ± 3.3	1.04 ± 0.14	-0.5	13.9	21.7
28	307.8921	38.9950	194	30.6	22.0	$0.25^{+0.25}_{-0.19}$	33.1	9.1	17.0 ± 3.3	0.7 ± 0.11	-0.5	14.0	21.7
29	307.9459	39.0174	104	15.6	7.0	$0.14^{+0.05}_{-0.07}$	12.2	2.8	21.6 ± 3.6	0.56 ± 0.09	0.2	13.9	21.7
30	307.3779	39.0166	92	16.2	9.5	$0.17^{+0.08}_{-0.09}$	11.6	3.1	24.8 ± 4.4	0.59 ± 0.09	-3.7	14.0	21.6

Continued on next page

Table A.9 – *Continued from previous page*

ID	RA (deg)	decl. (deg)	PA (deg)	σ_{maj} ($''$)	σ_{min} ($''$)	R_{eff} (pc)	M_{obs} ($M_\odot$)	M_{clip} ($M_\odot$)	T_K (K)	σ_{NH_3} (km s^{-1})	V_{NH_3} (km s^{-1})	$\log(N_{p-NH_3})$ (cm^{-2})	$\log(N_{H_2})$ (cm^{-2})
31	307.8351	39.0319	185	27.4	9.6	$0.2^{+0.17}_{-0.08}$	19.7	4.7	14.3 ± 3.3	0.27 ± 0.06	-0.1	13.9	21.7
32	307.9625	39.0403	170	12.0	10.2	$0.16^{+0.0}_{-0.02}$	13.6	3.5	23.7 ± 3.3	0.39 ± 0.06	-1.7	13.3	21.7
33	307.8092	39.1478	184	9.9	8.1	$0.12^{+0.01}_{-0.03}$	5.9	0.9	17.5 ± 3.9	0.21 ± 0.04	1.5	13.3	21.6
34	308.2332	39.4054	168	10.8	9.3	$0.14^{+0.01}_{-0.02}$	8.7	0.6	14.0 ± 4.0	0.39 ± 0.09	-3.8	13.8	21.7
35	308.5313	39.4177	49	14.1	11.5	$0.18^{+0.04}_{-0.01}$	19.5	4.1	19.7 ± 3.1	0.6 ± 0.08	-2.1	13.6	21.7
36	308.5291	39.4770	73	19.8	8.1	$0.15^{+0.08}_{-0.09}$	9.6	1.6	17.6 ± 4.2	0.37 ± 0.08	-0.9	13.7	21.7
37	308.2222	39.4983	48	10.3	9.0	$0.12^{+0.04}_{-0.02}$	7.6	0.9	14.9 ± 3.8	0.21 ± 0.05	-3.4	13.7	21.7
38	308.5202	39.5116	76	16.5	11.4	$0.2^{+0.1}_{-0.05}$	22.1	6.5	14.6 ± 2.5	0.48 ± 0.07	0.5	14.0	21.7
39	308.4727	39.5170	52	28.5	14.6	$0.33^{+0.24}_{-0.09}$	70.1	28.9	14.9 ± 1.4	0.29 ± 0.03	-1.4	14.0	21.7
40	308.6433	39.5787	211	18.2	15.9	$0.25^{+0.11}_{-0.02}$	26.3	5.1	14.1 ± 2.7	0.33 ± 0.05	4.5	13.4	21.6
41	308.8231	39.6453	177	10.8	9.1	$0.13^{+0.01}_{-0.02}$	8.4	0.9	18.7 ± 3.7	0.68 ± 0.12	7.8	14.0	21.6
42	309.0952	39.6732	130	30.5	13.5	$0.29^{+0.19}_{-0.11}$	44.6	9.5	12.0 ± 2.4	0.31 ± 0.04	4.6	13.9	21.7
43	308.6195	39.6769	177	23.6	14.1	$0.25^{+0.1}_{-0.1}$	32.0	5.6	14.0 ± 3.0	0.26 ± 0.05	4.8	13.5	21.7
44	308.3668	39.6871	76	18.0	15.2	$0.29^{+0.1}_{-0.05}$	86.3	32.6	14.4 ± 0.9	0.3 ± 0.02	0.8	14.3	21.8
45	308.6309	39.6908	163	13.1	7.7	$0.12^{+0.03}_{-0.07}$	6.9	0.6	13.3 ± 3.9	0.2 ± 0.05	4.3	13.8	21.7
46	309.1187	39.7126	72	34.3	15.8	$0.38^{+0.17}_{-0.14}$	115.1	54.2	13.1 ± 1.3	0.38 ± 0.03	3.9	14.1	21.7
47	308.3459	39.7129	208	20.1	14.5	$0.3^{+0.11}_{-0.06}$	85.9	33.3	15.9 ± 1.1	0.39 ± 0.03	1.3	14.2	21.8
48	308.6142	39.7167	75	20.5	10.2	$0.2^{+0.08}_{-0.09}$	19.3	2.1	11.9 ± 2.8	0.16 ± 0.03	5.0	13.7	21.8
49	308.6775	39.7493	182	22.8	20.4	$0.42^{+0.24}_{-0.09}$	206.8	126.5	18.4 ± 0.6	0.74 ± 0.02	6.0	14.5	21.8
50	308.9449	39.8238	211	26.8	11.3	$0.21^{+0.22}_{-0.09}$	26.7	6.9	11.5 ± 4.1	0.31 ± 0.07	1.1	13.5	21.7
51	309.3104	39.8201	80	14.7	13.2	$0.24^{+0.01}_{-0.02}$	39.7	15.9	22.0 ± 1.5	0.45 ± 0.03	6.9	14.4	21.7
52	308.9603	39.8463	70	30.8	18.5	$0.35^{+0.33}_{-0.1}$	70.1	25.8	11.4 ± 2.0	0.27 ± 0.03	1.6	14.0	21.7
53	309.4505	39.8286	210	19.0	11.4	$0.2^{+0.1}_{-0.05}$	58.8	20.1	16.2 ± 0.4	0.4 ± 0.01	5.5	14.4	21.7
54	309.0248	39.8299	190	20.7	9.7	$0.21^{+0.11}_{-0.07}$	27.8	4.6	12.6 ± 2.2	0.37 ± 0.05	5.3	14.0	21.7
55	309.2540	39.8435	68	36.0	12.5	$0.25^{+0.24}_{-0.18}$	37.5	9.5	13.3 ± 2.4	0.38 ± 0.06	3.5	13.7	21.7
56	309.2754	39.8414	202	16.8	7.1	$0.14^{+0.07}_{-0.07}$	11.2	0.7	17.6 ± 3.5	0.52 ± 0.1	3.9	13.7	21.7
57	309.4273	39.8480	51	16.3	11.2	$0.2^{+0.05}_{-0.01}$	60.8	25.0	18.2 ± 0.4	0.43 ± 0.01	6.0	14.6	21.7
58	309.3497	39.8475	181	14.9	10.9	$0.17^{+0.03}_{-0.05}$	13.8	2.0	14.0 ± 3.1	0.31 ± 0.06	3.5	13.9	21.7
59	309.0827	39.8493	160	15.9	9.2	$0.16^{+0.05}_{-0.05}$	12.4	2.1	12.4 ± 3.8	0.43 ± 0.09	5.1	13.6	21.7
60	308.3482	39.8515	118	13.2	7.3	$0.13^{+0.04}_{-0.02}$	7.1	0.7	10.1 ± 4.1	0.23 ± 0.06	1.2	14.1	21.7
61	309.2759	39.8671	76	27.1	17.0	$0.32^{+0.18}_{-0.09}$	76.4	19.9	13.1 ± 1.9	0.58 ± 0.05	3.6	13.8	21.7
62	309.2229	39.8600	77	15.2	6.1	$0.12^{+0.09}_{-0.05}$	8.4	0.7	14.2 ± 4.0	0.78 ± 0.13	3.3	14.0	21.7
63	309.2473	39.8717	190	12.1	6.0	$0.12^{+0.05}_{-0.03}$	8.1	0.2	13.0 ± 3.4	1.08 ± 0.16	3.3	14.4	21.7
64	308.8255	39.8894	212	23.7	11.9	$0.24^{+0.09}_{-0.07}$	37.4	12.0	20.6 ± 3.0	0.53 ± 0.07	-2.5	13.7	21.7
65	308.4474	39.8883	84	16.4	11.6	$0.18^{+0.03}_{-0.14}$	13.8	1.7	13.1 ± 3.5	0.15 ± 0.03	1.3	13.4	21.8
66	309.3154	39.8853	201	10.8	7.0	$0.13^{+0.01}_{-0.0}$	9.7	0.9	13.8 ± 2.9	0.31 ± 0.05	3.1	13.9	21.8
67	308.4240	39.9146	61	26.0	13.3	$0.26^{+0.12}_{-0.08}$	31.5	3.6	11.5 ± 2.3	0.29 ± 0.04	1.5	13.7	21.7
68	309.4527	39.9074	105	9.5	6.6	$0.11^{+0.01}_{-0.01}$	6.3	0.4	11.6 ± 3.4	0.22 ± 0.05	3.2	13.9	21.7
69	308.4860	39.9206	46	14.3	9.0	$0.14^{+0.07}_{-0.07}$	9.5	0.4	11.8 ± 3.1	0.17 ± 0.03	1.3	13.7	21.8
70	308.4638	39.9269	224	14.9	9.4	$0.16^{+0.02}_{-0.01}$	11.7	1.1	13.7 ± 3.9	0.49 ± 0.12	0.9	14.1	21.8
71	308.4103	39.9386	217	17.8	6.4	$0.14^{+0.1}_{-0.03}$	8.5	0.5	11.5 ± 2.5	0.21 ± 0.03	1.1	13.7	21.7
72	308.3569	39.9418	109	15.0	10.8	$0.19^{+0.04}_{-0.04}$	16.7	5.2	15.2 ± 2.0	0.29 ± 0.04	8.5	14.2	21.7
73	308.5785	39.9475	164	15.5	10.9	$0.19^{+0.06}_{-0.02}$	18.9	1.9	11.3 ± 2.7	0.18 ± 0.03	0.8	13.8	21.8
74	309.0812	39.9570	122	13.3	12.7	$0.18^{+0.07}_{-0.01}$	24.1	7.1	16.0 ± 2.8	0.45 ± 0.07	4.8	13.9	21.7
75	308.7757	39.9644	59	19.7	14.7	$0.24^{+0.04}_{-0.08}$	42.7	9.9	13.4 ± 2.9	0.41 ± 0.06	-1.4	13.9	21.8
76	308.1250	39.9614	107	14.1	7.9	$0.14^{+0.05}_{-0.06}$	12.6	4.1	24.3 ± 4.5	0.39 ± 0.07	2.7	13.9	21.7
77	308.5829	39.9839	84	31.7	16.6	$0.34^{+0.29}_{-0.14}$	84.4	26.8	10.8 ± 2.3	0.25 ± 0.03	0.8	14.2	21.8
78	308.5224	39.9643	167	11.6	6.1	$0.12^{+0.01}_{-0.03}$	8.4	0.6	11.2 ± 3.6	0.18 ± 0.04	-2.5	14.1	21.8
79	308.3540	39.9749	81	11.9	11.0	$0.16^{+0.04}_{-0.04}$	8.8	1.0	11.1 ± 3.3	0.15 ± 0.03	1.4	13.9	21.6
80	308.5208	39.9793	205	12.5	8.1	$0.15^{+0.04}_{-0.03}$	12.8	1.1	11.9 ± 3.3	0.1 ± 0.02	0.9	13.6	21.8
81	308.0914	40.0096	48	11.2	9.3	$0.15^{+0.02}_{-0.02}$	12.7	3.3	18.9 ± 3.4	0.42 ± 0.07	2.6	13.9	21.7
82	308.0706	40.0424	212	17.3	8.9	$0.13^{+0.1}_{-0.07}$	7.7	1.0	14.9 ± 4.2	0.25 ± 0.07	7.8	13.9	21.7
83	307.8022	40.0564	208	44.7	26.4	$0.62^{+0.53}_{-0.33}$	426.1	247.8	18.3 ± 0.7	0.63 ± 0.02	5.9	14.4	21.8
84	307.9396	40.0687	67	15.0	5.4	$0.12^{+0.07}_{-0.04}$	6.8	1.0	15.5 ± 4.4	0.35 ± 0.08	9.3	13.9	21.8
85	308.0682	40.1153	158	8.7	7.3	$0.12^{+0.01}_{-0.0}$	6.1	0.8	14.7 ± 2.7	0.2 ± 0.04	3.8	14.0	21.6
86	307.9533	40.1201	101	12.9	8.8	$0.14^{+0.07}_{-0.03}$	6.9	0.4	11.9 ± 3.7	0.12 ± 0.03	3.7	13.7	21.7
87	308.2001	40.1487	216	10.2	7.0	$0.11^{+0.04}_{-0.02}$	4.1	0.4	11.2 ± 3.2	0.32 ± 0.07	2.3	14.4	21.6
88	307.5984	40.1557	96	21.8	16.9	$0.31^{+0.09}_{-0.08}$	NaN	NaN	14.0 ± 1.4	0.44 ± 0.03	6.5	14.3	NaN
89	307.8877	40.1635	95	18.4	9.7	$0.18^{+0.08}_{-0.07}$	16.3	1.3	12.0 ± 3.8	0.12 ± 0.03	3.8	13.8	21.8
90	308.2034	40.1811	88	13.5	11.4	$0.18^{+0.02}_{-0.06}$	8.9	1.6	10.7 ± 2.0	0.13 ± 0.02	2.6	14.2	21.5
91	307.5358	40.1923	200	12.0	7.2	$0.13^{+0.04}_{-0.01}$	NaN	NaN	16.9 ± 2.9	0.3 ± 0.05	6.1	13.7	NaN
92	307.5210	40.2020	172	19.2	10.4	$0.17^{+0.12}_{-0.08}$	NaN	NaN	13.9 ± 3.7	0.37 ± 0.07	6.7	13.9	NaN

Continued on next page

Table A.9 – *Continued from previous page*

ID	RA (deg)	decl. (deg)	PA (deg)	σ_{maj} ($''$)	σ_{min} ($''$)	R_{eff} (pc)	M_{obs} ($M_\odot$)	M_{clip} ($M_\odot$)	T_K (K)	σ_{NH_3} (km s^{-1})	V_{NH_3} (km s^{-1})	$\log(N_{p-NH_3})$ (cm^{-2})	$\log(N_{H_2})$ (cm^{-2})
93	308.1366	40.2115	111	18.2	14.1	$0.24^{+0.1}_{-0.04}$	27.4	8.7	20.3 ± 2.1	0.48 ± 0.05	3.7	13.6	21.6
94	307.7446	40.2195	163	14.3	9.4	$0.15^{+0.02}_{-0.04}$	15.8	2.4	13.1 ± 3.2	0.41 ± 0.09	-2.4	14.3	21.7
95	307.5560	40.2270	198	19.0	13.4	$0.18^{+0.09}_{-0.09}$	NaN	NaN	14.8 ± 3.9	0.26 ± 0.07	7.4	13.5	NaN
96	307.9002	40.2307	134	10.3	7.5	$0.12^{+0.02}_{-0.03}$	7.5	0.7	12.8 ± 3.7	0.14 ± 0.03	4.3	13.9	21.8
97	308.1251	40.2331	223	13.3	8.2	$0.14^{+0.04}_{-0.02}$	8.5	1.5	23.3 ± 3.8	0.25 ± 0.04	3.7	14.0	21.6
98	307.5347	40.2362	175	12.9	7.8	$0.11^{+0.06}_{-0.08}$	NaN	NaN	14.2 ± 3.8	0.2 ± 0.04	7.2	14.0	NaN
99	308.0158	40.2425	223	16.7	7.1	$0.14^{+0.05}_{-0.05}$	7.0	0.6	13.0 ± 4.2	0.17 ± 0.04	3.1	13.4	21.7
100	307.6482	40.2461	209	15.4	8.0	$0.15^{+0.04}_{-0.05}$	NaN	NaN	15.0 ± 3.0	0.3 ± 0.05	4.3	14.0	NaN
101	308.1636	40.2636	57	21.2	6.4	$0.15^{+0.11}_{-0.06}$	7.2	1.6	22.7 ± 3.8	0.32 ± 0.06	5.7	13.9	21.6
102	307.4890	40.2609	148	24.5	13.0	$0.27^{+0.12}_{-0.07}$	NaN	NaN	17.8 ± 0.8	0.77 ± 0.03	5.9	14.4	NaN
103	307.3847	40.2731	99	14.2	5.3	$0.11^{+0.08}_{-0.02}$	NaN	NaN	11.9 ± 4.1	0.1 ± 0.02	0.2	13.5	NaN
104	307.5201	40.2763	172	18.1	10.7	$0.19^{+0.06}_{-0.02}$	NaN	NaN	16.6 ± 1.1	0.43 ± 0.03	6.9	14.2	NaN
105	307.9065	40.2864	104	10.1	8.3	$0.13^{+0.0}_{-0.0}$	11.0	0.9	12.8 ± 3.1	0.19 ± 0.04	2.0	14.0	21.9
106	307.9416	40.3144	153	36.6	24.5	$0.4^{+0.24}_{-0.13}$	234.1	69.5	12.1 ± 0.7	0.34 ± 0.01	1.7	14.4	21.9
107	308.1886	40.3031	188	12.7	8.8	$0.13^{+0.04}_{-0.09}$	5.2	0.5	13.2 ± 4.4	0.37 ± 0.09	0.0	13.8	21.7
108	307.9910	40.3081	160	20.5	15.1	$0.27^{+0.09}_{-0.03}$	115.3	54.2	12.1 ± 0.5	0.65 ± 0.02	1.5	14.7	21.8
109	308.0390	40.3153	149	31.3	8.9	$0.23^{+0.2}_{-0.1}$	25.9	5.5	12.1 ± 1.0	0.36 ± 0.02	0.4	14.1	21.8
110	308.0939	40.3358	67	43.9	26.7	$0.51^{+0.17}_{-0.18}$	376.5	235.9	15.0 ± 0.7	0.56 ± 0.02	0.9	14.2	21.8
111	308.2267	40.3250	112	14.4	7.4	$0.13^{+0.05}_{-0.04}$	5.5	0.5	12.5 ± 3.7	0.14 ± 0.03	0.5	13.8	21.6
112	307.6781	40.3230	132	22.7	13.4	$0.24^{+0.25}_{-0.08}$	NaN	NaN	15.0 ± 2.2	0.47 ± 0.05	-0.4	14.0	NaN
113	307.5925	40.3194	151	11.8	8.3	$0.14^{+0.02}_{-0.0}$	NaN	NaN	13.8 ± 2.9	0.19 ± 0.04	-0.2	13.7	NaN
114	308.1744	40.3258	217	12.7	9.5	$0.14^{+0.05}_{-0.07}$	7.1	0.8	14.6 ± 4.0	0.61 ± 0.12	0.6	14.0	21.7
115	308.1393	40.3291	219	15.9	10.7	$0.18^{+0.04}_{-0.04}$	26.1	5.9	11.9 ± 1.1	0.55 ± 0.03	1.7	14.2	21.7
116	307.9058	40.3292	170	19.0	14.2	$0.25^{+0.03}_{-0.02}$	69.5	18.0	11.8 ± 0.6	0.22 ± 0.01	1.1	14.4	21.9
117	307.8530	40.3319	214	10.8	9.3	$0.14^{+-0.0}_{-0.03}$	12.3	1.5	11.9 ± 2.8	0.18 ± 0.03	1.0	14.2	21.9
118	307.5920	40.3363	52	17.8	13.3	$0.22^{+0.05}_{-0.05}$	NaN	NaN	12.1 ± 2.5	0.18 ± 0.03	-0.1	13.9	NaN
119	307.7139	40.3423	116	24.7	13.7	$0.26^{+0.18}_{-0.08}$	41.7	8.0	10.2 ± 1.9	0.15 ± 0.02	0.2	14.0	21.6
120	307.8618	40.3560	185	26.1	20.5	$0.32^{+0.06}_{-0.1}$	95.9	32.5	10.7 ± 1.8	0.42 ± 0.03	0.0	14.2	21.8
121	308.2126	40.3584	141	28.3	12.0	$0.27^{+0.13}_{-0.12}$	28.2	5.0	11.8 ± 2.2	0.27 ± 0.04	0.8	14.0	21.7
122	308.1382	40.3657	159	22.3	14.5	$0.25^{+0.09}_{-0.07}$	30.3	6.8	13.2 ± 2.7	0.57 ± 0.08	1.7	14.1	21.7
123	308.2442	40.3692	220	15.3	9.7	$0.16^{+0.08}_{-0.09}$	9.9	1.8	12.2 ± 3.3	0.21 ± 0.04	0.5	14.1	21.7
124	307.8303	40.3736	150	26.6	21.1	$0.32^{+0.06}_{-0.15}$	103.0	38.8	12.7 ± 2.0	0.58 ± 0.05	0.2	14.2	21.8
125	308.0717	40.3979	124	51.9	27.3	$0.48^{+0.36}_{-0.31}$	101.2	25.4	16.2 ± 2.6	0.62 ± 0.08	0.7	13.7	21.8
126	308.0198	40.3785	210	15.9	13.1	$0.18^{+0.08}_{-0.08}$	12.9	1.4	13.8 ± 2.6	0.21 ± 0.04	1.1	13.9	21.8
127	308.0229	40.3996	91	13.4	7.9	$0.13^{+0.07}_{-0.03}$	6.0	0.1	17.2 ± 4.2	0.49 ± 0.1	0.5	14.2	21.8
128	308.1445	40.4052	84	11.0	8.6	$0.12^{+0.03}_{-0.05}$	4.5	0.2	14.0 ± 3.6	0.43 ± 0.09	0.4	13.8	21.7
129	307.6897	40.4132	188	16.1	8.9	$0.17^{+0.06}_{-0.07}$	NaN	NaN	11.9 ± 3.2	0.24 ± 0.05	9.4	13.9	NaN
130	308.1384	40.4302	176	22.8	11.2	$0.21^{+0.09}_{-0.06}$	16.1	2.7	15.6 ± 3.6	0.35 ± 0.07	0.1	13.8	21.7
131	308.0719	40.4565	108	30.3	13.5	$0.25^{+0.15}_{-0.21}$	21.0	3.0	13.9 ± 3.8	0.37 ± 0.08	0.5	13.7	21.6
132	307.7029	40.4483	64	10.9	9.0	$0.13^{+0.02}_{-0.02}$	NaN	NaN	19.7 ± 3.8	0.54 ± 0.09	10.0	14.3	NaN

Table A.10: Cygnus X North NH_3 (1,1) Leaves Catalog 1

ID	RA (deg)	decl. (deg)	PA (deg)	σ_{maj} ($''$)	σ_{min} ($''$)	R_{eff} (pc)	M_{obs} ($M_\odot$)	M_{clip} ($M_\odot$)	T_K (K)	σ_{NH_3} (km s^{-1})	V_{NH_3} (km s^{-1})	$\log(N_{p-NH_3})$ (cm^{-2})	$\log(N_{H_2})$ (cm^{-2})
0	310.0592	41.1720	224	24.7	15.2	$0.26^{+0.17}_{-0.09}$	31.3	6.1	10.3 ± 1.5	0.16 ± 0.01	5.5	14.0	21.7
1	310.0102	41.1755	142	30.8	15.4	$0.31^{+0.18}_{-0.17}$	43.5	9.7	10.0 ± 1.4	0.19 ± 0.02	5.3	14.1	21.7
2	309.9854	41.2135	46	23.1	9.5	$0.18^{+0.14}_{-0.16}$	15.3	2.0	16.4 ± 3.8	0.49 ± 0.09	-2.7	14.0	21.7
3	310.1076	41.2606	115	19.1	17.0	$0.19^{+0.07}_{-0.17}$	17.2	2.1	17.7 ± 3.7	0.82 ± 0.14	-4.5	14.1	21.7
4	309.7531	41.2946	219	36.7	25.5	$0.43^{+0.42}_{-0.2}$	103.7	48.5	15.1 ± 1.8	0.58 ± 0.05	8.5	14.1	21.6
5	310.2244	41.3259	137	10.8	8.9	$0.13^{+0.06}_{-0.04}$	6.4	1.3	11.0 ± 3.8	0.16 ± 0.04	5.3	13.9	21.6
6	309.9024	41.3304	109	15.4	11.0	$0.19^{+0.07}_{-0.02}$	26.0	11.8	24.3 ± 2.7	0.41 ± 0.05	-2.7	13.8	21.6
7	309.8784	41.3352	171	15.1	12.7	$0.22^{+0.01}_{-0.03}$	31.3	21.3	22.3 ± 1.8	0.45 ± 0.03	-2.8	14.1	21.6
8	309.7541	41.3469	109	19.2	12.0	$0.23^{+0.06}_{-0.02}$	28.4	7.1	14.6 ± 1.4	0.43 ± 0.03	9.4	14.1	21.6
9	309.8690	41.3582	131	36.4	12.9	$0.32^{+0.24}_{-0.15}$	59.9	30.4	20.3 ± 2.4	0.32 ± 0.04	-2.5	13.9	21.7
10	309.9737	41.4009	118	23.6	13.8	$0.22^{+0.11}_{-0.2}$	30.3	9.2	16.5 ± 3.9	0.63 ± 0.12	-3.5	14.1	21.7
11	309.9984	41.4232	93	17.3	10.0	$0.17^{+0.12}_{-0.13}$	14.3	2.8	14.9 ± 3.2	0.36 ± 0.07	-4.8	13.7	21.7
12	309.8336	41.4190	175	16.1	10.5	$0.17^{+0.07}_{-0.06}$	16.1	3.1	19.0 ± 3.4	0.37 ± 0.07	-2.1	13.5	21.7
13	310.0448	41.4464	145	9.8	7.4	$0.12^{+-0.0}_{-0.01}$	6.5	0.9	13.3 ± 2.5	0.22 ± 0.04	-5.3	13.7	21.7

Continued on next page

Table A.10 – *Continued from previous page*

ID	RA (deg)	decl. (deg)	PA (deg)	σ_{maj} ($''$)	σ_{min} ($''$)	R_{eff} (pc)	M_{obs} ($M_\odot$)	M_{clip} ($M_\odot$)	T_K (K)	σ_{NH_3} (km s^{-1})	V_{NH_3} (km s^{-1})	$\log(N_{p-NH_3})$ (cm^{-2})	$\log(N_{H_2})$ (cm^{-2})
14	310.0204	41.4661	139	12.2	9.3	$0.15^{+0.01}_{-0.01}$	31.6	8.3	20.9 ± 1.0	0.49 ± 0.02	-4.9	14.2	21.7
15	310.0262	41.4804	67	12.7	8.8	$0.15^{+0.02}_{-0.01}$	25.9	4.1	17.6 ± 0.7	0.32 ± 0.01	-3.8	14.2	21.7
16	310.0262	41.5357	158	19.6	15.2	$0.31^{+0.13}_{-0.05}$	115.6	62.9	18.6 ± 1.0	0.53 ± 0.02	-4.6	14.3	21.7
17	310.1191	41.5385	135	23.4	11.7	$0.23^{+0.1}_{-0.08}$	26.0	6.8	14.3 ± 3.0	0.31 ± 0.05	-5.4	13.4	21.7
18	309.3513	41.5367	136	14.2	5.5	$0.11^{+0.07}_{-0.04}$	10.3	1.2	16.6 ± 2.2	0.68 ± 0.07	-2.8	14.0	21.7
19	310.0730	41.5387	149	25.7	7.3	$0.17^{+0.14}_{-0.08}$	14.7	1.9	14.7 ± 3.0	0.22 ± 0.04	-4.9	13.9	21.7
20	309.3557	41.5543	99	17.7	14.1	$0.22^{+0.08}_{-0.04}$	43.6	12.6	15.8 ± 1.6	0.76 ± 0.06	-2.5	14.0	21.8
21	309.2983	41.5609	58	23.8	14.9	$0.26^{+0.12}_{-0.1}$	67.0	19.3	18.0 ± 2.4	1.21 ± 0.12	-2.1	13.8	21.8
22	309.2688	41.5666	204	13.4	7.6	$0.13^{+0.04}_{-0.03}$	13.7	1.6	18.8 ± 3.4	0.63 ± 0.1	-1.0	14.0	21.8
23	309.2530	41.5810	181	18.3	13.0	$0.24^{+0.07}_{-0.03}$	59.0	32.3	30.7 ± 2.6	1.01 ± 0.08	-1.9	13.7	21.8
24	310.1553	41.5899	56	12.5	9.9	$0.15^{+0.05}_{-0.04}$	9.1	1.6	16.0 ± 3.1	0.19 ± 0.04	-6.3	13.3	21.7
25	309.3565	41.5954	185	27.5	13.8	$0.3^{+0.21}_{-0.12}$	62.1	24.5	15.3 ± 2.0	0.56 ± 0.06	-1.8	13.9	21.8
26	309.2095	41.6042	174	27.1	25.2	$0.38^{+0.25}_{-0.14}$	143.0	84.3	23.5 ± 1.8	0.79 ± 0.05	-2.7	14.2	21.8
27	310.1620	41.6089	211	17.2	11.9	$0.2^{+0.07}_{-0.05}$	20.4	3.3	15.9 ± 3.2	0.24 ± 0.05	-5.8	13.8	21.6
28	309.1746	41.6190	224	18.1	13.6	$0.17^{+0.1}_{-0.08}$	19.6	2.4	16.6 ± 3.8	0.77 ± 0.13	-3.1	14.3	21.7
29	310.1405	41.6428	120	31.9	23.3	$0.43^{+0.24}_{-0.1}$	135.1	63.7	16.0 ± 1.5	0.38 ± 0.03	-5.7	14.0	21.7
30	309.0296	41.6670	174	26.2	15.4	$0.35^{+0.08}_{-0.11}$	97.8	56.1	22.1 ± 1.2	0.75 ± 0.03	11.3	14.3	21.6
31	308.9153	41.7133	106	13.3	8.5	$0.12^{+0.04}_{-0.06}$	5.8	0.9	11.6 ± 4.5	0.36 ± 0.09	-3.0	14.1	21.6
32	310.1206	41.7557	159	42.3	20.6	$0.48^{+0.31}_{-0.25}$	193.2	95.2	17.6 ± 1.4	0.78 ± 0.05	-4.2	14.1	21.7
33	310.0615	41.7525	154	21.9	10.7	$0.2^{+0.13}_{-0.07}$	19.7	3.1	15.9 ± 3.4	0.86 ± 0.13	-2.3	13.8	21.7
34	310.1917	41.8087	120	18.5	13.2	$0.17^{+0.06}_{-0.14}$	13.0	2.2	20.4 ± 3.4	0.38 ± 0.06	-6.6	13.9	21.8
35	310.1270	41.8266	109	19.4	8.4	$0.18^{+0.09}_{-0.04}$	59.8	17.7	18.2 ± 0.5	0.54 ± 0.01	-4.4	14.4	21.8
36	310.1385	41.8433	129	13.6	8.3	$0.15^{+0.02}_{-0.02}$	49.1	9.5	18.3 ± 0.5	0.66 ± 0.02	-4.8	14.4	21.8
37	309.2791	41.8503	113	21.0	10.1	$0.18^{+0.09}_{-0.14}$	13.9	1.1	16.5 ± 3.8	0.5 ± 0.1	8.8	13.9	21.7
38	309.1768	41.8540	132	18.1	13.7	$0.22^{+0.07}_{-0.04}$	23.8	6.7	20.3 ± 2.7	0.44 ± 0.06	12.9	13.9	21.7
39	310.2647	41.8562	58	17.3	8.5	$0.14^{+0.07}_{-0.07}$	10.7	1.9	16.9 ± 4.3	0.41 ± 0.1	0.2	13.8	21.7
40	310.4130	41.8617	128	13.4	9.5	$0.16^{+0.03}_{-0.02}$	9.8	1.6	12.5 ± 3.5	0.53 ± 0.1	8.9	14.1	21.6
41	310.1650	41.8810	169	26.3	14.1	$0.28^{+0.12}_{-0.1}$	60.7	26.7	20.2 ± 1.8	0.36 ± 0.03	-5.6	13.9	21.8
42	309.3125	41.8919	116	35.0	17.1	$0.36^{+0.17}_{-0.15}$	57.1	18.0	14.1 ± 2.4	0.4 ± 0.05	8.2	13.7	21.7
43	310.1438	41.8935	150	13.1	7.1	$0.13^{+0.06}_{-0.04}$	9.2	1.0	23.7 ± 3.9	0.57 ± 0.09	-6.4	13.9	21.8
44	310.1361	41.9072	218	10.5	7.5	$0.12^{+0.02}_{-0.01}$	8.8	0.7	18.5 ± 3.9	0.55 ± 0.09	-5.7	13.9	21.8
45	309.1422	41.9126	59	12.2	9.5	$0.15^{+0.02}_{-0.03}$	9.9	2.0	13.6 ± 2.7	0.38 ± 0.06	16.1	14.1	21.7
46	310.3367	41.9444	159	10.5	9.2	$0.14^{+0.01}_{-0.02}$	7.4	0.9	14.6 ± 3.4	0.25 ± 0.05	8.6	14.0	21.7
47	310.1195	41.9521	118	27.1	8.6	$0.2^{+0.21}_{-0.09}$	62.1	28.6	18.4 ± 0.9	0.5 ± 0.02	-6.4	14.3	21.8
48	310.1882	41.9629	89	16.0	14.5	$0.22^{+0.02}_{-0.03}$	38.2	18.9	24.9 ± 2.8	0.58 ± 0.06	-7.2	13.9	21.8
49	310.1377	41.9790	111	19.1	7.7	$0.16^{+0.08}_{-0.07}$	37.9	13.8	19.6 ± 1.0	0.49 ± 0.02	-6.3	14.1	21.8
50	309.9857	41.9990	79	40.0	20.0	$0.43^{+0.22}_{-0.15}$	163.3	79.3	15.3 ± 1.4	0.53 ± 0.04	8.3	14.2	21.7
51	309.1468	41.9885	145	27.4	16.4	$0.33^{+0.16}_{-0.1}$	71.3	27.8	14.8 ± 1.5	0.33 ± 0.03	12.3	13.9	21.7
52	309.1729	41.9833	140	12.6	6.5	$0.12^{+0.04}_{-0.03}$	7.2	1.2	13.3 ± 4.5	0.62 ± 0.13	12.3	13.9	21.7
53	309.6347	41.9860	50	12.4	8.7	$0.14^{+0.02}_{-0.05}$	9.0	0.3	13.0 ± 3.7	0.15 ± 0.03	3.2	13.5	21.7
54	309.7383	42.0087	203	23.3	16.7	$0.3^{+0.06}_{-0.04}$	32.8	4.7	10.2 ± 2.1	0.14 ± 0.01	3.3	13.9	21.7
55	309.4376	42.0066	171	14.9	13.7	$0.19^{+0.07}_{-0.04}$	17.4	0.8	13.4 ± 2.9	0.22 ± 0.04	3.2	13.8	21.8
56	309.4029	42.0207	125	39.0	23.3	$0.39^{+0.19}_{-0.22}$	82.6	10.0	12.0 ± 3.3	0.32 ± 0.06	3.6	13.7	21.8
57	309.6569	42.0154	187	20.7	14.8	$0.26^{+0.08}_{-0.07}$	36.4	5.8	10.9 ± 2.4	0.19 ± 0.03	3.6	13.8	21.7
58	309.7670	42.0199	75	16.1	12.9	$0.21^{+0.05}_{-0.03}$	16.1	2.7	10.1 ± 2.3	0.15 ± 0.02	3.4	14.1	21.7
59	309.1377	42.0136	48	9.3	6.7	$0.11^{+0.02}_{-0.02}$	5.7	0.6	13.3 ± 3.2	0.23 ± 0.05	11.9	14.1	21.7
60	310.1853	42.0250	115	21.1	11.4	$0.22^{+0.11}_{-0.11}$	30.0	7.5	21.1 ± 3.3	0.54 ± 0.08	-6.3	13.9	21.7
61	309.9638	42.0287	77	13.6	9.1	$0.16^{+0.03}_{-0.01}$	19.7	2.6	13.1 ± 2.6	0.3 ± 0.05	8.8	14.0	21.7
62	309.4327	42.0398	127	17.3	9.9	$0.15^{+0.08}_{-0.1}$	11.1	1.4	13.0 ± 3.0	0.17 ± 0.03	3.8	13.3	21.8
63	309.6706	42.0481	134	23.1	14.7	$0.25^{+0.09}_{-0.12}$	28.1	2.1	19.3 ± 3.2	0.41 ± 0.07	8.1	13.5	21.7
64	309.6957	42.0543	133	11.1	8.3	$0.13^{+0.01}_{-0.01}$	7.1	1.2	13.4 ± 3.4	0.18 ± 0.04	9.0	13.8	21.7
65	309.4483	42.0560	172	18.0	10.5	$0.19^{+0.06}_{-0.05}$	19.6	2.2	10.6 ± 3.2	0.18 ± 0.03	3.8	13.7	21.8
66	309.4124	42.0703	103	17.4	15.5	$0.21^{+0.09}_{-0.1}$	27.7	3.0	12.6 ± 2.4	0.35 ± 0.05	4.5	13.6	21.8
67	309.9355	42.0730	112	13.1	10.0	$0.15^{+0.05}_{-0.03}$	14.0	3.1	18.4 ± 3.3	0.37 ± 0.06	-6.8	14.0	21.7
68	309.5170	42.0751	204	15.5	10.3	$0.16^{+0.07}_{-0.11}$	13.1	1.7	15.9 ± 3.1	0.36 ± 0.06	-2.5	13.8	21.7
69	309.4275	42.0809	48	13.5	10.0	$0.14^{+0.07}_{-0.04}$	12.3	0.7	13.4 ± 2.9	0.33 ± 0.06	4.3	13.8	21.8
70	309.4622	42.0883	197	14.8	9.9	$0.16^{+0.04}_{-0.07}$	14.4	1.8	18.5 ± 4.6	0.36 ± 0.09	-1.5	14.1	21.8
71	309.6459	42.1033	120	25.3	19.0	$0.34^{+0.14}_{-0.09}$	78.1	32.0	19.5 ± 2.2	0.62 ± 0.06	8.1	13.9	21.7
72	309.1380	42.0943	187	22.5	14.6	$0.2^{+0.1}_{-0.18}$	17.4	2.8	14.8 ± 3.7	0.41 ± 0.08	12.9	13.5	21.7
73	309.0885	42.1123	205	34.4	20.4	$0.38^{+0.3}_{-0.17}$	92.9	32.0	19.1 ± 1.4	0.86 ± 0.05	14.7	14.0	21.7
74	309.4131	42.1134	70	30.0	14.5	$0.27^{+0.2}_{-0.11}$	39.8	8.8	20.2 ± 2.7	0.43 ± 0.06	-0.2	13.9	21.7
75	309.0404	42.1236	83	23.8	10.3	$0.19^{+0.12}_{-0.17}$	21.3	4.3	16.3 ± 2.3	0.52 ± 0.06	15.6	13.7	21.7

Continued on next page

Table A.10 – *Continued from previous page*

ID	RA (deg)	decl. (deg)	PA (deg)	σ_{maj} ($''$)	σ_{min} ($''$)	R_{eff} (pc)	M_{obs} ($M_\odot$)	M_{clip} ($M_\odot$)	T_K (K)	σ_{NH_3} (km s^{-1})	V_{NH_3} (km s^{-1})	$\log(N_{p-NH_3})$ (cm^{-2})	$\log(N_{H_2})$ (cm^{-2})
76	309.0027	42.1231	216	23.1	12.1	$0.21^{+0.18}_{-0.08}$	25.4	5.4	14.1 ± 2.5	0.53 ± 0.07	14.1	14.0	21.7
77	309.9779	42.1204	187	12.7	10.2	$0.13^{+0.05}_{-0.1}$	8.5	1.7	10.3 ± 3.2	0.36 ± 0.07	3.8	14.7	21.7
78	309.3160	42.1303	108	12.6	9.5	$0.15^{+0.02}_{-0.04}$	9.8	1.1	13.7 ± 2.8	0.3 ± 0.05	15.4	13.7	21.7
79	309.2862	42.1398	63	22.9	16.4	$0.31^{+0.13}_{-0.09}$	52.1	16.5	14.2 ± 1.5	0.52 ± 0.04	15.7	14.2	21.7
80	309.8744	42.1376	218	12.0	7.3	$0.13^{+0.04}_{-0.02}$	8.2	0.9	20.2 ± 3.5	0.3 ± 0.05	-6.3	13.9	21.7
81	309.5623	42.1466	51	14.9	8.3	$0.15^{+0.06}_{-0.01}$	8.5	1.4	11.9 ± 2.8	0.26 ± 0.04	15.9	13.9	21.7
82	309.1136	42.1478	66	17.4	12.3	$0.23^{+0.03}_{-0.03}$	22.6	8.5	16.4 ± 1.7	0.43 ± 0.04	15.2	14.1	21.7
83	309.0186	42.1655	108	48.6	35.5	$0.56^{+0.59}_{-0.41}$	287.0	115.0	15.5 ± 0.9	0.63 ± 0.03	14.2	14.3	21.7
84	309.8860	42.1735	168	15.3	10.1	$0.17^{+0.05}_{-0.05}$	10.6	0.6	14.4 ± 3.8	0.61 ± 0.11	8.7	13.8	21.7
85	309.3371	42.1889	208	19.7	12.7	$0.23^{+0.06}_{-0.04}$	34.1	7.8	16.3 ± 1.7	0.59 ± 0.05	15.9	14.0	21.7
86	309.2437	42.1952	174	24.2	21.6	$0.34^{+0.26}_{-0.08}$	203.5	117.8	20.4 ± 0.4	0.72 ± 0.01	15.2	14.6	21.7
87	309.8118	42.1961	89	17.4	6.1	$0.13^{+0.11}_{-0.08}$	11.3	0.8	25.0 ± 2.9	0.41 ± 0.05	-4.0	13.6	21.7
88	309.5867	42.1928	161	16.0	11.7	$0.2^{+0.08}_{-0.05}$	26.5	13.7	18.7 ± 2.4	0.42 ± 0.05	-2.2	14.3	21.7
89	309.3550	42.1940	216	10.2	6.8	$0.11^{+0.03}_{-0.01}$	6.6	0.7	14.4 ± 2.3	0.37 ± 0.05	14.8	13.6	21.7
90	309.4188	42.2005	90	14.5	11.0	$0.18^{+0.01}_{-0.01}$	13.1	1.6	12.7 ± 2.5	0.24 ± 0.04	15.7	14.0	21.7
91	309.8025	42.2150	58	26.6	8.1	$0.17^{+0.14}_{-0.13}$	17.3	2.4	26.9 ± 3.2	0.46 ± 0.05	-3.4	13.7	21.8
92	309.3769	42.2277	91	22.4	15.6	$0.29^{+0.08}_{-0.03}$	84.1	35.7	18.1 ± 1.0	0.46 ± 0.02	-1.7	14.1	21.7
93	309.0128	42.2244	197	19.3	17.3	$0.24^{+0.11}_{-0.1}$	39.5	7.8	18.2 ± 1.6	0.49 ± 0.04	13.9	13.9	21.7
94	309.2371	42.2193	91	10.7	6.8	$0.12^{+0.02}_{-0.0}$	16.2	2.4	16.7 ± 0.6	0.45 ± 0.01	16.5	14.4	21.7
95	308.9313	42.2389	120	26.1	17.0	$0.26^{+0.11}_{-0.23}$	34.7	9.3	16.5 ± 3.1	0.62 ± 0.09	14.4	13.9	21.7
96	309.3111	42.2393	144	21.5	10.6	$0.18^{+0.11}_{-0.08}$	10.8	0.9	15.2 ± 3.9	0.4 ± 0.09	-1.4	14.0	21.7
97	309.5473	42.2400	167	10.6	8.9	$0.14^{+0.05}_{-0.02}$	7.7	1.2	16.2 ± 2.2	0.29 ± 0.04	16.8	14.3	21.6
98	309.7897	42.2498	225	31.4	13.8	$0.25^{+0.2}_{-0.13}$	39.2	12.5	22.1 ± 3.8	0.64 ± 0.1	-2.5	14.1	21.9
99	309.3535	42.2498	217	20.2	17.5	$0.28^{+0.05}_{-0.04}$	64.2	15.4	17.9 ± 1.1	0.35 ± 0.02	-2.0	14.1	21.7
100	309.4530	42.2511	165	12.5	10.2	$0.16^{+0.05}_{-0.03}$	9.2	1.0	14.8 ± 2.7	0.35 ± 0.06	16.5	14.1	21.7
101	309.8935	42.2556	78	15.3	7.3	$0.13^{+0.08}_{-0.1}$	8.2	0.8	16.8 ± 2.8	1.12 ± 0.14	15.8	13.4	21.8
102	309.8170	42.2556	204	13.5	8.8	$0.14^{+0.04}_{-0.04}$	11.6	1.6	13.9 ± 2.6	0.31 ± 0.05	-3.9	13.6	21.9
103	309.8425	42.2679	186	48.6	15.9	$0.43^{+0.39}_{-0.22}$	170.4	85.4	18.3 ± 0.9	0.74 ± 0.03	18.4	14.3	21.8
104	309.3811	42.2715	151	18.3	13.9	$0.18^{+0.06}_{-0.12}$	21.1	3.1	16.0 ± 3.4	0.45 ± 0.08	15.8	13.5	21.7
105	308.9255	42.2679	74	13.9	11.3	$0.18^{+0.02}_{-0.04}$	19.5	3.7	19.0 ± 2.9	0.43 ± 0.06	13.2	13.5	21.7
106	309.1334	42.2816	133	27.7	10.3	$0.25^{+0.3}_{-0.11}$	33.5	6.5	13.4 ± 2.1	0.24 ± 0.03	3.1	14.0	21.7
107	309.3264	42.2745	174	12.4	6.6	$0.13^{+0.05}_{-0.02}$	16.1	2.6	17.9 ± 0.8	0.46 ± 0.02	17.4	14.3	21.7
108	309.7550	42.2834	210	17.3	9.0	$0.17^{+0.06}_{-0.09}$	33.4	12.0	25.1 ± 2.3	0.92 ± 0.07	-1.9	13.9	22.0
109	309.3902	42.2827	173	24.6	8.1	$0.16^{+0.17}_{-0.12}$	16.5	2.7	18.0 ± 4.2	0.4 ± 0.09	3.8	13.9	21.7
110	308.9175	42.2828	198	14.4	11.4	$0.18^{+0.02}_{-0.03}$	20.1	3.7	20.6 ± 3.7	0.38 ± 0.07	13.0	13.5	21.7
111	309.7576	42.3078	205	30.9	20.9	$0.38^{+0.09}_{-0.07}$	333.7	162.9	22.6 ± 0.8	0.74 ± 0.02	-1.9	14.4	22.0
112	309.4034	42.3107	165	14.5	9.8	$0.17^{+0.1}_{-0.05}$	11.3	2.0	16.4 ± 2.4	0.38 ± 0.05	-1.5	13.9	21.7
113	308.8782	42.3063	224	13.5	5.3	$0.11^{+0.04}_{-0.04}$	5.9	0.4	17.3 ± 4.5	0.95 ± 0.19	14.8	14.7	21.7
114	308.8895	42.3338	138	23.9	18.2	$0.39^{+0.17}_{-0.13}$	201.7	151.6	21.2 ± 0.9	0.65 ± 0.02	15.2	14.4	21.7
115	309.7207	42.3213	169	12.5	7.0	$0.13^{+0.04}_{-0.02}$	21.8	7.9	26.7 ± 3.7	0.68 ± 0.09	-2.3	13.8	22.0
116	309.3083	42.3316	62	12.6	9.4	$0.15^{+0.05}_{-0.02}$	13.2	2.2	16.2 ± 3.5	0.37 ± 0.07	-0.2	14.0	21.7
117	309.7487	42.3367	142	22.9	10.4	$0.21^{+0.11}_{-0.07}$	103.7	41.3	26.0 ± 1.3	0.71 ± 0.03	-2.3	14.2	22.1
118	309.7467	42.3827	83	43.1	10.6	$0.28^{+0.41}_{-0.17}$	640.1	272.7	25.0 ± 0.2	1.25 ± 0.01	-3.2	15.0	22.1
119	309.8153	42.3740	213	15.1	11.2	$0.2^{+0.05}_{-0.02}$	17.0	2.8	12.4 ± 1.9	0.29 ± 0.04	16.1	14.2	22.1
120	309.5600	42.3804	165	14.2	11.5	$0.15^{+0.06}_{-0.1}$	10.5	1.3	16.1 ± 3.6	0.27 ± 0.06	14.2	13.7	21.7
121	309.5882	42.3792	164	14.2	10.4	$0.17^{+0.07}_{-0.02}$	11.4	2.5	13.1 ± 2.7	0.36 ± 0.06	13.9	13.8	21.8
122	309.8773	42.3874	186	20.3	12.2	$0.23^{+0.12}_{-0.06}$	20.0	3.0	13.3 ± 2.6	0.39 ± 0.06	8.7	13.9	21.9
123	309.6921	42.4047	136	11.0	6.2	$0.12^{+0.02}_{-0.01}$	11.0	1.2	18.2 ± 1.9	0.46 ± 0.04	-2.2	13.7	22.1
124	309.5169	42.4104	223	13.9	13.1	$0.19^{+0.04}_{-0.04}$	24.8	5.0	14.2 ± 1.9	0.33 ± 0.04	8.4	13.7	21.7
125	309.5373	42.4168	172	11.9	8.8	$0.14^{+0.04}_{-0.02}$	14.1	2.3	15.4 ± 2.5	0.28 ± 0.05	8.2	13.7	21.7
126	309.7572	42.4205	114	18.4	8.0	$0.17^{+0.08}_{-0.06}$	180.2	37.4	20.9 ± 0.2	0.67 ± 0.0	-4.1	15.0	22.1
127	308.7175	42.4215	61	19.4	10.3	$0.18^{+0.13}_{-0.04}$	14.5	2.8	14.6 ± 3.7	0.84 ± 0.14	4.4	14.1	21.6
128	309.4521	42.4271	186	32.3	10.8	$0.26^{+0.2}_{-0.1}$	36.0	12.4	22.3 ± 3.1	0.3 ± 0.05	-0.6	13.6	21.6
129	309.6767	42.4323	85	18.3	11.6	$0.21^{+0.08}_{-0.03}$	26.4	10.0	17.6 ± 2.8	0.31 ± 0.05	-2.5	13.6	22.0
130	309.4163	42.4234	161	17.8	5.3	$0.13^{+0.09}_{-0.06}$	7.7	0.6	22.6 ± 4.5	0.23 ± 0.06	-0.4	13.4	21.6
131	309.7146	42.4553	206	19.9	16.3	$0.26^{+0.09}_{-0.07}$	92.8	39.8	17.8 ± 0.7	0.53 ± 0.02	-2.8	14.2	22.0
132	309.6871	42.4724	68	24.9	9.2	$0.2^{+0.2}_{-0.07}$	43.4	9.9	19.9 ± 0.9	0.39 ± 0.02	-3.3	14.0	22.0
133	309.7463	42.4862	64	26.5	15.7	$0.26^{+0.15}_{-0.1}$	67.1	15.3	17.7 ± 1.5	0.57 ± 0.05	-2.1	13.9	22.0
134	309.7195	42.5327	62	11.6	8.9	$0.13^{+0.04}_{-0.02}$	7.6	0.8	16.7 ± 3.5	0.33 ± 0.07	-2.4	13.6	21.9
135	309.8030	42.5437	46	20.5	12.0	$0.23^{+0.1}_{-0.05}$	29.1	7.0	13.9 ± 2.0	0.42 ± 0.05	8.7	13.9	21.8
136	309.6502	42.5441	120	13.2	10.7	$0.13^{+0.05}_{-0.07}$	8.5	0.7	19.8 ± 3.9	0.64 ± 0.11	-3.3	13.8	21.9
137	309.5605	42.5468	190	10.2	8.0	$0.12^{+0.0}_{-0.01}$	8.7	1.3	18.6 ± 1.9	0.64 ± 0.06	-2.4	13.6	21.8

Continued on next page

Table A.10 – *Continued from previous page*

ID	RA (deg)	decl. (deg)	PA (deg)	σ_{maj} ($''$)	σ_{min} ($''$)	R_{eff} (pc)	M_{obs} ($M_\odot$)	M_{clip} ($M_\odot$)	T_K (K)	σ_{NH_3} (km s^{-1})	V_{NH_3} (km s^{-1})	$\log(N_{p-NH_3})$ (cm^{-2})	$\log(N_{H_2})$ (cm^{-2})
138	309.5275	42.5541	198	26.0	9.5	$0.22^{+0.21}_{-0.07}$	31.1	8.9	18.6 ± 1.4	0.4 ± 0.03	-1.6	13.9	21.8
139	309.7823	42.5587	212	12.8	10.4	$0.15^{+0.03}_{-0.04}$	12.9	2.5	14.7 ± 2.4	0.31 ± 0.05	8.8	13.6	21.8
140	309.4874	42.5606	218	19.5	9.5	$0.19^{+0.13}_{-0.05}$	15.0	3.4	20.5 ± 2.8	0.37 ± 0.05	-1.4	13.8	21.7
141	309.7737	42.5718	203	10.3	7.5	$0.12^{+0.03}_{-0.0}$	7.5	0.6	13.0 ± 2.1	0.24 ± 0.03	8.6	13.8	21.8
142	309.6865	42.5758	79	12.7	5.4	$0.11^{+0.04}_{-0.04}$	8.5	0.9	18.6 ± 2.7	0.46 ± 0.06	-3.0	13.6	21.9
143	309.7295	42.5934	213	22.0	14.7	$0.24^{+0.14}_{-0.08}$	31.6	6.7	13.7 ± 2.4	0.32 ± 0.05	8.6	14.0	21.9
144	309.6780	42.5868	99	11.4	8.7	$0.14^{+0.0}_{-0.0}$	14.9	2.3	15.4 ± 2.2	0.42 ± 0.05	-3.1	13.9	21.9
145	309.4921	42.5911	213	13.6	7.3	$0.12^{+0.07}_{-0.03}$	5.3	0.5	19.4 ± 4.4	0.29 ± 0.07	-0.9	13.8	21.8
146	309.6459	42.5949	148	16.4	8.1	$0.15^{+0.07}_{-0.05}$	18.3	4.4	13.5 ± 1.7	0.3 ± 0.03	-2.6	13.9	21.9
147	309.6988	42.6064	49	16.5	8.7	$0.14^{+0.05}_{-0.08}$	16.1	2.0	15.2 ± 2.9	0.66 ± 0.1	8.6	13.8	21.9
148	309.6301	42.6034	161	17.2	9.4	$0.17^{+0.09}_{-0.04}$	25.3	9.9	26.2 ± 1.8	0.77 ± 0.05	9.3	13.8	21.9
149	309.6446	42.6285	194	39.8	21.6	$0.5^{+0.18}_{-0.19}$	464.1	374.6	26.8 ± 0.6	0.91 ± 0.02	9.5	14.5	21.9
150	308.6955	42.6118	166	16.6	9.5	$0.15^{+0.1}_{-0.06}$	8.4	1.2	14.2 ± 3.7	0.48 ± 0.09	3.7	14.0	21.6
151	309.5721	42.6168	200	19.7	9.5	$0.19^{+0.09}_{-0.06}$	37.6	9.5	14.3 ± 0.7	0.34 ± 0.01	-2.6	14.1	21.9
152	309.7220	42.6238	210	16.4	10.7	$0.2^{+0.04}_{-0.04}$	28.9	10.2	15.0 ± 1.2	0.24 ± 0.02	9.8	14.1	21.9
153	309.5459	42.6318	63	17.8	12.2	$0.21^{+0.06}_{-0.04}$	60.1	23.4	15.4 ± 0.6	0.42 ± 0.01	-2.1	14.2	21.9
154	309.7519	42.6287	197	16.4	11.4	$0.19^{+0.05}_{-0.03}$	18.9	2.6	15.8 ± 3.1	0.39 ± 0.07	10.1	13.3	21.8
155	309.6937	42.6317	56	10.5	7.2	$0.12^{+0.02}_{-0.0}$	16.2	1.0	18.5 ± 1.9	0.46 ± 0.04	10.0	14.0	21.9
156	309.5957	42.6374	78	21.3	11.3	$0.22^{+0.12}_{-0.05}$	36.1	7.2	15.0 ± 1.3	0.32 ± 0.03	-3.0	13.9	21.9
157	308.7366	42.6323	50	15.9	9.1	$0.17^{+0.06}_{-0.03}$	12.2	1.8	14.1 ± 2.0	0.38 ± 0.05	11.6	14.1	21.6
158	309.4807	42.6376	80	10.8	7.0	$0.12^{+0.03}_{-0.0}$	15.7	1.8	15.7 ± 0.7	0.35 ± 0.01	-1.0	14.1	21.8
159	309.5647	42.6559	150	22.6	18.7	$0.3^{+0.06}_{-0.05}$	76.3	24.5	15.1 ± 1.1	0.38 ± 0.02	-2.6	14.0	21.9
160	309.4509	42.6447	180	15.4	4.3	$0.12^{+0.06}_{-0.03}$	14.3	1.9	17.0 ± 0.9	0.42 ± 0.02	-0.8	14.1	21.8
161	309.4718	42.6494	150	11.8	6.6	$0.12^{+0.02}_{-0.03}$	12.9	0.9	15.4 ± 0.8	0.4 ± 0.02	-0.7	14.1	21.8
162	309.3975	42.6564	193	21.4	13.0	$0.26^{+0.1}_{-0.06}$	37.0	9.9	14.3 ± 1.5	0.26 ± 0.03	-0.2	13.9	21.7
163	309.6400	42.6663	140	29.0	19.1	$0.37^{+0.27}_{-0.12}$	157.1	75.8	17.8 ± 0.9	0.61 ± 0.03	12.8	14.3	21.9
164	308.7055	42.6604	111	23.9	15.9	$0.3^{+0.09}_{-0.09}$	42.7	12.0	12.6 ± 1.5	0.26 ± 0.03	12.7	14.1	21.6
165	309.5200	42.6644	192	21.9	17.9	$0.29^{+0.05}_{-0.07}$	169.1	65.2	14.9 ± 0.3	0.38 ± 0.01	-2.3	14.5	21.9
166	309.5855	42.6741	66	13.1	12.9	$0.18^{+-0.0}_{-0.01}$	24.9	3.0	14.7 ± 0.9	0.32 ± 0.02	-3.2	14.1	21.9
167	309.4875	42.6796	220	25.1	11.6	$0.24^{+0.11}_{-0.06}$	92.8	24.8	15.2 ± 0.4	0.46 ± 0.01	-1.4	14.4	21.8
168	309.3559	42.6788	201	20.9	11.0	$0.22^{+0.12}_{-0.07}$	22.2	4.0	13.9 ± 2.6	0.27 ± 0.04	0.4	13.9	21.7
169	309.4270	42.6841	121	16.8	11.5	$0.19^{+0.14}_{-0.06}$	17.7	3.6	12.0 ± 3.0	0.31 ± 0.05	-0.3	14.0	21.8
170	309.3949	42.6803	126	21.9	8.3	$0.16^{+0.09}_{-0.09}$	11.3	0.8	17.1 ± 3.8	0.26 ± 0.06	-0.3	13.4	21.7
171	309.7012	42.6796	97	12.0	6.5	$0.11^{+0.02}_{-0.04}$	7.9	1.3	16.7 ± 3.4	0.66 ± 0.11	11.8	14.1	21.8
172	309.6025	42.6962	113	32.6	9.2	$0.23^{+0.2}_{-0.11}$	40.0	6.8	14.7 ± 1.0	0.35 ± 0.02	-3.1	13.9	21.9
173	309.7123	42.6953	92	15.4	12.1	$0.2^{+0.06}_{-0.02}$	23.5	2.8	15.1 ± 1.8	0.28 ± 0.03	12.9	13.9	21.8
174	308.8052	42.6920	199	10.6	6.6	$0.12^{+0.02}_{-0.02}$	6.1	0.4	15.9 ± 3.7	0.56 ± 0.11	10.8	13.9	21.6
175	309.5203	42.6991	134	15.4	9.6	$0.17^{+0.04}_{-0.05}$	13.3	2.1	17.2 ± 3.3	0.31 ± 0.06	-2.0	13.5	21.8
176	309.3899	42.7017	222	20.8	8.4	$0.15^{+0.15}_{-0.05}$	9.4	2.3	14.2 ± 4.1	0.34 ± 0.09	-1.2	14.0	21.7
177	309.4653	42.7065	56	14.0	8.7	$0.15^{+0.05}_{-0.02}$	12.3	2.2	12.8 ± 2.8	0.35 ± 0.06	-1.0	13.8	21.8
178	309.5005	42.7174	127	16.4	8.4	$0.16^{+0.09}_{-0.02}$	9.4	1.5	14.6 ± 3.2	0.27 ± 0.06	-1.1	13.5	21.8
179	309.3741	42.7182	47	17.2	9.3	$0.17^{+0.12}_{-0.05}$	11.8	1.8	15.4 ± 3.5	0.49 ± 0.09	-0.7	13.8	21.7
180	309.4436	42.7264	225	25.2	14.3	$0.29^{+0.16}_{-0.07}$	50.0	17.1	14.4 ± 1.8	0.34 ± 0.04	-0.9	13.9	21.7
181	308.8296	42.7309	105	27.0	10.5	$0.24^{+0.19}_{-0.1}$	28.0	7.7	17.1 ± 2.8	0.44 ± 0.06	12.8	14.0	21.6
182	309.5981	42.7297	123	18.7	8.3	$0.16^{+0.08}_{-0.08}$	11.8	1.5	15.8 ± 4.4	0.3 ± 0.08	-2.9	13.8	21.8
183	309.4205	42.7468	142	12.5	10.2	$0.16^{+0.02}_{-0.01}$	12.3	1.9	13.9 ± 2.9	0.32 ± 0.06	-0.3	13.7	21.7
184	309.4080	42.7591	89	16.2	11.4	$0.19^{+0.03}_{-0.02}$	20.1	2.8	12.4 ± 2.3	0.25 ± 0.04	0.2	13.6	21.7
185	309.3775	42.7798	48	18.0	14.6	$0.24^{+0.06}_{-0.03}$	34.2	11.8	12.6 ± 2.0	0.23 ± 0.03	0.2	13.8	21.6
186	308.9387	42.8101	102	23.0	11.8	$0.24^{+0.12}_{-0.09}$	38.2	7.2	16.5 ± 2.4	0.42 ± 0.05	11.4	14.1	21.7
187	309.2974	42.8052	171	16.6	9.0	$0.15^{+0.1}_{-0.08}$	10.7	2.1	13.0 ± 4.0	0.44 ± 0.09	2.0	13.8	21.6
188	309.2772	42.8128	192	16.8	10.5	$0.18^{+0.07}_{-0.03}$	16.8	2.7	12.3 ± 3.6	0.35 ± 0.06	2.1	13.3	21.6
189	308.9723	42.8216	82	22.7	13.4	$0.2^{+0.18}_{-0.07}$	24.3	3.4	12.2 ± 4.4	0.54 ± 0.12	4.8	14.3	21.7
190	309.2436	42.8218	200	15.8	11.8	$0.21^{+0.07}_{-0.04}$	24.6	7.6	15.9 ± 1.9	0.39 ± 0.04	2.3	13.8	21.6
191	309.2739	42.8413	219	11.5	7.8	$0.13^{+0.01}_{-0.01}$	7.2	1.0	15.3 ± 3.0	0.2 ± 0.04	1.6	13.6	21.6
192	309.1533	42.8527	193	33.9	21.0	$0.45^{+0.31}_{-0.14}$	177.9	110.2	16.8 ± 1.0	0.51 ± 0.03	12.9	14.3	21.5
193	309.0271	42.8422	105	13.1	10.6	$0.15^{+0.05}_{-0.08}$	11.9	1.1	22.0 ± 4.6	0.92 ± 0.16	10.1	14.2	21.6
194	308.9552	42.8811	171	34.0	14.8	$0.35^{+0.19}_{-0.16}$	NaN	NaN	13.0 ± 1.7	0.33 ± 0.04	3.9	14.1	NaN
195	309.0956	42.8832	48	18.6	9.1	$0.15^{+0.08}_{-0.1}$	NaN	NaN	17.5 ± 2.5	0.73 ± 0.09	11.6	13.9	NaN
196	309.0671	42.8808	46	13.5	10.1	$0.17^{+0.07}_{-0.02}$	NaN	NaN	14.1 ± 1.5	0.48 ± 0.04	11.9	14.3	NaN
197	309.0100	42.8825	111	15.7	7.2	$0.13^{+0.08}_{-0.07}$	NaN	NaN	15.0 ± 4.4	0.88 ± 0.19	10.9	14.1	NaN
198	309.1893	42.9114	157	33.0	17.8	$0.37^{+0.38}_{-0.13}$	NaN	NaN	14.9 ± 1.3	0.35 ± 0.03	11.6	14.2	NaN
199	309.1178	42.9102	105	14.8	8.0	$0.14^{+0.04}_{-0.04}$	NaN	NaN	13.9 ± 4.1	0.48 ± 0.1	11.7	14.1	NaN

Table A.11: NGC7538 NH_3 (1,1) Leaves Catalog 1

ID	RA (deg)	decl. (deg)	PA (deg)	σ_{maj} ($''$)	σ_{min} ($''$)	R_{eff} (pc)	M_{obs} ($M_\odot$)	M_{clip} ($M_\odot$)	T_K (K)	σ_{NH_3} (km s^{-1})	V_{NH_3} (km s^{-1})	$\log(N_{p-NH_3})$ (cm^{-2})	$\log(N_{H_2})$ (cm^{-2})
0	348.8620	61.1181	139	32.1	20.6	$0.69^{+0.39}_{-0.33}$	285.6	193.5	23.4 ± 2.2	0.91 ± 0.07	-56.7	13.9	21.5
1	348.9680	61.1322	145	14.0	10.1	$0.3^{+0.06}_{-0.09}$	21.7	3.6	14.3 ± 3.4	0.46 ± 0.09	-55.7	13.9	21.4
2	348.8169	61.1278	191	14.8	7.8	$0.27^{+0.08}_{-0.18}$	22.2	4.9	12.7 ± 3.0	0.45 ± 0.08	-56.0	14.3	21.5
3	348.9377	61.1448	224	15.1	12.7	$0.38^{+0.11}_{-0.04}$	43.6	17.3	18.0 ± 2.5	0.36 ± 0.05	-54.8	13.8	21.4
4	348.8210	61.1466	203	14.8	7.2	$0.26^{+0.14}_{-0.23}$	17.4	2.6	11.9 ± 3.7	0.59 ± 0.12	-55.8	14.4	21.5
5	349.2294	61.2020	152	20.9	7.5	$0.27^{+0.24}_{-0.21}$	20.9	2.1	15.9 ± 3.6	0.53 ± 0.1	-53.6	13.8	21.4
6	349.2145	61.2320	50	18.5	13.2	$0.38^{+0.18}_{-0.14}$	40.2	6.7	16.2 ± 3.7	0.62 ± 0.11	-52.8	14.0	21.5
7	349.1750	61.2647	60	36.5	23.3	$0.81^{+0.41}_{-0.46}$	280.3	120.9	16.8 ± 2.3	0.54 ± 0.06	-52.3	13.5	21.5
8	348.6059	61.2528	148	21.4	8.2	$0.33^{+0.25}_{-0.12}$	36.6	14.7	16.4 ± 3.9	0.39 ± 0.08	-56.3	13.8	21.4
9	349.1789	61.3055	89	29.1	19.7	$0.5^{+0.29}_{-0.35}$	85.1	29.5	15.5 ± 3.6	0.92 ± 0.15	-53.1	14.0	21.6
10	349.1047	61.3026	194	10.7	7.2	$0.22^{+0.06}_{-0.06}$	24.6	4.5	16.0 ± 1.5	0.88 ± 0.06	-53.0	13.6	21.6
11	349.1310	61.3100	127	12.8	6.3	$0.23^{+0.06}_{-0.07}$	25.5	4.1	16.4 ± 1.3	0.82 ± 0.05	-53.5	14.1	21.7
12	348.8187	61.3430	130	26.4	11.3	$0.43^{+0.32}_{-0.23}$	152.8	39.7	14.1 ± 2.1	0.59 ± 0.06	-50.6	13.7	21.8
13	348.1818	61.3447	80	17.8	14.0	$0.45^{+0.11}_{-0.08}$	101.2	32.7	14.9 ± 2.3	0.74 ± 0.08	-55.3	13.9	21.7
14	349.1694	61.3430	213	10.8	9.6	$0.22^{+0.04}_{-0.17}$	15.9	1.3	20.4 ± 3.7	1.03 ± 0.15	-53.2	14.3	21.7
15	348.6798	61.3484	141	25.6	13.7	$0.45^{+0.24}_{-0.22}$	73.7	17.6	17.5 ± 3.9	0.4 ± 0.08	-49.7	14.0	21.6
16	348.8180	61.3600	118	18.8	10.4	$0.32^{+0.28}_{-0.18}$	85.0	17.6	13.5 ± 2.4	1.46 ± 0.15	-49.3	14.0	21.8
17	349.1407	61.3587	167	12.7	9.1	$0.24^{+0.16}_{-0.09}$	36.7	7.4	19.8 ± 1.3	1.39 ± 0.07	-53.6	13.8	21.8
18	349.0876	61.3598	152	15.4	10.2	$0.32^{+0.14}_{-0.11}$	79.5	24.4	14.6 ± 0.8	0.61 ± 0.03	-52.5	14.2	21.9
19	348.9793	61.3656	182	40.3	19.1	$0.8^{+0.56}_{-0.3}$	571.1	353.7	17.4 ± 0.8	0.81 ± 0.03	-52.6	14.2	21.8
20	348.8967	61.3618	135	14.0	8.3	$0.28^{+0.1}_{-0.07}$	51.8	4.8	14.0 ± 1.4	0.53 ± 0.04	-51.9	13.9	21.8
21	349.2577	61.3688	49	14.5	7.4	$0.22^{+0.09}_{-0.16}$	15.8	1.0	15.4 ± 4.1	0.44 ± 0.1	-51.8	14.1	21.6
22	349.0553	61.3754	207	23.6	15.7	$0.54^{+0.13}_{-0.11}$	424.0	179.6	15.5 ± 0.7	0.8 ± 0.03	-51.9	14.3	21.9
23	348.1828	61.3706	140	18.1	9.5	$0.35^{+0.12}_{-0.1}$	77.8	15.0	14.0 ± 2.2	0.52 ± 0.06	-54.4	13.9	21.8
24	349.1334	61.3783	134	28.3	12.8	$0.51^{+0.32}_{-0.17}$	260.5	82.8	15.9 ± 0.6	0.72 ± 0.02	-53.0	14.4	21.8
25	349.1650	61.3754	77	11.1	8.3	$0.23^{+0.07}_{-0.05}$	51.7	7.0	18.4 ± 0.8	1.05 ± 0.04	-52.0	14.2	21.8
26	348.1158	61.3758	126	14.8	9.5	$0.32^{+0.06}_{-0.04}$	127.2	23.3	15.3 ± 1.0	0.82 ± 0.04	-52.5	14.2	21.9
27	348.6142	61.3792	64	11.6	8.1	$0.24^{+0.05}_{-0.04}$	26.4	5.8	13.8 ± 3.4	0.46 ± 0.08	-52.9	13.9	21.6
28	348.8573	61.3800	176	21.8	8.3	$0.32^{+0.16}_{-0.19}$	47.4	10.6	14.9 ± 3.9	1.01 ± 0.19	-48.8	14.6	21.8
29	348.1475	61.3823	178	11.2	7.1	$0.23^{+0.03}_{-0.05}$	65.3	8.8	15.5 ± 0.9	0.64 ± 0.03	-54.7	14.3	21.9
30	349.3561	61.3914	194	16.2	6.8	$0.25^{+0.17}_{-0.16}$	19.6	4.0	14.5 ± 3.3	0.36 ± 0.07	-50.8	13.9	21.4
31	349.0111	61.4015	62	18.0	11.3	$0.37^{+0.1}_{-0.1}$	72.6	13.9	14.1 ± 1.9	0.41 ± 0.04	-52.9	13.8	21.8
32	349.0676	61.4029	47	23.5	9.7	$0.41^{+0.21}_{-0.15}$	69.4	18.7	14.9 ± 2.6	0.42 ± 0.06	-52.9	13.7	21.8
33	348.9744	61.4164	76	43.7	9.7	$0.51^{+0.58}_{-0.28}$	163.2	63.2	14.0 ± 2.3	0.83 ± 0.08	-52.5	13.8	21.8
34	348.0187	61.4092	197	28.3	14.7	$0.54^{+0.31}_{-0.18}$	160.4	33.0	15.8 ± 3.4	0.58 ± 0.1	-55.8	13.8	21.8
35	349.1990	61.4093	130	9.1	7.5	$0.22^{+0.0}_{-0.02}$	25.6	1.9	12.9 ± 1.2	0.66 ± 0.04	-51.9	13.9	21.7
36	348.5659	61.4156	104	13.1	10.4	$0.28^{+0.09}_{-0.12}$	33.4	4.2	10.8 ± 3.4	0.33 ± 0.07	-48.6	14.2	21.8
37	349.3035	61.4236	89	24.2	8.8	$0.36^{+0.29}_{-0.14}$	37.2	6.6	16.3 ± 4.1	0.69 ± 0.14	-52.2	14.1	21.5
38	348.3604	61.4178	136	13.3	6.7	$0.25^{+0.12}_{-0.04}$	156.6	27.7	20.1 ± 0.8	0.91 ± 0.03	-56.3	14.2	22.2
39	349.0301	61.4223	217	14.3	10.1	$0.34^{+0.04}_{-0.04}$	45.1	13.8	17.4 ± 2.1	0.51 ± 0.05	-53.1	13.4	21.7
40	348.3346	61.4229	149	13.7	11.0	$0.33^{+0.03}_{-0.05}$	279.1	86.9	17.6 ± 0.8	0.65 ± 0.02	-53.2	14.3	22.2
41	348.1103	61.4337	147	28.4	21.5	$0.66^{+0.33}_{-0.25}$	275.4	68.2	15.3 ± 2.4	0.5 ± 0.06	-55.7	13.7	21.9
42	349.2358	61.4322	131	16.4	10.7	$0.34^{+0.09}_{-0.1}$	46.0	8.5	15.6 ± 2.4	0.56 ± 0.06	-51.5	13.7	21.5
43	348.4427	61.4496	156	40.2	28.7	$0.94^{+0.59}_{-0.64}$	3041.4	2208.1	26.9 ± 0.6	1.21 ± 0.02	-56.4	14.5	22.2
44	348.1571	61.4445	142	10.5	7.5	$0.23^{+0.03}_{-0.01}$	34.6	2.8	12.0 ± 3.7	0.49 ± 0.09	-55.7	14.0	22.0
45	349.2767	61.4465	91	10.5	7.1	$0.23^{+0.04}_{-0.01}$	17.1	2.1	13.5 ± 3.3	0.41 ± 0.07	-51.5	13.8	21.5
46	348.9484	61.4619	75	29.0	12.3	$0.52^{+0.42}_{-0.22}$	173.1	94.9	15.4 ± 2.1	0.53 ± 0.06	-53.2	14.0	21.6
47	348.2268	61.4502	137	10.8	8.1	$0.23^{+0.07}_{-0.06}$	105.2	13.3	20.1 ± 0.8	0.94 ± 0.03	-58.0	14.3	22.0
48	348.5225	61.4516	184	17.4	6.4	$0.28^{+0.14}_{-0.09}$	130.5	28.9	23.0 ± 0.8	0.85 ± 0.03	-57.5	14.3	22.1
49	348.2411	61.4603	147	11.2	7.3	$0.24^{+0.04}_{-0.05}$	126.9	13.5	21.2 ± 0.9	1.6 ± 0.05	-57.2	14.3	22.0
50	348.2969	61.4751	126	29.5	16.7	$0.61^{+0.36}_{-0.3}$	392.6	196.3	19.2 ± 1.6	0.76 ± 0.05	-59.2	14.2	22.0
51	348.3725	61.4813	56	15.2	11.4	$0.35^{+0.14}_{-0.1}$	104.8	33.1	29.3 ± 2.6	0.93 ± 0.07	-58.5	13.8	22.1
52	348.9557	61.4957	91	15.7	10.2	$0.34^{+0.09}_{-0.06}$	73.3	16.9	14.0 ± 2.3	0.41 ± 0.05	-52.7	13.5	21.6
53	348.5167	61.5183	204	35.7	23.9	$0.83^{+0.48}_{-0.33}$	463.8	280.0	21.1 ± 1.9	0.66 ± 0.05	-55.8	14.0	21.7
54	348.9695	61.5118	86	13.2	8.1	$0.28^{+0.06}_{-0.06}$	46.7	8.4	13.7 ± 2.2	0.44 ± 0.05	-52.1	13.6	21.6
55	348.9835	61.5376	105	37.9	11.6	$0.45^{+0.56}_{-0.38}$	123.1	30.7	14.8 ± 2.2	0.49 ± 0.06	-51.5	13.9	21.6
56	349.0687	61.5900	86	16.4	11.0	$0.37^{+0.12}_{-0.04}$	98.4	35.8	15.6 ± 1.7	0.45 ± 0.04	-50.6	14.0	21.7
57	349.0372	61.6071	70	19.4	12.6	$0.45^{+0.1}_{-0.07}$	172.9	66.9	20.4 ± 1.6	0.57 ± 0.04	-50.2	13.9	21.8

Continued on next page

Table A.11 – *Continued from previous page*

ID	RA (deg)	decl. (deg)	PA (deg)	σ_{maj} ($''$)	σ_{min} ($''$)	R_{eff} (pc)	M_{obs} ($M_\odot$)	M_{clip} ($M_\odot$)	T_K (K)	σ_{NH_3} (km s^{-1})	V_{NH_3} (km s^{-1})	$\log(N_{p-NH_3})$ (cm^{-2})	$\log(N_{H_2})$ (cm^{-2})
58	348.9210	61.6102	146	15.6	11.5	$0.36^{+0.17}_{-0.09}$	55.2	12.6	14.2 ± 2.7	0.38 ± 0.06	-50.1	13.8	21.6
59	349.1925	61.6448	84	32.3	25.7	$0.96^{+0.33}_{-0.2}$	621.0	366.8	15.6 ± 1.0	0.61 ± 0.03	-51.4	14.2	21.7
60	349.0568	61.6289	156	15.4	10.6	$0.36^{+0.11}_{-0.05}$	76.8	30.2	18.8 ± 2.1	0.62 ± 0.06	-51.4	14.0	21.8
61	349.0081	61.6380	108	22.0	14.7	$0.49^{+0.17}_{-0.08}$	144.0	50.6	13.1 ± 2.8	0.51 ± 0.06	-52.3	13.7	21.8
62	349.1215	61.6389	211	10.9	6.3	$0.22^{+0.03}_{-0.03}$	21.3	3.2	18.1 ± 2.4	0.55 ± 0.06	-51.5	13.3	21.7
63	349.0942	61.6385	205	12.6	7.6	$0.26^{+0.03}_{-0.05}$	35.3	6.0	15.3 ± 2.1	0.47 ± 0.05	-51.4	13.7	21.8
64	349.0450	61.6478	150	18.1	11.3	$0.3^{+0.16}_{-0.17}$	39.2	7.3	18.6 ± 3.0	0.65 ± 0.09	-51.3	13.5	21.8
65	348.9884	61.6650	85	14.9	9.7	$0.34^{+0.03}_{-0.02}$	101.5	33.8	15.9 ± 1.8	0.54 ± 0.05	-48.2	14.2	21.7
66	348.9845	61.6933	83	31.7	15.1	$0.55^{+0.37}_{-0.23}$	186.4	67.5	12.7 ± 2.1	0.48 ± 0.05	-51.8	13.6	21.7
67	348.6898	61.7674	124	18.6	5.6	$0.23^{+0.21}_{-0.1}$	6.2	0.4	10.0 ± 3.0	1.42 ± 0.3	-58.1	15.5	21.2
68	348.9339	61.7927	77	19.1	17.5	$0.61^{+0.25}_{-0.08}$	416.1	247.8	20.8 ± 1.0	0.71 ± 0.03	-48.9	14.4	21.7
69	349.0691	61.7895	182	25.6	8.5	$0.37^{+0.27}_{-0.25}$	71.6	22.2	15.2 ± 3.2	0.71 ± 0.11	-49.7	13.7	21.7
70	349.0520	61.8005	160	15.9	8.5	$0.29^{+0.08}_{-0.11}$	53.0	9.9	15.1 ± 3.2	0.68 ± 0.1	-49.4	13.6	21.7
71	348.9485	61.8150	104	12.5	9.1	$0.26^{+0.12}_{-0.06}$	32.1	2.2	13.7 ± 2.9	0.4 ± 0.06	-49.1	13.7	21.7
72	349.0657	61.8166	166	15.7	7.4	$0.27^{+0.1}_{-0.09}$	34.3	2.3	11.8 ± 4.0	0.43 ± 0.11	-48.8	14.3	21.6

Appendix B

Continuation of Table 3.5

This appendix provides a continuation of the NH_3 (1,1) Leaves Catalog 2 shown in Table 3.5, which only presented the W3-west catalog. The catalogs for the remaining KEYSTONE clouds are listed below.

Table B.1: W3 NH_3 (1,1) Leaves Catalog 2

ID	α_{vir}	M_{vir} ($M_\odot$)	σ_{nt} (km s^{-1})	$\log\lvert\Omega_G\rvert$ (erg)	$\log\Omega_K$ (erg)	$\log\lvert\Omega_{Pw}\rvert$ (erg)	$\log\lvert\Omega_{Pt}\rvert$ (erg)	on-filament	hub	N_{proto}	Bad N(H_2) Pix
0	1.77	12.6	0.18	43.2	43.2	43.4	NaN	True	False	0	0.00
1	1.19	31.5	0.24	44.0	43.9	44.3	NaN	True	False	0	0.00
2	1.39	35.0	0.31	44.1	44.0	44.1	NaN	True	False	0	0.00
3	5.13	89.2	0.57	43.8	44.3	44.0	NaN	True	False	0	0.00
4	4.15	108.9	0.59	44.1	44.5	44.3	NaN	False	False	1	0.00
5	0.48	141.1	0.38	45.8	45.2	45.6	NaN	False	True	6	0.00
6	11.61	94.2	0.74	43.3	44.2	43.5	NaN	False	False	0	0.00
7	0.83	68.1	0.35	44.9	44.6	44.8	NaN	False	False	1	0.00
8	5.25	130.9	0.73	44.1	44.6	44.0	NaN	False	False	1	0.00
9	0.80	32.0	0.23	44.4	44.1	44.5	NaN	False	False	3	0.00
10	2.37	33.9	0.34	43.7	43.8	43.9	NaN	False	False	0	0.00
11	2.68	57.4	0.41	44.0	44.2	44.0	NaN	False	False	2	0.00
12	7.61	193.8	0.94	44.2	44.9	44.0	NaN	True	False	0	0.00
13	2.82	208.5	0.90	45.0	45.3	44.4	NaN	True	False	0	0.00
14	5.23	49.6	0.53	43.5	44.0	43.8	NaN	True	False	0	0.00
15	0.51	169.4	0.65	46.2	45.7	45.0	NaN	False	True	4	0.00
16	1.86	29.2	0.23	43.7	43.8	44.2	NaN	True	False	1	0.00
17	0.48	181.2	0.66	46.3	45.7	45.0	NaN	False	True	9	0.00
18	1.15	76.1	0.39	44.7	44.6	44.8	NaN	False	False	1	0.00
19	1.62	157.2	0.57	45.0	45.0	44.9	NaN	False	False	1	0.00
20	6.62	83.7	0.63	43.6	44.2	44.1	NaN	False	False	0	0.00
21	1.07	64.2	0.33	44.6	44.5	44.8	NaN	False	False	0	0.00
22	2.28	140.8	0.68	44.8	45.0	44.5	NaN	True	False	0	0.00
23	1.87	18.4	0.24	43.5	43.5	43.8	NaN	False	False	1	0.00
24	2.79	66.8	0.42	44.0	44.3	44.1	NaN	True	False	1	0.00
25	3.16	44.8	0.43	43.7	44.0	43.9	NaN	True	False	2	0.00
26	2.31	67.9	0.44	44.2	44.3	44.4	NaN	True	False	1	0.00
27	1.02	34.0	0.26	44.2	44.0	44.5	NaN	True	False	1	0.00
28	1.41	15.0	0.18	43.5	43.5	43.7	NaN	True	False	0	0.00
29	2.53	26.3	0.35	43.5	43.7	43.6	NaN	True	False	0	0.00
30	2.57	32.0	0.34	43.6	43.8	43.8	NaN	True	False	0	0.00
31	2.35	111.3	0.53	44.5	44.7	44.5	NaN	False	False	0	0.00
32	4.42	153.4	0.70	44.3	44.8	44.4	45.7	False	False	0	0.00
33	1.53	20.4	0.20	43.5	43.5	43.9	NaN	True	False	0	0.00
34	8.72	129.7	0.85	43.8	44.5	43.8	46.1	False	False	0	0.00
35	1.20	45.3	0.29	44.3	44.2	44.4	NaN	True	False	2	0.00
36	1.78	486.9	1.13	46.0	46.0	44.8	46.6	False	False	0	0.08
37	1.70	31.2	0.29	43.8	43.9	44.0	NaN	True	False	0	0.00

Continued on next page

Table B.1 – *Continued from previous page*

ID	α_{vir}	M_{vir} ($M_\odot$)	σ_{nt} (km s^{-1})	$\log\lvert\Omega_G\rvert$ (erg)	$\log\Omega_K$ (erg)	$\log\lvert\Omega_{Pw}\rvert$ (erg)	$\log\lvert\Omega_{Pt}\rvert$ (erg)	on-filament	hub	N_{proto}	Bad $N(H_2)$ Pix
38	2.53	274.3	0.99	45.3	45.5	44.3	NaN	False	False	3	0.00
39	2.41	19.8	0.23	43.2	43.4	43.7	NaN	True	False	0	0.00
40	1.28	82.2	0.45	44.8	44.7	44.6	45.8	True	False	1	0.00
41	0.61	74.6	0.32	45.1	44.7	45.0	NaN	True	False	2	0.00
42	2.09	34.5	0.33	43.8	43.9	43.9	NaN	True	False	0	0.00
43	1.03	20.3	0.30	44.1	43.9	43.4	NaN	True	False	0	0.00
44	1.15	24.2	0.32	44.1	44.0	43.5	NaN	True	False	0	0.00
45	1.66	101.7	0.46	44.7	44.7	44.7	NaN	True	False	0	0.00
46	0.98	56.0	0.30	44.6	44.4	44.5	NaN	True	False	4	0.00
47	6.53	111.0	0.74	43.9	44.5	43.7	NaN	True	False	0	0.00
48	1.38	34.2	0.33	44.1	44.1	43.9	NaN	True	False	1	0.00
49	3.88	148.4	0.67	44.4	44.8	44.4	NaN	True	False	0	0.00
50	1.75	39.5	0.34	44.0	44.0	44.1	NaN	True	False	0	0.00
51	3.43	119.8	0.61	44.3	44.7	44.3	NaN	True	False	2	0.00
52	5.80	75.4	0.54	43.6	44.2	43.8	NaN	False	False	0	0.00
53	2.06	19.5	0.26	43.4	43.5	43.6	NaN	True	False	0	0.00
54	1.42	29.1	0.29	44.0	43.9	43.9	NaN	True	False	2	0.00
55	1.58	18.4	0.21	43.5	43.5	43.7	NaN	True	False	0	0.00
56	2.17	22.4	0.29	43.5	43.6	43.6	NaN	True	False	0	0.00
57	1.51	17.6	0.19	43.5	43.5	43.7	NaN	False	False	0	0.00
58	1.19	53.8	0.35	44.5	44.4	44.4	NaN	True	False	1	0.00
59	1.10	23.9	0.21	43.9	43.8	44.1	NaN	True	False	0	0.00
60	2.21	16.4	0.20	43.2	43.4	43.4	NaN	True	False	0	0.00
61	0.61	37.5	0.22	44.7	44.2	44.6	NaN	True	False	1	0.00
62	0.87	30.0	0.21	44.3	44.0	44.3	NaN	True	False	0	0.00
63	3.29	24.3	0.35	43.2	43.6	43.3	NaN	True	False	0	0.00
64	7.32	67.0	0.57	43.4	44.0	43.7	NaN	False	False	0	0.00
65	2.46	57.9	0.40	44.0	44.2	44.1	NaN	False	False	1	0.00
66	4.46	120.4	0.62	44.1	44.6	44.3	45.9	False	False	0	0.00
67	1.73	254.9	0.70	45.4	45.4	45.0	47.0	False	False	1	0.00
68	2.46	17.7	0.20	43.1	43.3	43.6	NaN	False	False	0	0.00
69	1.52	296.4	0.65	45.5	45.5	45.4	46.9	True	False	3	0.00
70	2.29	25.2	0.25	43.4	43.6	43.8	NaN	False	False	0	0.00
71	1.15	71.3	0.38	44.7	44.6	44.6	NaN	False	False	3	0.00
72	2.52	58.2	0.42	44.0	44.2	44.2	NaN	False	False	0	0.00
73	4.84	214.6	0.74	44.4	44.9	44.7	46.2	True	False	0	0.00
74	1.74	483.0	1.10	46.0	46.0	44.7	46.8	False	False	3	0.14
75	4.12	76.3	0.63	44.0	44.5	43.6	NaN	False	False	0	0.00
76	1.83	39.0	0.33	44.0	44.0	44.2	45.8	True	False	0	0.00
77	1.73	193.1	0.60	45.1	45.2	45.0	46.4	True	False	2	0.00
78	7.84	59.6	0.56	43.2	43.9	43.5	NaN	True	False	0	0.00
79	3.19	78.4	0.51	44.1	44.4	44.2	45.7	True	False	0	0.00
80	3.28	104.3	0.56	44.2	44.6	44.2	NaN	True	False	0	0.00
81	10.63	165.9	0.93	43.8	44.6	43.7	NaN	True	False	0	0.00
82	5.46	93.7	0.62	43.8	44.3	43.9	NaN	True	False	0	0.00
83	5.19	37.2	0.37	43.1	43.6	43.6	NaN	True	False	0	0.00

Table B.2: MonR2 NH_3 (1,1) Leaves Catalog 2

ID	α_{vir}	M_{vir} ($M_\odot$)	σ_{nt} (km s^{-1})	$\log\lvert\Omega_G\rvert$ (erg)	$\log\Omega_K$ (erg)	$\log\lvert\Omega_{Pw}\rvert$ (erg)	$\log\lvert\Omega_{Pt}\rvert$ (erg)	on-filament	hub	N_{proto}	Bad $N(H_2)$ Pix
0	1.62	10.4	0.17	43.1	43.1	43.6	NaN	True	False	0	0
1	7.28	26.0	0.41	42.7	43.4	43.3	NaN	True	False	0	0
2	1.46	13.0	0.17	43.4	43.3	43.8	NaN	False	False	0	0
3	6.35	60.8	0.52	43.4	44.0	44.0	NaN	False	False	0	0
4	0.77	20.6	0.19	44.1	43.8	44.5	NaN	True	False	3	0
5	1.52	8.7	0.14	43.1	43.1	43.6	NaN	False	False	0	0
6	1.57	21.9	0.35	43.9	43.9	43.8	NaN	True	False	2	0
7	5.44	15.2	0.32	42.6	43.1	43.1	NaN	True	False	0	0
8	1.91	24.5	0.33	43.7	43.8	43.9	NaN	True	False	1	0
9	3.86	16.0	0.27	42.8	43.2	43.3	NaN	True	False	0	0
10	5.32	15.2	0.28	42.5	43.1	43.1	NaN	True	False	0	0
11	NaN	4.9	0.09	NaN	NaN	NaN	NaN	False	False	0	0
12	2.65	8.4	0.14	42.6	42.8	43.2	NaN	True	False	0	0

Continued on next page

Table B.2 – *Continued from previous page*

ID	α_{vir}	M_{vir} ($M_\odot$)	σ_{nt} (km s^{-1})	log|Ω_G| (erg)	logΩ_K (erg)	log|Ω_{Pw}| (erg)	log|Ω_{Pt}| (erg)	on-filament	hub	N_{proto}	Bad N(H_2) Pix
13	1.67	12.8	0.21	43.3	43.3	43.6	NaN	True	False	1	0
14	4.58	8.8	0.23	42.3	42.8	42.9	NaN	True	False	0	0
15	4.42	12.0	0.33	42.7	43.1	42.8	NaN	True	False	0	0
16	1.44	12.6	0.33	43.7	43.7	43.4	NaN	True	False	1	0
17	3.19	13.2	0.31	43.0	43.3	43.1	NaN	True	False	1	0
18	0.77	108.1	0.58	45.6	45.2	45.2	NaN	False	True	0	0
19	3.65	28.6	0.44	43.4	43.8	43.6	NaN	True	False	0	0
20	2.86	27.0	0.33	43.4	43.6	43.7	NaN	True	False	1	0
21	1.81	50.1	0.52	44.4	44.5	44.3	NaN	True	False	0	0
22	4.01	38.8	0.68	43.8	44.2	43.4	NaN	True	False	0	0
23	0.60	35.7	0.33	44.9	44.5	44.7	NaN	True	False	4	0
24	2.74	9.5	0.24	42.9	43.1	43.2	NaN	True	False	0	0
25	5.09	16.2	0.37	42.8	43.3	43.1	NaN	False	False	0	0
26	4.10	16.6	0.29	42.9	43.3	43.4	NaN	False	False	0	0
27	2.12	6.4	0.16	42.7	42.8	43.3	NaN	False	False	1	0
28	3.16	14.8	0.30	43.0	43.3	43.2	NaN	True	False	0	0
29	4.00	19.8	0.27	43.0	43.4	43.6	NaN	False	False	0	0
30	3.16	27.6	0.38	43.4	43.7	43.7	NaN	True	False	2	0
31	6.11	23.4	0.38	42.8	43.4	43.3	NaN	True	False	0	0
32	2.27	10.3	0.16	42.9	43.1	43.4	NaN	True	False	0	0
33	2.38	13.0	0.22	43.1	43.2	43.5	NaN	False	False	0	0
34	8.53	12.5	0.30	42.1	42.8	42.7	NaN	False	False	0	0
35	3.14	6.9	0.19	42.4	42.7	42.9	NaN	False	False	0	0
36	10.03	19.0	0.44	42.4	43.2	42.7	NaN	True	False	0	0
37	4.76	6.7	0.17	42.1	42.6	42.6	NaN	True	False	0	0
38	0.98	17.9	0.20	43.9	43.7	44.1	NaN	True	False	2	0
39	2.40	4.9	0.10	42.3	42.5	42.9	NaN	True	False	0	0
40	1.04	11.9	0.13	43.5	43.3	43.9	NaN	True	False	0	0
41	1.51	7.8	0.10	43.0	42.9	43.5	NaN	True	False	0	0

Table B.3: MonR1 NH_3 (1,1) Leaves Catalog 2

ID	α_{vir}	M_{vir} ($M_\odot$)	σ_{nt} (km s^{-1})	log|Ω_G| (erg)	logΩ_K (erg)	log|Ω_{Pw}| (erg)	log|Ω_{Pt}| (erg)	on-filament	hub	N_{proto}	Bad N(H_2) Pix
0	0.47	14.8	0.18	44.4	43.8	44.6	NaN	True	False	1	0
1	1.00	4.9	0.10	43.0	42.8	43.6	NaN	True	False	0	0
2	1.85	5.7	0.20	42.8	42.8	43.3	NaN	True	False	0	0
3	1.06	6.2	0.11	43.2	43.0	43.8	NaN	True	False	0	0
4	6.16	25.0	0.45	42.9	43.5	43.4	NaN	False	False	0	0
5	1.84	20.3	0.42	43.8	43.9	43.9	NaN	True	False	1	0
6	1.09	5.3	0.11	43.1	42.9	43.5	NaN	False	False	0	0
7	0.71	18.0	0.29	44.3	44.0	44.5	NaN	True	False	1	0
8	1.84	27.0	0.46	44.0	44.0	44.1	NaN	True	False	1	0
9	1.12	4.7	0.14	43.0	42.8	43.6	NaN	False	False	0	0
10	1.35	11.8	0.21	43.4	43.4	44.0	NaN	True	False	0	0
11	9.01	17.5	0.45	42.4	43.2	43.1	NaN	True	False	0	0
12	1.18	45.1	0.48	44.6	44.5	44.7	NaN	True	False	0	0
13	4.87	14.7	0.37	42.7	43.2	43.3	NaN	True	False	0	0
14	1.23	26.9	0.36	44.2	44.1	44.4	NaN	True	False	1	0
15	5.28	15.4	0.38	42.7	43.2	43.3	NaN	True	False	0	0
16	1.28	25.9	0.36	44.1	44.0	44.4	NaN	True	False	0	0
17	7.66	25.5	0.52	42.8	43.5	43.5	NaN	True	False	0	0
18	1.78	32.3	0.37	44.0	44.0	44.5	NaN	True	False	0	0
19	9.81	47.6	0.80	43.2	44.0	43.5	NaN	True	False	0	0
20	2.64	19.4	0.41	43.4	43.7	43.8	NaN	True	False	0	0
21	0.82	6.7	0.14	43.4	43.1	43.9	NaN	True	False	0	0
22	0.72	5.2	0.09	43.4	43.0	43.8	NaN	True	False	0	0
23	1.20	3.1	0.09	42.7	42.5	43.3	NaN	False	False	0	0
24	3.81	16.7	0.45	43.1	43.5	43.4	NaN	True	False	0	0
25	9.77	53.2	0.74	43.2	44.0	43.7	NaN	True	False	0	0
26	2.19	6.6	0.21	42.7	42.9	43.4	NaN	False	False	0	0
27	15.43	60.5	0.91	43.0	44.0	43.5	NaN	True	False	0	0
28	0.40	18.0	0.22	44.6	44.0	44.9	NaN	True	False	1	0
29	3.29	10.2	0.31	42.8	43.1	43.2	NaN	False	False	0	0

Continued on next page

Table B.3 – *Continued from previous page*

ID	α_{vir}	M_{vir} ($M_\odot$)	σ_{nt} (km s^{-1})	$\log\lvert\Omega_G\rvert$ (erg)	$\log\Omega_K$ (erg)	$\log\lvert\Omega_{Pw}\rvert$ (erg)	$\log\lvert\Omega_{Pt}\rvert$ (erg)	on-filament	hub	N_{proto}	Bad $N(H_2)$ Pix
30	0.72	11.5	0.26	44.0	43.7	44.2	NaN	True	False	0	0
31	1.36	3.7	0.12	42.7	42.6	43.2	NaN	False	False	0	0
32	1.50	3.2	0.10	42.5	42.5	43.2	NaN	True	False	0	0
33	5.08	20.5	0.47	43.0	43.5	43.4	NaN	True	False	0	0
34	0.68	4.6	0.16	43.5	43.1	43.7	NaN	True	False	0	0
35	0.45	15.6	0.26	44.6	44.0	44.6	NaN	True	False	0	0
36	4.10	28.4	0.50	43.4	43.8	43.9	NaN	True	False	0	0
37	1.96	58.5	0.48	44.3	44.4	44.7	NaN	True	False	0	0
38	29.94	102.0	1.22	42.9	44.2	43.4	NaN	True	False	0	0
39	14.50	183.5	1.19	43.8	44.7	44.1	NaN	True	False	0	0
40	0.62	12.9	0.18	44.1	43.6	44.5	NaN	True	False	1	0

Table B.4: Rosette NH_3 (1,1) Leaves Catalog 2

ID	α_{vir}	M_{vir} ($M_\odot$)	σ_{nt} (km s^{-1})	$\log\lvert\Omega_G\rvert$ (erg)	$\log\Omega_K$ (erg)	$\log\lvert\Omega_{Pw}\rvert$ (erg)	$\log\lvert\Omega_{Pt}\rvert$ (erg)	on-filament	hub	N_{proto}	Bad $N(H_2)$ Pix
0	0.86	21.7	0.20	44.1	43.9	44.2	NaN	True	False	0	0
1	2.21	95.6	0.56	44.5	44.7	44.4	NaN	True	False	3	0
2	11.64	55.2	0.67	43.0	43.9	43.2	NaN	False	False	2	0
3	8.76	44.7	0.57	43.0	43.8	43.4	NaN	True	False	0	0
4	0.76	67.1	0.36	45.0	44.7	45.0	NaN	True	False	1	0
5	4.80	17.5	0.33	42.8	43.2	43.3	NaN	False	False	0	0
6	1.53	11.4	0.20	43.3	43.3	43.6	NaN	True	False	0	0
7	1.36	34.3	0.34	44.2	44.1	44.3	NaN	True	False	1	0
8	2.43	24.2	0.31	43.5	43.7	43.9	NaN	False	False	0	0
9	0.89	18.1	0.24	44.0	43.8	44.1	NaN	True	False	2	0
10	0.86	109.7	0.50	45.3	45.1	45.0	NaN	True	False	0	0
11	1.37	20.8	0.25	43.7	43.7	44.1	NaN	False	False	0	0
12	3.91	26.2	0.39	43.2	43.6	43.6	NaN	False	False	0	0
13	5.47	38.9	0.48	43.2	43.8	43.7	NaN	False	False	0	0
14	2.73	39.4	0.42	43.8	44.0	44.0	NaN	False	False	0	0
15	12.45	141.9	0.96	43.6	44.5	43.8	NaN	True	False	0	0
16	1.23	11.3	0.17	43.4	43.3	43.8	NaN	True	False	1	0
17	1.43	64.8	0.47	44.6	44.6	44.5	NaN	True	False	1	0
18	2.39	29.9	0.41	43.7	43.9	43.8	NaN	True	False	0	0
19	3.47	18.6	0.33	43.0	43.4	43.4	NaN	True	False	0	0
20	1.96	11.1	0.23	43.1	43.2	43.6	NaN	True	False	0	0
21	1.80	49.6	0.39	44.2	44.2	44.4	NaN	True	False	0	0
22	1.67	56.1	0.47	44.4	44.4	44.4	NaN	True	False	2	0
23	2.18	14.2	0.29	43.3	43.4	43.5	NaN	True	False	0	0
24	1.23	34.0	0.35	44.3	44.1	44.3	NaN	True	False	3	0
25	1.59	62.6	0.44	44.5	44.5	44.3	NaN	True	False	1	0
26	1.40	19.1	0.25	43.7	43.6	43.9	NaN	True	False	1	0
27	3.73	38.3	0.55	43.7	44.1	43.5	NaN	True	False	2	0
28	0.88	61.9	0.41	44.9	44.7	44.8	NaN	True	False	3	0
29	0.55	42.0	0.31	44.9	44.5	44.9	NaN	True	False	4	0
30	3.75	33.3	0.37	43.4	43.7	43.6	NaN	True	False	2	0
31	1.44	44.8	0.44	44.4	44.4	44.2	NaN	False	False	3	0
32	12.14	95.8	0.84	43.4	44.3	43.6	NaN	True	False	0	0
33	1.91	54.3	0.44	44.3	44.3	44.2	NaN	True	False	1	0
34	3.76	31.9	0.40	43.4	43.7	43.6	NaN	True	False	0	0
35	1.85	17.5	0.26	43.5	43.5	43.5	NaN	True	False	0	0
36	2.75	44.1	0.38	43.7	44.0	44.1	NaN	True	False	0	0
37	7.77	46.1	0.54	43.1	43.8	43.5	NaN	True	False	0	0
38	4.20	21.0	0.33	43.0	43.4	43.4	NaN	True	False	0	0
39	2.32	95.6	0.48	44.4	44.5	44.6	NaN	False	False	0	0
40	1.92	9.8	0.16	43.0	43.1	43.4	NaN	True	False	0	0
41	6.94	30.2	0.44	42.9	43.5	43.2	NaN	True	False	0	0
42	10.26	61.3	0.59	43.1	43.9	43.2	NaN	False	False	1	0
43	2.34	12.1	0.17	42.9	43.1	43.4	NaN	True	False	0	0
44	9.91	33.0	0.42	42.6	43.4	43.1	NaN	False	False	0	0
45	1.79	66.8	0.36	44.3	44.3	44.5	NaN	True	False	1	0
46	6.43	46.0	0.48	43.2	43.8	43.3	NaN	True	False	0	0
47	9.36	36.3	0.47	42.8	43.5	42.9	NaN	False	False	1	0

Table B.5: NGC2264 NH_3 (1,1) Leaves Catalog 2

ID	α_{vir}	M_{vir} ($M_\odot$)	σ_{nt} (km s^{-1})	log|Ω_G| (erg)	logΩ_K (erg)	log|Ω_{Pw}| (erg)	log|Ω_{Pt}| (erg)	on-filament	hub	N_{proto}	Bad N(H_2) Pix
0	0.60	18.5	0.20	44.3	43.9	44.4	NaN	True	False	1	0
1	1.21	7.9	0.18	43.2	43.1	43.5	NaN	True	False	1	0
2	0.63	9.1	0.12	43.7	43.3	44.1	NaN	True	False	0	0
3	9.30	18.3	0.46	42.4	43.2	42.8	NaN	True	False	0	0
4	8.44	20.3	0.48	42.6	43.3	42.9	NaN	True	False	0	0
5	0.91	5.3	0.11	43.2	42.9	43.5	NaN	True	False	0	0
6	1.80	37.2	0.43	44.1	44.2	44.1	NaN	True	False	0	0
7	3.40	16.0	0.37	43.1	43.4	43.3	NaN	True	False	0	0
8	3.74	28.2	0.47	43.4	43.8	43.6	NaN	True	False	0	0
9	1.76	82.3	0.57	44.7	44.7	44.6	NaN	True	False	0	0
10	3.72	16.8	0.40	43.1	43.5	43.2	NaN	True	False	0	0
11	3.06	18.9	0.34	43.2	43.5	43.8	NaN	True	False	0	0
12	3.19	13.5	0.21	42.8	43.1	43.5	NaN	False	False	0	0
13	1.36	22.3	0.37	44.0	44.0	44.1	NaN	False	False	1	0
14	5.64	32.1	0.55	43.2	43.8	43.6	NaN	False	False	1	0
15	3.23	39.2	0.42	43.6	43.9	44.3	NaN	False	False	0	0
16	0.51	253.6	0.76	46.5	46.0	45.8	NaN	False	True	9	0
17	55.04	72.0	1.00	42.1	43.6	43.1	NaN	False	False	0	0
18	4.97	57.3	0.71	43.8	44.3	44.0	NaN	False	False	0	0
19	4.50	48.4	0.52	43.6	44.0	43.9	NaN	False	False	0	0
20	0.65	49.8	0.51	45.2	44.9	44.6	NaN	True	False	3	0
21	0.82	44.6	0.46	44.9	44.6	44.6	NaN	True	False	6	0
22	1.57	132.0	0.90	45.4	45.3	44.6	NaN	True	False	4	0
23	1.14	32.3	0.49	44.5	44.4	44.1	NaN	True	False	0	0
24	1.54	69.4	0.72	44.9	44.9	44.2	NaN	True	False	5	0
25	5.93	9.8	0.31	42.3	42.9	43.0	NaN	False	False	0	0
26	3.38	33.1	0.43	43.5	43.8	44.1	NaN	False	False	0	0
27	0.99	18.8	0.23	43.9	43.7	44.4	NaN	True	False	0	0
28	22.14	45.0	0.79	42.5	43.6	43.0	NaN	True	False	0	0
29	10.82	27.3	0.57	42.6	43.5	43.0	NaN	True	False	0	0
30	6.32	65.1	0.67	43.6	44.2	43.7	NaN	True	False	0	0
31	3.04	9.1	0.30	42.8	43.1	43.0	NaN	True	False	0	0
32	2.47	17.9	0.32	43.3	43.5	43.6	NaN	True	False	0	0
33	5.74	30.7	0.47	43.1	43.6	43.5	NaN	True	False	0	0
34	53.20	87.4	1.12	42.3	43.8	42.7	NaN	False	False	0	0
35	3.55	31.9	0.33	43.3	43.7	43.8	NaN	True	False	1	0
36	6.65	15.0	0.30	42.4	43.0	43.0	NaN	True	False	0	0
37	4.60	20.6	0.35	43.0	43.4	43.2	NaN	True	False	0	0
38	14.00	28.9	0.50	42.3	43.3	43.0	NaN	True	False	0	0
39	1.63	16.4	0.27	43.5	43.5	43.6	NaN	False	False	2	0
40	0.80	8.8	0.14	43.6	43.3	43.8	NaN	False	False	0	0
41	34.26	66.4	0.88	42.3	43.7	42.7	NaN	True	False	1	0

Table B.6: M16 NH_3 (1,1) Leaves Catalog 2

ID	α_{vir}	M_{vir} ($M_\odot$)	σ_{nt} (km s^{-1})	log|Ω_G| (erg)	logΩ_K (erg)	log|Ω_{Pw}| (erg)	log|Ω_{Pt}| (erg)	on-filament	hub	N_{proto}	Bad N(H_2) Pix
0	3.37	47.6	0.52	43.8	44.1	NaN	45.0	False	False	3	0
1	1.80	65.6	0.46	44.4	44.5	44.7	NaN	False	False	1	0
2	1.21	41.3	0.36	44.4	44.3	45.1	NaN	False	False	0	0
3	0.36	49.2	0.26	45.3	44.7	46.0	NaN	False	False	1	0
4	1.55	34.3	0.39	44.1	44.1	44.8	NaN	False	False	0	0
5	0.27	381.2	0.60	47.0	46.2	47.3	NaN	False	True	2	0
6	2.06	157.8	0.71	45.0	45.1	45.4	NaN	False	False	1	0
7	2.18	200.6	0.75	45.1	45.2	45.5	NaN	False	False	0	0
8	1.68	17.2	0.23	43.5	43.5	44.4	NaN	False	False	1	0
9	1.70	143.5	0.71	45.1	45.2	45.3	NaN	True	False	2	0
10	0.79	18.2	0.22	44.1	43.8	44.9	NaN	False	False	1	0

Continued on next page

Table B.6 – *Continued from previous page*

ID	α_{vir}	M_{vir} ($M_\odot$)	σ_{nt} (km s^{-1})	$\log\lvert\Omega_G\rvert$ (erg)	$\log\Omega_K$ (erg)	$\log\lvert\Omega_{Pw}\rvert$ (erg)	$\log\lvert\Omega_{Pt}\rvert$ (erg)	on-filament	hub	N_{proto}	Bad $N(H_2)$ Pix
11	0.63	15.5	0.18	44.1	43.7	44.9	NaN	False	False	1	0
12	2.26	83.8	0.61	44.5	44.7	45.0	NaN	True	False	1	0
13	1.17	148.4	0.59	45.3	45.2	45.8	NaN	True	False	2	0
14	1.08	22.4	0.28	44.1	43.9	44.8	NaN	False	False	0	0
15	0.79	10.6	0.10	43.8	43.5	44.6	NaN	False	False	0	0
16	1.75	174.0	0.66	45.1	45.2	45.7	NaN	False	False	3	0
17	1.41	126.8	0.58	45.1	45.0	45.6	NaN	True	False	1	0
18	6.21	93.6	0.77	43.9	44.5	44.6	NaN	True	False	0	0
19	1.15	91.8	0.54	45.1	45.0	45.3	NaN	False	False	1	0
20	6.71	129.3	0.83	44.0	44.7	44.7	NaN	False	False	0	0
21	1.02	81.6	0.49	45.1	44.9	45.4	NaN	True	False	1	0
22	0.38	29.3	0.22	45.0	44.3	45.6	NaN	True	False	0	0
23	20.62	554.1	1.72	44.3	45.4	44.9	NaN	True	False	0	0
24	3.93	192.4	0.93	44.7	45.1	45.1	NaN	True	False	0	0
25	1.83	58.4	0.50	44.4	44.5	44.9	NaN	True	False	0	0
26	3.75	86.3	0.67	44.2	44.5	44.8	NaN	True	False	0	0
27	1.02	18.8	0.27	44.0	43.9	44.6	NaN	True	False	0	0
28	1.14	71.5	0.45	44.8	44.7	45.5	NaN	True	False	0	0
29	2.76	66.5	0.61	44.2	44.5	44.7	NaN	True	False	0	0
30	1.02	148.1	0.59	45.4	45.2	45.8	NaN	True	False	0	0
31	0.68	39.8	0.44	45.0	44.6	45.0	NaN	True	False	1	0
32	0.41	77.1	0.48	45.8	45.2	45.7	NaN	True	False	1	0
33	1.68	132.1	0.64	45.0	45.1	45.5	NaN	True	False	0	0
34	1.87	18.1	0.26	43.5	43.6	44.3	NaN	False	False	0	0
35	1.29	69.6	0.41	44.7	44.6	45.4	NaN	False	False	0	0
36	0.53	143.9	0.51	45.9	45.4	46.2	NaN	False	False	0	0
37	0.88	110.7	0.58	45.4	45.2	45.7	NaN	True	False	1	0
38	2.94	52.2	0.46	43.9	44.2	44.7	NaN	False	False	0	0
39	1.04	108.3	0.61	45.3	45.1	45.5	NaN	True	False	0	0
40	2.63	115.2	0.65	44.6	44.8	45.2	NaN	False	False	0	0
41	1.44	106.6	0.60	45.0	45.0	45.3	NaN	True	False	0	0
42	8.56	220.9	1.03	44.2	44.9	44.9	NaN	False	False	0	0

Table B.7: M17 NH_3 (1,1) Leaves Catalog 2

ID	α_{vir}	M_{vir} ($M_\odot$)	σ_{nt} (km s^{-1})	$\log\lvert\Omega_G\rvert$ (erg)	$\log\Omega_K$ (erg)	$\log\lvert\Omega_{Pw}\rvert$ (erg)	$\log\lvert\Omega_{Pt}\rvert$ (erg)	on-filament	hub	N_{proto}	Bad $N(H_2)$ Pix
0	0.31	37.2	0.31	45.4	44.7	45.8	NaN	False	False	0	0.00
1	0.21	141.0	0.43	46.5	45.7	46.9	NaN	False	False	0	0.00
2	0.48	31.5	0.32	45.0	44.5	45.5	NaN	False	False	2	0.00
3	0.43	46.5	0.35	45.4	44.8	45.8	NaN	False	False	0	0.00
4	0.21	310.9	0.68	47.2	46.4	47.0	NaN	False	True	3	0.00
5	0.39	104.3	0.53	46.1	45.4	46.2	NaN	False	False	2	0.00
6	0.27	86.2	0.40	46.1	45.3	46.4	NaN	False	False	1	0.00
7	0.23	32.4	0.21	45.5	44.6	46.0	NaN	False	False	1	0.00
8	3.78	200.3	0.94	44.8	45.2	45.8	46.0	False	False	0	0.00
9	0.76	517.9	1.27	46.9	46.5	46.5	47.0	False	False	1	0.00
10	1.46	314.2	0.87	45.8	45.7	46.5	46.8	False	False	2	0.00
11	0.42	1103.0	1.52	47.9	47.3	47.2	47.4	False	True	1	0.59
12	2.69	681.6	1.61	46.1	46.3	46.2	46.6	False	False	0	0.00
13	0.77	57.3	0.45	45.1	44.8	45.8	45.5	True	False	1	0.00
14	2.37	105.6	0.74	44.8	44.9	45.4	45.6	False	False	0	0.00
15	0.64	433.8	0.87	46.6	46.2	46.9	47.1	True	False	8	0.00
16	1.55	122.3	0.65	45.1	45.1	45.5	45.8	True	False	1	0.00
17	1.07	157.7	0.62	45.5	45.3	46.1	46.4	False	False	1	0.00
18	1.54	157.3	0.80	45.4	45.3	45.6	45.9	True	False	1	0.00
19	3.98	140.4	0.90	44.6	45.0	45.2	45.4	True	False	0	0.00
20	1.12	148.2	0.63	45.4	45.3	45.9	46.2	False	False	0	0.00
21	1.08	89.7	0.59	45.2	45.0	45.5	45.5	True	False	0	0.00
22	1.13	78.9	0.52	45.0	44.9	45.6	NaN	True	False	0	0.00
23	1.17	67.0	0.54	44.9	44.8	45.3	NaN	True	False	0	0.00
24	0.55	69.5	0.37	45.4	44.9	46.0	NaN	True	False	1	0.00
25	1.31	136.0	0.70	45.3	45.2	45.7	NaN	True	False	0	0.00
26	1.33	52.5	0.46	44.6	44.6	45.2	NaN	False	False	0	0.00

Continued on next page

Table B.7 – *Continued from previous page*

ID	α_{vir}	M_{vir} ($M_\odot$)	σ_{nt} (km s^{-1})	$\log\lvert\Omega_G\rvert$ (erg)	$\log\Omega_K$ (erg)	$\log\lvert\Omega_{Pw}\rvert$ (erg)	$\log\lvert\Omega_{Pt}\rvert$ (erg)	on-filament	hub	N_{proto}	Bad $N(H_2)$ Pix
27	1.39	108.7	0.64	45.1	45.1	45.5	NaN	True	False	0	0.00
28	0.52	31.3	0.30	45.0	44.5	45.4	NaN	True	False	0	0.00
29	0.90	207.4	0.85	46.0	45.7	45.7	NaN	True	False	0	0.00
30	0.29	29.9	0.21	45.3	44.6	45.7	NaN	False	False	1	0.00
31	0.92	33.3	0.39	44.6	44.4	45.0	NaN	False	False	0	0.00
32	0.86	59.8	0.42	45.0	44.7	45.6	NaN	True	False	0	0.00
33	1.60	201.5	0.94	45.6	45.6	45.5	NaN	True	False	0	0.00
34	0.79	63.3	0.45	45.1	44.8	45.5	NaN	False	False	0	0.00
35	0.59	37.2	0.42	45.1	44.7	45.0	NaN	True	False	0	0.00
36	1.07	99.4	0.61	45.3	45.1	45.5	NaN	True	False	2	0.00
37	2.30	65.3	0.59	44.4	44.6	44.9	NaN	True	False	0	0.00

Table B.8: W48 NH_3 (1,1) Leaves Catalog 2

ID	α_{vir}	M_{vir} ($M_\odot$)	σ_{nt} (km s^{-1})	$\log\lvert\Omega_G\rvert$ (erg)	$\log\Omega_K$ (erg)	$\log\lvert\Omega_{Pw}\rvert$ (erg)	$\log\lvert\Omega_{Pt}\rvert$ (erg)	on-filament	hub	N_{proto}	Bad $N(H_2)$ Pix
0	0.30	37.8	0.27	45.4	44.6	45.6	NaN	True	False	0	0.00
1	1.57	152.1	0.66	45.2	45.1	45.6	NaN	True	False	0	0.00
2	0.53	63.7	0.32	45.2	44.7	45.9	NaN	False	False	0	0.00
3	0.30	300.0	0.65	46.9	46.2	46.6	NaN	True	False	3	0.00
4	0.66	52.5	0.36	45.0	44.6	45.4	NaN	True	False	0	0.00
5	1.64	98.0	0.62	44.9	44.9	45.1	NaN	True	False	0	0.00
6	0.21	393.4	0.67	47.3	46.5	46.8	NaN	False	True	8	0.00
7	1.42	79.5	0.49	44.7	44.7	45.4	NaN	True	False	1	0.00
8	0.43	77.9	0.32	45.5	44.9	46.1	NaN	False	False	2	0.00
9	0.21	161.6	0.37	46.5	45.6	46.9	NaN	True	False	2	0.00
10	1.38	62.6	0.49	44.6	44.6	45.1	NaN	True	False	0	0.00
11	0.35	53.0	0.30	45.4	44.8	45.8	NaN	False	False	0	0.00
12	0.28	35.9	0.23	45.3	44.5	45.9	NaN	False	False	0	0.00
13	0.32	52.8	0.26	45.5	44.8	46.0	NaN	False	False	1	0.00
14	1.63	155.4	0.65	45.1	45.1	45.6	NaN	False	False	0	0.00
15	0.43	75.0	0.41	45.6	45.0	45.7	NaN	True	False	1	0.00
16	0.16	89.0	0.25	46.3	45.3	46.8	NaN	False	False	2	0.00
17	0.52	82.1	0.38	45.4	45.0	45.9	NaN	True	False	1	0.00
18	0.51	35.6	0.32	45.0	44.5	45.3	NaN	True	False	0	0.00
19	1.05	66.1	0.41	44.8	44.6	45.5	NaN	False	False	0	0.00
20	1.09	164.2	0.59	45.4	45.3	45.9	NaN	False	False	0	0.00
21	0.38	27.6	0.21	44.9	44.3	45.6	NaN	False	False	0	0.00
22	0.30	171.6	0.48	46.4	45.7	46.4	NaN	True	False	1	0.00
23	0.42	21.9	0.17	44.6	44.0	45.1	NaN	False	False	0	0.00
24	5.38	343.6	1.11	44.9	45.4	45.4	NaN	False	False	0	0.00
25	1.66	474.4	1.01	45.9	46.0	46.1	NaN	False	False	1	0.00
26	0.42	87.5	0.38	45.7	45.1	46.0	NaN	False	False	0	0.00
27	8.35	424.3	1.36	44.7	45.5	45.1	NaN	False	False	0	0.00
28	0.58	63.2	0.38	45.3	44.8	45.5	NaN	True	False	0	0.00
29	0.53	564.9	0.81	46.8	46.3	46.8	NaN	False	False	5	0.00
30	0.29	80.0	0.37	45.9	45.2	46.1	NaN	False	False	0	0.00
31	0.94	183.7	0.58	45.6	45.4	46.0	NaN	False	False	0	0.00
32	0.51	27.0	0.22	44.7	44.2	45.3	NaN	True	False	0	0.00
33	0.43	52.3	0.37	45.4	44.8	45.5	NaN	False	False	0	0.00
34	0.36	113.2	0.48	46.1	45.4	45.9	NaN	False	False	1	0.00
35	1.04	66.3	0.42	44.8	44.6	45.4	NaN	False	False	0	0.00
36	0.69	56.4	0.37	45.1	44.7	45.3	NaN	True	False	0	0.00
37	0.30	143.4	0.42	46.2	45.5	46.5	NaN	False	False	0	0.00
38	0.25	42.7	0.23	45.6	44.7	45.9	NaN	False	False	0	0.00
39	1.55	99.2	0.58	44.9	44.9	45.3	NaN	True	False	0	0.00
40	0.52	371.7	0.75	46.6	46.1	46.5	NaN	False	False	6	0.00
41	0.73	82.2	0.48	45.3	45.0	45.6	NaN	False	False	0	0.00
42	0.61	84.1	0.42	45.4	45.0	45.8	NaN	True	False	0	0.00
43	2.59	283.2	0.91	45.2	45.5	45.6	NaN	True	False	0	0.00
44	0.31	531.4	0.77	47.3	46.5	46.8	NaN	False	True	4	0.01
45	0.44	208.5	0.59	46.3	45.7	46.3	NaN	False	False	1	0.00
46	0.18	29.9	0.18	45.5	44.5	46.0	NaN	False	False	1	0.00
47	2.71	252.9	0.99	45.3	45.5	45.1	NaN	True	False	0	0.00

Continued on next page

Table B.8 – *Continued from previous page*

ID	α_{vir}	M_{vir} ($M_\odot$)	σ_{nt} (km s^{-1})	log|Ω_G| (erg)	logΩ_K (erg)	log|Ω_{Pw}| (erg)	log|Ω_{Pt}| (erg)	on-filament	hub	N_{proto}	Bad N(H_2) Pix
48	1.00	439.6	0.86	46.2	46.0	46.4	NaN	True	False	0	0.00
49	1.98	110.4	0.56	44.7	44.8	45.4	NaN	True	False	0	0.00
50	1.21	136.5	0.53	45.2	45.1	45.9	NaN	False	False	0	0.00
51	6.05	599.3	1.36	45.2	45.8	45.6	NaN	False	False	0	0.00
52	2.43	185.6	0.83	45.0	45.2	45.3	NaN	False	False	0	0.00
53	1.27	97.1	0.52	45.0	44.9	45.5	NaN	False	False	0	0.00
54	0.98	342.8	0.85	46.1	45.9	46.0	NaN	False	False	0	0.00
55	0.50	50.6	0.35	45.2	44.7	45.6	NaN	True	False	0	0.00
56	0.93	364.4	0.84	46.2	45.9	46.3	NaN	True	False	0	0.00
57	0.21	233.2	0.44	46.8	45.9	47.1	NaN	True	False	3	0.00
58	5.42	331.9	1.06	44.8	45.3	45.4	NaN	False	False	0	0.00
59	0.56	215.7	0.59	46.1	45.7	46.4	NaN	True	False	2	0.00
60	0.42	178.9	0.53	46.2	45.6	46.4	NaN	True	False	0	0.00
61	1.26	100.3	0.58	45.1	45.0	45.4	NaN	True	False	0	0.00
62	4.04	191.7	0.84	44.6	45.0	45.3	NaN	False	False	0	0.00
63	1.85	183.4	0.76	45.2	45.3	45.6	NaN	True	False	0	0.00
64	0.29	209.5	0.53	46.6	45.9	46.5	NaN	True	False	1	0.00
65	0.35	129.7	0.43	46.1	45.4	46.4	NaN	True	False	1	0.00
66	1.36	64.9	0.40	44.6	44.5	45.0	NaN	True	False	0	0.00
67	0.54	167.0	0.58	46.0	45.6	46.1	NaN	True	False	1	0.00
68	4.00	163.3	0.80	44.5	44.9	45.2	NaN	False	False	0	0.00
69	0.34	187.9	0.44	46.3	45.6	46.3	NaN	True	False	3	0.00
70	0.54	130.5	0.48	45.8	45.3	46.2	NaN	True	False	0	0.00
71	0.94	38.7	0.30	44.5	44.3	45.0	NaN	True	False	0	0.00
72	1.36	180.9	0.73	45.4	45.4	45.6	NaN	True	False	0	0.00
73	0.61	35.4	0.30	44.8	44.4	44.9	NaN	True	False	0	0.00
74	0.30	59.3	0.30	45.6	44.9	45.7	NaN	True	False	2	0.00
75	0.67	78.5	0.46	45.3	45.0	45.6	NaN	True	False	0	0.00
76	0.44	409.6	0.73	46.8	46.2	46.7	NaN	True	False	0	0.00
77	1.91	86.0	0.54	44.6	44.7	45.3	NaN	False	False	0	0.00
78	0.18	76.8	0.25	46.1	45.1	46.7	NaN	True	False	0	0.00
79	0.33	12.6	0.12	44.5	43.8	45.1	NaN	True	False	0	0.00
80	0.21	166.5	0.40	46.6	45.7	46.9	NaN	True	False	4	0.00
81	0.34	23.0	0.19	44.8	44.2	45.7	NaN	False	False	0	0.00
82	0.37	195.8	0.49	46.3	45.7	46.6	NaN	True	False	3	0.00
83	0.41	33.5	0.25	45.0	44.4	45.6	NaN	False	False	0	0.00
84	0.29	188.0	0.45	46.4	45.7	46.8	NaN	False	False	4	0.00
85	0.54	80.6	0.42	45.5	45.0	46.0	NaN	False	False	0	0.00
86	2.09	290.4	0.77	45.3	45.4	46.1	NaN	False	False	0	0.00
87	0.44	1939.2	1.43	48.0	47.4	47.2	NaN	False	True	5	0.00
88	2.72	170.7	0.75	44.8	45.1	45.6	NaN	False	False	0	0.00
89	0.66	155.0	0.52	45.7	45.4	46.3	NaN	False	False	0	0.00
90	0.34	667.8	0.97	47.4	46.8	46.8	NaN	False	True	2	0.00
91	0.18	108.0	0.38	46.5	45.5	46.5	NaN	False	False	2	0.00
92	0.63	64.2	0.39	45.2	44.8	45.8	NaN	False	False	0	0.00
93	0.18	85.1	0.31	46.2	45.3	46.6	NaN	False	False	1	0.00
94	0.24	36.2	0.24	45.4	44.6	46.0	NaN	False	False	0	0.00
95	0.55	37.5	0.32	45.0	44.5	45.4	NaN	False	False	0	0.00
96	0.72	58.9	0.40	45.1	44.7	45.6	NaN	True	False	0	0.00
97	0.24	98.8	0.34	46.1	45.3	46.6	NaN	True	False	0	0.00
98	0.25	20.3	0.17	45.0	44.2	45.5	NaN	True	False	0	0.00
99	1.01	234.8	0.71	45.8	45.6	46.0	NaN	True	False	1	0.00

Table B.9: Cygnus X South NH_3 (1,1) Leaves Catalog 2

ID	α_{vir}	M_{vir} ($M_\odot$)	σ_{nt} (km s^{-1})	log|Ω_G| (erg)	logΩ_K (erg)	log|Ω_{Pw}| (erg)	log|Ω_{Pt}| (erg)	on-filament	hub	N_{proto}	Bad N(H_2) Pix
0	2.38	22.9	0.33	43.5	43.6	44.1	NaN	False	False	0	0
1	1.02	27.4	0.27	44.2	44.0	44.8	NaN	False	False	0	0
2	0.73	13.4	0.17	43.9	43.6	44.4	NaN	True	False	0	0
3	0.83	79.0	0.39	45.0	44.8	45.4	NaN	False	False	1	0
4	1.75	41.0	0.38	44.1	44.1	44.6	NaN	False	False	0	0
5	3.01	63.1	0.53	44.0	44.3	44.6	NaN	True	False	0	0
6	6.32	309.2	1.07	44.6	45.2	44.9	NaN	True	False	0	0

Continued on next page

Table B.9 – *Continued from previous page*

ID	α_{vir}	M_{vir} ($M_\odot$)	σ_{nt} (km s^{-1})	$\log\lvert\Omega_G\rvert$ (erg)	$\log\Omega_K$ (erg)	$\log\lvert\Omega_{Pw}\rvert$ (erg)	$\log\lvert\Omega_{Pt}\rvert$ (erg)	on-filament	hub	N_{proto}	Bad $N(H_2)$ Pix
7	1.21	58.2	0.45	44.7	44.6	44.8	NaN	True	False	0	0
8	2.21	71.2	0.54	44.4	44.5	44.7	NaN	True	False	0	0
9	1.04	12.4	0.15	43.6	43.4	44.2	NaN	False	False	0	0
10	1.19	55.1	0.39	44.6	44.5	44.9	NaN	True	False	0	0
11	2.05	81.4	0.57	44.5	44.7	44.6	NaN	False	False	0	0
12	1.33	53.0	0.45	44.6	44.5	44.6	NaN	False	False	1	0
13	0.49	94.1	0.42	45.6	45.1	45.5	NaN	False	False	3	0
14	0.59	163.4	0.58	45.9	45.5	45.5	NaN	False	False	4	0
15	1.20	20.1	0.27	43.9	43.8	44.2	NaN	False	False	1	0
16	1.00	50.0	0.35	44.6	44.4	45.0	NaN	False	False	0	0
17	1.97	42.3	0.40	44.0	44.1	44.5	NaN	True	False	1	0
18	1.69	98.8	0.53	44.8	44.8	44.9	NaN	True	False	4	0
19	1.96	143.5	0.73	45.0	45.1	44.8	NaN	True	False	3	0
20	5.22	43.0	0.52	43.4	43.9	43.9	NaN	False	False	0	0
21	3.83	107.6	0.68	44.3	44.7	44.4	NaN	True	False	1	0
22	3.01	133.8	0.76	44.7	44.9	44.6	NaN	True	False	2	0
23	1.95	14.2	0.25	43.3	43.4	43.8	NaN	True	False	1	0
24	9.50	74.0	0.71	43.3	44.1	44.0	NaN	True	False	0	0
25	2.93	74.6	0.59	44.2	44.5	44.4	NaN	True	False	0	0
26	1.59	75.2	0.45	44.6	44.6	44.9	NaN	True	False	1	0
27	7.45	241.3	1.03	44.4	45.0	44.6	NaN	True	False	0	0
28	3.86	127.6	0.69	44.3	44.7	44.8	NaN	True	False	0	0
29	4.14	50.3	0.55	43.7	44.1	44.0	NaN	False	False	1	0
30	5.63	65.6	0.58	43.6	44.2	44.1	NaN	False	False	0	0
31	1.13	22.3	0.26	44.0	43.8	44.5	NaN	False	False	0	0
32	2.50	34.0	0.38	43.8	44.0	44.1	NaN	False	False	0	0
33	1.84	10.8	0.18	43.2	43.2	43.7	NaN	False	False	1	0
34	2.92	25.5	0.38	43.4	43.7	44.0	NaN	False	False	1	0
35	3.64	70.9	0.59	44.0	44.4	44.3	NaN	False	False	0	0
36	2.69	25.7	0.35	43.5	43.7	44.1	NaN	False	False	0	0
37	1.33	10.1	0.19	43.4	43.3	43.9	NaN	True	False	0	0
38	2.30	50.8	0.47	44.1	44.3	44.5	NaN	False	False	1	0
39	0.57	39.8	0.28	44.9	44.4	45.1	NaN	False	False	2	0
40	1.34	35.3	0.32	44.2	44.1	44.7	NaN	False	False	0	0
41	7.66	64.3	0.67	43.4	44.1	43.9	NaN	False	False	0	0
42	0.80	35.6	0.30	44.5	44.2	44.9	NaN	False	False	1	0
43	0.82	26.1	0.25	44.3	44.0	44.8	NaN	False	False	0	0
44	0.43	36.8	0.29	45.1	44.5	45.1	NaN	False	False	0	0
45	1.30	9.0	0.18	43.3	43.2	43.8	NaN	False	False	0	0
46	0.56	64.2	0.37	45.3	44.8	45.3	NaN	False	False	3	0
47	0.65	55.7	0.38	45.1	44.7	45.1	NaN	False	False	1	0
48	0.60	11.5	0.14	44.0	43.5	44.6	NaN	False	False	0	0
49	1.15	237.9	0.73	45.7	45.6	45.5	NaN	False	False	2	0
50	0.96	25.7	0.30	44.2	44.0	44.5	NaN	False	False	2	0
51	1.55	61.7	0.44	44.5	44.5	44.7	NaN	False	False	0	0
52	0.49	34.1	0.26	44.9	44.3	45.2	NaN	False	False	3	0
53	0.68	39.9	0.39	44.9	44.6	44.5	NaN	False	False	1	0
54	1.27	35.4	0.37	44.3	44.2	44.5	NaN	False	False	1	0
55	1.12	42.1	0.37	44.5	44.3	44.8	NaN	False	False	0	0
56	3.87	43.3	0.51	43.7	44.0	44.1	NaN	False	False	0	0
57	0.75	45.5	0.42	45.0	44.6	44.5	NaN	False	False	1	0
58	1.58	21.8	0.30	43.8	43.8	44.3	NaN	False	False	1	0
59	2.60	32.1	0.42	43.7	43.9	44.1	NaN	False	False	0	0
60	1.41	10.0	0.22	43.3	43.3	43.9	NaN	True	False	0	0
61	1.48	113.0	0.57	45.0	44.9	45.1	NaN	False	False	0	0
62	8.71	73.0	0.77	43.5	44.2	43.8	NaN	False	False	0	0
63	16.09	129.9	1.07	43.5	44.5	43.8	NaN	False	False	0	0
64	2.05	76.6	0.52	44.5	44.6	44.7	NaN	False	False	3	0
65	0.75	10.3	0.13	43.7	43.4	44.3	NaN	True	False	0	0
66	1.67	16.2	0.30	43.6	43.6	43.9	NaN	False	False	0	0
67	0.90	28.4	0.28	44.3	44.0	44.8	NaN	True	False	0	0
68	1.37	8.7	0.21	43.3	43.2	43.7	NaN	True	False	1	0
69	0.88	8.4	0.15	43.5	43.3	44.1	NaN	True	False	0	0
70	3.61	42.3	0.48	43.6	44.0	44.2	NaN	True	False	0	0
71	1.24	10.6	0.20	43.4	43.3	44.0	NaN	True	False	0	0
72	1.44	24.0	0.28	43.9	43.8	44.4	NaN	False	False	0	0
73	0.62	11.7	0.16	44.0	43.6	44.5	NaN	False	False	0	0
74	1.78	42.8	0.44	44.2	44.3	44.3	NaN	False	False	0	0

Continued on next page

Table B.9 – *Continued from previous page*

ID	α_{vir}	M_{vir} ($M_\odot$)	σ_{nt} (km s^{-1})	$\log\lvert\Omega_G\rvert$ (erg)	$\log\Omega_K$ (erg)	$\log\lvert\Omega_{Pw}\rvert$ (erg)	$\log\lvert\Omega_{Pt}\rvert$ (erg)	on-filament	hub	N_{proto}	Bad N(H_2) Pix
75	1.09	46.5	0.40	44.6	44.4	44.8	NaN	False	False	1	0
76	2.30	29.0	0.37	43.8	43.9	44.0	NaN	False	False	0	0
77	0.36	30.4	0.24	45.0	44.4	45.3	NaN	True	False	0	0
78	0.90	7.5	0.16	43.5	43.2	43.9	NaN	True	False	0	0
79	0.95	8.3	0.13	43.4	43.2	44.1	NaN	False	False	0	0
80	0.50	6.4	0.07	43.8	43.3	44.1	NaN	True	False	0	0
81	2.53	32.2	0.41	43.8	44.0	44.1	NaN	False	False	0	0
82	1.69	13.1	0.23	43.4	43.4	43.9	NaN	True	False	0	0
83	0.60	257.6	0.62	46.2	45.8	46.1	NaN	False	False	4	0
84	2.83	19.4	0.34	43.3	43.5	43.9	NaN	False	False	0	0
85	1.50	9.1	0.18	43.2	43.2	43.7	NaN	False	False	0	0
86	0.92	6.4	0.09	43.2	43.0	44.0	NaN	False	False	0	0
87	3.39	14.0	0.31	42.9	43.2	43.6	NaN	False	False	0	0
88	NaN	66.4	0.43	NaN	NaN	NaN	NaN	False	False	1	0
89	0.54	8.8	0.10	43.9	43.4	44.4	NaN	False	False	0	0
90	0.92	8.1	0.10	43.3	43.1	44.2	NaN	False	False	0	0
91	NaN	17.1	0.29	NaN	NaN	NaN	NaN	False	False	0	0
92	NaN	27.9	0.36	NaN	NaN	NaN	NaN	False	False	0	0
93	2.42	66.4	0.47	44.2	44.4	44.6	45.2	True	False	1	0
94	1.90	30.1	0.40	43.9	44.0	44.2	NaN	True	False	0	0
95	NaN	19.3	0.25	NaN	NaN	NaN	NaN	False	False	0	0
96	0.89	6.7	0.12	43.4	43.1	43.9	NaN	False	False	1	0
97	2.12	18.0	0.23	43.4	43.5	43.9	44.5	True	False	0	0
98	NaN	8.7	0.18	NaN	NaN	NaN	NaN	False	False	0	0
99	1.29	9.1	0.15	43.3	43.2	44.0	NaN	False	False	0	0
100	NaN	18.8	0.29	NaN	NaN	NaN	NaN	False	False	0	0
101	3.41	24.4	0.30	43.2	43.6	44.0	44.5	False	False	0	0
102	NaN	159.2	0.76	NaN	NaN	NaN	NaN	False	False	3	0
103	NaN	4.9	0.07	NaN	NaN	NaN	NaN	False	False	0	0
104	NaN	41.8	0.42	NaN	NaN	NaN	NaN	False	False	0	0
105	0.85	9.4	0.18	43.7	43.4	44.0	NaN	True	False	0	0
106	0.24	57.3	0.33	45.8	45.0	45.5	NaN	True	False	4	0
107	4.12	21.4	0.36	43.0	43.4	43.9	NaN	False	False	0	0
108	0.99	114.0	0.64	45.4	45.2	45.0	NaN	True	False	1	0
109	1.34	34.7	0.35	44.2	44.1	44.7	NaN	True	False	0	0
110	0.45	169.2	0.55	46.2	45.6	45.8	NaN	False	False	6	0
111	1.33	7.2	0.12	43.1	43.0	43.9	NaN	False	False	0	0
112	NaN	59.2	0.46	NaN	NaN	NaN	NaN	False	False	2	0
113	NaN	10.2	0.17	NaN	NaN	NaN	NaN	False	False	0	0
114	7.53	53.3	0.60	43.3	43.9	44.0	NaN	False	False	0	0
115	2.20	57.3	0.55	44.3	44.4	44.4	NaN	False	False	0	0
116	0.29	19.9	0.21	45.0	44.3	44.9	NaN	True	False	2	0
117	0.76	9.4	0.17	43.7	43.4	44.2	NaN	False	False	0	0
118	NaN	14.6	0.17	NaN	NaN	NaN	NaN	False	False	1	0
119	0.32	13.3	0.14	44.5	43.8	44.7	NaN	False	False	0	0
120	0.66	62.8	0.41	45.2	44.8	45.2	NaN	False	False	0	0
121	0.95	26.7	0.26	44.2	44.0	44.8	NaN	False	False	1	0
122	2.85	86.4	0.56	44.3	44.5	44.8	NaN	False	False	0	0
123	1.25	12.3	0.20	43.5	43.4	44.1	NaN	False	False	0	0
124	1.08	111.3	0.57	45.2	45.1	45.2	NaN	False	False	1	0
125	1.96	198.3	0.62	45.0	45.1	45.7	NaN	True	False	0	0
126	1.10	14.3	0.20	43.7	43.5	44.4	NaN	True	False	0	0
127	5.70	34.3	0.48	43.2	43.7	43.9	NaN	True	False	0	0
128	5.54	25.1	0.43	43.0	43.5	43.8	NaN	False	False	0	0
129	NaN	14.4	0.22	NaN	NaN	NaN	NaN	False	False	0	0
130	2.05	33.1	0.33	43.8	43.9	44.5	NaN	True	False	0	0
131	2.01	42.2	0.36	44.0	44.1	44.7	NaN	True	False	0	0
132	NaN	43.0	0.53	NaN	NaN	NaN	NaN	False	False	0	0

Table B.10: Cygnus X North NH_3 (1,1) Leaves Catalog 2

ID	α_{vir}	M_{vir} ($M_\odot$)	σ_{nt} (km s^{-1})	$\log\lvert\Omega_G\rvert$ (erg)	$\log\Omega_K$ (erg)	$\log\lvert\Omega_{Pw}\rvert$ (erg)	$\log\lvert\Omega_{Pt}\rvert$ (erg)	on-filament	hub	N_{proto}	Bad N(H_2) Pix
0	0.45	14.0	0.14	44.3	43.7	44.8	NaN	True	False	0	0.00

Continued on next page

Table B.10 – *Continued from previous page*

ID	α_{vir}	M_{vir} ($M_\odot$)	σ_{nt} (km s^{-1})	$\log\lvert\Omega_G\rvert$ (erg)	$\log\Omega_K$ (erg)	$\log\lvert\Omega_{Pw}\rvert$ (erg)	$\log\lvert\Omega_{Pt}\rvert$ (erg)	on-filament	hub	N_{proto}	Bad $N(H_2)$ Pix
1	0.45	19.6	0.18	44.5	43.9	45.0	NaN	True	False	0	0.00
2	3.10	47.4	0.48	43.8	44.1	44.3	NaN	False	False	0	0.00
3	7.48	128.5	0.81	43.9	44.6	44.4	NaN	True	False	0	0.00
4	1.47	152.6	0.57	45.1	45.1	45.4	NaN	False	False	3	0.00
5	1.17	7.5	0.14	43.2	43.1	43.8	NaN	False	False	1	0.00
6	1.65	42.9	0.39	44.3	44.3	44.3	NaN	False	False	1	0.00
7	1.78	55.8	0.44	44.4	44.4	44.5	NaN	False	False	1	0.00
8	1.73	49.0	0.43	44.3	44.3	44.5	NaN	False	False	1	0.00
9	0.82	49.2	0.31	44.8	44.5	45.0	NaN	False	False	1	0.00
10	2.95	89.4	0.62	44.3	44.6	44.5	NaN	False	False	0	0.00
11	1.97	28.2	0.35	43.8	43.9	44.3	NaN	False	False	1	0.00
12	1.89	30.5	0.36	43.9	44.0	44.2	NaN	True	False	0	0.00
13	1.45	9.5	0.20	43.3	43.2	43.8	NaN	True	False	0	0.00
14	1.35	42.7	0.48	44.5	44.5	44.1	NaN	True	False	1	0.00
15	0.86	22.3	0.31	44.4	44.1	44.1	NaN	True	False	0	0.00
16	0.85	98.4	0.53	45.3	45.1	45.0	NaN	False	False	1	0.00
17	1.12	29.1	0.29	44.2	44.0	44.6	NaN	False	False	0	0.00
18	5.15	52.9	0.67	43.7	44.2	43.8	NaN	False	False	0	0.00
19	1.01	14.9	0.20	43.8	43.6	44.3	NaN	False	False	0	0.00
20	3.00	130.7	0.76	44.6	44.9	44.7	NaN	False	False	2	0.00
21	5.49	367.5	1.21	44.9	45.5	44.9	NaN	True	False	2	0.00
22	3.91	53.5	0.62	43.9	44.3	44.0	NaN	True	False	0	0.00
23	4.12	243.1	1.00	44.9	45.3	44.8	NaN	True	False	1	0.00
24	1.33	12.2	0.17	43.5	43.4	44.0	NaN	False	False	0	0.00
25	1.62	100.6	0.55	44.8	44.8	45.1	NaN	False	False	3	0.00
26	1.72	245.5	0.78	45.4	45.5	45.4	NaN	False	False	2	0.00
27	0.99	20.1	0.22	44.0	43.8	44.4	NaN	False	False	0	0.00
28	5.21	102.3	0.76	44.1	44.6	44.3	NaN	False	False	0	0.00
29	0.57	76.8	0.37	45.3	44.9	45.4	NaN	False	False	5	0.00
30	2.14	209.0	0.74	45.1	45.3	45.1	NaN	False	False	3	0.00
31	3.23	18.7	0.35	43.2	43.5	43.7	NaN	False	False	0	0.00
32	1.54	297.2	0.77	45.6	45.6	45.6	NaN	False	False	1	0.00
33	7.36	145.1	0.85	44.0	44.7	44.5	NaN	False	False	0	0.00
34	2.54	32.9	0.37	43.7	43.9	44.3	NaN	False	False	0	0.00
35	0.97	58.0	0.53	45.0	44.8	44.4	NaN	False	False	2	0.00
36	1.38	67.5	0.66	44.9	44.9	44.2	NaN	False	False	0	0.00
37	3.76	52.2	0.50	43.7	44.1	44.3	NaN	False	False	0	0.00
38	2.23	53.1	0.43	44.1	44.3	44.6	NaN	False	False	0	0.00
39	2.68	28.7	0.40	43.6	43.9	44.0	NaN	False	False	0	0.00
40	4.97	48.7	0.53	43.5	44.0	44.1	NaN	False	False	1	0.00
41	0.84	50.7	0.35	44.8	44.5	45.0	NaN	False	False	4	0.00
42	1.18	67.2	0.39	44.7	44.5	45.2	NaN	False	False	0	0.00
43	5.29	48.6	0.56	43.5	44.0	44.0	NaN	False	False	0	0.00
44	4.53	40.0	0.54	43.5	44.0	43.9	NaN	False	False	1	0.00
45	2.63	26.0	0.37	43.5	43.7	44.1	NaN	False	False	0	0.00
46	1.96	14.5	0.24	43.3	43.4	44.0	NaN	True	False	0	0.00
47	0.94	58.4	0.50	45.0	44.8	44.6	NaN	True	False	1	0.00
48	2.21	84.4	0.57	44.5	44.7	44.7	NaN	True	False	1	0.00
49	1.18	44.9	0.48	44.7	44.5	44.3	NaN	True	False	1	0.00
50	0.79	129.5	0.52	45.5	45.2	45.5	NaN	False	False	3	0.00
51	0.66	47.2	0.32	44.9	44.5	45.1	NaN	False	False	2	0.00
52	6.37	46.1	0.61	43.4	44.0	43.8	NaN	False	False	0	0.00
53	0.89	8.0	0.13	43.5	43.2	44.0	NaN	False	False	0	0.00
54	0.44	14.6	0.12	44.3	43.7	45.0	NaN	False	False	0	0.00
55	0.89	15.5	0.20	43.9	43.7	44.5	NaN	True	False	0	0.00
56	0.61	50.6	0.31	45.0	44.5	45.4	NaN	True	False	0	0.00
57	0.45	16.5	0.17	44.4	43.9	44.8	NaN	False	False	0	0.00
58	0.66	10.6	0.13	43.8	43.4	44.5	NaN	False	False	0	0.00
59	1.75	10.0	0.22	43.2	43.2	43.7	NaN	False	False	0	0.00
60	2.39	71.9	0.53	44.3	44.5	44.6	NaN	True	False	1	0.00
61	0.97	19.1	0.29	44.1	43.9	44.2	NaN	False	False	0	0.00
62	0.87	9.6	0.15	43.6	43.4	44.2	NaN	True	False	0	0.00
63	1.84	51.6	0.40	44.2	44.3	44.7	NaN	False	False	0	0.00
64	1.21	8.6	0.16	43.3	43.2	43.9	NaN	False	False	0	0.00
65	0.60	11.8	0.17	44.0	43.6	44.5	NaN	True	False	0	0.00
66	1.10	30.5	0.34	44.3	44.1	44.6	NaN	True	False	0	0.00
67	1.99	27.9	0.36	43.8	43.9	44.1	NaN	False	False	1	0.00
68	2.08	27.3	0.35	43.7	43.9	44.2	NaN	True	False	0	0.00

Continued on next page

Table B.10 – *Continued from previous page*

ID	α_{vir}	M_{vir} ($M_\odot$)	σ_{nt} (km s^{-1})	$\log\lvert\Omega_G\rvert$ (erg)	$\log\Omega_K$ (erg)	$\log\lvert\Omega_{Pw}\rvert$ (erg)	$\log\lvert\Omega_{Pt}\rvert$ (erg)	on-filament	hub	N_{proto}	Bad $N(H_2)$ Pix
69	1.59	19.5	0.32	43.7	43.7	44.1	NaN	True	False	0	0.00
70	1.88	27.1	0.34	43.8	43.9	44.2	NaN	True	False	0	0.00
71	1.81	141.8	0.62	45.0	45.0	45.2	NaN	True	False	2	0.00
72	2.29	39.7	0.40	43.9	44.0	44.5	NaN	False	False	0	0.00
73	3.08	286.0	0.86	45.1	45.3	45.4	NaN	True	False	0	0.00
74	1.56	62.0	0.42	44.5	44.5	44.9	NaN	True	False	0	0.00
75	2.64	56.3	0.51	44.1	44.3	44.4	NaN	True	False	0	0.00
76	2.47	62.9	0.52	44.2	44.4	44.6	NaN	True	False	0	0.00
77	2.23	19.0	0.36	43.5	43.6	43.9	NaN	False	False	1	0.00
78	1.88	18.5	0.29	43.5	43.6	44.1	NaN	True	False	0	0.00
79	1.77	92.1	0.52	44.6	44.7	45.1	NaN	True	False	0	0.00
80	2.24	18.2	0.28	43.4	43.6	43.9	NaN	True	False	0	0.00
81	1.72	14.6	0.25	43.4	43.4	44.1	NaN	False	False	0	0.00
82	2.24	50.6	0.42	44.0	44.2	44.7	NaN	False	False	0	0.00
83	0.82	234.7	0.63	45.9	45.6	45.9	NaN	True	False	1	0.00
84	6.16	65.1	0.60	43.5	44.1	44.2	NaN	True	False	0	0.00
85	2.50	85.1	0.59	44.4	44.6	44.7	NaN	False	False	1	0.00
86	0.89	181.7	0.71	45.8	45.5	45.2	NaN	True	False	2	0.00
87	2.71	30.6	0.39	43.7	43.9	44.0	NaN	True	False	0	0.00
88	1.67	44.3	0.41	44.2	44.3	44.5	NaN	False	False	1	0.00
89	2.83	18.7	0.36	43.3	43.6	43.8	NaN	False	False	0	0.00
90	1.25	16.3	0.22	43.7	43.6	44.4	NaN	False	False	0	0.00
91	2.72	47.1	0.45	44.0	44.2	44.3	44.9	True	False	0	0.00
92	0.84	70.7	0.45	45.1	44.8	45.0	NaN	False	False	4	0.00
93	1.70	67.1	0.49	44.5	44.5	44.7	NaN	True	False	1	0.00
94	1.75	28.3	0.44	44.0	44.1	43.8	NaN	False	False	1	0.00
95	2.97	103.1	0.61	44.4	44.7	44.8	NaN	True	False	0	0.00
96	3.13	33.9	0.39	43.5	43.8	44.4	NaN	False	False	0	0.00
97	2.22	17.1	0.27	43.3	43.5	43.9	NaN	False	False	1	0.00
98	2.87	112.5	0.63	44.5	44.7	44.9	45.6	True	False	1	0.00
99	0.73	46.9	0.34	44.9	44.5	44.9	NaN	False	False	2	0.00
100	2.72	25.1	0.34	43.4	43.7	44.1	NaN	False	False	0	0.00
101	19.37	158.5	1.12	43.4	44.5	44.0	NaN	False	False	0	0.00
102	1.59	18.6	0.30	43.7	43.7	44.2	44.6	False	False	0	0.00
103	1.42	241.2	0.73	45.5	45.5	45.6	46.4	False	False	1	0.00
104	2.00	42.3	0.45	44.1	44.2	44.3	NaN	True	False	0	0.00
105	2.00	38.9	0.41	44.0	44.1	44.3	NaN	True	False	0	0.00
106	0.67	22.4	0.22	44.4	44.0	44.7	NaN	True	False	0	0.00
107	1.93	31.1	0.45	44.0	44.1	43.9	NaN	True	False	0	0.00
108	4.25	141.9	0.91	44.5	45.0	44.5	45.4	True	False	0	0.00
109	1.96	32.3	0.39	43.9	44.0	44.2	NaN	True	False	0	0.00
110	1.67	33.6	0.37	44.1	44.1	44.3	NaN	True	False	0	0.00
111	0.65	218.0	0.73	46.2	45.8	45.6	46.5	True	False	2	0.00
112	2.74	31.0	0.37	43.6	43.8	44.2	NaN	True	False	0	0.00
113	16.95	99.2	0.95	43.2	44.2	43.7	NaN	False	False	0	0.00
114	0.88	176.8	0.64	45.7	45.5	45.3	NaN	False	False	1	0.00
115	2.94	64.3	0.67	44.3	44.6	44.2	45.5	False	False	0	0.00
116	2.05	27.0	0.36	43.8	43.9	44.1	NaN	False	False	1	0.00
117	1.11	114.7	0.70	45.4	45.3	44.9	45.8	True	False	0	0.00
118	0.67	430.5	1.24	46.9	46.5	45.4	46.4	True	False	1	0.15
119	1.34	22.8	0.28	43.9	43.8	44.8	NaN	False	False	1	0.00
120	1.59	16.7	0.25	43.6	43.6	44.1	NaN	False	False	0	0.00
121	2.31	26.3	0.35	43.6	43.8	44.3	NaN	False	False	0	0.00
122	2.00	40.2	0.38	44.0	44.1	44.8	NaN	False	False	0	0.00
123	2.66	29.3	0.45	43.7	43.9	44.1	44.3	False	False	1	0.00
124	1.09	27.1	0.32	44.2	44.1	44.4	NaN	True	False	0	0.00
125	1.18	16.6	0.27	43.9	43.7	44.0	NaN	True	False	0	0.00
126	0.44	78.7	0.66	46.0	45.4	44.6	45.5	True	False	1	0.00
127	8.51	123.2	0.83	43.8	44.5	44.2	NaN	False	False	1	0.00
128	1.03	37.1	0.28	44.4	44.2	44.7	NaN	True	False	0	0.00
129	1.10	29.1	0.30	44.2	44.1	44.8	44.9	False	False	0	0.00
130	1.90	14.5	0.21	43.4	43.5	43.8	NaN	True	False	0	0.00
131	0.86	80.0	0.52	45.2	45.0	45.1	45.6	False	False	0	0.00
132	0.90	39.0	0.37	44.7	44.4	44.7	45.0	False	False	1	0.00
133	1.40	93.7	0.57	44.9	44.9	45.1	45.8	True	False	0	0.00
134	2.59	19.8	0.32	43.4	43.6	44.1	NaN	True	False	0	0.00
135	1.62	47.3	0.41	44.3	44.3	44.8	NaN	True	False	0	0.00
136	6.83	58.4	0.63	43.4	44.1	44.1	NaN	False	False	0	0.00

Continued on next page

Table B.10 – *Continued from previous page*

ID	α_{vir}	M_{vir} ($M_\odot$)	σ_{nt} (km s^{-1})	$\log\lvert\Omega_G\rvert$ (erg)	$\log\Omega_K$ (erg)	$\log\lvert\Omega_{Pw}\rvert$ (erg)	$\log\lvert\Omega_{Pt}\rvert$ (erg)	on-filament	hub	N_{proto}	Bad $N(H_2)$ Pix
137	6.03	52.2	0.63	43.5	44.1	43.9	NaN	True	False	0	0.00
138	1.42	44.2	0.39	44.4	44.3	44.6	NaN	True	False	1	0.00
139	1.54	20.0	0.30	43.7	43.7	44.2	NaN	True	False	0	0.00
140	2.32	34.8	0.36	43.8	43.9	44.4	NaN	True	False	0	0.00
141	1.46	11.0	0.23	43.4	43.3	43.9	NaN	True	False	0	0.00
142	3.28	28.0	0.45	43.5	43.8	43.9	NaN	True	False	0	0.00
143	1.03	32.5	0.31	44.3	44.1	44.9	NaN	True	False	0	0.00
144	1.92	28.5	0.41	43.9	44.0	44.2	NaN	True	False	0	0.00
145	2.92	15.5	0.27	43.1	43.4	43.8	NaN	False	False	0	0.00
146	1.04	19.0	0.29	44.0	43.9	44.4	NaN	False	False	0	0.00
147	3.95	63.6	0.65	44.0	44.4	44.2	NaN	True	False	1	0.00
148	4.11	103.9	0.76	44.3	44.7	44.4	NaN	False	False	0	0.00
149	0.92	426.4	0.91	46.3	46.1	45.9	NaN	True	False	0	0.03
150	4.62	38.9	0.47	43.4	43.8	44.0	NaN	False	False	0	0.00
151	0.77	28.7	0.33	44.6	44.3	44.6	NaN	True	False	2	0.00
152	0.65	18.8	0.22	44.3	43.9	44.6	NaN	True	False	0	0.00
153	0.73	43.6	0.41	44.9	44.6	44.8	NaN	True	False	1	0.00
154	1.89	35.8	0.38	44.0	44.1	44.5	NaN	True	False	0	0.00
155	1.81	29.3	0.45	44.1	44.1	44.0	NaN	True	False	1	0.00
156	0.83	30.0	0.31	44.5	44.2	44.8	NaN	False	False	0	0.00
157	2.40	29.4	0.37	43.6	43.8	44.2	NaN	False	False	0	0.00
158	1.22	19.3	0.34	44.0	43.9	44.0	NaN	True	False	1	0.00
159	0.70	53.8	0.37	45.0	44.6	45.2	NaN	True	False	1	0.00
160	1.73	24.8	0.41	44.0	44.0	43.9	NaN	True	False	2	0.00
161	1.76	22.6	0.39	43.9	43.9	43.9	NaN	True	False	0	0.00
162	0.73	26.8	0.24	44.4	44.1	44.9	NaN	True	False	0	0.00
163	0.92	144.1	0.60	45.5	45.3	45.5	NaN	False	False	2	0.00
164	0.68	29.0	0.24	44.5	44.1	44.9	NaN	False	False	0	0.00
165	0.30	50.8	0.37	45.7	45.0	45.1	NaN	False	False	3	0.00
166	1.03	25.6	0.31	44.2	44.0	44.6	NaN	True	False	0	0.00
167	0.63	58.6	0.45	45.3	44.9	44.9	NaN	False	False	4	0.00
168	1.08	24.0	0.26	44.1	43.9	44.6	NaN	True	False	0	0.00
169	1.30	23.0	0.30	43.9	43.8	44.5	NaN	True	False	0	0.00
170	1.62	18.3	0.25	43.6	43.6	44.2	NaN	True	False	1	0.00
171	6.39	50.6	0.65	43.5	44.1	43.9	NaN	False	False	0	0.00
172	0.91	36.3	0.34	44.5	44.3	44.8	NaN	True	False	0	0.00
173	1.00	23.4	0.27	44.2	43.9	44.6	NaN	False	False	0	0.00
174	6.51	39.5	0.55	43.2	43.8	43.7	NaN	False	False	0	0.00
175	1.74	23.1	0.29	43.7	43.8	44.4	NaN	False	False	0	0.00
176	2.41	22.6	0.33	43.5	43.6	44.2	NaN	True	False	0	0.00
177	1.85	22.7	0.34	43.7	43.8	44.2	NaN	True	False	0	0.00
178	1.91	18.0	0.26	43.4	43.5	44.3	NaN	False	False	0	0.00
179	3.78	44.4	0.48	43.6	44.0	44.2	NaN	True	False	0	0.00
180	0.86	43.1	0.33	44.6	44.4	45.0	NaN	True	False	2	0.00
181	1.94	54.2	0.43	44.2	44.3	44.6	NaN	False	False	0	0.00
182	1.78	20.9	0.29	43.6	43.7	44.3	NaN	True	False	1	0.00
183	1.74	21.3	0.31	43.7	43.7	44.2	NaN	True	False	0	0.00
184	0.91	18.3	0.24	44.0	43.8	44.4	NaN	True	False	0	0.00
185	0.59	20.1	0.21	44.4	44.0	44.7	NaN	True	False	0	0.00
186	1.31	50.2	0.41	44.5	44.4	44.7	NaN	False	False	0	0.00
187	3.10	33.2	0.44	43.6	43.9	44.0	NaN	False	False	0	0.00
188	1.61	26.9	0.34	43.9	43.9	44.3	NaN	False	False	0	0.00
189	2.54	61.8	0.54	44.2	44.4	44.4	NaN	False	False	0	0.00
190	1.62	39.9	0.38	44.2	44.2	44.5	NaN	False	False	0	0.00
191	1.51	10.9	0.18	43.3	43.3	43.8	NaN	False	False	0	0.00
192	0.74	131.2	0.50	45.6	45.2	45.4	NaN	False	False	4	0.00
193	10.48	124.7	0.91	43.7	44.5	44.0	NaN	False	False	0	0.00
194	NaN	47.6	0.32	NaN	NaN	NaN	NaN	False	False	1	0.00
195	NaN	81.7	0.72	NaN	NaN	NaN	NaN	False	False	0	0.00
196	NaN	42.8	0.47	NaN	NaN	NaN	NaN	False	False	1	0.00
197	NaN	99.8	0.88	NaN	NaN	NaN	NaN	False	False	0	0.00
198	NaN	56.8	0.34	NaN	NaN	NaN	NaN	False	False	0	0.00
199	NaN	35.9	0.47	NaN	NaN	NaN	NaN	False	False	0	0.00

Table B.11: NGC7538 NH_3 (1,1) Leaves Catalog 2

ID	α_{vir}	M_{vir} ($M_\odot$)	σ_{nt} (km s^{-1})	$\log\lvert\Omega_G\rvert$ (erg)	$\log\Omega_K$ (erg)	$\log\lvert\Omega_{Pw}\rvert$ (erg)	$\log\lvert\Omega_{Pt}\rvert$ (erg)	on-filament	hub	N_{proto}	Bad $N(H_2)$ Pix
0	2.03	578.3	0.90	45.8	45.9	45.8	NaN	False	False	1	0.00
1	3.33	72.2	0.45	43.9	44.2	44.6	NaN	False	False	0	0.00
2	2.70	59.8	0.44	44.0	44.2	44.5	NaN	False	False	0	0.00
3	1.46	63.9	0.34	44.4	44.4	44.9	NaN	False	False	0	0.00
4	5.38	93.5	0.59	43.8	44.3	44.4	NaN	False	False	0	0.00
5	3.87	81.1	0.52	43.9	44.3	44.4	NaN	False	False	0	0.00
6	3.76	151.0	0.61	44.3	44.7	44.9	NaN	False	False	0	0.00
7	0.91	255.7	0.53	45.7	45.5	46.0	NaN	False	False	2	0.00
8	1.71	62.5	0.38	44.3	44.3	44.7	NaN	False	False	2	0.00
9	4.83	411.3	0.91	44.9	45.4	45.4	NaN	False	False	0	0.00
10	6.65	163.9	0.87	44.2	44.8	44.3	NaN	False	False	0	0.00
11	6.23	158.6	0.82	44.2	44.7	44.5	NaN	False	False	0	0.00
12	1.01	155.0	0.58	45.4	45.3	45.4	NaN	True	False	0	0.00
13	2.46	248.5	0.73	45.1	45.2	45.4	NaN	False	False	1	0.00
14	14.19	225.1	1.03	43.8	44.7	44.5	NaN	True	False	0	0.00
15	1.23	90.5	0.39	44.8	44.7	45.3	NaN	False	False	0	0.00
16	7.60	646.0	1.46	45.1	45.7	45.0	NaN	True	False	1	0.00
17	12.24	449.0	1.38	44.5	45.3	44.7	NaN	True	False	1	0.00
18	1.58	125.6	0.60	45.0	45.0	45.1	NaN	True	False	0	0.00
19	0.94	534.3	0.81	46.3	46.1	46.3	NaN	True	False	4	0.00
20	1.62	83.7	0.53	44.7	44.7	44.8	NaN	True	False	0	0.00
21	3.04	48.2	0.43	43.8	44.1	44.3	NaN	False	False	0	0.00
22	0.83	350.3	0.80	46.2	45.9	45.8	NaN	True	False	2	0.00
23	1.31	102.0	0.51	44.9	44.9	45.2	NaN	False	False	0	0.00
24	1.02	265.8	0.71	45.8	45.6	45.7	NaN	True	False	3	0.00
25	4.87	252.1	1.04	44.8	45.3	44.6	NaN	True	False	1	0.00
26	1.67	212.9	0.82	45.4	45.4	45.1	NaN	False	False	0	0.00
27	2.16	57.2	0.45	44.2	44.3	44.5	NaN	True	False	2	0.00
28	6.76	320.3	1.00	44.6	45.2	45.0	NaN	True	False	0	0.00
29	1.54	100.7	0.64	45.0	45.0	44.7	NaN	False	False	0	0.00
30	2.11	41.3	0.35	43.9	44.0	44.4	NaN	True	False	0	0.00
31	1.01	73.2	0.40	44.9	44.7	45.3	NaN	True	False	0	0.00
32	1.23	85.5	0.41	44.8	44.7	45.4	NaN	False	False	1	0.00
33	2.13	346.8	0.82	45.4	45.5	45.6	NaN	True	False	3	0.00
34	1.19	191.5	0.57	45.4	45.3	45.7	NaN	True	False	0	0.00
35	3.67	93.9	0.65	44.2	44.6	44.4	NaN	True	False	0	0.00
36	1.10	36.6	0.32	44.3	44.1	44.9	NaN	True	False	0	0.00
37	4.64	172.7	0.68	44.3	44.8	44.9	NaN	True	False	1	0.00
38	1.33	208.1	0.90	45.7	45.6	45.1	46.2	True	False	0	0.00
39	2.18	98.5	0.50	44.5	44.6	45.0	NaN	False	False	1	0.00
40	0.52	145.5	0.64	46.1	45.6	45.4	NaN	True	False	4	0.00
41	0.66	181.1	0.49	45.8	45.4	46.1	NaN	True	False	2	0.00
42	2.49	114.4	0.56	44.5	44.7	44.8	NaN	True	False	0	0.00
43	0.45	1354.1	1.21	47.7	47.1	46.9	48.2	False	True	2	0.02
44	1.72	59.3	0.48	44.4	44.4	44.8	NaN	False	False	0	0.00
45	2.53	43.3	0.40	43.8	44.0	44.3	NaN	True	False	0	0.00
46	0.91	156.7	0.52	45.5	45.2	45.5	46.4	True	False	0	0.00
47	1.86	196.2	0.93	45.4	45.5	44.8	NaN	True	False	1	0.00
48	1.55	202.9	0.84	45.5	45.5	45.1	46.4	True	False	0	0.00
49	4.68	593.9	1.60	45.5	46.0	44.9	NaN	True	False	1	0.00
50	0.92	360.9	0.75	46.1	45.9	46.1	47.2	True	False	0	0.00
51	2.95	309.2	0.92	45.2	45.5	45.4	46.5	False	False	0	0.00
52	0.91	66.8	0.40	44.9	44.7	44.9	NaN	True	False	1	0.00
53	0.83	383.0	0.65	46.1	45.8	46.2	47.2	False	False	2	0.00
54	1.30	60.6	0.43	44.6	44.5	44.7	NaN	True	False	2	0.00
55	1.00	122.6	0.49	45.2	45.0	45.3	NaN	True	False	4	0.00
56	0.89	87.6	0.44	45.1	44.9	45.2	NaN	True	False	0	0.00
57	0.95	164.6	0.56	45.5	45.3	45.4	NaN	True	False	1	0.00
58	1.16	64.2	0.37	44.6	44.5	45.0	NaN	False	False	0	0.00
59	0.61	377.2	0.60	46.3	45.9	46.3	NaN	False	False	4	0.00
60	1.92	147.4	0.61	44.9	45.0	45.2	NaN	True	False	0	0.00
61	0.95	136.5	0.50	45.3	45.1	45.6	NaN	True	False	1	0.00
62	3.39	72.3	0.54	44.0	44.4	44.4	NaN	True	False	0	0.00
63	1.85	65.4	0.47	44.4	44.5	44.7	NaN	True	False	0	0.00
64	3.38	132.5	0.64	44.4	44.7	44.9	NaN	True	False	0	0.00
65	1.06	107.2	0.53	45.2	45.0	45.1	NaN	True	False	1	0.00
66	0.74	137.2	0.47	45.5	45.2	45.6	NaN	True	False	0	0.00

Continued on next page

Table B.11 – *Continued from previous page*

ID	α_{vir}	M_{vir} ($M_\odot$)	σ_{nt} (km s^{-1})	$\log\lvert\Omega_G\rvert$ (erg)	$\log\Omega_K$ (erg)	$\log\lvert\Omega_{Pw}\rvert$ (erg)	$\log\lvert\Omega_{Pt}\rvert$ (erg)	on-filament	hub	N_{proto}	Bad $N(H_2)$ Pix
67	69.26	427.9	1.42	42.9	44.6	44.0	NaN	False	False	0	0.00
68	0.78	322.7	0.70	46.2	45.8	45.7	NaN	False	False	3	0.00
69	2.64	189.3	0.71	44.9	45.1	45.1	NaN	False	False	0	0.00
70	2.58	136.4	0.67	44.7	44.9	44.8	NaN	False	False	0	0.00
71	1.51	48.4	0.39	44.3	44.3	44.6	NaN	False	False	0	0.00
72	1.63	56.0	0.43	44.4	44.4	44.6	NaN	False	False	0	0.00

Bibliography

Adams, M. T., Strom, K. M., & Strom, S. E. 1979, ApJ, 230, L183

André, P., Di Francesco, J., Ward-Thompson, D., et al. 2014, in Protostars and Planets VI, ed. H. Beuther, R. S. Klessen, C. P. Dullemond, & T. Henning, 27

André, P., Men'shchikov, A., Bontemps, S., et al. 2010, A&A, 518, L102

Arzoumanian, D., André, P., Didelon, P., et al. 2011, A&A, 529, L6

Astropy Collaboration, Robitaille, T. P., Tollerud, E. J., et al. 2013, A&A, 558, A33

Auddy, S., Myers, P. C., Basu, S., et al. 2019, ApJ, 872, 207

Balázs, L. G., Ábrahám, P., Kun, M., Kelemen, J., & Tóth, L. V. 2004, A&A, 425, 133

Baldeschi, A., Elia, D., Molinari, S., et al. 2017, MNRAS, 466, 3682

Ball, N. M., & Brunner, R. J. 2010, International Journal of Modern Physics D, 19, 1049

Ballesteros-Paredes, J., Vázquez-Semadeni, E., Palau, A., & Klessen, R. S. 2018, MNRAS, 479, 2112

Battersby, C., Bally, J., Dunham, M., et al. 2014, ApJ, 786, 116

Baxter, E. J., Covey, K. R., Muench, A. A., et al. 2009, AJ, 138, 963

Benson, P. J., & Myers, P. C. 1983, ApJ, 270, 589

Bertoldi, F., & McKee, C. F. 1992, ApJ, 395, 140

Billington, S. J., Urquhart, J. S., Figura, C., Eden, D. J., & Moore, T. J. T. 2019, MNRAS, 483, 3146

Blitz, L., & Stark, A. A. 1986, ApJ, 300, L89

Blitz, L., & Thaddeus, P. 1980, ApJ, 241, 676

Bohlin, R. C., Savage, B. D., & Drake, J. F. 1978, ApJ, 224, 132

Bonatto, C., Santos, Jr., J. F. C., & Bica, E. 2006, A&A, 445, 567

Bonnell, I. A., Bate, M. R., & Vine, S. G. 2003, MNRAS, 343, 413

Bonnor, W. B. 1956, MNRAS, 116, 351

Bontemps, S., Motte, F., Csengeri, T., & Schneider, N. 2010, A&A, 524, A18

Boyden, R. D., Koch, E. W., Rosolowsky, E. W., & Offner, S. S. R. 2016, ApJ, 833, 233

Boyden, R. D., Offner, S. S. R., Koch, E. W., & Rosolowsky, E. W. 2018, ApJ, 860, 157

Bresnahan, D., Ward-Thompson, D., Kirk, J. M., et al. 2018, A&A, 615, A125

Burkhart, B. 2018, ApJ, 863, 118

Campbell, B. 1984, ApJ, 282, L27

Carpenter, J. M., Meyer, M. R., Dougados, C., Strom, S. E., & Hillenbrand, L. A. 1997, AJ, 114, 198

Caselli, P., Walmsley, C. M., Tafalla, M., Dore, L., & Myers, P. C. 1999, ApJ, 523, L165

Castelaz, M. W., Grasdalen, G. L., Hackwell, J. A., Capps, R. W., & Thompson, D. 1985, AJ, 90, 1113

Chabrier, G. 2003, PASP, 115, 763

Chen, H. H.-H., Pineda, J. E., Goodman, A. A., et al. 2019a, ApJ, 877, 93

Chen, H.-R. V., Zhang, Q., Wright, M. C. H., et al. 2019b, ApJ, 875, 24

Chen, M., Di Francesco, J., Rosolowsky, E., Pineda, J., & Friesen, R. in prep, ApJ

Chen, M. C.-Y., Di Francesco, J., Johnstone, D., et al. 2016, ApJ, 826, 95

Ching, T.-C., Lai, S.-P., Zhang, Q., et al. 2017, ApJ, 838, 121

Chollet, F., et al. 2015, Keras, https://keras.io

Clarke, S. D., Whitworth, A. P., Spowage, R. L., et al. 2018, MNRAS, 479, 1722

Colley, D. 1980, MNRAS, 193, 495

Comerón, F., Djupvik, A. A., Torra, J., Schneider, N., & Pasquali, A. 2019, A&A, 622, A134

Comerón, F., & Pasquali, A. 2012, A&A, 543, A101

Contreras, Y., Rathborne, J. M., Guzman, A., et al. 2017, MNRAS, 466, 340

Crapsi, A., Caselli, P., Walmsley, M. C., & Tafalla, M. 2007, A&A, 470, 221

Csengeri, T., Bontemps, S., Schneider, N., Motte, F., & Dib, S. 2011a, A&A, 527, A135

Csengeri, T., Bontemps, S., Schneider, N., et al. 2011b, ApJ, 740, L5

Cunningham, A. J., Krumholz, M. R., McKee, C. F., & Klein, R. I. 2018, MNRAS, 476, 771

Dahm, S. E. 2008, The Young Cluster and Star Forming Region NGC 2264 (ASP), 966

Devaraj, K., Church, S., Cleary, K., et al. 2014, 1–1

Di Francesco, J., Evans, II, N. J., Caselli, P., et al. 2007, Protostars and Planets V, 17

Di Francesco, J., Hogerheijde, M. R., Welch, W. J., & Bergin, E. A. 2002, AJ, 124, 2749

Di Francesco, J., Keown, J., Friesen, R., Bourke, T., & Caselli, P. 2018, arXiv e-prints, arXiv:1810.06701

Di Francesco, J., Keown, J., Ladjelate, B., et al. 2019, in prep, ApJ

Di Francesco, J., Sadavoy, S., Motte, F., et al. 2010, A&A, 518, L91

Didelon, P., Motte, F., Tremblin, P., et al. 2015, A&A, 584, A4

Dobashi, K., Matsumoto, T., Shimoikura, T., et al. 2014, ApJ, 797, 58

Duarte-Cabral, A., Bontemps, S., Motte, F., et al. 2014, A&A, 570, A1

—. 2013, A&A, 558, A125

Dunham, M. K., Rosolowsky, E., Evans, II, N. J., Cyganowski, C., & Urquhart, J. S. 2011, ApJ, 741, 110

Dunham, M. K., Rosolowsky, E., Evans, II, N. J., et al. 2010, ApJ, 717, 1157

Dunham, M. M., Crapsi, A., Evans, Neal J., I., et al. 2008, ApJS, 179, 249

Dunham, M. M., Allen, L. E., II, N. J. E., et al. 2015, ApJS, 220, 11

Dzib, S., Loinard, L., Mioduszewski, A. J., et al. 2011, in Revista Mexicana de Astronomia y Astrofisica Conference Series, Vol. 40, Revista Mexicana de Astronomia y Astrofisica Conference Series, 231–232

Ebert, R. 1955, ZAp, 37, 217

Elia, D., & Pezzuto, S. 2016, MNRAS, 461, 1328

Elmegreen, B. G., Lada, C. J., & Dickinson, D. F. 1979, ApJ, 230, 415

Evans, C. J., Smartt, S. J., Lee, J.-K., et al. 2005, A&A, 437, 467

Fabbro, S., Venn, K. A., O'Briain, T., et al. 2018, MNRAS, 475, 2978

Falgarone, E., & Puget, J. L. 1986, A&A, 162, 235

Fallscheer, C., Reid, M. A., Di Francesco, J., et al. 2013, ApJ, 773, 102

Federrath, C. 2016, MNRAS, 457, 375

Fiege, J. D., & Pudritz, R. E. 2000, MNRAS, 311, 105

Field, G. B., Blackman, E. G., & Keto, E. R. 2011, MNRAS, 416, 710

Fontani, F., Commerçon, B., Giannetti, A., et al. 2018, A&A, 615, A94

Friesen, R. K., Bourke, T. L., Di Francesco, J., Gutermuth, R., & Myers, P. C. 2016, ApJ, 833, 204

Friesen, R. K., Di Francesco, J., Shirley, Y. L., & Myers, P. C. 2009, ApJ, 697, 1457

Friesen, R. K., Medeiros, L., Schnee, S., et al. 2013, MNRAS, 436, 1513

Friesen, R. K., Pineda, J. E., co-PIs, et al. 2017, ApJ, 843, 63

Fukui, Y., et al. 2015, ApJ, 807, L4

Gao, Y., & Solomon, P. M. 2004, ApJ, 606, 271

Gatley, I., Becklin, E. E., Sellgren, K., & Werner, M. W. 1979, ApJ, 233, 575

Giannetti, A., Leurini, S., König, C., et al. 2017, A&A, 606, L12

Ginsburg, A., & Mirocha, J. 2011, PySpecKit: Python Spectroscopic Toolkit, Astrophysics Source Code Library, ascl:1109.001

Ginsburg, A., Glenn, J., Rosolowsky, E., et al. 2013, ApJS, 208, 14

Goldsmith, P. F. 2001, ApJ, 557, 736

Goodman, A. A., Rosolowsky, E. W., Borkin, M. A., et al. 2009, Nature, 457, 63

Gottschalk, M., Kothes, R., Matthews, H. E., Landecker, T. L., & Dent, W. R. F. 2012, A&A, 541, A79

Griffin, M., Abergel, A., Ade, P., et al. 2006, in Proc. SPIE, Vol. 6265, 62650A

Griffin, M. J., Abergel, A., Abreu, A., et al. 2010, A&A, 518, L3

Gritschneder, M., Burkert, A., Naab, T., & Walch, S. 2010, ApJ, 723, 971

Guesten, R., & Fiebig, D. 1988, A&A, 204, 253

Guilloteau, S., Wilson, T. L., Martin, R. N., Batria, W., & Pauls, T. A. 1983, A&A, 124, 322

Hacar, A., Tafalla, M., Kauffmann, J., & Kovács, A. 2013, A&A, 554, A55

Hachisuka, K., Brunthaler, A., Menten, K. M., et al. 2006, ApJ, 645, 337

Hampton, E. J., Medling, A. M., Groves, B., et al. 2017, MNRAS, 470, 3395

Hansen, C. E., Klein, R. I., McKee, C. F., & Fisher, R. T. 2012, ApJ, 747, 22

Hanson, M. M. 2003, ApJ, 597, 957

Hennebelle, P. 2013, A&A, 556, A153

Hennemann, M., et al. 2012, A&A, 543, L3

Henshaw, J. D., et al. 2013, MNRAS, 428, 3425

Henshaw, J. D., Longmore, S. N., Kruijssen, J. M. D., et al. 2016, MNRAS, 457, 2675

Herzberg, G., & Huber, K. 1979, Molecular Spectra and Molecular Structure: Constants of diatomic molecules, Molecular Spectra and Molecular Structure (Van Nostrand Reinhold)

Hester, J. J., Scowen, P. A., Sankrit, R., et al. 1996, AJ, 111, 2349

Heyer, M. H., Williams, J. P., & Brunt, C. M. 2006, ApJ, 643, 956

Hildebrand, R. H. 1983, QJRAS, 24, 267

Hill, T., André, P., Arzoumanian, D., et al. 2012a, A&A, 548, L6

Hill, T., Motte, F., Didelon, P., et al. 2012b, A&A, 542, A114

Hily-Blant, P., Walmsley, M., Pineau Des Forêts, G., & Flower, D. 2010, A&A, 513, A41

Ho, I. T., Medling, A. M., Groves, B., et al. 2016, Ap&SS, 361, 280

Ho, P. T. P., Barrett, A. H., Myers, P. C., et al. 1979, ApJ, 234, 912

Ho, P. T. P., & Townes, C. H. 1983, ARA&A, 21, 239

Hochreiter, S., Bengio, Y., & Frasconi, P. 2001, in Field Guide to Dynamical Recurrent Networks, ed. J. Kolen & S. Kremer (IEEE Press)

Hoffman, I. M. 2012, ApJ, 759, 76

Hoffman, I. M., & Seojin Kim, S. 2011, ApJ, 739, L15

Hoffmeister, V. H., Chini, R., Scheyda, C. M., et al. 2008, ApJ, 686, 310

Hogge, T., Jackson, J., Stephens, I., et al. 2018, ApJS, 237, 27

Hotzel, S., Harju, J., Lemke, D., Mattila, K., & Walmsley, C. M. 2001, A&A, 372, 302

Johnston, K. J., Stolovy, S. R., Wilson, T. L., Henkel, C., & Mauersberger, R. 1989, ApJ, 343, L41

Kallas, E., & Reich, W. 1980, A&AS, 42, 227

Kauffmann, J., Bertoldi, F., Bourke, T. L., Evans, II, N. J., & Lee, C. W. 2008, A&A, 487, 993

Kauffmann, J., & Pillai, T. 2010, ApJ, 723, L7

Kauffmann, J., Pillai, T., & Goldsmith, P. F. 2013, ApJ, 779, 185

Keown, J., Di Francesco, J., Teimoorinia, H., Rosolowsky, E., & Chen, M. C.-Y. 2019a, arXiv e-prints, arXiv:1909.08727

Keown, J., Schnee, S., Bourke, T. L., et al. 2016, ApJ, 833, 97

Keown, J., Di Francesco, J., Kirk, H., et al. 2017, ApJ, 850, 3

Keown, J., Di Francesco, J., Rosolowsky, E., et al. 2019b, ApJ, 884, 4

Kerr, R., Kirk, H., Di Francesco, J., et al. 2019, ApJ, 874, 147

Kim, J., Lee, J.-E., Choi, M., et al. 2015, ApJS, 218, 5

Kingma, D. P., & Ba, J. 2014, arXiv e-prints, arXiv:1412.6980

Kirk, H., Johnstone, D., & Di Francesco, J. 2006, ApJ, 646, 1009

Kirk, H., Myers, P. C., Bourke, T. L., et al. 2013a, ApJ, 766, 115

Kirk, H., Friesen, R. K., Pineda, J. E., et al. 2017, ApJ, 846, 144

Kirk, J. M., Ward-Thompson, D., Palmeirim, P., et al. 2013b, MNRAS, 432, 1424

Knödlseder, J. 2000, A&A, 360, 539

Koch, E. W., & Rosolowsky, E. W. 2015, MNRAS, 452, 3435

Koch, E. W., Ward, C. G., Offner, S., Loeppky, J. L., & Rosolowsky, E. W. 2017, MNRAS, 471, 1506

Könyves, V., André, P., Men'shchikov, A., et al. 2010, A&A, 518, L106

—. 2015, A&A, 584, A91

Kroupa, P. 2001, MNRAS, 322, 231

Krumholz, M. R., & McKee, C. F. 2008, Nature, 451, 1082

Kryukova, E., Megeath, S. T., Hora, J. L., et al. 2014, AJ, 148, 11

Kun, M. 1998, ApJS, 115, 59

Kun, M., Balog, Z., Kenyon, S. J., Mamajek, E. E., & Gutermuth, R. A. 2009, ApJS, 185, 451

Kun, M., Kiss, Z. T., & Balog, Z. 2008, Star Forming Regions in Cepheus (ASP), 136

Kun, M., & Prusti, T. 1993, A&A, 272, 235

Kurono, Y., Saito, M., Kamazaki, T., Morita, K.-I., & Kawabe, R. 2013, ApJ, 765, 85

Kutner, M. L., Dickman, R. L., Tucker, K. D., & Machnik, D. E. 1979, ApJ, 232, 724

Lada, C. J. 1976, ApJS, 32, 603

Lada, C. J., Forbrich, J., Lombardi, M., & Alves, J. F. 2012, ApJ, 745, 190

Lada, E. A. 1992, ApJ, 393, L25

Lang, K. R., & Willson, R. F. 1980, ApJ, 238, 867

Larson, R. B. 1981, MNRAS, 194, 809

Lee, C. W., Myers, P. C., & Tafalla, M. 1999, ApJ, 526, 788

Lee, J.-E., Di Francesco, J., Bourke, T. L., Evans, II, N. J., & Wu, J. 2007, ApJ, 671, 1748

Lee, J.-E., Lee, H.-G., Shinn, J.-H., et al. 2010, ApJ, 709, L74

Lee, K. I., Fernández-López, M., Storm, S., et al. 2014, ApJ, 797, 76

Levshakov, S. A., Henkel, C., Reimers, D., et al. 2013, A&A, 553, A58

Li, D., Kauffmann, J., Zhang, Q., & Chen, W. 2013, ApJ, 768, L5

Li, G.-X., Urquhart, J. S., Leurini, S., et al. 2016, A&A, 591, A5

Lindner, R. R., Vera-Ciro, C., Murray, C. E., et al. 2015, AJ, 149, 138

Liseau, R., Larsson, B., Lunttila, T., et al. 2015, A&A, 578, A131

Liu, T., Li, P. S., Juvela, M., et al. 2018, ApJ, 859, 151

Lombardi, M., Alves, J., & Lada, C. J. 2011, A&A, 535, A16

Lombardi, M., Lada, C. J., & Alves, J. 2008, A&A, 480, 785

Lovas, F. J. 2004, Journal of Physical and Chemical Reference Data, 33, 177

Lu, X., Zhang, Q., Liu, H. B., et al. 2018, ApJ, 855, 9

Mairs, S., Johnstone, D., Offner, S. S. R., & Schnee, S. 2014, ApJ, 783, 60

Mallick, K. K., Ojha, D. K., Tamura, M., et al. 2014, MNRAS, 443, 3218

Mangum, J. G., Emerson, D. T., & Greisen, E. W. 2007, A&A, 474, 679

Mangum, J. G., Wootten, A., & Mundy, L. G. 1991, ApJ, 378, 576

Margulis, M., & Lada, C. J. 1986, ApJ, 309, L87

Marsh, K. A., Kirk, J. M., André, P., et al. 2016, MNRAS, 459, 342

McKee, C. F. 1989, ApJ, 345, 782

McKee, C. F., & Zweibel, E. G. 1992, ApJ, 399, 551

Megeath, S. T., Herter, T., Beichman, C., et al. 1996, A&A, 307, 775

Megeath, S. T., Townsley, L. K., Oey, M. S., & Tieftrunk, A. R. 2008, Low and High Mass Star Formation in the W3, W4, and W5 Regions (ASP), 264

Men'shchikov, A. 2013, A&A, 560, A63

Men'shchikov, A., André, P., Didelon, P., et al. 2012, A&A, 542, A81

—. 2010, A&A, 518, L103

Merello, M., Molinari, S., Rygl, K. L. J., et al. 2019, MNRAS, 483, 5355

Minier, V., Booth, R. S., & Conway, J. E. 2000, A&A, 362, 1093

Minier, V., Tremblin, P., Hill, T., et al. 2013, A&A, 550, A50

Miville-Deschênes, M.-A., Martin, P. G., Abergel, A., et al. 2010, A&A, 518, L104

Molinari, S., Schisano, E., Faustini, F., et al. 2011, A&A, 530, A133

Molinari, S., Swinyard, B., Bally, J., et al. 2010, PASP, 122, 314

Montalban, J., Bachiller, R., Martin-Pintado, J., Tafalla, M., & Gomez-Gonzalez, J. 1990, A&A, 233, 527

Morgan, M., White, S., Lockman, J., et al. 2008, in Union Radio Scientifique Internationale XXIX General Assembly, J02p1

Moscadelli, L., Reid, M. J., Menten, K. M., et al. 2009, ApJ, 693, 406

Motte, F., Bontemps, S., & Louvet, F. 2018a, ARA&A, 56, 41

Motte, F., Bontemps, S., Schilke, P., et al. 2007, A&A, 476, 1243

Motte, F., Zavagno, A., Bontemps, S., et al. 2010, A&A, 518, L77

Motte, F., Nony, T., Louvet, F., et al. 2018b, Nature Astronomy, 2, 478

Murray, N. 2011, ApJ, 729, 133

Myers, P. C. 2009, ApJ, 700, 1609

Myers, P. C., Linke, R. A., & Benson, P. J. 1983, ApJ, 264, 517

Nakano, M., Soejima, T., Chibueze, J. O., et al. 2017, PASJ, 69, 16

Naranjo-Romero, R., Vázquez-Semadeni, E., & Loughnane, R. M. 2015, ApJ, 814, 48

Nguyen Luong, Q., Motte, F., Hennemann, M., et al. 2011, A&A, 535, A76

Nguyen-Lu'o'ng, Q., Motte, F., Carlhoff, P., et al. 2013, ApJ, 775, 88

Nishimura, A., Costes, J., Inaba, T., et al. 2017, arXiv e-prints, arXiv:1706.06002

Nishimura, A., Minamidani, T., Umemoto, T., et al. 2018, Publications of the Astronomical Society of Japan, 70, S42

Oey, M. S., Watson, A. M., Kern, K., & Walth, G. L. 2005, AJ, 129, 393

Offner, S. S. R., Bisbas, T. G., Viti, S., & Bell, T. A. 2013, ApJ, 770, 49

Offner, S. S. R., & Chaban, J. 2017, ApJ, 847, 104

Offner, S. S. R., & Liu, Y. 2018, Nature Astronomy, 2, 896

Ogura, K. 1984, PASJ, 36, 139

Ohashi, S., Sanhueza, P., Chen, H.-R. V., et al. 2016a, ApJ, 833, 209

Ohashi, S., Tatematsu, K., Sanhueza, P., et al. 2016b, MNRAS, 459, 4130

Ojha, D. K., Tamura, M., Nakajima, Y., et al. 2004, ApJ, 608, 797

Oliveira, J. M. 2008, Star Formation in the Eagle Nebula (ASP), 599

Oliver, R. J., Masheder, M. R. W., & Thaddeus, P. 1996, A&A, 315, 578

Olmi, L., Araya, E. D., Chapin, E. L., et al. 2010, ApJ, 715, 1132

Ortiz-León, G. N., Dzib, S. A., Kounkel, M. A., et al. 2017, ApJ, 834, 143

Pagani, L. P., & Nguyen-Q-Rieu. 1987, A&A, 181, 112

Palmeirim, P., André, P., Kirk, J., et al. 2013, A&A, 550, A38

Pattle, K. 2016, MNRAS, 459, 2651

Pattle, K., Ward-Thompson, D., Kirk, J. M., et al. 2015, MNRAS, 450, 1094

—. 2017, MNRAS, 464, 4255

Peretto, N., André, P., & Belloche, A. 2006, A&A, 445, 979

Peretto, N., Fuller, G. A., André, P., et al. 2014, A&A, 561, A83

Pérez-Beaupuits, J. P., Stutzki, J., Ossenkopf, V., et al. 2015, A&A, 575, A9

Peters, T., Banerjee, R., Klessen, R. S., & Mac Low, M.-M. 2011, ApJ, 729, 72

Pillai, T., Caselli, P., Kauffmann, J., et al. 2012, ApJ, 751, 135

Pillai, T., Kauffmann, J., Tan, J. C., et al. 2015, ApJ, 799, 74

Pillai, T., Kauffmann, J., Wyrowski, F., et al. 2011, A&A, 530, A118

Pineda, J. E., Goodman, A. A., Arce, H. G., et al. 2010, ApJ, 712, L116

Pirogov, L. E. 2009, Astronomy Reports, 53, 1127

Planck Collaboration, Abergel, A., Ade, P. A. R., et al. 2014, A&A, 571, A11

Poglitsch, A., Waelkens, C., Geis, N., et al. 2010, A&A, 518, L2

Pokhrel, R., Gutermuth, R., Ali, B., et al. 2016, MNRAS, 461, 22

Polychroni, D., Schisano, E., Elia, D., et al. 2013, ApJ, 777, L33

Povich, M. S., Churchwell, E., Bieging, J. H., et al. 2009, ApJ, 696, 1278

Purcell, C. R., Longmore, S. N., Walsh, A. J., et al. 2012, MNRAS, 426, 1972

Qiu, K., Zhang, Q., & Menten, K. M. 2011, ApJ, 728, 6

Ragan, S. E., Bergin, E. A., & Wilner, D. 2011, ApJ, 736, 163

Rapson, V. A., Pipher, J. L., Gutermuth, R. A., et al. 2014, ApJ, 794, 124

Rayner, T. S. M., Griffin, M. J., Schneider, N., et al. 2017, A&A, 607, A22

Redaelli, E., Alves, F. O., Caselli, P., et al. 2017, ApJ, 850, 202

Reid, M. A., & Wilson, C. D. 2005, ApJ, 625, 891

Ridge, N. A., Di Francesco, J., Kirk, H., et al. 2006, AJ, 131, 2921

Riener, M., Kainulainen, J., Henshaw, J. D., et al. 2019, A&A, 628, A78

Rivera-Gálvez, S., Román-Zúñiga, C. G., Jiménez-Bailón, E., et al. 2015, AJ, 150, 191

Rivera-Ingraham, A., Martin, P. G., Polychroni, D., & Moore, T. J. T. 2011, ApJ, 743, 39

Rivera-Ingraham, A., Martin, P. G., Polychroni, D., et al. 2013, ApJ, 766, 85

—. 2015, ApJ, 809, 81

Rivera-Ingraham, A., Ristorcelli, I., Juvela, M., et al. 2016, A&A, 591, A90

Román-Zúñiga, C. G., & Lada, E. A. 2008, Star Formation in the Rosette Complex (ASP), 928

Rosolowsky, E., & Leroy, A. 2006, PASP, 118, 590

Rosolowsky, E., Dunham, M. K., Ginsburg, A., et al. 2010, ApJS, 188, 123

Rosolowsky, E. W., Pineda, J. E., Kauffmann, J., & Goodman, A. A. 2008, ApJ, 679, 1338

Rygl, K. L. J., Wyrowski, F., Schuller, F., & Menten, K. M. 2010, A&A, 515, A42

Rygl, K. L. J., Brunthaler, A., Sanna, A., et al. 2012, A&A, 539, A79

Rygl, K. L. J., Goedhart, S., Polychroni, D., et al. 2014, MNRAS, 440, 427

Salpeter, E. E. 1955, ApJ, 121, 161

Sandell, G., Goss, W. M., & Wright, M. 2005, ApJ, 621, 839

Sandell, G., Wright, M., & Forster, J. R. 2003, ApJ, 590, L45

Sato, F., Mizuno, A., Nagahama, T., et al. 1994, ApJ, 435, 279

Schilke, P., Mauersberger, R., Walmsley, C. M., & Wilson, T. L. 1990, A&A, 227, 220

Schlafly, E. F., Green, G., Finkbeiner, D. P., et al. 2014, ApJ, 786, 29

Schnee, S., Brunetti, N., Di Francesco, J., et al. 2013, ApJ, 777, 121

Schneider, N., Bontemps, S., Simon, R., et al. 2006, A&A, 458, 855

Schneider, N., Csengeri, T., Bontemps, S., et al. 2010a, A&A, 520, A49

Schneider, N., Stutzki, J., Winnewisser, G., & Block, D. 1998, A&A, 335, 1049

Schneider, N., Motte, F., Bontemps, S., et al. 2010b, A&A, 518, L83

Schneider, N., Bontemps, S., Simon, R., et al. 2011, A&A, 529, A1

Schneider, N., et al. 2012, A&A, 540, L11

Schneider, N., Bontemps, S., Girichidis, P., et al. 2015, MNRAS, 453, L41

Schneider, N., Bontemps, S., Motte, F., et al. 2016, A&A, 591, A40

Schöier, F. L., van der Tak, F. F. S., van Dishoeck, E. F., & Black, J. H. 2005, A&A, 432, 369

Schuller, F., Menten, K. M., Contreras, Y., et al. 2009, A&A, 504, 415

Schwarz, G. 1978, The Annals of Statistics, 6, 461

Scoville, N. Z., Sargent, A. I., Sanders, D. B., et al. 1986, ApJ, 303, 416

Seifried, D., & Walch, S. 2015, MNRAS, 452, 2410

Seo, Y. M., & Youdin, A. N. 2016, MNRAS, 461, 1088

Seo, Y. M., Shirley, Y. L., Goldsmith, P., et al. 2015, ApJ, 805, 185

Shallue, C. J., & Vanderburg, A. 2018, AJ, 155, 94

Shirley, Y. L. 2015, PASP, 127, 299

Sipilä, O., Caselli, P., Redaelli, E., Juvela, M., & Bizzocchi, L. 2019, MNRAS, 487, 1269

Slysh, V. I., Kalenskii, S. V., & Val'tts, I. E. 1995, ApJ, 442, 668

Smith, R. J., Glover, S. C. O., Clark, P. C., Klessen, R. S., & Springel, V. 2014a, MNRAS, 441, 1628

Smith, R. J., Glover, S. C. O., & Klessen, R. S. 2014b, MNRAS, 445, 2900

Sohn, J., Lee, C. W., Park, Y.-S., et al. 2007, ApJ, 664, 928

Sokolov, V., Wang, K., Pineda, J. E., et al. 2017, A&A, 606, A133

Sousbie, T. 2011, MNRAS, 414, 350

Spezzano, S., Bizzocchi, L., Caselli, P., Harju, J., & Brünken, S. 2016, A&A, 592, L11

Stahler, S. W., & Palla, F. 2005, The Formation of Stars, 865

Stephens, I. W., Jackson, J. M., Whitaker, J. S., et al. 2016, ApJ, 824, 29

Straižys, V., Černis, K., & Bartašiūtė, S. 2003, A&A, 405, 585

Stutzki, J., & Guesten, R. 1990, ApJ, 356, 513

Stutzki, J., Stacey, G. J., Genzel, R., et al. 1988, ApJ, 332, 379

Sugiyama, K., Fujisawa, K., Doi, A., et al. 2008, PASJ, 60, 23

Surcis, G., Vlemmings, W. H. T., van Langevelde, H. J., & Hutawarakorn Kramer, B. 2012, A&A, 541, A47

Suzuki, H., Yamamoto, S., Ohishi, M., et al. 1992, ApJ, 392, 551

Svoboda, B. E., et al. 2016, ApJ, 822, 59

Swift, J. J., Welch, W. J., & Di Francesco, J. 2005, ApJ, 620, 823

Tafalla, M., Santiago-García, J., Myers, P. C., et al. 2006, A&A, 455, 577

Tan, J. C., Kong, S., Butler, M. J., Caselli, P., & Fontani, F. 2013, ApJ, 779, 96

Teimoorinia, H., & Keown, J. 2018, MNRAS, 478, 3177

Teixeira, P. S., Lada, C. J., Marengo, M., & Lada, E. A. 2012, A&A, 540, A83

Thronson, Jr., H. A., & Lada, C. J. 1983, ApJ, 269, 175

Tieftrunk, A. R., Gaume, R. A., Claussen, M. J., Wilson, T. L., & Johnston, K. J. 1997, A&A, 318, 931

Tieftrunk, A. R., Megeath, S. T., Wilson, T. L., & Rayner, J. T. 1998, A&A, 336, 991

Tigé, J., Motte, F., Russeil, D., et al. 2017, A&A, 602, A77

Traficante, A., Duarte-Cabral, A., Elia, D., et al. 2018, MNRAS, 477, 2220

Tremblin, P., Minier, V., Schneider, N., et al. 2013, A&A, 560, A19

Tremblin, P., Schneider, N., Minier, V., et al. 2014, A&A, 564, A106

Urquhart, J. S., Morgan, L. K., Figura, C. C., et al. 2011, MNRAS, 418, 1689

Urquhart, J. S., Figura, C. C., Moore, T. J. T., et al. 2015, MNRAS, 452, 4029

Uyanıker, B., Fürst, E., Reich, W., Aschenbach, B., & Wielebinski, R. 2001, A&A, 371, 675

Van Oort, C. M., Xu, D., Offner, S. S. R., & Gutermuth, R. A. 2019, ApJ, 880, 83

Vázquez-Semadeni, E., González-Samaniego, A., & Colín, P. 2017, MNRAS, 467, 1313

Vázquez-Semadeni, E., Palau, A., Ballesteros-Paredes, J., Gómez, G. C., & Zamora-Avilés, M. 2019, arXiv e-prints, arXiv:1903.11247

Vázquez-Semadeni, E., Ryu, D., Passot, T., González, R. F., & Gazol, A. 2006, ApJ, 643, 245

Walsh, J. R., Ogura, K., & Reipurth, B. 1992, MNRAS, 257, 110

Wang, H., Yang, J., Wang, M., & Yan, J. 2003, AJ, 125, 842

Wang, J., Townsley, L. K., Feigelson, E. D., et al. 2008, ApJ, 675, 464

Ward-Thompson, D., Di Francesco, J., Hatchell, J., et al. 2007, PASP, 119, 855

Ward-Thompson, D., Kirk, J. M., André, P., et al. 2010, A&A, 518, L92

Weingartner, J. C., & Draine, B. T. 2001, ApJ, 548, 296

Werner, M. W., Becklin, E. E., Gatley, I., et al. 1979, MNRAS, 188, 463

White, G. J., Nelson, R. P., Holland, W. S., et al. 1999, A&A, 342, 233

Wienen, M., Wyrowski, F., Schuller, F., et al. 2012, A&A, 544, A146

Williams, J. P., de Geus, E. J., & Blitz, L. 1994, ApJ, 428, 693

Williams, R. J. R., Ward-Thompson, D., & Whitworth, A. P. 2001, MNRAS, 327, 788

Willson, R. F., & Folch-Pi, F. J. 1981, AJ, 86, 1084

Wilson, B. A., Dame, T. M., Masheder, M. R. W., & Thaddeus, P. 2005, A&A, 430, 523

Wilson, T. L., Batria, W., & Pauls, T. A. 1982, A&A, 110, L20

Wilson, T. L., & Mauersberger, R. 1990, A&A, 239, 305

Wolf-Chase, G. A., Walker, C. K., & Lada, C. J. 1995, ApJ, 442, 197

Wright, N. J., Parker, R. J., Goodwin, S. P., & Drake, J. J. 2014, MNRAS, 438, 639

Wu, J., Evans, II, N. J., Gao, Y., et al. 2005, ApJ, 635, L173

Wu, J., Evans, II, N. J., Shirley, Y. L., & Knez, C. 2010, ApJS, 188, 313

Xu, Y., Moscadelli, L., Reid, M. J., et al. 2011, ApJ, 733

Yildirim, O., Pawiak, P., Tan, R. S., & Acharya, U. R. 2018, Computers in Biology and Medicine, 102, 411

Yonekura, Y., Dobashi, K., Mizuno, A., Ogawa, H., & Fukui, Y. 1997, ApJS, 110, 21

Zhang, Y. G., Gajjar, V., Foster, G., et al. 2018, ApJ, 866, 149